METALS SUPERCONDUCTORS

Electronic structure of Ce and Sm in hydrides and the 4*f* collapse in YbH_x

V. A. Shaburov, A. E. Sovestnov, Yu. P. Smirnov, and A. V. Tyunis

St. Petersburg Nuclear Physics Institute, Russian Academy of Sciences, 188350 Gatchina, Leningrad District, Russia

H. Drulis and M. Drulis

W. Trzebiatowski Institute of Low-Temperature and Structure Research, Polish Academy of Sciences, 50-950 Wroclaw, Poland

(Submitted December 22, 1997)
Fiz. Tverd. Tela (St. Petersburg) **40**, 1393–1396 (August 1998)

The population of the $4f$, $5d$, and $6s$ shells of rare-earth atoms in RH_x hydrides (R=Ce, Sm, Yb; $x \approx 2-3$) has been studied by the x-ray line-shift method. The population of the $5d$ and $6s$ shells of Ce and Sm atoms, and the charge on them in metals and hydrides, were determined from experiment and calculated within the Hartree–Fock–Dirac (Koopmans) model. The decrease of the charge on Ce and Sm revealed upon transition from the metal to the hydride argues unambiguously for the anionic (hydride) model. In YbH_x with $x \geqslant 2$, the structural transition is accompanied by a strongly pronounced electronic transition from divalent to a noninteger-valence state [$\bar{m}(x=2.25-2.708)=2.66\pm0.02$]. [S1063-7834(98)00108-7]

Macroscopic properties of rare-earth (RE) hydrides have been studied extensively (see, e.g., Refs. 1–3). The interest in these materials is stimulated primarily by their application potential for use as catalysts, in protection against penetrating radiation, as hydrogen accumulators etc. At the same time their microscopic properties, namely, metal valence, conduction-band features, the metal-hydrogen bonding etc. are known to a lesser extent. Moreover, there is still no consensus on the nature of chemical bonding in the hydrides.

The presently available experimental data permit formulation of two diametrically opposite models of the metal-hydrogen chemical bonding, namely, protonic, with positive hydrogen H^+, and anionic (hydride) with negatively charged hydrogen H^-. The anion model predicts depletion in electrons of the metal in the hydride (compared to the pure metal), and the protonic model, conversely, enrichment in electrons.

RE dihydrides have a CaF_2-type cubic lattice. Exceptions to this rule are EuH_2 and YbH_2, which crystallize in a SrH_2-type orthorhombic structure. Magnetic, structural, NMR, and other data (see, e.g., Ref. 1) indicate that Ce and Sm are trivalent in the di- and trihydrides, and Yb is divalent in YbH_2. It was found that YbH_x undergoes for $x \geqslant 2$ a structural transition from the orthorhombic to cubic phase.[4] Because all RE metals are trivalent in cubic binary hydrides, one could expect that the change in lattice symmetry would make possible the $Yb^2 \rightarrow Yb^{3+}$ transition. Indeed, photoemission studies suggest that ytterbium in $YbH_{2.6}$ is in a mixed-valence state.[5] In CeH_x, one observes a metal-insulator transition at $T=240$ K for $x>2.7$;[6] its mechanism can be connected with rearrangement of the Ce4*f* shell, as this occurs in the isomorphic $Ce_\gamma - Ce_\alpha$ transition in metallic cerium.[7] Magnetic data indicate that samarium in the hydride resides in the 3^+ state, while heat capacity measurements are interpreted as due to samarium being a mixture of Sm^{2+} and Sm^{3+} ions.[8] Thus determination of the electronic state of the RE atom in the hydrides of Ce, Sm, and Yb is of specific interest and could shed light on the character of metal-hydrogen chemical bonding.

1. EXPERIMENTAL RESULTS

It was shown earlier that the electronic structure of elements in compounds [population of the outer $s(p)$, d, and f electronic shells] can be studied successfully by the x-ray line-shift method (see, e.g., Refs. 9 and 10). Removal from an atom (or appearance in it) of a valence electron results in a change (shift) of the x-ray line energy, whose sign and magnitude, as well as the characteristic dependence of the shift on the line type ($K\alpha_{1,2}$, $K\beta_{1,3}$, $K\beta_{2,4}$), i.e., its ''signature,'' [10] permit identification of the type $[s(p),d,f]$ of this electron.

This paper reports a measurement of the shifts in the K x-ray lines of Ce, Sm, and Yb in hydrides relative to reference samples with known electronic structure: CeF_3, SmF_3, and YbS. The experimental arrangement and the measurement procedure are described in detail elsewhere (see, e.g., Refs. 10 and 11).

The samples of CeH_x ($x=2.06-2.96$), SmH_x ($x=2-2.77$), and YbH_x ($x=1.908-2.708$) to be studied were prepared by standard technology, namely, by direct reaction of hydrogen with the metal.[4] They were characterized by

TABLE I. Experimental shifts of $K\alpha_1$ and $K\beta_1$ lines of cerium and samarium (ΔE) in the CeH_x and SmH_x hydrides and metals (with CeF_3 and SmF_3 as references), and the hydride lattice parameters a.

	ΔE, meV			
	$K\alpha_1$	$K\beta_1$		
x	$T=300$ K	$T=300$ K	$T=77$ K	a, Å
		CeH_x		
0	50±4	−47±4	⋯	
2.06	25±4	−28±8	⋯	5.568±0.003
2.56	–	6±23	12±18	5.552±0.003
2.70	34±5	−8±6	−26±22	5.539±0.003
2.96	42±5	6±8	−22± 9	5.535±0.003
		SmH_x		
0	50±6	−7±8		
2.0	33±5	−2±14		5.372±0.002
2.16	33±7	5±15		5.362±0.002
2.33	44±7	50±15		5.354±0.002
2.77	36±6	49±15		5.341±0.002

x-ray diffraction and phase analysis, and the concentration dependences of their lattice parameters were determined. All the samples were single phase, with the exception of $YbH_{2.12}$, which contained a mixture of the orthorhombic with cubic phase. The Ce and Sm hydrides had fcc structure with the lattice parameters only weakly dependent on hydrogen concentration (see Table I).

1) CeH_x, SmH_x. The experimental shifts of the Ce and Sm $K\alpha_1$ and $K\beta_1$ lines in hydrides and metals with respect to trivalent references are listed in Table I, which also contains the lattice parameters $a(x)$.

The ratio of the effects for the $K\alpha_1$ and $K\beta_1$ lines of Ce and Sm in the hydrides, $r=\Delta E_{K\beta_1}/\Delta E_{K\alpha_1}$, differs substantially from that for RE mixed-valence ionic compounds (oxides, sulfides, chlorides, fluorides etc.), as well as intermediate-valence compounds. The value of $r=\Delta E_{K\beta_1}(\mathrm{Ln}^{(3\pm1)+}-\mathrm{Ln}^{3+})/\Delta E_{K\alpha_1}(\mathrm{Ln}^{(3\pm1)+}-\mathrm{Ln}^{3+})$, both experimental and calculated by the Hartree-Fock model, is positive for all RE elements and lies within the interval $r\approx 2-3$ ($r_{\max}=2.86\pm0.06$, $r_{\min}=2.03\pm0.19$ for Ce and Yb, respectively).[12] For metals and their hydrides, $r<1$.

It thus can be maintained that the electronic structure of Ce and Sm in the hydrides under study is metal-like in character, and that all RE metals, with the exception of Eu and Yb, are trivalent and have a configuration close to the commonly accepted $5d6s^2$.[13] As follows also from Table I, the metal-insulator transition in CeH_x ($T_{tr}\approx 240$ K) cannot be explained as due to promotion of the Ce $4f$ electron, because the shifts of the Ce $K\beta_1$ line at $T=300$ and 77 K are practically the same. Note also that our results do not bear out the conclusion of macroscopic heat-capacity studies[8] of samarium in SmH_x being in mixed-valence state ($Sm^{2+}-Sm^{3+}$); indeed, samarium remains trivalent throughout the x range investigated.

The electronic structure (population of the $5d$ and $6s$ states) of Ce and Sm in the hydrides was determined from experimental values of the x-ray line shifts using Hartree–Fock-type atomic calculations. To choose the model

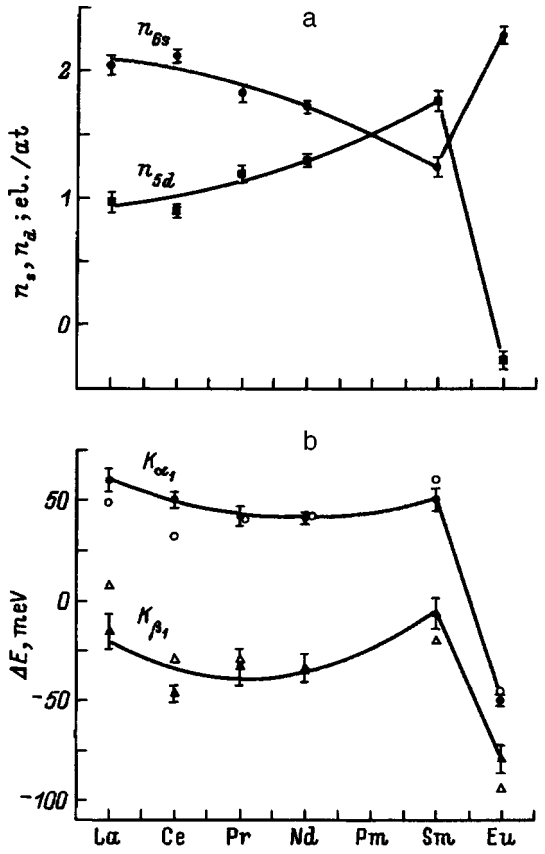

FIG. 1. (a) Population of $5d$ and $6s$ states, n_d and n_s, in RE metals; (b) experimental shifts of $K\alpha_1$ and $K\beta_1$ RE-metal lines (with RF_3 taken as references)—filled symbols; open symbols—calculations made within the Hartree-Fock-Dirac (Koopmans) model.

(Hartree–Fock–Dirac, Hartree–Fock–Slater, both with total electronic-shell relaxation and in single-electron approximation by Koopmans' theorem) which would provide the best fit to experiment, the electronic configurations of RE metals, from La through Eu, were determined. We solved the coupled equations

$$\Delta E_{\mathrm{calc}}(n_d,n_s)^{\alpha(\beta)}=\Delta E^{\alpha(\beta)},$$

$$n_d+n_s=n,$$

where $\Delta E_{\mathrm{calc}}(n_d,n_s)^{\alpha(\beta)}$ is the calculated $K_{\alpha(\beta)}$ line shift approximated by a second-order polynomial, $\Delta E^{\alpha(\beta)}$ are the experimental line shifts for RE metals, $n=2$ for Eu, and $n=3$ in all other cases. The Hartree–Fock–Dirac (Koopmans) model provides the best fit to experiment. The populations n_d and n_s thus obtained and the corresponding $\Delta E(n_d,n_s)^{\alpha(\beta)}$ are given in Fig. 1. We readily see that the RE metal configurations coincide satisfactorily with the $5d^16s^2$ configuration for trivalent metals, and with $6s^2$ for the divalent Eu ($n_s\approx 2$, $n_d\approx 1$ for RE=Ln–Sm, and $n_s\approx 2$, $n_d\approx 0$ for Eu). Satisfactory agreement is observed also for the experimental and calculated line shifts ΔE.

The calculational procedures [Hartree–Fock–Dirac (Koopmans)] tested on metals were used to determine the populations of the Ce and Sm $5d$ and $6s$ states in the hydrides under study. We solved a system of equations, which was similar to the above but did not contain any restriction

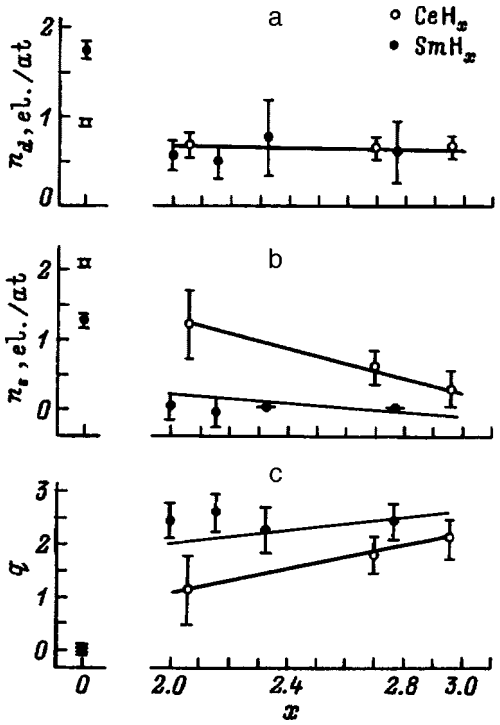

FIG. 2. Population of $5d$ and $6s$ states (a and b, respectively) and charge q (c) of cerium and samarium vs hydrogen concentration.

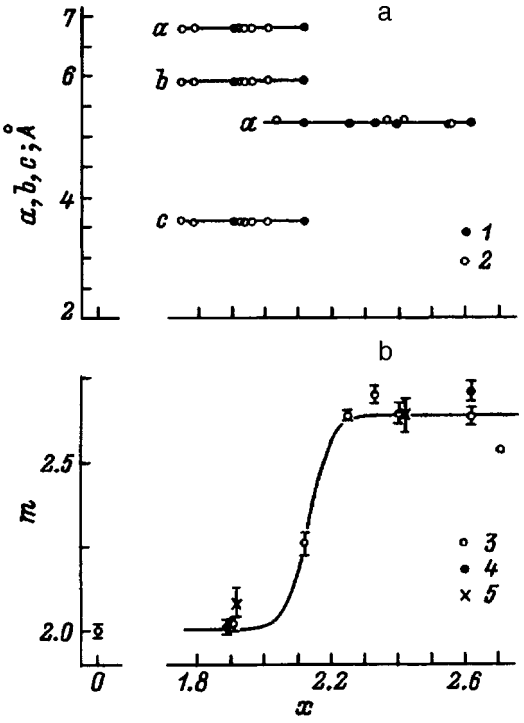

FIG. 3. (a) YbH_x lattice parameters a,b,c vs composition: *1*—our data, *2*—Ref. 4; (b) dependence of Yb valence in YbH_x *vs* composition and external conditions: *3*—$T=300$ K, *4*—$T=77$ K, *5*—$P\approx 12$ kbar.

on the total number of electrons n. The results of the calculations are presented graphically in Fig. 2, which shows that throughout the concentration range covered, $x\approx 2-3$, the population of the $5d$ states of Ce and Sm is practically constant, namely, the weighted mean $\overline{n_d}=0.62\pm 0.06$ 5d-el/Ce(Sm) atom, whereas that of Ce $6s$ states falls off monotonically down to zero, and n_s of Sm is close to zero over the whole x range studied. Photoelectron spectra of LaH_x and CeH_x exhibit a similar depletion of population.[14] The density of states near Fermi level in the hydrides is smaller than that in metals; indeed, it decreases in the dihydrides and practically vanishes in the trihydrides as one goes over from the metallic to semiconducting state.

Figure 2 displays also the dependence of the Ce and Sm charge state in the hydrides on x: $q(x)=3-[n_s(x)+n_d(x)]$. In all cases, the charge on the RE atom is positive. Thus formation of CeH_x and SmH_x involves extension of the outer $5d$ and $6s$ orbitals of the metal toward hydrogen, which argues unambiguously for the validity of the anionic (hydride) model of metal-hydrogen chemical bonding.

2) YbH_x. Figure 3 shows the dependence of the YbH_x lattice constants on hydrogen concentration. For $x\geqslant 2$, a structural transition from the orthorhombic to cubic phase occurs. This transition is accompanied by a sharp change in the Yb $K\alpha_1$ line energy [the weighted mean $\overline{\Delta E}_{K\alpha_1}(x=2.25-2.708)=-365\pm 8$ meV]. The sign and the anomalously large magnitude of the effect (the divalent-ytterbium compound YbS was used as a reference) argue unambiguously for the $4f$ character of the transition (the effects due to removal of $5d$ and $6s$ electrons are an order of magnitude smaller). The difference between the numbers of Yb $4f$ electrons in the hydride and in the reference was found as $\Delta n_{4f}(x)=\Delta E(x)/\Delta E(Yb^{3+}\text{-}Yb^{2+})$, where $\Delta E(x)$ is the experimental line shift, and $\Delta E(Yb^{3+}\text{-}Yb^{2+})$ is a calibration shift corresponding to the shift of the Yb $K\alpha_1$ line caused by the decrease of the $4f$-shell population by one. Obviously enough, the valence of Yb in the sample under study $m=m_{\text{ref}}+\Delta n_{4f}$. The value of $\Delta E(Yb^{3+}\text{-}Yb^{2+})$ was measured for the pair of ionic compounds Yb_2O_3–YbS and was found to be $\Delta E(Yb_2O_3\text{–}YbS)=-568\pm 7$ meV, and that calculated within the Hartree–Fock–Dirac (Koopmans) model, $\Delta E(Yb^{3+}\text{-}Yb^{2+})=-562$ meV. The valence state of Yb in the cubic phase is practically independent of hydrogen concentration, $\overline{m}(x=2.25-2.708)=2.66\pm 0.02$. The electronic structure of Yb was found to be fairly stable against variation in environmental conditions. For instance, cooling ($T=77$ K) or application of external pressure ($P\approx 12$ kbar) does not change the Yb valence in either orthorhombic or cubic samples (Fig. 3).

The heat capacity of YbH_x ($x=2.25, 2.37, 2.41$) was studied at low temperatures.[15] The temperature behavior of C_p/T was found to be typical of that of heavy-fermion systems. The quantity C_p/T extrapolated to $T\sim 0$ yields an anomalously large value of the electronic heat-capacity coefficient $\gamma\sim 860$ mJ/mole·K^2. The mechanism by which ''heavy'' electrons appear at Fermi level E_f remains largely unclear and can be associated with either the f level crossing the Fermi level (delocalization) or Kondo-type cooperative processes, where the f level lies comparatively deep below the Fermi level. In the first case, the number of f electrons will be fractional, and in the second, integer. Our data arguing for a noninteger valence of Yb in the cubic phase of YbH_x suggest that the heavy-fermion state in YbH_x origi-

nates apparently from delocalization of the Yb $4f$ electron. Note that cerium in heavy-fermion systems resides in an integer valence state ($n_{4f} \approx 1$),[16,17] whereas ytterbium (in the cases where its valence is known, as it is in Ref. 16) has a noninteger valence; moreover, in uranium-based heavy-fermion systems the valence states of U extend over a wide range from $U^{3+}(5f^3)$ to $U^{4+}(5f^2)$.[18] This difference indicates the existence of different formation mechanisms of the heavy-fermion state.

We note in conclusion that the sharp electronic transition from an integer to noninteger valence state, which was found to occur in YbH_x simultaneously with a structural transition, is a fairly rare (if not unique) phenomenon among rare-earth systems. All known $4f^n - 4f^{n\pm1}$ electronic transitions are isostructural (isomorphic), e.g., the $\gamma - \alpha$ transition in metallic Ce, in SmS, $Ce_{1-x}Th_x$, $Sm_{1-x}Gd_xS$ etc. (see, e.g., Ref. 19).

The authors thank O. I. Sumbaev for fruitful discussions and comments, E. G. Andreev for assistance in experiments, and P. L. Sokolova for help in preparing the manuscript.

Support of the Russian Fund for Fundamental Research (Grant 96-02-17811) is gratefully acknowledged.

[1] M. E. Kost, A. L. Shilov, V. N. Mikheeva *et al.*, *Rare-Earth Compounds: Hydrides, Borides, Carbides, Phosphides, Pnictides, Chalcogenides, and Pseudohalogenides* [in Russian], Nauka, Moscow, 1983.
[2] P. V. Gel'd, R. A. Ryabov, and L. P. Mokhracheva, *Hydrogen and the Physical Properties of Metals and Alloys* [in Russian], Nauka, Moscow, 1985.
[3] V. A. Gubanov, A. L. Ivanovskiĭ, and M. V. Ryzhkov, *Quantum Chemistry in Materials Sciences* [in Russian], Nauka, Moscow, 1987.
[4] R. Bischof, E. Kaldis, and L. Lacis, J. Less-Common Met. **94**, 117 (1983).
[5] S. Büchler, L. Schlapbach, R. Monnier, and L. Degiorgi, J. Phys. (Paris) **48**, 947 (1987).
[6] G. G. Libowitz, Ber. Bunsenges. Physik und Chemie **76**, 837 (1972).
[7] V. A. Shaburov, A. E. Sovestnov, and O. I. Sumbaev, Phys. Lett. A **49**, 83 (1974).
[8] J. Opyrchal and L. Bieganski, Solid State Commun. **26**, 965 (1978).
[9] O. I. Sumbaev, in *Modern Physics in Chemistry*, Vol. 1, No. 4 (Academic Press, New York, 1977), p. 33.
[10] O. I. Sumbaev, Usp. Fiz. Nauk **124**, 281 (1978) [Sov. Phys. Usp. **21**, 181 (1978)].
[11] V. A. Shaburov, I. M. Band, A. I. Grushko, T. B. Mezentseva, E. V. Petrovich, A. E. Sovestnov, Yu. P. Smirnov, O. I. Sumbaev, M. B. Trzhaskovskaya, and I. A. Markova, Zh. Éksp. Teor. Fiz. **65**, 1157 (1973) [Sov. Phys. JETP **38**, 573 (1973)].
[12] A. E. Sovestnov, Yu. V. Ganzha, Yu. S. Grushko, M. F. Kovalev, L. I. Molkanov, Yu. P. Smirnov, A. V. Tyunis, and V. A. Shaburov, LNPI Preprint No. 783, Leningrad (1982).
[13] K. A. Gschneidner, Jr., *Rare-Earth Alloys* [Van Nostrand, Princeton, 1961; IIL, Moscow, 1965].
[14] L. Schlapbach, J. Osterwalder, and H. C. Siegmann, J. Less-Common Met. **88**, 291 (1982).
[15] M. Drulis, H. Drulis, and B. Stalinski, J. Less-Common Met. **141**, 207 (1988).
[16] J. Röhler, *Handbook on the Physics and Chemistry of Rare Earths*, Vol. 10, edited by Gschneidner, Jr., L. Eyring, and S. Hüffner (Elsevier Science Publ., Amsterdam, 1987).
[17] V. A. Shaburov, Yu. P. Smirnov, A. E. Sovestnov, A. V. Tyunis, P. A. Alekseev, and V. N. Lazukov, Fiz. Tverd. Tela (St. Petersburg) **38**, 954 (1996) [Phys. Solid State **38**, 530 (1996)].
[18] A. V. Tyunis, V. A. Shaburov, Yu. P. Smirnov, and A. E. Sovestnov, Fiz. Tverd. Tela (St. Petersburg) **38**, 1598 (1996) [Phys. Solid State **38**, 880 (1996)].
[19] D. I. Khomskiĭ, Usp. Fiz. Nauk **129**, 443 (1979) [Sov. Phys. Usp. **22**, 879 (1979)].

Translated by G. Skrebtsov

Specific features of the electronic structure of cerium and its 4*d* and 5*d* partners in CeM_2 Laves phases (M=Fe, Co, Ni, Ru, Rh, Os, Pt, Mg, Al)

Yu. P. Smirnov, A. E. Sovestnov, A. V. Tyunis, and V. A. Shaburov

St. Petersburg Nuclear Physics Institute, 188350 Gatchina, Leningrad District, Russia
(Submitted December 22, 1997)
Fiz. Tverd. Tela (St. Petersburg) **40**, 1397–1400 (August 1998)

The x-ray line shift method has been used to study the electronic state of Ce (the $4f$ population) and of its $4d$ and $5d$ partners in the CeM_2 Laves phases (M=Fe, Co, Ni, Ru, Rh, Os, Pt, Mg, Al). It is shown that the valence of Ce in CeM_2 decreases monotonically from the limiting value $m \approx 3.35$ to $m \approx 3$ with decreasing intracrystalline compression of Ce atoms. The population of the outer $4d$ and $5d$ orbitals of Ru, Rh, and Os in the Laves phases has been found to be larger than that in metals. © *1998 American Institute of Physics.*
[S1063-7834(98)00208-1]

Ce present in CeM_2 Laves phases with $3d$ elements (M=Fe, Co, Ni) occurs in the intermediate-valence (IV) state. The valence states in these compounds were determined by different experimental techniques (see, e.g., Ref. 1), as well as in our studies,[2,3] which are based on the x-ray line shift method.[4] While cerium can exhibit IV state also in CeM_2 systems with $4d$ and $5d$ elements, these systems are less studied, and quantitative data on the Ce valence in them are either absent altogether or their accuracy is not high enough.[1]

It is generally believed that the IV of Ce in these systems results from intracrystalline compression of Ce atoms caused by the differences in the metallic radii of Ce_γ and of the M element.[1)] At the same time attempts at establishing a quantitative relationship between the IV of Ce and the parameters characterizing the degree of compression of Ce atoms in CeM_2 phases failed. One of the reasons accounting for this failure lies in that the IV states of Ce determined by different experimental methods (XPS, XAS, BIS, EELS etc.) differ considerably.

The present work uses the x-ray line-shift method to determine the $4f$ shell population (valence state) of Ce in Laves phases with $3d$, $4d$, and $5d$ elements (as well as with Mg and Al) CeM_2 (M=Fe, Co, Ni, Ru, Rh, Os, Pt, Mg, Al). The temperature dependence of Ce valence in some Laves phases was also measured ($T=77-1000$ K).

There are practically no data on the character of chemical bonding of $4d$ and $5d$ elements with Ce and with one another, i.e., on the change in the outer (valence) $4d$ and $5d$ shell population in Laves phases compared to metals. The $4d$ and $5d$ elements (Ru, Rh, Os, Pt) studied by us belong to transition metals with an almost completely filled d shell. It is therefore assumed that when a common conduction band forms in intermetallics, these elements will tend to fill their d shells at the expense of the electrons of the partner. To check this assumption, the shifts of the x-ray K lines of these elements in Laves phases were measured relative to those of the metals.

The Ce valence (m) in the Laves phases studied was derived from the experimental shifts of the Ce $K\beta_1$ line (ΔE) in the Laves phase relative to the trivalent Ce_γ which served as a reference. The experimental arrangement and measurement procedure were described in detail elsewhere (see, e.g., Ref. 4). It was shown[4] that rare-earth K line energies are most sensitive to the change in the number of $4f$ electrons n_{4f}, which determines their valence state (for instance, $|\Delta E^{4f}_{K\beta_1}| \approx 1500-1700$ meV for a change of n_{4f} by one, whereas when the number of $6s,6p,5d$ electrons changes by one, $|\Delta E^{6s,6p,5d}_{K\beta_1}| \approx 20-80$ meV).

The Ce valence in the Laves phase was found from experimental shifts ΔE using the relation

$$m = m_{Ce_\gamma} + \Delta n_{4f} = 3 + \Delta E/\Delta E(Ce^{4+} - Ce^{3+}), \qquad (1)$$

where $\Delta E(Ce^{4+} - Ce^{3+})$ is a calibration shift corresponding to the Ce $K\beta_1$ line shift caused by a change of the number of $4f$ electrons by one. As the calibration shift we took the experimental shift of the Ce $K\beta_1$ line for the CeF_4–CeF_3 pair of ionic compounds, which is -1727 ± 20 meV (Ref. 4).

The samples to be studied were prepared by arc melting and practically single phase, their crystallographic parameters being close to literature data.[6,7]

The experimental shifts of the Ce $K\beta_1$ line and of the valence of Ce in the Laves phases (m) are listed in Table I. Figure 1 plots these valences *vs* the Ce effective radius r^* characterizing the degree of Ce compression in a Laves phase. The real r_{Ce-Ce} separation in a Laves phase cannot serve as a criterion of the degree of compression, because it is determined not only by compression (the ''dimensional'' factor), but also by the Ce-M interaction, which is different for different M atoms (the ''chemical'' factor). To exclude the chemical factor, it was proposed[8] to take as a measure of Ce compression in a Laves phase the cerium-metal radius r^* found from the available crystallographic data. The lattice parameter a_{RM_2} for trivalent Laves phases RM_2 (R stands here for a rare earth) decreases linearly with increasing Z as a result of compression experienced by lanthanide atoms. The lattice parameter a_{CeM_2} for IV Laves phases does not fit

TABLE I. Experimental K line shifts ΔE in Ce, Ru, Rh, Os, and Pt, and Ce valence m in CeM_2 Laves phases.

		ΔE, meV				
		Ce	M_{exp}		M_{calc}	
Compound	m_{Ce}	$K\beta_1$	$K\alpha_1$	$K\beta_1$	$K\alpha_1$	$K\beta_1$
$CeFe_2$	3.36 ±0.01	−624±15				
$CeCo_2$	3.35 ±0.01	−599±12				
$CeNi_2$	3.22 ±0.01	−383±14				
$CeRu_2$	3.36 ±0.01	−621±17	+28±5	+41± 8	14	26
$CeRh_2$	3.16 ±0.01	−275±14	+11±4	+14±16	7	12
$CeOs_2$	3.35 ±0.01	−610±23	+43±6		6	···
$CePt_2$	3.00 ±0.01	6±11	+3±7		0	···
$CeMg_2$	3.000±0.003	−1± 6				
$CeAl_2$	2.998±0.003	4± 6				

Note: The reference are Ce_γ and M metals. M_{calc} stands for calculations made under the assumption that formation of an IV state involves promotion of a $4f$ electron into the d band of metal M.

to this relation and corresponds to that of the Laves phase of a rare earth with a smaller metallic radius. It is this radius derived from the $a_{RM_2}=f(r_R)$ relation that was proposed[8] to take as an effective radius r^* characterizing the degree of Ce compression in a Laves phase. The values of r^* presented in Fig. 1 were obtained by the above method using the values of r_R from Ref. 9 and a_{RM_2} from Refs. 6 and 7.

As seen from Fig. 1, in the small-compression region (large r^*) the Ce valence grows linearly with increasing compression up to the limiting value $m\approx 3.35$, to remain constant thereafter, despite the continuing increase of compression. This dependence of Ce valence on r^* can be explained in terms of the interconfigurational fluctuation model.[10] In this model, the IV state of Ce is considered as a resonance between the states Ce^{3+} $(4f^1)$ and Ce^{4+} $(4f^0+e)$. The Ce valence can be calculated within this model as

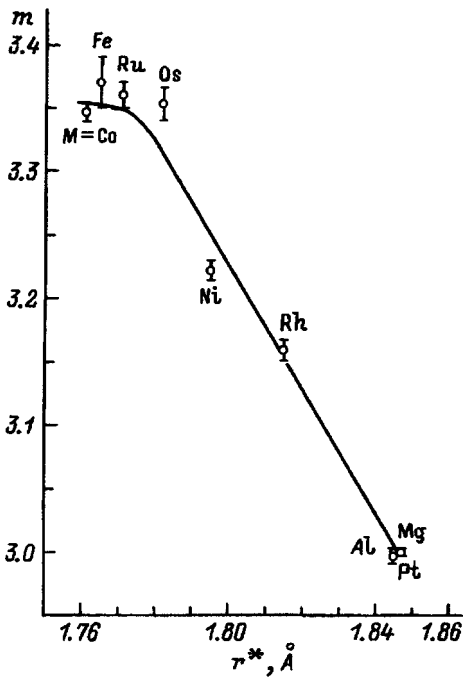

FIG. 1. Ce valence m in CeM_2 Laves phases vs effective Ce-metal radius r^*.

$$m=3+\left[1+\frac{M_3}{M_4}\exp\frac{E_{ex}}{kT+\Gamma}\right]^{-1}, \tag{2}$$

where E_{ex} is the energy difference between the Ce^{4+} and Ce^{3+} states, Γ is the Anderson hybridization energy (the $4f$-level width), and M_3 and M_4 are the statistical weights of the corresponding states.

As intracrystalline compression increases, the $4f$ level approaches the Fermi level and, accordingly, E_{ex} decreases, and m increases. In the limit as $E_{ex}\to 0$, the valence state is determined only by the statistical weights of the Ce^{3+} $(4f^1)$ and Ce^{4+} $(4f^0+e)$ states and by the final state of the electron e. It was shown[11] that in this limit the Ce valence can assume the values 3.14, 3.25, and 3.40, depending on where the $4f$ electron transfers when the IV state forms. The limiting value of the valence, $m\approx 3.35$, agrees well with the value $m_{calc}=3.40$ calculated under the assumption that $E_{ex}\approx 0$, and that the $4f$ electron transfers to the $np(d)_{3/2}$ states of the neighboring Ce or M metal atom.

Figure 2 plots temperature dependences $m(T)$ for some of the Laves phases studied. The Ce valence is seen to decrease with increasing temperature, although according to Eq. (2) m should grow with T for $E_{ex}=$const. This disagreement can be explained by assuming E_{ex} to be temperature dependent (in principle, theory allows this possibility[12]). The solid lines in Fig. 2 are plots of $m(T)$ calculated using Eq. (2) under the assumption of the simplest relation $E_{ex}(T)=E_0+\beta T$; it was also assumed that the width Γ of the $4f$ level does not depend on temperature. Experimental data on the heat capacity, magnetic susceptibility, and photoemission spectra suggest that the values of Γ for IV systems lie within the region 100–600 K.[13] The curves correspond to the following parameters E_0 and β (for $\Gamma=300$ K): 42 K and 1.8 for $CeNi_2$, 170 K and 2.3 for $CeRh_2$, −6 K and 0.4 for $CeCo_2$, and −10 K and 0.6 for $CeRu_2$. The excitation energies E_{ex} derived from the parameters E_0 and β thus found are in agreement with the values of E_{ex} obtained from the temperature dependences of magnetic susceptibility measured[14] for a broad class of compounds of intermediate-valence cerium.

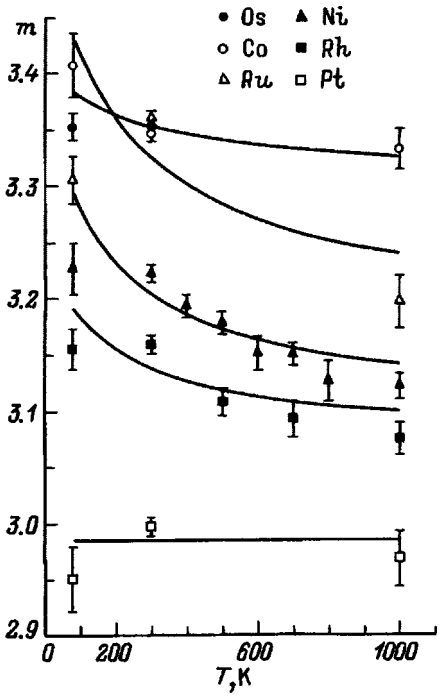

FIG. 2. Ce valence m in Laves phases *vs* temperature. Symbols-experiment, curves-plots of Eq. (2) with the parameters specified in text.

Table I presents also the shifts of the $K\alpha_1$ and $K\beta_1$ lines of Ru, Rh, Os, and Pt[2] in Laves phases relative to the corresponding metals. These lines exhibit slight positive shifts for all Laves phases. As we showed earlier,[15] positive shifts can appear either when valence $5(6)s(p)$ electrons are removed from the M atom, or when valence $4(5)d$ electrons are added to it.

The conduction band of $4d$ and $5d$ metals is derived from the comparatively narrow $4d,5d$ and broad $5s,6s$ subbands. Therefore when the number of electrons in the conduction band changes (for instance, as a result of formation of intermetallic compounds), the changes in the $5(6)s$ subbands will be small because of the low density of s states near the Fermi level. For this reason the positive shifts of the $K\alpha_1$ and $K\beta_1$ lines of M elements in Laves phases observed by us are more likely due to the increasing fraction of the $4d$ and $5d$ subbands of M elements in the total conduction band. By comparing the experimental shifts and the shifts calculated within the Hartree–Fock model, one can determine the required increase in the number of $4d,5d$ electrons of element M in the Laves phase compared to the M metal.

We obtained $\Delta n_d = 0.32 \pm 0.04$, 0.12 ± 0.04, 1.26 ± 0.18, and 0.04 ± 0.10 el/atom for $CeRu_2$, $CeRh_2$, $CeOs_2$, and $CePt_2$, respectively (the quoted errors are statistical). The calculation was made under the assumption that the valence configurations of M metals are $4d^7 5s^1$, $4d^8 5s^1$, $5d^7 6s^1$, and $5d^9 6s^1$ for Ru, Rh, Os, and Pt, respectively.[3)] One observes a certain correlation between the valence of Ce in Laves phases and Δn_d. This suggests that the population of the $4(5)d$ states increases at the expense of the additional valence electrons appearing when the IV state forms. This mechanism alone cannot, however, account for the experimental shifts (particularly for $CeOs_2$), which is seen from Table I presenting the K-line shifts of M metals ($\Delta E_{\mathrm{M\,calc}}$) calculated under the assumption that formation of an IV state promotes a $4f$ electron to the d band of metal M. An additional mechanism resulting in an increase of ΔE_{exp} could be redistribution of the valence s and d electrons of the M metal itself (electron promotion from the s to d subband of metal M).

The authors are grateful to O. S. Sumbaev for fruitful discussions and to P. L. Sokolova for assistance in preparing the manuscript.

Support of the Russian Fund for Fundamental Research (Grant 96-02-17811) is gratefully acknowledged.

[1)] In cubic Laves phases AB_2, the ratio of the closest distances between unlike atoms $r_{A-A}/r_{B-B} = 1.225 = k_0$ (see, e.g., Ref. 5). Because the ratio of the radii for pure components, $r_A/r_B = k$, differs from k_0, the A and B atoms in a Laves phase expand or contract. For CeM_2 Laves phases with IV, $k_0 = r_{Ce-Ce}/r_{M-M} < k = r_{Ce_\gamma}/r_M$, which corresponds to compression of Ce atoms.

[2)] For Pt we used the weaker $K\alpha_2$ line, because the energy of $K\alpha_1$ coincides to within a few linewidths with that of the W$K\beta_3$ line excited in the anticathode of the x-ray tube. The shifts of the $K\alpha_1$ and $K\alpha_2$ lines were shown[15] to differ only insignificantly.

[3)] The valence configurations of the $4d$ and $5d$ metals are known not well enough. The calculated values depend, however, only weakly on the starting valence configurations (variation of the population of the $5s$ and $6s$ orbitals, n_s, within a broad range of 0.5 to 1.5 changes Δn_d by not more than 15%).

[1] J. Röhler, *Handbook on the Physics and Chemistry of Rare Earths*, Vol. 10 (Elsevier Science Publ., Amsterdam, 1987).
[2] V. A. Shaburov, I. M. Band, A. I. Grushko, T. B. Mezentseva, E. V. Petrovich, Yu. P. Smirnov, A. E. Sovestnov, O. I. Sumbaev, M. B. Trzhaskovskaya, and I. A. Markova, Zh. Éksp. Teor. Fiz. **65**, 1157 (1973) [Sov. Phys. JETP **38**, 573 (1973)].
[3] A. E. Sovestnov, V. A. Shaburov, I. A. Markova, E. M. Savitskiĭ, O. D. Chistyakov, and T. M. Shkatova, Fiz. Tverd. Tela (Leningrad) **23**, 2827 (1981) [Sov. Phys. Solid State **23**, 1652 (1981)].
[4] O. I. Sumbaev, Usp. Fiz. Nauk **124**, 281 (1978) [Sov. Phys. Usp. **21**, 141 (1978)].
[5] M. E. Teslyuk, *Metallic Compounds with Laves-Phase Structure* [in Russian], Nauka, Moscow, 1969.
[6] K. H. J. Buschow, Rep. Prog. Phys. **40**, 1179 (1977).
[7] K. H. J. Buschow, Rep. Prog. Phys. **42**, 1373 (1979).
[8] I. R. Harris and R. C. Mansey, J. Less-Common Met. **13**, 591 (1967).
[9] K. A. Gschneidner, *Rare-Earth Metal Alloys* (IL, Moscow, 1965).
[10] L. L. Hirst, J. Phys. Chem. Solids **35**, 1285 (1974).
[11] V. A. Shaburov, Yu. P. Smirnov, A. E. Sovestnov, and A. V. Tyunis, JETP Lett. **41**, 259 (1985).
[12] D. K. Wohlleben, J. Phys. (Paris) **37**, C4-321 (1976).
[13] D. I. Khomskiĭ, Usp. Fiz. Nauk **129**, 443 (1979) [Sov. Phys. Usp. **22**, 879 (1979)].
[14] J. G. Sereni, G. L. Olcese, and C. Rizzuto, J. Phys. (Paris) **40**, C5-537 (1979).
[15] E. V. Petrovich, Yu. P. Smirnov, V. S. Zykov, A. I. Grushko, O. I. Sumbaev, I. M. Band, and M. B. Trzhaskovskaya, Zh. Éksp. Teor. Fiz. **61**, 1756 (1971) [Sov. Phys. JETP **34**, 935 (1971)].

Translated by G. Skrebtsov

On the propagation of electromagnetic waves in the tetrathiafulvalene family of organic conducting salts

V. G. Peschanskiĭ and D. A. Toryanik

Low-Temperature Physicotechnical Institute, Ukrainian Academy of Sciences, 310164 Khar'kov, Ukraine

S. N. Savel'eva

A. I. Ioffe Physicotechnical Institute, Russian Academy of Sciences, 194021 St. Petersburg, Russia
(Submitted January 20, 1998)
Fiz. Tverd. Tela (St. Petersburg) **40**, 1401–1404 (August 1998)

The propagation of electromagnetic waves is investigated theoretically in organic layered conductors with metallic conductivity in magnetic fields strong enough that the characteristic radius of curvature of a conduction-electron orbit is much smaller than its mean-free path l. It is shown that when groups of charge carriers with quasi-two- dimensional and quasi-one-dimensional energy spectra coexist in such a material, the penetration depth of the waves into it, which is a strong function of the polarization of the waves and the orientation of the magnetic field, also has an interesting dependence on the magnitude of the magnetic field and the low-dimensionality parameters of the charge-carrier spectra. This property makes it possible to recover details of the Fermi surface from the experimental data. © *1998 American Institute of Physics.* [S1063-7834(98)00308-6]

Organic conductors usually consist of layered or filamentary structures with marked anisotropy in their electrical conductivity. Members of the large family of ion-radical charge-transfer salts based on tetrathiafulvalene possess metallic conductivity not only along but also transverse to the layers. The similarities between these compounds and ordinary metals makes the concept of charged quasiparticles with arbitrary dispersion law an eminently suitable basis for discussing their electronic properties. Use of the topologically simplest model for the Fermi surface of a quasi-two-dimensional conductor, i.e., a slightly corrugated cylinder, has yielded good agreement with experiment in investigations of the magnetoresistance and Shubnikov-deHaas effect in the organic conductors $(BEDT–TTF)_2I_3$ and $(BEDT–TTF)_2IBr_2$.[1–6] However, the unusual behavior of the magnetoresistance in the $(BEDT–TTF)_2MHg(SCN)_4$ family of salts[7–15], where M = (K, Rb, Tl), indicates that the Fermi surface of these layered conductors is more complicated. One possible topological structure for the electronic energy spectra of this family of organic metals which agrees with the experimentally observed dependence of the resistance on the magnitude of the magnetic field implies a Fermi surface that includes not only a slightly corrugated cylinder but also two quasi-one-dimensional sheets consisting of slightly corrugated planes in which the charge carrier velocity is predominantly within the plane of the layers.[16,17] High-frequency phenomena in these conductors suggest strongly that the Fermi surface is a union of quasi-two-dimensional and quasi-one-dimensional sheets. In what follows we shall discuss the propagation of electromagnetic waves in conductors whose electronic energy spectra consist of two such sheets, i.e., one associated with a quasi-two-dimensional and one with a quasi-one-dimensional dispersion law for the charge carriers:

$$\varepsilon(\mathbf{p})=\sum_{n=0}^{\infty}\varepsilon_n(p_x,p_y)\cos\{anp_z/h\}, \tag{1}$$

$$\varepsilon'(\mathbf{p})=\sum_{n,m,q=0}^{\infty}A_{nmq}\{\cos(a_1np_x/h)\times\cos(a_2mp_y/h)\cos(aqp_z/h)\}. \tag{2}$$

We shall assume that the ratio of the numbers of conduction electrons in each energy band is arbitrary.

In this expression, a is the distance between layers, a_1 and a_2 are the periods of the crystal lattice in the layer planes, and h is Planck's constant. For the quasi- two-dimensional charge carrier spectrum the coefficients in Eq. (1) that multiply the cosines fall off rapidly with increasing values of the label n, so that the maximum value on the Fermi surface is $\varepsilon(\mathbf{p})=\varepsilon'(\mathbf{p})=\varepsilon_F$. The function $\max\{\varepsilon_F-\varepsilon_0(p_x,p_y)\}=\eta\varepsilon_F$ is much smaller than the Fermi energy ε_F, i.e., $\eta\ll 1$. For the quasi-one-dimensional charge carrier energy spectrum the primary contribution to the expression for the dispersion law $\varepsilon'(p)$ comes from terms with $m=q=0$. If we assume that $A_{100}=U\geqslant\varepsilon_F$, while all the remaining coefficients A_{nmq} equal zero, then the sheet of the Fermi surface corresponding to this energy band consists of the two planes $p_x=\pm(h/a_1)\arccos(\varepsilon_F/U)$. Let us include the slight corrugation of these planes by assuming that two other terms in Eq. (2) are nonzero, namely $A_{010}=\eta_1U\ll\varepsilon_F$ and $A_{001}=\eta_2U\ll\varepsilon_F$.

The complete system of equations that describes the propagation of electromagnetic waves in a conducting medium consists of the Maxwell equations

$$(\nabla\times\mathbf{H})=-i\omega\mathbf{E}+4\pi\mathbf{j}/c, \tag{3}$$

$$(\nabla\times\mathbf{E})=i\omega\mathbf{B}, \quad \mathbf{B}=\mathbf{H}+4\pi\mathbf{M}, \tag{4}$$

and a kinetic equation for the charge-carrier distribution function

$$f(\mathbf{p},\mathbf{r},t)=f_0(\varepsilon)-\psi(\mathbf{p},\mathbf{r})\exp\{-i\omega t\}\partial f_0(\varepsilon)/\partial\varepsilon,$$
$$\mathbf{v}\partial\psi/\partial\mathbf{r}+(e/c)(\mathbf{v}\times\mathbf{H})\partial\psi/\partial\mathbf{p}+(1/\tau-i\omega)\psi=e\mathbf{v}\mathbf{E}(\mathbf{r}), \tag{5}$$

which allows us to find the relation between the current density and the wave electric field $\mathbf{E}(\mathbf{r})$.

In Eq. (4), $\mathbf{M}$ is the magnetization of the conductor. Because the magnetic susceptibility $\chi_{ij}=\partial M_i/\partial B_j$ is usually vanishingly small in conductors without magnetic order, there is never a need to distinguish the magnetic field $\mathbf{H}$ from the magnetic induction $\mathbf{B}$ except for a few special cases when the deHaas–van Alphen effect is so strong that it leads to the formation of diamagnetic domains.[18,19] We will assume that the perturbation of the charge carrier system by the electric field of electromagnetic wave is so weak that we can limit ourselves to linear approximation. In the kinetic equation (5) we have already discarded the term $eE\partial\psi/\partial p$, which is quadratic in the perturbation. The collision integral $W_{\rm col}\{f\}$ will be treated in the τ approximation, i.e., $W_{\rm col}\{f\}=(f_0-f)/\tau$ where f_0 is the equilibrium Fermi distribution function for the charge carriers and τ is their mean free time, which we assume is the same for both groups of charge carriers. In this approximation the Maxwell equations become linear, and so the time dependence can be assumed to be harmonic, i.e., the electromagnetic wave can be regarded as monochromatic with frequency ω. This assumption does not in any way compromise the overall character of the problem as posed, since its solution when the time dependence of the field is arbitrary consists of a superposition of solutions to the Maxwell equations with different harmonics. Therefore, we shall replace the operation of time differentiation of the electromagnetic fields in Maxwell equations (3) and (4) by multiplication by $-i\omega$. In what follows, t will denote the time for motion of a charge in a magnetic field according to the equation

$$d\mathbf{p}/dt=(e/c)(\mathbf{v}\times\mathbf{H}). \tag{6}$$

Under anomalous-skin-effect conditions, i.e., when the skin depth δ is considerably smaller than the mean-free path of a charge carrier l, the reflection of carriers from the sample surface $r_s=0$ is strongly altered, and the kinetic equation must be supplemented by a boundary condition that reflects this scattering of conduction electrons from the surface:

$$\psi(\mathbf{p}_+,\mathbf{r}_s)=q(\mathbf{p}_-)\psi(\mathbf{p}_-,\mathbf{r}_s)+\int (d^3p)W(\mathbf{p},\mathbf{p}_+)$$
$$\times\{1-\Theta[v_x(\mathbf{p})]\}\psi(\mathbf{p},\mathbf{r}_s). \tag{7}$$

The specular reflection parameter of the sample surface $q(\mathbf{p})$, i.e., the probability of specular reflection of a conduction electron incident on the surface $\mathbf{r}_s=0$ with momentum $\mathbf{p}_-$, is related to the scattering indicatrix $W(\mathbf{p},\mathbf{p}')$ via the following expression:

$$q(\mathbf{p}_-)=1-\int d^3pW(\mathbf{p},\mathbf{p}_+)\{1-\Theta[v_x(\mathbf{p})]\}, \tag{8}$$

where $\Theta(\xi)$ is the Heaviside function. The incident $\mathbf{p}_-$ and reflected $\mathbf{p}_+$ momenta of the electrons are related by the condition for specular reflection, in which the energy and projection of the momentum onto the sample surface are conserved. When several groups of charge carriers are present, several channels for specular reflection are possible. Under anomalous skin effect conditions, this leads to an increase in the penetration depth of an electromagnetic field pulse when the applied magnetic field is parallel to the sample surface[20], as predicted by Azbel'[21]. The multichannel nature of specular reflection of electrons by the sample boundary strongly affects the transparency and surface impedance of a thin sample (since the thickness L is smaller or the same order as the mean-free path of a charge carrier), but turns out to have little effect on the penetration depth of electromagnetic waves in the conductor bulk (i.e., $L\gg l$). Therefore, in the analysis that follows we will not include interband transitions of charge carriers as they scatter within the sample and at its surface.

The integral term in the boundary condition (7) ensures that current cannot flow through the conductor surface; however, at high frequencies ω the solution to the kinetic equation does not depend strongly on this functional. In a magnetic field parallel to the sample surface and when charge carrier drift into the sample bulk along open electron orbits is negligible, we can write the equation for ψ in the following form:

$$\psi(t_H,p_H,\mathbf{r})=\int_\lambda^{t_H}dt\ e\mathbf{v}(t,p_H)\mathbf{E}(\mathbf{r}(t,p_H)-\mathbf{r}(\lambda,p_H))$$
$$\times\exp\{\nu(t-t_H)\}+q(\lambda,p_H)$$
$$\times[1-q(\lambda,p_H)\exp\{\nu(2\lambda-T)\}]^{-1}$$
$$\times\int_\lambda^{T-\lambda}dt\ e\mathbf{v}(t,p_H)\mathbf{E}(\mathbf{r}(t,p_H)-\mathbf{r}(\lambda,p_H))$$
$$\times\exp\{\nu(t-t_H+2\lambda-T)\}, \tag{9}$$

where $\nu=-i\omega+1/\tau$, and λ is the root of the equation

$$\mathbf{r}(t,p_H)-\mathbf{r}(\lambda,p_H)=\int_\lambda^t\mathbf{v}(t',p_H)dt'=\mathbf{r}-\mathbf{r}_s. \tag{10}$$

For conduction electrons that do not collide with the sample surface, we must set $\lambda=-\infty$.

Let us consider the propagation of electromagnetic waves along the x axis in a magnetic field $\mathbf{H}=(0,H\sin\vartheta,H\cos\vartheta)$ parallel to the sample surface. If the sample thickness considerably exceeds not only the mean free path of a charge carrier but also the skin depth, then to sufficient accuracy the distribution of ac electric field in the sample near the sample surface has the same form as it does in a half-space $x\geqslant 0$ occupied by conductor. According to Reuter and Sondheimer (see Ref. 22), we can continue the electric field as an even function into the region of negative x and Fourier-transform the current density and electric field:

$$\mathbf{j}(k)=2\int_0^\infty dx\mathbf{j}(x)\cos\, kx, \quad \mathbf{E}(x)=2\int_0^\infty dx\mathbf{E}(x)\cos\, kx. \tag{11}$$

Let us use the solution (9) of the kinetic equation to find the relation between the Fourier transforms of the current density and the ac electric field:

$$j_i(k)=\sigma_{ij}(k)E_j(k)+\int dk' Q_{ij}(k,k')E_j(k'), \tag{12}$$

where

$$\begin{aligned}\sigma_{ij}(k)&=2e^3H/c(2\pi h)^3\\ &\times\int dp_H\int_0^T dt v_i(t,p_H)\int_\infty^t dt' v_j(t',p_H)\\ &\times\exp\{\nu(t'-t)\}\cos\, k\{x(t'-p_H)-x(t,p_H)\}\\ &\equiv\langle e^2 v_i\hat{R}v_j\rangle,\end{aligned} \tag{13}$$

where $T=2\pi/\Omega$ is the period of the charge-carrier motion in a magnetic field.

The kernel $Q_{ij}(k,k')$ of the integral operator depends strongly on the state of the sample surface, i.e., on the probability that a conduction electron will undergo specular reflection from it. When the reflection of a charge carrier by the sample surface is close to specular, for electrons with a quasi-two-dimensional energy spectrum under anomalous skin-effect conditions the penetration depth of the electric field is the smallest parameter of the problem with dimensions of length. In this case, the second term in Eq. (12) is the largest term. However, for electrons with a quasi-one-dimensional spectrum including this term leads only to refinement of a numerical factor of order unity in the expression for the surface impedance.

In the Fourier representation, the Maxwell equations become

$$\{k^2-\omega^2/c^2\}E_\alpha(k)-4\pi i\omega j_\alpha(k)/c^2=-2E'_\alpha(0),$$
$$\alpha=(y,z). \tag{14}$$

Together with the constitutive equation (12), these equations allow us to find the Fourier transform of the ac electric field without difficulty, and then to find the electric field distribution in the conductor with the help of an inverse Fourier transform.

The electric field $E_x(x)$ must be determined from the solution to the Poisson equation

$$\text{div}\ \mathbf{E}=4\pi\langle\psi\rangle, \tag{15}$$

which reduces asymptotically to the condition of electric neutrality in conductors with high charge carrier densities

$$\langle\psi\rangle=0. \tag{16}$$

In a magnetic field strong enough that the diameter of an electron orbit $2r$ is much smaller than the skin depth, only the first term in Eq. (12) needs to be retained, and the skin depth is easily determined from the dispersion equation

$$\det\{\delta_{\alpha\beta}-\xi\tilde{\sigma}_{\alpha\beta}(k)\}=0,\ \alpha,\ \beta=(y,z), \tag{17}$$

where $\xi=4\pi i\omega/(k^2c^2-\omega^2)$,

$$\begin{aligned}\tilde{\sigma}_{\alpha\beta}(k)&=\sigma_{\alpha\beta}(k)+\sigma^{(1)}_{\alpha\beta}(k)-\{\sigma_{\alpha x}(k)+\sigma^{(1)}_{\alpha x}(k)\}\\ &\times\{\sigma_{x\beta}(k)+\sigma^{(1)}_{x\beta}(k)\}/\{\sigma_{xx}(k)+\sigma^{(1)}_{xx}(k)\}.\end{aligned} \tag{18}$$

The contribution to $\sigma_{\alpha\beta}(k)$ from charge carriers with quasi-one-dimensional energy spectrum is determined primarily by the component $\sigma^{(1)}_{xx}(k)$. Neglecting small corrections proportional to η_1^2 and η_2^2, this quantity has the form

$$\sigma^{(1)}_{xx}(k)=\frac{\sigma_1}{1+(kl_1)^2}, \tag{19}$$

where $l_1=\dfrac{v_x\tau}{1-i\omega\tau}$, σ_1 is the contribution of this group of charge carriers to the electrical conductivity along the x axis in a uniform electric field, and $v_x=-(Ua_1/h)\sin(\varepsilon_F/U)$.

The magnetic field dependence of $\sigma^{(1)}_{ij}(k)$ appears only in the next higher terms in the expansion in powers of the small parameters η_1 and η_2:

$$\sigma^{(1)}_{yy}(k)=\sum_{\pm}\frac{\eta_1^2\sigma_1 a_2^2/2a_1^2}{1+(k\pm eHa_2\cos\,\vartheta/\cosh)^2 l_1^2}, \tag{20}$$

$$\sigma^{(1)}_{zz}(k)=\sum_{\pm}\frac{\eta_2^2\sigma_1 a^2/2a_1^2}{1+(k\pm eHa\sin\,\vartheta/\cosh)^2 l_1^2}, \tag{21}$$

and including it does not significantly affect the skin depth for attenuation of the electromagnetic fields.

In strong magnetic fields, where $\gamma=1/\Omega\tau\ll 1$ and $|kl_1|\gg 1$, with sufficient accuracy the components $\tilde{\sigma}_{\alpha z}(k)$ and $\tilde{\sigma}_{z\beta}(k)$ are found to be the same as for a single group of charge carriers with a quasi-two-dimensional energy spectrum, i.e.,

$$\tilde{\sigma}_{zz}(k)\cong\sigma_{zz}(k), \quad \tilde{\sigma}_{yz}(k)=\tilde{\sigma}_{zy}(k)\cong\sigma_{yz}(k)\cong\sigma_{zz}\tan\,\vartheta. \tag{22}$$

However, the presence of the second group of charge carriers with a quasi-one-dimensional energy spectrum leads to a considerable change in the asymptotic behavior of the component

$$\tilde{\sigma}_{yy}(k)=\sigma_{zz}\tan^2\,\vartheta+(kr)^2\sigma_0^2/\sigma_1+\sigma_0\gamma^2, \tag{23}$$

where σ_0 is the $H=0$ contribution to the electrical conductivity along the x axis from charge carriers with a spectrum of the form (1); numerical factors of order unity in the next two terms of Eq. (23) are omitted.

Instead of saturating at a value of order σ_0, which occurs when $\sigma_1=0$, the component $\tilde{\sigma}_{yy}(k)$ decreases with increasing magnetic field over a rather wide range of fields, and the electromagnetic wave propagation turns out to be quite unlike the case where only one group of charge carriers is present. As a result, organic conductors of the family $(\text{BEDT–TTF})_2\text{MHg}\,(\text{SCN})_4$ must exhibit orientation- dependent effects, i.e., a strong dependence of the attenuation depth of the electric fields $E_y(x)$ and $E_z(x)$ on the orientation of the magnetic field relative to the layers.[23–25] This is because the integral

$$I(\vartheta)=T^{-1}\int_0^T dt\ \varepsilon_1(t)\exp\{iap_y(t)\tan\ \vartheta/h\}, \tag{24}$$

reduces to zero for certain values of the angle $\vartheta=\vartheta_c$, which strongly modifies the asymptotic behavior of the components $\sigma_{zz}(k)$, $\sigma_{yz}(k)$, and $\sigma_{zy}(k)$. In very strong magnetic fields, where r is the smallest parameter with the dimensions of length, the component $\tilde{\sigma}_{yy}(k)\cong\sigma_{zz}\tan^2\vartheta$ also decreases rapidly.

Suppose that for $\sigma_1=0$ we can assume, with sufficient accuracy, that $\tilde{\sigma}_{yz}(k)$ and $\tilde{\sigma}_{zy}(k)$ are negligibly small compared to the diagonal components of the matrix $\tilde{\sigma}_{\alpha\beta}(k)$, and the attenuation lengths of the electric fields $E_y(x)$ and $E_z(x)$ turn out to be quite different. Then the presence of the second group of charge carriers mixes waves with different polarizations. For $r\ll\delta_0=\{c/2\pi\omega(\sigma_0+\sigma_1)\}^{1/2}$, their attenuation lengths have the following form:

$$\delta_1=\delta_0/\eta,\quad \delta_2=\delta_0/\gamma, \tag{25}$$

i.e., even for samples pure enough that $l\eta\gg\delta_0$ there is a wave that attenuates over distances that greatly exceed the mean-free path of the conduction electrons.

Under anomalous-skin-effect conditions, when the penetration depth of an electromagnetic field is much smaller than the diameter of an electron orbit, the surface impedance of the conductor is sensitive to the state of its surface, and in the anomalous skin effect limit, where both the penetration depth $\delta_\perp$ of the wave electric field $E_y(x)$ and the penetration depth $\delta_\parallel$ of the wave electric field $E_z(x)$ are much smaller than r, the charge carrier group with spectrum (2) has practically no effect on the character of the electromagnetic wave propagation. When reflection of a charge carrier by the sample surface is close to specular, the relation between $\delta_\perp$ and $\delta_\parallel$ has the form

$$\delta_\perp=\eta^{4/5}\delta_\parallel. \tag{26}$$

For $\omega\tau\gg1$ and under cyclotron resonance conditions for charge carrier with the quasi-two-dimensional spectrum in a magnetic field, when the frequency of the waves is a multiple of the rotation frequency, the conduction electrons with the quasi-one-dimensional energy spectrum have only a slight effect on waves propagating along the direction in which they make the most important contribution to the electrical conductivity.

Thus, by investigating the surface impedance of these organic conductors over a wide range of magnetic fields we have obtained detailed information about the energy spectra of their various groups of charge carriers.

This paper was partially financed by the Science Ministry of Ukraine (Grant 2.4/192).

[1] M. V. Kartsovnik, V. N. Laukhin, V. V. Nizhankovskiĭ, and A. A. Ignat'ev, JETP Lett. **47**, 363 (1988).
[2] M. V. Kartsovnik, P. A. Kononovich, V. N. Laukhin, and I. F. Shchegolev, JETP Lett. **48**, 541 (1988).
[3] N. Toyota, T. Sasaki, K. Murata, Y. Honda, M. Tokumoto, H. Bando, N. Kinoshita, H. Anzai, T. Ishiguro, and Y. Muto, J. Phys. Soc. Jpn. **57**, 2616 (1988).
[4] W. Kang, G. Montanbaux, J. R. Cooper, D. Jerome, P. Batail, and C. Lenoir, Phys. Rev. Lett. **62**, 2559 (1989).
[5] M. V. Kartsovnik, P. A. Kononovich, V. N. Laukhin, S. I. Pesotskiĭ, and I. F. Shchegolev, Zh. Éksp. Teor. Fiz. **97**, 1305 (1990) [Sov. Phys. JETP **70**, 735 (1990)].
[6] R. Yagi, Y. Iye, T. Osada, and S. Kagoshima, J. Phys. Soc. Jpn. **59**, 3069 (1990).
[7] T. Sasaki and N. Toyota, Solid State Commun. **75**, 93 (1990).
[8] T. Osada, R. Jagi, A. Kawasumi, S. Kagoshima, N. Miura, M. Oshima, and G. Saito, Phys. Rev. B **41**, 5428 (1990).
[9] M. V. Kartsovnik, A. E. Kovalev, V. N. Laukhin, S. S. Pesotskiĭ, and N. V. Kushch, JETP Lett. **55**, 339 (1992).
[10] N. D. Kushch, L. I. Buravov, M. V. Kartsovnik, V. N. Laukhin, S. I. Pesotskii, R. P. Shibaeva, R. P. Rosenberg, E. B. Jagubskii, and A. V. Zvarikina, Synth. Met. **46**, 271 (1992).
[11] M. V. Kartsovnik, A. E. Kovalev, V. N. Laukhin, and S. I. Pesotskii, J. Phys. I **2**, 223 (1992).
[12] A. E. Kovalev, M. V. Kartsovnik, and N. D. Kushch, Solid State Commun. **87**, 705 (1993).
[13] A. E. Kovalev, M. V. Kartsovnik, R. P. Shibaeva, R. P. Rosenberg, and I. F. Shchegolev, Solid State Commun. **89**, 575 (1994).
[14] M. V. Kartsovnik, A. E. Kovalev, R. P. Shibaeva, R. P. Rosenberg, and N. D. Kushch, Physica B **201**, 459 (1994).
[15] M. V. Kartsovnik, A. E. Kovalev, V. N. Laukhin, I. F. Shchegolev, H. Ito, T. Ishiguro, N. D. Kushch, H. Mori, and G. Saito, Synth. Met. **70**, 811 (1995).
[16] R. Rossenau, M. L. Doublet, E. Canadell, R. P. Shibaeva, R. P. Rosenberg, N. D. Kushch, and E. B. Jagubskii, J. Phys. I **6**, 1527 (1996).
[17] T. Sasaki, H. Ozawa, H. Mori, S. Tanaka, T. Fukase, and N. Toyota, J. Phys. Soc. Jpn. **65**, 213 (1996).
[18] J. H. Condon, Phys. Rev. **145**, 526 (1966).
[19] I. A. Privorotskiĭ, Zh. Éksp. Teor. Fiz. **52**, 175 (1967) [Sov. Phys. JETP **25**, 112 (1967)].
[20] V. G. Peschanskiĭ, V. M. Kardenas, M. A. Lur'e, and K. Yasemides, Zh. Éksp. Teor. Fiz. **80**, 1645 (1981) [Sov. Phys. JETP **53**, 849 (1981)].
[21] M. Ya. Azbel', Zh. Éksp. Teor. Fiz. **39**, 400 (1960) [Sov. Phys. JETP **12**, 283 (1960)].
[22] G. E. H. Reuter and E. H. Sondheimer, Proc. R. Soc. London **195**, 336 (1948).
[23] V. G. Peschanskiĭ, S. N. Savel'eva, and Kh. Kkhier Bek, Fiz. Tverd. Tela (Leningrad) **34**, 1630 (1992) [Sov. Phys. Solid State **34**, 864 (1992)].
[24] V. G. Peschanskiĭ, Kh. Kkhier Bek, and S. N. Savel'eva, Fiz. Nizk. Temp. **18**, 1012 (1992) [Sov. J. Low Temp. Phys. **18**, 711 (1992)].
[25] V. G. Peschansky, Phys. Rep. **288**, 305 (1997).

Translated by Frank J. Crowne

Squeezed states of a particle in magnetic field

M. Ozana

Department of Theoretical Physics Umeå University, S-901 87 Umeå, Sweden

A. L. Shelankov

Department of Theoretical Physics Umeå University, S-901 87 Umeå, Sweden; Physicotechnical Institute, 194021 St. Petersburg, Russia

(Submitted January 26, 1998)
Fiz. Tverd. Tela (St. Petersburg) **40**, 1405–1412 (August 1998)

For a charged particle in a homogeneous magnetic field, we construct stationary squeezed states which are eigenfunctions of the Hamiltonian and the non-Hermitian operator $\hat{X}_\Phi = \hat{X}\cos\Phi + \hat{Y}\sin\Phi$, $\hat{X}$ and $\hat{Y}$ being the coordinates of the Larmor circle center and Φ is a complex parameter. In the family of the squeezed states, the quantum uncertainty in the Larmor circle position is minimal. The wave functions of the squeezed states in the coordinate representation are found and their properties are discussed. Besides, for arbitrary gauge of the vector potential we derive the symmetry operators of translations and rotations. © *1998 American Institute of Physics.* [S1063-7834(98)00408-0]

The problem of a charged quantum particle moving on a plane subject to a homogeneous magnetic field is met in various physical contexts, and it has been extensively studied in the literature and presented in text-books.[1] A specific feature of the problem is that the energy spectrum given by discrete Landau levels is multiply degenerate: the number of linearly independent eigenstates belonging to the Nth Landau level is proportional to the area of the plane accessible to the particle. The degeneracy is related to the translational invariance: as a classical Larmor circle can be put anywhere in the plane, a suitably defined operator of translation $\hat{T}_{\mathbf{a}} = e^{(i/h)\,\mathbf{a}\cdot\hat{\mathbf{P}}}$, $\hat{P}$ being the generator of translations, commutes with the Hamiltonian and upon acting on an energy eigenfunction $\psi_N(\mathbf{r})$ produces another eigenstate, shifted in space: $|\hat{T}_{\mathbf{a}}\psi_N(\mathbf{r})|^2 = |\psi_N(\mathbf{r}+\mathbf{a})|^2$.[2,3] Noncollinear translations do not commute in a magnetic field, and $[\hat{P}_x, \hat{P}_y] \neq 0$. The existence of two noncommuting Hermitian operators, $\hat{P}_y$, each of them commuting with the Hamiltonian leads[1] to the degeneracy.

The stationary wave functions corresponding to a degenerate Landau level may be chosen to be eigenfunctions of either $\hat{P}_x$ or $\hat{P}_y$ (but not both simultaneously). The eigenvalues of $\hat{P}_{x,y}$ are real, and the translation operator $e^{ia\hat{P}_x}$ (or $e^{ia\hat{P}_y}$) applied to the corresponding eigenfunction gives only an overall phase factor. The modulas remains unchanged by the translations, so that the eigenstates must be infinitely extended in the x (or y) direction. The wave functions of an electron in a magnetic field first found by Landau[1,4] provide an example: factorized as $e^{ipx}\chi(y)$, they are eigenfunctions of $\hat{P}_x$ and are infinitely extended in the x direction (strip-like states).

As discussed later, in the relation

$$\hat{\mathbf{P}} = \frac{e}{c}\,\mathbf{B}\times\hat{\mathbf{R}}, \tag{1}$$

$\hat{\mathbf{R}} = (\hat{X}, \hat{Y})$ has the meaning of the operator corresponding to the classical coordinate of the Larmor circle center (the guiding center); $\hat{X} = (c/eB)\hat{P}_y$ and $\hat{Y} = -(c/eB)\hat{P}_x$. The variable $\mathbf{R}$ has simple classical interpretation, and for this reason, it will be used below rather than $\mathbf{P}$.

Instead of $\hat{X}$ or $\hat{Y}$ ($\hat{P}_x$ or $\hat{P}_y$), one may choose their Hermitian linear combination $\hat{X}_\Phi = \hat{X}\cos\Phi + \hat{Y}\sin\Phi$ with a real Φ. The corresponding eigenstates are ''strips'' the orientation of which depends on the angle Φ. A different class of states can be obtained if the wave function is chosen to be an eigenfunction of the *non-Hermitian* operator $\hat{X}_\Phi$ with a complex ''angle'' $\Phi = \Phi_1 + i\Phi_2$. By virtue of the relation in Eq. (1), the eigenfunctions of $\hat{X}_\Phi$ are also eigenfunctions of $\hat{P}_{\Phi+\pi/2}$. In the case of a general complex Φ, eigenvalues of the non-Hermitian operator $\hat{P}_{\Phi+\pi/2}$ are complex numbers, and the above argument concerning an infinite extension of the state is not applicable; the eigenfunctions turn out to be localized (i.e., the wave function vanishes at infinity).

In the terminology of quantum optics (for a review see Ref. 5 and references therein) these states belong to the class of squeezed states, generalization of the coherent states. In optics the squeezed state is defined as an eigenfunction of a non-Hermitian operator, $\hat{x} - i\lambda\hat{p}$, built of two non-commuting variables, the coordinate and momentum of a harmonic oscillator (λ being the squeeze parameter). A distinctive feature of squeezed states is that the quantum uncertainty in the non-commuting variables is as minimal as allowed by the uncertainty relation (minimum uncertainty states). The purpose of the paper is to analyze properties of the squeezed states, eigenfunctions of $\hat{X}_\Phi$.

Solutions of the Schrödinger equation for a charge in a magnetic field corresponding to non-spreading wave packets with a classical dynamics—the coherent states in the modern terminology—were first built by Darwin as early as in 1928.[6] More recently, the coherent states in the magnetic field prob-

lem have been extensively studied by Malkin and Man'ko,[7] and Feldman and Kahn[8] (see also Refs. 9–11). In the coherent states, the quantum uncertainties in the *X*- and *Y*-coordinates of the Larmor center are equal. Various generalizations to the squeezed states have been done by Dodonov *et al.*[12,13] and Aragone:[14] In the general squeezed state, the uncertainty in one of the coordinates is reduced at the expense of the other one so that their product remains intact.

In the present paper, we consider *stationary* states, building the squeezed states from the energy eigenfunction belonging to a given Landau level. Being stationary, these states are of different kind than the moving squeezed wave packets of Refs. 12 and 14.

The paper is organized as follows. In Sec. 1, we review some general features of the quantum problem of a charge in a magnetic field. In Sec. 2, we define the squeezed states and explicitly find the wave functions in the coordinate representation. In Sec. 3, properties of the squeezed states are analyzed. In the Appendix, we suggest a method which allows one to construct symmetry operators for an arbitrary gauge of the vector potential and apply the method to the case of a homogeneous magnetic field.

1. GENERAL PROPERTIES

The Hamiltonian of a particle with mass m and electric charge e moving in the x-y plane in a magnetic field reads

$$\hat{H}=\frac{1}{2m}\left(\hat{\mathbf{p}}-\frac{e}{c}\,\mathbf{A}\right)^2, \tag{2}$$

here the vector potential $\mathbf{A}(A_x,A_y)$ corresponds to a homogeneous magnetic field perpendicular to the plane, $(\mathbf{curl}\,\mathbf{A})_z=B$. The choice of signs in some of the below formulas depends on the sign of eB; for definiteness, we assume $eB>0$. In terms of the ladder operators

$$\hat{c}=\frac{1}{\sqrt{2}l\omega_c}(\hat{v}_x+i\hat{v}_y),\quad \hat{c}^\dagger=\frac{1}{\sqrt{2}l\omega_c}(\hat{v}_x-i\hat{v}_y), \tag{3}$$

where $\hat{c}_{x,y}$ are the non-commuting components of the velocity operator

$$m\hat{\mathbf{v}}=\hat{\mathbf{p}}-\frac{e}{c}\,\mathbf{A},\quad [\hat{v}_x,\hat{v}_y]=i\,\frac{\hbar^2}{m^2l^2} \tag{4}$$

(the cyclotron frequency $\omega_c=|eB|/mc$ and the magnetic length $l=\sqrt{\hbar c/|eB|}$), the Hamiltonian Eq. (2) can be conveniently written as

$$\hat{H}=\hbar\omega_c\left(\hat{c}^\dagger\hat{c}+\frac{1}{2}\right),\quad [\hat{c},\hat{c}^\dagger]=1. \tag{5}$$

In the presence of a homogeneous magnetic field, the translations in the x-y plane and rotations around the z-axis remain symmetry elements. The reflection, σ_v, in a plane passing through the z axis (yOz, for definiteness), reverses the magnetic field and is not a symmetry transformation. However, the product $\sigma_T\equiv T\sigma_v$ of time-reversal T and σ_v, both reversing the field, is a valid symmetry.

It is well-known that the Hamiltonian Eq. (2) may not commute with the operators associated with the physical symmetries because the vector field $\mathbf{A}(\mathbf{r})$ has a lower symmetry than the corresponding magnetic field. If this is the case, the coordinate transformation should be accompanied by a certain gauge transformation which compensates the change in $\mathbf{A}(\mathbf{r})$.[3] A procedure of constructing the transformation, which is valid for arbitrary gauge of the vector potential, is presented in the Appendix.

As shown in the Appendix, the operators of finite translations, $\mathbf{r}\to\mathbf{r}+\mathbf{a}$, are built of the generator of translations

$$\hat{\mathbf{P}}=\hat{\mathbf{p}}-\frac{e}{c}\,\mathbf{A}+\frac{e}{c}\,\mathbf{B}\times\mathbf{r}. \tag{6}$$

The operator $\hat{\mathbf{P}}$ commutes with the Hamiltonian Eq. (2) as manifestation of the translation invariance preserved in a homogeneous magnetic field. The components of $\hat{\mathbf{P}}$ obey the commutation relation

$$[\hat{P}_x,\hat{P}_y]=-i\,\frac{e}{c}\,\hbar B. \tag{7}$$

Equation (6) is valid in an arbitrary gauge of the vector potential $\mathbf{A}$. In case of the symmetric gauge, $\mathbf{A}=1/2(\mathbf{B}\times\mathbf{r})$, Eq. (6) gives the expression first found by Zak.[2]

Presenting $\hat{\mathbf{P}}$ in the form in Eq. (1), one indeed recognizes in $\hat{\mathbf{R}}$ the center of the Larmor circle (the guiding center),

$$\hat{\mathbf{R}}=\hat{\mathbf{r}}+\frac{mc}{eB^2}\,\hat{\mathbf{v}}\times\mathbf{B}, \tag{8}$$

an integral of motion known from classical mechanics. The following commutation relations

$$[(\hat{\mathbf{R}})_l,(\hat{\mathbf{P}})_m]=i\hbar\,\delta_{lm}, \tag{9}$$

$$[\hat{X},\hat{Y}]=\frac{l^2}{i} \tag{10}$$

can be readily derived from Eqs. (7) and (8).

2. SQUEEZED STATES

From Eq. (10), the X and Y coordinates of the Larmor circle center are incompatible quantum variables. Given the commutator Eq. (10), their variances obey the standard (see e.g.[15]) uncertainly relation:

$$(\Delta X)^2(\Delta Y)^2\geqslant\frac{1}{4}\,l^4,$$

where the variance of a variable A is defined as $(\Delta A)^2=\langle(\Delta\hat{A})^2\rangle$ with $\Delta\hat{A}$ here and below standing for $\Delta\hat{A}=\hat{A}-\langle\hat{A}\rangle$. If the uncertainty relation is satisfied with the equality sign, it is said that the system is in a minimum uncertainty state or, in other words, in a coherent or, more generally, in a squeezed state.

We construct the stationary squeezed state, $|\mathbf{R},N\rangle$ as a simultaneous eigenfunction of the Hamiltonian Eq. (2) and the operator $\hat{X}_\Phi$,

$$\hat{X}_\Phi\equiv\hat{X}\cos\Phi+\hat{Y}\sin\Phi, \tag{11}$$

where Φ is a complex parameter $\Phi=\Phi_1+i\Phi_2$. Under a ϕ-rotation around the z-axis, Φ transforms to $\Phi\to\Phi'=\Phi-\phi$, and $\hat{X}_\Phi$ can be also represented as

$$\hat{X}_\Phi=\hat{X}'\cosh\Phi_2+i\hat{Y}'\sinh\Phi_2, \tag{12}$$

where $\hat{X}'=\hat{X}\cos\Phi_1+\hat{Y}\sin\Phi_1$ and $\hat{Y}'=-\hat{X}\sin\Phi_1+\hat{Y}\cos\Phi_1$ are the Cartesian components of the guiding center $\mathbf{R}$ in the principal axes where $\Phi_1'=0$.

The state $|\mathbf{R},\,N\rangle$ is found from the following system of equations

$$\hat{H}|\mathbf{R},\,N\rangle=\hbar\omega_c\left(N+\frac{1}{2}\right)|\mathbf{R},\,N\rangle, \tag{13}$$

$$\hat{X}_\Phi|\mathbf{R},\,N\rangle=(X\cos\Phi+Y\sin\Phi)|\mathbf{R},\,N\rangle. \tag{14}$$

The quantum numbers of a state are the Landau level number N, and the expectation value of the guiding center position, $\mathbf{R}(X,Y)$; two real parameters X and Y specify the complex eigenvalue X_Φ.

The operator $\hat{X}_\Phi$ is not Hermitian and the eigenvalue problem may or may not have solutions among physically admissible normalizable functions, $\langle\mathbf{R},\,N|\mathbf{R},\,N\rangle=1$. To find necessary conditions for the existence of physical solutions, we note that Eq. (14) leads to $\langle\mathbf{R},\,N|\Delta\hat{X}_\Phi^\dagger\Delta\hat{X}_\Phi|\mathbf{R},\,N\rangle=0$, or, using the representation in Eq. (12) and Eq. (10),

$$(\Delta X')^2+\tanh^2\Phi_2(\Delta Y')^2=-l^2\tanh\Phi_2. \tag{15}$$

Observing that the l. h. s. is positive definite, we conclude that Eq. (14) has normalizable solutions only if $\Phi_2<0$ (or, more generally, $eB\Phi_2<0$).

The real and imaginary parts of the relation $\langle\mathbf{R},\,N|(\Delta\hat{X}_\Phi)^2|\mathbf{R},\,N\rangle=0$, give

$$(\Delta Y')^2\tanh^2\Phi_2=(\Delta X')^2, \tag{16}$$

$$\langle\Delta\hat{X}'\Delta\hat{Y}'+\Delta\hat{Y}'\Delta\hat{X}'\rangle=0, \tag{17}$$

$$(\Delta X')^2(\Delta Y')^2=\frac{l^2}{4}. \tag{18}$$

The last relation follows from the first two combined with Eq. (15). Also,

$$(\Delta X')^2=\frac{l^2}{2}\,|\tanh\Phi_2|,\quad (\Delta Y')^2=\frac{l^2}{2}\,|\coth\Phi_2|. \tag{19}$$

According to Eq. (18), the eigenfunctions of $\hat{X}_\Phi$ indeed belong to the class of minimum uncertainly states. From Eq. (17), one sees that the physical meaning of Φ_1 is to show the orientation of the principal axes, along which the quantum fluctuations of the guiding center position are independent. It follows from Eq. (16) that Φ_2 controls the relative uncertainty of the projection of the guiding center onto the principal axes.

To find the wave functions of the squeezed states, we first consider the states from the Landau level $N=0$, $|\mathbf{R},0\rangle$ and solve the following system of equations

$$\hat{c}|\mathbf{R},0\rangle=0, \tag{20}$$

$$\hat{X}_\Phi|\mathbf{R},0\rangle=X_\Phi|\mathbf{R},0\rangle \tag{21}$$

(Eq. (20) is equivalent to Eq. (13) for the ground state $N=0$.) To find the explicit form of the wave functions, we choose the symmetric gauge

$$\mathbf{A}=\frac{1}{2}\,\mathbf{B}\times\mathbf{r}, \tag{22}$$

where different directions are treated on equal footing.

In the notations

$$\tilde{x}_\Phi=(x-X)\cos\Phi+(y-Y)\sin\Phi,$$

$$\tilde{y}_\Phi=-(x-X)\sin\Phi+(y-Y)\cos\Phi \tag{23}$$

($\tilde{y}_\Phi=\tilde{x}_{\Phi+\pi/2}$), the operators in Eq. (20) and Eq. (21) take the form

$$i\,\frac{\sqrt{2}}{l}\,e^{-i\Phi}\hat{c}=\frac{\partial}{\partial\tilde{x}_\Phi}+i\,\frac{\partial}{\partial\tilde{y}_\Phi}+\frac{1}{2l^2}\,(\tilde{x}_\Phi+i\tilde{y}_\Phi)+\frac{1}{2l^2}\,(X_\Phi+iY_\Phi), \tag{24}$$

$$\hat{X}_\Phi=\tilde{x}_\Phi-il^2\,\frac{\partial}{\partial\tilde{y}_\Phi}+X_\Phi, \tag{25}$$

where $Y_\Phi=-X\sin\Phi+Y\cos\Phi$.

In the coordinate representation, Eqs. (20) and (21) become a system of linear differential equations of the first order for $\Psi(\mathbf{r}|\mathbf{0},\,\mathbf{R})=\langle\mathbf{r}|\mathbf{R},\,0\rangle$. The normalized solution reads

$$\Phi(\mathbf{r}|0,\,\mathbf{R})=C_\Phi\exp\left(-\frac{1}{2l^2}\,(\tilde{x}_\Phi^2+i\tilde{x}_\Phi\tilde{y}_\Phi+i\tilde{x}_\Phi Y_\Phi-i\tilde{y}_\Phi X_\Phi)\right), \tag{26}$$

where C_Φ is the normalization constant

$$|C_\Phi|^2=\frac{1}{2\pi l^2}\,\sqrt{1-\exp 2i(\Phi^*-\Phi)}. \tag{27}$$

As expected, the function in Eq. (26) is normalizable and Eq. (27) is meaningful, only if $\mathrm{Im}\,\Phi<0$.

The normalized states for the Nth Landau level, eigenfunctions of the Hamiltonian in Eq. (5), can be now found from

$$\Psi(\mathbf{r}|N,\,\mathbf{R})=\frac{1}{\sqrt{N!}}\,(\hat{c}^\dagger)^N\Psi(\mathbf{r}|0,\,\mathbf{R}). \tag{28}$$

The calculation can be easily done with the help of the following identity

$$\hat{c}^\dagger=e^{-i\Phi}e^{\Lambda}\left(\frac{l\hbar}{i\sqrt{2}}\,\frac{\partial}{\partial\tilde{x}_\Phi}\right)e^{-\Lambda},$$

$$\Lambda\equiv\frac{1}{2l^2}\,(\tilde{x}_\Phi^2-i\tilde{x}_\Phi\tilde{y}_\Phi-i\tilde{x}_\Phi Y_\Phi+i\tilde{y}_\Phi X_\Phi). \tag{29}$$

After some algebra we obtain,

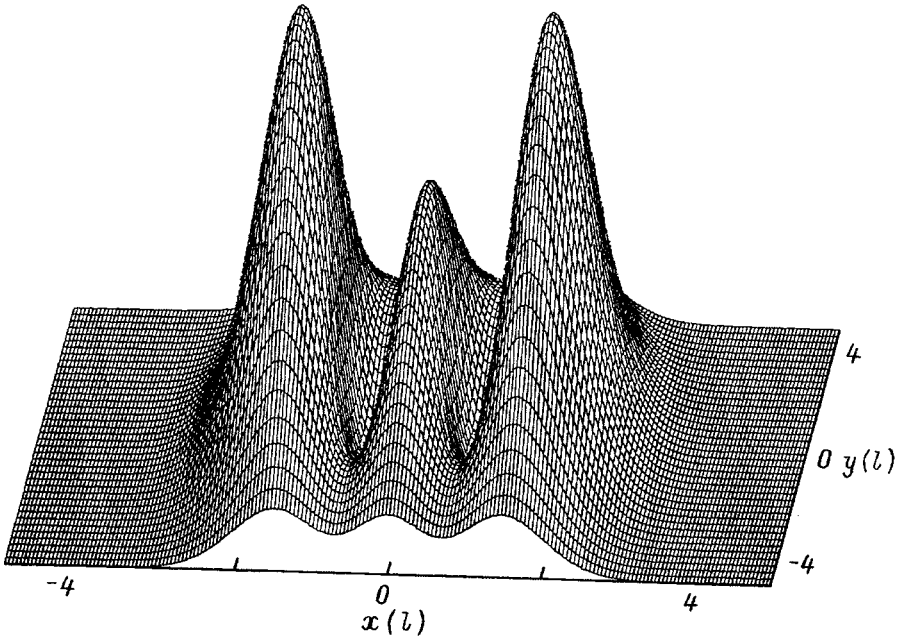

FIG. 1. The probability density for the state $N=2$, $|\tanh \Phi_2|=0.1$, $\Phi_1=0$ located at the origin $R=0$.

$$\Psi(\mathbf{r}|N,\ \mathbf{R})=C_\Phi \frac{(ie^{-i\Phi})^N}{\sqrt{2^N N!}} \times \exp\left(i \frac{e}{2\hbar c} \mathbf{B}\cdot(\mathbf{B}\times\mathbf{r}) - \frac{1}{2l^2}\tilde{x}_\Phi(\tilde{x}_\Phi+i\tilde{y}_\Phi)\right) H_N\left(\frac{\tilde{x}_\Phi}{l}\right), \tag{30}$$

where $H_N(\xi)$ is the Hermite polynomial, $H_N(\xi)=(-1)^N e^{\xi^2}(d^N e^{-\xi^2})/(d\xi^N)$. In the coordinate representation, this expression gives the wave function of the squeezed state $|\mathbf{R},\ N\rangle$ centered at $\mathbf{R}$ and belonging to the Nth Landau level [in the symmetric gauge Eq. (22)]; the ''rotation angle'' Φ in Eq. (23) is a complex parameter, $\mathrm{Im}\,\Phi<0$.

3. PROPERTIES

The basic features of squeezed states can be seen in Figs. 1 and 2, where the density and the current are plotted for a typical state: $N=2$, $\Phi=i\Phi_2$, $|\tanh \Phi_2|=0.1$. The squeezed state is localized in the sense that it has a finite extension in both x- and y-directions. Qualitatively, the squeezed state is a superposition of classical Larmor orbits of radius $\rho_N=\sqrt{2E_N/m\omega^2}$, the centers of which are positioned in the vicinity of $\mathbf{R}$ with a typical deviation $\Delta X'$ and $\Delta Y'$. From Eq. (19), $\Delta X'/\Delta Y'=|\tanh \Phi_2|<1$ so that the state is elongated in the direction of the principal y'-axis. When Φ_2 tends to zero, the elongation increases and the squeezed state asymptotically transforms into a ''strip'' (of length $\sim l/|\Phi_2|$).

The wave function of a squeezed state from the Nth Landau level has N isolated zeroes in the x-y plane. The zeroes are at the points on the line $\mathrm{Im}\,\tilde{x}_\Phi=0$, where the Hermite polynomial $H_H(\tilde{x}_\Phi/l)$ has its N roots. In the limit $\Phi_2 \to -\infty$, the zeroes gather together at the point $\mathbf{r}=\mathbf{R}$. This limit, where $\Delta X=\Delta Y=1/2$, gives the stationary coherent state introduced by Malkin and Man'ko,[7] the angular momentum eigenstate with the eigenvalue $L_z=-\hbar N$. In the coherent states, the probability density is rotationally invariant.

In quantum optics, squeezed states can be presented as the result of the action of the ''squeezed operator'' on the coherent state. Similar to Ref. 12, squeezed of the cylindrically symmetric coherent states ($\mathrm{Im}\,\Phi\to-\infty$) is achieved by applying

$$\hat{S}=\exp\left\{ \frac{i}{2l^2} r(\hat{X}'\hat{Y}'+\hat{Y}'\hat{X}') \right\}, \tag{31}$$

where $\tanh r=e^{2\Phi_2}$. In optics there are certain non-linear processes with the evolution operator in the form of $\hat{S}$.[16] A coherent state then evolves into the squeezed state. For the case of a particale in a magnetic field, the analogous problem of preparation of a squeezed state has been considered in Ref. 13.

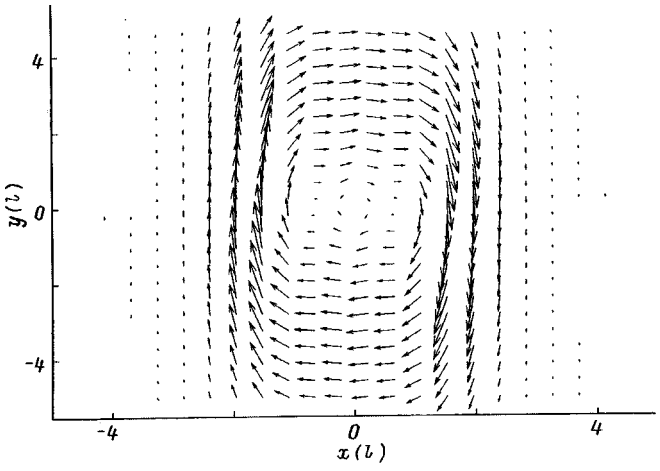

FIG. 2. The current density for the state $N=2$, $|\tanh \Phi_2|=0.1$, $\Phi_1=0$ located at the origin $R=0$.

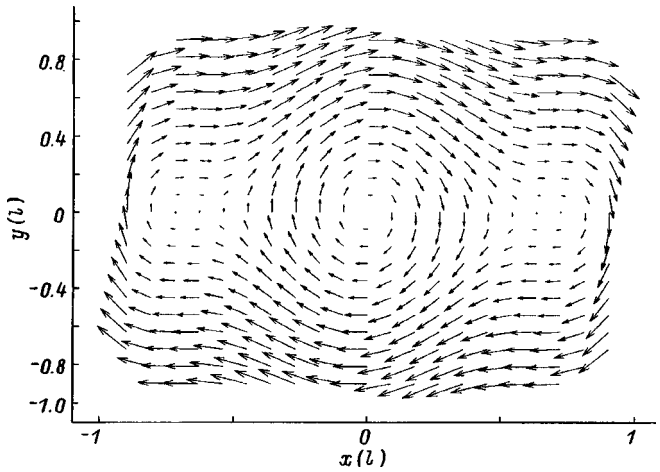

FIG. 3. Detail of the current density for the state $N=2$; $|\tanh \Phi_2|=0.1$, $\Phi_1=0$ located at the origin $R=0$.

As discussed in the Appendix, the product of the mirror and time reversal transformations is a valid symmetry element. As a consequence, the distribution of the density and current are mirror symmetric (relative to the principal axes) as also apparent in Figs. 1–4.

Within a given Landau level, the squeezed states, eigenfunctions of a non-Hermitian operator $\hat{X}_\Phi$, are nonorthogonal. For the states defined in Eq. (30) with the real positive normalization constant C_Φ Eq. (27), the overlap integral reads

$$\langle \mathbf{R};\Phi,N|\mathbf{R}';\Phi',n'\rangle = \delta_{NN'}\frac{(1-\exp[2i(\Phi^*-\Phi)])^{1/4}(1-\exp[2i(\Phi'^*-\Phi')])^{1/2}}{(1-\exp[2i(\Phi^*-\Phi')])^{1/2}} \times \exp\left(\frac{ie}{2\hbar c}\,\mathbf{B}\cdot(\mathbf{R}'\times\mathbf{R})+\frac{i}{2l^2}\,\frac{(X'_{\Phi'}-X_{\Phi'})(X'_{\Phi^*}-X_{\Phi^*})}{\sin(\Phi'-\Phi^*)}\right) \tag{32}$$

$(\mathrm{Re}(1-\exp[2i(\Phi^*-\Phi')])^{1/2}>0)$. The overlap of the states differing in the Larmor center position $\mathbf{R}$ or the parameter Φ does not depend on the Landau level number N as it follows from the Eq. (28) and the commutation relation in Eq. (5). Therefore, the overlap integral in Eq. (32) can be calculated using the Gaussian wave functions for $N=0$ in Eq. (26).

Repeating the derivation known in the theory of coherent states of a harmonic oscillator (see e.g. Ref. 5), one can show that the set of squeezed states is complete i.e. the closure relation,

$$\hat{1}=\sum_{N=0}^{\infty}\int \frac{d^2\mathbf{R}}{2\pi l^2}\,|\mathbf{R},\,N\rangle\langle\mathbf{R},\,N|, \tag{33}$$

is valid. As in the harmonic oscillator case, the states $|\mathbf{R},N\rangle$ with continuously varying $\mathbf{R}$ form an overcomplete set within the Nth Landau level. Repeating Perelomov's arguments,[17] one can show that the subset of states with $\mathbf{R}$'s on the sites of a periodic lattice is overcomplete if the lattice is too dense (the unit cell area $s_0<2\pi l^2$) and is not complete for a too dilute lattice ($s_0>2\pi l^2$). When $s_0=2\pi l^2$ (i.e., the flux through the unit cell equals to the flux quantum hc/e), the system of the functions is complete and it remains complete even if a single state is removed; it becomes incomplete, however, if any two states are removed.

In conclusion, stationary squeezed states of a charged particle in a homogeneous magnetic field have been constructed and analyzed. The distinctive feature of the squeezed states is the minimal quantum uncertainty of the position of the Larmor circle center. The family of the squeezed states is characterized by the squeezing parameter $\mathrm{Im}\,\Phi$ variation of which allows one to transform gradually strip-like states (infinitely extended in the direction controlled by $\mathrm{Re}\,\Phi$) to eigenfunctions of the angular momentum with rotationally invariant density distribution. The squeezed states have a rather simple structure: As it follows from Eqs. (30) and (23), a general squeezed state can be obtained from

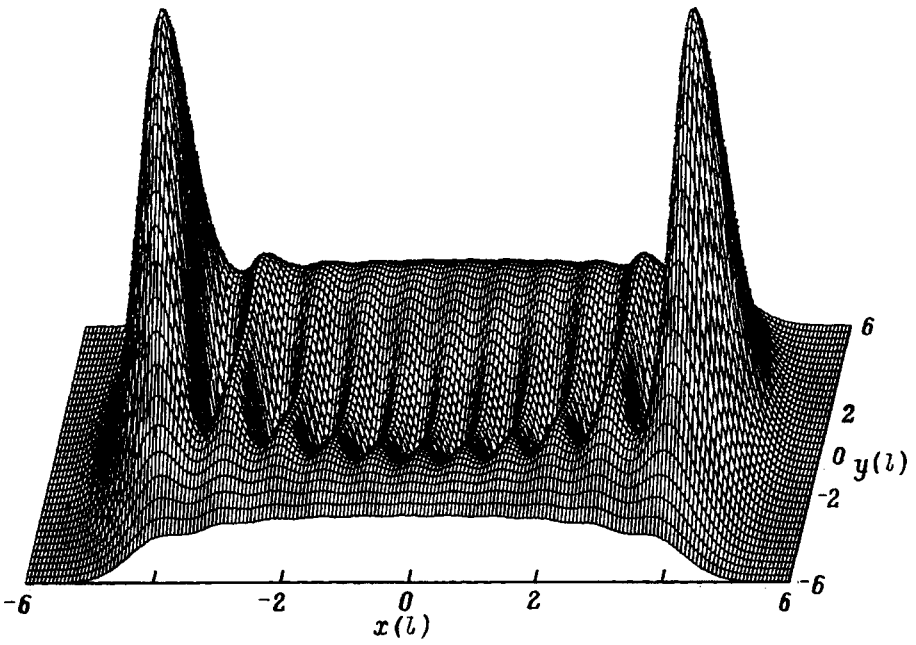

FIG. 4. The probability density for the state $N=10$; $|\tanh \Phi_2|=0.1$, $\Phi_1=0$ located at the origin $R=0$.

a Landau ''strip'' by a complex angle rotation of the coordinates. The simplicity of the construction gives the hope that the squeezed states may turn out to be useful.

We are grateful to Jørgen Rammer for reading the manuscript and valuable remarks. We also thank V. V. Dodonov for drawing our attention to Refs. 12 to 14

This work was supported by the Swedish Natural Science Research Council.

APPENDIX. SYMMETRIES OPERATORS

The physical symmetry of a system in an external magnetic field is controlled by the symmetry of the vector field $\mathbf{B}(\mathbf{r})$ (among other factors). However, the Hamiltonian, $\hat{H}=\hat{H}_{\mathbf{A}}$ contains the vector potential $\mathbf{A}(\mathbf{r})$ rather than $\mathbf{B}$. The vector field $\mathbf{A}(\mathbf{r}$ has a lower symmetry and, moreover, the spatial symmetry of $\mathbf{A}(\mathbf{r})$ is gauge dependent. For this reason, the Hamiltonian often does not commute with the operator corresponding to a physical symmetry element. A homogeneous magnetic field gives a simple example: the translation invariance is preserved but the vector potential is always $\mathbf{r}$-dependent. It is well-known[3] that the symmetry operator should include a certain gauge transformation which compensates the change of the $\mathbf{A}$ field generated by the symmetry transformation.

To build the modified operators on a regular basis, we suggest the following procedure. For any given symmetry element $\mathcal{O}$, it is always possible to find field $\mathbf{A}^{(\mathcal{O})}(\mathbf{r})$, $\mathbf{curl}\,\mathbf{A}^{(\mathcal{O})}=\mathbf{B}$, which is invariant relative to $\mathcal{O}$: $\mathcal{O}\mathbf{A}^{(\mathcal{O})}=\mathbf{A}^{(\mathcal{O})}$. Whatever gauge is chosen for $\mathbf{A}$ in Eq. (2), the gauge transformation, $\hat{G}_{\mathcal{O}}^{-1}\hat{H}_{\mathbf{A}}\hat{G}_{\mathcal{O}}$, specified by

$$\hat{G}_{\mathcal{O}}=e^{i\xi^{(\mathcal{O})}},\quad \xi^{(\mathcal{O})}(\mathbf{r})=\frac{e}{\hbar c}\int_0^{\mathbf{r}}d\mathbf{r}(\mathbf{A}-\mathbf{A}^{(\mathcal{O})}), \tag{A1}$$

changes the vector potential entering the Hamiltonian from $\mathbf{A}$ to $\mathbf{A}-\nabla_{\mathbf{r}}\chi^{(\mathcal{O})}=\mathbf{A}^{(\mathcal{O})}$, i.e., $\hat{G}_{\mathcal{O}}^{-1}\hat{H}_{\mathbf{A}}\hat{G}_{\mathcal{O}}=\hat{H}_{\mathbf{A}^{(\mathcal{O})}}$. By construction, $\mathcal{O}$ does not change the vector field $\mathbf{A}^{(\mathcal{O})}(\mathbf{r})$ and, therefore, the transformed operator $\hat{G}_{\mathcal{O}}^{-1}\hat{H}_{\mathbf{A}}\hat{G}_{\mathcal{O}}$ commutes with $\mathcal{O}$, i.e.

$$(\hat{G}_{\mathcal{O}}^{-1}\hat{H}_{\mathbf{A}}\hat{G}_{\mathcal{O}})\hat{\mathcal{O}}=\hat{\mathcal{O}}(\hat{G}_{\mathcal{O}}^{-1}\hat{H}_{\mathbf{A}}\hat{G}_{\mathcal{O}})$$

or

$$\hat{H}_{\mathbf{A}}(\hat{G}_{\mathcal{O}}\hat{\mathcal{O}}\hat{G}_{\mathcal{O}}^{-1})=(\hat{G}_{\mathcal{O}}\hat{\mathcal{O}}\hat{G}_{\mathcal{O}}^{-1})\hat{H}_{\mathbf{A}}.$$

Therefore, it is the operator

$$\hat{\mathcal{O}}_{\mathbf{A}}=\hat{G}_{\mathcal{O}}\hat{\mathcal{O}}\hat{G}_{\mathcal{O}}^{-1}, \tag{A2}$$

which commutes with the Hamiltonian $\hat{H}_{\mathbf{A}}$ and represents the symmetry element $\mathcal{O}$. As such, the operator $\mathcal{O}_{\mathbf{A}}$ depends on the gauge chosen for the vector potential $\mathbf{A}$ in the Hamiltonian, but its matrix elements are gauge invariant if the sandwiching functions are gauge transformed in the usual manner.

Equivalently, the symmetry operator in Eq. (A2) can be written as

$$\hat{\mathcal{O}}_{\mathbf{A}}=e^{i(\chi^{(\mathcal{O})}(\mathbf{r})-\chi^{(\mathcal{O})}(\hat{\mathcal{O}}\mathbf{r}))}\hat{\mathcal{O}}, \tag{A3}$$

or

$$\hat{\mathcal{O}}_{\mathbf{A}}=\hat{\mathcal{O}}e^{i(\chi^{(\mathcal{O})}(\hat{\mathcal{O}}^{-1}-\mathbf{r})-\chi^{(\mathcal{O})}(\mathbf{r}))}. \tag{A4}$$

Below, we analyze only the case of a homogeneous magnetic field but the method is generally applicable.

In the presence of a homogeneous magnetic field, the translations in the x-y plane and rotations around the z-axis remain (continuous) symmetry elements. As the reflection, σ_v, in a plane passing through the z axis (yOz, for definiteness), reverses the magnetic field, σ_v is not a symmetry element. We note here that the product of time-reversal T and σ_v, both reversing the field, is a symmetry element. We denote the product by $\sigma_T\equiv T\sigma_v$.

The transformation $\mathcal{O}$ changes the wave function as, $\psi\overset{\mathcal{O}}{\rightarrow}\hat{\mathcal{O}}\psi$, where $\hat{\mathcal{O}}$ denotes the operator associated with $\mathcal{O}$. For translations and rotations, the form of the operator $\hat{\mathcal{O}}$ is obvious; in the case of σ_T,

$$\hat{\sigma}_T\psi(x,y)=\psi^*(-x,y), \tag{A5}$$

and $\hat{\sigma}_T$ is an anti-linear anti-unitary operator. From $\hat{\mathcal{O}}^{-1}\hat{H}_{\mathbf{A}}\hat{\mathcal{O}}\equiv\hat{H}_{\mathcal{O}\mathbf{A}}$, the transformed vector field $\mathcal{O}\mathbf{A}$ can be found. Again, the result is obvious in case of rotations and translations. Under σ_T, which is the mirror reflection of the polar vector field $\mathbf{A}(\mathbf{r})$ in combination with time reversal ($\mathbf{A}\rightarrow-\mathbf{A}$), the vector potential transforms as: $\hat{\sigma}_T A_x(x,y)=A_x(-x,y)$, $\hat{\sigma}_T A_y(x,y)=-A_y(-x,y)$.

First, we consider the operator of a finite translation $\hat{\mathcal{O}}=\hat{T}_{\mathbf{a}}$, $\hat{T}_{\mathbf{a}}\psi(x,y)=\psi(x+a_x,y+a_y)$, $\mathbf{a}$ being the translation vector. The vector potential, $\mathbf{A}^{(\mathcal{O})}\equiv\mathbf{A}^{(\mathbf{a})}$, invariant relative to the translation along $\mathbf{a}$, $\mathbf{A}^{(\mathbf{a})}(\mathbf{r})=\mathbf{A}^{(\mathbf{a})}(\mathbf{r}+\mathbf{a})$, can be taken as,

$$\mathbf{A}^{(\mathbf{a})}=n((\mathbf{B}\times\mathbf{r})\cdot n),\quad \mathbf{a}=|\mathbf{a}|\mathbf{n}, \tag{A6}$$

(''Landau gauge''). Using Eq. (A3), the operator of magnetic translation reads

$$\hat{T}_{\mathbf{A}}^{(\mathbf{a})}=e^{(ie/ch)\int_{2+\mathbf{a}}^{2}d\mathbf{r}'(\mathbf{A}(\mathbf{r}')-\mathbf{A}^{(\mathbf{a})}(\mathbf{r}'))}e^{(i/h)\hat{\mathbf{p}}\cdot\mathbf{a}}, \tag{A7}$$

$\hat{\mathbf{p}}=(\hbar/i)\nabla$ being the canonical momentum. As a consequence of the physical translational invariance, this operator commutes with the Hamiltonian Eq. (2) for arbitrary gauge of the vector potential $\mathbf{A}(\mathbf{r})$.

Up to terms linear in $\mathbf{a}$, $\hat{T}_{\mathbf{A}}^{(\mathbf{a})}=1+(i/\hbar)\mathbf{a}\cdot(\hat{\mathbf{p}}-(e/c)\mathbf{A}+(e/c)\mathbf{A}^{(\mathbf{a})})$ or, using Eq. (A6), $\hat{T}_{\mathbf{A}}^{(\mathbf{a})}=1+(i/\hbar)\mathbf{a}\cdot(\hat{\mathbf{p}}-(e/c)\mathbf{A}+(e/c)\mathbf{B}\times\mathbf{r})$. From here, one reads off the expression for the generator of translations $\hat{\mathbf{P}}$ and derives Eq. (6).

This derivation of Eq. (6) links $\hat{\mathbf{P}}$ to the translational symmetry. The same expression for $\hat{\mathbf{P}}$ can be derived in a more intuitive manner. First, one considers the operator of the guiding center $\hat{\mathbf{R}}$, the expression for which in Eq. (8) can be guessed from the correspondence principle. Since $\mathbf{R}$ is a classical integral of motion, $\hat{\mathbf{R}}$ must commute with the Hamiltonian. Now, one defines $\hat{\mathbf{P}}$ by Eq. (1) and comes immediately to Eq. (6).

Next we consider rotations i.e., $\mathcal{O}=R$. The ''bare'' operator of a rotation around the z-axis is $\hat{R}=e^{1/\hbar(\mathbf{r}\times\hat{\mathbf{p}})_z\phi}$, ϕ being the angle of the rotation. The R-invariant vector potential is $\mathbf{A}^{(R)}=(1/2)\mathbf{B}\times\mathbf{r}$. Applying Eq. (A2), the symmetry operator reads:

$$\hat{R}_{\mathbf{A}}(\phi)=e^{i(e/ch)\int_0^2 d\mathbf{r}(\mathbf{A}-\mathbf{A}^{(R)})}e^{i/h(\mathbf{r}\times\mathbf{p})_z\phi}e^{-i(e/ch)\int_0^2 d\mathbf{r}(\mathbf{A}-\mathbf{A}^{(R)})}. \tag{A8}$$

In the limit $\phi\to 0$, $\hat{R}_{\mathbf{A}}(\phi)\approx 1+(i/\hbar)\hat{\mathcal{L}}_z\phi$, where the generator of rotations $\hat{\mathcal{L}}_z$ is

$$\hat{\mathcal{L}}_z=e^{i(e/ch)\int_0^{\mathbf{r}} d\mathbf{r}(\mathbf{A}-\mathbf{A}^{(R)})}(\mathbf{r}\times\hat{\mathbf{p}})_z e^{-i(e/ch)\int_0^2 d\mathbf{r}(\mathbf{A}-\mathbf{A}^{(R)})}.$$

Simplifying and using the expression for $\mathbf{A}^{(R)}$, one gets

$$\hat{\mathcal{L}}_z=\left(\mathbf{r}\times\left(\hat{\mathbf{p}}-\frac{e}{c}\mathbf{A}\right)\right)_z+\frac{e}{2c}(\mathbf{r}\times(\mathbf{B}\times\mathbf{r}))_z. \tag{A9}$$

For the case of a homogeneous magnetic field, this operator commutes with the Hamiltonian for arbitrary gauge of the vector potential and reduces to the usual angular momentum $\hat{L}_z=\mathbf{r}\times\hat{\mathbf{p}}$ when $\mathbf{A}$, $\mathbf{B}\to\mathbf{0}$. Also, $\hat{\mathcal{L}}_z=\hat{L}_z$ in the symmetric gauge $\mathbf{A}=(1/2)\mathbf{B}\times\mathbf{r}$.

The operator $\mathcal{L}_z$ can be written in the following identically equivalent forms

$$\hat{\mathcal{L}}_z=\frac{1}{2}\frac{eB}{c}\hat{\mathbf{R}}^2-\frac{mc}{eB}\hat{H}, \tag{A10}$$

$$\hat{\mathcal{L}}_z=\frac{1}{2}\frac{c}{eB}\hat{\mathbf{P}}^2-\frac{mc}{eB}\hat{H}, \tag{A11}$$

$\hat{H}$, and the (two-dimensional) vectors $\hat{\mathbf{P}}$ and $\hat{\mathbf{R}}$ are defined in Eqs. (2), (6), and (8) respectively. One sees that the integral of motion $\mathcal{L}_z$ is, actually, a function of the other conserving quantities $\mathbf{P}$ (or $\mathbf{R}$) and the energy H.

If the axis of the a rotation is shifted from the origin to the point $\mathbf{R}_0$, the generator of the rotations denoted as $\hat{\mathcal{L}}_{\mathbf{R}_{0,z}}$ reads

$$\hat{\mathcal{L}}_{\mathbf{R}_{0,z}}=\frac{1}{2}\frac{eB}{c}(\hat{\mathbf{R}}-\mathbf{R}_0)^2-\frac{mc}{eB}\hat{H}. \tag{A12}$$

Note that the vector potential enters $\mathcal{L}_z$ Eq. (A9) and the generator of translations $\hat{\mathbf{P}}$ Eq. (6) only in the gauge covariant combination $\hat{\mathbf{p}}-(e/c)\mathbf{A}$ so that their matrix elements are gauge invariant.

Finally, we consider the combined mirror and time-reversal transformation in Eq. (A5): $\mathcal{O}=\sigma_T$. One can check that $\hat{\sigma}_T$ does not change the Hamiltonian in Eq. (2) if the symmetric gauge Eq. (22) is chosen. Ultimately, this is the reason for the mirror symmetry in the distribution of the density and current seen in Figs. 1–4.

[1] L. D. Landau and E. M. Lifshitz, *Quantum Mechanics* (Pergamon Press, N.Y., 1977).
[2] J. Zak, Phys. Rev. **136**, A776 (1964).
[3] E. M. Lifshitz and L. P. Pitaevskii, *Statistical Physics*, Pt 2 (Pergamon Press, 1980).
[4] L. D. Landau, Z. Phys. **64**, 629 (1930).
[5] W. M. Zhang, D. H. Feng, and R. Gilmore, Rev. Mod. Phys. **62**, 867 (1990).
[6] G. C. Darwin, Proc. R. Soc. London **117**, 258 (1928).
[7] I. A. Malkin and V. I. Man'ko, Zh. Eksp. Teor. Fiz. **55**, 1014 (1968) [Sov. Phys. JETP **27**, 527 (1968)].
[8] A. Feldman and A. H. Kahn, Phys. Rev. B **1**, 4584 (1970).
[9] S. T. Pavlov and A. V. Prokhorov, Fiz. Tver. Tela (Leningrad) **32**, 11, 3451 (1990) [Sov. Phys. Solid State **32**, 2001 (1990)].
[10] E. I. Rashba, L. E. Zhukov, and A. L. Efros, Phys. Rev. B **55**, 5306 (1997).
[11] S. Varró, J. Phys. A: Math. Gen. **17**, 1631 (1984).
[12] V. V. Dodonov, E. V. Kurmyshev, and V. I. Man'ko, in *Proceedings of the Lebedev Physics Institute*, Vol. 176 ''Classical and quantum effects in electrodynamics,'' Nova Science, Commack, N.Y. (1988) p. 169.
[13] V. V. Dodonov, V. I. Man'ko, and P. G. Polynkin, Phys. Lett. A **188**, 232 (1994).
[14] C. Aragone, Phys. Lett. A **175**, 377 (1993).
[15] A. Messiah, *Quantum Mechanics* (North-Holland, Amsterdam, 1965).
[16] D. F. Walls and G. J. Milburn, in *Quantum Optics* (Springer-Verlag, Berlin, 1994), p. 137.
[17] A. M. Perelomov, Teor. Mat. Fiz. **6**, 213 (1971).

Published in English in the original Russian journal. Reproduced here with stylistic changes by the Translation Editor.

SEMICONDUCTORS AND INSULATORS

Analysis of quantum interference between elastic and inelastic electron scattering in disordered media

B. N. Libenson and V. V. Rumyantsev

St. Petersburg State Technical University, 195251 St. Petersburg, Russia
(Submitted November 26, 1997)
Fiz. Tverd. Tela (St. Petersburg) **40**, 1413–1417 (August 1998)

A comparative analysis is made of the kinematic and dynamic approaches to describing the quantum interference that occurs when electrons in a disordered medium are subjected to simultaneous large-angle elastic scattering and multiple inelastic scattering of long-wavelength type. It is shown that both the kinematic and dynamic approaches lead to the same angular dependence of the interference effect, but that the range of variation of the degree of coherence as the scattering angle changes is found to be a factor of 2 larger for the dynamic theory than it is for the kinematic description. © *1998 American Institute of Physics.* [S1063-7834(98)00508-5]

Quantum interference between elastically scattered electron waves is the cause of weak localization of conduction electrons and increased elastic reflection of particles incident on a disordered medium from the outside. Evidence for this interference is enhancement of scattering within a narrow cone with aperture angle $\Delta\chi\sim(kl)^{-1}\ll 1$ (where k is the modulus of the electron wave vector and l is the mean free path of the particle) in the neighborhood of the directly backward direction. For some time now, much attention has been focused on the influence of inelastic scattering of electrons on their transport in disordered media. The existence of inelastic scattering disrupts the quantum interference connected with preservation of phase memory by the electrons, and is the reason for dissipative processes. It has long been assumed that the only way that inelastic scattering affects the coherent transport of particles and waves is by giving rise to dissipative processes.

However, it has recently been shown that inelastic scattering does not lead to loss of phase memory in certain cases, and can contribute strongly to constructive interference. It was found that interference between elastically and inelastically scattered electron waves can lead to the appearance of a new type of weak localization of electrons that scatter with energies that differ from the energy these particles have when incident on the disordered medium. In other words, inelastic scattering can lead to a new coherent effect in the so-called scattering channel.[1] In this case the coherence turns out to arise from electron-wave interference associated with two possible ways to realize the following process: an electron undergoes one inelastic scattering (e.g., the electron can excite a plasmon or a well-defined atomic transition) followed by large-angle scattering, either single or multiple. The single inelastic scattering causes an electron to lose a portion of its energy. This loss, which can be a fixed quantity, also implies that the electron is now in the inelastic scattering channel. Because of elastic scattering, an electron that has lost a fixed energy can then leave the medium and reenter the vacuum by passing through the same surface it used to enter the medium with its original energy. When this happens, the flux of electrons with fixed energy loss can be measured.

The study of weak localization of electrons incident on a disordered medium from vacuum and reflected back into the vacuum is of special interest because in this case it is possibile to work with a flux of monokinetic particles and directly measure the characteristic angle for primary scattering connected with the phenomenon of weak localization. Electron energies for which quantum transport effects can be easily detected are in the range of hundreds of electron volts. Despite the relatively high particle energies (compared to the energy of a conduction electron), and hence small de Broglie wavelengths of these particles, the coherence length is found to be sizable at these energies, as shown in a number of papers,[1–5] ensuring that the quantum-transport effect is well-defined.

The new form of weak localization proposed here, i.e., weak localization of particles in the inelastic scattering channel, differs from ordinary weak localization (i.e., weak localization in the elastic scattering channel) in one important respect: there is a characteristic scattering angle for which the constructive interference is most strongly marked. In contrast to ordinary weak localization, the constructive interference for this new weak localization turns out to be strongest at a scattering angle χ that differs from π, and this difference can be considerable.

The reason why constructive interference is strongest at a scattering angle of π for ordinary weak localization has long been appreciated. In Ref. 6, Kanpiezer developed a

simple graphical method to illustrate this fact. Very recently we developed a similar kinematic approach[7] to describing interference between elastic and inelastic electron scattering and a corresponding graphical method to treat it. Our kinematic description implies that the characteristic primary scattering angle for constructive interference does not equal π; instead, it depends in a rather complicated way on the value of the energy lost, on the initial energy of the incident electron, and on other system parameters. In Ref. 7 we also discussed the structure of cross-type diagrams, and found that their contribution to the scattering cross section was comparable to the contribution from ladder-type diagrams. Our treatment focuses on cross-type diagrams in which two different types of lines, i.e., one associated with elastic, the other with inelastic scattering, cross each other. In studying the angular dependence of this new type of localization we need only analyze the structure of the simplest cross-type diagrams, which include only two interaction events (one event is an elastic and the other an inelastic interaction). As shown in Ref. 2, in an unbounded medium the possibility of multiple elastic collisions does not change the scattering angle that characterizes this new type of weak localization.

In Ref. 7 we showed that the coherent part of the scattering intensity is the sum of two terms $I(\chi)=I_1(\chi)+I_2(\chi)$. The first of these has a characteristic mathematical structure which allows us to construct an easily visualized model of the corresponding coherent part of the quantum transport intensity. This model has received the label "kinematic." Its use for describing the coherent part of a quantum transport makes it possible to understand why the characteristic scattering angle (associated with I_1) differs from π in the presence of inelastic processes. The kinematic model also allows us to estimate simply, without calculations, the range of scattering angles in which constructive interference can exist. The second term I_2 supplements the first with an expression for the intensity that describes all the coherent scattering processes. In other words, I_2 supplements the kinematic description of quantum transport, converting it to a complete dynamic description. The ratio $I_2(\chi)/I_1(\chi)$ can be either larger or smaller than unity. In Ref. 7 we showed by direct calculation of the total intensity $I(\chi)$ that the angular features of the intensity I correspond to the predictions of the kinematic model. However, a detailed analysis of the coherent part of the intensity I shows that the absolute value of I differs considerably from the value given by that part of the intensity I_1 corresponding to the kinematic description.

The goal of this paper is to clarify the reason why the predictions of the kinematic model are correct even in those cases where the conditions for applicability of this model are violated. To this end we have extended our analysis of the mechanism for the new weak localization. We investigate a case where electrons are transferred to the inelastic scattering channel by excitation of bulk plasmons, since this is exactly the case where $|I_2(\chi)|>I_1(\chi)$. In contrast to our previous paper,[7] in which we considered the total intensity $I=I_1+I_2$, here we thoroughly analyze intensities I_1 and I_2 individually. When we analyze and compare the expressions for $I_1(\chi)$ and $I_2(\chi)$, we find that the part of the scattering cross section that depends on scattering angle, which corresponds to I_2, practically coincides with the corresponding dependence of the quantity I_1. Moreover, these portions are equal in magnitude, so that the presence of I_2 leads to a doubling of the angle-dependent part of the coherence scattering cross section while preserving angular features that are present in the kinematic description.

1. WEAK LOCALIZATION IN THE KINEMATIC APPROXIMATION

The effect of coherence in inelastic scattering of electrons can be characterized by the function

$$M(\chi)=\frac{\int dqq^2w(q,\omega)\mathcal{G}_C(q,\omega,\chi)}{\int dqq^2w(q,\omega)\mathcal{G}_L(q,\omega)}, \tag{1}$$

which is the degree of coherence. This function depends on the scattering angle χ. The quantity $w(q,\omega)$ in this equation is the probability for excitation of a plasmon or any other long-wavelength excitation with energy $\hbar\omega$ and momentum q. The functions $\mathcal{G}_C$ and $\mathcal{G}_L$ correspond to cross-type and ladder diagrams respectively. According to Ref. 7, they are determined by the equations

$$\mathcal{G}_C(q,\omega,\chi)=2\int d\Omega_q \mathrm{Re}\frac{1}{(E-E_{\mathbf{k}-\mathbf{q}}-\hbar\omega+iU')(E-E_{\mathbf{k}'+\mathbf{q}}-iU')}, \tag{2}$$

$$\mathcal{G}_L(q,\omega)=\int d\Omega_q\left\{\left|\frac{1}{E-E_{\mathbf{k}-\mathbf{q}}-\hbar\omega+iU'}\right|^2+\left|\frac{1}{E-E_{\mathbf{k}'+\mathbf{q}}+iU'}\right|^2\right\}. \tag{3}$$

Here $\mathbf{k}$ is the momentum of an electron incident on the disordered medium, $\mathbf{k}'$ is the momentum of an electron in its final state, U' is the imaginary potential of the medium, and $\mathbf{q}$ is the momentum of a plasmon. Because the plasmons are long-wavelength in character we have $q<q_c\sim\omega_p/v_F$, where ω_p is the plasma frequency of the medium and v_F is the Fermi velocity. The integration in Eqs. (2) and (3) extends over all directions of the vector $\mathbf{q}$. The χ-dependence of $\mathcal{G}_C(\chi)$ is a consequence of weak localization.

To analyze the mechanism for weak localization we separate out the contribution to M that corresponds to the kinematic model. Consider the case $U'/\hbar\omega\ll 1$, where the

energy lost by an electron in exciting a bulk plasmon greatly exceeds the imaginary potential. The new weak localization affects the system most strongly in this limit, and the function $\mathcal{G}_C(q,\omega,\chi)$ takes the form

$$\mathcal{G}_c(q,\omega,\chi)=\frac{2}{\hbar^2}\int d\Omega_q\left\{\pi^2\delta(\mathbf{qv}-\omega)\,\delta(\mathbf{qv}'-\omega)-\mathcal{P}\frac{1}{(\mathbf{qv}-\omega)(\mathbf{qv}'-\omega)}\right\}. \tag{4}$$

Here $\mathbf{v}$ and $\mathbf{v}'$ are velocities of an electron in the initial and final states respectively. The symbol $\mathcal{P}$ denotes the principal value of the integral.

The term containing the product of two δ functions describes that part of the scattering process corresponding to the kinematic approach.[7] The principal value of the integral of the product of Green's functions supplements this equation, raising its accuracy to a point where it corresponds to the dynamic approach. The portion of the function M that corresponds to the kinematic approximation equals

$$\mathcal{G}_C(q,\omega,\chi)|_{\text{k.a.}}=\frac{2\pi^2}{\hbar^2}\int d\Omega_q\delta(\mathbf{qv}-\omega)\,\delta(\mathbf{qv}'-\omega)=\frac{2\pi^2\theta[qv\cos(\chi/2)-\omega]}{\hbar^2 qv\sin(\chi/2)\sqrt{(qv\cos(\chi/2))^2-\omega^2}}. \tag{5}$$

Here $\theta(x)=1$ for $x>0$ and 0 for $x<0$. Substituting Eq. (5) into Eq. (1), and taking into account that $w(q,\omega)\propto q^{-2}\theta(\omega_p/v_F-q)$, we obtain the following expression:

$$M(\chi)|_{\text{k.a.}}=\frac{U'}{2\hbar\sin(\chi/2)\ln(q_c v/\omega)}\times\int_{\omega/(v\cos\chi/2)}^{q_c}\frac{dq}{q\sqrt{(qv\cos\chi/2)^2-\omega^2}}=\frac{U'\theta(q_c v\cos\chi/2-\omega)}{4\hbar\omega\sin\chi/2\ln(q_c v/\omega)}\times\left\{\pi-2\sin^{-1}\left[\frac{\omega}{q_c v\cos\chi/2}\right]\right\}. \tag{6}$$

This equation is valid when the inelastic scattering involves excitation of a bulk plasmon. Here $q_c\sim\omega/v_F$ is the maximum possible momentum of the latter.

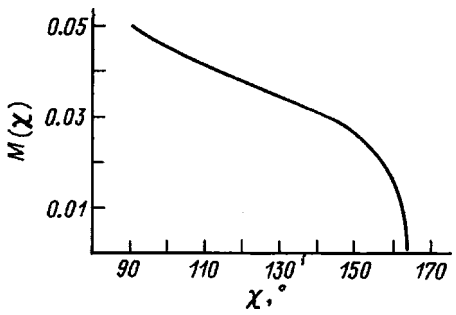

FIG. 1. Degree of coherence in the kinematic approximation. Along the abscissa we plot scattering angle χ for an electron with $q_c v/\omega_p=7$ and $U'/(\hbar\omega_p)=0.1$

Thus, the kinematic approximation corresponds to a rather simple function M, which is plotted in Fig. 1 for one possible set of parameters $q_c v/\omega$ and $U'/(\hbar\omega)$. It is easy to see that the angles at which we observe rapid changes in the function $M(\chi)|_{\text{k.a.}}$ exactly correspond to predictions that follow from the kinematic approach outlined in Ref. 7.

2. DYNAMIC CORRECTION TO THE KINEMATIC DESCRIPTION

The following portion of the function $\mathcal{G}_C$ extends the applicability of the kinematic approach:

$$\mathcal{G}_C|_{\text{d.a.}}=\frac{2}{\hbar^2}\mathcal{P}\int d\Omega_q\frac{1}{(\mathbf{qv}-\omega)(\omega-\mathbf{qv}')}, \tag{7}$$

by supplementing Eq. (5) to make up the complete expression (4). Calculation of this integral is a rather tedious procedure. Therefore, we immediately present the final result:

$$\mathcal{G}_C|_{\text{d.a.}}=\frac{2\pi^2\theta(qv-\omega/\cos\chi/2)}{\hbar^2 qv\sin(\chi/2)\sqrt{(qv\cos\chi/2)^2-\omega^2}}+\mathcal{G}_C|_{\text{d.gr.}} \tag{8}$$

Here the first term on the right side of Eq. (8) coincides with the function $\mathcal{G}_C|_{\text{k.a.}}$. The function $\mathcal{G}_C|_{\text{d.gr.}}$ has a complicated form and is given in the Appendix. The integral of this function over q is almost independent of the scattering angle χ, whereas the integral of the first term in Eq. (8) depends strongly on χ. This fact gives us license to treat the function $\mathcal{G}_C|_{\text{d.gr.}}$ as the source of a certain background whose origin is dynamic and does not contribute significantly to the angular dependence of the quantum transport.

3. DEGREE OF COHERENCE

From Eqs. (6) and (8) it follows that the expression for the degree of coherence M can be written in the form

$$M(\chi)=\frac{U'}{\hbar\,\sin(\chi/2)\int_{\omega/v}^{2k}dqqw(q,\omega)}\times\int_0^{2k}dqqw(q,\omega)\,\frac{\theta(qv\cos\chi/2-\omega)}{\sqrt{(qv\cos\chi/2)^2-\omega^2}}+M_{\text{ground}}=2M_{\text{k.a.}}+M_{\text{ground}}. \quad (9)$$

The probability function $w(q,\omega)$ is not specified here in order to emphasize that many future approaches will be correct so long as the inelastic scattering is caused by electron interactions with any long-wavelength elementary excitation, not simply with plasmons.

The dynamic correction to the kinematic approximation given in Eq. (9) consists of a sum $M_{\text{k.a.}}(\chi)+M_{\text{ground}}$. The function M_{ground} is determined from the following expression:

$$M_{\text{ground}}=\frac{\hbar U'v}{(2\pi)^2\int_0^{2k}dqqw(q,\omega)}\times\int_0^{2k}dqq^2w(q,\omega)\mathcal{G}_C|_{\text{d.gr.}}(q,\omega).$$

Since M_{ground} does not depend on the scattering angle, we are led to conclude that the dynamic correction to the degree of coherence in the kinematic approximation has exactly the same angular dependence as the kinematic approach, but because of the dynamic correction the range of variation of the degree of coherence is increased by exactly a factor of 2. The quantity M_{ground} is always negative; for this reason M is also negative over a wide range of scattering angles from $\chi_{\min}(q_cv/\omega)$ to $\chi=\pi$, where $\chi_{\min}$ decreases with decreasing q_cv/ω is.

4. DISCUSSION OF RESULTS

From the analysis given above it follows that the kinematic approach gives very good results when used to estimate the characteristic angles at which quantum interference is most important, even outside its limits of applicability, so long as the inelastic scattering channel is associated with excitations of long-wavelength type. The range of variation of the quantity $M(\chi)$ is increased by dynamic effects by a factor of 2. The contribution of the background coherent part to $M(\chi)$, which is dynamic in nature, is always negative.

Figure 2 clearly illustrates the relation between the kinematic and dynamic descriptions of the new type of localization when the inelastic behavior is associated with the generation of long-wavelength excitations with relatively large values of $q_cv/\omega=7$ (i.e., for sufficiently large electron velocities). Because of the coherent dynamic background, the degree of coherence changes sign at a scattering angle $\chi\simeq120°$. As the electron energy decreases, all the angular features of the function $M(\chi)$ shift to smaller scattering angles. In Fig. 3 we show the same three curves as in Fig. 2, but for $q_cv/\omega=3$, which corresponds to decreasing the electron energy by a factor of 5.5. In this case, as is clear from Fig. 3, the cross section for interference of elastic and inelastic scattering is negative over the entire observed range of scattering angles ($90<\chi<180°$). In order to compare these two examples, the parameter $U'/(\hbar\omega)$ was kept equal to 0.1 as before, even though the imaginary potential of the medium increases with decreasing electron energy.

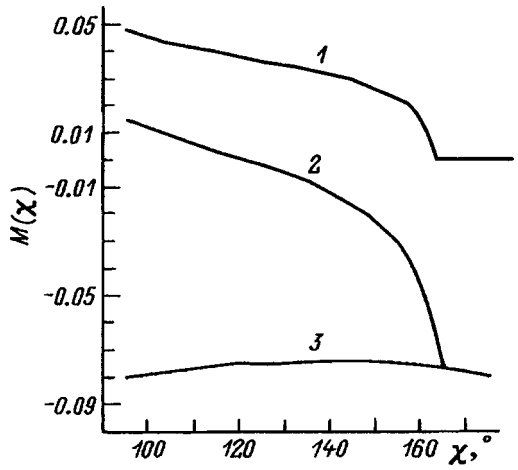

FIG. 2. Degree of coherence corresponding to the dynamic theory. The dynamic description is shown in curve *2*. Curve *1* corresponds to the kinematic approximation and is given for comparison. Curve *3* describes the function M_{ground}. Here $q_cv/\omega_p=7$, $U'/(\hbar\omega_p)=0.1$.

At relatively small electron energies the linear approximation in $U'/(\hbar\omega)$ used in this paper to describe the angular dependence of the degree of coherence may inadequate; however, the qualitative features of the function $M(\chi)$ discussed above remain in force. Exact theoretical expressions for the quantity $M(\chi)$ that are correct for any ratio $U'/(\hbar\omega)$ are given in our paper Ref. 7.

In conclusion, we should say that this work has practical value insofar as it identifies a strict correspondence between

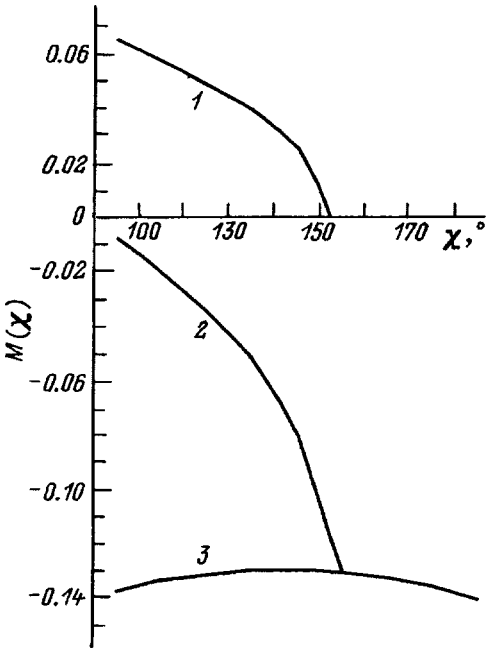

FIG. 3. Degree of coherence at low energies. $q_cv/\omega_p=3$, $U'/(\hbar\omega_p)=0.1$. The enumeration of the curves is the same as in Fig. 2.

the mathematical description and the graphical method of studying weak localization of electrons in the inelastic scattering channel. We hope that the theory of this new type of weak localization can serve as a stimulus for observing the effects we predict. Such experiments are feasible at this time, since the probability of seeing an angular dependence of the weak localization is quite large in the channel for excitation of bulk plasmons over a range of electron energies of hundreds of electron volts, which is the range for which the parameters for elastic and inelastic electron scattering given in this paper are realized.

APPENDIX

Form of the function $\mathcal{G}_C|_{\text{d.gr.}}$:

$$
\begin{aligned}
\mathcal{G}|_{\text{d.gr.}} = {} & \frac{4\pi\theta(qv-\omega)\,\text{sign}(qv+\omega/\cos\chi)}{\hbar^2 qv\sin(\chi/2)}\left\{\frac{\theta(qv-\omega/\cos\chi/2)}{\sqrt{q^2v^2\cos^2\chi/2-\omega^2}}\left[\arctan\left(\frac{qv+\omega+|qv\cos\chi+\omega|}{2\sin(\chi/2)\sqrt{q^2v^2\cos^2\chi/2-\omega^2}}\right)\right.\right. \\
& \left.\left. -\arctan\left(\frac{\cos\chi/2\sqrt{q^2v^2-\omega^2}+\omega\sin\chi/2}{\sqrt{q^2v^2\cos^2\chi/2-\omega^2}}\right)\right]+\frac{\theta(\omega/\cos\chi/2-qv)}{2\sqrt{\omega^2-q^2v^2\cos^2\chi/2}}\right. \\
& \times\left[\ln\left|\frac{qv+\omega+|qv\cos\chi+\omega|-2\sin\chi/2\sqrt{\omega^2-q^2v^2\cos^2\chi/2}}{qv+\omega+|qv\cos\chi+\omega|+2\sin\chi/2\sqrt{\omega^2-q^2v^2\cos^2\chi/2}}\right|\right. \\
& \left.\left.+\ln\left|\frac{\cos\chi/2\sqrt{q^2v^2-\omega^2}+\omega\sin\chi/2+\sqrt{\omega^2-q^2v^2\cos^2\chi/2}}{\cos\chi/2\sqrt{q^2v^2-\omega^2}+\omega\sin\chi/2-\sqrt{\omega^2-q^2v^2\cos^2\chi/2}}\right|\right]\right\}+\frac{4\pi\theta(qv-\omega)}{\hbar^2 qv\sin\chi/2}\left\{\frac{\theta(\omega/\cos\chi/2-qv)}{2\sqrt{\omega^2-q^2v^2\cos^2\chi/2}}\right. \\
& \times\left[\ln\left|\frac{qv\sin\chi/2-\sqrt{\omega^2-q^2v^2\cos^2\chi/2}}{qv\sin\chi/2+\sqrt{\omega^2-q^2v^2\cos^2\chi/2}}\right|+\ln\left|\frac{\cos\chi/2\sqrt{q^2v^2-\omega^2}-\omega\sin\chi/2+\sqrt{\omega^2-q^2v^2\cos^2\chi/2}}{\cos\chi/2\sqrt{q^2v^2-\omega^2}-\omega\sin\chi/2-\sqrt{\omega^2-q^2v^2\cos^2\chi/2}}\right|\right] \\
& \left.-\frac{\theta(qv-\omega/\cos\chi/2)}{\sqrt{q^2v^2\cos^2\chi/2-\omega^2}}\left[\arctan\left(\frac{\sqrt{q^2v^2\cos^2\chi/2-\omega^2}}{\cos\chi/2\sqrt{q^2v^2-\omega^2}+\omega\sin\chi/2}\right)+\arctan\left(\frac{\sqrt{q^2v^2\cos^2\chi/2-\omega^2}}{qv\sin\chi/2}\right)\right]\right\} \\
& +\frac{\pi\theta(\omega-qv)}{\hbar^2 qv\sin(\chi/2)\sqrt{\omega^2-q^2v^2\cos^2\chi/2}}\left[\ln\left|\frac{2\sin\chi/2\sqrt{\omega^2-q^2v^2\cos^2\chi/2}-\omega+qv\cos\chi}{2\sin\chi/2\sqrt{\omega^2-q^2v^2\cos^2\chi/2}+\omega-qv\cos\chi}\right|\right. \\
& +\ln\left|\frac{(qv-\omega\cos\chi)\sqrt{\omega^2-q^2v^2\cos^2\chi/2}-\omega\sin\chi/2(\omega-qv\cos\chi)}{(qv-\omega\cos\chi)\sqrt{\omega^2-q^2v^2\cos^2\chi/2}+\omega\sin\chi/2(\omega-qv\cos\chi)}\right|+\ln\left|\frac{2\sin\chi/2\sqrt{\omega^2-q^2v^2\cos^2\chi/2}+\omega+qv\cos\chi}{2\sin\chi/2\sqrt{\omega^2-q^2v^2\cos^2\chi/2}-\omega-qv\cos\chi}\right| \\
& \left.+\ln\left|\frac{\omega(\omega+qv\cos\chi)\sin\chi/2-(qv+\omega\cos\chi)\sqrt{\omega^2-q^2v^2\cos^2\chi/2}}{\omega(\omega+qv\cos\chi)\sin\chi/2+(qv+\omega\cos\chi)\sqrt{\omega^2-q^2v^2\cos^2\chi/2}}\right|\right].
\end{aligned}
$$

[1] B. N. Libenson, K. Yu. Platonov, and V. V. Rumyantsev, Zh. Éksp. Teor. Fiz. **101**, 614 (1992) [Sov. Phys. JETP **74**, 326 (1992)].
[2] G. Bergmann, Phys. Rev. B **28**, 2914 (1983); Phys. Rep. **107**, 1 (1984).
[3] V. V. Rumyantsev and V. V. Doubov, Phys. Rev. B **49**, 8643 (1994).
[4] E. V. Orlenko and V. V. Rumyantsev, J. Phys.: Condens. Matter **7**, 3557 (1995).
[5] E. A. Kanzieper and V. Freilikher, Phys. Rev. B **51**, 2759 (1995).
[6] E. A. Kanzieper, Phys. Rev. B **51**, 15 563 (1995).
[7] V. V. Rumyantsev, E. V. Orlenko, and B. N. Libenson, Zh. Éksp. Teor. Fiz. **111**, 1001 (1997) [JETP **84**, 552 (1997)].

Translated by Frank J. Crowne

NMR line shift of gallium in GaAs crystals in the temperature range 160–360 K

W. D. Hoffmann and D. Michel

Leipzig University, D-04103 Leipzig, Germany

I. G. Sorina and E. V. Charnaya

Scientific Institute for Physics Research of the St. Petersburg State Technical University, 198904 Petrodvorets, Russia

(Submitted January 23, 1998)
Fiz. Tverd. Tela (St. Petersburg) **40**, 1418–1419 (August 1998)

The shift in the nuclear magnetic resonance (NMR) line of ^{71}Ga isotopes in GaAs crystals is investigated in the temperature range 160–360 K. It is observed that the position of the resonance line is temperature-independent. The value of the shift relative to an isolated nucleus is 440 and 420 ppm for the three samples investigated. The roles of various contributions to the NMR line shift are discussed. © *1998 American Institute of Physics.* [S1063-7834(98)00608-X]

Single-crystal gallium arsenide (GaAs), which is one of the most widely used semiconductor compounds, has often been studied by nuclear magnetic resonance (NMR). Despite this, data on the temperature dependence of the NMR line shift of gallium nuclei in GaAs and its value at room temperature are quite contradictory.[1–5] In a number of recent papers devoted to NMR studies of bulk GaAs (for example, see Refs. 6 and 7), the shift in the resonance line is not discussed at all. The value of the shift in a GaAs crystal at room temperature was determined experimentally in Refs. 1, 2, and 5. In Ref. 3, Andrianov *et al.* investigated the NMR line shift at 4.2, 77, and 300 K, while in Ref. 4 Masterov *et al.* investigated the angular dependence of the NMR line shift and the difference between the shifts at 77 and 300 K. In Ref. 8 Barret *et al.* observed NMR in size-quantized GaAs/AlGaAs structures, and obtained information about the value of the shift by recording the signal from $Al_{0.1}Ga_{0.9}As$ barriers at $T=5.1$ K without optical pumping. The values obtained in Refs. 1–3, 5 and 8 for the shift are listed in Table I. Room-temperature chemical shifts in A_3B_5 compounds were calculated theoretically by Il'in *et al.* using the Popl single-electron method.[9] It is clear from the table that these theoretical calculations give the correct sign of the shift and a magnitude that agrees with the experimental numbers in order of magnitude. For comparison, we list values for the chemical shift in the crystal GaSb in the table as well.

In Ref. 3, it was reported that the NMR line shift for ^{71}Ga nuclei was a weak function of temperature in the range from 300 down to 77 K, which agrees with the values listed in Table I. As the temperature decreases from 77 to 4.2 K the observed shift begins to grow significantly, eventually reaching a value of approximately 250 ppm. However, the shift measured by Masterov *et al.* in Ref. 4 in the temperature range from 300 to 77 K had a value of ~ 100 ppm. Thus, there is no agreement regarding the temperature dependence of the NMR line shift of gallium nuclei in single-crystal GaAs at this time.

In this paper we investigate NMR line shifts for the isotope ^{71}Ga in three nominally pure GaAs crystals in the temperature range 160–360 K. Our measurements were made with an MSL-500 pulse spectrometer manufactured by Bruker. To observe the NMR signal we used a two-pulse quadrupole-echo sequence with pulse duration $\tau = 1.9\ \mu$s and repetition time $t=0.1$ s at a frequency $\omega_0 = 152.487$ MHz, which corresponds to the resonance frequency of an isolated nucleus. ^{71}Ga nuclei have spin $I=3/2$; however, since the GaAs crystal structure (cubic sphalerite, or zincblende) has cubic symmetry, no quadrupole splitting of the NMR line is observed. The precision of our thermal stabilization during these measurements was no worse than 0.5 K. The value of the shift was determined from the position of the line maximum. The error in determining the shift was 2 ppm, which is related to the finite width of the line. At room temperature we obtained the following values of the shift for the three samples we studied: $\delta = 440$, 440, and 420 ppm. Within the limits of error in our measurement of the line center, we observed no temperature dependence of the shift in any of the samples (see Fig. 1).

In semiconductor crystals, the NMR line shift is caused primarily by the chemical shift, although the Knight shift may also contribute.[10] The main ideas of the theory of chemical shifts were published by Ramsey in Refs. 11 and 12. According to these papers, this shift consists of two distinct terms:

$$\delta = \delta^d + \delta^p.$$

The diamagnetic term δ^d has the form

$$\delta^d = -\frac{e^2}{2mc^2}\left\langle \Psi_0 \left| \sum_i \frac{y_i^2 + z_i^2}{r_i^3} \right| \Psi_0 \right\rangle,$$

where e and m are the charge and mass of an electron, c is the velocity of light, Ψ_0 is the wave function of the ground state, and $\mathbf{r}_i$ is the radius vector to the i-th electron.

The paramagnetic term is written as follows:

TABLE I. NMR line shift of ^{71}Ga nuclei (in ppm)

Compound	T, K	Literature citation						
		[1]	[2]	[3]	[5]	[8]	Present work	[9] (Theory)
GaAs	160–360	⋯	⋯	⋯	⋯	⋯	440* 440* 420*	⋯
GaAs	300	200	270**	433***	216	⋯	440* 440* 420*	199
GaAs	77	⋯	⋯	458***	⋯	⋯	⋯	⋯
GaAs	4.2	⋯	⋯	705***	⋯	⋯	⋯	⋯
$Al_{0.1}Ga_{0.9}As$	5.1	⋯	⋯	⋯	⋯	230	⋯	⋯
GaSb	300	−80	0	⋯	−46	⋯	⋯	−39

*The measurements were made relative to a nominal frequency of an isolated ^{71}Ga nucleus.
**Measurements were made relative to the NMR line for ^{71}Ga nuclei in a crystal of GaSb.
***There is no reference point given in the paper.
Remaining data are presented relative to the position of the NMR line of a gallium nucleus in a standard water solution of $Ga(NO_3)_3$.

$$\delta^p = -\frac{2e}{m^2c^2}\frac{1}{\Delta E}\left\langle \Psi_0 \left| \sum_{k,i} \frac{l_k l_i}{r_k^3} \right| \Psi_0 \right\rangle,$$

where ΔE is the average excitation energy of the electrons from the ground state, and l_k is the orbital moment of the k-th electron.

In solids, the chemical shift is determined primarily by the paramagnetic term.[2,13,14] The diamagnetic contribution is by its nature practically temperature independent, since thermal broadening in the crystal, which in our temperature range corresponds to an insignificant 0.4%, can be neglected. The paramagnetic term is primarily determined by Van Vleck paramagnetism. This type of paramagnetism assumes that electrons are excited by the magnetic field to unoccupied shells. Since the difference between the energies of the excited states and the ground-state energy in GaAs considerably exceeds the thermal energy in our temperature interval, the paramagnetic contribution also turns out to be temperature independent.

Thus, in GaAs, only the Knight shift from free carriers can lead to any appreciable temperature dependence of the NMR line shift. The experimentally observed absence of such a temperature dependence that we report here implies that the contribution of the Knight shift is small, which is in agreement with earlier papers (see, e.g., Ref. 3). However, it is likely that the Knight contribution to the shift is the cause of the rather small discrepancy between measured values of the shift in the samples we studied.

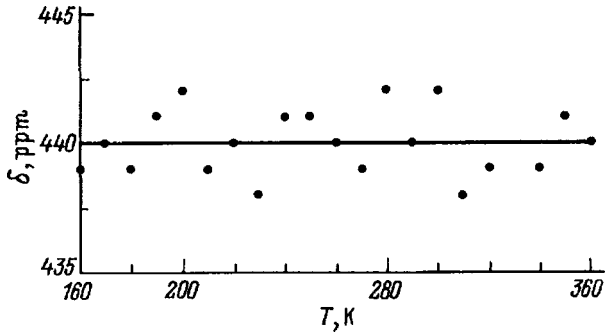

FIG. 1. Temperature dependence of the chemical shift of the NMR line of ^{71}Ga nuclei in one of the GaAs samples we studied.

This paper was partially supported by the Russian Fund for Fundamental Research (Grant 96-02-19523).

[1] H. Lütgemeier, Z. Naturforsch. **19a**, 1297 (1964).
[2] V. L. Bogdanov and V. V. Lemanov, Fiz. Tverd. Tela (Leningrad) **10**, 286 (1968) [Sov. Phys. Solid State **10**, 223 (1968)].
[3] D. G. Andrianov, Yu. B. Muravlev, N. N. Solov'ev, and V. I. Fistul', Fiz. Tekh. Poluprovodn. **8**, 604 (1974) [Sov. Phys. Semicond. **8**, 386 (1974)].
[4] V. F. Masterov, V. P. Maslov, and G. N. Talalakin, Fiz. Tekh. Poluprovodn. **11**, 1421 (1977) [Sov. Phys. Semicond. **11**, 837 (1977)].
[5] Oc Hee Han, H. K. C. Timken, and E. Oldfield, J. Chem. Phys. **89**, 6046 (1988).
[6] S. K. Buratto, D. N. Shykind, and D. R. Weitekamp, Phys. Rev. B **44**, 9035 (1991).
[7] M. Suemitsu, K. Terada, M. Mishijuma, and N. Miyamoto, Jpn. J. Appl. Phys. **31**, L1654 (1992).
[8] S. E. Barrett, R. Tycko, L. N. Pfeiffer, and K. W. West, Phys. Rev. Lett. **72**, 1368 (1994).
[9] N. P. Il'in and V. F. Masterov, Fiz. Tverd. Tela (Leningrad) **20**, 557 (1978) [Sov. Phys. Solid State **20**, 321 (1978)].
[10] A. Abragam, *Nuclear Magnetism* (Moscow, 1963), 551 pp.
[11] N. F. Ramsey, Phys. Rev. **77**, 567 (1950).
[12] N. F. Ramsey, Phys. Rev. **78**, 699 (1950).
[13] S. Hafner, J. Phys. Chem. Solids **27**, 1881 (1966).
[14] A. Leshe and S. Grande, *The Chemical Bond in Crystals* [in Russian], Nauka i Tekhnika, Minsk, 1969.

Translated by Frank J. Crowne

Optical spectra and a tail in the density of states of the disordered solid solution $ZnSe_{1-c}Te_c$

A. A. Klochikhin

St. Petersburg Nuclear Physics Institute, Russian Academy of Sciences, 188350 Gatchina, Leningrad District, Russia

S. A. Permogorov and A. N. Reznitskiĭ

A. F. Ioffe Physicotechnical Institute, Russian Academy of Sciences, 194021 St. Petersburg, Russia
(Submitted January 27, 1998)
Fiz. Tverd. Tela (St. Petersburg) **40**, 1420–1425 (August 1998)

A calculational scheme is presented to determine the density of states in the fluctuation tail for the disordered solid solution $ZnSe_{1-c}Te_c$ at concentrations below the threshold for percolation over sublattice sites. Zero-phonon absorption and luminescence bands in the region of the exciton ground state are found using an approach developed earlier. Phonon coupling is taken into account, and vibronic absorption and luminescence bands are obtained. Experimental data are shown to be in a good agreement with the calculations. © *1998 American Institute of Physics.* [S1063-7834(98)00708-4]

The disordered solid solutions $ZnSe_{1-c}Te_c$ stand apart from other II-VI compounds, because they are obtainable within the whole concentration range despite the relatively large lattice mismatch (lattice constants 5.668 and 6.089 Å for the Se and Te compounds, respectively). The interest in these systems stems from their application potential in quantum electronics.

The absorption and luminescence of $ZnSe_{1-c}Te_c$ solid solutions indicate the formation of fluctuation-induced tails in the density of states of localized excitons.[1–4] The diffuse band edge suggests that the $ZnSe_{1-c}Te_c$ solid solution is a system where substitution of Te for Se creates a strong perturbation of the valence-band electronic states, at least for Te concentrations $c \leqslant 0.30$. This conclusion is buttressed also by the fact that for low concentrations $c \approx 0.01$ the tail of the fluctuation states exhibits structural features,[1–4] which originate from localized states of small clusters consisting of two or three Te atoms. As the Te concentration increases and the average level of potential decreases, the perturbation introduced by each Te atoms decreases too, so that for $c \geqslant 0.35$ the fluctuation tail in $ZnSe_{1-c}Te_c$ becomes comparable in depth to that in $CdSe_{1-c}Se_c$.[1–4]

The $ZnSe_{1-c}Te_c$ solid solution differs from a number of other compounds of this type in a strong electron-phonon interaction, which for $c \leqslant 0.30$ gives rise in luminescence spectra to structureless features with a halfwidth ≈ 0.1 eV.[1–4] The increase of the Fröhlich coupling with LO phonons compared to the starting crystals provides supportive evidence for the onset of fairly deep exciton localization in this concentration interval, which makes possible vibronic transitions assisted by phonons whose vectors occupy a sizable part of the Brillouin zone. The decrease in localization depth with increasing Te concentration ($c > 0.3$) results also in a noticeable weakening of Fröhlich interaction, which is accompanied by a narrowing of the luminescence band and the appearance of a characteristic structure associated with LO phonons.[1,3,4]

The optical characteristics of the solid solution at the interband absorption edge are dominated by fluctuation-induced localized states of the valence band-tail. We are going to present in this work a general scheme for calculation of the density of fluctuation states, of the intrinsic luminescence band profile, and of absorption spectrum in the region of the density-of-states tail for the $ZnSe_{1-c}Te_c$ solid solution. Because the possibility of optical recombination is limited by the exciton lifetime for transition (tunneling) to lower localized states in the tail, which is accompanied by phonon emission, in order to describe the luminescence one has to find the energy distribution of such states which have no or strongly suppressed channels for nonradiative depletion. In other words, one has to know the distribution of spatially isolated localized states. In a general case, this problem is an aspect of quantum percolation theory. Isolated states in lattice models were considered in Refs. 5–8. An analog of such isolated states is in our case the states forming in potential wells of tellurium-atom clusters and, accordingly, of complexes of such clusters (superclusters).

Thus calculation of a spectrum of isolated states reduces to finding the distribution of localized tail states among superclusters in the continuum model, i.e., to a problem similar to percolation over overlapping spheres.[9–15] By applying the relations developed in classical percolation theory for overlapping spheres, to the calculation of the distribution of states over superclusters, one can establish the position of the zero-phonon luminescence band with respect to the maximum of the exciton ground-state zero-phonon absorption band and the mobility edge.

The calculation of the absorption and luminescence spectra will take into account exciton interaction with both optical and acoustic phonons. Within the concentration re-

gion of interest here, it is assumed that the electron cannot follow adiabatically the fast motion of a localized hole and interacts by Coulomb law with the hole density distribution averaged over the fluctuation well. The results obtained in this work are used to describe the luminescence spectra of the $ZnSe_{1-c}Te_c$ solid solution, for which a wealth of experimental data is available.[1–4]

1. LOCALIZED CLUSTER STATES. THE SUM RULE

We shall assume a macroscopic volume V of the solid solution consisting of N lattice sites to be filled in a random manner by atoms of two species, A and B. The diagonal matrix element of a one-band Hamiltonian $F_{\rm n}$ takes the value E_A if the site is occupied by atom A, and $E_{\rm B}$ in the opposite case. We are going to consider in this work the situation where the atomic concentration of the narrow-gap solid-solution component A is less than the critical value for percolation over the sites of the anion sublattice, $c<p_c\approx 0.2$. In these conditions, atoms A can form only clusters of finite size.

If the perturbation introduced by a cluster consisting of n atoms A exceeds the critical level and results in a splitting of a state from the bottom of the virtual-crystal band, then all higher-order clusters will likewise split off such states. In the low-concentration domain, clusters made up of two and more Te atoms in $ZnSe_{1-c}Te_c$ split off localized states.[1] We shall assume in zero approximation that the cluster wave functions do not overlap, and consider the resulting split-state spectrum. Within such an approach, the medium beyond the cluster is described in terms of the virtual-crystal approximation.

A. Isolated-cluster approximation

In this approximation, the equation of motion for any cluster can be written

$$\{\mathbf{I}+\mathbf{g}^{vc}(\omega)\mathbf{\Delta}\}_{\mathbf{nm}}\varphi^{\Delta}_{\Lambda}(\mathbf{m})=\mathbf{0}, \tag{1}$$

where $\mathbf{I}$ is the identity matrix, $\mathbf{\Delta}=\Delta_{\mathbf{n}}\delta_{\mathbf{nm}}$ is the perturbing potential at a site, $\mathbf{n}$ and $\mathbf{m}$ run through the values corresponding to the coordinates of the sites occupied by the cluster, and $\mathbf{g}^{vc}(\omega)$ is a fragment of the single-particle Green's function matrix confined to the cluster volume.

We use next the approach developed in the theory of impurity lattice dynamics[16] to obtain the eigenfunctions and eigenvalues of matrix $[\mathbf{g}^{vc}(\omega)\mathbf{\Delta}]$ whose rank is equal to the cluster size

$$\sum_{\mathbf{m}\in\mathcal{C}_{st,\varkappa}}[\mathbf{g}^{vc}(\omega)\mathbf{\Delta}]_{\mathbf{n,m}}\Phi^{\sigma}(\mathbf{m},\omega)=\lambda^{\sigma}(\omega)\Phi^{\sigma}(\mathbf{n},\omega), \tag{2}$$

where the summation runs over the sites occupied by the cluster. The eigenfunctions thus found form a complete orthonormal system

$$\sum_{\sigma}\Phi^{\sigma}(\mathbf{m},\omega)\Phi^{\sigma}(\mathbf{n},\omega)=\delta_{\mathbf{nm}}. \tag{3}$$

Using these eigenvalues and eigenfunctions, we can rewrite the matrix $\{\mathbf{I}+\mathbf{g}^{vc}(\omega)\mathbf{\Delta}\}^{-1}$ in the form

$$\{\mathbf{I}+\mathbf{g}^{vc}(\omega)\mathbf{\Delta}\}^{-1}_{\mathbf{nm}}=\sum_{\sigma}\frac{\Phi^{\sigma}(\mathbf{n},\omega)\Phi^{\sigma}(\mathbf{m},\omega)}{1-\lambda_{\sigma}(\omega)}. \tag{4}$$

In this approximation, a localized state splits off if for at least one of the σ's there exists a value $\omega=\omega_{\rm loc}>0$ that satisfies the condition

$$\lambda_{\sigma}(\omega_{\rm loc})=1. \tag{5}$$

The first to split off is always the siteless state; it has the deepest localization energy and provides the largest contribution to optical processes.

The wave functions of the split-off localized states normalized to unity can be written, accordingly, as

$$\phi^{\sigma}(\mathbf{n})=\sum_{\mathbf{m}\in\mathcal{C}_{st,\varkappa}}G^{vc}_{\mathbf{n,m}}(\omega)\Phi^{\sigma}_{\mathbf{m}}(\omega)\times\left|\sum_{\mathbf{n,m}\in\mathcal{C}_{st,\varkappa}}\Phi^{\sigma}_{\mathbf{n}}G'^{vc}_{\mathbf{n,m}}(\omega)\Phi^{\sigma}_{\mathbf{m}}\right|^{-1/2}, \tag{6}$$

where $G'^{vc}_{\mathbf{n,m}}(\omega)=\dfrac{\partial}{\partial\omega}G'^{vc}_{\mathbf{n,m}}(\omega)$.

The probability for a cluster consisting of s atoms of species A and of t atoms B on the periphery to appear is

$$g_{st}c^{s}(1-c)^{t}, \tag{7}$$

where g_{st} is the number of clusters which have the same number of atoms A and the same number of atoms B forming the perimeter but are realized in different spatial configurations. Limiting ourselves to siteless states only, we can write for the averaged density of states

$$\rho(\omega)=\sum_{s}\sum_{\varkappa=1}^{g_{st}}\sum_{\mathbf{n}}|\phi^{st,\varkappa}_{\mathbf{n}}|^{2}c^{s}(1-c)^{t}\delta(\omega-\omega^{st,\varkappa}_{loc}). \tag{8}$$

We have labeled here the eigenfunctions and eigenvalues according to the clusters they belong to. The integrated density of states split off from the band bottom of a virtual crystal calculated per site

$$\mathcal{N}(0)=\int_{0}^{E_L}\rho(\omega)d\omega=\sum_{st,\varkappa}g_{st}c^{s}(1-c)^{t}=\sum_{s}n_{s}(c), \tag{9}$$

where E_L is the Lifshits boundary for a solid solution; it coincides with the total number of clusters per site.

To calculate the number of states with localization energy in excess of ω, we have to set the upper limit of integration in Eq. (9) equal to this quantity, and begin summation on the right-hand side with a cluster size s which gives rise to a state with localization energy ω. In these conditions, the total number of split-off states will in no case exceed the number of atoms of the narrow-gap component, which is determined by the expression

$$N_A=N\sum_{s=1}^{\infty}n_{s}(c)s. \tag{10}$$

Sums of type (9) converge rapidly within the whole concentration interval. Because functions $n_s(c)$ are known for many lattices for at least a few lowest values of s, the sum rule we

have obtained can be used to estimate the number of states split off from the band bottom of the virtual crystal. To give an illustration, for a cubic fcc lattice[5,6]

$$n_1(c)=c(1-c)^{12}, \quad n_2(c)=12\,c^2(1-c)^{18},$$
$$n_3(c)=c^3[24\,(1-c)^{23}+126\,(1-c)^{24}]. \tag{11}$$

Our estimate of the probability of formation of a four-atom cluster yields

$$n_4(c)\approx 10^3 c^4(1-c)^{30}. \tag{12}$$

In accordance with the sum rule (9), these functions can be employed to estimate the number of states created below the virtual-crystal band minimum. Additional useful information can be obtained if one knows at least approximately the dependence of localization energy on the number of A atoms in the cluster. This would provide an insight into both the magnitude and behavior of the integrated density of states and the pattern of density-of-states variation.

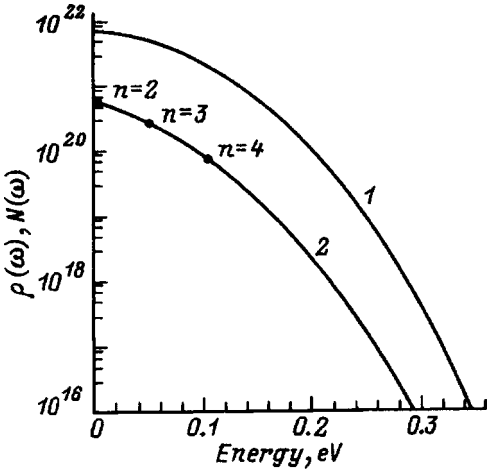

FIG. 1. Calculated (*1*) density of states $\rho(\omega)$ and (*2*) integrated density of states $\mathcal{N}(\omega)$ in the fluctuation tail for the $ZnSe_{1-c}Te_c$ solid solution ($c=0.15$). Filled circles - estimates of the integrated density of states made by the sum rule.

B. Approximate description of the $\rho(\omega)$ relation

To describe the $\rho(\omega)$ relation in the vicinity of the mobility edge and below it, we assume that in zero approximation all states with localization energy ω_j in excess of some energy ω_0 can be considered localized and well isolated from one another. The value of ω_0 measured relative to E_G should be chosen so that the total number of states with energy in excess of this value

$$\mathcal{N}(\omega_0)=\int_{\omega_0}^{E_L}\rho(\omega)d\omega \tag{13}$$

satisfies the condition

$$\mathcal{N}(\omega_0)a^3\ll 1\,. \tag{14}$$

Here $a\approx\sqrt{\hbar^2/2M\omega_0}$ determines the characteristic exponential-decay length of the wave function of a single quantum well outside it.

The quantity ω_0 plays the part of the upper boundary of the region within which the theory is valid. ω_0 and the position of the mobility edge ω_{ME} turn out to be of the same order of magnitude, and they are both larger than the Urbach parameter ε_U, which determines the exponential decay of the density of localized states for energies above ω_{ME}.

To calculate the $\rho(\omega)$ relation, we use the effective-mass approximation and the approach developed in Refs. 17–20. To estimate the absolute value of the density of states, we find the coefficient of proportionality by joining the approximate value of the integrated density of states with the function found by means of the sum rule for the interval between the localization energies for clusters with $s=3$ and 4 atoms of species A. The results of these calculations are displayed in Fig. 1. The localization energies for clusters with $s=2-4$ were found in the effective mass approximation for spherical potential wells of the corresponding size. This procedure gives the density of states presented in Fig. 1 for $\omega\geqslant\omega_0$, and permits extrapolation of this function to the region $\omega\leqslant\omega_0$.

C. Zero-phonon absorption and luminescence bands

We shall use for description of the zero-phonon absorption band the method developed earlier in Refs. 17 and 18. It permits one to describe the $1s$ exciton band profile in terms of the model of a localized hole and an electron bound to it by Coulomb interaction (referred to as model II in Refs. 17 and 18) for $\omega\geqslant\omega_0$, i.e., the main part of the zero-phonon absorption band.

The main parameters of the problem that determine the Urbach slopes are $\Delta=|E_A-E_B|$ and Δ/E_{cr}, with the critical value of the perturbation potential in the lattice version of the model related to the electron Green's function through

$$E_{cr}^{-1}=G_{\mathbf{nn}}^{vc}(0).$$

Experimental values of the Urbach energy $\varepsilon_U(c)$ were extracted from absorption coefficient measurements[1,3]. This provided a possibility for estimating the parameters Δ and Δ/E_{cr}, which were found to be ≈ 1 eV and ≈ 0.8 eV, respectively.

a) *Zero-phonon luminescence line*. When atoms of two species are distributed in a random way, the fluctuation-induced potential wells are likewise scattered randomly throughout the crystal volume. In a very crude approximation, the states of interest to us here are isolated from one another. This is valid, however, only for states with a sufficiently high localization energy. As one approaches the mobility edge, a progressively larger part of these states begins to belong not to a single cluster but rather to their complexes (superclusters).

Following the calculational scheme adopted in Ref. 18, we shall assume that one can specify for each cluster a sphere of radius $R_{int}>a$ such that, if for a given concentration of localized states within the sphere volume $4\pi R_{int}^3/3$ there is, on the average, more than one potential well with localization energy equal to or greater than that in this well, then an exciton will have a possibility of transferring from the upper to the lower state of this complex. The quantity R_{int} cannot exceed the distance between two wells for which the

time of the phonon-assisted exciton transition between them is of the order of the exciton radiative lifetime.

The theory of percolation over overlapping spheres[9–15] yields a dependence on the number of spheres in the volume of interest for such characteristics as the average number of clusters $\langle n_s \rangle$ consisting of s overlapping spheres per sphere. When applied to our problem, $\langle n_1 \rangle$ is the number of isolated localizing potential wells, $\langle n_2 \rangle$ is that of superclusters made up of pair wells, and so on.

Using the well-known expression for $\langle n_1 \rangle$,[9–14] we come to

$$\langle n_1(\omega) \rangle \approx \exp(-[R_{\rm int}/\overline{r(\omega)}]^3) \equiv \exp\{-2\mathcal{P}(\omega)\}. \quad (15)$$

Here

$$\overline{r(\omega)} = \left(\frac{3}{4\pi} \frac{1}{\mathcal{N}(\omega)} \right)^{(1/3)}, \quad (16)$$

and $\langle n_1(\omega) \rangle \equiv \langle n_1[\mathcal{N}(\omega)] \rangle$.

The concentration of potential wells $\mathcal{N}(\omega)$ with localization energy bounded on one side by the magnitude of ω, and on the other, by the Lifshits boundary E_L, is determined by a relation of type (13). The function $\mathcal{P}(\omega)$ is the density of localized excitons in units of the first virial coefficient. In classical percolation theory, the data obtained by various authors on the magnitude of the critical density $\mathcal{P}(\omega)$ for percolation over spheres are collected in Ref. 13. These values are confined in the interval $1.17 \geqslant \mathcal{P}_{\rm cr}^{\rm cl} \leqslant 1.40$. As seen from Eqs. (15) and (16), the value $\mathcal{P}(\omega_{ME})$ depends in our case on the parameter $R_{\rm int}$ we have introduced and the integrated density at percolation threshold $\mathcal{N}(\omega_{ME})$. We shall use the results of extrapolation of power expansions in sphere concentration in the low-concentration domain for $s=2,3,4$ quoted in Ref. 18.

We shall assume that a localized state can either undergo radiative recombination or transfer to another state lying lower in energy by emitting a certain number of phonons. Using the classification of localized states according to their belonging to superclusters of different size, we can maintain that the states belonging to single wells can only recombine. States belonging to pair superclusters, $s=2$, can be divided into two types, viz., one of them (the lower) can only recombine at zero temperature, whereas the other (the upper one) is capable of decaying to the lower one with emission of phonons.

Obviously enough, the total concentration of states capable only of recombining can be written

$$\mu_0(\omega) \equiv \mu_{\rm rad}(\omega) = \Big\langle \sum_{s=1}^{\infty} n_s(\omega) \Big\rangle. \quad (17)$$

Here $n_s(\omega)$ is the number of superclusters consisting of s potential wells with localization energy larger than or equal to ω per well, and the angular brackets denote averaging over all possible realizations of the supercluster of a given size.

Within the model considered here, $\mu_{\rm rad}(\omega)$ is the fraction of states with the total lifetime equal to the radiative lifetime

$$\tau^{(0)} \equiv \tau_{\rm rad}, \quad (18)$$

which we shall consider independent of localization energy. The other states of a supercluster will have lifetimes limited by phonon-assisted decays. For example, the upper states of pair clusters and the second states of larger clusters (the supercluster states are labeled in order of decreasing localization energy) will have the only possibility for decay. The number of decay channels involving phonon emission increases with increasing state number in the supercluster.

By analogy with Eq. (17), the number of states having s decay channels can be written

$$\mu_s(\omega) = \left\langle \sum_{k=s+1}^{\infty} n_k(\omega) \right\rangle. \quad (19)$$

The sums (17) and (19) are dominated, with a good enough accuracy, by their lower limit,[15] i.e., by a few of their leading terms.

b) *Profile of the zero-phonon luminescence band.* Steady-state concentration of occupied states under continuous and sufficiently weak interband excitation is proportional to the density of states at the given energy and their lifetime. Because the contribution of each populated state to the spectral emission density coincides with that to the absorption coefficient of the $1s$ state, we can present the zero-phonon luminescence band in the form

$$I_{1s}^0(\omega) \sim \alpha_{1s}^0(\omega) P(\omega) \tau_{\rm rad}, \quad (20)$$

where

$$P(\omega) = \sum_{s=1}^{\infty} \mu_{(s-1)}(\omega) \tau^{(s-1)}/\tau_{\rm rad} \equiv \sum_{s=1}^{\infty} P^{(s-1)}(\omega) \quad (21)$$

gives the total relative population of states with localization energy ω, which belong to superclusters of different size. Recalling the expressions for $\langle n_s \rangle$,[18] the first two terms in $\mathcal{P}(\omega)$ yield

$$I^0(\omega) \sim \alpha^0(\omega) \tau_{\rm rad} [\exp\{-2\mathcal{P}(\omega)\} + \mathcal{P}(\omega) \times \exp\{-3.073\,\mathcal{P}(\omega)\}]. \quad (22)$$

Superclusters of the minimum size are responsible in all cases for the major contribution, while the higher terms provide only small corrections, both in the low-concentration domain, $\mathcal{N}(\omega)/\mathcal{N}(\omega_{ME}) \ll 1$, where their number is proportional to the concentration powers $\mathcal{P}(\omega)$ growing with supercluster size, and in the vicinity of the mobility edge because of the additional exponentially small factors.

Electron-phonon coupling affects the shape of absorption and luminescence spectra because absorption and recombination are accompanied by emission of both acoustic and optical phonons.

To describe the interaction of excitons with both LO and LA phonons, we use the approach of Ref. 18. The calculation of the $\alpha_{1s}(\omega)$ and $I_{1s}(\omega)$ spectra will take into account Fröhlich interaction with longitudinal optical phonons and deformation and piezoelectric interactions with longitudinal acoustic phonons. The main parameters of the solid solution needed for the calculation (electron and hole effective masses, the constants of the deformation potential and of

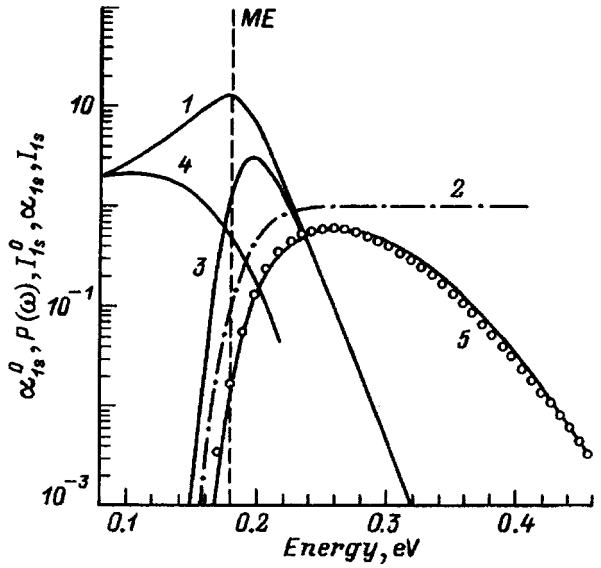

FIG. 2. Calculated relations: (*1*) zero-phonon absorption band profile $\alpha^0_{1s}(\omega)$, (*2*) the fraction of radiative states $P(\omega)$, (*3*) zero-phonon luminescence band $I^0_{1s}(\omega)$, (*4*) absorption band $\alpha_{1s}(\omega)$, and (*5*) $1s$ luminescence band $I^0_{1s}(\omega)$ with inclusion of phonon coupling; open circles - luminescence spectrum of $ZnSe_{1-c}Te_c$ obtained for $c=0.15$ and $T=2$ K.

piezoelectric and Fröhlich interactions) will be derived by linear interpolation between their values for the terminal compounds.

2. RESULTS OF THE CALCULATION AND DISCUSSION

As evident from Eq. (20) for the zero-phonon luminescence band, only a relatively small fraction of fluctuation states lying in the region of small absorption coefficients dominates the luminescence process. The maximum in the distribution of these radiative states is redshifted with respect to that of absorption maximum even without taking into account the interaction with lattice vibrations, which agrees qualitatively well with available experimental data on disordered systems. Interaction with phonons gives rise to additional Stokes shifts of the absorption and emission bands in opposite directions.

We calculated the luminescence spectrum profile for the $ZnSe_{1-c}Te_c$ solid solution for $c=0.15$. The localized-exciton wave function was taken as a product of the wave function of a localized hole by the electron Coulomb function (model II). Because in this concentration region the exciton binding energy $E_{ex}(c)$ is substantially smaller than the localization energy of radiative states, the electron cannot follow adiabatically the motion of the hole and interacts with its distribution averaged over the fluctuation well, which is actually the postulate of model II.

Figure 2 presents the results of the calculation and an experimental spectrum. A satisfactory fit to experiment is observed when up to 10 LO phonon replicas are taken into account.

We note in conclusion that the above approach to describing optical spectra of disordered crystalline systems can be generalized to a two-dimensional case by including the corresponding changes in the consideration of the density of fluctuation states and in the relations following from percolation theory.

A possible version is the case of a three-dimensional density of states and two-dimensional supercluster statistics, provided the solid solution layer is sufficient for accommodating three-dimensional fluctuation-induced clusters but still not large enough for three-dimensional superclusters to form.

Support of the INTAS Foundation (Grant 94-324) and of the Russian Fund for Fundamental Research (Grants 96-02-16933 and 97-02-18138) is gratefully acknowledged.

[1] S. Permogorov and A. Reznitsky, J. Lumin. **52**, 201 (1992).
[2] A. Naumov, S. Permogorov, A. Reznitsky, S. Verbin, and A. Klochikhin, J. Cryst. Growth **101**, 713 (1990).
[3] A. Yu. Naumov, S. A. Permogorov, T. B. Popova, A. N. Reznitskiĭ, V. Ya. Zhulaĭ, V. A. Novozhilov, and G. T. Petrovskiĭ, Fiz. Tekh. Poluprovodn. **21**, 350 (1987) [Sov. Phys. Semicond. **21**, 213 (1987)].
[4] A. Yu. Naumov, S. A. Permogorov, T. B. Popova, A. N. Reznitskiĭ, V. Ya. Zhulaĭ, V. A. Novozhilov, and N. N. Spendiarov, Fiz. Tekh. Poluprovodn. **21**, 377 (1987) [*sic*].
[5] P. G. de Gennes, P. Lafore, and J. P. Millot, J. Phys. Chem. Solids **11**, 105 (1966).
[6] P. G. de Gennes, P. Lafore, and J. P. Millot, J. Phys. Radium **20**, 624 (1959).
[7] Y. Cho and Y. Toyozawa, J. Phys. Soc. Jpn., Suppl. **26**, 71 (1969).
[8] S. Kirkpatrick and T. P. Eggarter, Phys. Rev. B **6**, 3598 (1972).
[9] D. F. Holcomb and J. J. Rehr, Jr., Phys. Rev. **183**, 733 (1969).
[10] V. K. S. Shante and S. Kirkpatrick, Adv. Phys. **20**, 325 (1971).
[11] J. W. Essam, Rep. Prog. Phys. **43**, 833 (1980).
[12] G. E. Pike and C. H. Seager, Phys. Rev. B **10**, 1421 (1974).
[13] S. W. Haan and R. Zwanzig, J. Phys. A **10**, 1547 (1977).
[14] W. T. Elam, A. R. Kerstein, and J. J. Rehr, Jr., Phys. Rev. Lett. **52**, 1516 (1984).
[15] A. Bunde and S. Havlin, in *Fractals and Disordered Systems*, edited by A. Bunde and S. Havlin, Springer-Verlag, Berlin, Heidelberg/New York/London/Paris/Tokyo/Hong Kong/Barcelona/Budapest (1997), p. 97.
[16] N. X. Xinh, A. A. Maradudin, and R. A. Goldwell-Horsfall, J. Phys. (Paris) **26**, 717 (1965).
[17] A. A. Klochikhin, S. A. Permogorov, and A. N. Reznitskiĭ, JETP Lett. **65**, 289 (1997).
[18] A. A. Klochikhin, S. A. Permogorov, and A. N. Reznitskiĭ, Fiz. Tverd. Tela (St. Petersburg) **39**, 1170 (1997) [Phys. Solid State **39**, 1035 (1997)].
[19] A. A. Klochikhin and S. G. Ogloblin, Phys. Rev. B **48**, 3100 (1993).
[20] A. A. Klochikhin, Phys. Rev. B **52**, 10979 (1995).

Translated by G. Skrebtsov

Photoelectric properties of tin disulfide

G. B. Dubrovskiĭ and A. I. Shelykh

A. I. Ioffe Physicotechnical Institute, Russian Academy of Sciences, 194021 St. Petersburg, Russia
(Submitted February 3, 1998)
Fiz. Tverd. Tela (St. Petersburg) **40**, 1426–1427 (August 1998)

[S1063-7834(98)00808-9]

In recent years, investigations of the crystal structure and electrical and optical properties of layered compounds of type MX_2 (where M is a metal and X is a chalcogen) have elicited considerable interest. Many of these compounds possess polytypes, which ensures that a whole range of crystal modifications, each having different properties, can exist for a single chemical compound. One such compound is the wide- gap semiconductor SnS_2. At this time, more than ten polytypes of this compound are known; depending on the structure of the polytype, the width of the bandgap varies over a wide range from 0.81 to 3.38 eV.[1] The commonest polytype of SnS_2 has a sequence $(A\gamma B)(A\gamma B)$ of alternating layers, and is usually denoted by $2H$ according to its sulfur layers. However, since its unit cell contains only one molecule, it is the simplest structure this compound can have and, hence, should be denoted by $1H$. The width of the forbidden band of this modification, according to optical measurements, is 2.18 eV.[2]

SnS_2 crystals are rather strongly photosensitive, a fact of considerable interest since the photosensitivity is present in the visible region of the spectrum. However, very few papers have made it their task to study the photoconductivity of these crystals,[3–5] and as far as we know no one has investigated the photo-EMF. In order to fill in this gap, we measured the photoconductivity and photo-EMF of SnS_2 crystals doped during growth with Cu, Au, Zn, Cd, In, Ga, and P impurities. Our measurements were made in the constant-current regime, using a monochromator as a light source with a photon energy range from 1 to 4 eV. The contacts were made using silver paste. In order to measure the photoconductivity, they were deposited on one surface and screened from the light. The photo-EMF was measured on the opposite side of the sample as the immediate vicinity of the contact was illuminated by a fixed beam from the monochromator.

Our results are shown in Fig. 1. It is clear from this data that a well-defined strong maximum is observed in the photoconductivity spectrum at an energy of about 2.3 eV, which was practically the same for all the samples, a weaker peak at an energy of 2.85 eV, which in some samples had the form of a shoulder, and a maximum in the neighborhood of 1.65 eV, which did not appear in all samples. The first feature is obviously connected with the edge of the fundamental absorption band and corresponds to an indirect optical transition to the absolute minimum of the conduction band. The peak at energy of 2.85 eV is probably associated with direct transitions to a higher-lying minimum, which agrees with optical data of Ref. 6 indicating the existence of a direct minimum at an energy of 2.88 eV. Previously, Shibata *et al.*[5] reported seeing this feature in the photoconductivity spectrum in the form of a shoulder at an energy of 2.8 eV.

As for energies smaller than the width of the forbidden gap, Patil *et al.*[3] reported a maximum at an energy of 1.45 eV at liquid-nitrogen temperatures, which disappeared at room temperature. In Ref. 4, Nakata *et al.* observed weak peaks in the photosensitivity in the energy range from 1.4 to 1.9 eV, which disappeared in a humid atmosphere, which probably means that they are related to the surface. No assumptions about the nature of the photosensitivity in this region were advanced. The photoconductivity we observed in the neighborhood of 1.65 eV was seen in samples with various impurity contents; however, not all samples with the same impurity content were photosensitive in this region. This leads us to conclude that the effect is not associated with an impurity mechanism. In our opinion, its cause is most likely the presence of layers in the sample with a different polytype structure. Our previous x-ray investigations (see Ref. 7) showed that the majority of SnS_2 crystals consist of intergrowths of two or more polytypes. The next most common polytypes after $1H$ are referred to as $4H$ and $6H$ based on their sulfur layers, with forbidden-gap widths of 1.89 and 1.59 eV respectively.[1] The presence of thin layers of these polytypes in some samples could lead to the observed long-wavelength photosensitivity. A broad maximum in the photo-EMF spectra is also observed in this wavelength range, whose position almost coincides with the peak in the photoconductivity spectra.

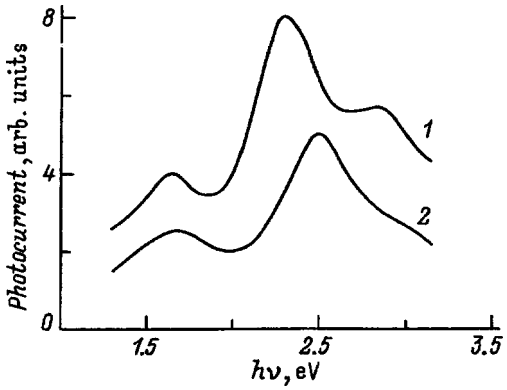

FIG. 1. Spectral dependence of photoconductivity (curve *1*) and photo-EMF (curve *2*) in crystals of $1H$ SnS_2 at room temperature.

It is clear from Fig. 1 that the principal maximum of the photo-EMF spectrum is located at an energy of 2.5 eV. The origin of this maximum is undoubtedly the same as that of the photoconductivity maximum at an energy of 2.5 eV, i.e., indirect transitions of electrons from the valence band to the absolute minimum of the conduction band. The shift of this maximum to shorter wavelengths is obviously associated with the fact that the photo-EMF is generated by the separation of electron-hole pairs in a region whose size is the same order as the diffusion length from the metallic contact. If the diffusion length is much smaller than the sample size, then the photo-EMF maximum will occur in the region of strong absorption deep in the fundamental absorption band, i.e., it shifts towards the short-wavelength spectral region.

We note one interesting feature of the spectral dependence of the photo-EMF, which could have practical application. In certain samples, we observe a change in the sign of the photo-EMF in the neighborhood of the principal maximum as the wavelength of the incident light was varied. Additional research is required in order to explain this effect.

This work was carried out with the financial support of the Russian Fund for Fundamental Research (Grant 97-02-18300).

[1] S. Acharya and O. N. Srivastava, Phys. Status Solidi A **65**, 717 (1981).
[2] G. B. Dubrovskiĭ and N. S. Zhdanovich, Fiz. Tverd. Tela (St. Petersburg) **38**, 272 (1996) [Phys. Solid State **38**, 153 (1996)].
[3] S. G. Patil and R. N. Tredgold, J. Phys. D **4**, 718 (1971).
[4] R. Nakata, M. Yamaguchi, S. Zembutsu, and M. Sumita, J. Phys. Soc. Jpn. **32**, 1153 (1972).
[5] T. Shibata, Y. Mukanushi, T. Miura, and T. Kishi, J. Phys. Chem. Solids **51**, 1297 (1990).
[6] G. Domingo, R. S. Itoga, and C. R. Kannewurf, Phys. Rev. **143**, 536 (1966).
[7] A. V. Golubkov, G. B. Dubrovskiĭ, and A. V. Prokof'ev, Fiz. Tverd. Tela (St. Petersburg) **36**, 2666 (1994) [Phys. Solid State **36**, 1453 (1994)].

Translated by Frank J. Crowne

Specific features of Bi_2Te_3 doping with Sn

M. K. Zhitinskaya and S. A. Nemov

St. Petersburg State Technical University, 195251 St. Petersburg, Russia

T. E. Svechnikova

A. A. Baikov Institute of Metallurgy, Russian Academy of Sciences, Moscow, Russia
(Submitted February 12, 1998)
Fiz. Tverd. Tela (St. Petersburg) **40**, 1428–1432 (August 1998)

The effect of doping bismuth telluride with tin, on its electrophysical properties, has been studied. It is shown that the main features in the transport coefficients of Bi_2Te_3:Sn can be explained by the existence of resonant Sn states within the valence band. The existence of resonant Sn states was confirmed by codoping Bi_2Te_3:Sn with the electroactive impurity I.
 [S1063-7834(98)00908-3]

Bismuth telluride is the main component of materials employed in room-temperature thermoelectric power converters. Therefore a search for impurities capable of increasing the thermoelectric efficiency of Bi_2Te_3 and of related compounds is not only interesting from the scientific standpoint but has potential application as well. Both literature and our data suggest tin as a promising impurity in this respect.[1–4] Tight-binding calculations show that Group-IV elements substituting for Te in Bi_2Te_3 can produce resonant states within the allowed band.[1] Experimental studies[2–4] revealed some features in the dependences of electrical conductivity (σ) and Hall (R) coefficients on temperature and pressure, which can be attributed to the presence of tin impurity states. These features are, however, not so clearly pronounced as the manifestations of the resonant states of Group III impurities in PbTe and other IV-VI semiconductors.[5] This is apparently due to a number of factors, such as the strong anisotropy in the physical properties, the small formation energy of various, including antisite, lattice defects, the higher carrier concentration (by an order of magnitude, $\sim 1 \times 10^{19}$ cm^{-3}), as well as the complex structure of the electron and hole energy spectra.

The experience gained in investigation of the resonant states originating from Group III elements in IV-VI semiconductors[5,6] shows that such levels can be detected by codoping the material with an electroactive impurity, which, while not creating any levels itself, affects the position of the chemical potential μ and the filling by electrons of the impurity states. Such additional impurity for bismuth telluride is iodine, which exhibits a strong donor action. The existence of an impurity band is most clearly revealed by the pinning of the chemical potential under variation of the impurity concentration.

The present work reports a study of the thermoelectric, galvano- and thermomagnetic properties of Bi_2Te_3 crystals doped with Sn, as well as with Sn and a codopant. We used iodine as the codopant.

1. EXPERIMENT

The transport coefficients were studied in Czochralski-grown bismuth telluride single crystals. The composition of the samples doped only with tin can be specified by the formula $Bi_{2-x}Sn_xTe_3$, where $x=0$, 0.002, 0.005, 0.007, and 0.01 ($x=0.01$ in Bi_2Te_3 corresponds to the atomic concentration of 6×10^{19} cm^{-3}). Samples codoped with tin and iodine have the formula $Bi_{2-x}Sn_xTe_3+ySbI_3$, where $x=0.005$ and $y=0.05$, 0.1, and 0.15 wt %.

The high degree of perfection of the crystals was confirmed by scanning tunneling microscopy, as well as by measurements of the transverse Nernst-Ettingshausen effect[7] (Qe/k_0). The Sn and I impurity content was monitored by chemical and x-ray microprobe analysis. The uniformity of impurity distribution in the samples was estimated from measurements of the Seebeck coefficient S at $T=300$ K.

We measured in single-crystal samples the following independent components of the transport tensors: R_{123} and R_{321} of the Hall coefficient, S_{11} of thermopower, σ_{11} of the electrical conductivity, and Q_{123} of the Nernst-Ettingshausen effect. Axis 3 in this notation lies in the direction of the trigonal crystal axis. The indices of the coefficients identify, in the order they are given, the following directions: the first — the electric field being measured, the second — the electric current or temperature gradient, and the third — the magnetic field. The measurements were carried out within the 77–420 K temperature range.

Figure 1 displays the dependence of the hole concentration (p) on the amount of the impurity introduced (N_{imp}). [The hole concentration was determined from the larger Hall coefficient component R_{321} using the relation $p=(eR_{321})^{-1}$]. Also shown are data on the doping of Bi_2Te_3 with tin and a chlorine impurity introduced in the form of $CdCl_2$,[4] as well as with donor (an excess of Te and I) and acceptor (an excess of Bi and Pb) impurities[8–10]. When bismuth telluride is doped with lead or iodine, the carrier concentration (p or n) increases usually proportional to the amount of the impurity introduced, namely, the electrical activity of lead is 1.4–1.7 hole, depending on the lat-

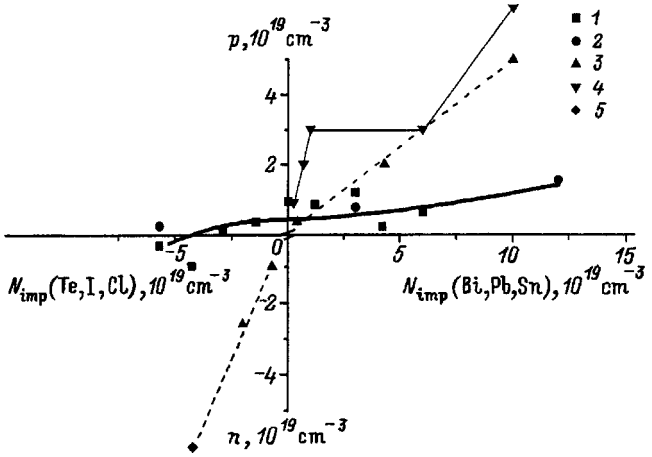

FIG. 1. Hole and electron concentrations (p,n) in Bi_2Te_3 at 77 K vs impurity content (N_{imp}): *1* — this work, dopants: Sn, Sn + I; *2* — Ref. 4: Sn, Sn+Cl; *3* — Ref. 8: Bi, Te; *4* — Ref. 9: Pb; *5* — Ref. 10: SbI_3.

tice site occupied by the Pb atoms, and that of iodine,[9] 1.3 −1.4 electron per impurity atom introduced.

By contrast, we observe the hole concentration to vary only weakly with the tin content in Bi_2Te_3. For instance, for tin present in concentrations $N_{Sn}=(1.2-6)\times10^{19}$ cm^{-3} the hole concentration varied within a narrow interval from 2×10^{18} to 5×10^{18} cm^{-3}, which argues for "soft" stabilization of the chemical potential.

Figure 1 presents also results obtained by codoping Bi_2Te_3 with tin and a halogen electroactive impurity introduced into Bi_2Te_3 in the form of a compound (SbI_3 in this work, and $CdCl_2$ in Ref. 4). We readily see a substantial difference in doping action between the iodine and chlorine[4] impurities in Bi_2Te_3 and Bi_2Te_3:Sn. In the latter case, the variation in the hole concentration is much less pronounced, which confirms stabilization of the hole concentration in Sn-doped Bi_2Te_3 samples.

The temperature dependence of the transport coefficients is shown graphically in Figs. 2–4. We see that the temperature dependences of the Seebeck and Hall coefficients in samples with tin undergo substantial changes compared to those for undoped Bi_2Te_3. The temperature dependences $R(T)$ of the samples containing Sn change from the rising pattern typical of Bi_2Te_3 to the strongly decreasing course (see Fig. 2). The Seebeck coefficient for tin-containing samples is noticeably larger in the high-temperature region. One observes simultaneously a considerable falloff of the Hall ($R\sigma$) and Nernst ($|Qe/k_0|$) hole mobility.

Note that, for low tin concentrations ($x=0.002$ and 0.005), the presence of tin atoms practically does not affect the hole concentration. The temperature dependences $R(T)$, as well as the magnitude and temperature behavior of the mobility $R\sigma(T)$ for these compositions, are identical with those obtained for undoped Bi_2Te_3. It may be conjectured that because of its higher electronegativity tin, like indium, is capable of suppressing the formation of Bi_{Te}-type antisite defects.

Crystals codoped by Sn and I also exhibited features in the transport coefficients, namely, the falloff of $R_{ijk}(T)$ throughout the temperature range studied and a sharp decrease in hole mobility in the cleavage plane, $R_{123}\sigma_{11}$, which was determined both from the electrical conductivity and from the Nernst-Ettingshausen effect ($|Q_{123}e/k_0|$).

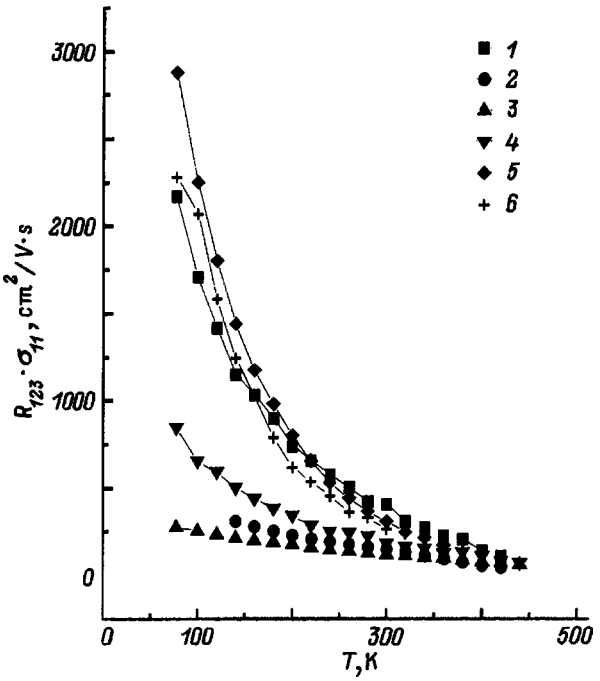

FIG. 2. Temperature dependence of the Hall mobility $R_{123}\sigma_{11}$. x_{Sn}: *1* — 0, *2* — 0.002, *3* — 0.005, *4* — 0.007, *5* — 0.01, *6* — 0.005 + 0.05 wt.% SbI_3.

2. DISCUSSION OF RESULTS

The above features in the transport coefficients of tin-doped Bi_2Te_3 samples are similar in many respects to those

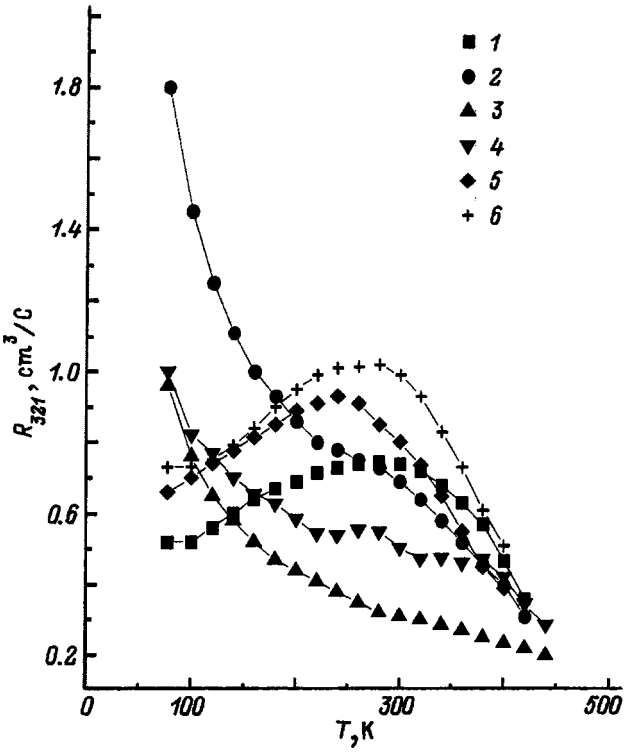

FIG. 3. Temperature dependence of the Hall coefficient R_{321}. Same notation as in Fig. 2.

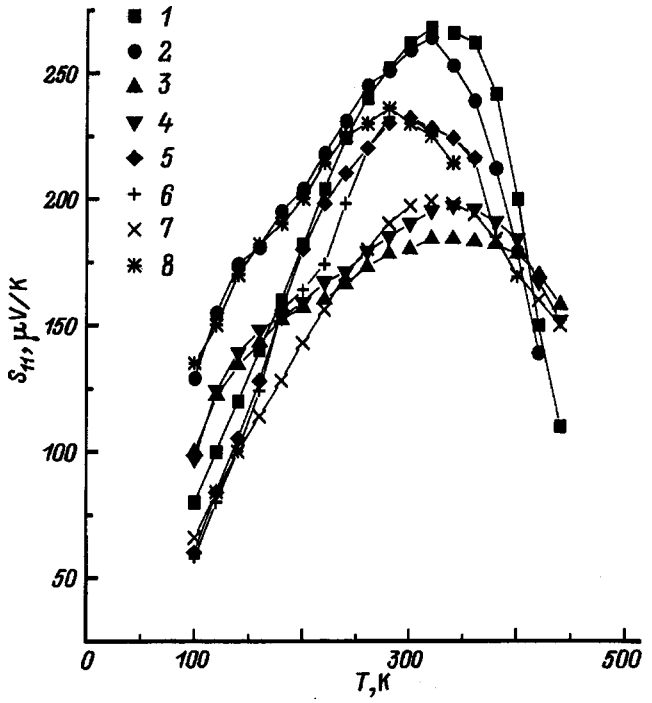

FIG. 4. Temperature dependence of the Seebeck coefficient S_{11}. Same notation as in Fig. 2; 7,8 — data from Ref. 4.

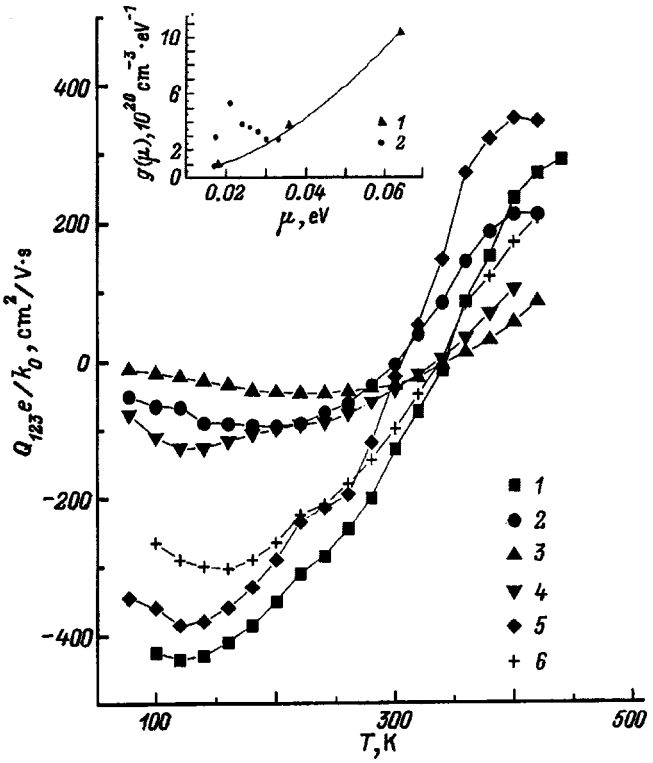

FIG. 5. Temperature dependence of the coefficient of the transverse Nernst-Ettingshausen effect Q_{123}. Same notation as in Fig. 2. Inset shows the density of states $g(\mu)$ for (*1*) stoichiometric samples and (*2*) tin-doped Bi_2Te_3 single crystals.

observed[5] to occur in Tl-doped lead chalcogenides, and can also be interpreted in terms of the model of impurity resonant states. Indeed, stabilization of the carrier concentration can be related to the existence of Sn impurity states within the valence band of Bi_2Te_3 (with a density of states proportional to Sn content), the strong temperature dependence of the Hall coefficient — to a temperature-induced shift of the Sn impurity states, and the abrupt drop of the Hall and Nernst hole mobilities — to hole resonant scattering into the Sn impurity band. It should be pointed out, however, that these features are much weaker than those observed in the IV-VI compounds. Therefore additional arguments are required to prove the existence of Sn resonant states. Besides, doping of Bi_2Te_3, particularly with metals (e.g., with Pb, In, or Tl), increases the amount of defects and the nonuniformity of the material. Note that in nonuniform semiconductors the temperature dependences of the transport coefficients (in particular, of the Hall coefficient) can in certain conditions simulate the behavior of a homogeneous semiconductor with impurity levels. This pitfall should be borne in mind in analysis and interpretation of experimental data. We studied[7] the effect of inhomogeneities (crystal quality) on the transverse Nernst–Ettingshausen and Hall effects and confirmed the high quality of the Czochralski-grown Bi_2Te_3:Sn crystals. Thus the specific features in the behavior of transport coefficients observed experimentally in these crystals can be accounted for by differences in the energy spectra of *p* Bi_2Te_3 samples doped with tin and without it, in other words, by the existence of Sn impurity resonant states.

The experimental data obtained permitted us to determine the band structure parameters, namely, the effective mass of the density of states m_d^* and the band gap ε_g in Bi_2Te_3:Sn crystals. The method used to determine these parameters is described in detail elsewhere.[3] Note that the values of m_d^* and ε_g obtained for Bi_2Te_3:Sn samples with hole concentrations outside the region of the sharp mobility fall-off coincide with the literature data available for undoped *p*-Bi_2Te_3.

Estimation of the position of the chemical potential in samples within the stabilization region shows that the Sn level lies between the valence-band subbands near the edge of the additional extremum. Extrapolation of the temperature dependence of the chemical potential $\mu(T)$ to $T=0$ made for samples with different Sn contents yields for the energy of the impurity states $\varepsilon_1 \approx \mu(0) \approx 0.02-0.03$ eV.

For low enough temperatures (up to 140 K in our case) and for degenerate statistics, the four transport coefficients permit one to determine the density of states in the band using the relation $\alpha_\infty=(k_0/e)(\pi^2/3)(1/n)(k_0T)g(\mu) = S_{11}e/k_0+Q_{123}e/(R_{123}\sigma_{11}k_0)$. This is an isotropic quantity depending only on the chemical potential level. Our estimates showed an increase in the density of states $g(\varepsilon)$ in the region of Fermi energies of 0.02–0.03 eV for temperatures close to 100 K (see the inset to Fig. 5). In our opinion, the observed bell-shaped profile of $g(\varepsilon)$ for Bi_2Te_3:Sn argues for the existence of a band of Sn impurity states near the edge of the second valence band with a broadening $\Gamma \sim 0.01$ eV. This value of the broadening of the impurity states is in accord with the idea of resonant hole scattering into the Sn band. Indeed, resonant scattering can reduce effectively the mobility only in samples whose Fermi level lies within the impurity band, and at temperatures such that the

temperature-induced broadening of the Fermi distribution function $k_0T \sim \Gamma$. (Bi_2Te_3:Sn crystals exhibited a considerable decrease of mobility near 100 K).

The effect of carrier resonant scattering on transport coefficients (in particular, on the Seebeck coefficient) was discussed in considerable detail in a review paper Ref. 6. It was shown[6] that resonant scattering has a clearly pronounced selective character, namely, only carriers with energies close to the energy of the impurity states undergo strong scattering. A certain relative arrangement of the impurity band, the edge of the valence band, and of the chemical potential level may result in conditions conducive to strong scattering of carriers with a comparatively low energy ($\varepsilon - \mu < 0$, "cold") and weak scattering of energetic ones ($\varepsilon - \mu > 0$, "hot"). This should increase the average energy in the flow and, hence, increase the thermopower for a given carrier concentration. If the decrease in carrier mobility due to resonant scattering is not too large, the thermoelectric power $S^2\sigma$ may increase. Note that our experimental data show that doping Bi_2Te_3 with tin does indeed increase the Seebeck coefficient. The thermopower $S^2\sigma$ and the figure of merit Z increased in two samples compared to undoped p Bi_2Te_3. These samples exhibited an increase in thermopower accompanied by a relatively small decrease in mobility. It may be conjectured that the Sn impurity band in these samples is filled by holes to a larger extent than in the other crystals due to the formation of native (antisite) defects.

To conclude, the results obtained in this work argue for the existence of Sn impurity states within the valence band of Bi_2Te_3, near the top of the additional extremum. This gives us grounds to hope that it will be possible to detect impurity resonant states in solid solutions of the V-VI compounds used traditionally in thermoelectric power converters, and to use these states to improve the thermoelectric characteristics of Bi_2Te_3-based materials.

[1] P. Pecheur and G. Toussaint, in *Proceedings of the 8th International Conference on Thermoelectric Energy Conversion* (Nancy, 1989), p. 176.
[2] V. A. Kulbachinskii, M. Inoue, M. Sasaki, H. Negishi, W. X. Gao, K. Takase, Y. Giman, P. Lostak, and J. Horak, Phys. Rev. B **50**, 16921 (1994).
[3] M. K. Zhitinskaya, S. A. Nemov, T. G. Abaidulina, and T. E. Svechnikova, in *Proceedings of the 14th International Conference on Thermoelectrics* (St. Petersburg, Russia, 1995), p. 56.
[4] G. T. Alekseeva, P. P. Konstantinov, V. A. Kutasov, L. N. Luk'yanova, and Yu. I. Ravich, Fiz. Tverd. Tela (St. Petersburg) **38**, 2998 (1996) [Phys. Solid State **38**, 1639 (1998)].
[5] V. I. Kaĭdanov and Yu. I. Ravich, Usp. Fiz. Nauk **145**, 51 (1985) [Sov. Phys. Usp. **28** 31, (1985)].
[6] V. I. Kaĭdanov, S. A. Nemov, and Yu. I. Ravich, Fiz. Tekh. Poluprovodn. **26**, 201 (1992) [Sov. Phys. Semicond. **26**, 113 (1992)].
[7] M. K. Zhitinskaya, S. A. Nemov, and T. E. Svechnikova, Fiz. Tekh. Poluprovodn. **31**, 441 (1997) [Semiconductors **31**, 375 (1997)].
[8] J.-P. Fleurial, L. Gailliard, R. Triboulet, H. Scherrer, and S. Scherrer, J. Phys. Chem. Solids **49**, 1237 (1988).
[9] H. Süssmann, A. Priemuth, and U. Pröhl, Phys. Status Solidi A **82**, 561 (1984).
[10] W. M. Yum and F. D. Rosi, Solid–State Electron. **10**, 1121 (1972).

Translated by G. Skrebtsov

Photoluminescence of *a*-Si:H films grown by plasma-enhanced chemical vapor deposition and doped with erbium from the metallorganic compound $Er(HFA)_3 \cdot DME$

V. B. Voronkov, V. G. Golubev, A. V. Medvedev, A. B. Pevtsov, and N. A. Feoktistov

A. I. Ioffe Physicotechnical Institute, Russian Academy of Sciences, 194021 St. Petersburg, Russia

N. I. Gorshkov and D. N. Suglobov

''V. G. Khlopin Radium Institute'' Scientific Research Association, 194021 St. Petersburg, Russia
(Submitted February 12, 1998)
Fiz. Tverd. Tela (St. Petersburg) **40**, 1433–1436 (August 1998)

Using standard low-temperature (<300 °C) plasma-enhanced chemical vapor deposition (PE CVD) technology, films of *a* Si(Er) : H were obtained that emitted light in the neighborhood of 1.54 μm at room temperature. The Er source was the specially synthesized fluorine-containing metallorganic complex $Er(HFA)_3 \cdot DME$ (where $HFA = CF_3C(O)CHC(O)CF_3$ and $DME = CH_3OCH_2CH_2OCH_3$), which possesses a low transition temperature to the gas phase (of order 100 °C) at working pressures (0.1−0.5 Torr) for the PE CVD method. Distinctive features of the photoluminescence spectrum of *a*-Si(Er):H were investigated in the range 0.5 −1.7 μm for $T = 77$ and 300 K. The presence of photoconductivity in the synthesized films is evidence of their satisfactory electronic quality. © *1998 American Institute of Physics.* [S1063-7834(98)01008-9]

Materials based on silicon doped with erbium are interesting primarily because they could be used to make silicon-based optoelectronic devices that operate in the wavelength vicinity of 1.5 μm, which coincides with the region of minimum loss and dispersion in optical-fiber communication lines. Films of amorphous hydrogenated silicon (*a* Si:H) doped with erbium exhibit enhanced photoluminescence (PL) intensity[1,2] compared with Si crystals at this wavelength, as well as weak temperature quenching. Two basic methods are used to introduce Er into *a* Si:H: 1) ion implantation[3], and 2) magnetron sputtering of a mosaiclike erbium-silicon target in an atmosphere of silane.[1,4] In both cases, the synthesized films exhibit PL in the neighborhood of 1.54 μm at room temperature. A common deficiency of these methods is the high concentration of intrinsic defects in the resulting films, which makes their future use in fabricating optoelectronic devices problematic. Rogers *et al.*[5] and Andry *et al.*[6] used a modification of the technology of plasma- enhanced chemical-vapor deposition (PE CVD), which is usually used to obtain device-quality films of *a*-Si:H, to synthesize Si(Er) films. Erbium was introduced into the film by the metallorganic compounds tris (2, 2, 6, 6-tetramethyl-3, 5-heptanedionato) erbium(III) (see Ref. 5) and tris (bis trimethyl silyl amido) erbium(III) (see Ref. 6) during PE CVD at $T = 430$ °C under cyclotron-resonance conditions, which ensures epitaxial growth of Si. In this case, PL at a wavelength of 1.54 μm was recorded at helium temperatures. It is important to note that when an optimally chosen metallorganic compound is used as the doping component during PE CVD, it is possible to ensure that the erbium incorporates into the growing film in the form of optically active erbium complexes previously created in the metallorganic compound structure.

In this paper, we used standard low-temperature (<300 °C) PE CVD technology,[7] of the sort normally used to make device-quality individual layers and multilayer *a*-Si:H structures for solar cells, to make films of *a* Si(Er):H. We then investigated their PL at nitrogen and room temperatures. The films are doped with erbium directly during deposition of the *a* Si:H from a specially synthesized metallorganic complex $Er(HFA)_3 \cdot DME$ (where $HFA = CF_3C(O)CHC(O)CF_3$ and $DME = CH_3OCH_2CH_2OCH_3$). The distinctive features of this compound are its resistance to the action of moisture in the air and its low sublimation temperature: 100−120 °C at pressures of order 0.1 Torr. Experiments in which we used the $Er(HFA)_3 \cdot DME$ complex to obtain films of *a* Si(Er):H that emit at a wavelength of 1.54 μm are described in the brief publication Ref. 8.

1. PREPARATION OF SAMPLES

We paid particular attention to choosing a metallorganic compound that would make the Er^{3+} ions incorporate into the film in a chemical environment suitable for converting them into optically active centers. It was established in Refs. 9 and 10 that C, O, and F impurities are capable of increasing the intensity of 1.54 μm emission in silicon doped with erbium. Among these impurities, the fluorine ion has the smallest radius, a consequence of which is that a fluoride environment for the erbium leads to less distortion of the silicon lattice and perhaps to narrowing of the 1.54 μm line.[11] Note also that there is an analogous use of hydrogen fluoride in the role of a passivator of broken bonds in amorphous silicon films,[12] which leads to suppression of nonradiative recombination centers. Furthermore, the larger electronegativity of fluorine compared to nitrogen and oxygen leads to a stronger ligand field surrounding the Er^{3+} ion.

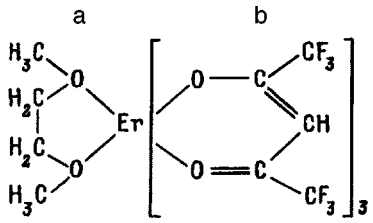

FIG. 1. Structure of the $Er(HFA)_3 \cdot DME$ complex. a—additional ligands for dimethoxyethane $DME = CH_3OCH_2CH_2OCH_3$, b—β-diketonate ligands of hexafluoracetylacetone $HFA = CF_3C(O)CHC(O)CF_3$.

These considerations serve as a basis for choosing a fluorine-containing metallorganic compound for fabrication experiments geared to obtaining emitting films of *a* Si(Er):H.

The most frequently encountered metallorganic compounds used to incorporate rare-earth elements into semiconductor materials are β-diketonate complexes with the formula ML_3 (where M is a rare-earth metal and L is $(CH_3)_3CC(O)CHC(O)C(CH_3)_3$).[13,14] A promising way to obtain a fluoride environment for the erbium atom is to use hexafluoroacetylacetone (HFA) as an acidoligand. However, it is not possible to obtain unsolvated β-diketonate complexes of rare-earth elements with this acidoligand, and the rare-earth hexafluoroacetylacetates are usually isolated in the form of dihydrates $M(HFA)_3(H_2O)_2$. When the latter are heated, internal hydrolysis takes place with the formation of nonvolatile metal-containing products. In order to avoid this, we replaced the two molecules of water by a bidentate ligand, i.e., 1, 2-Dimethoxyethane—(DME) (see Ref. 15). As a result, we obtained the more volatile compoundM $(HFA)_3 \cdot DME$, which has reasonable thermally stability but also considerable vapor pressures at a temperature of 90–100 °C in the forevacuum. The saturation pressure of the vapor at 127 °C was 124.0 Pa. In Ref. 16 we described our studies of thermolysis of vapors of this compound, and showed that for temperatures 320–340 °C it decomposes on a heated substrate to form films of MF_3 (where M=Nd, Eu, Er) without any noticeable carbon impurity.

In this paper, we used the method of Refs. 15 and 16 to synthesize the compound $Er(HFA)_3 \cdot DME$ (Fig. 1), which was then used in experiments on doping *a*-Si:H films with erbium as they grow.

Amorphous films of *a* Si(Er):H were grown by high-frequency decomposition of an argon-silane mixture in a glow discharge plasma. The parameters of the fabrication process were as follows: the content of silane in argon was 10%, the pressure was 0.1–0.2 Torr, the frequency was 17 MHz, the rf power was 0.03–0.1 W/cm^2, the substrate temperature was 200–250 °C, and the flux of gas mixture was 5–10 sccm.

The erbium was introduced by sublimation of a $Er(HFA)_3 \cdot DME$ powder. A charge of 0.1 g of material was placed in a boat made of stainless steel at a distance of about 4 cm from the discharge gap, where the substrate was placed with the growing *a*-Si:H film. The rate of sublimation was varied by heating the boat from 25 to 200 °C. As a substrate we used fused quartz and crystalline silicon. The film thicknesses were determined by *in situ* laser interferometry to be in the range of 2000 to 3000 Å for the different samples. These films were then annealed at $T = 300$ °C under normal pressure in a flux of pure nitrogen (50 sccm) for 15 minutes.

2. RESULTS OF EXPERIMENT AND DISCUSSION

The impurity concentrations in the film,as determined by secondary ion mass spectroscopy (SIMS), were: for erbium 10^{19} cm^{-3}, for fluorine 2×10^{20} cm^{-3}, for oxygen 10^{20} cm^{-3}, and for carbon 3×10^{20} cm^{-3}. The presence of considerable amounts of carbon in the film shows that the mechanism that disrupts the metallorganic complex in a high-frequency glow- discharge plasma is quite different from thermolysis on a heated substrate. In the latter case, as already reported, ErF_3 films form with very little carbon. Note that the concentrations of oxygen and fluorine were roughly an order of magnitude larger than the concentration of erbium ions in the synthesized sample. Thus, the ratio of impurities is quite sufficient to form octahedral complexes, i.e., complexes where a metal ion is surrounded by six ligands at the vertices of an octahedron. It is this configuration that is optimal for obtaining effective luminescence from an Er^{3+} ion via the radiative transition $^4I_{13/2} \rightarrow {}^4I_{15/2}$.[5,6]

The width of the optical forbidden gap (E_g) for *a*-Si(Er):H films defined by the method of Tauc, is 2.0–2.1 eV. The values we obtained exceeds E_g for standard *a*-Si:H, which is associated with the presence of carbon and oxygen impurities. The dark conductivity of the films did not exceed $10^{-10}\Omega^{-1}\times\text{cm}^{-1}$. The photoconductivity was at a level of $10^{-7}\Omega^{-1}\cdot\text{cm}^{-1}$.

We used an automated KSVU-23 setup in the synchronous detection regime to measure the photoluminescence of the films. As a detector we used a cooled germanium photodiode and a photomultiplier (for measurements in the wavelength range $<$7000 Å). The PL was excited by the 4880 Å line of an Ar^+ laser in the power range 5–280 mW.

The PL spectra at room and nitrogen temperatures are shown in Fig. 2. At low temperatures three bands appear in the spectrum. The narrow line (with a width of $\approx$7 meV at half-height) centered around $\lambda \approx 1.54$ μm is associated with the intracenter transition $^4I_{13/2} \rightarrow {}^4I_{15/2}$ of the Er^{3+} ion. At room temperature the lines are considerably broadened on the short-wavelength side, and their intensity is decreased by roughly a factor of 4.

Our measurements of the integrated PL intensity at nitrogen temperatures in the neighborhood of 1.54 μm as a function of excitation power showed that this dependence is linear up to values of the laser excitation power of $\approx$250 mW, and then the signal saturates (Fig. 3). It is obvious that in the linear region the excitation of intracenter luminescence of the erbium ions is proportional to the concentration of electron-hole pairs.[17] Our results are analogous to the data of Refs. 1 and 3, where they were interpreted as Auger processes in which the energy to excite the erbium centers comes from nonradiative transitions of electrons from the conduction band to defect levels in the amorphous silicon.

The observed ''two-humped'' structure of the spectrum in the region $0.5-1.2\mu$m (Fig. 2) is characteristic of inho-

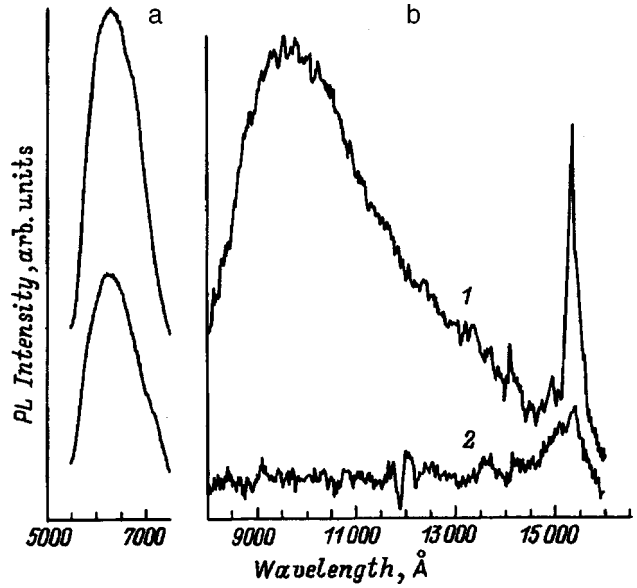

FIG. 2. PL spectra of *a*-Si(Er) : H films at nitrogen (*1*) and room (*2*) temperatures. The laser excitation power was 40 mW. a—spectra recorded by a photomultiplier, b— spectra recorded by a cooled germanium photodiode.

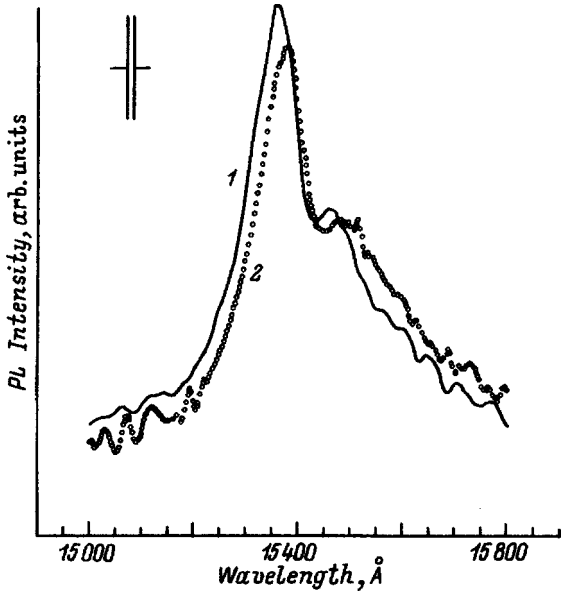

FIG. 4. Comparison of PL spectra (T = 77 K) of *a*- Si(Er) : H films obtained by various fabrication methods: *1*—using the technique developed in this paper, *2*—using the MASD technique with an erbium-silicon target.

mogeneous amorphous hydrogenated films of mixed silicon-carbon and silicon-oxygen compounds.[18] The broad band near 1 μm comes from well-known ''tail- tail'' transitions in undoped *a* Si:H (see Ref. 18) The prolongation of the line into the long- wavelength region is a consequence of the considerable concentration of oxygen in our samples.[18] As we might expect, this line undergoes strong temperature quenching connected with the thermally activated transition of nonequilibrium carriers to nonradiating states. The band in the neighborhood of $0.5-0.8$ μm is also associated with carbon and oxygen impurities in the film.

Figure 4 shows our measured PL spectra on an expanded scale. The measurements were made under identical excitation conditions and recording conditions for two samples of *a* Si(Er):H: 1) A sample synthesized according to the methods developed in this paper; 2) a sample prepared using a magnetron sputtering technique (Magnetron- Assisted Silane Decomposition, or MASD) on an erbium-silicon target in an argon-silane plasma. The PL peak of the second sample, obtained using MASD, is centered at $\lambda = 1.537$ μm, which matches data from the majority of papers that have dealt with crystalline and amorphous films of Si(Er). The short-wavelength shift (20 Å) of the PL spectrum from that of sample No. 1, i.e., an *a*-Si(Er):H film doped with erbium from $Er(HFA)_3 \cdot DME$, is evidence that the ligand field has a different value compared with the previous case, and hence that the impurity environment for the Er^{3+} ion is different. For a concrete answer to the question of what the nature and number of impurity centers surrounding the erbium ion are, additional research is required, e.g., the fine structure of *x*-ray absorption (Extended X-ray Arbsoption Fine Structure, or EXAFS) or Mossbauer spectra.

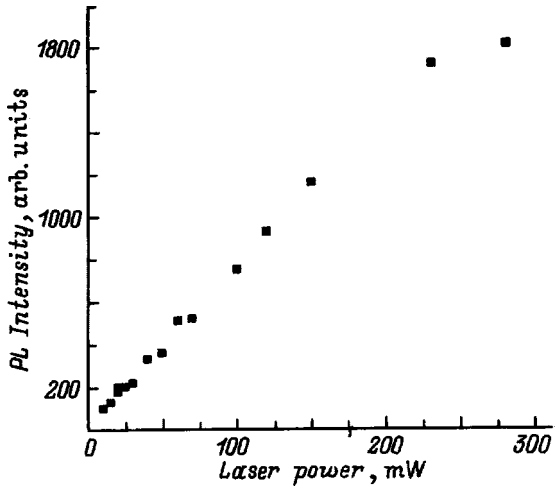

FIG. 3. Dependence of the integrated PL intensity of *a*- Si(Er) : H films in the neighborhood of 1.54 μm on the laser excitation power at T = 77 K.

The authors are grateful to B. T. Melekh for useful discussions, A. N. Kuznetsov for providing the *a*-Si(Er):H samples obtained from MASD using a silicon- erbium target, and to B. Ya. Ber for the SIMS measurements.

This work was carried out with the support of the Russian Fund for Fundamental Research (Project No. 98-02-17350).

[1] M. S. Bresler, O. V. Gusev, V. Kh. Kudoyarova, A. N. Kuznetsov, P. E. Pak, E. I. Terukov, I. N. Yassievich, B. P. Zakharchenya, W. Fuhs, and A. Sturm, Appl. Phys. Lett. **67**(24), 3599 (1995).
[2] E. I. Terukov, V. Kh. Kudoyarova, M. M. Mezdrogina, V. G. Golubev, A. Sturm, and W. Fuhs, Fiz. Tekh. Poluprovodn. **30**, 820 (1996) [Semiconductors **30**, 440 (1996)].
[3] J. H. Shin, R. Serna, G. N. van den Hoven, A. Polman, W. G. J. M. vanSark, and A. M. Vredenberg, Appl. Phys. Lett. **68**, 997 (1996).
[4] A. R. Zanatta and L. A. O. Nunes, Appl. Phys. Lett. **70**, 511 (1997).
[5] J. L. Rogers, P. S. Andry, W. J. Varhue, E. Adams, M. Lavoie, and P. B. Klein, J. Appl. Phys. **78**, 6241 (1995).
[6] P. S. Andry, W. J. Varhue, F. Lapido, K. Ahmed, P. B. Klein, P. Hengen-

hold, and J. Hunter, J. Appl. Phys. **80**, 551 (1996).
[7] *Physics of Amorphous Hydrogenated Silicon*, Issue 1, G. Jounopoulos and J. Lyukovski (Eds.), Mir, Moscow (1987), 363 pp.
[8] V. B. Voronkov, V. G. Golubev, N. I. Gorshkov, A. V. Medvedev, A. B. Pevtsov, D. N. Suglobov, and N. A. Feoktistov, Pis'ma Zh. Tekh. Fiz. **24** (1998) [Tech. Phys. Lett. **24** (1998)] (to be published).
[9] J. Michel, J. L. Benton, R. F. Ferrante, D. C. Jacobson, D. J. Eaglesham, E. A. Fitzgerald, Y. H. Xie, J. M. Poate, and L. C. Kimerling, J. Appl. Phys. **70**, 2672 (1991).
[10] F. Priolo, G. Franzo, S. Coffa, A. Polman, S. Libertino, R. Barklie, and D. Carey, J. Appl. Phys. **78**, 3874 (1995).
[11] W.-X. Ni, K. B. Joelsson, C.-X. Du, I. A. Buyanova, G. Pozina, W. M. Chen, G. V. Hansson, B. Monemar, J. Cardenas, B. G. Svensson, Appl. Phys. Lett. **70**, 3383 (1997).
[12] A. Madan, in *Physics of Amorphous Hydrogenated Silicon*, Issue 1, G. Jounopoulos and J. Lyukovski (Eds.), Mir, Moscow (1987), p. 310.
[13] M. Morse, B. Zheng, J. Palm, X. Duan, and L. C. Kimerling, Mater. Res. Soc. Symp. Proc. **422**, 41 (1996).
[14] A. J. Kenyon, P. F. Trwoga, M. Federighi, C. W. Pitt, Mater. Res. Soc. Symp. Proc. **358**, 117 (1995).
[15] N. P. Grebenshchikov, G. V. Sidorenko, and D. N. Suglobov, Radiokhimiya **32**, *6*, 14 (1990).
[16] N. I. Gorshkov, D. N. Suglobov, and G. V. Sidorenko, Radiokhimiya **37**, *3*, 196 (1995).
[17] V. F. Masterov and L. V. Zakharenkov, Fiz. Tekh. Poluprovodn. **24**, 610 (1990) [Sov. Phys. Semicond. **24**, 383 (1990)].
[18] R. Street, Adv. Phys. **30**, 593 (1981).

Translated by Frank J. Crowne

Spin fluctuations and electronic semiconductor-metal transitions in iron monosilicide

A. A. Povzner, A. G. Volkov, and P. V. Bayankin

Ural State Technical University, 620002 Ekaterinburg, Russia
(Submitted February 16, 1998)
Fiz. Tverd. Tela (St. Petersburg) **40**, 1437–1441 (August 1998)

This paper discusses the effect of dynamic zero-point and thermal spin-density fluctuations (SDF) on the electronic spectrum of the nearly-ferromagnetic semiconductor FeSi. It is shown that near T=0° zero-point SDF can lead to so much splitting of the electron states of the valence and conduction band that a ''gapless'' ground state arises. As the temperature increases, the forbidden gap in the spectrum of *d* electrons first reappears due to suppression of zero-point fluctuations and then disappears again, as the amplitude of thermal spin fluctuations increases. It is these transformations of the electronic spectrum that are the reason for the anomalous changes in the magnetic susceptibility with temperature observed experimentally.
 [S1063-7834(98)01108-3]

1. The nearly-ferromagnetic compound FeSi has complicated electronic and magnetic properties, whose nature has not been clarified completely and remains a subject for discussion at this time.[1–7] According to the results of band calculations of the electron spectrum based on the single-particle approximation,[8] the compound is a semiconductor with an energy gap between the conduction and valence bands (both in the *s* and *p* spectra and in the *d* spectrum) with a width $E_g^0 \approx 0.12$ eV. However, investigations of the optical conductivity[2] show that the width of the forbidden gap in the *d*-electron spectrum $E_g(T)$ $(E_g(0)=E_g^0)$ decreases with increasing temperature and becomes equal to zero for $T \geqslant T_g \approx 120$ K. Moreover, the studies of its electronic and magnetic properties in Ref. 7 indicate that the electronic state of FeSi is ''gapless'' at low temperatures as well $(T<T_g' \approx 5$ K), and that there is a regime in which the magnetic susceptibility $(\chi(T))$ increases roughly as a Curie law. It should also be kept in mind that $\chi(T) \cong 0$ in the semiconducting phase $(5<T<120$ K), while for $T>T_g$ it begins to increase rapidly, leading to the formation of a broad temperature maximum (in the range $500<T<600$ K). For $T>600$ K the function $\chi(T)$ once more follows a Curie–Weiss law.[1]

In Ref. 3 the extreme change in the susceptibility at relatively high temperatures $(T>T_g)$ was explained qualitatively by postulating that temperature-induced local magnetic moments form. This reflects the existence of itinerant *d* electrons in the system, which fluctuate in the space of exchange ξ fields. In this case an analogy can be made between orientational fluctuations of the ξ fields and fluctuations of atomic magnetic moments localized at sites of a crystal lattice (as in, e.g., magnetic insulators). Although this hypothesis has been confirmed by inelastic neutron-scattering experiments, the approach proposed in Ref. 3 and developed in Ref. 4 does not explain all the data on electronic properties of FeSi. This is because the spin-field and charge-field fluctuation amplitudes are determined by using a crude static approximation, which is valid only at high temperatures. For this reason, the theory agrees quantitatively with the observed function $\chi(T)$ only at temperatures $T>T^* \approx 600$ K (see Ref. 1), for which the amplitude of the temperature-induced local magnetic moments saturates (see Refs. 3 and 4), and gives only a qualitative description of experiments above the temperature T_g. Moreover, this theorey cannot explain the experimental fact[7] that $\chi(T)$ follows the Curie-Weiss law at low temperatures $T<5$ K. In the recently published Refs. 2, 5, and 6, the electronic and magnetic properties of FeSi are derived by representing the compound as a strongly-correlated Kondo system; however, their approach has not improved the situation. Although there are analogies between the properties of FeSi and Kondo systems based on rare-earth metals (for example, CeNiSn, $CeBi_4Pt$, and SmB_6), they do not lead to a quantitative description of the observed function $\chi(T)$, nor the chain of transformations of the electron spectrum observed in FeSi.

2. In order to determine the spin fluctuation amplitude more accurately, we will use the fluctuation-dissipation theorem, according to which

$$\langle m^2 \rangle = \langle m^2 \rangle_T + \langle m^2 \rangle_0 = \sum_q \int_0^\infty \mathrm{Im}(\chi(\mathbf{q},\omega,T))[f_B(\omega/T)+(1/2)]d\omega, \quad (1)$$

where $\chi(\mathbf{q},\omega,T)$ is the generalized dynamic magnetic susceptibility, $\mathbf{q}$ is the fluctuation quasimomentum, and ω is the fluctuation frequenc. The squared amplitude of thermal spin density fluctuations (SDF) $\langle m^2 \rangle_T$ corresponds to the term with the Bose–Einstein function $f_B(\omega/T)$, while the term with the factor 1/2 corresponds to the amplitude of zero-point SDF $\langle m^2 \rangle_0$.

Let us calculate $\chi(\mathbf{q},\omega,T)$ within the framework of the Hubbard model, which includes both band motion of electrons and their intra-atomic interaction. The latter leads not only to interelectron correlations but also to spin fluctuations.[3] In this case we will use the following generating functional Ref. 9 in the interaction representation:

$$\Phi(\mathbf{h}_q)=\left\langle T_\tau \exp\left\{ U\sum_{q'} [\mathbf{S}_{q'}\mathbf{S}_{-q'}-(1/4)N_{q'}N_{-q'}] + \mathbf{h}_q\mathbf{S}_{-q}+\mathbf{h}_{-q}\mathbf{S}_q \right\}\right\rangle_0 . \quad (2)$$

Here T_τ is an operator that orders according to the imaginary time τ, T is the temperature in energy units, $\langle \dots \rangle_0$ is a quantum-statistical average with respect to the Hamiltonian H_0 for band motion of the electrons (see Refs. 3, 9, and 10),

$$S_q^z=\frac{1}{2}\sum_\sigma \sigma N_{q,\sigma}, \quad S_q^+=\sum_k a^+_{k+q,\sigma}a_{k,-\sigma}, \quad S_q^-=(S_{-q}^+)^+,$$

$$N_q=\sum_\sigma N_{q,\sigma}, \quad N_{q,\sigma}=\sum_k a^+_{k+q,\sigma}a_{k,\sigma}$$

are the Fourier transforms of the spin-density operators $\mathbf{S}_q$ and charge-density operators N_q, $q=(\mathbf{q},\omega_n)$ is a four-vector, $\omega_n=2\pi nT$ are boson Matsubara frequencies, n is an integer, and $a^+_{k,\sigma}$ and $a_{k,\sigma}$ are creation and annihilation operators of an electron with four-vector quasimomentum $k=(\mathbf{k},\omega_{2n+1})$ and spin σ, where $\omega_{2n+1}=((2n+1)\pi T)$ are fermion Matsubara frequencies.

The derivatives of $\Phi(\mathbf{h}_q)$ with respect to the generating field vector components $\mathbf{h}_q$ (after reducing $\mathbf{h}_q$ to zero) give the following Matsubara spin Green's functions

$$\chi_q^{\alpha,\beta}(T)=\langle T_\tau S_q^\alpha S_{-q}^\beta\rangle=T^{-1}\frac{\partial^2\Phi(\mathbf{h}_q)}{\partial h_q^\alpha \partial h_q^\beta}, \quad (3)$$

whose analytic continuation to the real axis ($\omega_n\to\omega+i\vartheta$ with $\vartheta\to 0$) coincides with $\chi(\mathbf{q},\omega,T)$. Recall also that the thermodynamic potential of this almost ferromagnetic system of d-electrons is $\Omega=-T\ln(\Phi(0))$.

We shall calculate $\Phi(\mathbf{h}_q)$ in the same approximation as we did the thermodynamic potential for the electronic system in Ref. 11; however, we shall not include the spontaneous magnetization and we shall include zero-point spin fluctuations. In this case we use the Stratonovich–Hubbard transformation (see Ref. 3) to reduce our many-body problem to the study of motion of noninteracting electrons in fluctuating exchange $\boldsymbol{\xi}$ and charge η fields. Then, by analogy with Ref. 11, if we perform the quantum-statistical average in Eq. (2) and sum the resulting series (i.e., resulting from this average) in the approximation of quasi-uniform electron form factors, in addition to those terms that correspond to the Stoner amplification factor ($D_0(\mathbf{q},\omega)$) we have

$$\Phi(\mathbf{h}_q)=\int_0^\infty\int_0^{2\pi}\prod_{q',\gamma}(dr_{q',\gamma}\,d\theta_{q',\gamma}/2\pi)(d\eta_{q'}/2\pi) \times\exp\left\{-\sum_{q'}[|\xi_{q'}-\mathbf{h}_q|^2-|\eta_{q'}|^2 + r^2_{q',\gamma}(D_0^{-1}(q')-D_0^{-1}(0))-\ln r_{q',\gamma}] + \sum_{\nu,\sigma'}\Phi_0(i\eta_\nu+\sigma'|\boldsymbol{\xi}_\nu|)\right\}, \quad (4)$$

where

$$\xi_{q,\gamma}=r_{q,\gamma}\exp(\theta_{q,\gamma}), \quad \nu=(\nu,\tau),$$

$$\sum_\nu(\dots)=\sum_\nu T\int_0^{T^{-1}}(\dots)d\tau,$$

$$\Phi_0(i\eta_\nu+\sigma'|\xi_\nu|)=\sum_{\omega_{2n+1}}\ln(i\omega_{2n+1}-\varepsilon_{\sigma'}(\mathbf{k},\xi_\nu,\eta_\nu)+\mu),$$

$$\varepsilon_{\sigma'}(\mathbf{k},\xi_\nu,\eta_\nu)=\varepsilon_{\mathbf{k}}+i\eta_\nu+\sigma'\xi_\nu,$$

$$\chi_{\mathbf{q}}^0=\sum_{\mathbf{k}}\frac{f(\varepsilon_{\mathbf{k}})-f(\varepsilon_{\mathbf{k}+q})}{i\omega_n-\varepsilon_{\mathbf{k}}+\varepsilon_{\mathbf{k}+q}}, \quad (5)$$

$\varepsilon_{\mathbf{k}}$ is the energy of a d-electron in the single-particle approximation, $D_0^{-1}(\mathbf{q})=(1-U\chi_{\mathbf{q}}^0)$, $\gamma=x,y,z$, $\sigma'=\pm 1$ is the spin quantum number corresponding to a quantization axis connected with the $\boldsymbol{\xi}$ fields that fluctuate in space and time, $f_F(\varepsilon-\mu)$ is the Fermi–Dirac function, and μ is the chemical potential determined from the condition of electrical neutrality (where $N=-\partial\Omega/\partial\mu$ is the number of d electrons). In order to estimate the functional integrals in Eq. (4), taking into account dynamic spin fluctuations, we will use the saddle-point method in the variable $r_{q,\gamma}$, η_q[11] taking into account fluctuations in the modulus of the exchange and charge fields. When we then integrate $\Phi(\mathbf{h}_q)$ over $\theta_{q,\gamma}$, calculate the spin correlators Eq. (3), and analytically continue them to the real axis, we find an expression for the generalized dynamic susceptibility

$$\chi(\mathbf{q},\omega,T)=U^{-1}[(D^{-1}(\varepsilon,T)+D_0^{-1}(\mathbf{q},\omega) + D_0^{-1}(0,0))^{-1}-1], \quad (6)$$

in which

$$D^{-1}(\xi,T)=1-\frac{U}{3}\chi_0^{\parallel}(\xi,T)-\frac{2U}{3}\chi_0^{\perp}(\xi,T), \quad (7)$$

$$\chi_0^{\parallel}(\xi,T)=2g(\mu+\xi)g(\mu-\xi)/\sum_\sigma g(\mu+\sigma'\xi), \quad (8)$$

$$\chi_0^{\perp}(\xi,T)=\frac{1}{2\xi}\sum_{\sigma'}\sigma'\int_{-\infty}^{\infty}g(\varepsilon+\sigma'\xi)f_F(\varepsilon-\mu)d\varepsilon, \quad (9)$$

where the expressions for $\chi_0^{\parallel}(\xi,T)$ and $\chi_0^{\perp}(\varepsilon,T)$ coincide formally with expressions for the longitudinal and transverse susceptibilities of a ferromagnet in the mean-field approximation if we replace $\xi=U\langle m^2\rangle^{1/2}$ by UM_0 (where M_0 is the uniform spontaneous magnetization). Furthermore, here

$$g(\mu)=\int_{-\infty}^{\infty}g(\varepsilon)\left(-\frac{\partial f_F(\varepsilon-\mu)}{\partial\varepsilon}\right)d\varepsilon, \quad (10)$$

where $g(\varepsilon)$ is the density of single-electron d-states.

Finally, using the relation between the electron density of states and the thermodynamic potential (see Ref. 12), we find the following expression

$$g(\varepsilon,\xi)=\frac{1}{2}\sum_\sigma g(\varepsilon+\sigma'\xi), \quad (11)$$

which formally coincides with the expression found earlier in Ref. 10, but which includes the dynamic thermal and zero-point spin fluctuations in accordance with Eq. (1).

The system of equations (6)–(11) allows us to analyze the experimental data for the intensity of paramagnetic neutron scattering:

$$J(\mathbf{q},\omega,T)\sim \mathrm{Im}\chi(\mathbf{q},\omega,T). \tag{12}$$

as we calculate the effect of spin fluctuations on the electron density of states and magnetic susceptibility $\chi(T) \equiv \chi(0,0,T)$.

3. On the one hand, neutron-diffraction studies of paramagnetic spin-fluctuation excitations in FeSi confirm the conclusion that the amplitude of temperature-induced local magnetic moments saturates above $T^*\approx 600$ K;[13] on the other hand, they show the inappropriateness of representing the exchange fields by orientational fluctuations alone for $T<T^*$.[14] The fluctuation representations we develop here imply that the expression for $\chi(\mathbf{q},\omega,T)$ should contain the longitudinal susceptibility $\chi_0^{\parallel}$ as well as the transverse susceptibility $\chi_0^{\perp}$. Moreover, according to Ref. 14, the intensity of neutron scattering by spin fluctuations varies with frequency according to a Lorentz law and decreases with increasing temperature from 77 to 600 K by roughly a factor of 1.5. In this case the half-width of the Lorentz function $J(\mathbf{q},\omega,T)$ turns out to be smaller than its characteristic value for a material with local magnetic moments.

The change in intensity can be explained if we take into account that the Pauli susceptibility, which figures into Eqs. (6) and (7) and determines the exchange amplification factor $D_0(\mathbf{q},\omega)$, can be approximated by the expression (see, e.g., Ref. 3)

$$\chi^0(\mathbf{q},\omega)\approx\chi^0(0,0)(1-aq^2+(ib\omega/|\mathbf{q}|)), \tag{13}$$

where the coefficients a and b depend on the characteristics of the band structure, while the vectors $\mathbf{k}$ and $\mathbf{q}$ are given in units of the modulus of the Brillouin vector q_B.

However, since detailed information about the electronic spectrum $\varepsilon_{\mathbf{k}}$ of FeSi is not available at this time, the parameters a and b can be determined only by comparing the expression for the scattering intensity Eq. (12), obtained after substituting Eqs. (6)–(10) into Eq. (12) and taking into account approximation (13), with the experimental data[13,14]. In this case we obtain values of $a\cong a_1\cong 0$ and $b\cong b_1\cong 10/U$ that can be used to successfully describe the observed change in the intensity with temperature. In particular, the spectral half-width $J(\mathbf{q},\omega,T)$ (i.e., the value of the frequency for which $J(\mathbf{q},\omega,T)$ is decreased by a factor of 2) coincides with the results of Ref. 14 for $T<T^*$. Moreover, in the range where the temperature-induced local magnetic moment amplitude saturates, it coincides with the values derived in Ref. 13. Within the context of approximation (13) we obtain according to Eq. (1)

$$\langle m^2\rangle_T = b(T^2/U)D(\xi)[D^{-1}(\xi)+a]^{-1}, \tag{14}$$

while

$$\langle m^2\rangle_0 = (3/\pi bU)[1-D^{-2}(\xi)a^{-2}] \tag{15}$$

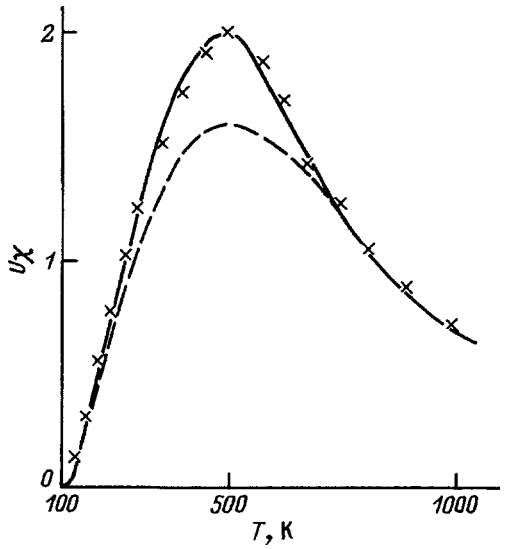

FIG. 1. Temperature dependence of the uniform magnetic susceptibility of FeSi ($\chi(T)\equiv\chi(0,0,T)$) for $T>T_g$. The crosses denote experimental data from Ref. 1. The solid curve comes from calculations using Eq. (6) taking into account the longitudinal and transverse spin fluctuations; the dashed curve shows results of calculations using Eq. (17) without including the contribution associated with the longitudinal spin fluctuations.

for $D^{-1}(\xi)<a$ and zero otherwise. Then if we set values $a=a_1$ and $b=b_1$ in Eqs. (14) and (15), the average SDF amplitude will contain only the contribution from thermal fluctuations

$$\xi = U\langle m^2\rangle_T^{1/2} = \sqrt{Ub_1}TD(\xi), \tag{16}$$

while the amplitude of zero-point spin fluctuations will equal zero. When we calculate the temperature dependence of the paramagnetic susceptibility $\chi(T)$ within these approximations, we find that in the temperature range $T>T^*$ the transverse (orientational) SDF dominate:

$$\chi(T)=\chi_0^{\perp}(\xi,T)[1-U\chi_0^{\perp}(\xi,T)]^{-1}, \tag{17}$$

while for $T<T^*$ the contribution associated with longitudinal spin fluctuations is enhanced, which takes into account the term $\chi_0^{\parallel}$ in Eqs. (6) and (7). The results of these calculations are given in Fig. 1. For $T_g'<T<T_g$ the quantity $\chi(T)$ equals zero, since the chemical potential lies in the energy gap and the semiconducting phase is realized.

The density of states of the semiconducting phase calculated from Eqs. (11) and (16) is shown in Fig. 2, while the width of the forbidden gap varies according to the law

$$E_g(T)=E_g^0-2\xi(T)=E_g^0-2\sqrt{Ub_1}T. \tag{18}$$

The value of T_g obtained from Eq. (18) agrees with the experimentally measured value[1)] of the optical conductivity and temperature dependence of the magnetic susceptibility.[1,2] However, these calculations do not predict a gapless state below $T_g'\approx 5$ K, which disagrees with the experimental data[7].

There have benn no neutron diffraction studies of spin fluctuations in the ground state of FeSi. Despite this, we can describe them by using a model in which

$$E_g=E_g^0-U\langle m^2\rangle_0^{1/2}\approx 0, \tag{19}$$

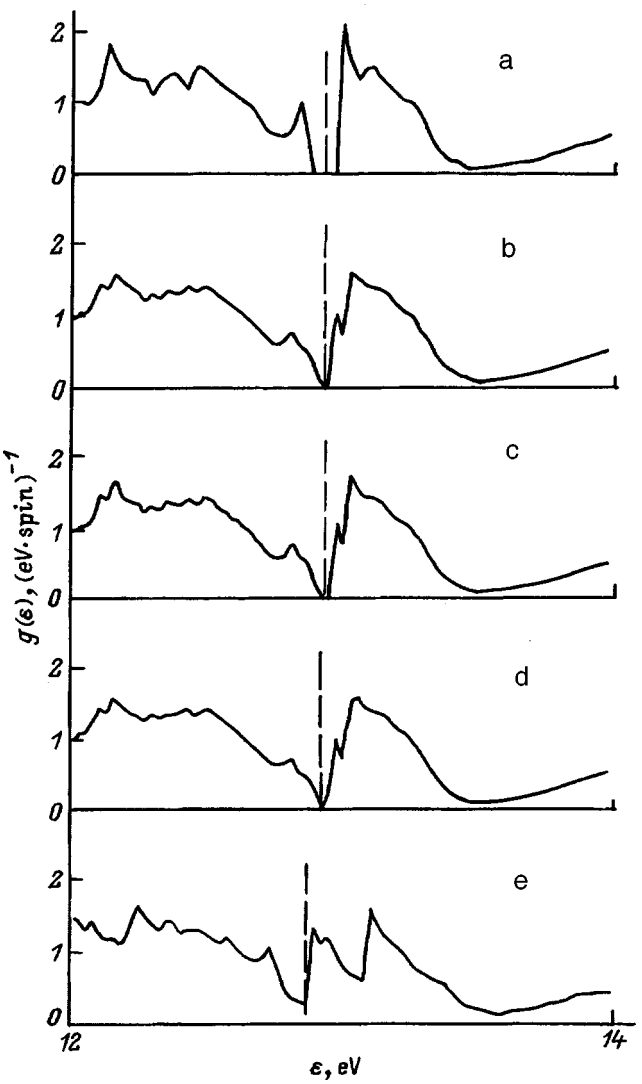

FIG. 2. Dependence of the electron density of states of FeSi on energy at various temperatures. The dashed line corresponds to the position of the chemical potential. a—model curve of the density of electron states unrenormalized by spin fluctuations, constructed from the data of Ref. 8; b–e—electron density-of-states curves at $T=0$, 50, 100, and 300 K respectively.

as $T\to 0$ K. From this model, we estimate the amplitude of the zero-point fluctuations to be $\langle m^2\rangle_0^{1/2}=0.08$ (in units of the Bohr magneton). Assuming also that the zero-point fluctuations disappear below $T_g'\approx 5$ K, we find from Eq. (15) the values $a=a_2=0.1$ and $b=b_2=30/U$. In this case the following approximate relation holds within this model:

$$\chi(T)\approx\chi_0^{\|}(\xi,T)\left[1-\frac{1}{3}U\chi_0^{\|}(\xi,T)\right]^{-1}, \tag{20}$$

according to which the longitudinal (not transverse) zero-point spin fluctuations are found to have a decisive influence on the value of the paramagnetic susceptibility.

Our numerical analysis of Eq. (20) is limited by the precision of the band calculations from Ref. 8, and is impossible for $T<1$ K. However, in the temperature range above 1 K (when $T>|\mu\pm\xi-(E_g^0/2)|$) and up to the point where the zero-point fluctuations disappear (according to our assumptions, at 5 K) $\chi^{\|}$ decreases with increasing temperature due to Fermi excitations (see Eqs. (8), (10), and Fig. 2a). Thus, in approximate agreement with the experiments of Ref. 7, the results of our numerical calculations based on Eqs. (20) and (8) can be approximated by the expressions

$$U\chi\approx C/(T+\Theta),$$

$$U\chi^{\|}\approx C/(T+\Theta_0), \tag{21}$$

where $C\approx 1$ K, $\Theta\approx 0.02$ K, $\Theta_0\approx 0.35$ K, and T is the temperature (in K).

4. Thus, it is clear that the reason for the transformations of the electron spectrum in nearly ferromagnetic FeSi, and possibly the transformations that occur in the strongly correlated rare-earth element compounds as well (i.e., those compounds that do not undergo magnetic phase transitions despite the fact that they are close to these states theoretically), is the splitting of the electronic spectra in the fluctuating exchange fields. The amplitudes of these fields are associated both with thermal and zero-point SDF; the values of the latter can turn out to be quite large in the ground state, and decrease considerably with increasing temperature. Moreover, these nearly-ferromagnetic semiconductors exhibit both orientational (transverse) and longitudinal spin fluctuations (i.e., fluctuations of the modulus of the spin density vector) over a wide temperature range. Inclusion of the latter is particularly important at low temperatures, and allows us to achieve not only qualitative but also quantitative agreement with experimental data on the temperature dependence of the magnetic susceptibility, the temperature at which the energy gap ''collapses'' and that at which the electronic phase transitions take place. The picture set forth here of the temperature-induced changes of the density of states of d electrons agrees not only with the function $\chi(T)$ but also with experimental data on the electrical resistivity.[15] In particular, within its framework we can interpret the change in the value of the temperature coefficient of electrical resistivity as the system passes from the ''gapless'' state to a semiconductor phase, and also the change in sign of the electrical resistivity at $T>250$ K, when the dip in the curve for $g(\varepsilon,\xi)$ at $\varepsilon\approx\mu$ disappears (see Fig. 2c–e).

Of course, this picture of transformations of the electronic structure of FeSi induced by spin fluctuations is in need of further experimental confirmation and refinement. Experimental studies of paramagnon scattering of neutrons and optical conductivity below 5 K would be especially interesting in this context. Moreover, in light of the similarity of the properties of FeSi and strongly correlated compounds based on rare-earth metals, there is a need for further development of analogous spin-fluctuation approaches for these materials as well. However, this requires that we begin with more general models that take into account hybridization anomalies in the electronic spectra.

[1)]When the static approximation of Ref. 10 is used, the computed value of T_g exceeds the value found from experiment by roughly a factor of 3.

[1] V. Jaccarino, G. R. Wertheim, J. H. Werneic, L. R. Walker, and S. Arays, Phys. Rev. **160**, 46 (1967).
[2] Z. Schlesinger, Z. Fizk, H. T. Zhang, and M. B. Maple, Phys. Rev. Lett. **71**, 1748 (1993).
[3] T. Moriya, *Spin Fluctuations in Itinerant Electron Magnetism* [Springer-Verlag, Berlin, New York, 1985; Mir, Moscow, 1988, 288 pp.].
[4] P. V. Gel'd, A. A. Povzner, and A. G. Volkov, Dok. Akad. Nauk SSSR **283**(2), 358 (1985) [Sov. Phys. Dokl. **30**, 585 (1985)].
[5] C. Fu, M. P. Krijn, and S. Doniach, Phys. Rev. B **49**, 2219 (1994).
[6] C. M. Varma, Phys. Rev. B **50**, 9952 (1994).
[7] M. B. Hunt, M. A. Chernicov, T. Felder, and H. R. Ott, Phys. Rev. B **50**, 14 933 (1994).
[8] L. I. Vinokurova, A. V. Vlasov, and É. T. Kulatov, Bull. IOFAN **32**, 26 (1991).
[9] A. A. Povzner, Fiz. Nizk. Temp. **19**, 90 (1993) [Low Temp. Phys. **19**, 65 (1993)].
[10] A. G. Volkov, A. A. Povzner, and P. V. Gel'd, Fiz. Tverd. Tela (Leningrad) **26**, 1675 (1984) [Sov. Phys. Solid State **26**, 1015 (1984)].
[11] P. V. Gel'd, A. A. Povzner, and A. G. Volkov, Dok. Akad. Nauk Ross. **333**(3), 321 (1993) [Dokl. Akad. Nauk SSSR **38**, 470 (1993)].
[12] A. A. Abrikosov, L. P. Gor'kov, and I. E. Dzyaloshinskiĭ, *Methods of Quantum Field Theory in Statistical Physics* [Prentice-Hall, Englewood Cliffs, N. J., 1963; Fizmatgiz, Moscow, 1962, 444 pp.].
[13] K. Tajima, Y. Endoh, J. W. Fincher, and G. Shirane, Phys. Rev. B **38**, 6954 (1988).
[14] M. Kohgi and Y. Ishikawa, Solid State Commun. **37**, 833 (1981).
[15] P. V. Gel'd, A. A. Povzner, Sh. Sh. Abel'sjiĭ, and L. F. Romashyova, Dok. Akad. Nauk SSSR **313**(5), 1107 (1990) [Sov. Phys. Dokl. **35**, 758 (1990)].

Translated by Frank J. Crowne

Optical spectra of triply-charged rare-earth ions in polycrystalline corundum

A. A. Kaplyanskiĭ, A. B. Kulinkin, A. B. Kutsenko, S. P. Feofilov, R. I. Zakharchenya, and T. N. Vasilevskaya

A. F. Ioffe Physicotechnical Institute, Russian Academy of Sciences, 194021 St. Petersburg, Russia
(Submitted February 16, 1998)
Fiz. Tverd. Tela (St. Petersburg) **40**, 1442–1449 (August 1998)

Solid samples of polycrystalline corundum α-Al_2O_3 activated by triply-charged rare-earth ions RE^{3+} ($R=Eu^{3+}$, Er^{3+}, Pr^{3+}) were synthesized by the sol-gel technology. Characteristic narrow-line optical absorption and luminescence spectra produced by intraconfigurational $4f-4f$ transitions in RE^{3+} ions have been measured. RE^{3+} ions have been established to form one dominant type of optical centers in the corundum matrix, and the energy diagram of Eu^{3+} and Er^{3+} Stark levels in corundum has been determined. © *1998 American Institute of Physics.* [S1063-7834(98)01208-8]

Although the spectroscopic properties of rare-earth (RE) ions in dielectric crystals have been studied in numerous works, the latter contain practically no information on the characteristics of RE ions acting as activators in crystalline corundum $\alpha\,Al_2O_3$. Indeed, while Al^{3+} ions in the corundum lattice are easily replaced by iron-group $3d$ ions (as exemplified by ruby $\alpha\,Al_2O_3$:Cr^{3+}), incorporation of RE^{3+} ions which are larger in size into the corundum host is difficult to achieve by traditional high-temperature methods of crystal growth. A recent communication[1] reported on doping corundum single crystals by Er^{3+} ions by the fast-ion-implantation technique. The present work (as also Ref. 2) deals with the first studies of optical spectra of triply charged RE ions (Eu^{3+}, Er^{3+}, Pr^{3+}) in polycrystalline corundum $\alpha\,Al_2O_3$ prepared by the sol-gel technique. It is shown that RE^{3+} ions embedded in the corundum lattice form a distinct dominant type of centers with a characteristic $f-f$ narrow-line spectrum. The energy diagram of the Eu^{3+} and Er^{3+} levels in corundum has been determined.

1. PREPARATION AND CHARACTERIZATION OF SAMPLES

$\alpha\,Al_2O_3$ corundum doped with the RE ions Eu^{3+}, Er^{3+}, and Pr^{3+} was prepared by the sol-gel technology using the alkoxy method, with the aluminum alkoxides $Al(OR)_3$ used as the starting materials. The initial stage in preparing Al_2O_3 by the sol-gel technology consists in forming aggregation-stable colloidal solutions (sols and gels of the aluminum monohydroxide γ AlOOH), which were obtained by hydrolysis of $Al(OR)_3$. The stability of γ-AlOOH sols against aggregation within a broad range of electrolyte concentrations[3] permits one to introduce precisely monitored amounts of salts of RE elements, which spread uniformly throughout the sol volume. The sols were aged and dehydrated at 80–100 °C to produce gels and xerogels. These processes are accompanied by chemisorption of RE^{3+} ions at the surface of the colloidal aluminum-monohydroxide particles involving formation of Al-O-RE–type bridging bonds. Note that formation of such bonds by traditional crystal-growth methods would require much higher temperatures, which are determined by the melting points of the corresponding oxides (about 2000 °C).

In the final stage, Al_2O_3 samples were obtained by firing the xerogels. At 450 °C, the temperature corresponding to the minimum of the second endothermal feature in the DTA curve,[4] aluminum monohydroxide looses water to transform to $\gamma\,Al_2O_3$, which is the first low-temperature aluminum-oxide modification stable up to 900 °C. The optical and other physicochemical properties of $\gamma\,Al_2O_3$ were studied in samples annealed at 750 °C for an hour. Annealing at 750 °C produced a solid transparent highly porous $\gamma\,Al_2O_3$:RE^{3+} sample made up of nm-scale crystalline particles which were close in size and had a structurally disordered cubic lattice of the γ phase of Al_2O_3. Heating $\gamma\,Al_2O_3$ above 900 °C converts it to corundum through a series of polymorphic transformations $\gamma\rightarrow\delta\rightarrow\theta\rightarrow\alpha$-$Al_2O_3$.

The phase composition of the samples was monitored by x-ray diffractometry. Figure 1 presents diffraction patterns of aluminum-oxide samples annealed at 1350 °C, which had different concentrations c (at. %) of the RE ion (Eu^{3+}) (it is the calculated concentration introduced in the liquid-phase stage of the preparation). For low Eu^{3+} contents ($c\leqslant 1$ at. %), one observes reflections characteristic of the α-Al_2O_3 lattice, which indicates that the sample is single phase (corundum). For higher Eu^{3+} concentrations, the diffraction pattern (3–5 in Fig. 1) exhibits, besides the corundum signature, reflections characteristic of the $EuAlO_3$ oxide, which implies crystallization of a new phase. We shall consider subsequently results obtained primarily on single-phase α-Al_2O_3 samples with a low RE impurity concentration. These solid, very strong samples are polycrystalline and are made up of closely packed, fairly large (0.1–0.5 μm) corundum crystallites (see Fig. 2 displaying an image of the α-Al_2O_3:Er^{3+} sample surface obtained with an atomic-force microscope). Because the optically uniaxial corundum crystals are misoriented, the polycrystalline sample turns out to be optically nonuniform and strongly scatters visible light.

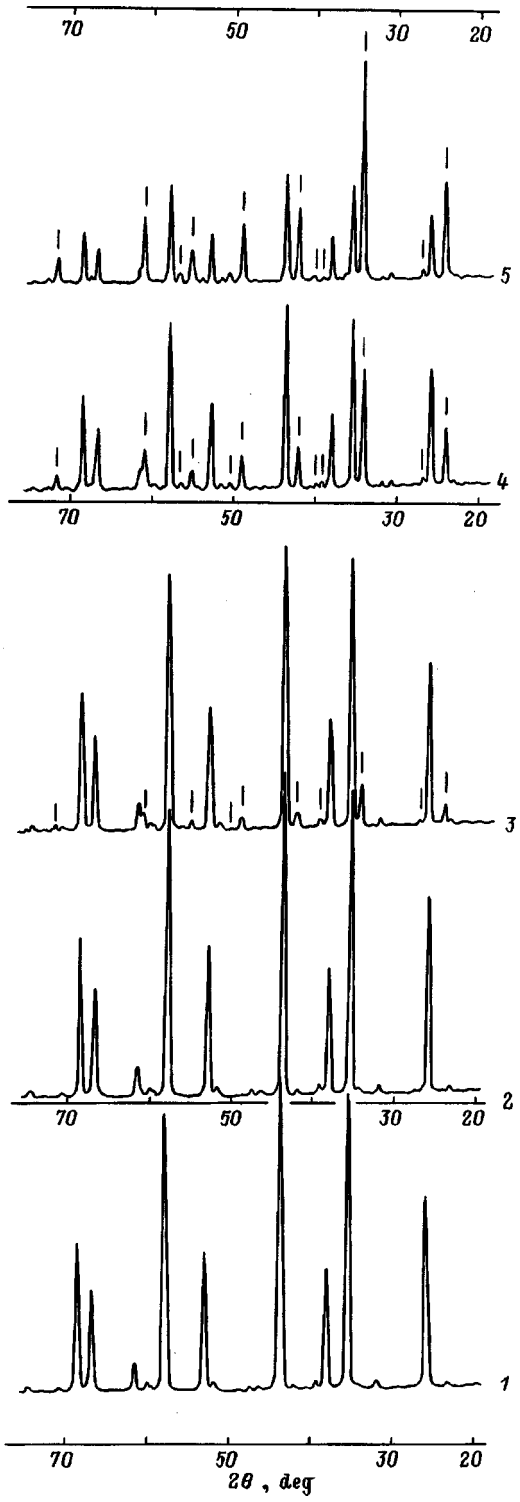

FIG. 1. X-ray diffraction patterns of aluminum oxide samples annealed at 1400 °C and having different concentrations of Eu added during the sol-gel preparation. *c* (at. %): *1*—0, *2*—0.1, *3*—1.5, *4*—5, *5*—20. The bars identify the $EuAlO_3$ reflections.

2. OPTICAL SPECTRA

The main studies of optical spectra of RE^{3+} ions in polycrystalline corundum were carried out on low-concentrated samples with Eu^{3+} ($4f^6$) ions, because they have one of the simplest energy-level and optical-transition diagrams, as well with Er^{3+} ions ($4f^{11}$). Besides RE^{3+} spectra of polycrystalline $\alpha\,Al_2O_3$ corundum which has a regular lattice, we consider briefly inhomogeneously broadened spectra of these ions in high-porosity nanocrystalline samples of a structurally disordered γ phase of Al_2O_3, which are obtained by the same sol-gel technique but at a lower temperature (750 °C). The luminescence and absorption spectra were measured by standard spectroscopic methods at 77 and 5 K.

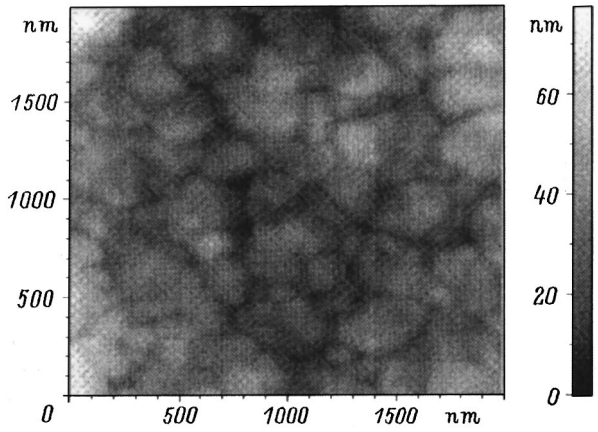

FIG. 2. Atomic-force microscope image of the surface of Er-doped $\alpha\,Al_2O_3$.

A. Spectra of Eu^{3+} ions

1) $\gamma\,Al_2O_3$:Eu^{3+}. The luminescence spectra of Eu^{3+} excited nonselectively via high-lying excited states exhibit clearly inhomogeneously broadened structured bands due to transitions from the lower radiative level of Eu^{3+} $^5D_0$ to the ground-multiplet levels $^7F_0$, $^7F_1$, $^7F_2$, $^7F_3$, and $^7F_4$ (Fig. 3a). The relative intensity and width of the bands produced in transitions to the ^7F_n levels, as well as the observed number of components in the structure of the $^5D_0$–^7F_n bands associated with the crystal-field splitting of the lower ^7F_n level, are, on the whole, similar to those of Eu^{3+} spectra in disordered crystals[5] and glasses.[6] Note that in the case of γ-Al_2O_3:Eu^{3+} part of the inhomogeneous broadening, which is comparatively large for Eu^{3+}, is due to structural disorder on the cation sublattice of the host. The $^5D_0$–^7F_n decay kinetics occur on the ms scale and are nonexponential, which is due to dispersion of the characteristic times in the nonuniform ensemble of Eu^{3+} centers in the disordered host lattice.

We have succeeded in observing a certain narrowing of luminescence bands in the region of the transitions $^5D_0$–$^7F_1$, $^7F_2$, $^7F_3$, and $^7F_4$ (Fig. 3b) by selective excitation of $\gamma\,Al_2O_3$:Eu^{3+} within the inhomogeneously broadened profile of the $^7F_0$–$^5D_0$ transition. The small extent of narrowing of these nonresonant fluorescence bands under selective resonant excitation argues for the absence of a clear correlation between the energies of the $^7F_0$–$^5D_0$ and $^5D_0$–^7F_n ($n\neq 0$) transitions in Eu^{3+} ions residing in the disordered γ-Al_2O_3 lattice.

2) $\alpha\,Al_2O_3$:Eu^{3+}. α-Al_2O_3:Eu^{3+} samples prepared by annealing high-porosity $\gamma\,Al_2O_3$:Eu^{3+} at 1350 °C exhibit fairly intense Eu^{3+} luminescence, whose spectral and kinetic characteristics differ substantially from those of Eu^{3+} in the nanocrystalline γ phase of Al_2O_3 discussed above. Optical

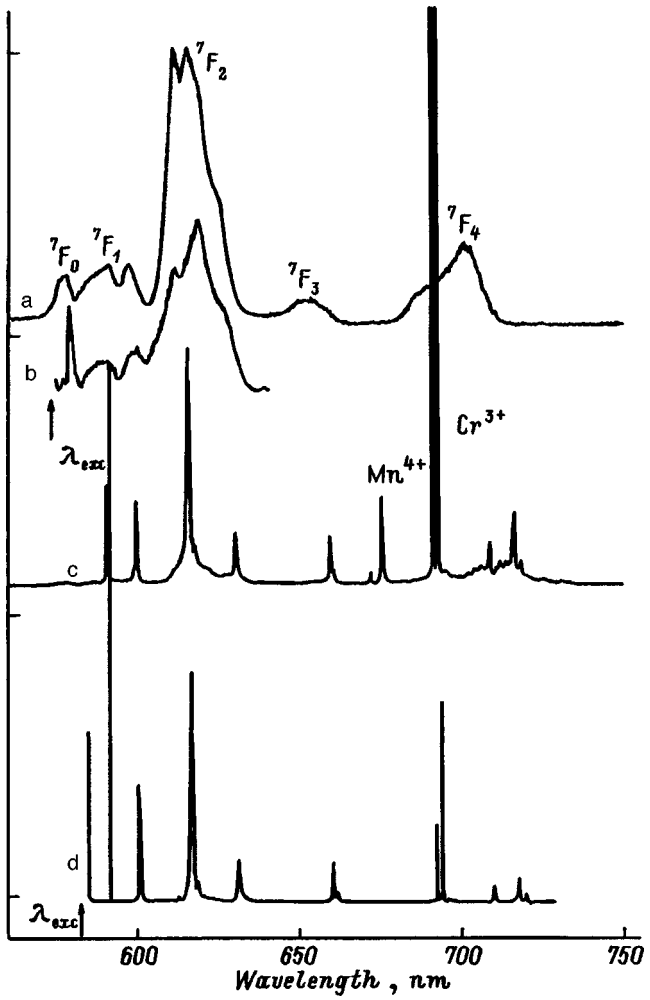

FIG. 3. 77 K fluorescence spectra of Eu^{3+} in aluminum oxide in (a,b) γ phase and (c,d) α phase. a,c—nonresonant excitation at $\lambda_{exc}=350-420$ nm, b—$\lambda_{exc}=575$ nm, d—$\lambda_{exc}=584.5$ nm.

nonselective excitation of Eu^{3+} via its high-lying states with 350–420 nm light reveals narrow (~ 0.1 nm) emission lines in the region of transitions from $^5D_0$ to levels of the ground multiplet ^7F: $^5D_0-^7F_1$ (two lines), $^5D_0-^7F_2$ (three lines), $^5D_0-^7F_3$, and $^5D_0-^7F_4$, with no indication of the $^5D_0-^7F_0$ transition (Fig. 3c). In the vicinity of these lines one observes a weaker, structured background, whose relative intensity depends on prehistory of the α-Al_2O_3:Eu^{3+} sample (anneal regime and temperature and Eu concentration). The spectrum of the sample shown in Fig. 3c exhibits also characteristic lines belonging to accidental impurities Cr^{3+} and Mn^{4+}, which coincide in position with the well-known R lines (the $^2E-^4A_2$ transition) of these ions observed in bulk α-Al_2O_3 corundum crystals. The observation of these lines may serve as an additional argument for the crystal lattice of the samples under study belonging to the α phase of Al_2O_3.

We studied also the luminescence excitation spectrum of Eu^{3+} by means of a tunable laser. A narrow excitation peak was found about 584.5 nm, whose position corresponds to the expected energy of the $^7F_0-^5D_0$ transition of Eu^{3+}. Selective optical excitation of Eu^{3+} ions at the $^7F_0-^5D_0$ energy gives rise to the whole narrow-line luminescence spectrum $^5D_0-^7F_{1,2,3,4}$, which is observed also under nonselective Eu^{3+} excitation through the high-lying states, but both the background near the Eu^{3+} lines and the lines that do not belong to Eu^{3+} (the R lines of Cr^{3+} and Mn^{4+}) are considerably weaker in this case (Fig. 3d). The practically close coincidence of the line spectra $^5D_0-^7F_{1,2,3,4}$ obtained under nonselective excitation in the 350–420-nm region with those excited selectively in the $^7F_0-^5D_0$ transition shows that the luminescence of the α-Al_2O_3:Eu^{3+} samples is dominated by one type of Eu^{3+} centers only. Table I presents the energy diagram of the levels of this main Eu^{3+} center, which is seen in the spectra and was derived from spectral positions of the luminescence lines and of the $^7F_0-^5D_0$ excitation line. Interestingly, one of the $^5D_0-^7F_1$ emission components (591.3 nm) produced in selective laser excitation of the $^7F_0-^5D_0$ transition (Fig. 3d) is much more narrow (<0.01 nm) than the lines obtained under nonresonant excitation, which implies correlation between the positions of the $^5D_0$, $^7F_0$, and $^7F_1$ levels. After termination of the excitation, the α-Al_2O_3:Eu^{3+} luminescence decays exponentially with a characteristic time $\tau=2$ ms.

TABLE I. Energies of the Stark sublevels of Eu^{3+} ions in α-Al_2O_3.

Term	Energy, cm^{-1}
$^7F_0$	0
$^7F_1$	202, 458
$^7F_2$	898, 943, 1268
$^7F_3$	1970, 1991
$^7F_4$	3024, 3169, 3209
$^5D_0$	17 109

The narrow-line spectrum of the luminescence and its strictly exponential decay indicate that the Eu^{3+} ions responsible for the luminescence occupy predominantly one fixed position in the regular crystal lattice which does not have structural disorder. It is such a lattice that characterizes the α-Al_2O_3 phase, to which the samples under study belong according to the conditions of preparation and to the results of x-ray diffraction analysis. It may be added that the observed $^5D_0-^7F_{0,1,2,3,4}$ line spectrum coincides with none of the known luminescence spectra of Eu^{3+} ions present in various crystalline europium oxides [Eu_2O_3 (Ref. 7) and $EuAlO_3$ (Ref. 8)], phases which can form in small amounts in annealed Al_2O_3:Eu^{3+} samples, particularly at high Eu concentrations (Fig. 1). A luminescence spectrum of the $EuAlO_3$ impurity phase coinciding with the available data[8] was observed by us only under selective excitation at a wavelength that could not excite the main narrow-line spectrum of the α-Al_2O_3:Eu^{3+} samples. Thus the narrow-line Eu^{3+} luminescence spectrum observed under both nonselective and selective excitation belongs to none of the possible impurity ''concentrated phases'' containing europium. It appears natural to assign this spectrum to Eu^{3+} ions in α-Al_2O_3 corundum.

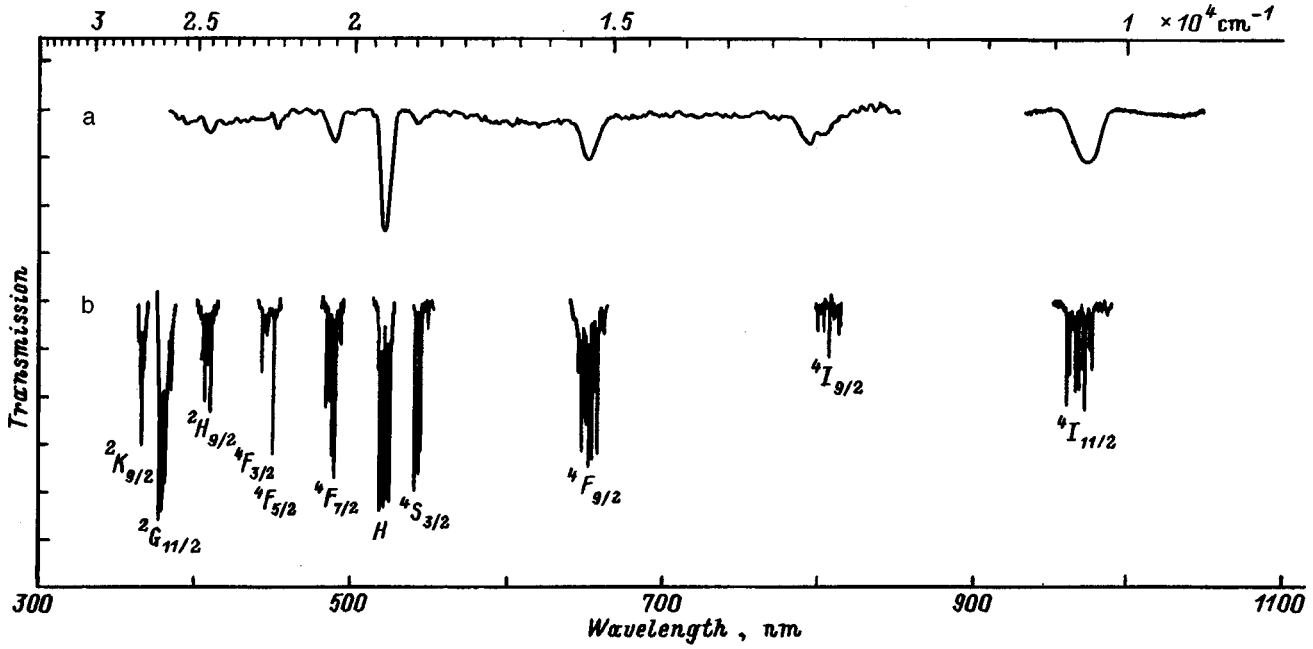

FIG. 4. Absorption spectrum of Er^{3+} ions in aluminum oxide in (a) γ phase and (b) α phase. $T=77$ K.

B. Spectra of Er^{3+} ions

1) γ Al_2O_3:Er^{3+}. The absorption spectrum of solid high-porosity nanocrystalline samples of the γ phase of Al_2O_3:1 at. %Er^{3+} exhibited all visible and near-IR transitions from the $^4I_{15/2}$ ground state to the levels $^4I_{13/2,11/2,9/2}$, $^4F_{9/2,7/2,3/2}$, $^4S_{3/2}$, and $^2H_{11/2,9/2}$ characteristic of Er^{3+} (Fig. 4a). The bands corresponding to these transitions are inhomogeneously broadened (the broadening ~ 200 cm^{-1}), which is due to structural disorder of the γ-Al_2O_3 lattice.

Er^{3+} luminescence in γ-Al_2O_3 samples was observed under resonant excitation of the $^4I_{15/2}$–$^4F_{5/2}$ transition by an Ar laser at 488.0 nm. We succeeded in detecting here a weak, inhomogeneously broadened, structured luminescence band $^4S_{3/2}$–$^4I_{15/2}$ in the green region and a strong structured IR band peaking at 1.53 μm, which corresponds to the well-known $^4I_{13/2}$–$^4I_{15/2}$ transition. The observed IR luminescence spectrum of our nanocrystalline γ-Al_2O_3:Er^{3+} samples prepared by sol-gel technology turns out to be very close to the spectrum of Er^{3+} in thin polycrystalline Al_2O_3 films obtained by magnetron sputtering on oxidized silicon.[9]

2) α Al_2O_3:Er^{3+}. The $T=77$ K absorption spectrum exhibits in place of all the above inhomogeneously broadened absorption bands of γ Al_2O_3:Er^{3+} (Fig. 4a) close groups of narrow lines produced in transitions between the Stark sublevels of the lower state, $^4I_{15/2}$, and the sublevels of the upper states $^4I_{13/2,11/2,9/2}$, $^4F_{9/2,7/2,5/2,3/2}$, $^4S_{3/2}$ and $^2H_{11/2,9/2}$ (Fig. 4b).

The luminescence spectrum of α-Al_2O_3:Er^{3+} samples obtained at $T=77$ K under excitation by a He–Cd laser at 441.6 nm of the Er^{3+} upper levels $^4F_{3/2}$ exhibits transitions from several lower lying states: $^4S_{3/2}$ ($^4S_{3/2}$–$^4I_{15/2}$ and $^4S_{3/2}$–$^4I_{13/2}$ transitions), $^4F_{9/2}$ ($^4F_{9/2}$–$^4I_{15/2}$ transition), and $^4I_{13/2}$ (the $^4I_{13/2}$–$^4I_{15/2}$ IR transition, see Fig. 5). In the corresponding spectral regions one observes close groups of narrow lines caused by transitions between the Stark sublevels of the upper and lower states.

A comprehensive analysis of the complex line structure in the absorption and luminescence spectra of α Al_2O_3:Er^{3+}

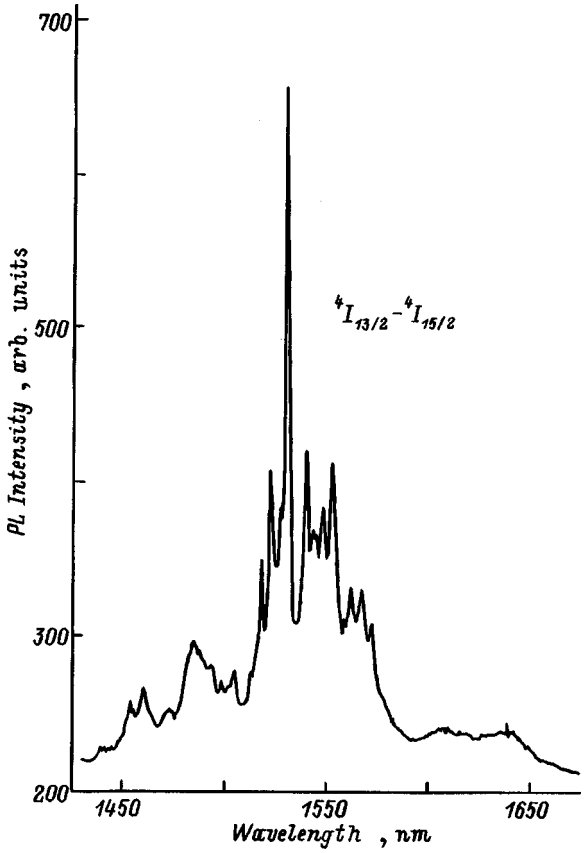

FIG. 5. IR luminescence spectrum of Er^{3+} ions in α Al_2O_3 ($^4I_{13/2}$–$^4I_{15/2}$ transition). $T=300$ K.

TABLE II. Energies of the Stark sublevels of Er^{3+} ions in α Al_2O_3.

Term	Number of components	Energy, cm^{-1}
$^4I_{15/2}$	8	0, 51, 168, 218, 267, 382, 437, 514
$^4F_{9/2}$	5	15 260, 15 342, 15 373, 15 396, 15 480
$^4S_{3/2}$	2	18 403, 18 488
$^2H_{11/2}$	6	19 120, 19 164, 19 190, 19 242, 19 275, 19 305
$^4F_{7/2}$	4	20 479, 20 555, 20 619, 20 687
$^4F_{5/2}$	3	22 193, 22 262, 22 227
$^4F_{3/2}$	2	22 528, 22 653
$^2H_{9/2}$	5	24 480, 24 528, 24 667, 24 697, 24 765

measured at 77 and 5 K suggests the existence of a single dominant physical type of Er^{3+} center in corundum, which is responsible for the experimentally-observed line spectra of Er^{3+}. Table II presents an energy diagram of the Stark structure of Er^{3+} electronic states in α-Al_2O_3 crystals, within which one can identify the main lines in the absorption and luminescence spectra of α Al_2O_3:Er^{3+} observed experimentally. The diagram is based on measurements of absorption and luminescence spectra obtained at 5 K. At such a low temperature, only the lowest Stark sublevel is populated in the initial state of the ion, and the energy of the final electronic state is extracted directly from the spectral line positions. As follows from Table II, the number of the Stark sublevels seen in absorption spectra for all Er^{3+} electronic states $^{2S+1}L_J$ is $J+1/2$, which implies crystal-field-induced lifting of degeneracy to the maximum extent possible for the levels of the Kramers ion Er^{3+} $(4f^{11})$. The Stark-energy

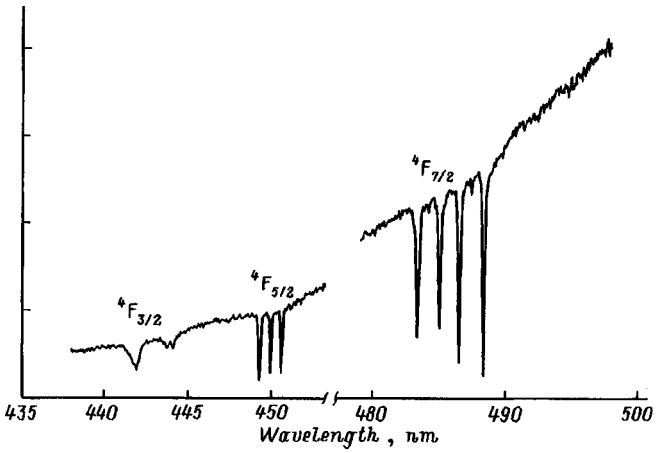

FIG. 6. 5 K absorption spectrum of α Al_2O_3: 1 at. % Er^{3+} obtained in the region of the $^4I_{15/2}$-$^4F_{3/2,5/2,7/2}$ transitions.

structure of excited states was found from 5 K absorption spectra corresponding to transitions from the lowest Stark-split sublevel of the $^4I_{15/2}$ ground state. The number of absorption lines observed at 5 K and produced in transitions to the states $^4I_{13/2,11/2,9/2}$, $^4F_{9/2,7/2,5/2,3/2}$, $^4S_{3/2}$, and $^2H_{11/2,9/2}$ (7, 6, 5, 5, 4, 3, 2, 2, 6, and 5, respectively) is equal in all cases to the maximum possible number $(J+1/2)$ of the Stark sublevels under complete lifting of degeneracy of the final excited states (see, e.g., Fig. 6). The Stark structure of the $^4I_{15/2}$ ground state was determined from 5 K eight-line experimental luminescence spectra $^4S_{3/2}$–$^4I_{15/2}$ and $^4F_{9/2}$–$^4I_{15/2}$ produced by transitions from the lowest Stark-split component

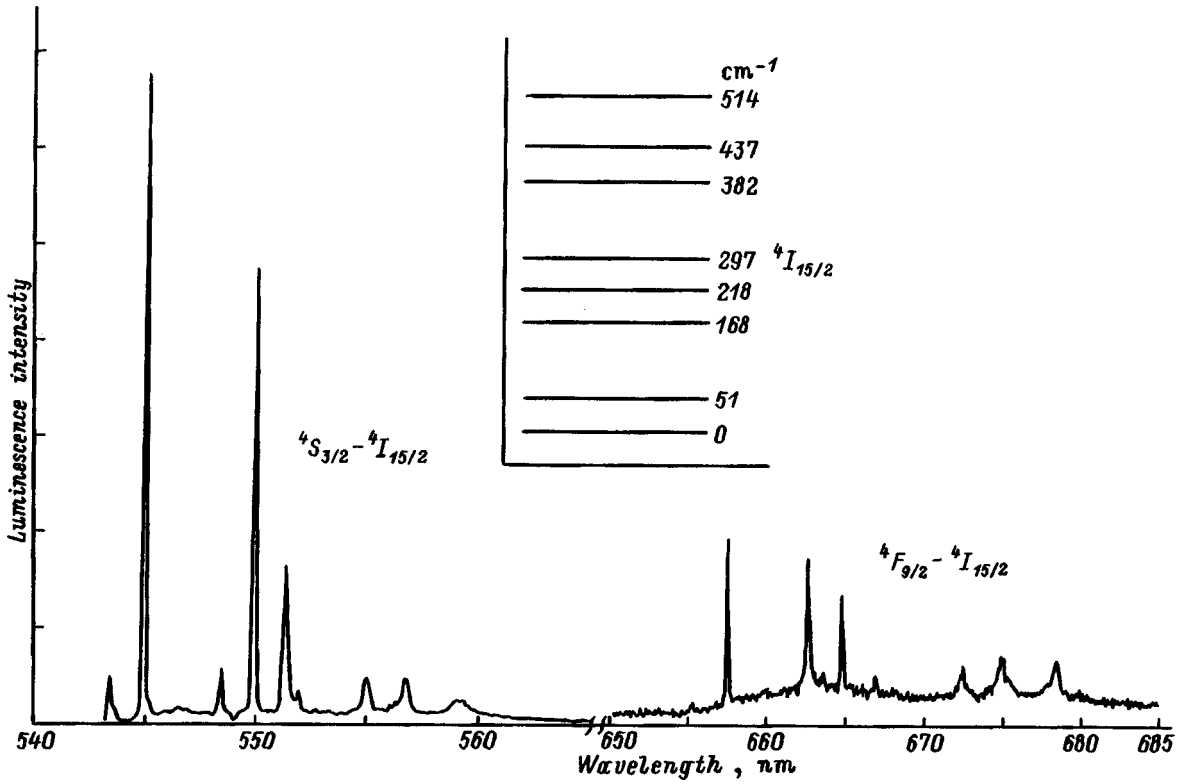

FIG. 7. Luminescence spectrum of α Al_2O_3: 1 at. %Er^{3+} obtained at $T=5$ K ($^4S_{3/2}$–$^4I_{15/2}$ and $^4F_{9/2}$–$^4I_{15/2}$ transitions). Inset: the Stark structure of the ground state $^4I_{15/2}$.

$^4S_{3/2}$, $^4F_{9/2}$ to the eight Stark sublevels of $^4I_{15/2}$. Note that the experimental α-Al_2O_3:Er^{3+} spectra produced in these and all other transitions exhibit practically all theoretically possible optical transitions between the Stark sublevels of the various Er^{3+} electronic states, with their particular intensities.

Most of the absorption and luminescence lines are narrow, and their width ($\sim$0.1 nm) is caused by inhomogeneous broadening. One observes at the same time a very strong broadening of some lines in the spectra of absorption ($^4I_{15/2}$–$^4F_{3/2}$, Fig. 6) and luminescence (three long-wavelength lines in the $^4S_{3/2}$–$^4I_{15/2}$ spectrum, Fig. 7). Remarkably, in both cases the energy spectrum of Er^{3+} contains below the final levels other states at a distance of about 500 cm^{-1} (the $^4F_{5/2}$ level below $^4F_{3/2}$, the Er^{3+} ground level below the upper $^4I_{15/2}$ Stark sublevels). According to Ref. 10, the frequency region of 500 cm^{-1} is characterized by a high density of phonon states of $\alpha\,Al_2O_3$. Thus the final states we have been discussing can relax rapidly in single-phonon processes with emission of 500 cm^{-1} phonons, which shortens the lifetime of the states and results in the observed broadening of the spectral transitions involved.

The above line spectra of $\alpha\,Al_2O_3$:Er^{3+} belonging to one dominant type of Er^{3+} ions in the corundum lattice are observed in pure form in single-phase samples (corundum) containing Er^{3+} at low concentration ($c \leqslant 1$ at. %). At the same time, the spectra of samples with higher Er concentrations, as well as of samples which were not annealed to the single-phase state, usually exhibit additional narrow lines in the region of the Er^{3+} transitions. These lines may originate both from interacting Er^{3+} ions in corundum and from Er^{3+} ions bound in crystalline phases other than corundum in a heterophase sample.

Note also that excitation of Er^{3+} ions in the $^4I_{15/2}$–$^4I_{11/2}$ transition reveals upconverted luminescence due to transitions from the higher lying $^4S_{3/2}$ and $^4F_{9/2}$ levels to the ground state. The mechanisms responsible for this luminescence will be the subject of further studies.

C. Spectra of Pr^{3+} ions

We observed in the Pr^{3+} luminescence spectrum transitions from the two upper states, $^1D_2$ and $^3P_0$, to the ground-multiplet $^3H_{4,5,6}$ levels under nonselective excitation by light of a Hg lamp ($\lambda = 350$–420 nm). The large number of the multiplet components and superposition of the $^1D_2$–$^3H_4$ and $^3P_0$–$^3H_6$ transitions makes the spectrum fairly complex. The luminescence spectrum of $\gamma\,Al_2O_3$:Pr exhibits broad bands, which is connected with strong inhomogeneous broadening due to the γ phase being structurally disordered. In the luminescence spectra of $\alpha\,Al_2O_3$:Pr the structure of these bands is resolved to reveal fairly narrow lines. By tuning the laser frequency to the $^3H_4$–$^1D_2$ transition in $\alpha\,Al_2O_3$:Pr, one can find the wavelengths at which a distinct narrow-line luminescence spectrum is excited (Fig. 8). At helium temperature the spectrum consists of three lines, with two of them forming a stronger doublet (40 cm^{-1}). It appears natural to assign these three lines to transitions from the lowest Stark sublevel $^1D_2$ to the $^3H_4$ sublevels. As the temperature is raised through liquid nitrogen to room level, one observes a short-wavelength replica of the doublet, which corresponds to transitions from the $^1D_2$ sublevel lying 179 cm^{-1} above the lower $^1D_2$ sublevel. This line luminescence decays exponentially with $\tau \approx 0.12$ ms. The narrow-line pattern of the α-Al_2O_3:Pr^{3+} spectra indicates formation of regular Pr^{3+} centers in corundum.

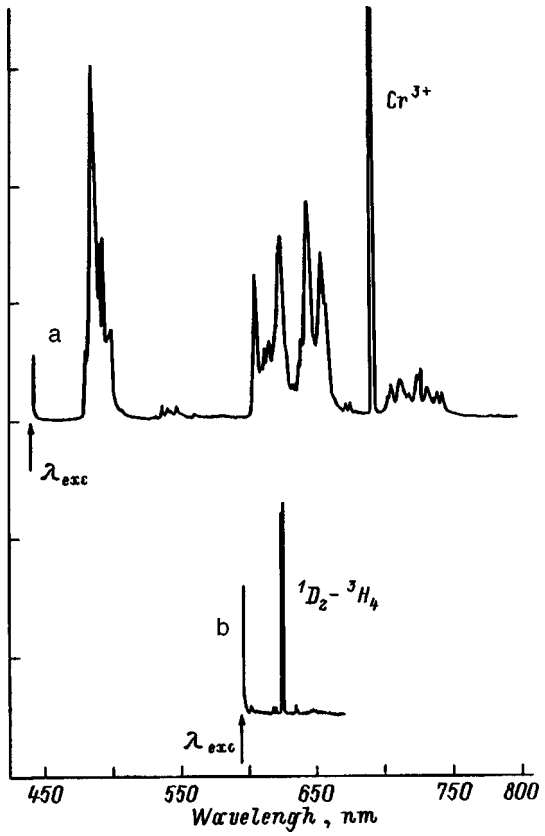

FIG. 8. Fluorescence spectra of Pr^{3+} in aluminum oxide obtained at 77 K in the α phase. a—nonresonant excitation at $\lambda_{exc} = 441.6$ nm, b—$\lambda_{exc} = 595.9$ nm.

3. DISCUSSION

The results we obtained show that triply-charged rare-earth ions RE^{3+} ions ($4f^n$) can be incorporated into the crystal lattice of corundum $\alpha\,Al_2O_3$ in polycrystalline samples prepared by sol-gel technology. RE^{3+} ions form in the corundum lattice a characteristic type of optical centers with a line spectrum typical of this $4f^n$ ion, which is produced in f–f transitions between the crystal-field-split levels of the $4f^n$ manifold. The observed small inhomogeneous linewidth is typical of the f–f spectra of RE^{3+} ions embedded in bulk dielectric crystal hosts. RE^{3+} impurity ions are distributed in the bulk of α-Al_2O_3 crystallites (localization of these ions on crystallite surface would result in multiplicity of optical centers and in a larger inhomogeneous linewidth). As for the local symmetry of the RE^{3+} centers, the conclusion of the local crystal-field symmetry being noncubic (which directly follows from the observation of the remaining purely Kramers-type degeneracy of Er^{3+} levels and of the splitting of the Eu^{3+} level $^7F_1$) can apparently be refined; namely,

observation of the doublet (rather than triplet) splitting of the $^7F_1$ level (the two $^5D_0-^7F_n$ components in Figs. 3c and 3d) is possibly an indication of an axial character of the center symmetry.

The problem of the detailed physical structure (on the atomic scale) of the RE^{3+} center in the lattice of corundum $\alpha\,Al_2O_3$ remains open. The extremely large difference between the ionic radii of RE^{3+} (0.88 Å and 0.95 Å for Er^{3+} and Eu^{3+}, respectively) and of the Al^{3+} ion (0.51 Å) casts doubt on the applicability of the model of simple isocharge substitution $RE^{3+}(Al^{3+})$, which is valid for the case of corundum activation by iron-group ions. At the same time the $RE^{3+}(Al^{3+})$ substitution can, in principle, be accompanied by a substantial rearrangement of the nearest environment, which would provide the space necessary for incorporation of the larger RE^{3+} ion (the discussion[11] of the model of Y^{3+} centers in Al_2O_3 included the formation of vacancies in the oxygen octahedron surrounding the ion). A study[1] of the location of implanted Er^{3+} ions in the α-Al_2O_3 lattice made by the Rutherford backscattering and channeling techniques led to a conclusion that Er^{3+} localizes in octahedral voids of the lattice. Although the Er^{3+} luminescence spectra in the IR region ($^4I_{13/2}-^4I_{15/2}$) obtained on our α-Al_2O_3:Er^{3+} samples and on Er^{3+}-implanted corundum single crystals[12] are generally close, their detailed comparison presents difficulties because of the different conditions in which they were taken (spectral resolution). One has to bear in mind that the conditions typical of the sol-gel method, where activation by rare earths occurs simultaneously with formation of nanoparticles of aluminum oxide at moderate temperatures, are conducive to formation of specific centers with the RE^{3+} ion. To reveal the detailed structure of these centers, it is planned to use methods (magnetic resonance etc.) sensitive to the atomic environment of the RE^{3+} ions.

The authors are grateful to O. B. Gusev for cooperation in measurements of IR luminescence spectra of Er^{3+}-doped corundum, to A. N. Titkov and A. V. Ankudinov for assistance in atomic-force microscope studies, and to S. A. Basun for measurements of low-temperature spectra of the Er^{3+}-doped corundum.

Support of ''Physics of Solid-State Nanostructures'' and ''Laser Physics'' programs is gratefully acknowledged.

[1] E. Alves, M. F. da Silva, G. N. van den Hoven, A. Polman, A. A. Melo, and J. C. Soares, Nucl. Instrum. Methods Phys. Res. B **106**, 429 (1995).
[2] S. P. Feofilov, A. A. Kaplyanskii, A. B. Kutsenko, T. N. Vasilevskaya, and R. I. Zakharchenya, Mater. Sci. Forum **239/241**, 687 (1997); S. P. Feofilov, A. A. Kaplyanskii, and R. I. Zakharchenya, J. Lumin. **72/74**, 41 (1997).
[3] B. E. Yoldas, J. Appl. Chem. Biotech. **23**, 803 (1973); R. I. Zakharchenya, I. K. Meshkovskiĭ, and F. S. Kaplan, Dokl. Akad. Nauk SSSR **314**, 393 (1990) [*sic*].
[4] R. I. Zakharchenya and T. N. Vasilevskaya, J. Mater. Sci. **29**, 2806 (1994).
[5] K. W. Jang and R. S. Meltzer, Phys. Rev. B **52**, 6431 (1995).
[6] Th. Schmidt, R. M. Macfarlane, and S. Völker, Phys. Rev. B **50**, 15707 (1994).
[7] M. Buijs, A. Meyerink, and G. Blasse, J. Lumin. **37**, 9 (1987); B. Bihari, H. Eilers, and B. M. Tissue, *ibid.* **75**, 1 (1997).
[8] J. P. van der Ziel and L. G. Van Uitert, Phys. Rev. **180**, 343 (1969).
[9] G. N. van der Hoven, E. Snoeks, A. Polman, J. W. M. van Uffelen, Y. S. Oei, and M. K. Smit, Appl. Phys. Lett. **62**, 3065 (1993).
[10] H. Bialas and H. J. Stolz, Z. Phys. B **21**, 319 (1975).
[11] M. K. Loudjani, C. Haut, and S. Parisot, Radiat. Eff. Defects Solids **134**, 233 (1995).
[12] G. N. van der Hoven, Thesis, Universiteit Ultrecht (1996).

Translated by G. Skrebtsov

The theory of photorefractive resonance

V. V. Bryksin and M. P. Petrov

A. I. Ioffe Physicotechnical Institute, Russian Academy of Sciences, 194021 St. Petersburg, Russia
(Submitted February 5, 1998)
Fiz. Tverd. Tela (St. Petersburg) **40**, 1450–1459 (August 1998)

A theory is proposed to describe holograms in thin photorefractive crystals and the self-diffraction of two writing laser beams, one of which is periodically modulated in phase. In linear approximation with respect to the amplitude of the phase modulation, expressions are derived for the AC component of the intensity of various diffraction orders. Oscillations in the intensity are observed having a well-defined resonance character connected with excitation of photorefraction waves, and the frequency position of the resonance peaks is related to the period of the grating by the dispersion law of these oscillations. The results obtained are in good agreement with available experimental data. © *1998 American Institute of Physics.* [S1063-7834(98)01308-2]

Holograms are written in photorefractive crystals via photoexcitation of electrons, which then form a bulk charge in the crystal. This charge then gives rise to a nonuniform electric field, which in turn spatially modulates the index of refraction via the electrooptic effect. Writing can take place both in the steady-state (static) regime and under nonstationary conditions when some one of the parameters (applied electric field, amplitude and phase of the incident beam, etc.) change with time.[1] There have been quite detailed studies of effects connected with writing in an AC electric field[2,3] or when the phase of one of the writing beams varies like a sawtooth.[4–7] In the latter case, resonance excitation of traveling holographic gratings (i.e., index of refraction gratings) was observed when the translation velocity of the interference pattern coincides with some characteristic velocity of the hologram.[5] In analyzing nonstationary writing mechanisms, it is customary to use the concept of photorefractive waves (refractive index waves) excited by light incident on the crystal. In the simplest case, the dynamics of these waves coincides with that of trap recharging waves,[8,9] although the dynamics of the system could be otherwise under conditions where self-diffraction of light caused by the generation of interference patterns in the bulk of the crystal plays an important role,[10]. In such situations, photorefraction waves do not reduce to trap recharging waves.

In this paper we consider hologram writing and self-diffraction of light when one of the waves is periodically phase-modulated. This regime is of considerable practical interest, because it can be used to record phase-modulated optical beams with almost arbitrary wave fronts.[11] In this paper we focus most of our attention on the range of low spatial frequencies, where diffusion of charge carriers can be neglected and the primary mechanism for holographic writing is drift of electrons in an applied electric field. Analysis shows that in this case resonance excitation of photorefractive waves is possible if the frequency of the phase modulation and the period of the interference pattern satisfy the wave dispersion relation. We will refer to this phenomenon as photorefractive resonance and investigate it both in the linear and nonlinear writing regimes. We use the term ''linear writing regime'' if a sinusoidal interference pattern leads to a strictly sinusoidal shape for the spatial variation of the refractive index. The case where a sinusoidal interference pattern leads to a nonsinusoidal (although still periodic) spatial variation of the refractive index will be referred to as the ''nonlinear'' regime of hologram writing. The nonlinear regime at low spatial frequencies is currently of great interest, because in this case even a rather thick crystal can be treated as a thin hologram, i.e., diffraction from it is not subject to the Bragg boundaries. Therefore, it is possible to observe diffraction from gratings that consist of higher spatial harmonics of the original hologram. Our theoretical results are in very good agreement with available experimental data.

1. BASIC EQUATIONS

When two coherent beams are incident on a crystal, one of which is periodically modulated in phase (Fig. 1), the resulting interference pattern oscillates about an equilibrium position and the rate of generation of photoelectrons $g(x,t)$ in the conduction band has the form

$$g(x,t)=WI(x,t)=g_0\{1+m\cos(kx+\Theta\cos\Omega t)\}. \quad (1)$$

Here the incident light intensity $I(x,t)=I_0\{1+m\times\cos(kx+\Theta\cos\Omega t)\}$, where I_0 is the total intensity, Θ and Ω are the amplitude and frequency of the phase modulation, $k=2\pi/\Lambda$ is the wave vector of the interference pattern (Λ is the spatial period of the interference pattern), $W=\beta\alpha/P_0$, β is the quantum yield of the photoconductivity, α is the coefficient of light absorption, P_0 is the energy of a photon of writing light, and $g_0=WI_0$.

The induced internal electric field $E(x,t)$ is determined by a system of nonlinear differential equations.[12] The first of these is the equation of continuity:

$$\frac{\partial\rho(x,t)}{\partial t}=-\frac{\partial j(x,t)}{\partial x}, \quad (2)$$

where ρ is the charge density, j is the current density, and

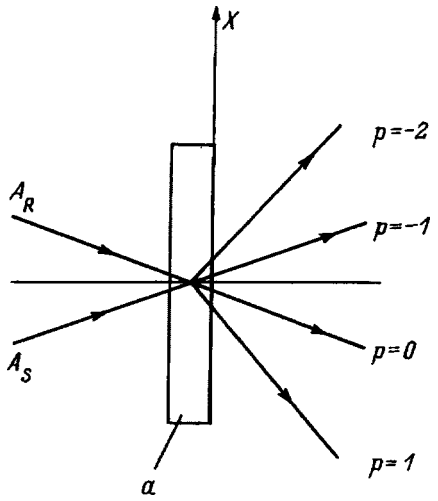

FIG. 1. Sketch illustrating the propagation directions of the writing beams and diffraction orders. The complex amplitudes of the beams in the plane of the crystal have the form $A_S=A_{S0}\exp(ik_Sx)$, $A_R=A_{R0}\exp(ik_Rx+i\Theta\cos\Omega t)$. *a*—a thin photorefractive crystal.

$$j(x,t)=e\mu n(x,t)[E_0+E(x,t)]+eD\frac{\partial n(x,t)}{\partial x}. \tag{3}$$

Here $n(x,t)$ is the concentration of photoelectrons, and μ and D are their mobility and diffusion coefficient [$\mu=eD/(k_BT)$]. The quantity E_0 is the applied external electric field, and $E(x,t)$ is the induced internal electric field.

The charge density and field are related via the Poisson equation

$$\frac{\partial E(x,t)}{\partial x}=\frac{4\pi}{\varepsilon}\rho(x,t). \tag{4}$$

Here ε is the static dielectric permittivity. In what follows it will be convenient to eliminate the charge density from Eqs. (2) and (4). After integrating over coordinates we obtain an equation for the current

$$\frac{\varepsilon}{4\pi}\frac{\partial E(x,t)}{\partial t}+j(x,t)=j_0(t). \tag{5}$$

Here $j_0(t)$ is the total current through the external circuit, which is determined below.

These equations must be supplemented by a balance relation for the bound charge density $N(x,t)$ (donors ionized by light). Here we need to specify a model for the recombination. In this paper we use the simplest model

$$\frac{\partial N(x,t)}{\partial t}=g(x,t)-\frac{n(x,t)}{\tau}, \tag{6}$$

where τ is the lifetime of the photoelectrons. Note that this model for the recombination imposes serious limitations on the final results obtained. On one hand, it assumes the presence of a high concentration of unoccupied locations at trapping centers N_A, so that the recombination takes the simple form n/τ. On the other hand, it does not take into account the depletion of donor centers. A more complete model of recombination is discussed in Ref. 12. The model we use here is applicable to a situation where the external applied field E_0 (and the diffusion field E_D, see below) are much smaller than the maximum possible amplitude of the internal field $E_q=eN_A/\varepsilon k$, where N_A is the concentration of unoccupied trapping sites (i.e., the concentration of compensated traps).[1,12]

In the model used here, the concentration of bound charge N can easily be eliminated from the problem by substituting Eq. (6) into the continuity equation (2), which takes the form

$$\frac{\partial n(x,t)}{\partial t}=g(x,t)-\frac{n(x,t)}{\tau}+\frac{1}{e}\frac{\partial j(x,t)}{\partial x}. \tag{7}$$

Thus, the problem of determining the internal field reduces to solving the system of two equations (5) and (7) for the quantities $E(x,t)$ and the concentration of free electrons $n(x,t)$. However, the Poisson Eq. (4) determines only the concentration of bound charge and therefore is not of interest to us.

The last quantity to determine is the current through the external circuit $j_0(t)$ using the condition

$$\int_0^L E(x,t)dx=0, \tag{8}$$

where L is the length of the sample.

As before, the system of equations (5) and (7) is too complicated for an analytic investigation, and requires some sort of simplifying assumptions. The first of these is that the balance equation for the photoelectron density can be treated within a quasistatic approximation, which in Eq. (7) amounts to neglecting the term $\partial n/\partial t$. The quasistatic approximation is valid if $\Omega_m\tau\ll 1$, where Ω_m is the maximum characteristic frequency of the problem, and applies to almost all cases of practical interest (see Ref. 1).

The second approximation we will use in this paper is to assume that the amplitude of oscillations in the grating Θ is small (see Eq. 1), and look for a solution to the system (5) and (7) to linear accuracy in Θ. That is, we will discuss contributions to the grating oscillations at the fundamental frequency Ω only, ignoring effects at multiples of this frequency and other accompanying phenomena. In particular, this approximation lets us write relation (1) in the form

$$\begin{aligned} g(x,t)&\cong g_0\{1+m\cos kx-m\Theta\sin kx\cos\Omega t\}\\ &\equiv g^{(0)}(x)+\delta g(x,t),\\ \delta g(x,t)&=-g_0m\Theta\sin kx\cos\Omega t\\ &=-\frac{1}{2}g_0m\Theta[\sin(kx+\Omega t)+\sin(kx-\Omega t)]. \end{aligned} \tag{9}$$

In steady state, the approximate solution to the system of Eqs. (5) and (7) that is linear in Θ can be written as the sum of a time-independent contribution and a small oscillatory correction:

$$E(x,t)=E^{(0)}(x)+\mathrm{Re}\,\delta E(x)\exp(i\Omega t),$$

$$n(x,t)=n^{(0)}(x)+\mathrm{Re}\,\delta n(x)\exp(i\Omega t),$$

$$j(x,t)=j^{(0)}(x)+\mathrm{Re}\,\delta j(x)\exp(i\Omega t),$$

$$j_0(t)=j_0^{(0)}+\mathrm{Re}\,\delta j_0 \exp(i\Omega t). \tag{10}$$

The system of nonlinear equations for the dc component is easily solved because $j^{(0)}(x)=J_0^{(0)}$, which does not depend on coordinates. Then $n^{(0)}(x)=\tau g^{(0)}(x)$ and

$$j_0^{(0)}=e\mu n^{(0)}(x)[E_0+E^{(0)}(x)]+eD\frac{dn^{(0)}(x)}{dx}. \tag{11}$$

The value of the current $j_0^{(0)}$ is determined from Eq. (11) using condition (8), which takes the following form when periodic boundary conditions are used:

$$\int_0^{2\pi/k} E^{(0)}(x)dx=0. \tag{12}$$

Then Eqs. (11) and (12) and some simple transformations give

$$j_0^{(0)}=e\mu\tau g_0\sqrt{1-m^2}E_0, \tag{13}$$

$$E^{(0)}(x)+E_0=E_0\frac{\sqrt{1-m^2}}{1+m\cos kx}+E_D\frac{m\sin kx}{1+m\cos kx}, \tag{14}$$

where $E_D=Dk/\mu=kk_BT/e$ is the diffusion field.

We now can address the primary problem, i.e., findng the oscillatory corrections to the internal electric field $\delta E(x)$ [see Eq. (10)]. The equations for this quantity are now ordinary linear differential equations, and hence rather simple to solve.

2. OSCILLATORY PART OF THE INTERNAL ELECTRIC FIELD

We obtain the following equations for the corrections δn and δE from Eq. (10) that are linear in Θ from Eqs. (3), (5), and (7):

$$\frac{\delta n}{\tau}+i\Omega\frac{\varepsilon}{4\pi e}\frac{d\,\delta E}{dx}=-g_0 m\Theta\sin kx,$$

$$\delta j_0-i\Omega\frac{\varepsilon}{4\pi}\delta E=e\mu n^{(0)}\delta E+e\mu\,\delta n(E_0+E^{(0)})+eD\frac{d\,\delta n}{dx}. \tag{15}$$

By eliminating δn from these and converting to the dimensionless coordinate $z=kx$, we obtain the desired equation for the quantity δE:

$$(1+m\cos z+i\omega)\,\delta E-i\omega kL_0\left(1+\frac{E^{(0)}}{E_0}\right)\delta E'-i\omega(kL_D)^2$$

$$\times\,\delta E''=\frac{4\pi}{\varepsilon}\tau_M\delta j_0+m\Theta(E_0+E^{(0)})\sin z+mE_D\Theta\cos z. \tag{16}$$

Here the dash denotes differentiation with respect to z. We have introduced the diffusion and drift lengths $L_D=\sqrt{D\tau}$ and $L_0=\mu E_o\tau$, and also a dimensionless frequency $\omega=\Omega\tau_M$. The quantity $\tau_M^{-1}=4\pi e\mu n_0/\varepsilon=4\pi e\mu g_0\tau/\varepsilon$ has the sense of a Maxwell relaxation time for the uniform generation rate g_0.

The second order differential equation (16) (which is of Hill type) can be solved by assuming the periodicity condition $\delta E(z)=\delta E(z+2\pi)$. Then according to Eq. (12), the current δj_0 is determined from the condition that the zero Fourier component of the field $\delta E(z)$ reduce to zero.

In obtaining an analytic solution to Eq. (16) we will limit ourselves to the case where diffusion processes are unimportant, setting $L_D=0$, $E_D=0$. This approximation is applicable for sufficient small values of the spatial wave vector K. As a result, taking Eq. (14) into account we obtain a first-order equation

$$(1+m\cos z)(1+m\cos z+i\omega)\,\delta E-i\omega d\,\delta E'$$

$$=m\Theta E_0\sqrt{1-m^2}[\sin z+A(1+m\cos z)]. \tag{17}$$

Here $d=kL_0\sqrt{1-m^2}$. The constant $A=4\pi\tau_M\times\delta j_0/\varepsilon E_0 m\sqrt{1-m^2}$ is proportional to the current δj_0 and also can be determined from the condition that the zero Fourier component of the internal field reduce to zero.

The overall solution (Eq. 17) has the form

$$\delta E(z)=\exp[\lambda z+\chi(z)]\times\left\{C+\int_0^z dz'\,\varphi(z')\exp[-\lambda z'-\chi(z')]\right\}, \tag{18}$$

where

$$\lambda=(1+i\omega+m^2/2)(i\omega d)^{-1},$$

$$\chi(z)=(i\omega d)^{-1}m\sin z(2+i\omega+m\cos z),$$

$$\varphi(z)=-\frac{m\sqrt{1-m^2}\Theta E_0}{i\omega d}[\sin z+A(1+m\cos z)]. \tag{19}$$

The constant of integration C in Eq. (18) is determined from the condition of periodicity of the solution to Eq. (12):

$$C=-(1-e^{-2\pi\lambda})^{-1}\int_0^{2\pi}dz\,\varphi(z)\exp[-\lambda z-\chi(z)]. \tag{20}$$

In studying diffraction we are interested in the Fourier components of the field:

$$\delta E_p=\frac{1}{2\pi}\int_0^{2\pi}dz\,\delta E(z)\exp(-ipz). \tag{21}$$

To determine them we expand the following function in a Fourier series:

$$\exp\chi(z)=\sum_{p=-\infty}^{\infty}r_p\exp(ipz),$$

$$r_p=\frac{1}{2\pi}\int_0^{2\pi}dz\exp\left\{-ipz+\frac{m}{i\omega d}\sin z(2+i\omega+m\cos z)\right\}. \tag{22}$$

Expanding Eq. (18) in a Fourier series and using the definition of the constant C Eq. (20) and the expansion Eq. (22), we obtain after some algebraic transformations

$$\delta E_p=\frac{m\sqrt{1-m^2}\Theta E_0}{2i}\sum_{p'=-\infty}^{\infty}\frac{r_{p'+p}}{1+i\omega-p'\omega d+m^2/2}\times[r_{p'+1}-r_{p'-1}+A(2r_{p'}+mr_{p'+1}+mr_{p'-1})]. \tag{23}$$

In this case we have used the relation $\chi(z)=-\chi(-z)$.

We now can explicitly determine the constant A from the condition Eq. (12) that $\delta E_0=0$:

$$A=-\sum_{p=-\infty}^{\infty}\frac{r_p(r_{p+1}-r_{p-1})}{(1+i\omega-p\omega d+m^2/2)}\times\left\{\sum_{p=-\infty}^{\infty}\frac{r_p(2r_p+mr_{p+1}+mr_{p-1})}{1+i\omega-p\omega d+m^2/2}\right\}^{-1}. \tag{24}$$

Further studies of the Fourier components of the field in general form require numerical calculations. We can obtain a simple analytic result in the limit of small illumination contrasts, where $m\ll 1$. In this case

$$r_p=\delta_{p,0}-m\frac{2+i\omega}{2\omega d}(\delta_{p,1}-\delta_{p,-1})+\frac{m^2}{4\omega d}\times\left\{\left[\frac{(2+i\omega)^2}{2\omega d}-1\right]\delta_{p,2}+\left[\frac{(2+i\omega)^2}{2\omega d}+1\right]\delta_{p,-2}\right\}+\ldots.$$

This implies that the first of the set of Fourier components of the field has the form

$$\delta E_1=-\frac{1}{2}mi\Theta E_0\frac{1}{1+i\omega+\omega d}, \tag{25}$$

$$\delta E_2=\frac{1}{4}m^2i\Theta E_0\frac{2+i\omega}{(1+i\omega+\omega d)(1+i\omega+2\omega d)}. \tag{26}$$

The Fourier components with negative p can be found from the relation $\delta E_p(\omega)=\delta E^*_{-p}(-\omega)$. At weak contrasts, the Fourier components of the field fall off rapidly, because in this case $\delta E_p\propto m^{|p|}$.

Another important limiting case is that of high frequencies. In the limit $\omega\to\infty$ we can carry out the summation of the series in Eq. (23). Here we present only the final result of this summation, omitting the details of the calculation:

$$\delta E_p=\frac{\pi m\sqrt{1-m^2}\Theta E_0}{2i^{p-1}\omega d\sinh(\pi/d)}I_{p+i/d}\left(\frac{m}{d}\right)\times\left[I_{1-i/d}\left(\frac{m}{d}\right)+I_{-1-i/d}\left(\frac{m}{d}\right)\right], \tag{27}$$

where $I_\nu(x)$ is a modified Bessel function with complex index. Thus, in the high-frequency regime all the Fourier components of the field fall off as $1/\omega$ for any modulation of the illumination. From this expression it is not difficult to find an expression for δE_p under conditions of strong contrast, where $m\to 1$, i.e., $d\to 0$ in the region of high frequencies, which is correct for any p:

$$\delta E_p=(-1)^p\Theta E_0\omega^{-1}\tanh\alpha\exp(-|p|\alpha), \tag{27a}$$

where $\cosh\alpha=m^{-1}$. Note that this expression is correct for $d\ll 1$, i.e., not only for strong contrast but also for sufficiently weak fields E_0 and arbitrary values of m. In particular, it agrees with Eqs. (25) and (26) for $m\ll 1$ when $\alpha=\ln(2/m)\gg 1$. An important property of the field δE_p at high contrast is the slow decrease of its amplitude with increasing p. On the other hand, the Fourier components of this limit are real and antisymmetric under the replacement $\omega\to-\omega$. This implies that, in the absence of diffusion, there are no oscillations. At high contrast, however, the high-frequency asymptotic behavior of the diffraction peaks is changed (see below).

As for the limit $\omega\to 0$, we can obtain it easily from Eq. (16) by the direct substitution $\omega=0$. The exact result, which is also correct in the presence of diffusion, has the form

$$\delta E_p\Big|_{\omega=0}=ip\Theta E_p^{(0)}, \tag{28}$$

where $E_p^{(0)}$ is the Fourier component of the stationary field Eq. (14), and

$$E_p^{(0)}=\left(\frac{-m}{1+\sqrt{1-m^2}}\right)^p(E_0+iE_D). \tag{29}$$

In Eq. (29) we have $p>0$; for $p<0$ we must use the relations $E_p^{(0)}=E_{-p}^{(0)*}$ and $E_0^{(0)}=0$. It is interesting to note that Eq. (28) is correct not only for the model under discussion here, where the steady-state Fourier components are determined from Eq. (29), but in the most general case as well. In fact, for $\Omega=0$ according to Eq. (1) we have a relation between the exact steady-state solution $E(z)$ for arbitrary values of Θ and the solution for $\Theta=0$: $E(z)=E^{(0)}(z+\Theta)$. For the Fourier components this implies that $E_p=E_p^{(0)}\exp(ip\Theta)$, which in turn implies Eq. (28) to linear approximation in Θ.

Now let us discuss the characteristics of the diffracted light.

3. DIFFRACTION BY AN OSCILLATING GRATING

Let us consider diffraction of light by a thin hologram written by two beams A_S and A_R, where $A_S=A_{S0}\exp(ik_Sx)$ and $A_R=A_{R0}\exp(ik_Rx+i\Theta\cos\Omega t)$. The hologram is considered to be thin if its thickness h satisfies the condition $h\ll\Lambda^2n_0/\lambda$, where n_0 is the refractive index of the light. For a thin hologram we can introduce a transmission coefficient $T(x,t)=\exp[i\varphi(x,t)]$ such that the light amplitude $A_{\rm out}$ directly behind the hologram is related to the amplitude of the incident light $A_{\rm in}$ by the expression $A_{\rm out}(x,t)=T(x,t)\times A_{\rm in}(x,t)$. In our case $\varphi(x,t)=QE(x,t)$ is the phase advance of the beam passing through the hologram due to modulation of the index of refraction, where Q is a parameter that depends on the electrooptic properties of the crystal. In crystals with point groups 23 and $\bar{4}3m$ cut, for instance, along $\langle 110\rangle$, when the wave vector of the grating is directed along the [001] axis and the polarization of the incident light is parallel to the $[1\bar{1}0]$ axis, we have $Q=\pi r_{41}n_0^3h/\lambda$, where r_{41} is the electrooptic coefficient. Note that for $m\ll 1$ and $\Theta=0$ the diffraction efficiency of the hologram is related to Q by the expression $\eta=(QE_1^{(0)})^2$, where $E_1^{(0)}$ is the first Fourier component of the stationary field Eq. (29).

Let us expand $T(x,t)$ in a Fourier series in spatial harmonics, taking into account that $E(x,t)=E^{(0)}(z)+\mathrm{Re}\,\delta E(z)\exp(i\Omega t)$ [see Eq. (10)] (we have switched to the dimensionless coordinate $z=kx$). Limiting ourselves to linear approximation in $\delta E(z)$ (i.e., in Θ), we obtain

$$T(x,t)=\sum_{p=-\infty}^{\infty}(B_p+ib_p)\exp(ipz),$$

$$B_p=\frac{1}{2\pi}\int_0^{2\pi}dz\,\exp(-ipz+iQE^{(0)}(z)),$$

$$b_p=\frac{Q}{2\pi}\int_0^{2\pi}dz\,\exp(-ipz+iQE^{(0)}(z))\mathrm{Re}[\,\delta E(z)e^{i\Omega t}]. \tag{30}$$

Taking into account that the diffraction efficiency $\eta\ll 1$, we can limit ourselves in Eq. (30) to the lowest approximation in Q. As a result we have

$$B_p=\delta_{p,0}+iQE_p^{(0)}, \tag{31}$$

$$b_p(t)=\frac{Q}{2}\,\delta E_p(\omega)e^{i\Omega t}+\frac{Q}{2}\,\delta E_p(-\omega)e^{-i\Omega t}. \tag{32}$$

The Fourier components $E_p^{(0)}$ and δE_p were determined in the previous section. The expressions (31) and (32) describe first-order diffraction of light by phase gratings with spatial harmonics pk. All the higher orders of diffraction for any individual grating can be neglected, since we are limiting ourselves to small diffraction efficiencies.

Now let us find the amplitude and intensity of the light diffracted by these gratings. We note that in enumerating the diffraction order a certain ambiguity arises. For example, the zero order for beam A_R coincides with the minus first-order for beam A_S, and conversely. Let us use the convention of labeling the observed diffraction beams with an index p that corresponds to the first diffraction order of beam A_R by the grating with wave vector pk. Accordingly the relation between k_R and k_S is defined to be $k_S=k_R-k$, where $k>0$. Assuming as before that $\Theta\ll 1$, we will write the expression for the amplitude of the beam with label p in the form

$$A_p=[A_{R0}(B_p+i\Theta B_p\cos\Omega t+ib_p(t))+A_{S0}(B_{p+1}+ib_{p+1}(t))]\exp[i(k_R+pk)x].$$

Accordingly we have for the intensity

$$I_p(t)=|A_p|^2=|A_{R0}(B_p+i\Theta B_p\cos\Omega t+ib_p(t))+A_{S0}(B_{p+1}+ib_{p+1}(t))|^2.$$

Omitting the contribution to Eq. (30) that is quadratic in Θ, we obtain the oscillatory part of the light intensity in the p-th diffracted beam in the form:

$$\delta I_p(t)=2\,\mathrm{Re}\{i\Theta\cos\Omega tA_{S0}A_{R0}B_{p+1}^*B_p+i(A_{R0}B_p^*+A_{S0}B_{p+1}^*)(A_{R0}b_p(t)+A_{S0}b_{p+1}(t))\}. \tag{33}$$

The Bragg peaks with $p=0,\,-1$ are proportional to the first power of this parameter for small Q, whereas the remaining peaks are proportional to Q^2. Therefore we first investigate the case $p=0$ separately. Using Eqs. (31) and (32), we obtain from Eq. (33)

$$\delta I_0=A_{S0}A_{R0}Q\mathrm{Re}\{[2\Theta E_1^{(0)}+i\,\delta E_1(\omega)+i\,\delta E_1\times(-\omega)]\cos\Omega t-[\,\delta E_1(\omega)-\delta E_1(-\omega)]\sin\Omega t\}. \tag{34}$$

As we noted above, as $\Omega\to\infty$ the quantity δE_p reduces to zero. Therefore, at high frequencies the function $\delta I_1(\omega)$ reaches a plateau. According to Eq. (29),

$$\delta I_0\Big|_{\Omega\to\infty}=-2Q\Theta A_{S0}A_{R0}\frac{mE_0}{1+\sqrt{1-m^2}}\cos\Omega t. \tag{35}$$

However, in the limit $\Omega\to 0$ according to Eqs. (34) and (28), the quantity δI_0 reduces to zero.

In the previous section, we obtained expressions for the quantity δE_1 for arbitrary frequency but weak modulation [see Eq. (25)]; therefore we can write the total function $\delta I_0(\omega)$ for $m\ll 1$ as follows:

$$\delta I_0=-A_{S0}A_{R0}QmE_0\Theta\omega\times\frac{\sqrt{1+\omega^2(3+d^4)+\omega^4(1+d^2)^2(3-2d^2)+\omega^6(1+d^2)^4}}{1+2\omega^2(1-d^2)+\omega^4(1+d^2)^2}\times\cos(\Omega t+\varphi_0), \tag{36}$$

where the phase is given by the relation

$$\tan\varphi_0=\frac{1+\omega^2(1+d^2)}{\omega[1-d^2+\omega^2(1+d^2)^2]}. \tag{37}$$

The peak with $p=-1$ is determined by the relation $\delta I_{-1}=-\delta I_0$.

For peaks with $p\neq 0,-1$, we find from (33)

$$\delta I_p=Q\mathrm{Re}(A_{R0}E_p^{(0)*}+A_{S0}E_{p+1}^{(0)*})(A_{R0}b_p+A_{S0}b_{p+1}). \tag{38}$$

In obtaining Eq. (38) we take into account that according to Eq. (29) the quantity $E_p^{(0)}E_{p+1}^{(0)*}$ is real. This implies that as $\Omega\to\infty$ the intensity δI_p for $p\neq 0,-1$ reduces to zero as ω^{-1} [see Eq. (27)] and that the high-frequency plateau characteristic of Bragg peaks is absent.

This result is closely related to the fact that in this paper we have neglected all effects connected with the finite concentration of acceptors N_A, and hence with finite values of the field E_q (see Sec. 1). In most cases this is correct; for example, in $Bi_{12}SiO_{20}$ the field E_q reaches values of order 100 kV/cm with a grating period $\Delta\sim 10\ \mu$m (see Ref. 13) and increases still more with increasing Λ. However, in other materials, for example, in $Bi_{12}TiO_{20}$, the field E_q is approximately an order of magnitude smaller (or at least is several times smaller[14]) and it is important to include it. There is reason to assume that including the field E_q can lead to the appearance of a phase difference $\Delta=\arctan(E_0/E_q)$ between harmonics of the constant field, i.e., $\mathrm{Im}E_p^{(0)}E_{p'}^{(0)*}\neq 0$. As a result, an additional contribution to the expression

(40) for the intensity of peaks with $p \neq 0, -1$ appears, whose amplitude does not depend on the frequency Ω and is given by the expression [see Eq. (33)]

$$\delta I_p = -2Q^2 \Theta A_{S0} A_{R0} \cos \Omega t \, \mathrm{Im} E_p^{(0)} E_{p+1}^{(0)*}. \tag{39}$$

In the limit $\Omega \to \infty$ the quantities b_p reduce to zero, and Eq. (39) describes the high-frequency plateau for non-Bragg peaks. This implies that measurements of the high-frequency plateau yield information about the value of the field E_q. As for the static limit $\Omega \to 0$, according to Eqs. (32) and (28) in this case we have $b_p = ip\Theta E_p^{(0)} \cos \Omega t$. Substituting this value of b_p into Eq. (33) gives the result $\delta I_p|_{\omega=0} = 0$ for any form of the Fourier components $E_p^{(0)}$.

Furthermore, when E_q is included, a shift appears in the static field grating and the components $E_p^{(0)}$ become complex quantities even in the absence of diffusion. Equation (38) predicts a contribution to the intensity of the peaks that is proportional to $\mathrm{Im}\, b_p$ that differs strongly from the contribution proportional to $\mathrm{Re}\, b_p$, which describes the intensity in the limit $E_q \to \infty$. Thus, there are some new experimental possibilities for recording effects connected with the field E_q, and hence measuring this quantity (and with it the concentration of acceptors N_A).

Note also that in the limit of strong contrast and high frequencies, when relation (27a) is valid, the quantity b_p is pure imaginary. Therefore, in the absence of diffusion, when the Fourier components of the static field $E_p^{(0)}$ are real, for strong contrast the high-frequency asymptotic behavior no longer varies as ω^{-1} as is the case for weak contrast.

We now return to the case of weak contrast, assuming that $E_q \to \infty$. In the limit of weak modulation $m \ll 1$, Eq. (38) simplifies, because $E_p^{(0)}, b_p \propto m^p$ and fall off rapidly as p increases. Without including the diffusion contribution to $E_p^{(0)}$ we have for $p \geqslant 1$ that

$$\delta I_p = Q^2 (-2)^{-p} m^p A_{R0}^2 E_0 C_p \cos(\Omega t + \varphi_p), \tag{40}$$

where the amplitude C_p and phase φ_p are defined by the relations

$$C_p = \{[\mathrm{Re}(\delta E_p(\omega) + \delta E_p(-\omega))]^2 + [\mathrm{Im}(\delta E_p(\omega) - \delta E_p(-\omega))]^2\}^{1/2},$$

$$\tan \varphi_p = \frac{\mathrm{Im}(\delta E_p(\omega) - \delta E_p(-\omega))}{\mathrm{Re}(\delta E_p(\omega) + \delta E_p(-\omega))}. \tag{41}$$

In what follows we shall discuss the peaks with $p \geqslant 1$. The expressions for peaks with $p \leqslant -2$ can be obtained from the relation $\delta I_{-p-1} = (A_{S0}/A_{R0})^2 \delta I_p$. From Eq. (41), taking Eq. (25) into account we have for the peak with $p = 1$

$$C_1 = m\Theta E_0 \frac{\omega d}{\sqrt{1 + 2\omega^2(1-d^2) + \omega^4(1+d^2)^2}},$$

$$\tan \varphi_1 = \frac{1 - \omega^2(1+d^2)}{2\omega}. \tag{42}$$

Figure 2 shows the computed relations for δI_0 and δI_1 based on Eqs. (36) and (42).

Note that in obtaining expression (34) for the intensity of the Bragg peak with $p = 0$ we have omitted terms proportional to Q^2. However, a situation is possible where this contribution plays a dominant role. This will happen for the case of anisotropic diffraction if we place a polarization analyzer at the output directed along an axis orthogonal to the polarization of light incident on the crystal. Since the beams diffracted in first order have a polarization direction perpendicular to the polarization of the incident beam for anisotropic diffraction, there will be no interference between the diffracted and undiffracted beams. This happens, e.g., for an external field along the $[1\bar{1}0]$ axis and light polarization parallel to the [001] axis in crystals of classes 23 and $\bar{4}3m$. In this case we can find the ac component of the signal δI_0 proportional to Q^2 from Eq. (38) obtained above for the non-Bragg peaks by setting $p = 1$:

$$\delta I_0 = Q A_{R0}^2 \mathrm{Re} E^{(0)*} b_1. \tag{43}$$

This implies that in this situation the peak with $p = 0$ is given by the same expressions as the peak with $p = 1$ [see Eqs. (40)–(42)] with the substitution $A_{S0}^2 \to A_{R0}^2$.

For the peak with $p = 2$ the corresponding expressions have the very awkward forms

$$C_2^2 = \left[\frac{3m^2\Theta E_0 \omega d}{D(d)D(2d)}\right]^2 [4 - (3 + 40d^2)\omega^2 - (19 + 50d^2$$

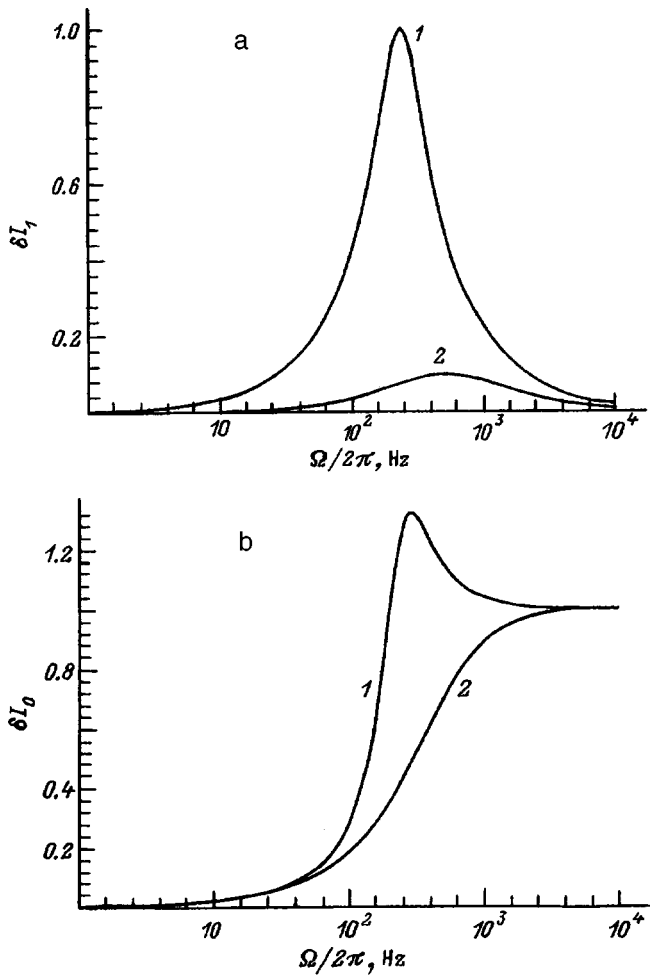

FIG. 2. Dependence of signals δI_1 (a) and δI_0 (b) (in relative units) on frequency $\Omega/2\pi$, $\tau_M = 3 \times 10^{-4}$ s. $d = 2$ (*1*) and 0.2 (*2*).

$$-132d^4)\omega^4+(4+110d^2+309d^4-160d^6)\omega^6$$
$$+(30+200d^2+303d^4-200d^6+64d^8)\omega^8$$
$$+(17+100d^2+279d^4+360d^6-240d^8)\omega^{10}$$
$$+(1+d^2)^2(1+4d^2)^2\omega^{12}],$$

$$\tan\varphi_2=[2-\omega^2(1+10d^2)-\omega^4(4+15d^2-8d^4)$$
$$-\omega^6(1+d^2)(1+4d^2)]\omega^{-1}[1-\omega^2(2+5d^2)$$
$$-\omega^4(3+5d^2-4d^4)]^{-1}, \quad (44)$$

where

$$D(d)=1+2\omega^2(1-d^2)+\omega^4(1+d^2)^2.$$

These complicated relations simplify considerably in the physically most interesting limiting case where $\omega \ll 1$ but ωd is arbitrary:

$$C_2 \cong \frac{6m^2\Theta E_0\omega d}{|1-\omega^2d^2||1-4\omega^2d^2|}, \quad \tan\varphi_2 \cong \frac{2}{\omega}. \quad (45)$$

The expression for C_2 has poles at frequencies $\omega = d^{-1}, (2d)^{-1}$ ($\Omega=(kL_0\tau_M)^{-1}$, $(2kL_0\tau_M)^{-1}$). The corresponding expressions for peaks with $p=0,1,-1,-2$ have poles at only one frequency $\omega=d^{-1}$ [see Eqs. (36) and (42)]. The existence of this pole structure as $\omega\to 0$ but for finite values of ωd is quite evident from the general expression (23), where we see a pole at arbitrary values of m at the points $\omega=(1+m^2/2)/pd$, where p is an integer. Rather than discuss the physical nature of these resonance peaks, we turn our attention to one more feature of the interference pattern.

Up to now we have discussed the case where the relation between intensities of beams R and S and the contrast m is unrefined. If there is no additional illumination in the experiment, the intensities A_{S0} and A_{R0} are related to the modulation depth m by the expression $m=2A_{R0}A_{S0}/(A_{R0}^2+A_{S0}^2)$, i.e.,

$$\frac{A_{R0}}{A_{S0}}=\frac{1\pm\sqrt{1-m^2}}{m}. \quad (46)$$

Using Eqs. (46) and (29), we transform relation (38) for the diffraction peaks with $p\neq 0,-1$ to the form

$$\delta I_p = Q^2A_{S0}^2\mathrm{Re}E_{p+1}^{(0)*}\left(1-\frac{1\pm\sqrt{1-m^2}}{1+\sqrt{1-m^2}}\right)$$
$$\times\left(b_{p+1}+\frac{1\pm\sqrt{1-m^2}}{m}b_p\right). \quad (47)$$

The plus sign is chosen for $A_{R0}>A_{S0}$ and the minus sign in the opposite case. From this it follows that when there is no additional illumination the oscillatory part of the non-Bragg diffraction maxima with positive p is completely quenched if $A_{R0}>A_{S0}$ (i.e., only peaks with negative p oscillate). Conversely, for $A_{R0}<A_{S0}$ the oscillatory parts of the non-Bragg peaks with negative p are completely quenched.

4. PHOTOREFRACTIVE WAVES AND THE RESONANCE CHARACTER OF DIFFRACTION

We now turn to elucidating the physical reason, alluded in the previous section, why the diffraction is resonant in character when $d\gg 1$ (i.e., $kL_0\gg 1$). For this we will consider a photoconductor described by Eqs. (3), (5) and (7) under conditions of uniform illumination, $g(x,t)=g_0$. In this case the system of equations has a trivial solution $n(x,t)=g_0\tau\equiv n^{(0)}$, $j(x,t)=j_0=e\mu n^{(0)}E_0$, $E(x,t)=0$. We consider small corrections to this solution: $n(x,t)=n^{(0)}+\delta n(x,t)$, $j(x,t)=j_0+\delta j(x,t)$. As a result we obtain the linearized system of equations

$$\frac{\varepsilon}{4\pi}\frac{\partial E}{\partial t}+e\mu(n^{(0)}\delta E+\delta nE_0)+eD\frac{\partial\delta n}{\partial x}=0,$$
$$\frac{\partial\delta n}{\partial t}=-\frac{\delta n}{\tau}-\frac{\varepsilon}{4\pi e}\frac{\partial^2E}{\partial x\partial t}. \quad (48)$$

Making the substitutions $E(x,t)=E\exp(iqx-i\nu t)$, $\delta n(x,t)=\eta\exp(iqx-i\nu t)$, we obtain the relation

$$\frac{1}{\nu\tau_M}(1-i\nu\tau_M)(1-i\nu\tau)=qL_0+i(qL_D)^2. \quad (49)$$

In the low-frequency limit $\nu\tau\ll 1$, $\nu\tau_M\ll 1$, neglecting diffusion ($L_D\to 0$) we obtain the dispersion relation of the eigenmodes of oscillation of the system (electron density and electric field):

$$\nu=(qL_0\tau_M)^{-1}=\frac{4\pi en^{(0)}}{q\varepsilon E_0\tau}. \quad (50)$$

The lifetime of these oscillations can be long if a number of conditions hold: $\nu\tau\ll 1$, $\nu\tau_M\ll 1$, and the wave vector lies in the interval $(\mu E_0\tau)^{-1}=L_0^{-1}\ll q\ll eE_0/k_BT$. Characteristic oscillations of this kind in the electric charge were first discussed in semiconductors in Refs. 8 and 9, where they received the name trap recharging oscillations. In photorefractive crystals waves of charge are transformed into waves of dielectric permittivity via the mechanism of the Pockels effect. As we have already shown above. such oscillations can be thought of as photorefractive waves.

Up to now we have discussed spatially uniform media only. When a hologram has been written, the medium is no longer spatially uniform, but rather is modulated periodically such that $n^{(0)}=n^{(0)}(kx)$ and $n^{(0)}(kx)=n^{(0)}(kx+2\pi)$. In this case, when the inequalities listed above are fulfilled Eq. (48) takes the form

$$n^{(0)}(kx)\,\delta E+\delta nE_0=0, \quad \frac{\delta n}{\tau}=-\frac{\varepsilon}{4\pi e}\frac{\partial^2E}{\partial x\partial t}.$$

Substituting a solution of the form $E(x,t)=E(x)\exp(-i\nu t)$, $\delta n(x,t)=\eta(x)\exp(-i\nu t)$ into these equations, we obtain

$$\nu\frac{dE}{dx}=\frac{4\pi ien^{(0)}(kx)}{\varepsilon E_0\tau}E.$$

From this equation, using the condition of periodicity in space for the field $E(x)$ we obtain the dispersion relation

$$\nu=\frac{2e}{lk\varepsilon E_0\tau}\int_0^{2\pi}dzn^{(0)}(z)=\frac{4\pi en_0^{(0)}}{lk\varepsilon E_0\tau}\equiv\frac{\nu_0}{l}, \tag{51}$$

where $l=1,2,3\ldots$, and $n_0^{(0)}=n_0=g_0\tau$ is the zero Fourier component of the photoelectron density (see, also, Sec. 1). Relation (51) is the discrete analog to the dispersion equation (50). It shows that the spectrum of photorefractive waves in a periodically modulated medium is discrete in character: ''photorefractons'' propagate with wave vectors k and frequency $\nu=\nu_0/l$. In this case the intrinsic modes are no longer plane waves, but are modulated spatially in phase. For small values of m, Bragg peaks ($p=0,-1$) are generated from scattering by one photorefracton with $l=1$, and a resonance occurs for $\Omega=\nu_0$. The diffraction peaks with $p=1$, -2 are generated from scattering by one photorefracton with $l=2$ (resonance at $\Omega=\nu_0/2$) or by a photorefracton with $l=1$ (resonance at $\Omega=\nu_0$), etc. In this case we should keep in mind that the law of conservation of momentum holds in a periodic system up to discrete values of pk, $p=0,\pm1,\pm2,\ldots$, i.e., here we must speak of a law of conservation of quasimomentum or of umklapp processes. For strong contrast (m close to unity) we must take into account the participation of the entire discrete set of photorefractons in generating any one diffraction peak, a consequence of which is that the frequency dependence of all the diffraction peaks is multipolar in character at a set of frequencies $\Omega=\nu_0/l$, where l is an integer. It is this pole structure that is exhibited by the general relation (23) when we make the replacement $i\omega\to0$ in the denominator, which corresponds to the condition mentioned above for existence of the photorefractons $\omega=\Omega\tau_M=\nu\tau_M\ll1$. However, for arbitrary values of m, as follows from Eq. (23), the resonance is somewhat shifted and occurs at $\Omega=(1+m^2/2)\nu_0/l$.

In conclusion, we emphasize once more that, because these photorefractive waves are attenuated, sharp resonances of the diffraction peaks are observed only at sufficiently strong electric fields E_0, where the condition $ke\mu E_0\tau\gg1$ holds. This simultaneously imposes a bound from above on the period of spatial modulation at a fixed electric field E_0. On the other hand, in avoiding attenuation of photorefractons due to diffusion the period of modulation should not be so small that $k\ll eE_0/(k_BT)$.

5. DISCUSSION OF RESULTS OBTAINED

In this paper we have set up a theory for phenomena that occur in a photorefractive crystal illuminated by two beams of coherent light, one of which is periodically modulated in phase at a frequency Ω. We have established that the steady holographic grating in the refractive index is accompanied by a dynamic (oscillating) grating. For the approximations made in this paper (neglect of diffusion and the contribution from the field E_q) the stationary grating is unshifted with respect to the interference pattern.

The oscillatory grating has two components. One of them is unshifted with respect to the steady-state grating and is described by the real part of b_p, while the other is shifted by an angle of $\pi/2$ [the imaginary part of b_p, see Eq. (32)]. The amplitude of the unshifted component has a maximum at a frequency $\Omega_r=\nu_0$ [see Eq. (51)] in the linear writing regime. The height and width of this maximum (i.e., the quality of the resonance) are determined by the product of the grating wave vector and the drift length kL_0. In the nonlinear regime the theory predicts a series of maxima at frequencies $\Omega_r=\nu_0/l$ for sufficiently large values of the parameter kL_0, where l is an integer [see Eq. (51)].

The appearance of this resonance is associated with excitation of photorefractive waves in the photorefractive medium when the period of the holographic grating and the period of the phase modulation of the writing beam coincide with the corresponding period and frequency of the photorefractive waves. Therefore, the phenomena mentioned above can be described as photorefractive resonance. Experimentally this effect was observed in Ref. 15, and probably in Ref. 16. A comparison shows that the theory is in good agreement with experiment.

The shifted component also oscillates in time, but the character of its frequency dependence is different from that of the unshifted component. Here the amplitude of oscillation does not reduce to zero for $\Omega\to0$ [see Eqs. (28) and (32)], although for sufficiently high values of kL_0 we also may observe a maximum at $\Omega=\Omega_r$. As $\Omega\to\infty$ the amplitudes of both components (shifted and unshifted) reduce to zero. The shifted component determines the frequency dependence of the Bragg orders of diffraction Eq. (34).

The processes that occur during diffraction of light can be described qualitatively in the following way. The primary process consists of diffraction by the static grating. Moreover, diffraction takes place by the unshifted and shifted components of the oscillatory grating. When two beams incident on the crystal diffract into the same direction, several beams propagate which interfere among themselves. Depending on the index of the diffraction order we can separate out some dominant diffraction beam. As we already mentioned above, in directions $p=1,-2$, for example, diffraction from the static and unshifted oscillating components is recorded, while for $p=0,-1$ it is record from the static and shifted components of the hologram. It is interesting to note that for $\Omega\to0$ signals from the static and shifted oscillatory hologram compensate each other exactly, and the ac signal reduces to zero. This phenomenon is well known.[17] It is very important for practical applications, because it ensures the property of adaptivity, i.e., suppression of parasitic low-frequency phase fluctuations.

This work was supported by the Russian Fund for Fundamental Research (Grants Nos. 96-02-16848*a* and 98-02-18254).

[1] M. P. Petrov, S. I. Stepanov, and A. V. Khomenko, *Photorefractive Crystals in Coherent Optical Systems*, Vol. 59 (Springer Series in Optical Sciences, Springer-Verlag, 1991).
[2] S. I. Stepanov and M. P. Petrov, Opt. Commun. **53**, 292 (1985).
[3] G. Pauliat, A. Villing, J. C. Launay, and G. Roosen, J. Opt. Soc. Am. B **7**, 1481 (1990).
[4] J. P. Huignard and A. Marrakchi, Opt. Commun. **38**, 249 (1981).
[5] S. I. Stepanov, V. V. Kulikov, and M. P. Petrov, Opt. Commun. **44**, 19 (1982).
[6] Ph. Refreiger, L. Solymar, H. Rajbenbach, and J. P. Huignard, J. Appl. Phys. **58**, 45 (1985).

[7] T. E. McClelland, D. J. Webb, B. I. Sturman, M. Mann, and K. N. Ringhofer, Opt. Commun. **113**, 371 (1995).
[8] R. F. Kazarinov, R. A. Suris, and B. I. Fuks, Fiz. Tekh. Poluprovodn. **6**, 572 (1972) [Sov. Phys. Semicond. **6**, 500 (1972)]; R. A. Suris, and B. I. Fuks, *ibid.* **12**, 2319 (1978) [*ibid.* **12**, 1380 (1978)]; *ibid.* **13**, 138 (1979) [*ibid.* **13**, 79 (1979)].
[9] N. G. Zhdanova, M. S. Kagan, R. A. Suris, and B. I. Fuks, Zh. Éksp. Teor. Fiz. **74**, 364 (1978) [Sov. Phys. JETP **47**, 189 (1978)].
[10] S. Bruegnot, M. Defour, and J. P. Huignard, Opt. Commun. **134**, 599 (1997).
[11] T. J. Hall, M. A. Fiddy, and M. S. Ner, Opt. Lett. **5**, 484 (1980).
[12] N. V. Kukhtarev, V. B. Markov, S. G. Odulov, M. S. Soskin, and V. L. Vinetskii, Ferroelectrics **22**, 949 (1979).
[13] J. P. Huignard and P. Guenter, in *Photorefractive Materials and their Applications II*, (Springer-Verlag, Berlin, Heidelberg, 1989), p. 205.
[14] M. P. Petrov, A. V. Shamraĭ, V. M. Petrov, and I. Zoubulis, Fiz. Tverd. Tela (St. Petersburg) **39**, 1990 (1997) [Phys. Solid State **39**, 1749 (1997)].
[15] M. P. Petrov, V. M. Petrov, V. V. Bryksin, I. Zouboulis, A. Gerwens, and E. Kraetzig, Opt. Lett. **22**, 1083 (1997).
[16] M. Vasnetsov, P. Buchhave, and S. Lyuksyutov, Opt. Commun. **137**, 181 (1997).
[17] S. I. Stepanov, *Optical Holography with Writing in Three-Dimensional Media*, Yu. N. Denisyuk (ed.) [in Russian], Nauka, Leningrad, 1983.

Translated by Frank J. Crowne

Space-time resolved optical spectroscopy of barium fluoride

V. F. Shtan'ko and E. P. Chinkov

Tomsk Polytechnical Institute, 634004 Tomsk, Russia
(Submitted December 3, 1997)
Fiz. Tverd. Tela (St. Petersburg) **40**, 1460–1463 (August 1998)

Space-time-resolved spectroscopy is used to study the spectral–kinetic characteristics of transient absorption and rapidly decaying luminescence in a BaF_2 crystal bombarded by an accelerated electron beam of nanosecond duration. Creation of spatially-inhomogeneous primary products of radiolysis is observed, and an interrelationship between these products and the intrinsic properties of the BaF_2 crystal is established. © *1998 American Institute of Physics.* [S1063-7834(98)01408-7]

Under the action of ionizing radiation in nominally pure fluorite crystals at temperatures not higher than room temperature, autolocalized excitons (AE) are created, which are usually represented as different configurations of closely arranged F,H pairs.[1–4] Their spectra are usually divided into an electron component and a hole component of absorption by autolocalized excitons.[1] However, this division is very arbitrary since absorption in the series CaF_2, SrF_2, BaF_2 grows noticeably in the spectral region lying between these components. The natural luminescence of fluorites is linked with radiative transitions from singlet and triplet states of autolocalized excitons.[1] Singlet luminescence is not observed in BaF_2, but, as in some alkali-halide crystals,[5] a rapidly decaying luminescence (RDL) ($\tau<1$ ns) is observed in the ultraviolet. The RDL yield in BaF_2 is significantly higher than in CaF_2 and SrF_2. The authors of Ref. 6 ascribe RDL to core–valence transitions, and the authors of Ref. 5 ascribe it to singlet luminescence of autolocalized excitons with an unrelaxed hole nucleus. The efficiency of creation of closely arranged F,H pairs, and also the RDL yield, depend on the temperature and excitation density.[1–7] Below we shall show that these characteristics are determined in significant measure by the prehistory of the crystal.

The aim of the present paper is to examine transient absorption and rapidly decaying luminescence in nominally pure BaF_2 crystals by space-time-resolved pulsed spectroscopy.

1. EXPERIMENT

The method of pulsed spectroscopy was described in Ref. 8, and a precision measurement technique was discussed in Ref. 4. The maximum energy of the accelerated electrons was 0.28 MeV, the duration of the (current) pulse at half-height was 12 ns, and the temporal resolution was 7 ns. Crystals, grown by the Stockbarger method at the State Optical Institute (GOI) in St. Petersburg, were cleaved from one block in the form of wafers with dimensions $8\times8\times0.5$ mm with allowance for the direction of growth. A segment of the surface of the sample, ~3.75 mm^2 in area, was irradiated by a stopped-down beam. The energy density ($0.2\ J\cdot cm^{-2}$) was measured calorimetrically, with a standard deviation over the irradiated surface of $\pm5\%$. The repetition rate of the pulsed electron beam was $\sim10^{-3}$ Hz. In the present work we used the usual measurement geometry (sample oriented at some angle to the propagation direction of the electron beam[8]) and also the geometry with normal incidence of the electron beam. The transient absorption spectra and RDL spectra were recorded over the entire penetration depth of the electrons in the sample (~250 μm) and over the entire irradiated surface (~3.75 mm^2) as well as from microzones of dimensions 25×38 μm. The distribution of the luminescence light sum (the spectral region 300 $-$400 nm was culled out with the help of light filters) was recorded from the focal plane, located at a depth of ~100 μm from the irradiated surface. This was done photographically with the help of an MPD-1 microscope using fine-grain photographic film of the type ''Mikrat.'' Photometry of the images was performed on an MF-2 microphotometer with resolution $\sim0.3\times0.5$ μm.

2. EXPERIMENTAL RESULTS

Figure 1 (curve *1*) shows the transient absorption spectrum of a BaF_2 crystal cleaved from the lower part of the block, measured using the usual experimental scheme (sample oriented at an angle of 55° to the propagation direction of the electron beam). The characteristic form of the spectrum is in qualitative agreement with the data of Ref. 5. Relaxation of the induced absorption is described by an exponential law with several time constants. The time constant 250 ± 50 ns describes $\sim95\%$ of the falloff of the optical density in the region of the electron component. The spectral distribution of the temporal components isolated by graphical analysis of the relaxation kinetics of the absorption at fixed photon energies without allowance for the complicated structure of the spectrum is shown in Fig. 1 by curves *2–4*.

The intensity distribution of the induced absorption along an arbitrary coordinate (x) in the sample surface was measured in perpendicular geometry 10 ns after termination of the electron pulse, at a fixed wavelength (1.90 eV) with a spatial resolution of 25×38 μm. Results are plotted in Fig. 2a. The distribution of the luminescence light sum along an

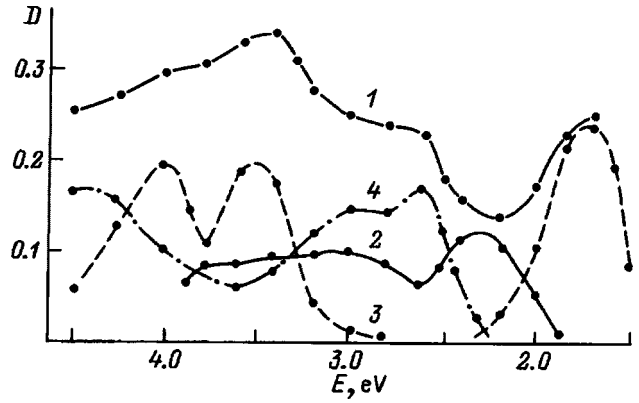

FIG. 1. Spectrum of transient absorption of a BaF_2 crystal, measured at 295 K 10 ns after termination of the electron pulse (*1*), and spectral distribution of the temporal components (*2–4*) in the relaxation of the induced absorption: *2* — 60 ns, *3* — 250±50 ns, *4* — 400±50 ns. Sample situated at an angle of 55° to the direction of incidence of the electron beam.

arbitrary direction in the irradiated surface, measured from darkening of the photographic film with resolution ~0.3 ×0.5 μm, is shown in Fig. 2b.

Curves *2* and *3* of Fig. 3 show the transient absorption spectra of a BaF_2 crystal cleaved from the upper part of the block, measured in perpendicular geometry from arbitrarily chosen microzones but of the same area as above. Curve *1* plots the transient absorption spectrum measured in the same geometry but from an area of ~3.75 mm^2. RDL spectra measured in perpendicular geometry from the same microzones as the absorption are shown in Fig. 4 by curves *2* and

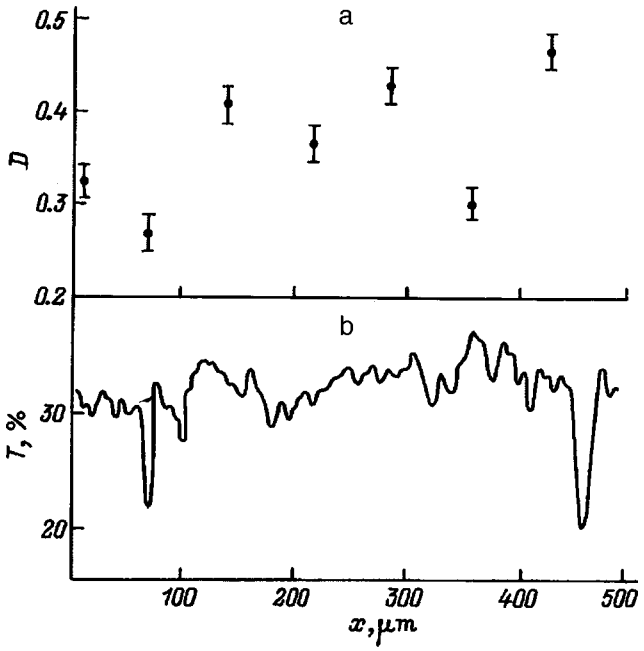

FIG. 2. Spatial distribution of the intensity of the induced absorption (a) and the light sum of the luminescence (b) along an arbitrary coordinate *x* on the irradiated surface of the BaF_2 crystal at 295 K. a — measured in perpendicular geometry 10 ns after termination of a 1.90 eV pulse with resolution 25×38 μm; b — transparency of the photographic film *T*, measured with resolution 0.3×0.5 μm. Photograph of crystal in its own light (spectral region 300−400 nm extracted using light filters) taken in the focal plane, located at a depth of ~100 μm from the irradiated surface.

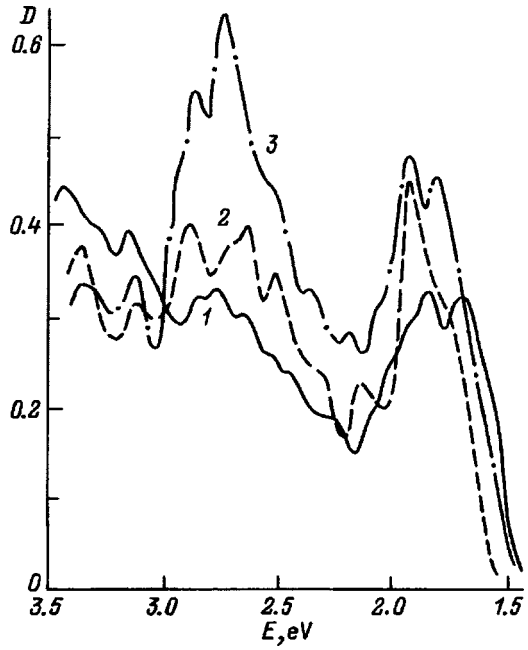

FIG. 3. Spectra of the transient absorption of a BaF_2 crystal, measured in perpendicular geometry at 295 K 10 ns after termination of pulse. *1* — from the irradiated surface (area 3.75 mm^2), *2, 3* — from microzones of identical area (25×38 μm), separated by a distance of ~430 μm.

3. The distance between the microzones was ~430 μm. For comparison, Fig. 4 also shows the RDL spectrum (curve *1*) measured in the usual geometry from an irradiated surface of area ~3.75 mm^2. The RDL intensity of the microzones is

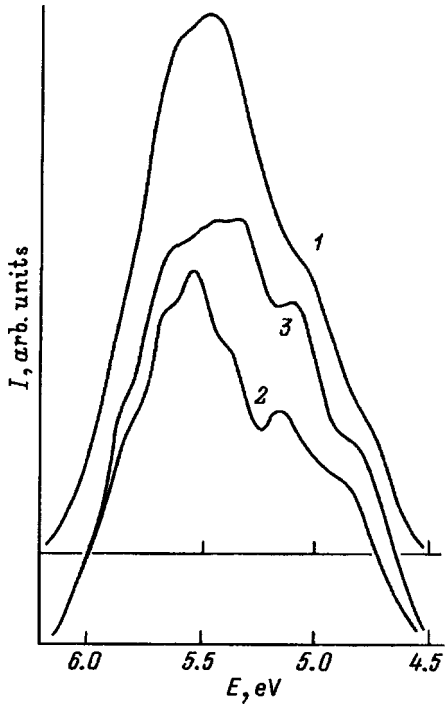

FIG. 4. Spectra of rapidly decaying luminescence of a BaF_2 crystal, measured at 295 K. *1* — in a geometry in which the sample is situated at an angle of 55° to the direction of incidence of the electron beam, *2, 3* — in the perpendicular geometry from the same microzones from which the induced absorption was measured (see curves *2* and *3* in Fig. 3).

roughly three orders of magnitude lower than that of the entire irradiated surface. Analysis of the data obtained reveals the following regularities: first, a complex structure is observed in the spectra of both the rapidly decaying luminescence and the transient absorption; second, the intensity, spectral composition of the transient absorption and rapidly decaying luminescence, and also the distribution of the luminescence light sum depend to a significant extent on the coordinates of the irradiated surface.

3. DISCUSSION

Violation of the condition of dispersed creation of autolocalized excitons is usually linked with the appearance of additional channels of discharge of the electronic excitations in a defective lattice. In this case, the efficiency of creation of autolocalized excitons in unaffected segments of the lattice is diminished.[9] It is well known[10] that homologous cation impurities can enter into BaF_2 crystals in high concentrations. Spectral analysis of our samples directly demonstrates the presence of calcium and strontium impurities. Besides this, a qualitative agreement of the spectral distributions of the components with time constants 60 ns and 400 ± 50 ns in BaF_2 (curves *2* and *4* in Fig. 1) with the distributions of the electron and hole components of the autolocalized-exciton absorption in SrF_2 and CaF_2 is observed.[1,4] Application of the Alentsev–Fock method[11] to the analysis of the structure of the transient absorption spectra in fluorites has also revealed agreement of the spectral positions of the maxima of the band series in these crystals (a detailed analysis will be given in a separate paper). Consequently, we can assume the formation of CaF_2 and SrF_2 phase inclusions in BaF_2.

The radically inhomogeneous variation in space of the intensity of the selective bands [Figs. 2a and 3] in the region of the electron component of autolocalized-exciton absorption (~ 1.90 eV) suggests a significant influence of the intrinsic structure of the BaF_2 crystal on the distribution of the autolocalized excitons over configurations. (It is usually assumed[1,5] that creation of autolocalized excitons takes place in an unaffected BaF_2 lattice.) The data presented in Fig. 3 (curves *2* and *3*) also show that the efficiency of defect creation in the phase inclusions is also a function of the coordinates. A clear spatial correlation is observed here between the processes of defect creation in the host matrix and in the phase inclusions [Figs. 2a and 3]. Since localization of electronic excitations occurs at the stage of free electrons and holes and is very sensitive to changes in the crystal-lattice potential,[12] it may be assumed that creation of autolocalized excitons in the BaF_2 lattice takes place in the vicinity of a defect. This probably also explains the spatially inhomogeneous variation of the efficiency of creation of autolocalized excitons and their distribution over configurations.

It was concluded above, on the basis of integrated spectral–kinetic measurements (Fig. 1), that homologous cation impurities in BaF_2 form phase inclusions. Spatially resolved measurements [Figs. 2a and 3] suggest the possibility of forming a buffer layer, i.e., a transitional region from the CaF_2 or SrF_2 phase to the BaF_2 lattice. First, the distribution of temporal components in the relaxation of the transient absorption in BaF_2 (curves *2* and *4* in Fig. 1) is somewhat broadened in comparison with the spectral distribution of the components of the autolocalized-exciton absorption in nominally pure crystals of CaF_2 and SrF_2. Second, the efficiency of creation of autolocalized excitons both in a nominally pure crystal and in its phase inclusions should be a function of the crystal temperature and the excitation density. However, the intensity of the induced absorption in the region $2.2-4$ eV in BaF_2 (curve *3* in Fig. 3) exceeds its value in SrF_2 and CaF_2 crystals by nearly a factor of three under identical irradiation conditions. Consequently it may be assumed that a homologous impurity does not form a pure phase since there exists an efficient channel for discharge of electronic excitations.

Spatially inhomogeneous creation of primary defects in BaF_2 also can be inferred from an examination of the distribution of the light sum of the natural luminescence. It is usually assumed[1,5] that it arises from the same energy states of the autolocalized excitons as the absorption. As follows from the data plotted in Fig. 2b, the distribution of the light sum over the irradiated surface presents a complex picture. Relatively narrow ($\sim 10\ \mu$m) regions appear against the background of large fragments (up to 100 μm) with roughly the same distribution of the luminescence light sum. Optical micro-inhomogeneities in the BaF_2 crystal are also clearly visible from the effects of birefringence on local strain fields in crossed polarizers. Such inhomogeneities are also found in other fluorite crystals.[13]

Recently it was shown[14] that optical pre-excitation of autolocalized excitons in the region of the electronic components, synchronous with electron bombardment, is accompanied both in CaF_2 and in BaF_2 by spectrally selective changes in the intensity of the rapidly decaying luminescence, which clearly contradicts the model of core–valence transitions. Since the creation of primary defects in BaF_2 exhibits a clear dependence on the intrinsic structure of the crystal, interest has been shown in tracking changes in the intensity and the spectrum of the rapidly decaying luminescence on the basis of space-time resolved measurements (Fig. 4). A comparison of the data displayed in Figs. 3 and 4 provides unambiguous evidence of a spatial correlation between the processes of creation of primary defects and excitation of the rapidly decaying luminescence. The dramatic spatial inhomogeneity of occurrence of these processes suggests that their efficiency is determined to a significant degree by the intrinsic structure of the lattice. The data obtained in the present work indicate the presence of a developed defect structure of BaF_2 crystals and are in good agreement with the results of Ref. 10. Since the level of intrinsic defects in CaF_2 and SrF_2 is significantly lower than in BaF_2 (Ref. 10), a dramatic difference is observed in the RDL yields in these matrices.

To sum up, the results of this study can be considered as alternative arguments for the RDL model not only within the framework of the model of core–valence transitions,[6] but also as forms of ''hot'' luminescence of autolocalized excitons.[5] In conjunction with data on the sublinear density dependence of the efficiency of creation both of closely ar-

ranged (autolocalized) excitons and of spatially separated F, H pairs,[3,5,7] the results obtained here suggest a direct link between the processes of creating primary defects and the intrinsic properties of crystals having the fluorite structure. Spatially-resolved pulsed spectroscopy is an informative method for investigating the primary products of radiolysis in real crystals.

[1] R. T. Williams, M. N. Kabler, W. Hayes, and J. P. H. Stott, Phys. Rev. B **14**, 725 (1976).
[2] N. N. Ershov, N. G. Zakharov, and P. A. Rodnyĭ, Opt. Spektrosk. **53**, *1*, 89 (1982) [Opt. Spectrosc. **53**, 51 (1982)].
[3] L. A. Lisitsyna, V. M. Lisitsyn, and E. P. Chinkov, Izv. Vuzov. Fiz., *1*, 13 (1995).
[4] E. P. Chinkov and V. F. Shtan'ko, Fiz. Tverd. Tela (St. Petersburg) **39**, 1197 (1997) [Phys. Solid State **39**, 1060 (1997)].
[5] I. P. Denisov, V. A. Kravchenko, A. V. Malovichko, and V. Yu. Yakovlev, Fiz. Tverd. Tela (Leningrad) **31**, 22 (1989) [Sov. Phys. Solid State **31**, 1110 (1989)].
[6] M. Yu. Aleksandrov, V. N. Makhov, P. A. Rodnyĭ, T. I. Syreĭshchikova, and M. N. Yakimenko, Fiz. Tverd. Tela (Leningrad) **26**, 2865 (1984) [Sov. Phys. Solid State **26**, 1734 (1984)].
[7] V. F. Shtan'ko and V. I. Oleshko, Zh. Tekh. Fiz. **59**(3), 99 (1989) [Sov. Phys. Tech. Phys. **34**, 312 (1989)].
[8] É. D. Aluker, V. V. Gavrilov, R. G. Deĭch, and S. A. Chernov, *Fast-acting Radiation-Stimulated Processes in Alkali-Halide Crystals* [in Russian], Zinatne, Riga (1987), 183 pp.
[9] L. A. Lisitsyna, V. M. Reĭterov, V. M. Lisitsyn, E. P. Chinkov, and L. M. Trofimova, Opt. Spektrosk. **55**, 875 (1983) [Opt. Spectrosc. **55**, 526 (1983)].
[10] W. Hayes and A. M. Stoneham, in *Crystals with the Fluorite Structure*, Ch. 4, edited by W. Hayes (Oxford, 1974), pp. 185–280.
[11] M. V. Fok, Trudy FIAN **59**, 3 (1972).
[12] V. I. Korepanov, V. M. Lisitsyn, and L. A. Lisitsyna, Izv. Vuzov, *11*, 94 (1996).
[13] L. Dressler, Cryst. Res. Technol. **21**, *4*, K53 (1986).
[14] V. F. Shtank'ko and E. P. Chinkov, Pis'ma Zh. Tekh. Fiz. **23**(21), 45 (1997) [Tech. Phys. Lett. **23**, 837 (1997)].

Translated by Paul F. Schippnick

Effect of overlap of localized orbitals on the band structure of insulators under pressure

V. G. Baryakhtar

Institute of Magnetism, Ukrainian Academy of Sciences, 252142 Kiev, Ukraine

E. V. Zarochentsev, E. P. Troitskaya, and Yu. V. Eremeĭchenkova

Donetsk Physicotechnical Institute, Ukrainian Academy of Sciences, 340114 Donetsk, Ukraine

(Submitted January 8, 1998)
Fiz. Tverd. Tela (St. Petersburg) **40**, 1464–1472 (August 1998)

A new method for calculating the energy spectra of compressed insulators based on the cluster expansion is proposed. The dependence on the compression of the spectra of both the conduction band and the valence bands is uniquely determined by the values of the overlap integrals of the orbitals of pairs of isolated atoms. The overlap integrals and the matrices defined by them are calculated numerically for inert-gas crystals and their properties and values are analyzed for different lattice constants. Numerical calculations of the bands of the compressed crystal in the various proposed models are carried out and discussed for neon. © *1998 American Institute of Physics.* [S1063-7834(98)01508-1]

Contemporary theoretical studies of the properties of insulators under pressure generally take two different tacks. The first approach—the quantum-chemical approach (c.f., Ref. 1 for crystals of inert gases)—considers an individual atom in a crystal and calculates the total energy of the crystal. The second approach proceeds to calculate the band structure. Here we are looking at calculations within the framework of density functional theory,[2–4] the method of Green's functions,[5,6] and methods using the muffin-tin (MT) approximation (PPV, KKR, LMTO, etc.).[7,8] A general feature of the above-enumerated methods is the use of specific approximations for the crystal potential, whose applicability to compressed crystals is unclear.

In order to avoid uncontrollable approximations in the calculation of bands under pressure, it is necessary that certain conditions be fulfilled: 1) to calculate the energy spectrum of occupied states methods can be used that are based on localized orbitals (LO) while to calculate the conduction bands the most acceptable method is the modified[9–11] GPW method;[12] 2) in the GPW method it is necessary to describe the states of the filled bands using the Wannier functions of the crystal; 3) it is necessary to have a sufficiently accurate orthogonalization of the localized basis orbitals with each other and with the GPW.

The second and third requirements in Refs. 9–11 were satisfied approximately—to first order in the overlap integrals

$$S_{\alpha\beta}^{\mathbf{lm}}=\langle \mathbf{l}\alpha|\mathbf{m}\beta\rangle \tag{1}$$

of the atomic orbitals $\varphi_\alpha(\mathbf{r}-\mathbf{l})=|\mathbf{l}\alpha\rangle$. The valence bands were calculated in Ref. 9 quite roughly although it should be noted that their pressure dependence was apparently faithfully reproduced.[9–11] This has to do, first, with the fact that Refs. 9–11 constructed a theory without any adjustable parameters or any of the traditional approximations (the X_α approximation, the local pseudopotential approximation, etc.). The insulator–metal transition at $\Delta V/V_0=0.77\pm0.02$ was predicted within the framework of this theory.

A further development of this theory, satisfying the above-enumerated points, is the application of Löwdin's exact orthogonalization[13–15] of the basis linear orbitals (LO) in combination with the cluster expansion (CE).[14–16] The necessity of using the cluster expansion (instead of first order in the overlap integrals) is due to the fact that for large compressions the overlap integrals become quite large. Even in its lowest order the cluster expansion contains a sum over a definite subsequence of the series in overlap integrals[16,17] and thereby removes the restriction $|S|\ll 1$, which is basic to the theory.[9–11,18]

In the present work we restrict the discussion to ideal crystals of inert gases under high pressures. The insulator–metal transition (metallization) in inert-gas crystals (IGC) has been predicted, detected, and investigated, along with structural phase transitions.[19–21] The most accessible inert gas for experiment is xenon. Metallization of Xe takes place in the hcc phase at 1.5 Mbar (molar volume $\nu_\mu=10.2$ cm^3/mol).[20] According to Ref. 21, Xe also transitions to the metallic state in the hcc structure at 1.32 Mbar ($\nu_\mu=10.5$ cm^3/mol).

To calculate the conduction bands of an insulator under pressure, we propose to use the CEOPW method. However, in contrast to Refs. 9–11, here we approximate the Wannier functions of the occupied states by linear combinations of orthogonalized (according to the prescription of Löwdin[13]) atomic orbitals and use the cluster expansion to calculate them.

The main idea of the present work is that the effective potential needed to calculate the band characteristics and thermodynamic properties is defined by just the overlap integrals S of the orbitals of an isolated atom. We also inves-

tigate the behavior of S and the bands with decrease of the interatomic distance d (in the instance of inert-gas crystals).

1. BASIS AND CLUSTER EXPANSION

Let us start from a consideration of the filled states in the crystal.[16,17] For a system of noninteracting atoms a natural set of one-electron wave functions consists of the functions of filled Hartree–Fock electron states in the atom $|\mathbf{l}\alpha\rangle$. Here $\mathbf{l}$ ranges over all lattice sites (cells) of the crystal from 1 to N. The orbital number α varies from 1 to $Z/2$ (Z is the number of electrons in an atom of the crystal; for simplicity we consider only monoatomic crystals), i.e., α is in fact the set nl consisting of the principal quantum number and the orbital quantum number.

We introduce atomic orbitals $|\mathbf{l}\alpha\rangle_{\mathrm{CE}}$ which have been orthogonalized according to Löwdin's prescription,[13] and the matrices $\mathcal{P}$ and P, which we will need in what follows,

$$|\mathbf{l}\alpha\rangle_{\mathrm{CE}}=\sum_{\mathbf{m}\beta}(T^{-1/2})^{\mathbf{ml}}_{\beta\alpha}|\mathbf{m}\beta\rangle=|\mathbf{l}\alpha\rangle-\sum_{\mathbf{m}\beta}\mathcal{P}^{\mathbf{ml}}_{\beta\alpha}|\mathbf{m}\beta\rangle,$$

$$\mathcal{P}=I-T^{-1/2},\quad P=I-T^{-1} \tag{2}$$

(P is the single-particle density matrix of the crystal). The metric matrix $T^{\mathbf{ml}}_{\beta\alpha}$, by definition, is equal to

$$T^{\mathbf{ml}}_{\beta\alpha}=\begin{cases}\langle\mathbf{l}\alpha|\mathbf{m}\beta\rangle, & \mathbf{l}\neq\mathbf{m},\\ \delta_{\mathbf{lm}}\delta_{\alpha\beta}, & \mathbf{l}=\mathbf{m},\end{cases}\quad T=I+S,\ \ S=S^{+}. \tag{3}$$

The matrix T is defined in the space of atomic orbitals centered on the lattice sites,[14,15,22] and I is the unit matrix.

To find the matrices $\mathcal{P}$ and P it is advisable to use the cluster expansion. This expansion for the density matrix (i.e., for P) was suggested in Ref. 14 (see also Refs. 15 and 22), and for the matrix $\mathcal{P}$, in Refs. 16 and 17. The sense of the cluster expansion is conveniently elucidated in instance of some of its lowest orders (for details of the general theory, see Refs. 16 and 17). The first order for the quantity A contains two-particle clusters (the $2C$ approximation)

$$A^{(2)}=\sum_{\mathbf{l}<\mathbf{m}}A[\mathbf{l},\mathbf{m}], \tag{4}$$

where $A[\mathbf{l},\mathbf{m}]$ is a two-particle cluster. Each term in expansion (4) takes exact account of the overlap of orbitals within the corresponding two-particle cluster. One set of such clusters runs over the entire crystal. The second order (the three-particle cluster approximation) has the form

$$A^{(3)}=\sum_{\mathbf{l}<\mathbf{m}<\mathbf{n}}\{A[\mathbf{l},\mathbf{m},\mathbf{n}]-A[\mathbf{l},\mathbf{m}]-A[\mathbf{m},\mathbf{n}]-A[\mathbf{l},\mathbf{n}]\}. \tag{5}$$

Each of the terms in Eq. (5) contains the exact contribution of a pairwise overlap within the three-particle cluster after subtraction of all possible exact contributions of two-particle clusters contained in the given three-particle cluster. The terms of all subsequent orders of the cluster expansion have an analogous structure, so that

$$A=A^{(2)}+A^{(3)}+\ldots+A^{(N)},$$

and all terms except for $A^{(N)}A[\mathbf{l}_1\ldots\mathbf{l}_N]$ mutually cancel and only $A=A^{(N)}$ remains (for more details, see Refs. 14 and 22). The advantage of the cluster expansion is that it is possible to cut it off at a small number of terms, thereby avoiding the necessity of calculating with the T matrix of order $L\times L$ (L is the dimension of the crystal).

In the present work we restrict the discussion to the approximation of two-particle clusters. In the interesting case of calculating the band structure

$$A=\begin{cases}\mathcal{P}; & A[\mathbf{m},\mathbf{n}]=I-T[\mathbf{m},\mathbf{n}]^{-1/2},\\ P; & A[\mathbf{m},\mathbf{n}]=I-T[\mathbf{m},\mathbf{n}]^{-1},\end{cases} \tag{6}$$

$$T[\mathbf{m},\mathbf{n}]^{\mathbf{ll}'}_{\alpha\beta}=\begin{cases}S^{\mathbf{ll}'}_{\alpha\beta}; & \mathbf{l}\ \text{and}\ \mathbf{l}'[\mathbf{m},\mathbf{n}],\\ \delta_{\mathbf{ll}'}\delta_{\alpha\beta}; & \mathbf{l}\ \text{and/or}\ \mathbf{l}'[\mathbf{m},\mathbf{n}].\end{cases} \tag{7}$$

Thus, when using the two-particle cluster approximation the problem of Löwdin orthogonalization of the atomic orbitals of the entire crystal reduces to the analogous problem for the corresponding two-atom clusters.

2. BAND STRUCTURE

The single-particle Schrödinger equation (the Hartree–Fock equation) of a band electron with Bloch function $\psi_{\mathbf{k}}$ is

$$\left[\hat{T}+\sum_{\mathbf{l}}V^{\mathbf{l}}_{ne}+2\int\frac{\rho(\mathbf{r}'|\mathbf{r}')d\mathbf{r}'}{|\mathbf{r}-\mathbf{r}'|}\right]\Psi_{\mathbf{k}v}(\mathbf{r})-\int\frac{\rho(\mathbf{r}'|\mathbf{r}')\psi_{\mathbf{k}}(\mathbf{r}')d\mathbf{r}'}{|\mathbf{r}-\mathbf{r}'|}=\varepsilon_{\mathbf{k}}\psi_{\mathbf{k}v}. \tag{8}$$

In the Hartree–Fock method the density matrix $\rho(\mathbf{r}|\mathbf{r}')$ itself in Eq. (8) depends on the unknown functions $\psi_{\mathbf{k}v}$. However, usually (see Ref. 12) all the terms on the left-hand side, except for the kinetic energy operator $\hat{T}=(\hbar^2/2m)\nabla^2$, are denoted as the potential $V^{\mathbf{l}}$ acting identically on any electron and satisfying the main Ansatz of the band calculations

$$V(\mathbf{r})=\sum_{\mathbf{l}}V(\mathbf{r}-\mathbf{l}). \tag{9}$$

This approach is used in the CELO method[16] discussed below. A more flexible scheme is the one in which the one-electron potential $V(\mathbf{r})$ is constructed differently for the occupied (valence bands) and free (conduction band) states. Let us consider just this situation, assuming that in the insulator the occupied states are described in the basis of localized orbitals $|\mathbf{l}\alpha\rangle_{\mathrm{CE}}$, and the conduction band can be described within the framework of the GPW method.

The wave function of the filled electron states in the crystal in the single-particle approach is the Slater determinant[15] with columns (rows) consisting of one-electron functions: Bloch or Wannier. The spatial part of this determinant is formed in our case of Bloch functions of the valence electrons $|\mathbf{k}v\rangle$ ($\mathbf{k}$ is the wave vector, and v is the number of the filled band), constructed according to the usual rules[12] from the orthogonal basis $|\mathbf{l}\alpha\rangle_{\mathrm{CE}}$, i.e.,

$$|\mathbf{k}v\rangle=N^{-1/2}\sum_{\mathbf{l}\alpha}C_{\alpha v}\exp(i\mathbf{kl})|\mathbf{l}\alpha\rangle_{\mathrm{CE}}, \tag{10}$$

where $C_{\alpha v}$ are variational parameters subject to determination.

The Hamiltonian H of the problem is

$$H=\sum_i h_i+\sum_{i<j} v_C(\mathbf{r}_i-\mathbf{r}_j), \quad h_i=T_i+V_i, \tag{11}$$

where T_i and V_i are the kinetic energy operator and the one-electron potential acting on the ith electron due to the nuclei, and $v_C(r)=e^2/r$.

Performing a series of obvious transformations, we reduce the secular equation for finding the energy $E_{\mathbf{k}v}$ and the wave functions $C_{\alpha v}$ of the valence bands to the following form:

$$\sum_\beta [V_{\alpha\beta}(\mathbf{k};\{C\})+\delta_{\alpha\beta}(\varepsilon_\beta-E_{\mathbf{k}v})]C_{\beta v}=0; \tag{12}$$

for $V_{\alpha\beta}=0$ this equation gives the energy levels of an isolated atom ε_β. In Eqs. (12) the one-electron potential $V_{\alpha\beta}$ vanishes for $S^{\mathbf{lm}}_{\alpha\beta}=0$. System of equations (12) is equally suitable for any method whose basis is a set of localized orbitals. It is suitable for the Hartree–Fock (HF) approach, the hole bands approach, and the LCAO approach (see Ref. 23). In the CEHF approach the potential $V_{\alpha\beta}$ has the form

$$V_{\alpha\beta}(\mathbf{k};C)=\varepsilon_\alpha S_{\alpha\beta}(\mathbf{k})+N^{-1}\sum_{\mathbf{l},\mathbf{n}} \exp[i\mathbf{k}(\mathbf{l}-\mathbf{n})] \times\left\{\sum_{\mathbf{m}\neq\mathbf{n}}\langle\mathbf{l}\alpha|v_a^{\mathbf{m}}|\mathbf{n}\beta\rangle+(V^{(1)}[\mathcal{P}])^{\mathbf{ln}}_{\alpha\beta} +(V^{(2)}[\mathcal{P};C])^{\mathbf{ln}}_{\alpha\beta}\right\}, \tag{13}$$

where

$$S_{\alpha\beta}(\mathbf{k})=\sum_{\mathbf{h}\neq\mathbf{0}} S^{\mathbf{h0}}_{\alpha\beta}\exp[i\mathbf{kh}], \tag{14}$$

v_a is the self-consistent potential of the neutral atom, and $S^{\mathbf{h0}}_{\alpha\beta}$ is given by formula (1). The terms of the crystal potential $V_{\alpha\beta}(\mathbf{k};C)$ in Eqs. (12) are derived in the Appendix. In the calculation of the hole bands[18] it is necessary to set $V^{(2)}=0$ in Eqs. (13), and in the CELO and LCAO methods, also some of the terms involving $V^{(1)}$ (see Appendix). The potential $V^{(1)}$ is a function of the matrix $\mathcal{P}$ and vanishes when $\mathcal{P}=\mathbf{0}$ (or $S=0$). It has the form

$$V^{(1)}[\mathcal{P}]=V_h^{(1)}[\mathcal{P}]+V_{ee}^{(1)}[\mathcal{P}]. \tag{15}$$

Expressions for $V_h^{(1)}$ and $V_{ee}^{(1)}$ are given in the Appendix. The potential $V^{(2)}$ depends on the overlap of basis functions directly through $\mathcal{P}$ and implicitly through the variational parameters $C_{\alpha v}$ (see Appendix). The potential $V^{(2)}$ is a direct consequence of the nonlinearity of the Hartree–Fock equations.

Let us now consider the conduction bands and briefly describe the CEOPW method.[16,17] The test functions of the conduction bands $|\mathbf{k}c\rangle$ are constructed from the orthogonalized waves

$$|\mathbf{k}\rangle_{\text{CEOPW}}=\left(1-\sum_{\mathbf{k}'v}|\mathbf{k}'v\rangle\langle\mathbf{k}'v|\right)|\mathbf{k}\rangle \tag{16}$$

as

$$|\mathbf{k}c\rangle=\sum_{\mathbf{g}} a_{\mathbf{g}}(k)|\mathbf{k}+\mathbf{g}\rangle_{\text{CEOPW}}, \tag{17}$$

where $a_{\mathbf{g}}(\mathbf{k})$ are variational parameters and $|\mathbf{k}v\rangle$ are functions of the filled bands (10).

The secular equation for finding the spectrum $E_{\mathbf{k}c}$ and functions $a_{\mathbf{g}}(\mathbf{k})$ has the form

$$\sum_{\mathbf{g}'}\left\{\left[\frac{\hbar^2}{2m}(\mathbf{k}+\mathbf{g})^2-E_{\mathbf{k}c}\right]\delta_{\mathbf{gg}'}+V_C(\mathbf{g}'-\mathbf{g})+V_{\text{ex}} \times(\mathbf{k}+\mathbf{g}',\mathbf{k}+\mathbf{g})+V_{\text{PK}}(\mathbf{k}+\mathbf{g}';\mathbf{k}+\mathbf{g})\right\}a_{\mathbf{g}'}(\mathbf{k})=0. \tag{18}$$

Here V_C, V_{ex}, and V_{PK} are the form-factors of the Coulomb and exchange potentials, and the Phillips–Kleinman potential. Expressions for these quantities in the cluster approach are derived and discussed in detail in Ref. 16. In the present work we discuss only their dependence on the overlap integrals.

The coefficients of Eq. (18) depend on the overlap integrals through the so-called lattice Fourier transform of the $\mathcal{P}$ and P matrices. In general form

$$A_{\alpha\beta}(\mathbf{k})=\sum_{\mathbf{h}} A^{\mathbf{h0}}_{\alpha\beta}\exp(i\mathbf{kh}), \tag{19}$$

$A=S,\mathcal{P},P$ and $\alpha,\beta=1s,2s,2p_x,2p_y,2p_z$ for Ne, which is discussed below. The matrices $A_{\alpha\beta}(k)$ can be expressed in terms of the basis overlap integrals $A^{\mathbf{h0}}_{\alpha\beta}$ $(\mathbf{h}=\sqrt{2}(0,0,1))$

$$A^{\mathbf{h0}}_{\alpha\beta}\begin{Bmatrix}S_{\alpha\beta}\\ \mathcal{P}_{\alpha\beta}\\ P_{\alpha\beta}\end{Bmatrix}=A_\sigma,A_\pi,A_{ns,2p},A_{ns,ms},$$

where $n=1,2$, $A_\sigma=A_{2p_z,2p_z}$, $A_\pi=A_{2p_x,2p_x}$, and $A_{ns,2p}=-A_{2p,ns}$. The quantities $A_{\alpha\beta}(\mathbf{k})$ in Eq. (19) in the nearest-neighbor approximation are equal to

1) s-s overlap

$$A_{ns,ms}(\mathbf{k})=\gamma^{ss}(\mathbf{k})A_{ns,ms}, \tag{20a}$$

2) s-p overlap, $n=1,2$, $\alpha=x,y,z$

$$A_{ns,2p_\alpha}(\mathbf{k})=-A_{2p_\alpha,ns}(\mathbf{k})=\gamma^{sp}_\alpha(\mathbf{k})A_{ns,2p}, \tag{20b}$$

3) p-p overlap

$$A_{2p_\alpha,2p_\beta}(\mathbf{k})=A_{2p_\beta,2p_\alpha}(\mathbf{k})=\gamma^{\sigma}_{\alpha\beta}(\mathbf{k})A_\sigma+\gamma^{\pi}_{\alpha\beta}(\mathbf{k})A_\pi. \tag{20c}$$

The quantities $\gamma^{\alpha\beta}(\mathbf{k})$ depend only on the structure of the crystal and the orbital quantum number

$$\gamma^{\alpha\beta}(\mathbf{k})=\sum_{\mathbf{h}} n(\alpha\beta)\exp(i\mathbf{kh}). \tag{21}$$

Here $n(\alpha\beta)=1,-1,0$ depending on the specific value of $\mathbf{h}$. We will not give here specific expressions for $\gamma^{\alpha\beta}(\mathbf{k})$.

3. OVERLAP OF ATOMIC ORBITALS

From Eq. (13) (also see Appendix) it follows that the crystal potential $V_{\alpha\beta}(\mathbf{k};\{C\})$ acting on the valence electron

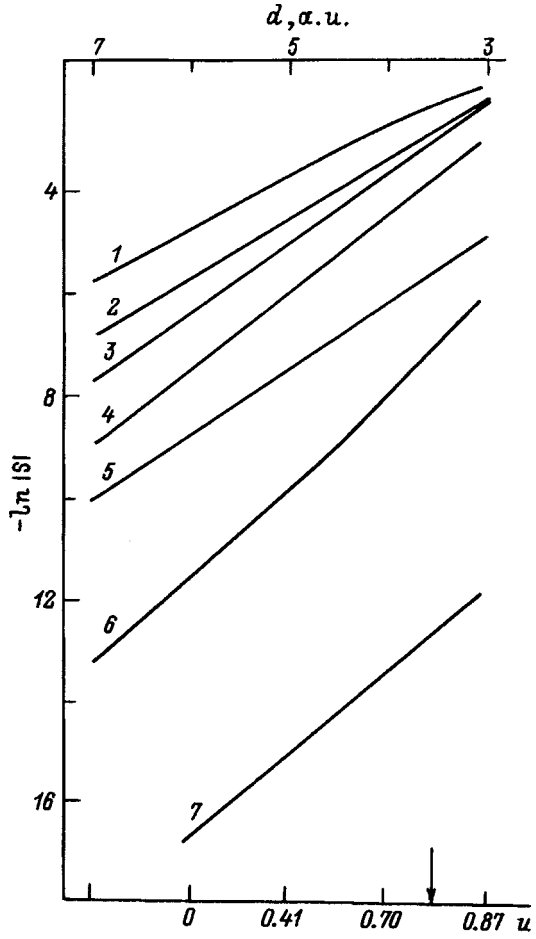

FIG. 1. Overlap integrals of neon nearest-neighbors plotted versus compression $u=\Delta V/V_0$ (lower axis) and distance d ($d_0=5.96230$ a.u., Ref. 24, upper axis) of the following orbital pairs: *1*—$2p2p(\sigma)$, *2*—$2s2p$, *3*—$2p2p(\pi)$, *4*—$2s2s$, *5*—$1s2p$, *6*—$1s2s$, *7*—$1s1s$. In this and in the following figures the arrow indicates the calculated value of the metallization compression.[1] The hash-marks of the lower axis are at the same positions as those of the upper axis and show the compression values corresponding to the given distances.

is defined by the overlap of the electron wave functions of the atoms of the crystal. The cluster expansion (to any order) operates only by means of the pairwise overlap integrals, in terms of which the single-particle basis (2) is introduced. The Coulomb and exchange potentials in expression (13) also depend on the overlap of orbitals of neighboring atoms and can also be written in terms of the $S^{\mathbf{lm}}_{\alpha\beta}$ (Refs. 8 and 22). As for the potential acting on the extra electron (in the conduction band), the dependence of all its terms on $S^{\mathbf{lm}}_{\alpha\beta}$ is explicit.[16] In this Section we consider the behavior of $S^{\mathbf{lm}}_{\alpha\beta}$, and also the matrices $\mathcal{P}$ and P, as functions of the interatomic distance (which imitates the external pressure in a cubic crystal).

Figures 1 and 2 plot the dependence of the basis overlap integral S on the interatomic distance d (or compression $u=\Delta V/V_0$, where V is the volume) (the z axis is directed toward the nearest neighbor) for Ne and Kr (having 10 and 36 electrons per atom, respectively). In the calculations we used atomic functions from the tables of Clementi and Rosetti.[26]

A general property of $\ln|S|$, as expected, is its growth with decrease of d. The linearity of $\ln|S|\sim(d_0-d)$ holds up quite well, especially for the high-energy states and not too large compressions. The structure of $S(d)$ in neon (Fig. 1) is extraordinarily simple whereas in krypton (Fig. 2) the dependence of $\ln|S|$ with participation of the inner shells is nonlinear and even nonmonotonic. Deviation of the curve $\ln|S|=f(d)$ from a straight line is due to the fact that nonmonotonicity begins to show up for significant compressions as well as the presence of zeros of the radial atomic functions. This also explains the nonmonotonicity of the largest S for d in the metallization range ($u\sim0.7-0.8$). Another peculiarity is the substantially greater rate of growth of the curve $\ln|S|$ for overlap of the d states [Fig. 2b].

From Fig. 3 it can be seen that Ne stands apart from the series of inert-gas crystals. For it the deviations δ are equal to $\sim1\%$ whereas for Ar, Kr, and Xe the deviations group around 10%. Compressions corresponding to the insulator–metal transition for the four inert-gas crystals lie in the interval $u_c=0.7-0.8$ (Fig. 3 plots calculated values of u_c from Ref. 1; for Ne u_c coincides with our value[9–11,27]).

Dependences of the first few $S_{\alpha\beta}(\mathbf{k})$, Eq. (19), are plotted in Fig. 4. The curves for $\mathcal{P}_{\alpha\beta}(\mathbf{k})$ and $P_{\alpha\beta}(\mathbf{k})$ have a similar form. It can be seen [Fig. 4a] that all the $S_{\alpha\beta}(\mathbf{k})$ ($\alpha,\beta=1s,2s,2p_x,2p_y,2p_z$) have the same order of magnitude although the $S^{\mathbf{h0}}_{\alpha\beta}$ differ among themselves by one order. This is as it is because $S^{\mathbf{h0}}_{\alpha\beta}$ is multiplied by γ (Fig. 4), but the contribution of S_σ to $S_{\alpha\beta}(\mathbf{k})$ is 2–4 times greater than that of S_π [Fig. 4b]. This explains why addition of S_π has not significant effect on the result for the conduction bands (Table I). At the same time, addition of the remaining overlap integrals (s-s and s-p overlaps) changes the band structure.

Among all the basis overlap integrals the largest for all the cryocrystals is S_σ. In Refs. 9 and 11 only it was taken into account. However, the smallness of the remaining overlap integrals relative to S_σ still does not allow us to conclude that they can be neglected. The quantities $\gamma^{\alpha\beta}(\mathbf{k})$, Eq. (20), can alter the magnitude of the contributions from the $S_{\alpha\beta}$. For example, S_π is considerably smaller than S_σ; however, $\gamma^\pi(\mathbf{k})$ is two times larger than γ^σ at the Γ point, so that the contributions of these two integrals to $S(\mathbf{k})$ turn out to be of the same order. The situation is the same on the ΓX line, so that taking S_π into account noticeably ''smooths out'' the curve of the overlap $S_{2p_y,2p_y}(\mathbf{k})$ on this line, etc. From this reason we calculated bands with different sets of overlap integrals S (Table I).

In the preceding Sections we showed how to take into account the entire series of overlap integrals S by introducing the matrices $\mathcal{P}$ and P. We will now show what quantitative effect the cluster expansion has for the case of neon. Although in neon the nondiagonal blocks, for example, the matrices $P[\mathbf{0l}]^{\mathbf{0l}}_{\alpha\beta}$, are equal to $S^{\mathbf{0l}}_{\alpha\beta}$ ($u=0.75$) with good accuracy ($\sim1\%$) (Fig. 3), the contributions of the diagonal blocks turn out to be on the order of $\sim25\%$. For this reason the curves $P_{\alpha\beta}(\mathbf{k})$ are shifted relative to the curve $S_{\alpha\beta}(\mathbf{k})$ by a constant offset equal to

$$P_{\alpha\beta}(\mathbf{k})-S_{\alpha\beta}(\mathbf{k})=\sum_{\mathbf{h}} P[\mathbf{h0}]^{\mathbf{00}}_{\alpha\beta},$$

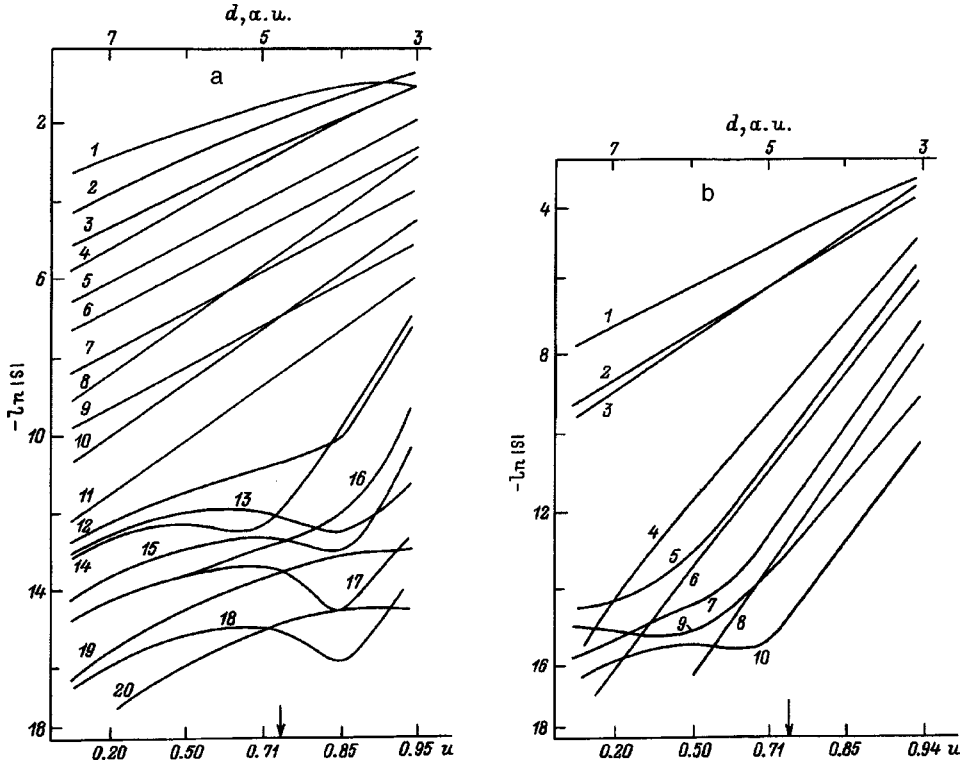

FIG. 2. The largest overlap integrals S in Kr ($d_0=7.547080$ a.u., Ref. 25). *a*—overlap of the s and p orbitals: *1*—$4p4p(\sigma)$, *2*—$4s4p$, *3*—$4p4p(\pi)$, *4*—$4s4s$, *5*—$3s4p$, *6*—$3p4p(\pi)$, *7*—$2s4p$, *8*—$3s4s$, *9*—$1s4p$, *10*—$2s4s$, *11*—$1s4s$, *12*—$3s3p$, *13*—$3s2p$, *14*—$3p3p(\sigma)$, *15*—$2s3p$, *16*—$3p3p(\pi)$, *17*—$2s4p$, *18*—$1s2p$, *19*—$2s2s$, *20*—$1s2s$; *b*—overlap of the d orbitals: *1*—$3d_{z^2}4p$, *2*—$3d_{xz}4p$, *3*—$3d_{z^2}4s$, *4*—$3d_{z^2}3dz^2$, *5*—$3d_{z^2}3p$, *6*—$3d_{xz}3d_{xz}$, *7*—$3d_{xz}3p$, *8*—$3d_{xy}3d_{xy}$, *9*—$3d_{z^2}2p$, *10*—$3d_{xz}2p$.

regardless of **k**.

Figure 5 shows the cluster contributions, i.e., the deviations of the elements of the matrix $\mathcal{P}$ from the corresponding values of S. What distinguishes the matrices $\mathcal{P}$ and P qualitatively from the overlap integrals S is that their diagonal elements are not equal to zero (Fig. 5). It is clear that for neon these differences (as was already noted) are insignificant up to the transition pressures, but for other, heavier crystals they are important.

4. DISCUSSION

From the band-structure theory that we have just constructed (see Secs. 2 and 3 and Ref. 16) it follows that the bands of an insulator depend only on the quantities $S^{\mathbf{lm}}_{\alpha\beta}$ (1). Any external forces that do not alter the structure of the wave functions of an electron in the atoms making up the crystal act on the crystal only by varying the distances $\mathbf{l}-\mathbf{m}$ and through overlap of the atomic orbitals. In this sense the quantities $S^{\mathbf{lm}}_{\alpha\beta}$ are the only correction parameters of the theory. Of these only the ones that are for nearest neighbors (e.g., in Ne) are important, and only for the tops of the valence bands. Thus, the set of quantities $S^{\mathbf{lm}}_{\alpha\beta}$ uniquely determines all the properties of insulators: both their electron spectra (through the matrices $\mathcal{P}$ and P) and the adiabatic potential (through the matrix P, Refs. 15 and 29). The problem of calculating the properties of insulators can be broken down into two steps: calculation of the set $S^{\mathbf{lm}}_{\alpha\beta}$ and calculation for given $S^{\mathbf{lm}}_{\alpha\beta}$ of the spectra, thermodynamics, and kinetics.

Table I displays the results of calculations for the bottom of the conduction band of neon. The calculations were based on the GPW method in various models. In all the models, for the energies of the occupied states we used the energies of the isolated atoms.[26] In this way we excluded the effect of approximations on the valence band.

Table II displays results of calculations for the tops of the valence bands and the bottoms of the conduction bands of compressed neon in various models of the valence bands. To calculate the conduction bands, as in Table I, we used the GPW method, but, like for the hole bands, we calculated the

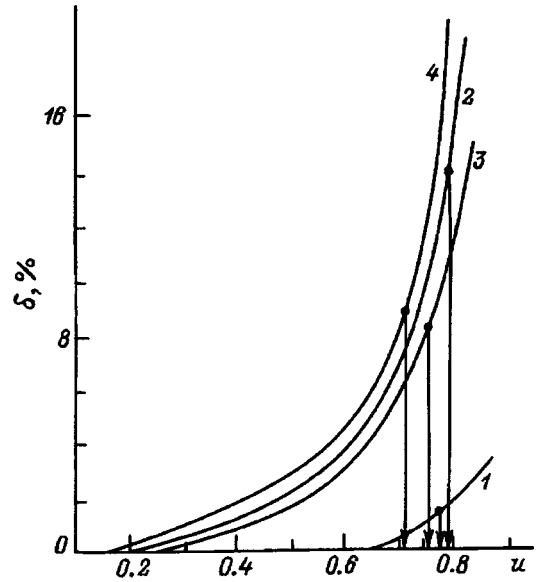

FIG. 3. Difference $\delta=|(\mathcal{P}-0.5S)/S|\cdot 100\%$ of the largest elements $\mathcal{P}^{(\sigma)}_{np,np}$ of the matrix $\mathcal{P}$ from their first order in the overlap integrals as a function of interatomic distance d and compression u for Ne (*1*), Ar (*2*), Kr (*3*), and Xe (*4*).

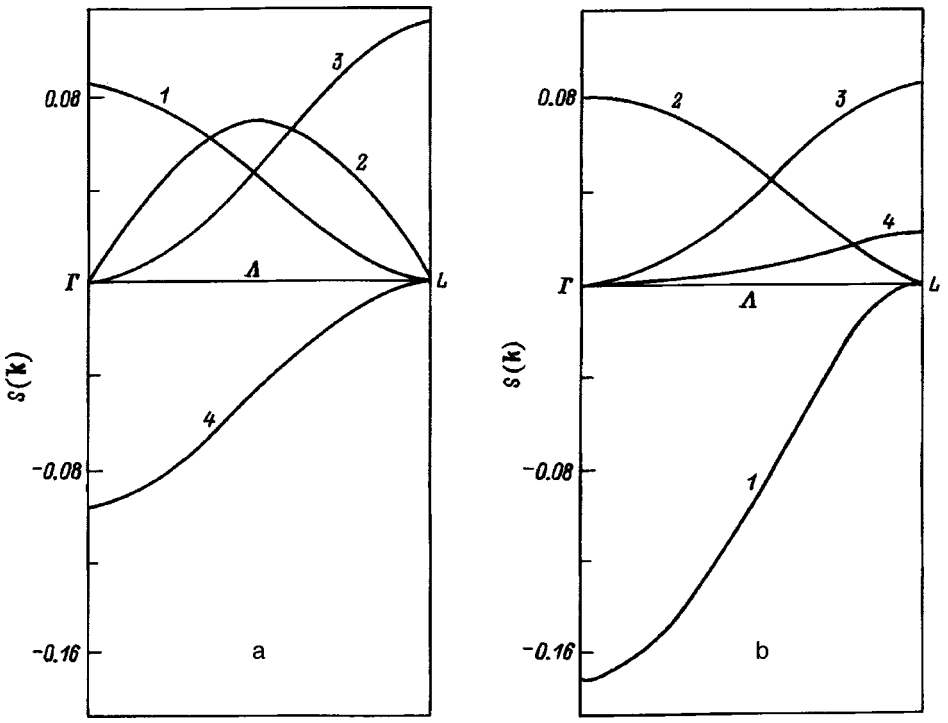

FIG. 4. Lattice Fourier transforms of the nearest-neighbor overlap integrals in fcc neon on the $\Gamma-L$ line. Compression $u=0.6$. a—maximum nonzero overlap integrals ($\alpha\neq\beta=x,y,z$): *1*—$S_{2s;2s}$, *2*—$S_{2s;2p_\alpha}=-S_{2p_\alpha;2s}$, *3*—$S_{2p_\alpha;2p_\beta}=S_{2p_\beta;2p_\alpha}$, *4*—$S_{2p_\alpha;2p_\alpha}$; b—contributions of S_σ and S_π to $S_{2p_x;2p_x}$ (*1* and *2*) and to $S_{2p_x;2p_y}$ (*3* and *4*).

filled bands in the LCAO approximation[12] and the CELO approximation[16] (see Sec. 2 and the Appendix).

The main result following from Tables I and II is that metallization under pressure appears as a result of vanishing of the indirect gap $E(X_n)-E(\Gamma_{15})$ or $E(L_n)-E(\Gamma_{15})$. For an uncompressed crystal the presence or absence of orthogonalization of the atomic functions does not play a role. Differences between the models show up starting at $u=0.6$. The most sensitive bands to overlap of the atomic functions are the bands at the X and L points.

Table II reveals the influence of the different models of the valence bands and the conduction bands. An increase in the energy of any of the valence bands lowers the energy in

TABLE I. Conductivity bands of compressed neon near the fundamental gap in different models.

		$\Delta V/V_0$				
BZ Point	Model	0.0	0.6	0.7	0.75	0.8
	1	2.55	9.31	14.09	18.86	24.66
	2	2.56	9.49	14.34	18.49	25.02
Γ_1	*3*	2.56	9.55	14.42	18.55	25.07
	4	2.54	7.31	14.61	18.69	25.53
	5	2.54	8.30	16.38	18.96	25.44
	1	8.35	17.57	20.99	21.46	−5.35
	2	8.16	17.80	20.44	17.15	−5.82
L_n	*3*	8.13	16.50	15.02	7.11	−9.50
	4	8.13	16.89	16.81	11.77	1.33
	5	8.13	17.32	19.24	17.36	8.22
	1	9.25	15.94	15.47	3.36	−8.90
	2	9.25	16.06	13.48	1.08	−9.02
X_n	*3*	9.25	16.04	13.01	0.49	−9.33
	4	9.26	16.47	19.55	21.29	14.37
	5	9.26	16.32	19.16	21.10	21.16
$2p$ level, calculation				−23.13, Ref. 26		
$2p$ level, experiment				−21.5, Ref. 28		

Note: Energies given in eV. Γ_1, L_n, and X_n are the lowest points of the conduction band in the models: *1*—without orthogonalization of the atomic functions, *2*—with orthogonalization of the atomic functions to first order in S_σ, *3*—to first order in S_σ and S_π, *4*—all S taken into account to first order, *5*—CEOPW.

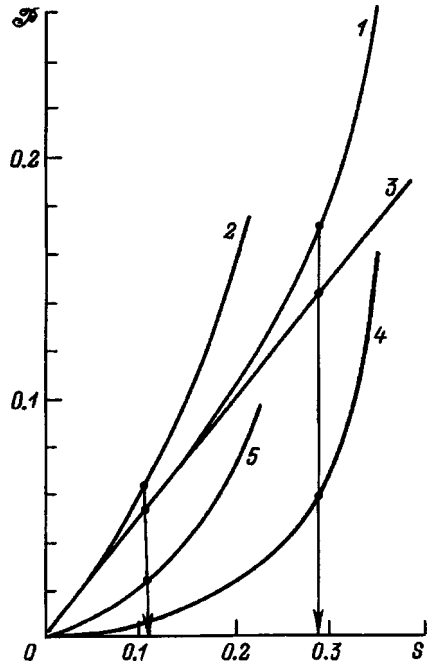

FIG. 5. Largest elements of the nondiagonal (*1*,*2*) and diagonal (*4*,*5*) blocks of the matrix $\mathcal{P}$ in Xe as functions of the corresponding overlap integral S. Curve *3*—dependence on S of the first order of the power-series expansion of S of the elements of the nondiagonal blocks of the matrix $\mathcal{P}$. *1*—$|\mathcal{P}^{(\sigma)}_{05p15p}|$, *2*—$|\mathcal{P}_{05s15s}|$, *4*—$|\mathcal{P}^{(\sigma)}_{15p15p}|$, *5*—$|\mathcal{P}_{15s15s}|$. Arrows indicate the values of S at the metallization point.[1]

TABLE II. Band structure of compressed neon near the fundamental gap in different models.

Band	BZ Point	Model		$\Delta V/V_0$ 0.0	0.6	0.7	0.75	0.8
$E_{\mathbf{k}v}$	Γ_{15}		*a*	−23.00	−22.55	−22.24	−22.01	−21.78
			b	−22.99	−22.52	−22.26	−22.14	−22.22
			c	−20.43	−14.90	−7.70	3.64	
$E_{\mathbf{k}c}$	Γ_1	*2*	*a*	2.56	9.54	14.38	18.51	25.04
			b	2.56	9.54	14.37	18.51	25.04
			c	2.56	9.49	14.34	18.49	
		5	*a*	2.54	8.79	12.86	20.93	25.46
			b	2.54	8.78	11.04	19.21	25.46
			c	2.54	8.30	16.38	18.96	
	L_n	*2*	*a*	8.16	17.81	20.78	18.63	2.58
			b	8.16	17.81	19.78	16.45	0.81
			c	7.63	12.82	−9.71	−88.89	
		5	*a*	8.13	17.38	19.54	18.17	10.43
			b	8.13	17.11	18.44	15.53	4.24
			c	7.60	12.25	−4.44	−58.80	
	X_n	*2*	*a*	9.25	16.01	10.61	−3.37	13.50
			b	9.25	16.10	16.28	8.25	1.35
			c	9.25	15.01	−4.16	−40.18	
		5	*a*	9.26	16.31	19.15	21.08	23.56
			b	9.26	16.33	19.18	21.12	23.63
			c	9.26	16.31	3.83	−44.80	
$E(L_n)-E(\Gamma_{15})$		*2*	*c*	28.06	27.72	−2.01	−92.53	
		5	*c*	28.03	27.15	3.26	−62.64	
$E(X_n)-E(\Gamma_{15})$		*2*	*c*	29.68	29.91	4.16	−43.82	
		5	*c*	29.69	31.21	11.53	−48.44	

Note: Energies are given in eV. The numerals *2* and *5* denote models for calculating the conduction bands $E_{\mathbf{k}c}$ (see Table I), the letters denote models for calculating the valence bands $E_{\mathbf{k}v}$: *a*—LCAO, Ref. 12; *b*—CELO, Ref. 16; *c*—Ref. 18 (hole bands).

the lowest conduction band at the corresponding point in the Brillouin zone, and vice versa. This is most clearly visible in model *c*, where a strong increase in the energy of the $2p$ bands (for the energies of the $1s$ and $2s$ bands unchanged) leads to decrease in the energies of the conduction bands at the *L* and *X* points, significantly lowering the metallization pressure.

The lower part of Table II gives the values of the indirect gaps. The insulator–metal transition appears at the *L* point at a compression of ~0.69 or ~0.71 in models *2* and *5*, respectively. The insignificant lowering of the transition pressure in comparison with the results of Refs. 9–11 is due mainly to a refinement of $E_{\mathbf{k}v}$ in the Phillips–Kleinman potential. Taking all orders in *S* into account is not so important in Ne. Thus, the insulator–metal transition pressure in Ne was predicted in Refs. 9–11 quite accurately. It corresponded to a pressure of 5 ± 2 Mbar (Ref. 9). As follows from Ref. 30, pressures of ~6 Mbar have already been reached, which is quite close to the insulator–metal transition pressure in Ne.

The band structure for different compressions and metallization were taken into account in Ref. 4 for Ar and Kr and in Ref. 3 for Xe (see also Ref. 2). All these studies employed density functional theory in the local density approximation to calculate four tops of valence bands and bottoms of conduction bands. The remaining filled states were taken to be fixed in comparison with the states of the isolated atom and were included in the core. Collapse of the indirect gaps was obtained. However, the local density approximation always underestimates the band gap.[2]

To wrap up, let us dwell briefly on the generalization of the cluster approach. The appearance in the theory of only pairwise overlap integrals $S^{\mathbf{lm}}_{\alpha\beta}$ is a consequence of the single-particle nature of the basis. In systems where two-electron states are important, three-particle clusters and the corresponding overlap integrals $S^{\mathbf{lmn}}_{\alpha\beta\gamma}$ will play an important role.

In conclusion we would like to express our gratitude to I. V. Abarenkov for his constant interest in this work and for valuable discussions.

This work was carried out with the partial support of the International Science Foundation (Grant No. U9B000).

APPENDIX

The self-consistent potential $v_a^{\mathbf{m}}$ of a neutral atom **m** is equal to

$$v_a^{\mathbf{m}}=v_{en}^{\mathbf{m}}+v_C^{\mathbf{m}}+v_{\mathrm{ex}}^{\mathbf{m}},$$

where

$$v_{en}^{\mathbf{m}}=v_{en}(\mathbf{r}-\mathbf{m})=Ze^2/|\mathbf{r}-\mathbf{m}|,$$

$$v_C^{\mathbf{m}}=\mathbf{v}_C(\mathbf{r}-\mathbf{m})=2\sum_{\gamma}\langle\mathbf{m}\gamma|v_C(\mathbf{r}-\mathbf{r}')|\mathbf{m}\gamma\rangle,$$

$$v_{\mathrm{ex}}^{\mathbf{m}}|f\rangle=-\sum_{\gamma}\langle\mathbf{m}\gamma|v_C(\mathbf{r}-\mathbf{r}')|f\rangle|\mathbf{m}\gamma\rangle. \tag{A1}$$

The potentials $V^{(1)}$ and $V^{(2)}$ in expression (13) have a large number of terms, and to write them all down it is advantageous to use the graphical representation. We introduce the elements from which we will construct the effective potential $V_{\alpha\beta}(\mathbf{k};\{C\})$ of system (12)

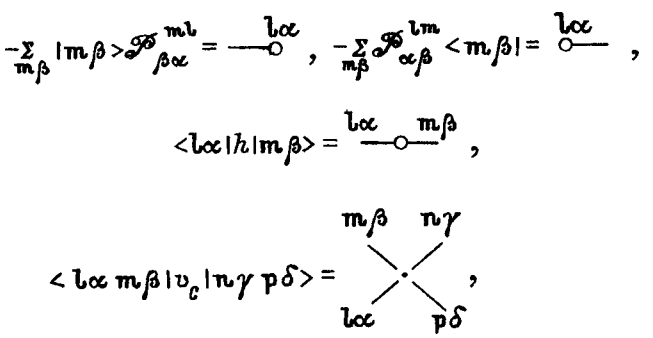

(A2)

where $h=\hbar^2/2m\ \Delta+\sum_{\mathbf{m}}v_{en}^{\mathbf{m}}$.

Let us consider the potential $V^{(1)}$ in Eq. (13). First of all, we note that whereas $V_h^{(1)}$ in Eq. (15) has the simple form

$$V_h^{(1)}[\mathcal{P}]=-\{\mathcal{P}h+h\mathcal{P}\}+\mathcal{P}h\mathcal{P}, \tag{A3}$$

or graphically

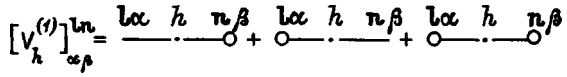

(A4)

($\mathcal{P}$ and h are matrices), the Coulomb potential $V_{ee}^{(1)}$ is a fourth-degree polynomial in the matrix $\mathcal{P}$. We represent it in the form

$$[V_{ee}^{(1)}]_{\alpha\beta}^{\mathbf{ln}}=\sum_{\mathbf{m}\gamma}[2U_{\alpha\gamma\gamma\beta}^{\mathbf{lmmn}}-U_{\alpha\gamma\beta\gamma}^{\mathbf{lmnm}}]. \tag{A5}$$

For U the graphical representation

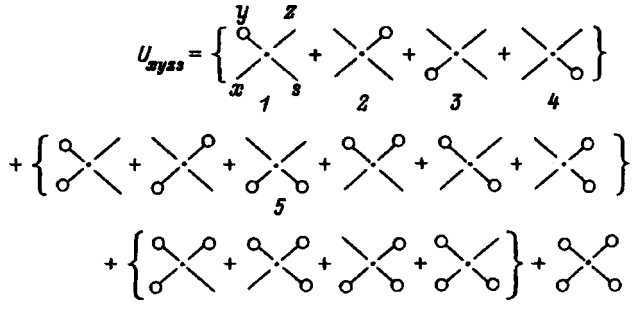

(A6)

is valid, where

$$U_{xyzs}\rightarrow\begin{cases}U_{\alpha\gamma\gamma\beta}^{\mathbf{lmmn}}\text{—in the Coulomb term,}\\ U_{\alpha\gamma\beta\gamma}^{\mathbf{lmnm}}\text{—in the exchange term.}\end{cases} \tag{A7}$$

It is no trouble to write out an analytical expression for $V^{(1)}$.

The potential (A6) corresponds to calculation of the valence bands using the Hartree–Fock method. The CELO approximation[16] obtains if in the potential (A6) we retain only diagrams 3, 4, and 5. Taking only diagrams 1 and 4 into account gives the potential used for the hole bands.[18]

The second term in expression (13) is a correction to the self-consistent procedure and has the form

$$\{V^{(2)}[\mathcal{P};\{C\}]\}_{\mathbf{l}\alpha;\mathbf{n}\beta}=N^{-1}\sum_{\mathbf{q}}\sum_{\mathbf{mj}}\sum_{\gamma\sigma}\exp[-i\mathbf{q}(\mathbf{m}-\mathbf{j})]\times\left[\sum_{v}^{n_l}C_{\delta v}^{*}(\mathbf{q})C_{\gamma v}(\mathbf{q})-\delta_{\delta\gamma}\right]\times[2\tilde{U}_{\alpha\delta\gamma\beta}^{\mathbf{lmjn}}-\tilde{U}_{\alpha\delta\beta\gamma}^{\mathbf{lmnj}}], \tag{A8}$$

where

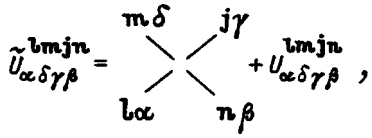

(A9)

the term $U_{\alpha\delta\gamma\beta}^{\mathbf{lmjn}}$ on the right in Eq. (A9) is given by diagrams (A6), and the index v numbers the filled bands.

[1] A. V. Tulub, V. F. Brattsev, and M. V. Pak, Opt. Spektrosk. **74**, 464 (1993) [Opt. Spectrosc. **74**, 279 (1993)].
[2] Y. Li, J. B. Krieger, M. R. Norman, and G. J. Iafrate, Phys. Rev. B **44**, 10437 (1991).
[3] Shindo Koichi and Nishikawa Astushi, J. Phys. Soc. Jpn. **60**, 3579 (1991).
[4] I. Kwon, L. A. Collins, and J. D. Kress, Phys. Rev. B **52**, 15 165 (1995).
[5] C. Helio and S. G. Louie, Phys. Rev. B **46**, 6688 (1992).
[6] R. W. Godby and R. J. Needs, Phys. Rev. Lett. **62**, 1169 (1989).
[7] A. K. McMahan, Phys. Rev. B **33**, 5344 (1986).
[8] Yu. Kh. Vekilov and L. Z. Kimlat, Fiz. Tekh. Vysok. Davl. **9**, 84 (1982).
[9] E. V. Zarochentsev and E. P. Troitskaya, Fiz. Tverd. Tela (Leningrad) **27**, 1212 (1985) [Sov. Phys. Solid State **27**, 1935 (1985)].
[10] E. V. Zarochentsev and E. P. Troitskaya, Fiz. Tverd. Tela (Leningrad) **30**, 2367 (1988) [Sov. Phys. Solid State **30**, 1365 (1988)].
[11] E. V. Zarochentsev, K. B. Tolpygo, and E. P. Troitskaya, Phys. Status Solidi B **127**, 175 (1985).
[12] J. M. Zaĭman, Solid State Phys. **26**, 1 (1971).
[13] P. O. Lövdin, *Theoretical Investigation into Some Properties of Ionic Crystals, Thesis.* Uppsala (1948), 126 pp.
[14] I. V. Abarenkov and I. M. Antonova, Fiz. Tverd. Tela (Leningrad) **20**, 565 (1978) [Sov. Phys. Solid State **20**, 326 (1978)].
[15] I. V. Abarenkov, I. M. Antonova, V. G. Baryakhtar, V. L. Bulatov, and E. V. Zarochentsev, *Computer Methods in Solid State Physics. Electronic Structure of Ideal and Defective Crystals* [in Russian], Naukova Dumka, Kiev (1991), 450 pp.
[16] Yu. V. Eremeĭchenkova, E. V. Zarochentsev, and E. P. Troitskaya, Theor. Math. Phys. **106**(3), 498 (1996).
[17] E. P. Troitskaya, Yu. V. Eremeĭchenkova, and E. V. Zarochentsev, Fiz. Tekh. Vysok. Davl. **4**, *3–4*, 7 (1994).
[18] V. K. Sribnaya and K. B. Tolpygo, Fiz. Nizk. Temp. **6**, 366 (1980) [Sov. J. Low Temp. Phys. **6**, 175 (1980)].
[19] A. P. Jephcoat, H. K. Mao, L. M. Finger, D. F. Cox, R. J. Hemley, and C. S. Zha, Phys. Rev. Lett. **59**, 2670 (1987).
[20] R. Reichlin, K. I. Brister, A. K. McMahan, M. Ross, S. Martin, V. K. Vohra, and A. L. Ruoff, Phys. Rev. Lett. **62**, 669 (1989).

[21] K. A. Goettel, J. H. Eggert, J. F. Silvera, and W. C. Moss, Phys. Rev. Lett. **62**, 665 (1989).
[22] I. V. Abarenkov and I. M. Antonova, Phys. Status Solidi **38**, 783 (1970).
[23] E. P. Troitskaya, E. V. Zarochentsev, and Yu. V. Eremeĭchenkova, Fiz. Tekh. Vysok. Davl. **6**, *3*, 31 (1996).
[24] D. N. Batchelder, D. L. Losee, and R. O. Simmons, Phys. Rev. **162**, 767 (1967).
[25] J. Skalyo, Jr. and Y. Endoh, Phys. Rev. B **9**, 1797 (1974).
[26] E. Clementi and C. Rosetti, At. Data Nucl. Data Tables **14**(3–4), 177 (1974).
[27] E. P. Troitskaya, Author's Abstract of Doctoral Dissertation [in Russian], Kiev (1987), 27 pp.
[28] V. V. Sobolev, *Bands and Excitons of Cryocrystals* [in Russian], Shtiintsa, Kishinev (1986), 204 pp.
[29] E. P. Troitskaya, Yu. V. Eremeĭchenkova, and E. V. Zarochentsev, Fiz. Tekh. Vysok. Davl. **5**, *4*, 5 (1995).
[30] N. E. Christensen, A. L. Ruoff, and C. O. Rodriguez, Phys. Rev. B **52**, 9121 (1995).

Translated by Paul F. Schippnick

Effect of annealing on the dielectric permittivity of strontium titanate films in the $SrTiO_3/Al_2O_3$ structure

A. M. Prudan, E. K. Gol'man, A. B. Kozyrev, A. A. Kozlov, V. E. Loginov, and A. V. Zemtsov

St. Petersburg Electrical-Engineering University, 197376 St. Petersburg, Russia
(Submitted December 4, 1997; resubmitted March 3, 1998)
Fiz. Tverd. Tela (St. Petersburg) **40**, 1473–1478 (August 1998)

The paper reports an experimental study of the structure of a strontium titanate film on a sapphire substrate and of the dielectric properties of capacitors based on a $SrTiO_3/Pt/Al_2O_3$ multilayer system before and after a high-temperature anneal. The macro- and microstructure of $SrTiO_3$ films and its variation induced by the annealing have been investigated. The temperature and field dependences of the dielectric permittivity of strontium titanate films have been determined, and their comparison with similar data for single crystals carried out. The mechanisms by which annealing can affect the capacitor capacitance and the properties of $SrTiO_3$ films are discussed. © *1998 American Institute of Physics.* [S1063-7834(98)01608-6]

The crystal structure of strontium titanate films ($SrTiO_3$, STO) prepared by different techniques on dielectric substrates is, as a rule, preferentially oriented with respect to the substrate surface [(100),(110),(111)]. The temperature dependence of the capacitance of structures based on STO films differs radically from the relation calculated using data for a single crystal. One of possible reasons for this difference may be the small size of film grains and the presence in them of growth-induced and thermal strains.

High-temperature annealing is a widely accepted technological operation to improve the film characteristics.[1–4] Its effect on the structure and stoichiometric composition of STO films deposited by magnetron sputtering on Al_2O_3 substrates was studied in considerable detail.[1,2] The problems of the dielectric permittivity of STO films (ε) and of the anneal-induced changes in the dielectric characteristics of films in the multilayer $SrTiO_3/Al_2O_3$ system remain, however, open. This work discusses technique for determining the dielectric permittivity and analyzes the mechanisms by which high-temperature annealing affects the properties of strontium titanate films.

1. EXPERIMENT

STO films were prepared by rf magnetron sputtering of a stoichiometric target in an $0.7\ O_2 + 0.3$ Ar ambient at a pressure $P \cong 4$ Pa. The substrate plates measuring $12.0 \times 12.0 \times 0.5$ mm were cut from single-crystal sapphire (r cut). Platinum (Pt) electrodes with a gap $s = 2.5 - 4.0$ μm were produced by photolithography on the plate surface. The substrate temperature was maintained constant during the STO deposition ($T = 700$ °C). On reaching an STO film thickness $h = 0.8$ μm, the deposition was completed, and the system was cooled to room temperature at a rate of ~ 10 deg/min. After x-ray diffraction and dielectric measurements, the multilayer system $SrTiO_3/Pt$ (planar capacitor electrodes)/Al_2O_3 was annealed in air at $T = 1050$ °C for two hours. After this, the electrophysical properties were measured again.

X-ray diffraction using a ''Geigerflex'' instrument showed the crystal structure of STO films to have (100) preferred orientation with respect to the Al_2O_3 surface both before and after the anneal. Similar results were obtained in Ref. 2. Recrystallization enhances the (300) higher-order reflection. Essentially, annealing also changes substantially the (100) interplanar spacing from $a = 0.3938$ nm to 0.3900 nm, which brings it closer to the single-crystal lattice constant ($a_0 = 0.3902$ nm). This is accompanied by a decrease of the halfwidth of the (200) diffraction maximum from 1.0 to 0.45°. Estimation of the crystallite dimension along the normal to the film made from the halfwidth of this maximum yields 10 nm before, and 50 nm after the anneal.

Electron microscope images of the surface of an annealed film exhibit a mosaic pattern. No such pattern was observed before the anneal. The visible grain dimension does not exceed 0.3 μm. Note also that the thickness of the STO film decreased after the high-temperature anneal by 30–40%.

X-ray and electron microscope studies suggest that STO films grown on sapphire substrates have a fine-grained microstructure. Annealing makes the crystallites larger while not affecting their preferred orientation relative to the substrate, and reduces the growth-induced deformation of the STO unit cell.

The design of the planar capacitors under study shown in Fig. 1 permits one to study the dielectric properties of the same area of a film before and after a high-temperature anneal. The capacitance was measured at a frequency $f = 1$ MHz by the four-probe technique with an E 7-12 impedance meter. Figure 2 displays the temperature dependences of the total capacitance, $C(0,T)$, under zero bias ($U_i = 0$) before and after a high-temperature anneal. The inset shows fragments of the temperature dependence of the capacitance of the same capacitor for $U_i > 0$, which reveal the presence of

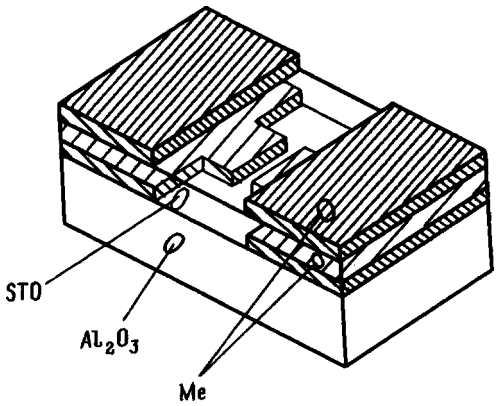

FIG. 1. Schematic design of the planar capacitor under study. Dimensions: $2.0\times1.0\times0.5$ mm, $h=0.8$ μm, $s=(3\pm1)\mu$m, $w=300$ μm.

an extremum and its shift in temperature with increasing voltage. We readily see that annealing increases the derivative $dC(0,T)/dT$ near $T=80$ K and reduces noticeably the capacitance throughout the temperature range covered (78–290 K). The voltage-capacitance characteristics $C(U,T_i)$ (Fig. 3) were obtained at two temperatures ($T_i=78$ and 290 K). Annealing reduces the $C(0,T_i)/C(200\text{ V},T_i)$ ratio at 78 K to a greater extent than that measured at room temperature. We analyze below the mechanism by which annealing may affect the dielectric properties of a film.

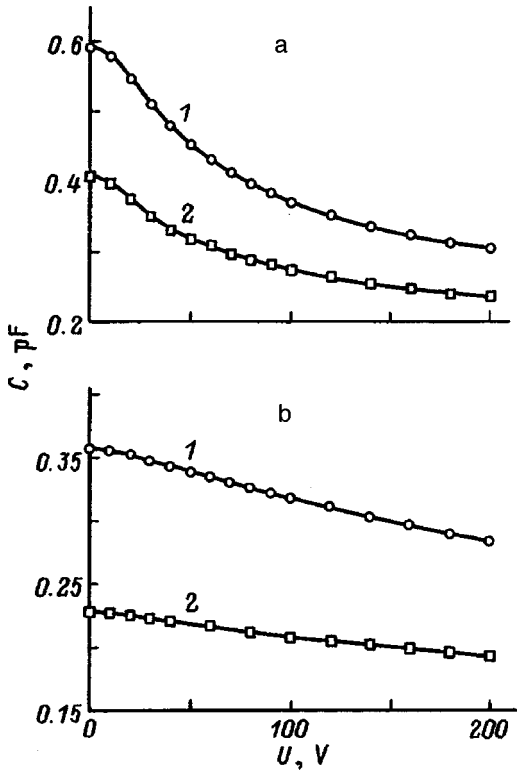

FIG. 3. Voltage-capacitance characteristics of a planar capacitor using (*1*) unannealed and (*2*) annealed $SrTiO_3$ film for two temperatures T(K): (a) 78 and (b) 290.

2. MODEL CONCEPTS

The interelectrode space in a planar capacitor is filled by a many-layered material. The capacitance can in this case be calculated by the method of partial capacitances[5]

$$C=\sum_{i=1}^{N} C_i. \tag{1}$$

Each term C_i in Eq. (1) characterizes the electric-field energy in the bulk of the material with dielectric permittivity ε_i and can be calculated by conformal mapping. Let us simplify Eq. (1) by retaining the terms $C_1\equiv C_P$ and C_2 associated with the volume of the STO film (C_2) and with the other parts of the space (substrate + surrounding air, C_P). Only the term C_2 can be expected to be strongly temperature dependent.

The Curie function, $f(T)=a/(T-T_C^*)$, is usually employed in describing the temperature dependence of the dielectric permittivity of ferroelectrics. Figure 4 presents the results of testing the experimental data on $C_j(T_j)-C_P$ for fitting this relation. In both cases (before and after annealing) there are intervals within which the $C_2(T)$ relations are well described by this function. Annealing changes the parameters of this function. For the characteristic temperature T_C^*

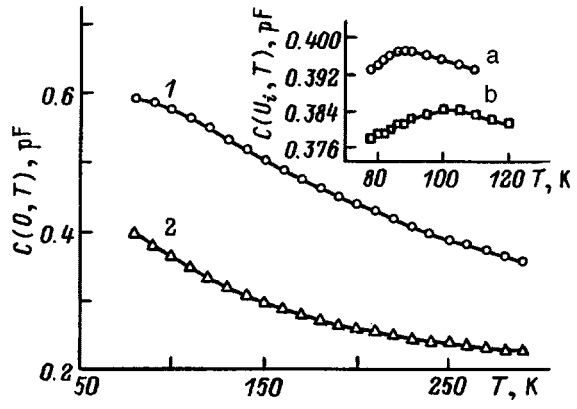

FIG. 2. Temperature dependence of the total planar-capacitor capacitance under zero bias, $C(0,T)$, (*1*) before and (*2*) after annealing of the $SrTiO_3$ film. Inset shows a capacitance *vs* temperature plot for two bias voltages U(V): (a) 80 and (b) 90.

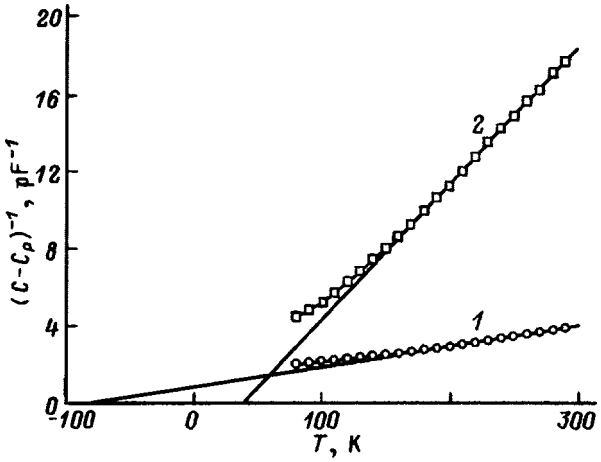

FIG. 4. Temperature dependence of the inverse capacitance of a planar capacitor based on (*1*) unannealed and (*2*) annealed $SrTiO_3$ film with no bias applied.

these changes are anomalous and range from -80 to $+40$ K. The latter is probably connected with a change in the spatial nonuniformity of dielectric permittivity within the volume of the $SrTiO_3$ film due to its recrystallization. Connection of the capacitances in series

$$(C_2)^{-1}=(C_F)^{-1}+(C_N)^{-1} \tag{2}$$

is the simplest model taking this nonuniformity into account. Note that Eq. (2) loses the pictorial simplicity of a capacitor design with ferroelectric (C_F) or nonferroelectric (C_N) filling, and one will have to invoke methods for determining C_F and C_N which do not require the knowledge of geometrical dimensions of the capacitor.

We assume that only the $C_F(T)$ component is temperature dependent, whereas the other two (C_P, C_N) do not depend on temperature. The $C_F(T)$ dependence originates from the ferroelectric properties of the strontium titanate film:

$$C_F(T)=\varepsilon_0\varepsilon(T)F_F, \tag{3}$$

where F_F is the form factor. In the paraphase region, the dielectric permittivity of a ferroelectric obeys the Curie law

$$\varepsilon(T)=C_C/(T-T_C). \tag{4}$$

Component $C_F(T)$ and the capacitance of the series connection of C_N and C_F follow a similar behavior but with different parameters C_C and T_C. The total capacitance of the capacitor can in this case be written

$$C(T)=C_P+\left(\frac{T-T_C}{A}+\frac{1}{C_N}\right)^{-1}, \tag{5}$$

where $A=\varepsilon_0 C_C F_F$ is a parameter of the function.

By analyzing the temperature dependence of the derivative dC/dT one can determine the parameters A and $(T_C/A+1/C_N)$ and, accordingly, the magnitude of component C_P.[6] For the capacitors we studied C_P lies within $0.10-0.18$ pF. Calculation of C_P based on the geometric dimensions of a planar capacitor yields the same values.

To determine component C_N, we shall use one more property of ferroelectrics having a second-order phase transition. Application of an electric field shifts the maximum in the $\varepsilon(E_i,T)$ dependence to higher temperatures. The proposed method is based on a connection between the dielectric permittivities at the maximum with the field on, $\varepsilon(E_i,T_m)$, and without it, $\varepsilon(0,T_m)$, measured at the same temperature. The corresponding expression can be determined by using the relation connecting the electric field E with polarization P:

$$E=\frac{1}{\varepsilon_0\varepsilon(0,T)}P+\beta P^3-\gamma P^5, \tag{6}$$

where ε_0 is the dielectric constant, β and γ are constants determining the dielectric nonlinearity, and $\varepsilon(0,T)$ is the small-signal dielectric permittivity. Differentiating Eq. (6) with respect to polarization yields the following relation for the dielectric permittivity $\varepsilon(E,T)$ of a ferroelectric in a static electric field:

$$\frac{1}{\varepsilon_0\varepsilon(E,T)}=\frac{1}{\varepsilon_0\varepsilon(0,T)}+\frac{\beta}{3}P^2-\frac{\gamma}{5}P^4. \tag{7}$$

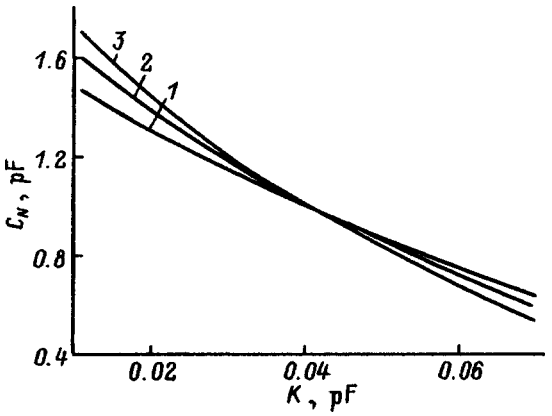

FIG. 5. Calculated dependence of component C_N on generalized constant K for three values of $C(U_i,T_m)$: *1* — 0.467 pF (75 V and 85 K), *2* — 0.459 pF (80 V and 88 K), *3* — 0.451 pF (85 V and 90 K).

For $E=\text{const}(T)$, the temperature derivative of the right-hand side of Eq. (6) is zero. The temperature derivative of the right-hand side of Eq. (7), taken at the temperature $T=T_m$ corresponding to the maximum of the temperature dependence $\varepsilon(E_i,T)$, is likewise zero. Solving jointly the two equations yields the following relation

$$\frac{1}{\varepsilon_0\varepsilon(E_i,T_{mi})}-\frac{2}{\varepsilon_0\varepsilon(0,T_{mi})}=\frac{10\gamma}{36\beta^2}\left(\frac{3}{\varepsilon_0\varepsilon(E_i,T_{mi})}-\frac{4}{\varepsilon_0\varepsilon(0,T_{mi})}\right)^2. \tag{8}$$

If the third terms on the right-hand side of Eqs. (6) and (7) are small corrections, then Eq. (8) gives for the $\varepsilon(0,T_{mi})/\varepsilon(E_i,T_{mi})$ ratio a value of two. Experimental data obtained[7] on single-crystal $SrTiO_3$ support this result.

Equality (8) can be recast in terms of integrated capacitor characteristics

$$\left(\frac{1}{C_2(U_i,T_{mi})}-\frac{2}{C_2(0,T_{mi})}+\frac{1}{C_N}\right)=K\left(\frac{3}{C_2(U_i,T_{mi})}-\frac{4}{C_2(0,T_{mi})}+\frac{1}{C_N}\right)^2, \tag{9}$$

where $C_2(U_i,T_{mi})=C(U_i,T_{mi})-C_P$ is the partial capacitance characterizing the electric-field energy in a ferroelectric film, and

$$K=\frac{10\gamma F_F}{36\beta^2}. \tag{10}$$

Equality (9) contains two unknowns, C_N and K. Figure 5 plots the roots C_N of Eq. (9) for different K. The $C_N(K)$ relations calculated for three experimental values of $C(U_i,T_{mi})$ and $C(0,T_{mi})$ are seen to intersect at a point whose coordinates give the values of C_N and K we have been looking for.

High-temperature annealing of the multilayer structure $SrTiO_3$/Pt (planar capacitor electrodes)/Al_2O_3 increases component C_N from one to 45 pF while affecting constant K to a much lesser extent.

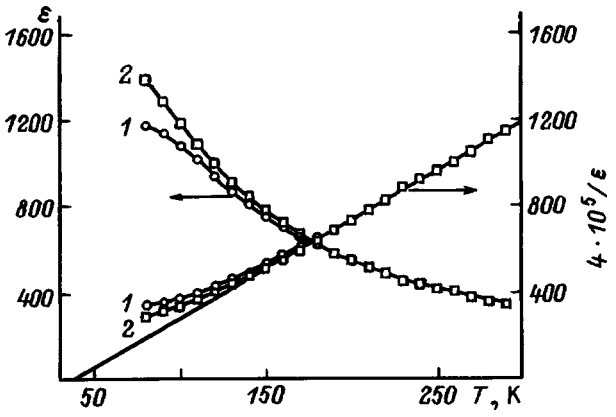

FIG. 6. Temperature behavior of the dielectric permittivity of a strontium titanate film in a multilayer structure (*1*) before and (*2*) after high-temperature anneal. Straight lines are fits on the linear portions of the temperature dependence of inverse dielectric permittivity.

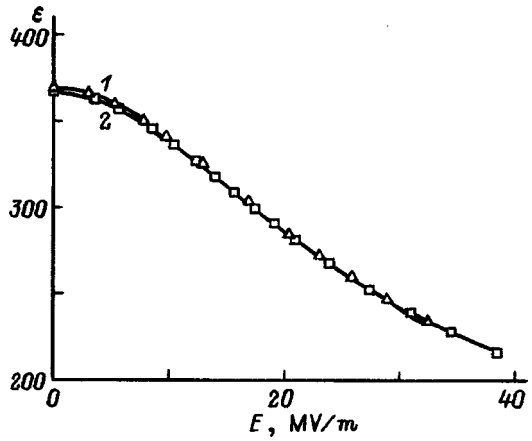

FIG. 7. Dielectric permittivity of a strontium titanate film vs effective electric-field strength at $T=290$ K. (*1*) annealed film, (*2*) unannealed film.

By our model, the total capacitance of a planar capacitor based on a $SrTiO_3/Al_2O_3$ multilayer structure depends nonlinearly on the dielectric permittivity ε of a strontium titanate film

$$\varepsilon=\frac{1}{\varepsilon_0 F_F}\left(\frac{1}{C-C_P}-\frac{1}{C_N}\right)^{-1}. \tag{11}$$

The form factor F_F needed to determine ε can be found from

$$F_F=\frac{1}{\varepsilon_0 C_C}\frac{d}{dT}\left(\frac{1}{C-C_P}\right). \tag{12}$$

The derivative on the right-hand side of Eq. (12) is determined by fitting function (5) to the experimental data on $C(T)$ for temperatures $T\geqslant 180$ K, and the Curie constant C_C is a true constant of strontium titanate,[8] which is not affected by external conditions: $C_C=8.9\times10^4$ K.

Figure 6 shows temperature dependences of the dielectric permittivity of the strontium titanate film before and after the high-temperature anneal. The anneal affects the permittivity only for $T<180$ K and shifts the low-temperature boundary of the region within which the Curie relation is valid (Fig. 6) from $T=180$ to 150 K and brings it closer to the boundary temperature for the single crystal ($T=100$ K). No noticeable effect of annealing on the Curie temperature ($T_C=39\pm3$ K) was found.

The capability of a ferroelectric to change its dielectric permittivity under application of an external electric field is characterized by dielectric nonlinearity constants of the first (β), second (γ), and higher orders [see Eq. (7)]. Two of them (β and γ) enter the generalized constant K defined earlier. Assuming the first-order nonlinearity constants for single-crystal and film strontium titanate to be the same ($\beta=8.9\times10^9$ m$^5/C^2$ F),[9] the numerical value of γ will lie within the interval $(0.8-1.3)\times10^{10}$ m$^9/C^4$ F and coincide with the data quoted in Ref. 10.

It may be expected that components C_P and C_N are only weakly affected by an external field compared to the ferroelectric component C_F. In this approximation, the measured $C(U)$ characteristics and the values of C_P and C_N permit one to find the field dependence of the dielectric permittivity of $SrTiO_3$ film (Fig. 7). The electric field E was calculated using Eqs. (6) and (7). It has the meaning of the effective strength of a field, which is uniform in the ferroelectric and is responsible for the observed changes in the dielectric permittivity. Annealing does not affect the $\varepsilon(E)$ behavior at room temperature (Fig. 7). At low temperatures, in particular, at $T=78$ K, it brings about an increase of the $\varepsilon(0)/\varepsilon(35\ \text{MV/m})$ from 4.7 to 5.8 (Fig. 7).

Figure 8 plots the effective electric field in a strontium titanate film, E, vs the real potential difference of the bias field between the planar-capacitor electrodes. Except for the initial portion of the relation, the field increases linearly with potential difference (Fig. 8), and its derivative $dU/dE=5.5\ \mu$m, as expected, is slightly larger than the electrode gap width $s=(3.0\pm1.0)\ \mu$m. This gives us grounds to believe that the $\varepsilon(E)$ relations displayed in Fig. 7 do not contain serious errors.

3. DISCUSSION OF RESULTS

There is a considerable scatter among literature data on the dielectric permittivity of $SrTiO_3$ films. For instance, for $T=300$ K they extend from $\varepsilon=90$ to 350.[10–13] In many

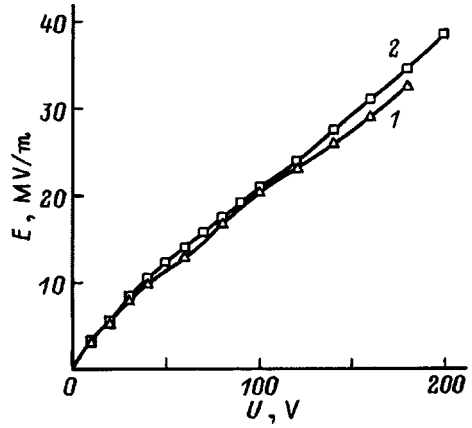

FIG. 8. Effective electric-field strength in a strontium titanate film (*1*) before and (*2*) after anneal vs real potential difference between the capacitor electrodes at $T=290$ K.

cases they have the meaning of effective values, i.e., they were derived from the capacitance of a capacitor and its geometrical dimensions. The film being polycrystalline, its dielectric permittivity is not uniform over the volume. The main reason for the nonuniformity is probably connected with the manifestation of boundary conditions for the polarization vector within a single crystallite.[14]

Film recrystallization during a high-temperature anneal reduces the number of grains in the active planar-capacitor region. Within the model discussed here, grain growth in size gives rise to an increase of component C_N. The anneal-induced thinning of the STO film reduces the form factor F_F entering the expression for the capacitance C_F. Equation (3) shows that this results in a decrease of the absolute value of C_F.

In the high-temperature region ($T>180$ K), single-crystal and film strontium titanate are indistinguishable in the dielectric permittivity and its temperature dependence. Differences are observed to occur at low temperatures. Annealing brings noticeably closer the dielectric properties of single-crystal and film $SrTiO_3$ for $T<180$ K, which reveals one more mechanism of its effect, namely, a decrease of mechanical strains u.

Mechanical action affects considerably the dielectric permittivity of a ferroelectric.[8] Taking strain into account in the Ginzburg-Devonshire expansion yields, in the first approximation, the electrostriction correction to the small-signal dielectric permittivity $\varepsilon(0,T,0)$:

$$\varepsilon^{-1}(0,T,u)=\varepsilon^{-1}(0,T,0)+\varepsilon_0 G u, \tag{13}$$

where G are the electrostriction tensor components. For $SrTiO_3$, the first term on the right-hand side of Eq. (13) falls off monotonically with decreasing temperature. In this case $\varepsilon(0,T,u)$ and $\varepsilon(0,T,0)$ may be indistinguishable in the high-temperature region, to become different again upon deep cooling. The annealing of the $SrTiO_3/Al_2O_3$ multilayer structure and its subsequent slow cooling to room temperature results in a reduction of growth-induced strains in the film. The latter, according to Eq. (13), increases the dielectric permittivity only in the low-temperature region (Fig. 6). This is responsible also for the apparent increase of the dielectric nonlinearity of a strontium titanate film at $T=78$ K observed to occur (Fig. 7) after annealing.

Investigators showed that the fine-grained structure of $SrTiO_3$ films prepared by magnetron sputtering invalidates the assumption that the capacitance of a planar capacitor is linearly related to the dielectric permittivity of a strontium titanate film. The proposed method for treating experimental data permits one to determine the temperature and field dependences of dielectric permittivity of a $SrTiO_3$ film. They coincide in a number of respects with similar relations obtained for a single crystal. High-temperature annealing of a multilayer structure increases the grain size in the film and reduces mechanical strain in the lattice. Accordingly, the dielectric permittivity of $SrTiO_3$ films increases in the low-temperature domain.

The authors thank O. G. Vendik for fruitful discussions and valuable criticisms.

[1] Yu. Ya. Tomashpol'skiĭ, M. A. Sevost'yanov, G. E. Ratnikov, and A. F. Fedotov, Kristallografiya **20**, 194 (1975) [Sov. Phys. Crystallogr. **20**, 116 (1975)].
[2] B. M. Gol'tsman, N. V. Zaĭtseva, Yu. L. Kretser, V. V. Lemanov, and T. A. Shaplygina, Fiz. Tverd. Tela (St. Petersburg) **37**, 3723 (1995) [Phys. Solid State **37**, 2052 (1995)].
[3] V. M. Mukhortov, Ya. S. Nikitin, M. G. Radchenko, V. A. Aleshin, Yu. I. Golovko, and V. P. Dudkevich, Zh. Tekh. Fiz. **56**, 1372 (1986) [Sov. Phys. Tech. Phys. **56**, 805 (1986)].
[4] R. Kalyanaraman, R. D. Vispute, S. Oktyabrsky, K. Dovidenko, K. Jagannadham, J. Narayan, J. D. Budai, N. Parikh, and A. Suvkhanov, Appl. Phys. Lett. **71**, 1709 (1997).
[5] E. Chen and S. Y. Chou, IEEE Trans. Microwave Theory Tech. **45**, 939 (1997).
[6] A. M. Prudan, E. K. Gol'man, A. B. Kozyrev, R. N. Kyutt, and V. E. Loginov, Fiz. Tverd. Tela (St. Petersburg) **39**, 1024 (1997) [Phys. Solid State **39**, 920 (1997)].
[7] K. Bethe, Philips Res. Rep. **2**, 1 (1970).
[8] E. Hegenbarth and C. Frenzel, Cryogenics **7**, 331 (1967).
[9] G. V. Belokopytov, Fiz. Tverd. Tela (St. Petersburg) **37**, 1953 (1995) [Phys. Solid State **37**, 1063 (1995)].
[10] S. Komatsu and A. Kazuhide, Jpn. J. Appl. Phys. **34**, 3597 (1995).
[11] Yu. A. Boĭkov, I. P. Pronin, Z. G. Ivanov, and T. Claeson, Fiz. Tverd. Tela (St. Petersburg) **38**, 1100 (1996) [Phys. Solid State **38**, 609 (1996)].
[12] T. Hirano, M. Taga, and T. Kobayashi, Jpn. J. Appl. Phys. **32**, L1760 (1993).
[13] F. A. Miranda, C. H. Mueller, and G. A. Koepf, Supercond. Sci. Technol. **8**, 755 (1995).
[14] O. G. Vendik, S. P. Zubko, and L. T. Ter-Martirosyan, Fiz. Tverd. Tela (St. Petersburg) **38**, 3654 (1996) [Phys. Solid State **38**, 1991 (1996)].

Translated by G. Skrebtsov

DEFECTS. DISLOCATIONS. PHYSICS OF STRENGTH

Heating of slip lines and bands as a quasi-athermic mechanism of plastic deformation of crystals at low temperatures

G. A. Malygin and O. V. Klyavin

A. F. Ioffe Physicotechnical Institute, Russian Academy of Sciences, 194021 St. Petersburg, Russia
(Submitted January 30, 1998)
Fiz. Tverd. Tela (St. Petersburg) **40**, 1479–1485 (August 1998)

We discuss theoretically a mechanism of violation of the Arrhenius law for the rate of plastic deformation, on the one hand, and of the appearance of plateau-like segments in the temperature dependence of the thermal-activation parameters, on the other, during deformation of crystals at low (<10 K) temperatures, which is associated with heating of the crystal by slip lines and bands. Via a self-consistent solution of the heat-conduction equation with allowance for variation of its coefficients and the rate of plastic deformation with temperature it is found that both a stable and an unstable regime (in the thermal sense) of propagation of slip lines and expansion of slip bands are possible depending on the ratio between the heating level and the level of strain hardening of the strain localization sites. The first regime is associated with the appearance of quasi-athermic plateaus in the temperature dependences of the thermally-activation parameters, and the second one leads to an instability (stepped) in the plastic deformation that is characteristic at low temperatures. © *1998 American Institute of Physics.* [S1063-7834(98)01708-0]

The mechanism for the appearance of anomalous plateaus in the temperature dependence of the fluidity limits and their rate coefficients[1–4] and the violation of the Arrhenius law for the plastic deformation rate[1,2] during deformation of crystals at low temperatures (<20 K) have been the subject of recent discussion.[5–10] As was noted in Refs. 7–10, the widely discussed idea of quantum athermicity as the reason for the appearance of plateau-like segments in these curves finds itself in contradiction to the absence of similar segments in the temperature curves of the shear stresses for strains below the fluidity limit[10] and with the existence in the temperature interval where these plateaus are located of a stepped, discontinuous deformation.[1,4,7] Since the latter is due to a thermal instability of the plastic deformation of the crystals at low temperatures,[9–13] both these facts are evidence of the absence of a noticeable influence of athermic quantum fluctuations (zero oscillations[2,3] and dislocation tunneling[1,4]) on the surmounting by the dislocations of barriers having short radius of action, and preservation in the investigated temperature interval (>0.5 K) of the thermal-activation nature of the motion of the dislocations. This state of affairs is also indicated by the fact that when the temperature is raised abruptly the creep rate of the crystals investigated in Ref. 14 at $1.3-4.2$ K experiences discontinuous growth. In light of this contradiction, a quasi-athermic mechanism was considered in Ref. 9 for the appearance of plateaus and violation of the Arrhenius law for the plastic deformation rate, where this mechanism is associated with heating of strain localization sites (slip lines and bands) by the energy dissipated upon the motion of the dislocations. Local thermal excitation of the crystal above the temperature of the cooling medium causes the thermal component of the flow stresses to drop, as a result of which a quasi-athermic segment arises in the temperature dependence of these stresses. Direct evidence of heating of the strain localization sites is provided by the formation of helium bubbles at the exit sites of the slip lines and bands at the surface of crystals deformed at $2.2-4.2$ K (Refs. 10 and 15).

The estimates made in Refs. 9 and 16 show that sufficiently dense groups of dislocations (with a linear density of 10^6 m^{-1}) moving with high speed (10^2-10^3 m$\cdot$s^{-1}) can cause local lattice heating of appreciable intensity. Evidence of the existence of such dislocation groups during low-temperature deformation of metallic crystals is provided, for example, by data[17] on the formation of electric pulses of microsecond duration as a result of entrainment of electrons by the dislocations. The appearance of such groups of dislocations at low temperatures is promoted by the high sensitivity of the dislocation speed V to fluctuations of the effective stresses τ^* at these temperatures ($\partial \ln V/\partial \ln \tau^*)\approx 10^3-10^4$. For comparison, at moderate temperatures it is on the order of 1–10.

This circumstance can explain, in particular, the microstepped, discrete character of the creep curves of polycrystalline copper at $1.4-4.2$ K (Ref. 18). Small-to-moderate fluctuations of the local stresses, leading to the formation of dynamic slip lines as a result of activation of one or more Frank–Read sources, cause an abrupt growth of the deformation. The finite magnitude of each such deformation jump and the logarithmic character on the whole of the creep curve[18] indicate that as a consequence of strain hardening the speed of dislocations in such dynamic slip lines and bands

falls after the deformation jump to values characteristic of thermally activated motion of the dislocations. Since the formation of dynamic slip lines and bands at low temperatures is accompanied by their heating, a plateau-like, quasi-athermic segment appears in the temperature dependence of the logarithmic creep coefficient: one more characteristic anomaly of low-temperature crystal plasticity.[19]

Thus, the question of the thermal regime in which plastic deformation of crystals at low and superlow temperatures develops locally is of fundamental significance for this temperature interval.

The goal of the present paper is to analyze in detail heating of crystals by dynamic slip lines and bands with allowance for the fact that during their formation, strain hardening lowers the dislocation speed while heating of the crystal by the dislocations increases it. The relationship between these two factors (heating and hardening) determines whether plastic deformation of the crystals at the level of individual slip lines and bands develops stably or unstably, in the thermal sense. In the case when strain hardening predominates, quasi-athermic segments appear in the temperature dependences of the thermal-activation parameters and Arrhenius's law for the plastic deformation rate is seen to be violated. On the other hand, when heating predominates, the deformation diagrams acquire stepped discontinuities under certain conditions.

Taking the above-said into account, Sec. 1 describes a model of dynamic slip lines (bands). Section 2 carries out a self-consistent calculation of the local temperature distribution and the dislocation speed distribution in this model. Section 3 discusses the obtained results and compares them with experiment.

1. MODEL OF DYNAMIC SLIP LINES

As experiment shows, plastic deformation of a crystal begins with activation of dislocation sources in the bulk or on the surface of the deformed crystal. As they move along the slip plane, the dislocations multiply by double transverse slipping,[10] as a result of which the slip line is converted into an expanding slip band. Another consequence of multiplication of dislocations is strain hardening, as a result of which the dislocation speed in the band drops to values characteristic of thermally activated plastic deformation. Only dislocations in the tip (''nose'') of an unfinished slip line and one the edge of an expanding slip band continue to propagate with high, dynamic speeds.

At present there is no generally accepted theoretical model for the evolution of the dislocation density distribution in a forming slip band, starting from the formation stage of a planar accumulation of dislocations upon activation of a dislocation source of Frank–Read type. In the present work we describe this evolution by the expression

$$\rho(r,z,t)=\rho_n\left[1-\exp\frac{r-ut+l}{l}\right]\left[1-\exp\frac{z-u_zt+w}{w}\right], \tag{1a}$$

$$\rho=0, \quad n=n_0, \quad ut>r>ut-l, \quad u_zt>z>u_zt-w. \tag{1b}$$

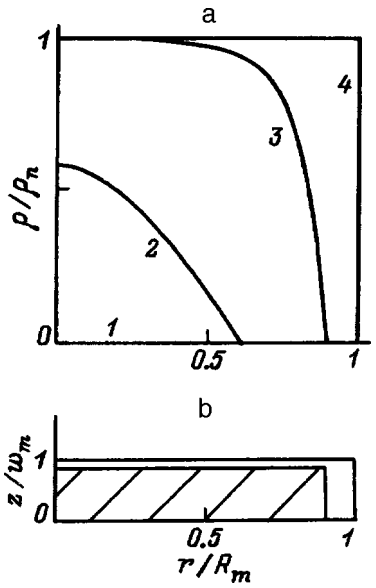

FIG. 1. Density distribution of dislocations (a) along a slip band (b) for different ratios of the length of its dynamic part l to its overall length $l/R_m=1.0$ (*1*), 0.4 (*2*), 0.1 (*3*), and 0 (*4*). The hatched region is the deformation-hardened part of the band for $l/R_m=0.1$.

Here ρ is the dislocation density in the strain hardened, quasistatic part of the slip line (band), n is the linear density of dislocations at the tip (nose) and on the edge of the slip band, equal to n_0; l and w are respectively the length of the nose and the width of the active edge of the band, both of which depend on microscopic parameters of the processes of dislocation multiplication and diffusion,[20] u and u_z are the lengthening and expanding speeds of the bands, t is time reckoned from commencement of activation of a circular dislocation source at the point $r=0$, $z=0$ in cylindrical coordinates, and ρ_n is the maximum dislocation density in the strain-hardened part of the slip band. Expression (1) was obtained with the help of a self-similar solution of the equations[20] describing the evolution of the dislocation density at the initial stage of deformation, when dislocation annihilation is still absent. The expression inside the first set of brackets in Eq. (1a) describes the evolution of the dislocation density associated with lengthening of the band, and the second describes the evolution associated with its expansion.

Figure 1a depicts the dislocation distributions as described by Eq. (1a) in the initial slip plane of the dislocations (the $z=0$ plane) for different ratios of the total length of the slip line $L=2R_m=2ut$ to the length of its nose l. Since the speed of unilateral expansion of the slip band $u_z=(w/l)u$, its total width $w_m=(w/l)R_m$ and, consequently, $w_m/w=R_m/l$. This means that the dislocation density distribution over width (thickness) of the slip bands (along the z axis) has a form analogous to the curves in Fig. 1a. Figure 1b shows the shape of the band (half of it is shown) in the case when the ratio of the length of the nose to the total length of the slip line, equal to the ratio of the width of its dynamic part to its total width, is equal to 0.1 ($l/R_m=w/w_m=0.1$).

Since the dislocation speeds within the limits of the slip band vary over a wide range, the expression for the disloca-

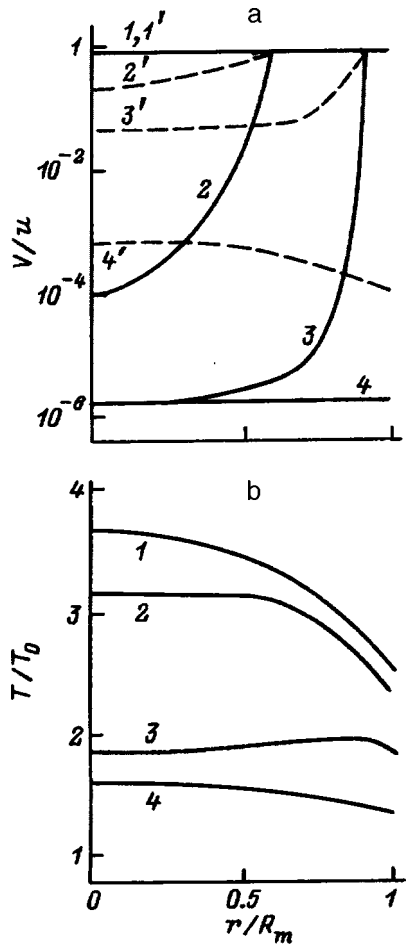

FIG. 2. Distribution of the dislocation speed (a) and temperature (b) along a slip band in the absence of heating (*1–4*) and for heating (*1′–4′*) of the crystal by dislocations for different ratios of the lengths of its dynamic and deformation-hardened parts [see Fig. 1a].

tion speed V should contain both a thermal-activation and an above-barrier (u) component

$$V=u\left(1+\frac{u}{u_s}\exp\frac{H(\tau^*)}{kT}\right)^{-1}. \tag{2}$$

Here $H(\tau^*)$ is the activation energy, $\tau^*=\tau-\tau_\mu$ where τ^* and τ are respectively the effective stress and the applied stress, $\tau_\mu=\alpha b\mu\rho^{1/2}$, α is the interdislocation interaction constant, b is the Burgers vector, μ is the shear modulus, T is temperature, k is Boltzmann's constant, and u_s is the preexponential factor in the expression for the thermally activated dislocation speed.

Curves *1–4* in Fig. 2a illustrate the distribution of dislocation speeds along a slip band in the $z=0$ plane for $H(\tau^*)=H_c[1-(\tau^*/\tau_c)^q]^p$ and different ratios between its static and dynamic parts (Fig. 1a). The calculation was done for the following parameter values: $\tau/\tau_c=0.975$, $\alpha b\mu\rho_n^{1/2}/\tau_c=0.2$, $\tau_m^*/\tau_c=(\tau-\alpha b\mu\rho_n^{1/2})/\tau_c=0.775$, $\alpha b=0.15$ nm, $H(\tau_m^*)/kT=\ln(u_s/V)=25$, $u/u_s=0.1$, and $\rho_n=10^{12}$ m^{-2}, which corresponds to formation of a slip line (band) for motion of dislocations in the Peierls relief in a metallic crystal ($\tau_c/\mu=10^{-3}$, $p=1$, $q=5/4$) at low deformation temperatures.[21] Here τ_c is the Peierls stress at $T=0$.

It is clear from the calculated curves in Fig. 2a that with growth of the dislocation density ρ and expansion of the region of deformation hardening $(R_m-1)/R_m$ the dislocation speed in the slip plane varies from purely dynamic (curve *1*) to primarily thermally activated (curve *3*) to completely thermally activated (curve *4*). The last variant corresponds to escape of the slip plane to the boundary (surface) of the crystal. Only dislocations in a layer of thickness w at the edge $z=w_m$ of the slip band continue to propagate with dynamic speeds u.

2. HEATING OF THE CRYSTAL BY A SLIP BAND

The local thermal regime in which formation of a slip band takes place is defined by the equation of heat conduction

$$c\frac{\partial T}{\partial t}=\nabla(\varkappa\nabla T)-f\frac{h}{d}(T-T_0)+\beta\tau\dot{\varepsilon}. \tag{3}$$

Here t is time, c is the heat capacity, $\varkappa$ and h are the coefficients of bulk thermal conductivity and surface heat transfer, d is the characteristic transverse dimension of the crystal, f and β are coefficients of the order of unity which depend, respectively, on the shape of the cross section of the crystal and the degree of conversion of the work of plastic deformation into heat, $\dot{\varepsilon}=b\rho_m V$ is the plastic deformation rate, ρ_m is the density of mobile dislocations, and T_0 is the temperature of the cooling medium.

Since formation of dynamic slip lines occurs during times of the order of a few microseconds,[14,17] and the relaxation time of heat escaping from the crystal to the cooling medium $t_h=cd/fh$, as estimates and experiment show,[17] is of the order of several milliseconds, local heating of the crystal by such a band will depend only on the relaxation rate of heat in the bulk of the crystal. In this case, solution of Eq. (3) in cylindrical coordinates for a forming slip band, as described in Sec. 1, has the form[22] ($\Delta T=T-T_0$)

$$\Delta T(r,z,t)=\frac{\beta\tau\dot{\varepsilon}_m}{8c}\int_0^t\frac{dt'}{[\pi a(t-t')]^{3/2}}\int_0^{ut'}2\pi\eta\,d\eta \times\int_0^{u_z t'}U(\eta,\xi,t')G(r,z,t|\eta,\xi,t')\,d\xi,$$

$$G(r,z,t|\eta,\xi,t')=I_0\left[\frac{r\eta}{2a(t-t')}\right]\exp\left[-\frac{r^2+\eta^2+(z-\xi)^2}{4a(t-t')}\right], \tag{4}$$

where $U=V/u$ is the dimensionless dislocation speed, $\dot{\varepsilon}_m=b\rho_m u$ is the maximum plastic deformation rate in the band, $\rho_m\approx n_0/w$ is the mean density of mobile dislocations in the band, ut' and $u_z t'$ are intermediate values of the length and width of the band, $I_0(x)$ is the zeroth-order Bessel function with imaginary argument, and $a=\varkappa/c$ is the thermal diffusion coefficient.

The solution (4) of Eq. (3) assumes that the level of local heating of the crystal $\Delta T/T_0$ is sufficiently small and has no noticeable influence on the dislocation speed (2) or the heat capacity of the crystal and its thermal conductivity or the

coefficient of surface heat transfer. In most crystals at low temperatures these quantities vary according to a power law: $c=c_mT^n$, $\varkappa=\varkappa_mT^m$, $h=h_mT^r$. Here c_m, $\varkappa_m$, and h_m are coefficients that depend respectively on the mechanisms of heat storage and heat conduction, and on the state of the cooling medium. In reality, the level of heating of the crystal ΔT can substantially exceed the medium temperature T_0. For this reason, Eq. (3) is in general nonlinear. If the exponents n and m in the power laws for c and $\varkappa$ are equal, then it is possible by making the substitution $T=T_0\psi^{\frac{1}{n+1}}$ to reduce Eq. (3) to the form

$$c(T_0)\frac{\partial\psi}{\partial t}=\varkappa(T_0)\nabla^2\psi-(n+1)\frac{2h(T_0)}{fd}\psi^{\frac{r+1}{n+1}}(1-\psi^{-\frac{1}{n+1}})+(n+1)T_0^{-1}\beta\tau\dot{\varepsilon}(\psi) \tag{5}$$

with constant values of c and $\varkappa$. Solving Eq. (5) in the absence of surface heat transfer ($h=0$), we obtain

$$T=T_0[1+(n+1)T_0^{-1}\Delta T(r,z,t,T)]^{\frac{1}{n+1}}. \tag{6a}$$

It is obvious that for $\Delta T/T_0\ll 1$ solution (6a) goes over to solution (4). For $n=1$ it describes heating of a slip band in metallic crystals with the electronic contribution to the heat capacity predominant while for $n=3$ it describes heating in crystals where the phonon mechanism of heat storage and heat conduction predominates.

Since the dislocation speed $U(r,z,t,T)$ in expressions (5) and (6a) vary substantially as a result of heating, we solved Eq. (6a) self-consistently by the method of iterations. Results of solution of Eq. (6a) are plotted in Fig. 2b for $n=1$ and the above-indicated (Fig. 1) values of the ratio $m_l=l/R_m$ of the length of the dynamic part of the slip band to its total length. The value of the relative heating found in this way can be written as a function of the parameters[22] to

$$\Delta T(r,z,t,T_0)/T_0=\frac{2\beta\tau\dot{\varepsilon}_m w}{\pi^{1/2}uc(T_0)T_0}\times\Omega\left(\frac{r}{R_m},\frac{z}{w_m},m_r,m_z,m_l\right). \tag{6b}$$

The parameters $m_r=R_m/2R_0$, $R_0=2a/u$ (Ref. 22), and $m_z=m_r(w/l)^2$ determine the degree of heat localization and the nature of the dependence of the level of heating on the length $2R_m$ and width (thickness) w_m of the slip band and on the ratio between the length of the band and its dynamic part l. As can be seen from Fig. 2b, as the length of the dynamic (deformation-unhardened) part of the band grows, its heating temperature also grows. The results plotted in Fig. 2b were obtained for the following parameter values: $m_r=0.2$, $R_0=2.5$ mm, $w/l=10^{-2}$, $m_z=2\times10^{-5}$, $a=0.25\ \mathrm{m^2\cdot s^{-1}}$, $u=2\times10^2\ \mathrm{m\cdot s^{-1}}$. They correspond to actual parameters of slip lines and bands at the initial stage of deformation of metallic crystals ($2R_m=2$ mm, $w_m=10\ \mu$m, $w=1\ \mu$m, $\rho_n=\rho_m=10^{12}\ \mathrm{m^{-2}}$) at low temperatures ($\tau\approx20$ MPa, $\beta=0.6$, $c=\gamma_eT_0\approx2\times10^2\ \mathrm{J\cdot m^{-3}\cdot K^{-1}}$, $T_0\approx2$ K), where γ_e is the coefficient of the electronic specific heat.

3. DISCUSSION

It follows from the calculated results [Fig. 2b] that heating of a slip band can be significant both for the case when it is of a purely dynamic character (curve *1*, $T/T_0=3.7$) and in the strain-hardened state (curve *4*, $T/T_0=1.6$). The distribution of dislocation speeds in such heated slip bands is illustrated by curves $1'-4'$ in Fig. 2a. In comparison with the case of no heating (curves *1–4*) the dislocation speeds in heated bands are several orders higher. For weak or moderate deformation hardening (curves *2* and *3*) the quasistatic regions of the bands acquire a dynamic or almost dynamic character (curves $2'$ and $3'$).

This means that thermally activated motion of dislocations in such slip bands is unstable in the thermal sense. Because of intense heating of regions of the crystal neighboring the band, this motion can initiate the generation of new dynamic slip lines and bands. Such a correlated, avalanche-like growth of plastic deformation in a bounded volume of the crystal can lead to a jump in the deforming stress if the growth time of the thermal flare-up is longer than the relaxation time of heat escaping from the crystal due to surface heat transfer and longer than the relaxation time of the deforming stress, which depends on the rigidity and dynamic characteristics of the loading apparatus. These two circumstances, as is well known, define the criterion of thermal instability of low-temperature plastic deformation.[8,13] In Ref. 17 it was established that from 10 to 20 individual slip lines participate in each such avalanche-like growth of deformation.

If the conditions for avalanche-like development of plastic deformation are absent, then on the macroscopic level, deformation develops stably. On the microscopic level, as a consequence of the discreteness and cooperative nature of deformation and the associated heating of individual slip lines and bands typical of the dislocation mechanism, deformation takes place at some effective temperature T^* greater than the temperature of the cooling medium T_0. Taking expressions (6a) and (6b) into account, we can write down the following expression for the effective temperature:

$$T^*=T_0[1+(\Theta/T_0)^{n+1}]^{\frac{1}{n+1}} \tag{7a}$$

or

$$T^*=\Theta[1+(T_0/\Theta)^{n+1}]^{\frac{1}{n+1}}, \tag{7b}$$

where

$$\Theta=\left[(n+1)\frac{2\beta\tau\dot{\varepsilon}_m}{\pi^{1/2}uc_m}\Omega\left(\frac{r}{R_m},\frac{z}{w_m},m_r,m_z,m_l\right)\right]^{\frac{1}{n+1}}. \tag{7c}$$

As calculation shows [Fig. 2b], heating of slip lines and bands has a fairly uniform character over both the length and width (thickness) of the band; therefore it may be assumed that the temperature Θ has a constant value in the volume occupied by the band.

It follows from Eq. (7b) that as $T_0\to0$ the heating temperature of the band $T^*\to\Theta$. The characteristic temperature Θ of appearance of quasi-athermic effects depends on the

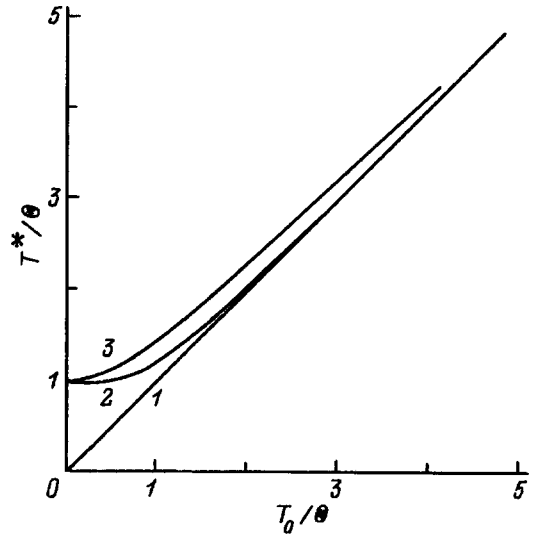

FIG. 3. Effective temperature T^* as a function of temperature of the cooling medium T_0 in the absence of heating (*1*) and for heating of the crystal by dislocations by the phonon (*2*) and electron (*3*) mechanisms respectively of heat storage and heat conduction.

length $L=2R_m$ and width w_m of the slip band, and in the case of strain hardening, on the length of the dynamic part of the band, l. Since $\Omega\sim l$ in expression (7c) for $l/2R_0<1$ and $\Omega\sim l^{1/2}$ for $l/2R_0>1$, at the very initial stage of deformation (in the optical elasticity limit[10]), when the length of the slip lines amounts to a few tens of microns, the level of heating is too small to have a noticeable effect on the dislocation speed. This may explain the absence of a plateau-like segment in the temperature dependence of the optical fluidity limit in LiF crystals.[10] But when the length of the lines becomes comparable with the transverse dimensions of the crystal, then heating, as was shown above, has a substantial influence on the dislocation speed and, consequently, on the thermal component of the flow stresses, which results in the appearance of plateau-like segments in the temperature dependence of the fluidity limit of the crystal.[10] Note that by virtue of the nonlinear nature of the equation of heat conduction the temperature Θ of the appearance of quasi-athermic effects (7c) depends not too strongly on the whole on the length and width of the slip bands: $\Theta\sim(lw_m)^{\frac{1}{n+1}}$. Estimates based on formula (7c) show that for values of the thermal, dynamic, and deformational parameters typical for low temperatures, $\Theta=1-10$ K. For high-strength alloys it can be substantially greater.

For purely electronic ($n=1$) and purely phonon-mediated ($n=3$) mechanisms of heat storage and heat conduction, according to formula (7b) we have the following functional forms of the dependence of the effective temperature T^* on the temperature of the cooling medium T_0:

$$T^*=\Theta[1+(T_0/\Theta)^2]^{1/2}, \tag{8a}$$

$$T^*=\Theta[1+(T_0/\Theta)^4]^{1/4}. \tag{8b}$$

The form of these dependences is illustrated by curves *2* and *3* in Fig. 3. As a consequence of its greater nonlinearity, the effective temperature of heating, T^*, in crystals with a predominantly phonon mechanism of heat storage and heat conduction (e.g., in alkali-halide crystals) varies more abruptly with the temperature T_0 of the cooling medium than is the case for metals. To illustrate the quasi-athermic effects for a predominantly phonon mechanism of heat storage, Fig. 4 plots the temperature dependence of the critical shear stresses τ^* and the corresponding rate sensitivity coefficient $\partial\tau^*/\partial\ln\dot{\varepsilon}$ in the absence of heating (curves *1* and *2*) and in the presence of heating (curves *1′* and *2′*) of the slip lines and bands. The calculation was based on the following relations:

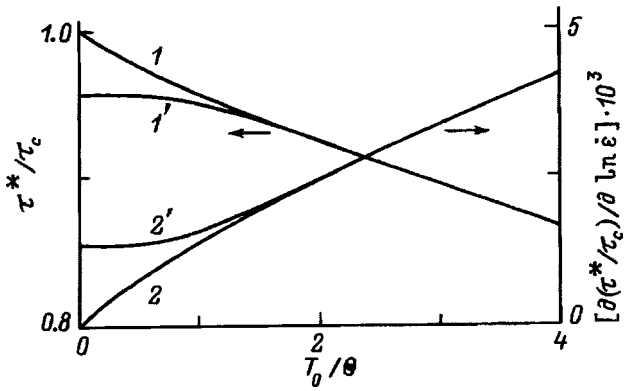

FIG. 4. Temperature dependence of the critical shear stresses (*1,1′*) and their rate coefficients (*2,2′*) in the absence of heating (*1,2*) and for heating (*1′,2′*) of the crystal by slip lines for predominance of the phonon mechanism of heat storage.

$$\tau^*=\tau_c[1-(T/T_c)^{1/q}]^{1/p}, \quad T_c=\frac{H_c}{k\ln(\nu/\dot{\varepsilon})}, \tag{9a}$$

$$\frac{\partial(\tau^*/\tau_c)}{\partial\ln\dot{\varepsilon}}\approx\frac{1}{pq\ln(\nu/\dot{\varepsilon})}\left(\frac{T}{T_c}\right)^{1/q}, \tag{9b}$$

which follow from the expression for the rate of thermally activated plastic deformation (2), where ν is the pre-exponential factor in the Arrhenius formula for this rate. Curves *1* and *2* illustrate the nature of these curves for $p=1$, $q=5/4$ (the Peierls relief), $\ln(\nu/\dot{\varepsilon})=25$ and $T=T_0$, while curves *1′* and *2′* illustrate the nature of these curves for $\Theta/T_c=2\times10^{-2}$ and $T=T^*$ (8b).

The appearance of quasi-athermic segments in the temperature curves of the critical shear stresses and their rate coefficients strongly depresses the values of the ratio $H/kT_0\ln(\nu/\dot{\varepsilon})$ at temperatures $T_0<\Theta$ for the experimentally determined activation energy of the plastic deformations, i.e., it leads to a violation of the Arrhenius law for the plastic deformation rate, according to which the value of the indicated ratio should be strictly equal to unity. This state of affairs serves as a basis for concluding that the deviation from this law and the apparent athermicity of deformation at temperatures below Θ are due to the coming into play of athermic quantum mechanisms by which dislocations overcome local barriers.[2–4]

According to Ref. 2, if the effective temperature T^* depends on T_0, then the ratio

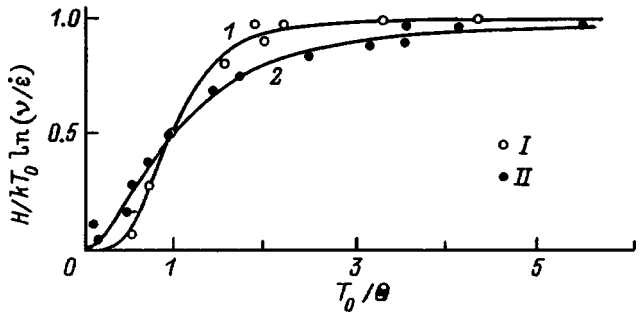

FIG. 5. Violation of the Arrhenius law for the plastic deformation rate in KBr (Ref. 1) (I) and α Fe (Ref. 2) (II). The theoretical curves were calculated according to Eq. (11) for $n=3$ (*1*) and 1 (*2*).

$$\frac{H}{kT_0 \ln(\nu/\dot{\varepsilon})} = \left(\frac{T_0}{T^*}\right)\frac{\partial T^*}{\partial T_0} \tag{10}$$

depends only on the nature of the dependence of the effective temperature T^* on the temperature of the cooling medium, T_0. Thus, in the case of local heating (7) we have

$$\frac{H}{kT_0 \ln(\nu/\dot{\varepsilon})} = \frac{(T_0/\Theta)^{n+1}}{1+(T_0/\Theta)^{n+1}}. \tag{11}$$

Curves *1* and *2* in Fig. 5 illustrate the functional dependence (11) for predominance of the phonon term ($n=3$) and electronic term ($n=1$) in the specific heat. Experimental data indicating the violation of the Arrhenius law for the rate of thermally activated plastic deformation in crystals of KBr (Ref. 1) and α iron[2] plotted in this figure are found to be in quite good agreement with the theoretical curves. They confirm a more abrupt deviation from the Arrhenius law $H/kT_0 \ln(\nu/\dot{\varepsilon})=1$ in the alkali-halide crystal KBr ($n=3$, $\Theta=2.7$ K) in comparison with α Fe ($n=1$, $\Theta=6.6$ K).

Thus, our results demonstrate that local heating of the crystal by moving dislocations, because of its substantial magnitude at low deformation temperatures, complicates the thermal-activation analysis of the mechanisms of plastic deformation of crystals at temperatures <20 K. Therefore, revealing the influence of quantum effects on the surmounting by dislocations of barriers having short radius of action against the background of this heating becomes essentially impossible. The athermic plateaus in the temperature dependence of the thermal-activation parameters observed at temperatures $T<20$ K, as was shown above (see also Refs. 9 and 23), are linked with thermal effects, as is the instability (jumplike discontinuity) of the plastic deformation that is characteristic at low temperatures and grows as the deformation temperature is decreased.[24,25]

In this regard, it bears mention that in comparison to long-range internal stresses from accumulations of same-sign dislocations as a possible cause of avalanche-like growth of plastic deformation and jumps in the deforming stress at low temperatures,[26] local heating possesses a greater time lag and longer range of action, which facilitates spatial correlation and temporal synchronization[17] of the dislocation avalanches. Due to the small time lag of the internal stresses, the work of the dislocation sources initiated by them terminates rapidly as a result of strain hardening (Fig. 2a) while dislocation heating of the crystal makes it possible, as was shown above, to overcome this hardening and thus hastens the development of the thermal instability of low-temperature plastic deformation of crystals.

Weakening and disappearance of the influence of thermal effects on the thermal-activation characteristics measured at low temperatures can be achieved by thinning the crystal-foils to cross sections with transverse dimension of the order of $10-20$ μm. In this case, as estimates show, the relaxation time of heat escaping into ^{3}He and ^{4}He $t_h=cd/2h\approx10^{-5}$ s becomes comparable to the heating time of the crystal by a dynamic slip line of length $L\approx1-2$ mm, $t=L^2/4a$, as it propagates across a wide face of the crystal.

[1] T. Suzuki and H. Koizumi, in *Dislocations in Solids. Proceedings of the IXth Yamada Conference*, edited by H. Suzuki. (Univ. Press, Tokyo, 1985), p. 159.
[2] E. Kuramoto, Y. Aono, K. Kitajima, K. Maeda, and S. Takeuchi, Philos. Mag. A **A39**, *6*, 717 (1979).
[3] V. V. Pustovalov, Fiz. Nizk. Temp. **15**, 901 (1989) [Sov. J. Low Temp. Phys. **15**, 497 (1989)].
[4] V. D. Natsik, G. I. Kirichenko, V. V. Pustovalov, V. P. Soldatov, and S.É. Shumilin, Fiz. Nizk. Temp. **22**, 965 (1996) [Low Temp. Phys. **22**, 740 (1996)].
[5] V. V. Abraimov and V. P. Soldatov, Fiz. Nizk. Temp. **7**, 1058 (1981) [Sov. J. Low Temp. Phys. **7**, 453 (1981)].
[6] Yu. Ossipyan and V. S. Bobrov, Cryst. Res. Technol. **19**, *6*, 825 (1984).
[7] O. V. Klyavin, G. A. Malygin, and Yu. M. Chernov, Fiz. Tverd. Tela (St. Petersburg) **38**, 191 (1996) [Phys. Solid State **38**, 105 (1996)].
[8] G. A. Malygin, Fiz. Tverd. Tela (St. Petersburg) **39**, 1392 (1997) [Phys. Solid State **39**, 1235 (1997)].
[9] G. A. Malygin, Fiz. Tverd. Tela (St. Petersburg) **39**, 2019 (1997) [Phys. Solid State **39**, 1806 (1997)].
[10] O. V. Klyavin, *Physics of Plasticity of Crystals at Helium Temperatures* [in Russian], Nauka, Moscow, 1987.
[11] S. N. Komnik and V. V. Demirskii, Cryst. Res. Technol. **19**, *6*, 863 (1984).
[12] L. P. Kubin and Yu. Estrin, Cryst. Res. Technol. **19**, *6*, 853 (1984).
[13] G. A. Malygin, Fiz. Met. Metalloved. **81**, *3*, 5 (1996).
[14] A. C. Arco and J. Weertman, Acta Metall. **17**, *5*, 687 (1969).
[15] O. V. Klyavin and A. V. Nikiforov, Izv. Akad. Nauk SSSR, Ser. Fiz. **37**, *11*, 2411 (1973).
[16] G. A. Malygin, Fiz. Tverd. Tela (Leningrad) **19**, 3152 (1977) [Sov. Phys. Solid State **19**, 1845 (1977)].
[17] V. S. Bobrov and M. A. Lebedkin, Fiz. Tverd. Tela (St. Petersburg) **35**, 1881 (1993) [Phys. Solid State **35**, 939 (1993)].
[18] V. A. Koval', V. P. Soldatov, and V. I. Startsev, in *Physical Processes of Plastic Deformation at Low Temperatures* [in Russian], Naukova Dumka, Kiev (1974), p. 339.
[19] V. I. Startsev, V. P. Soldatov, V. D. Natsik, and V. V. Abraimov, Phys. Status Solidi A **59**, *1*, 377 (1980).
[20] G. A. Malygin, Fiz. Tverd. Tela (St. Petersburg) **37**, 3 (1995) [Phys. Solid State **37**, 1 (1995)].
[21] T. Mori and M. Kato, Philos. Mag. A **43**, *6*, 1315 (1981).
[22] G. A. Malygin, Fiz. Nizk. Temp. **5**, 1338 (1979) [Sov. J. Low Temp. Phys. **5**, 633 (1979)].
[23] G. A. Malygin, Fiz. Tverd. Tela (St. Petersburg) **40**, 684 (1998) [Phys. Solid State **40**, 629 (1998)].
[24] N. N. Kuz'menko and V. V. Pustovalov, Fiz. Nizk. Temp. **5**, *12*, 1433 (1979) [Sov. J. Low Temp. Phys. **5**, 676 (1979)].
[25] G. I. Kirichenko, V. D. Natsik, V. V. Pustovalov, V. P. Soldatov, and S. É. Shumilin, Fiz. Nizk. Temp. **23**, *9*, 1010 (1997) [Low Temp. Phys. **23**, 758 (1997)].
[26] A. Zeeger, in *Dislocations and Mechanical Properties of Crystals* (Wiley, New York, 1957), p. 63.

Translated by Paul F. Schippnick

MAGNETISM AND FERROELECTRICITY

Vortex states in antiferromagnetic crystals

A. Bogdanov and A. Shestakov

Donetsk Physicotechnical Institute, National Academy of Sciences of Ukraine, 340114 Donetsk, Ukraine
(Submitted November 3, 1997)
Fiz. Tverd. Tela (St. Petersburg) **40**, 1486–1493 (August 1998)

It is shown that axially symmetric two-dimensional nonuniform states can exist in easy-axis and cubic antiferromagnets lacking inversion symmetry, in the form of two-dimensional spatially modulated structures (magnetic vortex lattices) and isolated two-dimensional structures (vortices). The structure and equilibrium dimensions of the lattices and vortices have been determined by numerical solution of differential equations. © *1998 American Institute of Physics.* [S1063-7834(98)01808-5]

It is known that in acentric magnets there can exist specific, symmetry-induced exchange-relativistic interactions, which enter the energy of the system in the form of terms linear in the first spatial derivatives.

These invariants were used[1] to account for the thermodynamic stability of spiral structures in magnets lacking an inversion center. In contrast to the wide-spread exchange spirals,[2,3] the modulated structures considered in Ref. 1 had a large period and a fixed direction of M rotation (chirality).

Such modulated structures have by now been discovered in a number of cubic helical magnets[4–13] and other noncentrosymmetric crystals,[14–18] in magnetic superlattices,[19,20] and a number of other systems[2,3]. Theoretical studies of spiral structures associated with the Dzyaloshinsky interaction were carried out.[21–28]

It has been shown, using a simple model representation, that inversionless magnets can support, besides one-dimensional modulated structures (spirals), a system of isolated vortices as well.[29] The size of these vortices is proportional to the Dzyaloshinsky interaction energy, i.e., such vortices should collapse in a regular magnet. It was also shown that, in the region where modulated structures exist, vortex states are thermodynamically stable within a certain field interval. The vortex and spiral structures in easy-axis ferro- and antiferromagnets were studied.[29,30]

A systematic theoretical study of isolated and interacting vortices in easy-axis ferromagnets lacking inversion symmetry was carried out.[31,32] The equilibrium parameters of isolated vortices and vortex lattices, and the boundaries of existence of localized states and modulated phases were determined by numerical solution of differential equations, as well as by analytical techniques. The force of interaction between two isolated vortex lines was calculated.[33] Studies were also made of vortex states in cubic helimagnets,[34] and of the effect of basal-plane anisotropy on vortex-state stability[35].

This work explores specific features of vortex states in easy-axis and cubic antiferromagnets lacking inversion symmetry.

1. EASY-AXIS ANTIFERROMAGNETS

For a two-sublattice antiferromagnet with Dzyaloshinsky interaction, the nonequilibrium thermodynamic potential can be written to terms quadratic in components of the total magnetization vector $\mathbf{m}=(\mathbf{M}_1+\mathbf{M}_2)/2M_0$ and of the antiferromagnetism vector $\mathbf{l}=(\mathbf{M}_1-\mathbf{M}_2)/2M_0$ (here $\mathbf{M}_i$ is the magnetization of the ith sublattice, $M_0=|\mathbf{M}_i|$) in the form

$$W=\int w dV=\int [A(\partial l/\partial x_i)^2+A'(\partial l/\partial x_i)^2+w_0-w_d]dV, \tag{1}$$

where A,A' are nonuniform-exchange constants, w_0 is the uniform part of energy, and w_d contains invariants linear in the first spatial derivatives.

We write the uniform part of energy, w_0, for the antiferromagnets under study in the following standard form[36,37]

$$w_0=M_0^2[2\lambda\mathbf{m}^2-2\mathbf{Hm}/M_0-\beta l_z^2], \tag{2}$$

where λ is the intersublattice exchange-interaction constant, β is the second-order uniaxial-anisotropy constant, and $\mathbf{H}$ is the magnetic field. Usually $\lambda\gg\beta$. We shall also limit ourselves to the case of low temperatures, where one may assume $m^2+l^2=1$, $ml=0$.[37]

For $\beta>0$, Z is the easy-magnetization axis. It is well known (see, e.g., Ref. 37), that in this case for $H_z=H_{sf}=M_0\sqrt{2\lambda\beta}$ and $H_x=H_y=0$ a first-order phase transition takes place from the antiferromagnetic ($\mathbf{l}\|\mathbf{Z}$) to spin-flop ($\mathbf{l}\perp\mathbf{Z}$) phase. Limiting ourselves to the ($\mathbf{H}\|\mathbf{Z}$) case and minimizing Eq. (1) in m, we obtain

$$m=h\frac{H_{sf}}{2\lambda M_0}, \tag{3}$$

where $h=H/H_{sf}$. In the vicinity of the spin-flop transition $m\ll l$, because $H_{sf}=M_0\sqrt{2\lambda\beta}\ll 2\lambda M_0$. Assuming now $|l|=1$, we come to the following expression for w_0:[29]

$$w_0=w_0^0+M_0^2\beta|1-\beta^2|\sin^2(\theta-\theta_0), \tag{4}$$

where

$$w_0^0=\beta M_0^2,\quad \theta_0=0,\quad h<1,$$

$$w_0^0=\beta M_0^2 h^2,\quad \theta_0=\pi/2,\quad h>1.$$

Here θ is the angle between **l** and **OZ**, $h^2=H^2/2\beta\lambda M_0^2$, and w_0^0 is the ground-state energy density.

The expressions for w_d for easy-axis antiferromagnets were derived in Ref. 29 (in the $m\ll l$ approximation). In particular, for antiferromagnets belonging to the crystallographic classes C_{nv} and D_n the expressions for w_d have the form

$$w_d=DM_0^2\left(l_z\frac{\partial l_x}{x}-l_x\frac{\partial l_z}{x}+l_z\frac{\partial l_y}{y}-l_y\frac{\partial l_z}{y}\right)\quad \text{for}\quad C_{nv}, \tag{5}$$

$$w_d=DM_0^2\left(l_z\frac{\partial l_x}{y}-l_x\frac{\partial l_z}{y}+l_z\frac{\partial l_y}{x}-l_y\frac{\partial l_z}{x}\right)$$

$$+D'M_0^2\left(l_x\frac{\partial l_y}{z}-l_y\frac{\partial l_x}{z}\right)\quad \text{for}\quad D_n. \tag{6}$$

The last term in Eq. (6) may result in formation of modulated structures propagating along the easy axis **Z**. Because we consider here only states uniform along **Z**, we shall assume D' to be identically zero. The case of C_n symmetry, where w_0^0 is a linear combination of Eqs. (5) and (6), does not yield qualitatively new results and therefore will be disregarded subsequently.

The presence of such invariants in the thermodynamic potential was shown to entail invariably formation of nonuniform states in the vicinity of the spin-flop transition.[29] The stability boundaries of such states can be determined by considering the energy of a plane domain wall separating states with opposite directions of **l** (the 180° domain wall). Calculations revealed[29] that nonuniform spatially modulated states in antiferromagnets are thermodynamically stable for

$$h_1<h<h_2,\quad \text{where}\quad h_{1,2}^2=1\mp\nu^2,\quad \nu^2=\frac{\pi D^2}{16A\beta}. \tag{7}$$

Note that, because coefficient D in Eqs. (2) and (3) is of the exchange-relativistic origin ($D\sim\sqrt{A\beta}$),[38] the lower critical field h_1 may vanish for some crystals, i.e. for such crystals spatially modulated structures will become energetically preferable starting with $H=0$. At the same time the upper critical field will always be lower than the exchange fields ($h_2\ll 2\lambda M_0/H_{sf}$). This relates, for instance, to the inversionless rhombohedral easy-axis antiferromagnet $BiFeO_2$ [space group C_{3v}^6, Néel temperature $T_N=673$ K (Ref. 39)]. In zero and weak fields it exhibits a modulated structure. In a fairly high field, a magnetic-field-induced transition from a helical, spatially modulated to a uniform antiferromagnetic phase was observed to occur, which was accompanied by a strong variation of electrical polarization.[40]

Let us turn now to an analysis of two-dimensional spatially modulated states. Consider an isolated vortex with the axis directed along **Z**; at vortex center the antiferromagnetism vector **l** is parallel to the applied magnetic field **H**. Introduce spherical coordinates for vector **l**, and cylindrical ones, for the spatial variables

$$\mathbf{l}=(\sin\theta\cos\psi,\ \sin\theta\sin\psi,\ \cos\theta),$$

$$\mathbf{r}=(r\cos\varphi,\ r\sin\varphi,\ z).$$

Written in these variables, Eqs. (2) and (3) will assume the following form for C_{nv} symmetry

$$w_d=\cos(\varphi-\psi)\left[\frac{\partial\theta}{\partial r}+\frac{1}{r}\sin\theta\cos\theta\frac{\partial\psi}{\partial\varphi}\right]$$

$$+\sin(\varphi-\psi)\left[\sin\theta\cos\theta\frac{\partial\psi}{\partial r}-\frac{1}{r}\frac{\partial\theta}{\partial\varphi}\right], \tag{8}$$

and for D_n symmetry:

$$w_d=\sin(\varphi-\psi)\left[\frac{\partial\theta}{\partial r}+\frac{1}{r}\sin\theta\cos\theta\frac{\partial\psi}{\partial\varphi}\right]$$

$$+\cos(\varphi-\psi)\left[\sin\theta\cos\theta\frac{\partial\psi}{\partial r}-\frac{1}{r}\frac{\partial\theta}{\partial\varphi}\right]. \tag{9}$$

Thus the energy of a two-sublattice antiferromagnet with Dzyaloshinsky interaction can be presented as

$$E=\frac{W-W_0^0}{2\pi LAM_0^2}$$

$$=\int\left[\left(\frac{d\theta}{d\rho}\right)^2+\frac{\sin^2\theta}{\rho^2}-2\pi\left(\frac{d\theta}{d\rho}+\frac{\sin\theta\cos\theta}{\rho}\right)\right.$$

$$\left.+4\pi^2\frac{A\beta}{D^2}|1-h^2|\sin^2(\theta-\theta_0)\right]\rho d\rho, \tag{10}$$

$$\rho=r/r_0,\quad r_0=\frac{2\pi A}{D}. \tag{11}$$

Here L is vortex length along the **Z** axis, and r_0 is the period of the spiral structure for $h=1$.

Euler's equation for functional (1) reads

$$\frac{d^2\theta}{d\rho^2}+\frac{1}{\rho}\frac{d\theta}{d\rho}-\frac{\sin 2\theta}{2\rho^2}+2\pi\frac{\sin^2\theta}{\rho}$$

$$-\cos 2\theta_0 2\pi^2\frac{A\beta}{D^2}|1-h^2|\sin 2\theta=0. \tag{12}$$

The solutions to Eq. (10) subject to the boundary conditions

$$\theta(0)=0,\quad \theta(R)=\pi \tag{13}$$

describe an axial structure (vortex) of radius R. Equation (10) does not lend itself to analytic solution, and therefore numerical methods were invoked. The character of the solutions depends essentially on the applied magnetic field, namely, on whether h lies within or outside the $[h_1,h_2]$ interval.

For $h_1<h<h_2$, the boundary problem under study has solutions only for finite radii R, and for $h<h_1$ or $h>h_2$, both for finite R and for $R=\infty$. Note that in the second case ($h\notin[h_1,h_2]$) none of the finite-radius solutions corresponds to the minimum in energy density (see below), in other words, such solutions are unstable.

We shall conveniently use in place of h in what follows the parameter

$$B^* = -\cos 2\theta_0 \frac{4}{\pi}\sqrt{\frac{A\beta}{D^2}|1-h^2|}. \quad (14)$$

For $h=h_{1,2}$, $B^*=\mp 1$, for $h<h_1$, $B^*<-1$, and for $h>h_2$, $B^*>1$.

Consider the solutions for each of these cases in more detail.

1) $h_1<h<h_2(-1<B^*<1)$. Since everywhere within this region the domain-wall energy is negative,[29] the structures formed in these conditions will have the maximum possible distribution of inhomogeneity in the bulk of the sample. The spiral[1] may serve as an example of such a state. Another example is the magnetic-vortex lattice, whose thermodynamic stability was proven for inversionless magnets within a certain magnetic-field range.[32]

As already mentioned, the stabilization of two-dimensional modulated structures is connected with the presence in the magnet energy of invariants linear in the first spatial derivatives. These terms lower the energy of the system only for a certain direction of change of the order parameters. In particular, in the case of a uniaxial antiferromagnet with Dzyaloshinsky interaction the sign of parameter D [see Eq. (2)] determines the energetically favorable direction of rotation of vector **l**. Therefore from the various axial-structure lattices present in antiferromagnets only those in which the given direction of antiferromagnetism vector rotation is preserved are capable of reducing the energy of the system. This condition is obviously upheld in lattices where vector **l** is parallel to **OZ** at cell center, and antiparallel to it at the cell boundary. We shall call such structures π lattices.

The equilibrium states of two-dimensional lattices in antiferromagnets are determined by solving coupled differential equations for $\theta(x,y)$ and $\Psi(x,y)$ which minimize functional (1). This problem is difficult to solve even by numerical techniques. The problem can, however, be considerably simplified by invoking the circular-cell approximation[32,41]. Within this approximation, a unit cell of the lattice with hexagonal (or square) cross section is replaced by a circular cylinder of the same volume. Accordingly, the boundary conditions for π lattices are replaced by those for circular ones, i.e., by Eq. (11).

Application of this approximation to the calculation of the equilibrium lattice structure restores the axial symmetry and reduces the problem to integration of Eq. (10) subject to boundary conditions (11), with subsequent minimization of

$$F = \frac{E}{\pi R_2} \quad (15)$$

in R [the energy E is given by Eq. (10)].

Calculations showed that throughout the region $h_1<h<h_2$ $(-1<B^*<1)$ the energy density (15) has a minimum at finite cell dimensions R. Figure 1 displays the equilibrium cell dimensions and the period of the helical structure as functions of parameter B^* [Eq. (14)]. Within a broad range $-1<B^*<1$, equilibrium lattice periods depend only weakly on the field, but start to increase without limit as B^* approaches ± 1 (i.e., as $h\to h_{1,2}$). Figures 2–5 plot the evolution of equilibrium cell structures with increasing magnetic field in π lattices. In the vicinity of the lower critical field h_1 $(B^*\approx -1)$, the nonuniformities in the distribution of **l** in π lattices become localized within a narrow transition region. This can be easily understood if one recalls that, in a magnetic field $h<1$ $(B^*<0)$, states with $\theta=\pi/2$ possess a higher energy than those with $\theta=0, \pi$. In π lattices, the

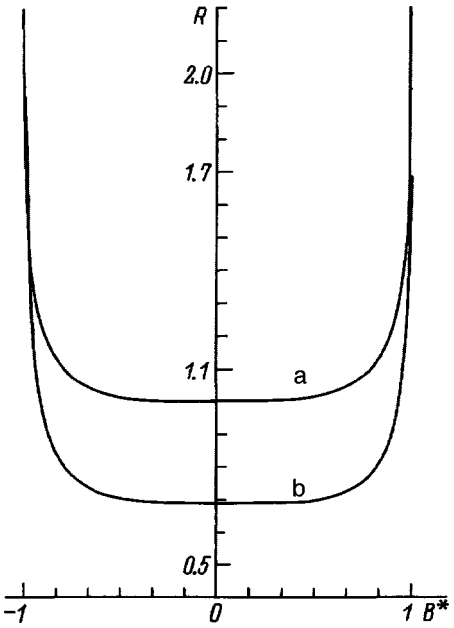

FIG. 1. Periods of (a) spiral structure and (b) vortex lattice *vs* parameter B^*.

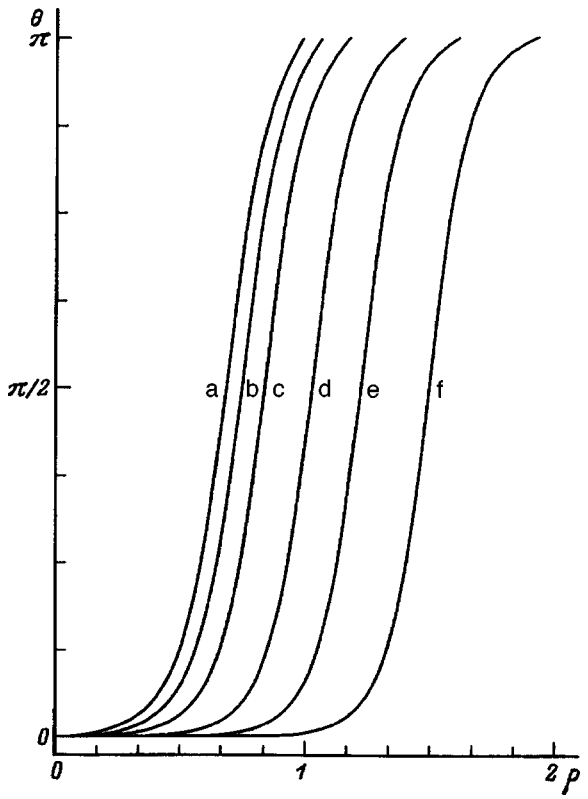

FIG. 2. Equilibrium structures of unit cells of the magnetic-vortex lattice for B*: (a) −0.91, (b) −0.93, (c) −0.95, (d) −0.97, (e) −0.98, and (f) −0.99.

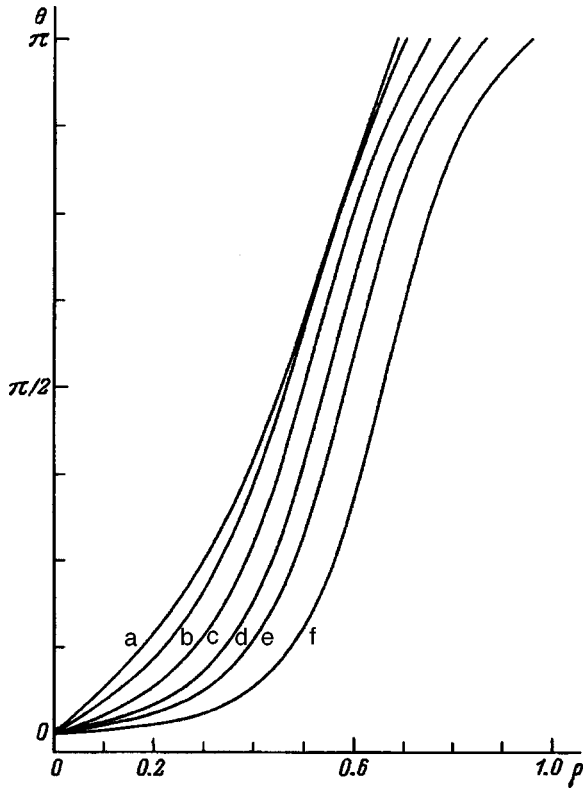

FIG. 3. Equilibrium structures of unit cells of the magnetic-vortex lattice for B*: (a) 0, (b) −0.5, (c) −0.7, (d) −0.8, (e) −0.85, and (f) −0.9.

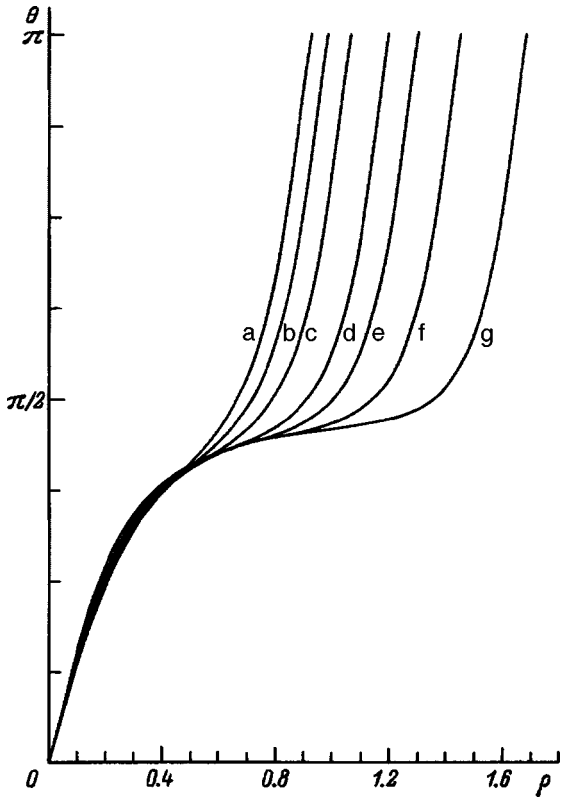

FIG. 5. Equilibrium structures of unit cells of the magnetic-vortex lattice for B*: (a) 0.91, (b) 0.93, (c) 0.95, (d) 0.97, (e) 0.98, (f) 0.99, and (g) 0.999.

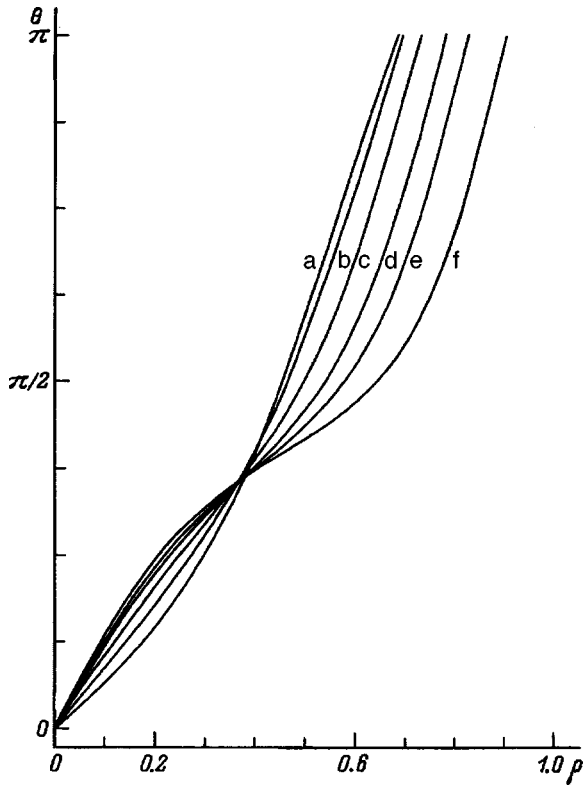

FIG. 4. Equilibrium structures of unit cells of the magnetic-vortex lattice for B*: (a) 0, (b) 0.5, (c) 0.7, (d) 0.8, (e) 0.85, and (f) 0.9.

$\theta=\pi/2$ states are realized inside the cells. It is in the region of states close to $\pi/2$ that nonuniformities are localized in the lattices.

In the opposite limiting case, i.e., close to the upper critical field h_2 ($B^*\approx 1$), nonuniformities in the distribution of **l** in π lattices are localized both at cell boundaries (where $\theta\approx\pi$) and at cell center (where $\theta\approx 0$). This is due to the fact that for $h>1$ ($B^*>0$) states with $\theta=\pi/2$ possess a lower energy than those with $\theta=0$, π.

Throughout the region where modulated structures exist the energy density of π lattices is higher than that of the helical state (Fig. 6). Hence the one-dimensional spatially modulated state is here thermodynamically stable. In the presence of linear defects, however, magnetic vortex lattices can form. There is a report of observation of a magnetic vortex lattice in $BiFeO_3$.[42]

Similar to a helical structure, a magnetic-vortex lattice transfers to a uniform state through unlimited growth of the period of the system with $h\to h_{1,2}$ ($B^*\to\pm 1$). Obviously enough, the energies of all modulated structures become equal at $h=h_{1,2}$.

2) $h<h_1(B^*<-1)$. The form of the solution depends in this case substantially on

$$a=\left.\frac{d\theta}{d\rho}\right|_{\rho=0}. \tag{16}$$

Figure 7 shows phase patterns for several values of parameter a. If a is greater than some critical value $a(h)$, the solutions $\theta(\rho)$ describe structures with finite radii and a non-

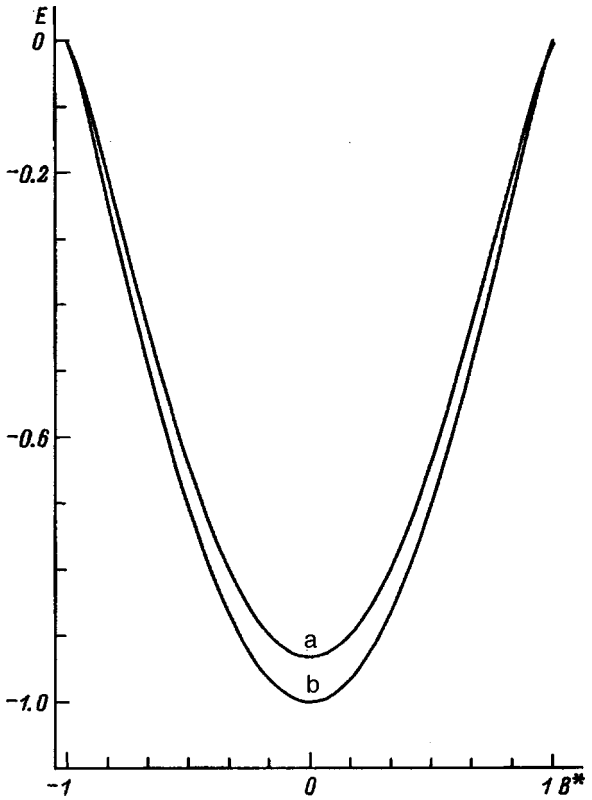

FIG. 6. Dependence of the energy density of (a) magnetic-vortex lattice and (b) spiral structure on parameter B^*.

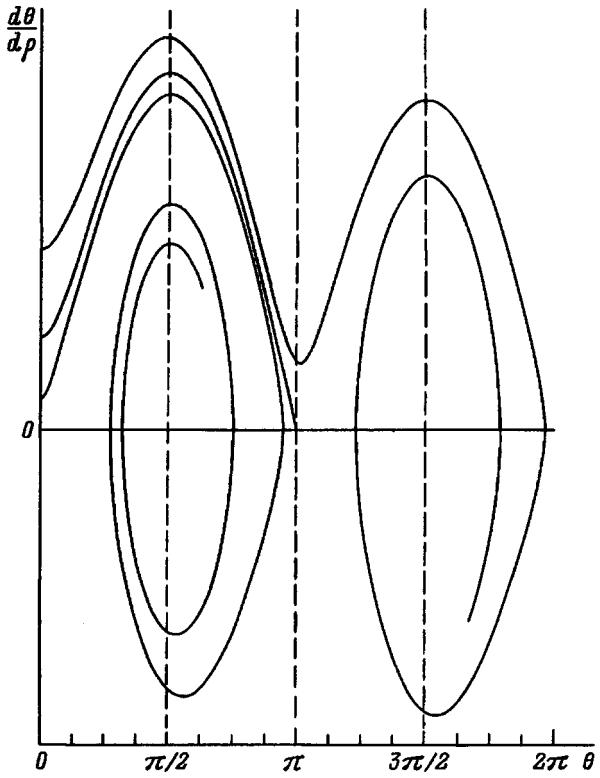

FIG. 7. Phase patterns of $\theta(\rho)$ solutions for $h<h_1$ ($B^*<-1$).

zero derivative at finite points for boundary conditions (11). In the phase plane (Fig. 7), to these solutions correspond portions of the trajectories terminating at the pole $3\pi/2$. There are no such solutions for $a<a_0$. As already mentioned, all these solutions are unstable. Finally, at $a=a_0$ localized solutions for boundary conditions (11) describing isolated vortices in the bulk of an antiferromagnet are realized. The phase pattern of this solution has a separatrix character. Figure 8 displays profiles of localized solutions for a number of fields below h_1 ($B^*<-1$). As one moves away from h_1 (as h decreases), vortex localization becomes increasingly stronger. As one approaches h_1, the vortices expand, a narrow transition region begins to form in them between the core with $\theta=0$ and the outer region with $\theta=\pi$, i.e., a "domain wall", until for $h>h_1$ ($B^*>-1$) no localized axial structures exist any more in the antiferromagnet.

3) $h>h_2$ ($B^*>1$). In contrast to the $h<h_1$ case, the phase patterns of the solutions displayed in Fig. 9 have poles at the points $(\pi,n), n=0,1,2,\ldots$, whereas the separatrix solutions terminate at point $(\pi/2,0)$. Thus for $h_2<h(B^*>1)$ we have localized solutions for the boundary conditions $\theta(\infty)=\pi/2$. In other words, for $h>h_2$ there can exist in an antiferromagnet vortices with $\mathbf{l}\|\mathbf{Z}$ at vortex center, and with $\mathbf{l}\perp\mathbf{OZ}$ for $\rho\to\infty$. Note that in this case the $\theta=0$ state at vortex center is not energetically preferable. The vortex profiles for $h>h_2$ are displayed in Fig. 10.

Thus inversionless uniaxial antiferromagnets can support two-dimensional, spatially modulated structures (magnetic vortices) as metastable states. For $h<h_1$, localized vortices with $\theta=0$ can exist at vortex center, and with $\theta=\pi$, off the

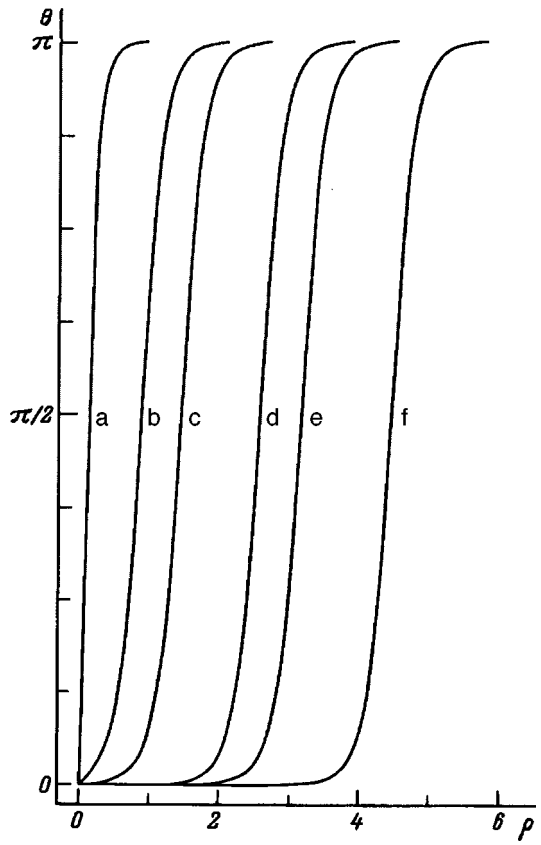

FIG. 8. Isolated magnetic vortices for B^*: (a) -1.5, (b) -1.03, (c) -1.01, (d) -1.003, (e) -1.002, and (f) -1.001.

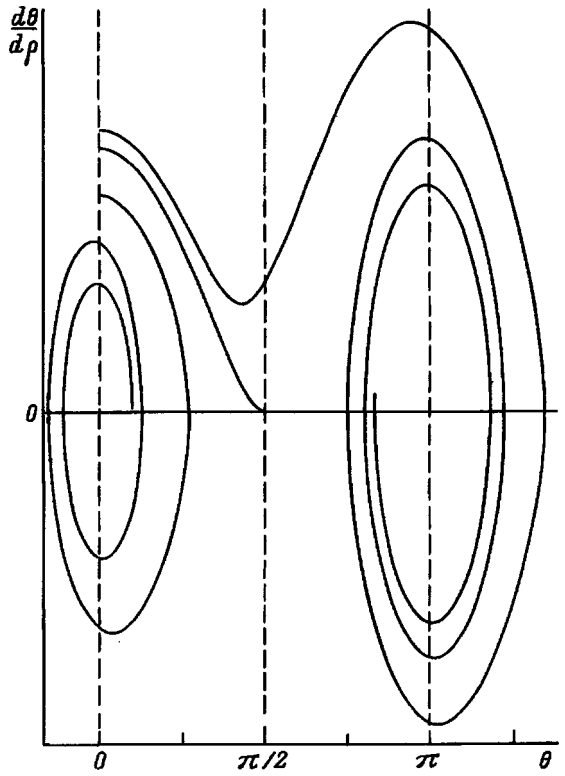

FIG. 9. Phase patterns of $\theta(\rho)$ solutions for $h>h_2$ ($B^*>1$).

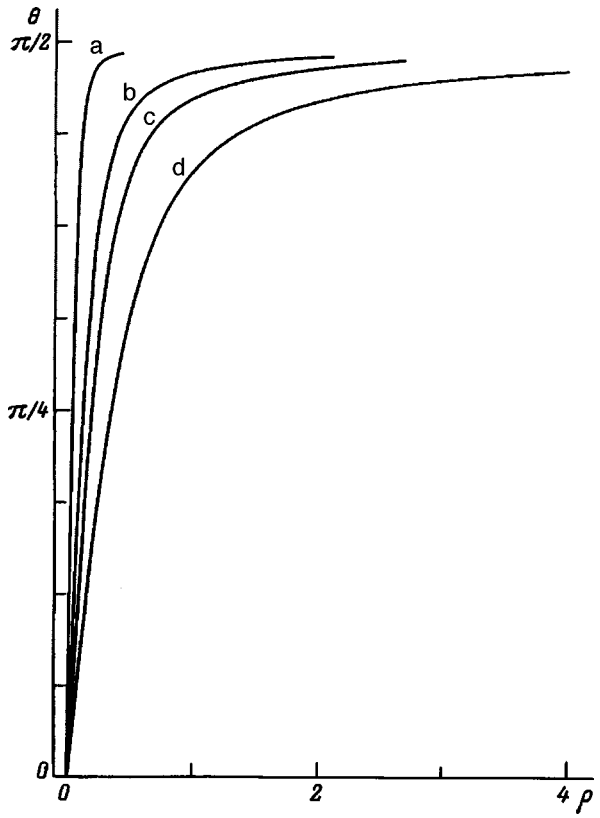

FIG. 10. Isolated magnetic vortices for B^*: (a) 5.0, (b) 2.0, (c) 1.5, and (d) 1.01.

center. As h approaches h_1, the vortices expand, a narrow transition region between the core with $\theta=0$ and the outer region with $\theta=\pi$ ("domain wall") begins to form (Fig. 8), until at $h=h_1$ localized axial structures in the antiferromagnet vanish, and a magnetic-vortex lattice appears. For h close to h_1, there exists a narrow transition region between the $\theta=0$ and $\theta=\pi$ states (Fig. 2). As the field increases, the vortex profiles become smoother (Figs. 3 and 4), and at $h\approx 0.7-0.9$ a shelf appears near $\theta=\pi/2$ (Fig. 5). As $h\to h_2$, the cells grow rapidly in size, until at $h=h_2$ localized solutions (isolated vortices) set in again. In contrast to the $h<h_1$ case, however, for $h>h_2$ we have $\theta(\infty)=\pi/2$.

2. CUBIC ANTIFERROMAGNETS

As already pointed out, modulated structures can exist not only in uniaxial but in cubic inversionless antiferromagnets as well.

For cubic antiferromagnets, the nonequilibrium thermodynamic potential coincides with (1) to within terms quadratic in the components of vectors **m** and **l**, but the expressions for w_0 and w_d are here somewhat different. For the crystallographic classes O and T the expressions for w_d can be written

$$w_d = DM_0^2 \mathbf{I}\mathrm{rot}\mathbf{I}. \tag{17}$$

The uniform part of the energy for the cubic antiferromagnets under study can be presented in the form

$$w_0 = M_0^2[2\lambda \mathbf{m}^2 - 2\mathbf{Hm}/M_0]. \tag{18}$$

Note that in this case any nonzero magnetic field orients the magnetic moments in such a way that $\mathbf{H}\perp\mathbf{l}$. Limiting ourselves to the $\mathbf{H}\perp\mathbf{Z}$ case, it can be shown that

$$w_0 = -\frac{H^2}{2\lambda}\sin^2\theta, \tag{19}$$

where, as before, θ is the angle between **l** and the **OZ** axis.

Transforming now to spherical coordinates for vector **l**, and to cylindrical coordinates for the spatial variables, and looking for axially symmetric solutions of the type $\theta=\theta(\rho)$, $\psi=\psi(\varphi)$, Eq. (16) can be written

$$w_d = D\sin(\psi-\varphi)\left(\frac{\partial\theta}{\partial r}+\frac{\sin\theta\cos\theta}{r}\frac{\partial\psi}{\partial\varphi}\right). \tag{20}$$

Similar to the way this was done in Ref. 32, one can obtain

$$\psi=\varphi\pm\pi/2\,. \tag{21}$$

Thus the energy density of a cubic two-sublattice antiferromagnet (crystallographic classes T and O) can be presented in the form

$$\frac{\varepsilon}{AM_0^2}=\frac{1}{\pi R^2}\int_0^R\left[\left(\frac{d\theta}{d\rho}\right)^2+\frac{\sin^2\theta}{\rho^2}-2\pi\left(\frac{d\theta}{d\rho}+\frac{\sin\theta\cos\theta}{\rho}\right)-\frac{\pi^4}{4}h^2\sin^2\theta\right]d\rho, \tag{22}$$

where

$$\rho=r/r_0,\quad r_0=2\pi A/D, \tag{23}$$

$$h = H/H_c, \quad h_c \pi^2 \sqrt{\lambda/2}. \tag{24}$$

Note that Eq. (22) coincides to within an insignificant constant with Eq. (10) for $\theta_0 = \pi/2$, which means that a cubic magnet behaves in a magnetic field as a uniaxial antiferromagnet in fields above the spin-flop transition point, namely, for $H < H_c$ a vortex lattice can exist, with the energy density of the helical state being always (within the region of existence of nonuniform structures) less than that of the vortex lattice. The cell radius grows rapidly with H approaching H_c, so that $R \to \infty$ for $H \to H_c$ (Fig. 1). For $H > H_c$, isolated vortices with $\mathbf{l} \| \mathbf{H}$ can occur at vortex center, and those with $\mathbf{l} \perp \mathbf{H}$, far away from the center.

To conclude, we have shown that easy-axis and cubic antiferromagnets which lack inversion symmetry can support both two-dimensional spatially modulated structures (magnetic-vortex lattices) and isolated two-dimensional structures (vortices).

Throughout the region where modulated structures occur in easy-axis and cubic antiferromagnets, there can exist, besides the one-dimensional modulated structure (spiral), also a two-dimensional spatially modulated structure (magnetic-vortex lattice) representing a metastable state.

In strong magnetic fields, easy-axis and cubic antiferromagnets lacking inversion symmetry can support localized axial structures, namely, isolated magnetic vortices with $\theta = 0$ at vortex center and with $\theta = \pi/2$ far away from the center.

In weak magnetic fields, isolated magnetic vortices with $\theta = 0$ at vortex center and with $\theta = \pi$ far away from vortex center can occur in easy-axis antiferromagnets.

Support of the Alexander von Humboldt Foundation in providing computer facilities and access to literature is gratefully acknowledged. The authors express deep gratitude to A. Hubert for a discussion of the work and valuable criticisms, and to A. S. Kovalev and S. V. Tarasenko for fruitful discussions.

[1] I. E. Dzyaloshisky, Zh. Éksp. Teor. Fiz. **46**, 1420 (1964) [Sov. Phys. JETP **19**, 960 (1964)].
[2] Yu. A. Izyumov, Usp. Fiz. Nauk **144**, 439 (1984) [Sov. Phys. Usp. **27**, 845 (1984)].
[3] Yu. A. Izyumov, *Neutron Diffraction from Long-Period Structures* [in Russian], Energoatomizdat, Moscow (1987), 200 pp.
[4] Y. Ishikawa, K. Tajima, D. Bloch, and M. Roth, Solid State Commun. **19**, 525 (1976).
[5] B. Lebech, J. Bernhard, and T. Freltoft, J. Phys.: Condens. Matter **1**, 6105 (1989).
[6] J. Beille, J. Voiron, F. Towriq, M. Roth, and Z. Y. Zhang, J. Phys. F **11**, 2153 (1981).
[7] J. Beille, J. Voiron, M. Roth, and Z. Y. Zhang, Solid State Commun. **43**, 399 (1983).
[8] H. Watanabe, Y. Tazuke, and H. Nakajima, J. Phys. Soc. Jpn. **54**, 3978 (1985).
[9] H. Watanabe, J. Phys. Soc. Jpn. **58**, 1035 (1989).
[10] B. Lebech, P. Harris, J. S. Pedersen, K. Mortensen, C. I. Gregory, N. R. Bernhoeft, M. Jermy, and S. A. Brown, J. Magn. Magn. Mater. **140/144**, 119 (1995).
[11] T. Sato, T. Nemoto, E. Ohta, M. Sakata, T. Sakakibara, and T. Goto, J. Magn. Magn. Mater. **70**, 411 (1987).
[12] T. Sato, T. Ando, T. Oku, and M. Furusaka, Phys. Rev. B **49**, 11864 (1994).
[13] T. Sato, T. Anto, T. Oku, and M. Furusaka, J. Magn. Magn. Mater. **140/144**, 1785 (1995).
[14] A. Zheludev, G. Shirane, Y. Sasago, N. Kiode, and K. Uchinokura, Phys. Rev. B **54**, 15163 (1996).
[15] A. Zheludev, S. Maslov, G. Shirane, Y. Sasago, N. Kiode, and K. Uchinokura, Phys. Rev. Lett. **78**, 4857 (1997).
[16] A. Akimitsu, K. Siratori, G. Shirane, M. Iizumi, and T. Watanabe, J. Phys. Soc. Jpn. **44**, 172 (1978).
[17] J. Adachi, N. Achiwa, and M. Mekata, J. Phys. Soc. Jpn. **49**, 545 (1980).
[18] I. Sosnowska and A. K. Zvezdin, J. Magn. Magn. Mater. **140/144**, 167 (1995).
[19] T. M. Giebułtowicz, H. Luo, N. Samarth, J. K. Furdyna, and J. J. Rhyne, IEEE Trans. Magn. **29**, 3383 (1993).
[20] T. M. Giebułtowicz, V. Nuñez, H. Luo, N. Samarth, and J. K. Furdyna, J. Appl. Phys. **73**, 6090 (1993).
[21] V. G. Bar'yakhtar and E. P. Stefanovskiĭ, Fiz. Tverd. Tela (Leningrad) **11**, 1946 (1969) [Sov. Phys. Solid State **11**, 1566 (1969)].
[22] P. Bak and M. H. Jensen, J. Phys. C **13**, L881 (1980).
[23] O. Nakanishi, A. Yanase, A. Hasegawa, and M. Kataoka, Solid State Commun. **35**, 995 (1980).
[24] M. Kataoka and O. Nakanishi, J. Phys. Soc. Jpn. **50**, 3888 (1981).
[25] M. L. Plumer and M. B. Walker, J. Phys. C **14**, 4689 (1981).
[26] M. L. Plumer, J. Phys.: Condens. Matter **2**, 7503 (1981).
[27] V. A. Golovko and D. G. Sannikov, Zh. Éksp. Teor. Fiz. **82**, 959 (1982) [Sov. Phys. JETP **55**, 562 (1982)].
[28] Yu. A. Izyumov and V. M. Laptev, Zh. Éksp. Teor. Fiz. **88**, 165 (1985) [Sov. Phys. JETP **61**, 95 (1985)].
[29] A. N. Bogdanov and D. A. Yablonskiĭ, Zh. Éksp. Teor. Fiz. **96**, 253 (1989) [Sov. Phys. JETP **69**, 142 (1989)].
[30] A. N. Bogdanov, M. V. Kudinov, and D. A. Yablonskiĭ, Fiz. Tverd. Tela (Leningrad) **31**, 99 (1989) [Sov. Phys. Solid State **31**, 1707 (1989)].
[31] A. Bogdanov and A. Hubert, Phys. Status Solidi B **186**, 527 (1994).
[32] A. Bogdanov and A. Hubert, J. Magn. Magn. Mater. **138**, 255 (1994).
[33] A. N. Bogdanov, JETP Lett. **62**, 247 (1995).
[34] A. Bogdanov and A. Hubert, J. Appl. Phys. **79**, 1536 (1996).
[35] B. A. Ivanov and A. K. Kolezhuk, Fiz. Nizk. Temp. **21**, 355 (1995) [J. Low. Temp. Fiz. **21**, 275 (1995)].
[36] V. G. Bar'yakhtar, A. N. Bogdanov, and D. A. Yablonskiĭ, Usp. Fiz. Nauk **156**, No. 1, 47 (1988) [Sov. Phys. Usp. **31**, 810 (1988)].
[37] E. A. Turov, *Physical Properties of Magnetically Ordered Crystals* [in Russian], AN SSSR, Moscow (1963), 224 pp.
[38] T. Moriya, Phys. Rev. **120**, 91 (1960).
[39] J. R. Teagyl, R. Gerson, and W. J. James, Solid State Commun. **8**, 1073 (1970).
[40] Yu. F. Popov, A. K. Zvezdin, G. P. Vorob'ev, A. M. Kadomtsev, V. A. Murashov, and D. N. Rakov, JETP Lett. **57**, 69 (1993).
[41] A. Hubert, *Theorie der Domänenwände in Geordneten Medien* [Springer, Berlin, 1974; Mir, Moscow, 1972, 308 pp.].
[42] M. M. Tegeranchi, G. A. Esina, Yu. F. Popov, and A. K. Zvezdin, in *Abstracts of the XV All-Russian School-Seminar* (1996), p. 297.

Translated by G. Skrebtsov

Nuclear magnetic relaxation in ferrimagnetic $Y_3Fe_{5-x}Si_xO_{12}$ films

V. N. Berzhanskiĭ and A. I. Gorbovanov

Simferopol' State University, 333036 Simferopol', Ukraine

S. N. Polulyakh and N. V. Pronina

Tavricheskiĭ Ecological Institute, 333013 Simferopol', Ukraine

(Submitted December 1, 1997)
Fiz. Tverd. Tela (St. Petersburg) **40**, 1494–1497 (August 1998)

The effect of silicon impurities on the damping of spin-echo signals from the ^{57}Fe nuclei of tetrahedral Fe^{3+} ions in epitaxial yttrium-iron-garnet films was investigated. It was found that for silicon concentrations $0.015 \leqslant x \leqslant 0.037$ the damping of the spin echo is a two-component process, which made it possible to separate nuclei into two types, differing by both the longitudinal and transverse magnetic relaxation times. For silicon concentrations $0.044 \leqslant x \leqslant 0.073$ the decay of the echo can be described by one exponential and all nuclei in the sample have the same transverse relaxation times and the same longitudinal relaxation times. The experimental results are interpreted on the basis of the supposition that impurity ''macromolecules'' form around the Si^{4+} ions. The relaxation times of the iron nuclei in a ''macromolecule'' are much shorter than the relaxation times of iron nuclei belonging to the matrix ions. The radius of a ''macromolecule'' is estimated on the basis of percolation theory. © *1998 American Institute of Physics.* [S1063-7834(98)01908-X]

Yttrium iron garnet (YIG) is a ''classic'' ferrimagnet, the dissipative properties of whose electronic subsystem have been well studied.[1] At the same time, the nuclear relaxation processes (both intrinsic and extrinsic) have not been adequately studied. In Refs. 2 and 3 attempts were made to investigate the intrinsic nuclear relaxation mechanisms, for which purpose YIG samples enriched with the magnetic isotope ^{57}Fe were specially synthesized. In Ref. 2, in an investigation of epitaxial YIG films enriched with the magnetic isotope up to 100% it was observed experimentally that increasing the concentration of magnetic nuclei decreases both the longitudinal and the transverse nuclear magnetic relaxation times at temperature $T=77$ K. This signifies that the nuclear-nuclear interactions are dominant and are responsible for nuclear relaxation in specially undoped YIG films.

Our objective in the present work is to investigate extrinsic nuclear magnetic relaxation processes associated with the influence of impurities with strong spin-orbit coupling, which give rise to an efficient relaxation channel in the electronic system of YIG.[1] Such a channel can be produced either by directly introducing the appropriate *d* or *f* impurity ions or by introducing heterovalent diamagnetic impurities, which lead to the appearance of iron ions having valence differing from the main valence. We used the latter method and chose as the dopant Si^{4+} ions, whose effect on the magnetic properties of YIG is well known.[4]

1. EXPERIMENT

YIG films with different silicon content were synthesized for the investigations: $Y_3Fe_{5-x}Si_xO_{12}$ ($x=0.015$, 0.026, 0.037, 0.044, and 0.073). The films were grown by liquid-phase epitaxy on gadolinium-gallium garnet substrates oriented in the (111) plane. To increase the amplitude of the nuclear spin-echo signal the charge used for synthesis of the samples was enriched to 50% with the magnetic isotope ^{57}Fe.

The spin-echo signals from the ^{57}Fe nuclei of the Fe^{3+} ions occupying magnetically-isotropic tetrahedral positions in the structure of the garnet were investigated experimentally. The relaxation properties of the echo signals were investigated at temperature $T=77$ K in the absence of an external magnetic field. The nuclear spin echo signals excited in such polydomain samples probably belong to the nuclei of iron ions located in domain walls.[5] Despite the enrichment with the magnetic isotope, the ratio of the amplitude of the echo signal to the noise amplitude was low, and it was the main source of errors in the experimental results.

The NMR spectra were obtained by registering the frequency dependence of the amplitude of a double-pulse echo signal. The NMR spectra for nuclei of tetrahedrally coordinated iron ions in silicon-doped YIG films were identical to the NMR spectra in both film[2] and bulk[3,5] YIG samples having no impurities and consisted of a single, inhomogeneously broadened spectral line at frequency 64.35 MHz.

A double-pulse sequence $90°-\tau-180°-\tau$ was used to determine the transverse magnetic relaxation time. The transverse magnetic relaxation time T_2 characterizes the exponential decay of the amplitude of the double-pulse spin-echo signal:

$$V(\tau)=V(0)\exp\{-2\tau/T_2\}, \tag{1}$$

where V is the amplitude of the echo signal and τ is the duration of the time interval between the exciting pulses.

Figure 1*a* shows the numerical values obtained for the transverse magnetic relaxation times by fitting the expression

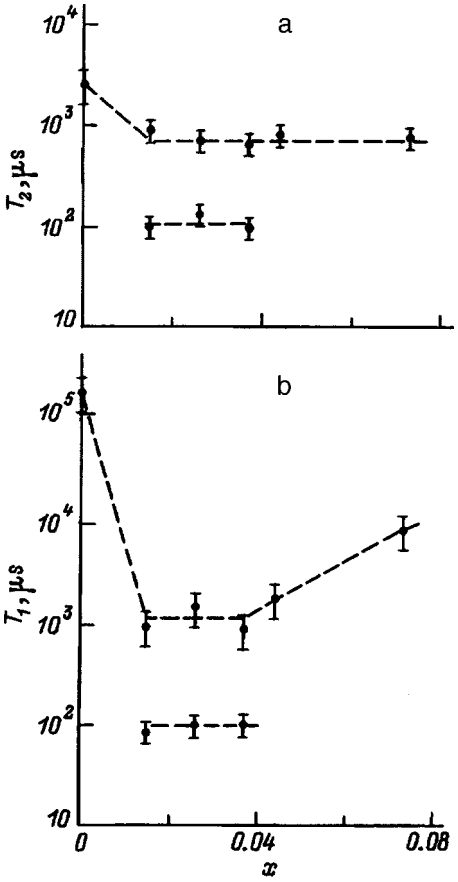

FIG. 1. Transverse (a) and longitudinal (b) magnetic relaxation times versus the silicon concentration.

(1) to the experimentally observed decay of the double-pulse echo signals. For low silicon concentrations ($0.015 \leqslant x \leqslant 0.037$) the experimentally observed decay of the echo is described by two exponentials (1) with different relaxation times. For high silicon concentrations ($x \geqslant 0.044$) the component with the short relaxation time vanishes. In silicon-doped YIG films the value of T_2 for the component with the long relaxation time does not depend on the dopant concentration.

A triple-pulse sequence $90°-\tau-90°-T-90°-\tau$ was used to measure the longitudinal relaxation time T_1.[6] For low silicon concentrations the experimental decay of the triple-pulse echo signal likewise separated into two exponential curves with two longitudinal relaxation times (see Fig. 1*b*). A further increase of the impurity concentration resulted in an echo decay described by a single exponential. The longitudinal relaxation time increased but remained less than the longitudinal relaxation time for the undoped sample.

2. DISCUSSION OF THE EXPERIMENTAL RESULTS

To analyze the experimental results we shall consider the valence of ions in silicon-doped YIG. The Si^{4+} ions replacing the tetrahedral Fe^{3+} ions in the garnet lattice lead to the appearance of excess electrons. Following the well-known models of the electronic structure of $Y_3Fe_5O_{12}Si$,[4] we shall assume that the excess electron is delocalized in a region near a Si^{4+} impurity ion. The delocalization region, including the octa- and tetrahedral iron ions closest to the Si^{4+} ion, comprise a magnetic impurity ''macromolecule.'' We shall assume that the excess electron is localized on a definite iron ion, transforming it into a Fe^{2+} ion, only for some time interval and that it is capable of migrating from one iron ion of the ''macromolecule'' to another under the action of thermodynamic fluctuations. Therefore the assumption of a migrating excess electron is equivalent to the assumption of the appearance of a dynamic defect — an iron ion with a low valence, migrating in a certain region near the Si^{4+} ion. In contrast to the main Fe^{3+} ions, the magnetic Fe^{2+} ions possess a strong spin-orbit coupling, which is the reason why they have the dominant effect on the electronic[1] and (in accordance with Ref. 5) nuclear relaxation.

At a low silicon concentration, when the regions of delocalization of the excess electrons belonging to different silicon ions do not overlap, there exist two types of iron ions. Ions of the first type belong to impurity ''macromolecules'' and participate in ''intramolecular'' electronic exchange $Fe^{3+} \leftrightarrow Fe^{2+}$. If n is the number of such ions, then an intermediate valence state $Fe^{(3-1/n)+}$ is realized for ions of the first type as a result of time-averaging. Ions of the second type lie outside the ''macromolecules'' and are ordinary, trivalent iron ions. Such a division of iron ions into two types makes it possible to analyze the experimental results on nuclear magnetic relaxation.

At low concentrations of silicon impurity ions the existence of two relaxation times (see Fig. 1) attests to the existence of two types of nuclei. Nuclei of the first type have shorter relaxation times and $T_1 \approx T_2$. It is known[7] that such a ratio between the longitudinal and transverse relaxation times occurs when nuclear relaxation is due to fluctuations of both the longitudinal and transverse components of the local magnetic fields at the nuclei and the correlation time τ_c of these fluctuations is much shorter than the reciprocal of the magnetic resonance frequency ω_0 ($\tau_c \ll \omega_0^{-1}$). Thermodynamic transitions of iron ions from a trivalent into a divalent state and back are a source of fluctuations of the local magnetic fields at the nuclei belonging to these ions, and they lead to the appearance of a rapidly decaying component of the nuclear echo.

It follows from the estimates given below for the radius of a ''macromolecule'' that the number n of ions in a macromolecule is at least 10. Assuming the localization time of a migrating electron on an iron ion is the same for all ions, we find that the lifetime of an ion in the Fe^{3+} state is at least an order of magnitude longer than the lifetime of this ion in the Fe^{2+} state, and the difference of the resonance frequencies of the nuclei belonging to iron ions with intermediate valence and nuclei belonging to Fe^{3+} ions is so small that it cannot be resolved in the NMR spectra. Therefore nuclei of the first type are located directly in the regions of delocalization of the excess electrons.

Nuclei of the second type are located outside the regions of delocalization of the excess electrons. From the standpoint of the analysis of nuclear magnetic relaxation processes, the main feature of the regions of delocalization of excess electrons is the presence of Fe^{2+} ions there, on account of which these regions can be regarded as magnetic ''macromol-

ecules'' with strong spin-orbit coupling. We shall assume that the effect of ''macromolecules'' on the relaxation of nuclei of the second type is similar to the effect of paramagnetic impurities on the nuclear magnetic relaxation in diamagnetic solids.[7] On account of the conventional magnetic dipole-dipole interactions[7] and/or interactions via ''virtual'' magnons,[5] the Fe^{2+} ions interact with nuclei of the second type, which are located in a certain region close to but not coinciding with the region of delocalization of an excess electron. On account of the strong interactions between nuclei in YIG films enriched with the magnetic isotope,[2] the spin temperature becomes equalized in the subsystem of the type-II nuclei and the longitudinal relaxation time turns out to be the same for all of these nuclei. Moreover, the impurity magnetic ''macromolecules'' have the effect that the relaxation times of type-II nuclei are shorter than in undoped YIG (see Fig. 1).

It should be noted that the secular part of the nuclear-nuclear interactions is suppressed because of the small variance of the resonance frequencies of nuclei belonging to Fe^{3+} ions and ions with an intermediate valence. On account of this the equalization of the spin temperature between the subsystems of nuclei of the two types is suppressed, and at low silicon concentrations nuclei of two types with different relaxation times are observed.

At high silicon concentrations ($x \geqslant 0.044$) the regions of delocalization of the excess electrons supplied by different Si^{4+} ions overlap, and the excess electrons form an impurity band. These electrons give rise to fluctuations of the local magnetic fields at the nuclei and are responsible for the relaxation of the longitudinal component of the nuclear magnetization.

The existence of a transition from isolated regions of delocalization of excess electrons to an impurity band makes it possible to estimate the effective radius R of a ''macromolecule'' on the basis of percolation theory. Following Ref. 8, we have for the effective radius R the expression

$$R = \left(\frac{3B_c}{4\pi N} \right)^{1/3}, \qquad (2)$$

where N is the threshold volume density of the regions at which merging of the regions occurs and B_c is a dimensionless parameter which represents the average number of bonds per site in the percolation theory. An estimate for the threshold concentration of silicon impurities $0.037 \leqslant x_c \leqslant 0.044$ follows from the results of the NMR experiment. Since a cubic unit cell of the crystal structure of YIG with cell parameter $a_0 \approx 12.37 \times 10^{-10}$ m contains eight formula units,[9] the threshold volume density of ''macromolecules'' for which an impurity band forms lies in the range $1.56 \times 10^{26} \leqslant N \leqslant 1.86 \times 10^{26}$ m^{-3}. The numerical values obtained for the parameter B_c for the ''sphere problem'' by different methods are presented in, for example, Ref. 8 and lie in the range $2.4 \leqslant B_c \leqslant 3.0$. Substituting the values given for N and B_c into the expression (2), we obtain an estimate for the radius of the impurity ''macromolecules'' $14.6 \times 10^{-10} \leqslant R \leqslant 16.6 \times 10^{-10}$ m.

In summary, in this paper it was shown that a two-component nuclear echo, which can be attributed to the presence of two types of nuclei belonging to iron ions inside and outside impurity ''macromolecules,'' is observed in silicon-doped YIG films. The increase in the longitudinal relaxation time at above-threshold impurity density is due to the formation of an impurity band. An estimate of the radius of an impurity macromolecule shows that it is somewhat greater than the cell parameter of YIG.

In closing, we note that the known mechanisms of nuclear relaxation in solids give a qualitative explanation of the experimental data. Quantitative investigations require detailed information about both the electronic and magnetic structures of silicon-doped YIG films. This information cannot be obtained solely from NMR experiments.

This work was supported in part by the Soros International Program (Grant No. SPU062005).

[1] A. G. Gurevich and G. A. Melkov, *Magnetic Oscillations and Waves* [in Russian], Nauka, Moscow, 1994, 460 pp.
[2] V. N. Berzhanskiĭ and S. N. Polulyakh, Fiz. Tverd. Tela (Leningrad) **31**, 256 (1989) [Sov. Phys. Solid State **31**, 1423 (1989)].
[3] M. P. Petrov and A. P. Paugurt, Fiz. Tverd. Tela (Leningrad) **12**, 2829 (1970) [Sov. Phys. Solid State **12**, 2284 (1970)].
[4] V. F. Kovalenko and É. L. Nagaevm Usp. Fiz. Nauk **148**, 561 (1986) [Sov. Phys. Usp. **29**, 297 (1986)].
[5] M. I. Kurkin and E. A. Turov, *NMR in Magnetically Ordered Materials and Its Application* [in Russian], Nauka, Moscow, 1990, 244 pp.
[6] A. A. Vashman and I. S. Pronin, *Nuclear Magnetic Relaxation Spectroscopy* [in Russian], Nauka, Moscow, 1986, 231 pp.
[7] A. Abragam, *The Principles of Nuclear Magnetism* [Clarendon Press, Oxford, 1961; Inostr. Lit., Moscow, 1963, 551 pp.].
[8] B. I. Shklovskiĭ and A. L. Éfros, *Electronic Properties of Doped Semiconductors* [Springer-Verlag, N. Y.; Nauka, Moscow, 1979, 416 pp.].
[9] Yu. M. Yakovlev and S. Sh. Gendelev, *Ferrite Single Crystals in Radio Electronics* [in Russian], Sov. radio, Moscow, 1975, 300 pp.

Translated by M. E. Alferieff

Structure and stability of 0° domain walls localized at defects in a (001)-crystal plate with combined anisotropy

R. M. Vakhitov and V. E. Kucherov

Bashkir State University, 450074 Ufa, Russia
(Submitted December 16, 1997)
Fiz. Tverd. Tela (St. Petersburg) **40**, 1498–1502 (August 1998)

An analysis is made of the conditions of formation and the stability region of static-soliton–type magnetic nonuniformities in a (001)-crystal plate with combined anisotropy. It is shown that if demagnetizing fields in the plate are taken into account, static solitons can localize at certain defects for appropriate parameters of the material. The soliton stability region was found to be bounded by two extreme values of the material parameters, namely, those at which the soliton is unstable against collapse and at which it expands. It was also found that the soliton stability region differs considerably from that predicted theoretically in the model disregarding the finite size of the sample and the presence of defects. © *1998 American Institute of Physics.* [S1063-7834(98)02008-5]

Two types of anisotropy of different nature were observed to form under certain conditions in some magnetic materials, such as ferrite-garnet single-crystal plates, namely, induced uniaxial and natural crystallographic (cubic).[1] This combined anisotropy affects substantially the magnetic properties of these crystals and, in particular, influences the formation and topological features of their domain structure.[2,3] Studies show that the equilibrium orientations of the magnetization vector **M** in domains and the possible magnetic nonuniformities in the plate depend essentially on the orientation of its surface, as well as on the relative magnitude of the induced-uniaxial and cubic anisotropies. It was shown[4] that within the region of values of $\varkappa = K_1/K_u$ (K_1 and K_u are, respectively, the induced-uniaxial and cubic-anisotropy constants) where the unstable state of vector **M** (the hard-magnetization axis) becomes stable (or, more accurately, metastable) waists appear in the domain-wall (DW) structure, which act as nuclei of a new phase and initiate rearrangement of the domain structure of the sample. On the other hand, the existence of a metastable axis in the spin rotation plane may give rise to magnetic nonuniformities of a particular type, viz. 0° domain walls or static solitons. Landau-Lifshits equations yield solutions corresponding to 0° domain walls for all three types of crystals, (001), (011), and (111); for a (001) plate they can be written

$$\tan\theta = \pm a\cosh\xi, \quad \varphi = 0,\pi, \quad \varphi_0 = \pi n/2, \quad n \in Z,$$
$$a = (\varkappa - 1)^{-1/2}, \quad \xi = by/\Delta_0, \quad b = (\varkappa - 1)^{1/2}, \tag{1}$$

where θ and φ are the polar and azimuthal angles of vector **M**, φ_0 is the angle defining domain-wall orientation relative to the crystallographic axes, $\Delta_0 = \sqrt{A/K_u}$ is the wall width in a uniaxial crystal,[3] A is an exchange parameter, and y is the coordinate along which the magnet is nonuniform. These solutions are actually magnetic nonuniformities which, in contrast to domain walls (i.e., topological solitons[5]), separate domains with the same orientation of vector **M** (**M**$\|[100]$ or **M**$\|[010]$) and, similar to dynamic solitons, are bell shaped. They exist in two types, which differ in the direction of deflection of vector **M** from the (001) plane and are characterized by energy E_s, effective width Δ_s, and amplitude θ_s (i.e., maximum deflection angle of vector M from the uniform state) as follows[4]

$$E_s = K_u L D \Delta_0 \{[\varkappa a^2/(b(a^2+1)) - a^2 b - 2/b]/\sqrt{a^2+1} + [\varkappa/(b(a^2+1)) + b]\},$$
$$\Delta_s = 2\Delta_0 \{[\pi - 2\arctan\sqrt{1+2a^2}]\sqrt{1+a^2} + \ln[(\sqrt{1+a^2} + \sqrt{1+2a^2})/a]\}/b, \tag{2}$$
$$\theta_s = \arctan(a) - (\pi/2), \quad E_0 = 4\sqrt{AK_u}.$$

For $\varkappa \to 1$ we obtain $E_s \to 0$, $\Delta_s \to \infty$, and $\theta_s \to 0$, which means that the soliton expands and disappears. At the same time for $K_u \to 0$ ($\varkappa \to \infty$) the soliton expands without limit to transform into two 90° DW's propagating away from one another (with $E_s \to 2\sqrt{A/K_u}$, $\Delta_s \to \infty$, and $\theta_s \to \pm\pi/2$).

A study of the second variation in energy made to determine the stability region for solutions of type (1) showed that solitons are not stable formations.[5] At the same time an analysis of experimental[6,7] and theoretical[8,9] investigations suggests that magnetic nonuniformities of this type can form in magnetic materials under certain conditions. It is at the search for such conditions for a (001) plate that our study is aimed. The choice of this crystal was motivated by the simplicity and informativeness of the case under study, as well as by its being poorly investigated.

1. MODEL OF THE STATIC SOLITON

Consider an infinite plane-parallel plate of thickness D with combined anisotropy. We select a coordinate frame with the axis $OZ\|[001]$ perpendicular to the plate plane, and with $OX\|[100]$. Then for the energy of magnetic nonunifor-

mities in a (001) plate, including the nonuniform exchange interaction, combined anisotropy, and DW magnetostatic energies, we shall obtain

$$E=\int_V \{A[(d\theta/dy)^2+\sin^2\theta(d\varphi/dy)^2]+K_u\sin^2\theta + K_1[\sin^4\theta\sin^2(\varphi-\varphi_0)\cos^2(\varphi-\varphi_0) + \sin^2\theta\cos^2\theta]+2\pi M_s^2(\sin\theta\sin\varphi - \sin\theta_m\sin\varphi_m)^2\}dV, \quad (3)$$

where θ_m and φ_m are the angles determining the direction of **M** in domains, M_s is the saturation magnetization, and V is the plate volume.

In the region where $\varkappa>1$, Euler's equations minimizing (3) contain solutions of type (1), which are known[10] to be unstable. This results from the fact that Eq. (3) does not include the factors responsible for the break-up of the sample into domains. One of them is the presence in the plate of demagnetizing fields, whose contribution to energy (3) for Bloch domain walls can be written[11]

$$E_{ms}=M_s^2L\int_{-\infty}^{\infty}\int_{-\infty}^{\infty}\cos\theta(y)\cos\theta(y') \times\ln[1+D^2/(y-y')^2]dydy', \quad (4)$$

where L is the dimension of the plate along the OX axis (in the limit, $L\to\infty$). Because for static solitons θ varies within the interval $0<\theta<\pi/2$, which corresponds to the plus sign in Eq. (1), or $\pi/2<\theta<\pi$ [the minus sign in Eq. (1)], we obtain $E_{ms}>0$, so that magnetostatic energy (4) provides a positive contribution to the total energy (2). This means that inclusion of demagnetizing fields in the case under study will always tend to decrease the soliton dimensions, which are determined by the quantities θ_s and Δ_s.

The presence of defects in a sample is another factor affecting domain-structure formation. As a result of its inclusion, the material parameters (A,K_u,K_1,M_s) become coordinate dependent.[8,12] We shall assume in this case that only K_u and K_1 are functions of y

$$K_u(y)=\begin{cases}K_u, & \text{for } |y|>l/2,\\ K_u+\Delta K_u, & \text{for } |y|\leqslant l/2,\end{cases}$$

$$K_1(y)=\begin{cases}K_1, & \text{for } |y|>l/2\,.\\ K_1-\Delta K_1, & \text{for } |y|\leqslant l/2\,.\end{cases} \quad (5)$$

The defect chosen in this way is obviously a model representation of real defects in crystals and may be considered as a planar magnetic inclusion. A similar situation may arise in the presence of chemical or structural nonuniformities of other types (dislocations, misorientations etc.), which likewise perturb the translational symmetry of the crystal and can give rise to local changes in induced-uniaxial and cubic-anisotropy constants.[13,14]

As this will be shown later, taking into account these two factors is justified in an analysis of static-soliton stability, while making at the same time practically unsolvable the corresponding Euler's equations describing the magnetization distribution in a (001) plate. Therefore we shall solve this problem by variational analysis and assume that these factors do not affect significantly the topology of the static soliton and can only change its parameters. As a trial function $\theta=\theta(y)$ we shall take the relation describing the variation of vector **M** in a static soliton of the type (1), where a and b will be assumed to be variational parameters. Taking into account the finiteness of the sample and the nonuniformity of the induced-uniaxial and cubic-anisotropy constants, the energy of a static soliton can now be written

$$\begin{aligned}\varepsilon_s=(E_s+E_{ms})/K_uLD\Delta_0+(\Delta\varkappa_u-\Delta\varkappa_1a^2/(a^2+1)/2)\\ \times\ln\{[\sqrt{a^2+1}-\tanh(b(l/2-\xi)/\Delta_0)]\\ \times[\sqrt{a^2+1}-\tanh(b(l/2-\xi)/\Delta_0)]\\ \times[\tanh(b(l/2+\xi)/\Delta_0)+\sqrt{a^2+1}]^{-1}\\ \times[\tanh(b(l/2-\xi)/\Delta_0)+\sqrt{a^2+1}]^{-1}\}/(2b\sqrt{a^2+1})\\ -\Delta\varkappa_1a^2\{\tanh(b(l/2+\xi)/\Delta_0)/\\ [a^2+1-\tanh^2(b(l/2+\xi)/\Delta_0)]\\ +\tanh(b(l/2-\xi)/\Delta_0)/[a^2+1-\tanh^2(b(l/2-\xi)/\Delta_0)]\}/\\ (2b(a^2+1)), \quad (6)\end{aligned}$$

where $\Delta\varkappa_1=\Delta K_u/K_u$, $\Delta\varkappa_1=\Delta K_1/K_u$, and ξ is a parameter defining the soliton position relative to defect center.

We thus see that the above model of the static soliton describes more adequately the real situation in crystals, which makes it realistic compared to the idealized case treated in Refs. 5 and 10.

2. STABLE STATES OF THE STATIC SOLITON

To determine the structure and stability region of the static soliton, one obviously has to minimize the energy $\mathcal{E}$ in variational parameters, with subsequent solution of the equations thus obtained for a and b. These equations are, however, very cumbersome and cannot be solved in known functions, and therefore one has to invoke numerical methods. In this case one uses the method of minimization of Hook and Jeeves[15].

An analysis of the results obtained by numerical minimization shows that the static soliton as a localized state of vector **M** is stable and can exist in certain regions of the values of material and defect parameters. As follows from Fig. 1, the static soliton is localized at defect center. Its displacement away from defect center gives rise to considerable forces of quasi-elastic nature, which deform the soliton and make it shrink. These forces depend considerably on both the displacement ξ and parameter $\varkappa$, and result in the collapse of the soliton at defect edges. The critical value of the amplitude falls off rapidly with increasing $\varkappa$ practically to zero (curve *3* in Fig. 1b). Note that the soliton always decreases in size with increasing $\varkappa$, which is in accord with Eqs. (2).

The parameters of the static soliton are determined to a considerable extent by those of the defect. As evident from Fig. 2a, the soliton width is directly proportional to the defect dimension l, and for $l\to\infty$ it grows without limit, while $\theta_s\to 0$, i.e., the soliton spreads out. This can be accounted for

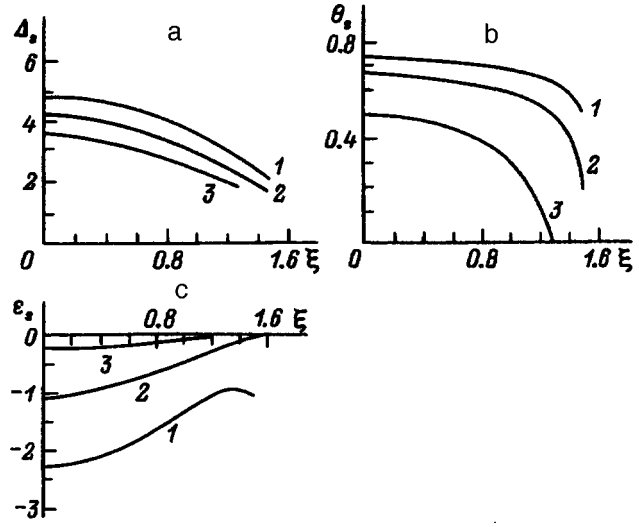

FIG. 1. (a) Energy, (b) amplitude, and (c) energy of soliton vs displacement of its center from defect center for the following material parameters: $Q=1.5$, $\Delta_0=0.15$, $l=4.5$, $D=10$, $\Delta\varkappa_u=-1$, $\Delta\varkappa_1=2.7$. $\varkappa$: *1* — 1.7, *2* — 2.0, *3* — 2.3.

by the fact that the $l\to\infty$ situation corresponds to the absence of the defect, and in this case the soliton is known[10] to be an unstable formation. On the other hand, there is a minimum value of l below which the soliton becomes unstable and collapses. The existence of a lower boundary for l means that in order for a stable soliton to form the defect has to possess a certain minimum energy depending both on l and on the quantities $\Delta\varkappa_1$ and $\Delta\varkappa_u$. Indeed, Figs. 3 and 4 show the existence in this case of threshold values of $\Delta\varkappa_1$ and $\Delta\varkappa_u$ at which the soliton collapses. These critical values may lie in the negative region as well (curve *3* in Figs. 3 and 4). This implies that stable states are possible also if one of these parameters does not ''feel'' a defect. In this case, however, the values of the other parameter will be confined to the positive region. In the case where one of the defects is absent, the critical values of $\Delta\varkappa_u$ and $\Delta\varkappa_1$ determine obviously the minimum energy of the other, ''existing'' defect, which

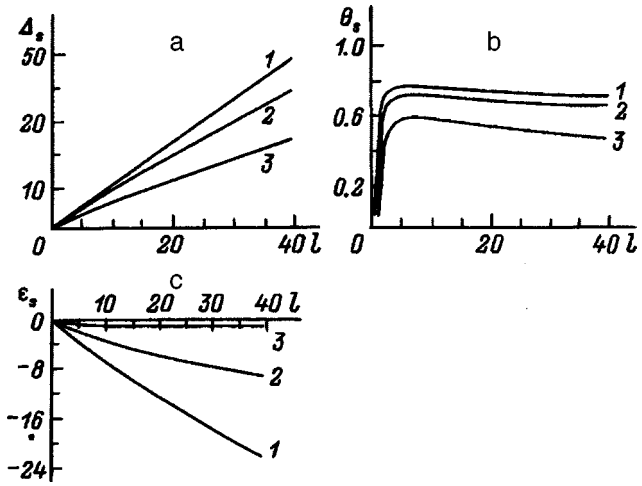

FIG. 2. Soliton parameters vs defect width l. Notation of curves and values of the material parameters same as in Fig. 1.

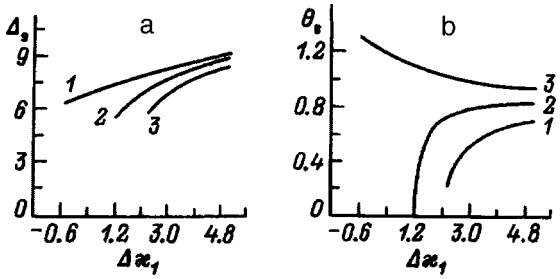

FIG. 3. Soliton size vs cubic-anisotropy defect parameter $\Delta\varkappa_1$ for the following material parameters: $Q=0.5$, $\Delta_0=0.15$, $D=10$, $l=5$, $\Delta\varkappa_u=1$, $\xi=0$. Notation of curves same as in Fig. 1.

is necessary for the soliton to nucleate. If both defects are present (both in cubic and induced-uniaxial anisotropies), the minimum energy is determined by their combined contribution.

The influence of demagnetizing fields in the plate on the soliton stability region is dominated by contribution (4) to the total energy (3), which is inversely proportional to the Q factor. As seen from Fig. 5, taking into account the finiteness of the sample reduces the region of soliton stability. Here likewise exists a threshold value of Q at which the soliton becomes unstable against collapse. On the other hand, for $Q\to\infty$ (demagnetizing fields become negligible, for instance, at the compensation point) the soliton parameters approach asymptotically some values which can be obtained without taking into account magnetostatic effects. This may serve as one more argument for the validity of the approach used in the numerical minimization of energy (6), because numerical solution of expression (4) representing a double integral over an infinite region of an integrand which contains a logarithmic singularity at the line $y=y'$ meets with certain difficulties.

The curves relating the soliton parameters to plate thickness (Fig. 6) exhibit an interesting feature, namely, an extremum in D. This can be attributed to the fact that the energy of soliton interaction with a defect decreases with increasing thickness following a linear law, whereas the magnetostatic energy increases (quadratically for small D). Accordingly, the first factor tends to increase the soliton dimensions (θ_s,Δ_s), and the second, to reduce them. At the value of D where the soliton reaches the maximum dimensions, the two factors cancel. At the same time the values of D at which θ_s and Δ_s attain a maximum, and E, a minimum, do not coin-

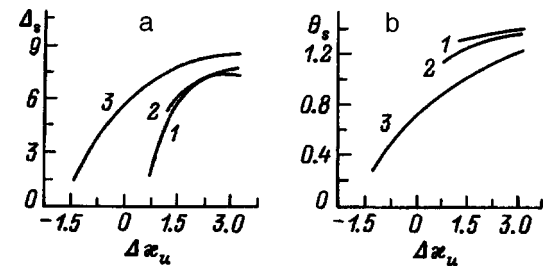

FIG. 4. Soliton size vs induced-uniaxial anisotropy defect parameter $\Delta\varkappa_u$. Notation of curves and material parameters same as in Fig. 3 (except for $\Delta\varkappa_1=2.9$).

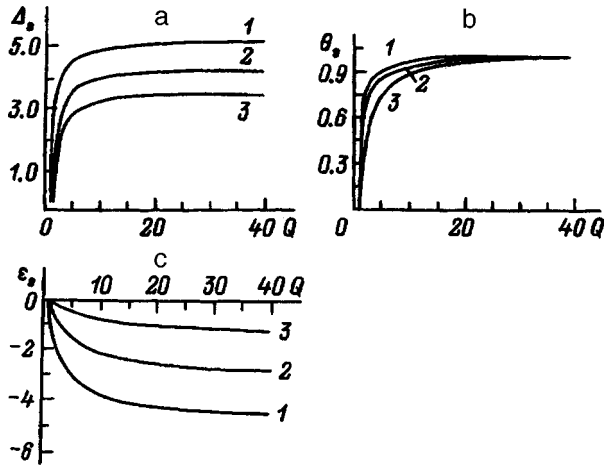

FIG. 5. Soliton parameters vs Q factor of material. Notation of curves and material parameters same as in Fig. 1 (except for $l=3.4$).

cide. This is due to the fact that θ_s depends on one variational parameter only (a), while Δ_s and E_s, on two parameters (a and b), and that their functional dependences on a and b are different [see Eq. (2)]. We see also from Fig. 6 that the soliton width grows with increasing Δ_0 [in accordance with expression (2) for Δ_s], whereas θ_s decreases. This can be assigned to the effect of magnetostatic stray fields increasing with increasing DW width. The latter factor upsets the soliton equilibrium conditions, which, in its turn, gives rise to a decrease of the soliton amplitude.

To conclude, our studies show that a static soliton can exist as a stable formation only for certain types of defects, which provide a negative contribution to the energy, and within certain regions of material parameters. The upper boundary of stability (if it does exist at all) originates from the spreading of the soliton and was predicted already by the idealized model[4,10]. The regions of soliton stability calculated in the above papers (for instance, in parameter $\varkappa$) differ considerably from our results. The lower boundary of soliton stability, connected with soliton collapse, determines the minimum defect energy required for a soliton to nucleate. In connection with this the following comment appears appropriate: first, the lower boundary of stability has not been found before despite repeated studies of the interaction of 0° DW's with defects in crystals (see, e.g., Refs. 8 and 9). This situation can be attributed to the neglect of demagnetizing fields in the plate. Second, one can draw a certain analogy with the theory[16] of magnetic bubbles, by which the region of bubble-domain existence is bounded by the collapse fields and the elliptical instability. This suggests that magnetic nonuniformities of the solitary type obey some general relations. Third, the presence of a defect in a magnet, which was considered earlier as affecting adversely the statics and dynamics of magnetic nonuniformities, is in this case a necessary prerequisite to the existence of solitons. This, in its turn, suggests possible application potential of the latter.

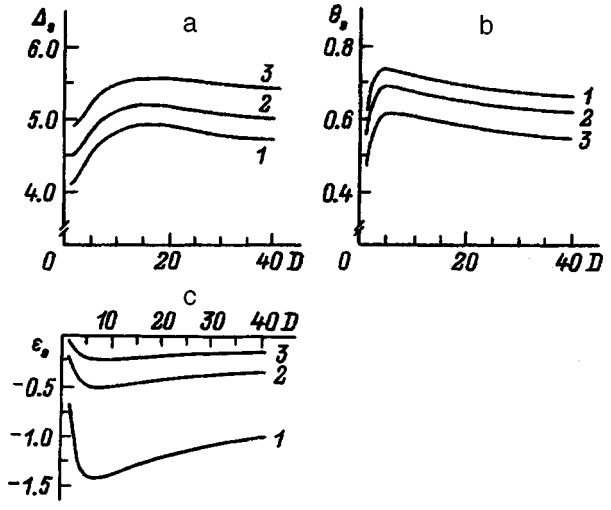

FIG. 6. Soliton parameters vs plate thickness. $Q=1.5$, $l=4.5$, $\Delta\varkappa_u=-1$, $\Delta\varkappa_1=2.7$, $\xi=0$, and $\varkappa=2$. Δ_0: *1* — 0.15, *2* — 0.35, *3* — 0.55.

[1] S. Tikazumi, *Physics of the Ferromagnetism. Magnetic Characteristics and Applications* (Mir, Moscow, 1987), 419 pp.
[2] J. Simsova, S. Krupička, M. Marusko, and I. Tomas, Acta Phys. Slov. **31**, 121 (1981).
[3] R. M. Vakhitov, R. M. Sabitov, and M. M. Farztdinov, Fiz. Tverd. Tela (Leningrad) **27**, 1852 (1985) [Sov. Phys. Solid State **27**, 1111 (1985)].
[4] R. M. Sabitov and R. M. Vakhitov, Izv. Vyssh. Uchebn. Zaved. Fiz. No. 8, 51 (1988).
[5] A. M. Kosevich, Fiz. Met. Metalloved. **53**, 420 (1982).
[6] A. M. Balbashov, A. V. Zalesskiĭ, E. V. Krivenko, and E. V. Sinitsyn, Pis'ma Zh. Tekh. Fiz. **14**, 293 (1988) [Sov. Tech. Phys. Lett. **14**, 129 (1988)].
[7] G. S. Kandaurova and L. A. Pamyatnykh, Fiz. Tverd. Tela (Leningrad) **31**, 132 (1989) [Sov. Phys. Solid State **31**, 1351 (1989)].
[8] M. A. Shamsutdinov, V. G. Veselago, M. M. Farztdinov, and E. G. Ekomasov, Fiz. Tverd. Tela (Leningrad) **32**, 497 (1990) [Sov. Phys. Solid State **32**, 288 (1990)].
[9] V. G. Veselago, I. V. Vladimirov, R. A. Doroshenko, and V. V. Plavskiĭ, Preprint No. 53, Moscow (1989), 36 pp.
[10] R. M. Sabitov, R. M. Vakhitov, and R. S. Fakhretdinova, in *Dynamics and Statics of Domain Structures in Magnetically Ordered Crystals* [in Russian], Ural Branch, AN SSSR, Ufa (1988), pp. 22–40.
[11] R. M. Vakhitov and A. R. Yumaguzin, in *Structural, Magnetoelastic, and Dynamic Effects in Ordered Media* [in Russian], Bash. State University, Ufa (1997), pp. 87–92.
[12] A. I. Mitsek and S. S. Semyannikov, Fiz. Tverd. Tela (Leningrad) **11**, 1103 (1969) [Sov. Phys. Solid State **11**, 899 (1969)].
[13] V. K. Vlasko–Vlasov, L. M. Dedukh, M. V. Indenbom, and V. I. Nikitenko, Zh. Éksp. Teor. Fiz. **84**, 277 (1983) [Sov. Phys. JETP **57**, 159 (1983)].
[14] A. B. Dichenko and V. V. Nicolaev, J. Magn. Magn. Mater. **53**, 71 (1985).
[15] B. D. Bunday, *Basic Optimization Methods* (Radio i Svyaz, Moscow, 1988), 128 pp.
[16] A. A. Thiele, Bell Syst. Tech. J. **48**, 3287 (1969).

Translated by G. Skrebtsov

Magnetic state of nickel-zinc ferrites at high zinc concentrations

Yu. G. Chukalkin and A. E. Teplykh

Institute of Metal Physics, Russian Academy of Sciences (Ural Department), 620219 Ekaterinburg, Russia
(Submitted December 19, 1998)
Fiz. Tverd. Tela (St. Petersburg) **40**, 1503–1504 (August 1998)

Neutron diffraction and magnetic methods are used to investigate ferrites from the system Zn_xFe_{1-x} $[Ni_{1-x}Fe_{1+x}]O_4$. In these investigations, no diffraction effects were observed that would indicate ordered positions for the perpendicular projections of spins at 4.2 K over the entire ferrimagnetic range of concentrations x. However, the high-field magnetic susceptibility and intense small-angle scattering of neutrons observed at helium temperatures in samples with $x>0.45$ are evidence of local angular structures with effective sizes of 1–10 nm. The temperatures at which these local angular structures are disrupted are determined. © *1998 American Institute of Physics.* [S1063-7834(98)02108-X]

It is known that the replacement of nickel ions by ions of zinc in the ferrite system Zn_xFe_{1-x} $[Ni_{1-x}Fe_{1+x}]O_4$ leads to a gradual change in the ferrimagnetic ordering until the material is antiferromagnetic.[1] At high zinc concentrations ($x>0.4$), the magnetic state of these ferrites is observed to deviate from Néel ferrimagnetic ordering due to competition between the inter- and intrasublattice negative-exchange interactions. This phenomenon has been a subject of discussion for many years. Based on neutron diffraction data, Satya-Murthy *et al.*[2] and Vologin *et al.*[3] have asserted that there is some sort of long-range ordering in the perpendicular projections of the spins. This picture is rejected by the authors of Refs. 4–6, who argue that an explanation of the data based on the concept of a disordered angular structure is physically more justifiable . To resolve this argument, we have undertaken a detailed study of the nickel-zinc ferrites using neutron diffraction and magnetic methods.

We synthesized polycrystalline samples with zinc concentrations $x=0$, 0.15, 0.30, 0.45, 0.60, 0.68, 0.75, 0.90, and 1.0 the usual ceramic technique. Our neutron diffraction studies were carried out at 4.2 K using a multidetector diffractometer at a wavelength of $\lambda=0.181$ nm. The magnetization of the samples was measured using a vibrational magnetometer in magnetic fields up to 1.6×10^6 A/m. The dynamic susceptibility χ_{ac} at a frequency of 60 Hz was measured using a mutual inductance bridge.

In Fig. 1 we observe that the concentration dependence of the magnetic moment n_B begins to depart slightly from the linear increase predicted by the collinear theory of Néel (the dashed line in Fig. 1) at $x=0.45$. For zinc concentrations greater than 0.6 n_B is observed to decrease rapidly. Extrapolating n_B to zero shows that the magnetic moment vanishes at $x\sim0.8$. It is this concentration interval that is of the most interest. Our neutron diffraction studies of samples at 4.2 K did not reveal any diffraction effects that would indicate ordering of the positions of the perpendicular spin projections. However, at low temperatures, the high-field susceptibility of ferrimagnetic samples with $x=0.60$, 0.68, and 0.75 showed clear signs of a noncollinear magnetic structure. An intense small-angle scattering (curve *2* in Fig. 1) was also characteristic for these samples, indicating the presence of magnetic inhomogeneities with respect to the z projection of the magnetic moments. These observations argue in favor of a local angular structure. Based on values of the quasimomentum transfers $q=4\pi\sin\Theta/\lambda$ (where Θ is the scattering angle) at which the small angle scattering is observed, we estimate that the effective sizes of the magnetic inhomogeneities were 1–10 nm.

Analysis of the data from Refs. 5 and 6 leads us to expect that these local angular structures transform into collinear ferrimagnetic ordering as the temperature increases. Since frozen-in noncollinear spin configurations with these effective dimensions will be an obstacle to domain walls at low temperatures, measurement of the dynamic susceptibility is a convenient way to observe them and study their possible evolution. Figure 2 shows that there is a large falloff in χ_{ac} at

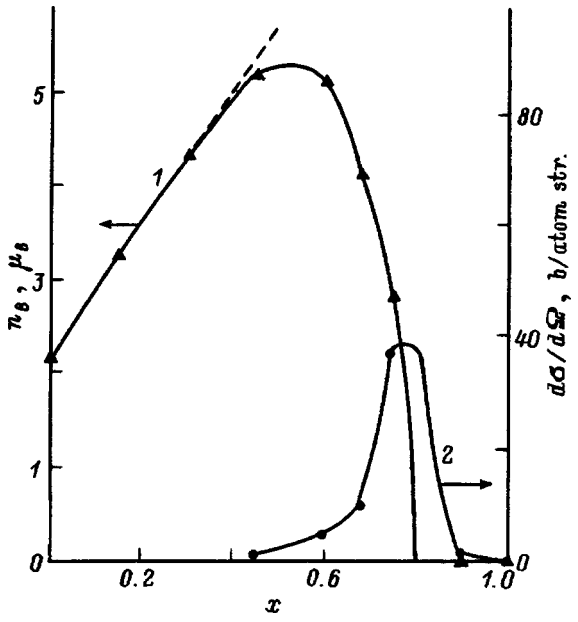

FIG. 1. Concentration dependence of the magnetic moment (*1*) and small-angle neutron scattering cross section ($q=0.79$ nm^{-1}) at 4.2 K (*2*).

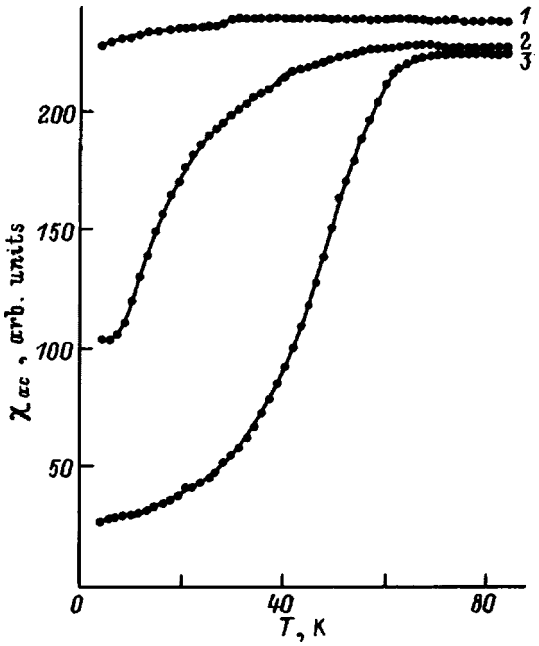

FIG. 2. Temperature dependences of the dynamic susceptibility for samples with $x=0.45$ (*1*), 0.60 (*2*), and 0.75 (*3*).

low temperatures for the samples with $x=0.45$, 0.60, and 0.75, most obviously for the two last compounds. The temperatures at which this falloff begins were 33, 57, and 67 K for samples with $x=0.45$, 0.60 and 0.75 respectively. Below these temperatures we also observed irreversibility of the static magnetization, which is characteristic of interacting ferri- and antiferromagnetic phases.[7] Taken as a whole, these data suggest that these temperatures correspond to disruption of the local angular structures.

The ferrites with zinc contents $x=0.90$ and 1.0 were not ferrimagnetic. Distinctive features of antiferromagnetic ordering in zinc ferrite ($x=1.0$) were discussed in detail in our previous Ref. 8. Our neutron-diffraction data indicated no long-range magnetic order of any kind in the sample with $x=0.90$, only short-range antiferromagnetic order.

The authors are grateful to Prof. B. N. Goshchitskiĭ for useful discussions.

Support for this work came from the GNTP ''Current Research in Condensed Matter Physics,'' in the area of ''Neutron-Diffraction Studies,'' Projects Nos.96-104 and 96/301.

[1] S. Krupichka, *Physics of Magnetic-Oxide Ferrites*, Vol. 1 [in Russian] (Moscow, 1976), 353 pp.
[2] N. S. Satya-Murthy, M. G. Natera, S. I. Youssef, R. J. Begum, and C. M. Srivastava, Phys. Rev. **181**, 969 (1969).
[3] V. G. Vologin, S. F. Dubinin, V. D. Parhomenko, and S. K. Sidorov, Solid State Commun. **29**, *5*, 447 (1979).
[4] J. Piekoszewski, J. Suwalski, and L. Dabrowski, Acta Phys. Pol. A **51**, *2*, 179 (1977).
[5] S. C. Bhargava and N. Zeman, Phys. Rev. B **21**, 1717 (1980).
[6] S. M. Zhilyakov, V. V. Ivolga, E. P. Naĭden, and T. N. Simonova, Izv. vuzov. Fizika **7**, 23 (1986).
[7] Yu. G. Chukalkin, V. R. Shtirts, and B. N. Goshchitskin, Fiz. Tverd. Tela (Leningrad) **30**, 3201 (1988) [Sov. Phys. Solid State **30**, 1841 (1988)].
[8] Yu. G. Chukalkin and V. R. Shtirts, Fiz. Tverd. Tela (Leningrad) **30**, 2919 (1988) [Sov. Phys. Solid State **30**, 1683 (1988)].

Translated by Frank J. Crowne

Study of the magnetic properties of ferrites in the $CuGa_xAl_xFe_{2-2x}O_4$ system having a frustrated magnetic structure

L. G. Antoshina and E. N. Kukudzhanova

Lomonosov Moscow State University, 119899 Moscow, Russia
(Submitted January 12, 1998)
Fiz. Tverd. Tela (St. Petersburg) **40**, 1505–1509 (August 1998)

This paper reports a first preparation of samples of the $CuGa_xAl_xFe_{2-2x}O_4$ system ($x=0.0$, 0.1, 0.2, 0.3, 0.4, 0.5, 0.6, and 0.7) and a study of temperature dependences of their spontaneous magnetization σ_s, coercive force H_c, and of the longitudinal, $\lambda_\parallel$, and transverse, $\lambda_\perp$, magnetostriction. Our experimental data have established that compositions with $x>0.4$ undergo two magnetic phase transitions, namely, from the paramagnetic to cluster spin-glass state at the Curie temperature T_C, and another transformation, at $T_{tr}<T_C$, from the cluster spin glass to a frustrated magnetic structure. It was found that the coercive force of ferrites with a frustrated magnetic structure is an order of magnitude lower than that of ferrimagnetically ordered ferrites. The behavior of the magnetostriction of frustrated ferrites was studied. Such ferrites were found to exhibit a considerable positive magnetostriction of the paraprocess λ_{para}. It was shown that the magnetostriction of spin-glass ferrites is lower by nearly an order of magnitude. © *1998 American Institute of Physics.* [S1063-7834(98)02208-4]

Considerable attention has been focused recently on the study of magnetic properties of materials capable of taking on both the frustrated magnetic and the spin-glass structure.[1] There are many publications dealing with investigation of the magnetic properties of dilute alloys, both experimental and theoretical, while studies of strongly diluted ferrites are relatively scarce. Because ferrites with frustrated magnetic structure possess novel magnetic characteristics, experimental investigation in this area appears to be very important both for development of new magnetic materials for possible applications and from the standpoint of further theoretical progress in the physics of ferrites. Of particular interest are studies performed in the vicinity of magnetic phase transitions, because the magnetic properties of frustrated materials become manifest in different ways than they do in nondilute magnetic substances.

A frustrated magnetic structure and the spin-glass state in ferrites having the spinel structure can be obtained both by diluting the ferrites with nonmagnetic ions and by introducing magnetic ions with a strong negative exchange BB interaction.[2] This results in enhanced competition between the exchange AB and BB interactions, and magnetic order, rather than extending throughout the sample, sets in in isolated, spontaneously magnetized regions. If such isolated magnetized regions maintain long-range magnetic order, this structure is called frustrated, and if they are comparatively small and short-range ordered, the magnetic structure is of the cluster spin-glass type.

This work studies the magnetic properties of copper-containing spinel ferrites as a function of dilution by nonmagnetic ions Ga^{3+} and Al^{3+}. Substitution of nonmagnetic for magnetic ions on the A and B sublattices in materials of such composition increases the role of negative intrasublattice BB and AA coupling compared to negative intersublattice AB interactions. This gives rise to enhanced competition between negative intra- and intersublattice interactions, which, in its turn, favors the onset of the spin-glass state and of a frustrated magnetic structure.

We chose as subjects for study samples of the $CuGa_xAl_xFe_{2-2x}O_4$ system with $x=0.0$, 0.1, 0.2, 0.3, 0.4, 0.5, 0.6, and 0.7. The choice of these compositions was based on a theoretical calculation[3] of the diagram of magnetic ordering (ferrimagnetic, antiferromagnetic, paramagnetic, and spin glass) in spinel ferrites as a function of nonmagnetic-ion content in the A and B sublattices of the ferrites. Because Ga^{3+} ions tend to occupy tetrahedral lattice positions, and Al^{3+} ions, octahedral positions of the spinel structure, we prepared ferrites having spinel structure, where nonmagnetic ions substitute for the magnetic ones simultaneously on the A and B sublattices.

The samples were prepared by ceramic technology. The first anneal was carried out at 750 °C for 20 h, and the second, at 900 °C for 20 h, with subsequent slow cooling. Both anneals were made in air. The measurements of magnetization σ and of the coercive force H_c were performed by the ballistic method in fields of up to 10 kOe within the 80–650 K temperature range. The relative error of magnetization measurements was approximately 3%. Magnetostriction was measured by means of strain gauges in magnetic fields of up to 12 kOe within the temperature range of 80–650 K. The relative magnetostriction measurement error was less than 3%.

These studies showed that spontaneous magnetization σ_s and the coercive force H_c in $x<0.4$ compositions vanish at the Curie point T_C. In samples with $x>0.4$, the coercive force becomes zero at T_C, and spontaneous magnetization drops sharply at a lower temperature T_{tr}. For illustration, Fig. 1 presents $\sigma_s(T)$ and $H_c(T)$ curves for the composition

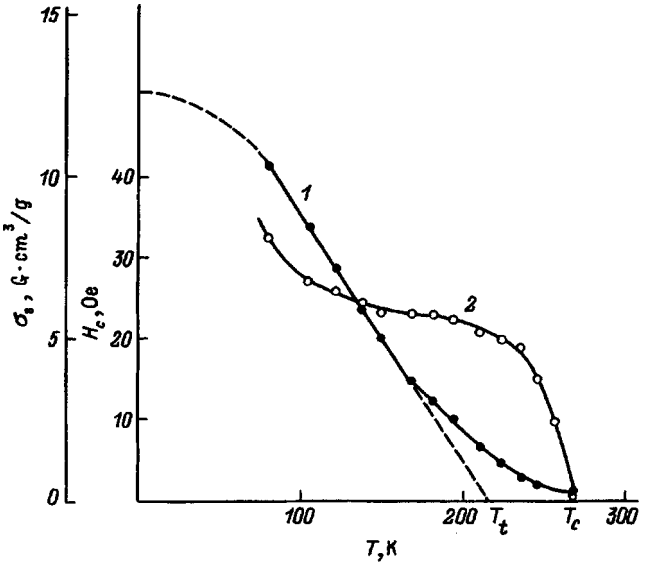

FIG. 1. Temperature dependence of (*1*) spontaneous magnetization σ_s and (*2*) coercive force H_c for a $x=0.7$ ferrite.

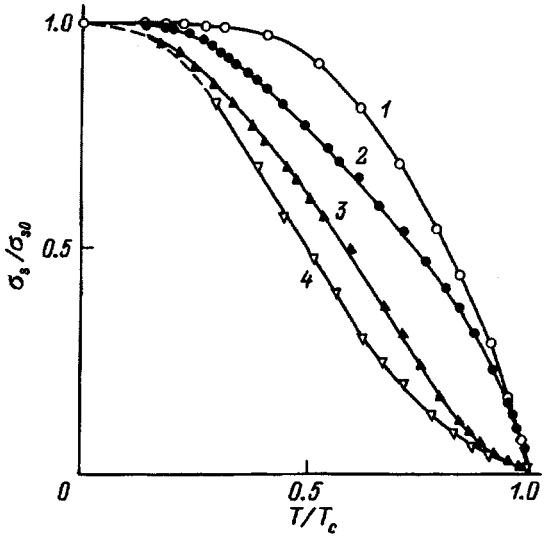

FIG. 2. Temperature dependence of relative spontaneous magnetization for (*1*) $CuFe_2O_4$, (*2*) $CuGa_{0.3}Al_{0.3}Fe_{1.4}O_4$, (*3*) $CuGa_{0.5}Al_{0.5}FeO_4$, and (*4*) $CuGa_{0.7}Al_{0.7}Fe_{0.6}O_4$.

with $x=0.7$. We readily see that σ_s decreases nearly linearly with increasing temperature within a broad temperature range, 80–170 K. Extrapolation of the linear portion of the $\sigma_s(T)$ relation to zero magnetization permitted us to determine the transition temperature $T_{tr}=215\pm5$ K, whereas the coercive force remains fairly large at this temperature and vanishes only at $T_C=270\pm5$ K.

It was shown theoretically[4,5] that if a magnetic compound has a paramagnetism–spin-glass transition, then further cooling should give rise to a second phase transition from spin glass to a mixed magnetic phase (magnetic phase + spin glass). It should be pointed out that theory[3] allows the onset of a spin-glass state in spinel ferrites with $x>0.4$ having the same amounts of nonmagnetic ions on the *A* and *B* sublattices. Based on our experimental results and on the conclusions drawn in Refs. 3–5, we put forward a suggestion that samples with $x>0.4$ undergo at T_C a transition from the paramagnetic to cluster spin-glass state, and at T_{tr}, from the cluster spin glass to a mixed magnetic phase. We observed a similar behavior of magnetization and of the coercive force in a study of the $CuFe_{2-x}Cr_xO_4$ system on samples with a high Cr^{3+} concentration.[2] In these chromite ferrites, the frustrated magnetic structure and the cluster spin glass form as a result of competition between the intersublattice negative *AB* and negative, both direct and indirect, intrasublattice *BB* interactions.

Extrapolation of the $\sigma_s(T)$ relation to $T=0$ yielded for all compositions the values of σ_{s0} with an error not above 5%. Figure 2 shows $(\sigma_s/\sigma_{s0})(T/T_C)$ plots for samples with $x=0.0$, 0.3, 0.5, and 0.7. We see that while for the samples with $x=0.0$ and 0.3 the $(\sigma_s/\sigma_{s0})(T/T_C)$ curves are *Q* type by Néel, for $x=0.5$ and 0.7 these relations follow an anomalous behavior, namely, within a considerable temperature interval the spontaneous magnetizations decrease linearly with increasing temperature to drop noticeably below T_C. Our studies of the residual magnetization σ_r in samples with $x=0.5$, 0.6, and 0.7 showed that it does not reverse sign throughout the temperature interval covered, so that the observed sharp decrease of σ_s at $T=T_{tr}$ is not connected in any way with the compensation temperature.

We calculated the magnetic moments $n_{0\,\mathrm{exp}}$ for all the $CuGa_xAl_xFe_{2-2x}O_4$ samples using the values of σ_{s0}. Figure 3 displays $H_c(x)$ relations (for $T=80$ K) and $n_{0\,\mathrm{exp}}(x)$, as well as $T_C(x)$ and $T_{tr}(x)$ for this compound. We see that for compositions with $x=0.0-0.4$ the magnetic moment $n_{0\,\mathrm{exp}}$ is approximately equal to 1.1 μ_B, which is in accord with

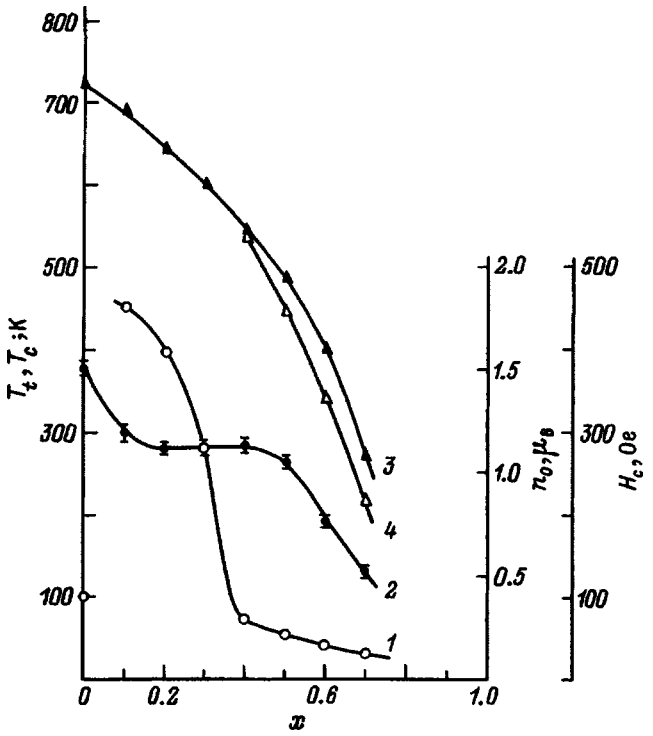

FIG. 3. (*1*) Coercive force H_c (for $T=80$ K), (*2*) magnetic moment $n_{0\,\mathrm{exp}}$, (*3*) Curie temperature T_C, and (*4*) transition temperature T_{tr} *vs* composition for samples of the $CuGa_xAl_xFe_{2-2x}O_4$ system.

$n_{0\,\mathrm{calc}}$ calculated under the assumption that Ga^{3+} ions occupy A sites, and Al^{3+} ions, B sites in the spinel lattice, and that starting with $x \geqslant 0.5$, $n_{0\,\mathrm{exp}}$ decreases considerably with increasing x. We believe that such a behavior of the magnetic moment $n_{0\,\mathrm{exp}}$ also may be considered as supporting our assumption of the formation of a frustrated magnetic structure in ferrites with $x \geqslant 0.5$. The Curie temperature T_C and the transition temperature T_{tr} (for compositions where such a transition takes place) decrease monotonically with increasing x for samples of this system.

It was established that the coercive force decreases strongly with increasing x up to $x=0.4$, after which the decrease slows down. The value of H_c for frustrated ferrites ($x>0.4$) is considerably smaller than that for ferrimagnetically ordered ferrites. For instance, at 293 K the $x=0.5$ composition has $H_c=31$ Oe, whereas for $x=0.2$, $H_c=315$ Oe. This suggests a conclusion that the onset of a frustrated magnetic structure results in a decrease of the ferrite magnetic anisotropy. Thus we have experimentally established the possibility of preparing magnetic materials with a low coercive force by creating in them a frustrated magnetic structure.[6]

It was found that the magnetization isotherms $\sigma(H)$ of all samples do not saturate. In order to learn whether this is due to the paraprocess or some other reason, we studied the behavior of the longitudinal, $\lambda_\parallel$, and transverse, $\lambda_\perp$, magnetostriction. It is known that within the region of technical magnetization the magnetostrictions $\lambda_\parallel$ and $\lambda_\perp$ are anisotropic, whereas in the region of the paraprocess they behave isotropically. Measurements of the longitudinal, $\lambda_\parallel$, and transverse, $\lambda_\perp$, magnetostrictions made on all $CuGa_xAl_xFe_{2-2x}O_4$ samples revealed that the $\lambda_\parallel(T)$ and $\lambda_\perp(T)$ relations and the $\lambda_\parallel(H)$ and $\lambda_\perp(H)$ isotherms behave differently in the $x<0.4$ and $x>0.4$ compositions. For illustration, Fig. 4 presents isotherms of the longitudinal, $\lambda_\parallel$, and transverse, $\lambda_\perp$, magnetostrictions obtained for a $x=0.7$ composition. We see that the $\lambda_\parallel(H)$ and $\lambda_\perp(H)$ relations are isotropic throughout the temperature region studied already in magnetic fields $H>1$ kOe, i.e., one observes here a substantial positive magnetostriction of the paraprocess λ_{para}. This implies that the role of technical magnetization in this sample is insignificant. As evident from Fig. 5, the $x=0.3$ sample also exhibits considerable magnetostriction of the paraprocess at low temperatures, which decreases strongly with increasing temperature, to practically vanish at $T=293$ K. Magnetostriction behaves in this way usually in noncollinear ferrimagnets in the low-temperature domain. The paraprocess sets in as a result of noncollinear ferrimagnetic ordering setting in in these materials. The results obtained suggest that introduction of nonmagnetic ions into the $x=0.3$ sample induced formation of a noncollinear ferrimagnetic structure at low temperatures.

We used the experimental values of the $\lambda_\parallel$ and $\lambda_\perp$ magnetostriction (in a field $H=12$ kOe) to calculate for all samples the volume, ω, and anisotropic, λ_t, magnetostriction as a function of temperature. The volume magnetostriction was calculated using the relation $\omega=\lambda_\parallel+2\lambda_\perp$, and the anisotropic one, from $\lambda_t=\lambda_\parallel-\lambda_\perp$. As seen from Fig. 6 presenting the results of measurements made on the $x=0.7$ composition, the $\lambda_\parallel$ and $\lambda_\perp$ magnetostrictions have positive sign and are approximately equal in magnitude, namely, magnetostriction λ_t is negative and very small, and magnetostriction ω, by contrast, is positive and fairly large. In the spin-glass state, however, i.e., for $T>215$ K, the magnetostrictions $\lambda_\parallel$, $\lambda_\perp$, and ω decrease by nearly an order of magnitude.

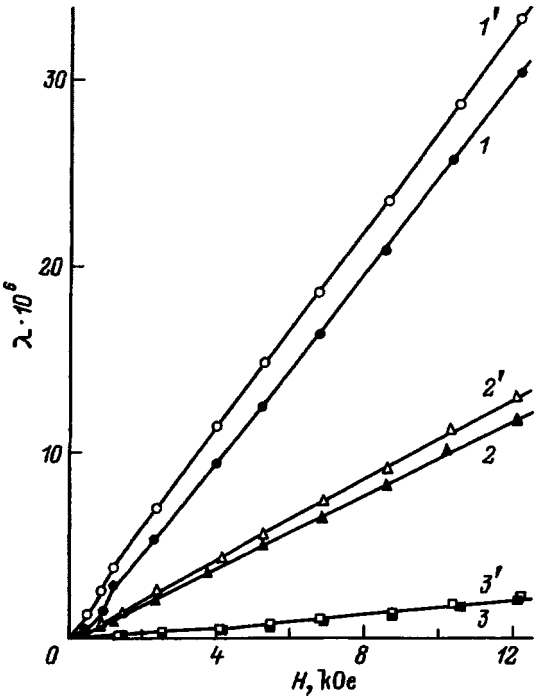

FIG. 4. Isotherms of (*1–3*) longitudinal magnetostriction $\lambda_\parallel$ and (*1′–3′*) transverse magnetostriction $\lambda_\perp$ for a $x=0.7$ ferrite obtained at different temperatures T(K): *1, 1′* — 89.5, *2, 2′* — 143, *3, 3′* — 245.5.

For comparison, Fig. 7 presents temperature dependences $\lambda_\parallel(T)$, $\lambda_\perp(T)$, $\omega(T)$, and $\lambda_t(T)$ for a $x=0.3$ ferrite

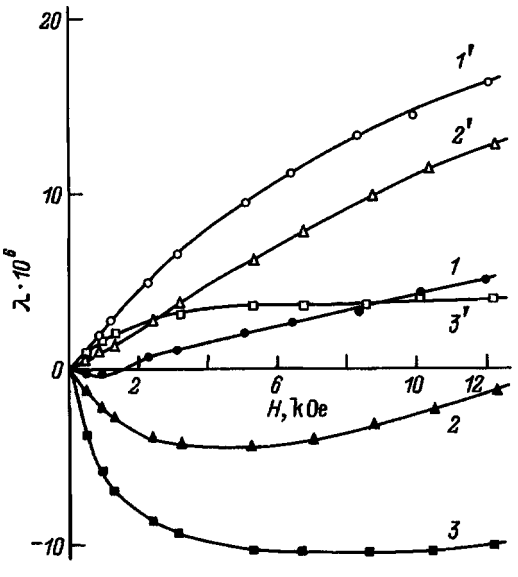

FIG. 5. Isotherms of (*1–3*) longitudinal magnetostriction $\lambda_\parallel$ and (*1′–3′*) transverse magnetostriction $\lambda_\perp$ for a $x=0.3$ ferrite obtained at different temperatures T(K): *1, 1′* — 82, *2, 2′* — 147, *3, 3′* — 294.

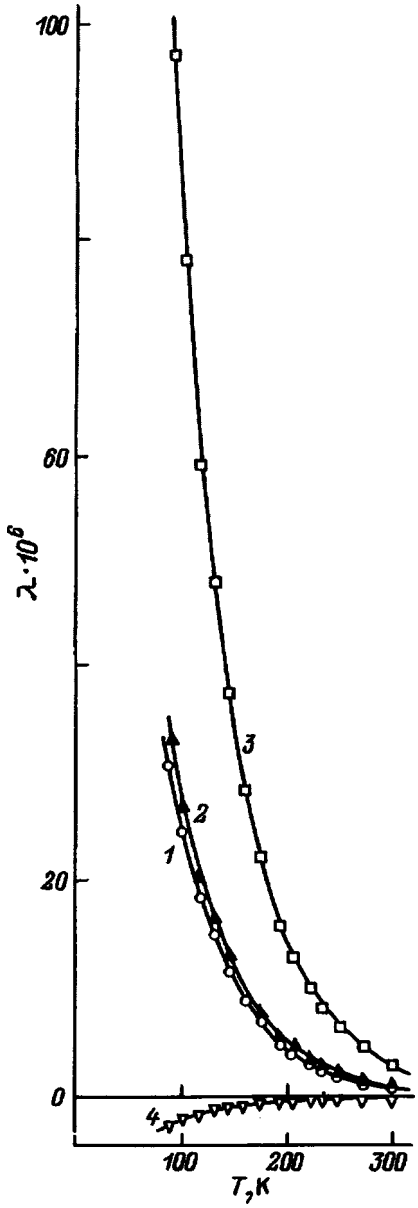

FIG. 6. Temperature dependences of (*1*) longitudinal $\lambda_{\parallel}$, (*2*) transverse $\lambda_{\perp}$, (*3*) volume ω, and (*4*) anisotropic, λ_t, magnetostrictions obtained in a field $H=12$ kOe for a $x=0.7$ ferrite.

with ferrimagnetic ordering. We readily see that these relations behave differently from those for a $x=0.7$ ferrite. For instance, in the sample with $x=0.3$ the volume magnetostriction ω is nearly three times smaller and reverses sign at ≈ 230 K from positive to negative, whereas λ_t is almost an order of magnitude larger.

We believe that the strong paraprocess in the samples with frustrated magnetic structure ($x>0.4$) is caused by the alignment of the magnetic moments of individual, spontaneously magnetized regions with the field, and the small magnitude of their anisotropic magnetostriction λ_t is connected with a small magnetic anisotropy.

Of particular interest is the observation of practically identical temperature and field dependences of the longitudinal, $\lambda_{\parallel}$, and transverse, $\lambda_{\perp}$, magnetostrictions in samples with frustrated magnetic structure ($x=0.5-0.7$). This implies that application of a field extends a sample nearly to the same degree both along and across its direction within a broad temperature range. We have observed such a behavior of the $\lambda_{\parallel}(T)$, $\lambda_{\perp}(T)$, $\lambda_{\parallel}(H)$, and $\lambda_{\perp}(H)$ relations for the first time. We believe that this phenomenon originates from the presence of a frustrated magnetic structure, and it is difficult to account for within the current theories describing magnetostriction of ferrites.

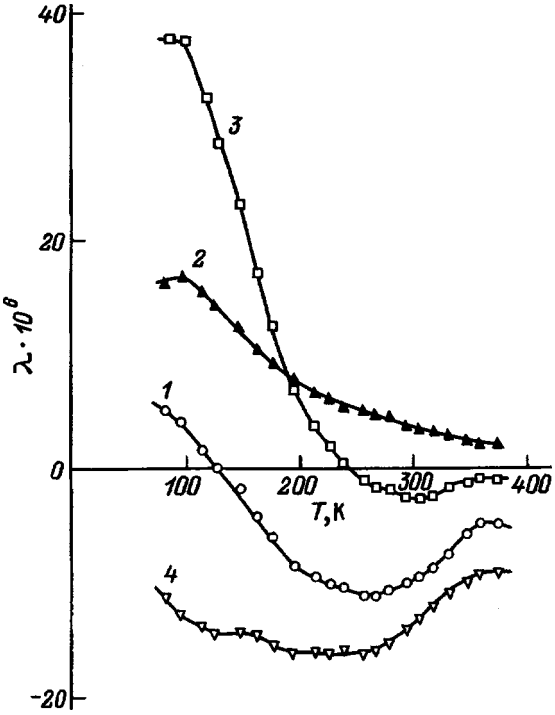

FIG. 7. Temperature dependences of (*1*) longitudinal $\lambda_{\parallel}$, (*2*) transverse $\lambda_{\perp}$, (*3*) volume ω, and (*4*) anisotropic, λ_t, magnetostrictions obtained in a field $H=12$ kOe for a $x=0.3$ ferrite.

Thus we have prepared for the first time samples of the $CuGa_xAl_xFe_{2-2x}O_4$ system, and studied the behavior of their magnetization, coercive force, and magnetostriction. It has been established that, depending on the content of nonmagnetic ions, this system can exhibit ferrimagnetic ordering, frustrated magnetic structure, or the cluster spin-glass state.

Our studies of frustrated ferrites showed them to possess a number of anomalous magnetic properties, which may prove to be useful for further progress in the theory of ferrites as well as for practical applications in the development of new magnetic materials.

The authors are grateful to A. N. Goryaga for valuable criticisms.

[1] V. S. Dotsenko, Usp. Fiz. Nauk **163**, 6, 1 (1993) [Phys. Usp. **36**, 455 (1993)].
[2] L. G. Antoshina, A. N. Goryaga, E. N. Kukudzhanova, and I. A. Fil'gus, Zh. Eksp. Teor. Fiz. **111**, 1732 (1997) [JETP **84**, 948 (1997)].
[3] C. P. Poole and H. A. Farach, Z. Phys. B **47**, 55 (1982).
[4] J. L. van Hemmen, Phys. Rev. Lett. **49**, 409 (1982).
[5] A. C. D. van Enter and J. L. van Hemmen, Phys. Rev. A **29**, 355 (1984).
[6] L. G. Antoshina, A. N. Goryaga, and E. N. Kukudzhanova, in *Abstracts of the 13th Conference on Soft Magnetic Materials (September 24–26, 1997)* (Grenoble, 1997), p. 237.

Translated by G. Skrebtsov

Phase transitions in a domain wall of the four-sublattice antiferromagnet La_2CuO_4 in a magnetic field

M. A. Shamsutdinov

Bashkir State University, 450074 Ufa, Russia

V. N. Nazarov

Institute of the Physics of Molecules and Crystals Russian Academy of Sciences, 450075 Ufa, Russia

(Submitted January 12, 1998)
Fiz. Tverd. Tela (St. Petersburg) **40**, 1510–1513 (August 1998)

The effect of an external magnetic field on the characteristics of domain walls was studied in a four-sublattice antiferromagnet La_2CuO_4. It was shown that a transition of domain-wall structure from one type into other types is possible for certain values of the fields. The critical fields of the transition were determined. The phase diagram of the stability of different types of domain walls was constructed. © *1998 American Institute of Physics.* [S1063-7834(98)02308-9]

Metal-oxide compounds, the class of compounds to which antiferromagnetic La_2CuO_4 belongs, are now being widely investigated both theoretically and experimentally. For a certain variation of its chemical composition, La_2CuO_4 exhibits high-temperature superconductivity, in studying whose nature a great deal of attention is devoted to the magnetic properties. This crystal possesses a tetragonal lattice with one ''octahedral molecule'' CuO_6[1,2] and is a four-sublattice weakly-collinear antiferromagnet with Néel temperature $T_N \approx 325$ K.[3] In this crystal it is possible to distinguish CuO_2 planes where all interactions are much stronger than the corresponding interplanar interactions. This circumstance makes it possible to introduce dimensionless ferromagnetism m_j and antiferromagnetism l_j $(j=1,2)$ vectors within the CuO_2 layers.[2,4]

The structure of domain walls in the four-sublattice antiferromagnet La_2CuO_4 was studied theoretically in Ref. 4 . Four types of domain walls (DWs), differing by the spin-rotation law in different sublattices, were found. The conditions for stability were determined in Ref. 5 , and the drift velocity of these DWs in an ac magnetic field was measured in Ref. 6 . The effect of an external magnetic field on DW structure in four-sublattice antiferromagnets has not been investigated. It is known that a magnetic field induces spin-reorientational transitions in the interior of a La_2CuO_4 crystal.[7] Similar transitions can also occur in a domain wall. A transition of one type of DW into another with a different spin-rotation plane has been observed in zero field in rare-earth orthoferrites[8] and in a nonzero field in collinear antiferromagnets with orthorhombic symmetry.[9,10] Such structural rearrangements of domain walls can be interpreted as phase transitions occurring in the walls.[8] Spin-reorientational transitions induced in DWs by an external magnetic field have been investigated theoretically only in a two-lattice model.[11,12]

The present paper is devoted to the investigation of the effect of an external magnetic field on the characteristics of 180° domain walls and on the spin-reorientational transitions in DWs in the four-sublattice antiferromagnet La_2CuO_4.

1. STRUCTURE OF A DOMAIN WALL IN A MAGNETIC FIELD

To study the structure of DWs we proceed from the following form of the free energy:[2,6]

$$W = 2M_0 \int \left\{ \sum_{j=1}^{2} \left[\frac{1}{2} H_e m_j^2 + H_D [m_j l_j]_x + \frac{1}{2}(H_{AZ} l_{jz}^2 - H_{AY} l_{jy}^2) - H m_j + \frac{1}{4} \alpha M_0 (\partial l_j / \partial x_i)^2 \right] + h_e' l_1 l_2 - h_a' (l_{1x} l_{2x} - l_{1y} l_{2y}) \right\} dr. \quad (1)$$

Here the Cartesian z axis is parallel to the direction C_4 and perpendicular to the CuO_2 planes, M_0 is the saturation magnetization of the sublattices, H_e and h_e' describe, respectively, the uniform intra- and interplane (primed) exchange interaction, H_D is the Dzyaloshinskiĭ field, H_{AZ} and H_{AY} are, respectively, the tetragonal and orthorhombic anisotropy fields, h_a' is the interplanar anisotropy field, α is the nonuniform exchange constant, H is the external magnetic field, and $x_i = x, y, z$.

In a uniform state with no external magnetic field and $\beta_1 = 2(H_{AZ} + H_{AY})/M_0 > 0$, $\beta_2 = 2(H_{AY} + H_D^2 H_e^{-1})/M_0 > 0$, $\delta_y = 2(h_e' + h_a')/M_0 > 0$ the vectors l_1 and l_2 are collinear to the y axis and antiparallel to one another.[4,5] In what follows we shall consider the case where the external magnetic field intensity, lying in the CuO_2 plane, is perpendicular to the vector l_j, i.e., $H \| x$. For $H \ll H_e$ the equilibrium direction of l_j does not change in the uniform state, m_j remaining much less than l_j. It is convenient to describe the DW structure in a spherical coordinate system $(l_j^2 \approx 1)$ $l_j = (-1)^{j+1} \times (\sin\theta_j \cos\varphi_j, \cos\theta_j, \sin\theta_j \sin\varphi_j)$. Proceeding from Eq. (1), it is possible to derive a system of four equations in the

variables θ_j and φ_j which admits two special classes of solutions. One class ($\varphi_1=\varphi_2=0$) corresponds to rotation of the vectors l_j in CuO_2, i.e., the xy plane. The second class of solutions ($\varphi_1=\varphi_2=\pi/2$) corresponds to rotation of the vectors l_j in the xz plane. In the zero-field case, to each class of solutions there are associated two types of DWs, differing by the spin-rotation law. Spin rotation in a domain wall can occur with and without destruction of the antiparallelism of the antiferromagnetism vectors l_j. Calculations show that an external magnetic field does not change the zero-field distribution law of l_j.[5] Only the DW thickness and energy can change. Under conditions of spin rotation with antiparallelism preserved the angles θ_j vary according to the law

$$\theta_1=\theta_2=2\tan^{-1}[\exp(\pi x/x_p)], \tag{2}$$

where $p=1A$ for $\varphi_1=\varphi_2=0$ and $p=2A$ in the case $\varphi_1=\varphi_2=\pi/2$. The dependence of the DW thickness on the external field in such a case is determined by the expressions

$$x_{1A}=\pi(\alpha/(\beta_2+\chi_\perp H^2/M_0^2+\delta_y-\delta_x))^{1/2},$$

$$x_{2A}=\pi(\alpha/(\beta_1+\delta_y-\delta_z))^{1/2}, \tag{3}$$

where $\delta_x=2(h_e'-h_a')/M_0$, $\delta_z=2h_e'/M_0$, $\chi_\perp=2M_0/H_e$. For $H=0$ the DWs described by Eq. (2), i.e., with index A, were termed acoustic.[4]

In two domain walls inwhich the antiparallelism of l_j ($\theta_1=-\theta_2$) is destroyed the exchange energy increases; such DWs ($1E$, $2E$) were termed exchange walls.[4] The distribution of θ_1 in them also is determined by an expression of the form (2), except that in this case, as calculations show, the DW thicknesses equal

$$x_{1E}=\pi(\alpha/(\beta_2+\chi_\perp H^2/M_0^2+\delta_y+\delta_x))^{1/2},$$

$$x_{2E}=\pi(\alpha/(\beta_1+\delta_y+\delta_z))^{1/2}. \tag{4}$$

One can see from Eqs. (3) and (4) that the thicknesses of the $1A$ and $1E$ (with spin rotation in the xy plane) domain walls decrease as the magnetic field intensity increases, while the thicknesses of the $2A$ and $2E$ walls (with spin rotation in the yz plane) do not depend on the field.

The energy of a 180° DW is inversely proportional to its thickness, i.e., $E_p=4\pi M_0^2\alpha/x_p$ ($p=1A$, $1E$, $2A$, $2E$). Analysis shows that the energies of two domain walls ($1A$, $1E$) in which the spins rotate in the CuO_2 plane increase as the magnetic-field intensity increases. In the case of the two other types of DWs ($2A$, $2E$), in which the spins turn in a plane parallel to the C_4 axis and perpendicular to the direction of the external magnetic field, the surface energy of a wall does not depend on the field.

A resulting magnetization equal to $M_x=4M_0H/H_e$ appears along the magnetic field in the entire sample. The other components of the magnetization in the case of all domain walls except DW-$2E$ equals zero. In the interior of a DW-$2E$ wall there exists a magnetization along the y axis, equal to $M_y=(4M_0H_D/H_e)\cosh^{-1}(\pi x/x_{2E})$. This circumstance apparently can be used to observe DW-$2E$. Such a domain wall should move in a magnetic-field gradient.

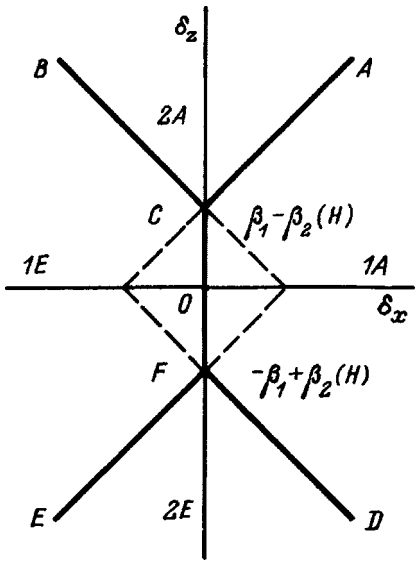

FIG. 1. Phase diagrams of domain-wall stability in fields $H<H_k$. Two types of DWs — $1A$ and $1E$ — are stable in the region bounded by the dashed lines.

2. SPIN-REORIENTATIONAL TRANSITIONS IN A DOMAIN WALL

We now proceed to the question of the stability of different types of DWs and phase transitions which are induced in a domain wall by an external magnetic field. Domain-wall stability can be determined by analyzing the second variation of the energy (1).

Let us analyze the condition for the stability of one of the four types of DWs, for example $1A$. Analysis shows that such a wall is stable if

$$\beta_1-\beta_2(H)+\delta_x-\delta_z\geqslant 0, \tag{5}$$

$$\beta_1-\beta_2(H)+\delta_x+\delta_z\geqslant 0, \tag{6}$$

$$s-(\beta_2(H)-\delta_x-\delta_y)/(\beta_2(H)-\delta_x+\delta_y)\geqslant 0, \tag{7}$$

where

$$\beta_2(H)=\beta_2+\chi_\perp(H/M_0)^2, \quad s=(\sqrt{1+4\Delta_{1A}}-1)/2,$$

$$\Delta_{1A}=2\beta_2(H)/(\beta_2(H)-\delta_x+\delta_y). \tag{8}$$

The equalities in Eqs. (5)–(7) correspond to lines of instability of DWs. Similar conditions can also be obtained for the other types of domain walls. Figures 1 and 2 show the regions of stability of different DWs in the $\delta_x\delta_z$ plane. Figures 1 and 2 correspond to the cases $H<H_k$ and $H>H_k$, respectively, where

$$H_k=M_0[(\beta_1-\beta_2)/\chi_\perp]^{1/2}=(H_eH_{AZ}-H_D^2)^{1/2}. \tag{9}$$

In the field $H=H_k$ there exists in the $\delta_x\delta_z$ plane a fourth point (the point to which the regions of stability of the four types of DWs converge) which arises when the triple points C and F merge with O in Fig. 1 (C_1 and F_1 with O in Fig. 2). The existence of triple and quadruple points attests to the fact that, from the thermodynamic standpoint (the Gibbs phase rule), a DW in the four-sublattice antiferromagnet La_2CuO_4 is a multicomponent heterogeneous medium,

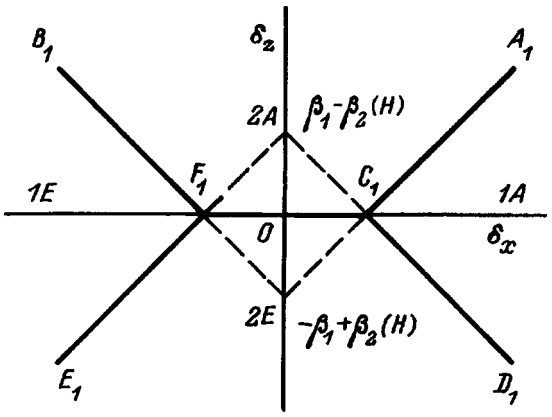

FIG. 2. Phase diagrams of domain-wall stability in fields $H>H_k$. Two types of DWs — $2A$ and $2E$ — are stable in the region bounded by the dashed lines.

where the intra- and interplanar anisotropies as well as the interplanar exchange interaction play the role of the components.

When the inequality (5) breaks down, DW-1A become unstable and transform into DW-2A (the line AC in Fig. 1, A_1C_1 in Fig, 2). The transition field equals

$$H_1=H_k\left(1+\frac{\delta_x-\delta_z}{\beta_1-\beta_2}\right)^{1/2}. \tag{10}$$

In the case when the inequality (6) breaks down a transition of DW-1A into DW-2E occurs (the line FD in Fig. 1, C_1D_1 in Fig. 2). The field H_2 of such a transition can be represented in the form

$$H_2=H_k\left(1+\frac{\delta_x+\delta_z}{\beta_1-\beta_2}\right)^{1/2}. \tag{11}$$

We note that the field of the transition of DW-1E into DW-2A (DW-2E) can be obtained by replacing in $H_1(H_2)$ the parameter δ_x by $-\delta_x$.

Such rearrangements of DW structure can be regarded as a peculiar kind of spin-reorientational transition occurring only in a domain wall. As shown in the case of rare-earth orthoferrites,[11] such transitions can occur by menas of first- and second-order phase transitions. It should be noted that, to determine the character of the phase transition in the case of the types of rearrangement of DW structure which were studied above, it is necessary to include in Eq. (1) terms which are proportional to the fourth power of the components l_j. The values of the phase-transition fields with $H_{AZ}\gg h'_e h'_a$ are close to H_k. Estimates in the case of the antiferromagnet La_2CuO_4, according to the data of Ref. 13 , show that $H_k \approx 5\times 10^3$ Oe, while the values of the phase-transition fields should lie in the interval 10^3-10^4 Oe.

Let us now consider the transition of DW-1A into DW-1E. For $H<H_k$ this transition occurs by menas of a first-order phase transition (the line CF in Fig. 1) with $\delta_x=0$. In the case $H>H_k$ the situation changes sharply and the transition of DW-1A into DW-1E can occur via DW-2A ($\delta_z>0$) or DW-2E ($\delta_z<0$) (see Fig. 2). Finally, let us analyze the transition of DW-2A into DW-2E. For $H<H_k$ such a transition can occur only via DW-1A ($\delta_x>0$) or DW-1E ($\delta_x<0$). In the case $H>H_k$ a rearrangement of the DW-2A structure into DW-2E occurs as a first-order phase transition (the line F_1C_1 in Fig. 2) with $\delta_z=0$. Thus, the character of the phase transitions can change at the critical field H_k corresponding to the quadruple point in the $\delta_x\delta_z$ plane.

We call attention to the possibility of observing a magnetic phase transition in a domain wall. The rearrangement of DW structure can be observed by investigating the dependence of the susceptibility of a sample on the external magnetic field. As shown in the case of orthoferrites,[11] the susceptibility should increase as H approaches the phase-transition fields. A phase transition in a DW of a collinear antiferromagnet has been observed experimentally by such a method.[12]

In summary, our investigations show that as the intensity of the external magnetic field increases, at certain critical values DWs with spin rotation in the CuO_2 plane become unstable. A rearrangement of the DW structure, which can be regarded as a peculiar kind of spin-reorientational transition, occurs. The character of these transitions can change in a certain field, equal to the field at which a quadruple point exists, i.e. a point where the regions of stability of the four types of DWs converge. Above the phase-transition fields DWs with spin rotation in a plane parallel to the C_4 axis and perpendicular to the magnetic field become stable. As a result, as the intensity of the external magnetic field parallel to the CuO_2 plane and perpendicular to the direction of the antiferromagnetism vectors in domains increases, the regions of stability of of DW-1A and DW-1E in the $\delta_x\delta_z$ plane become narrower, while the regions of stability of DW-2A and DW-2E become wider.

This work was supported by a grant from MOPO of the Russian Federation in the field of fundamental natural science.

[1] A. S. Borovik-Romanov, A. I. Buzdin, N. M. Kreĭnes, and S. S. Krotov, JETP Lett. **47**, 697 (1988).
[2] V. G. Bar'yakhtar, V. M. Loktev, and D. A. Yablonskiĭ, Preprint ITF-88-81R, Kiev (1988).
[3] B. I. Belevtsev, N. V. Dalakova, and A. S. Panfilov, Fiz. Nizk. Temp. **23**, 375 (1997) [Low Temp. Phys. **23**, 274 (1997)].
[4] V. G. Bar'yakhtar, A. L. Sukstanskiĭ, and D. A. Yablonskiĭ, Fiz. Tverd. Tela (Leningrad) **32**, 1231 (1990) [Sov. Phys. Solid State **32**, 723 (1990)].
[5] A. L. Sukstanskiĭ, Preprint DonFTI-90-20, Donetsk (1990).
[6] V. S. Gerasimchuk and A. L. Sukstanskiĭ, Fiz. Nizk. Temp. **20**, 142 (1994) [Low Temp. Phys. **20**, 114 (1994)].
[7] V. N. Krivoruchko and T. E. Primak, Fiz. Nizk.Temp. **19**, 871 (1993) [Low Temp. Phys. **19**, 620 (1993)].
[8] A. V. Zalesskiĭ, A. M. Savvinov, I. S. Zheludev, and A. N. Ivashchenko, Zh. Eksp. Teor. Fiz. **68**(4), 1449 (1975) [Sov. Phys. JETP **41**, 723 (1975)].
[9] A. N. Bogdanov, V. A. Galushko, V. T. Telepa, and D. A. Yablonskiĭ, JETP Lett. **40**, 1279 (1984).
[10] A. N. Bogdanov, V. G. Telepa, P. P. Shatskiĭ, and D. A. Yablonskiĭ, Zh. Éksp. Teor. Fiz. **90**, 1738 (1986) [Sov. Phys. JETP **63**, 1018 (1986)].
[11] M. A. Shamstudinov, M. M. Farztdinov, and A. A. Khalfina, Fiz. Tverd. Tela (Leningrad) **31**, 112 (1989) [Sov. Phys. Solid State **31**, 237 (1989)].
[12] A. N. Bogdanov and A. I. Puzynya, Fiz. Tverd. Tela (St. Petersburg) **38**, 2072 (1996) [Phys. Solid State **38**, 1143 (1996)].
[13] V. E. Kataev, E. F. Kukovitskiĭ, Yu. I. Talanov, and G. B. Teĭtel'baum, JETP Lett. **48**, 101 (1988).

Translated by M. E. Alferieff

Effect of the susceptibility on the magnetic phase diagrams of a ferrimagnet with magnetic instability

N. P. Kolmakova and M. Yu. Nekrasova

Bryansk State Technical University, 241035 Bryansk, Russia

R. Z. Levitin

M. V. Lomonosov Moscow State University, 119899 Moscow, Russia

(Submitted January 14, 1998)
Fiz. Tverd. Tela (St. Petersburg) **40**, 1514–1518 (August 1998)

The magnetic phase diagrams of a two-sublattice ferrimagnet with a magnetically unstable subsystem are calculated taking account of the susceptibility. Analytic expressions are obtained for the phase-transition fields and critical values of the parameters of the ferrimagnet. The evolution of the magnetic phase diagrams as the susceptibility of the unstable sublattice increases is analyzed. © *1998 American Institute of Physics.* [S1063-7834(98)02408-3]

In the last few years a great deal of attention has been devoted to the experimental and theoretical study of ferrimagnets in which one of the magnetic sublattices is magnetically unstable, i.e., in a magnetic field it undergoes a metamagnetic transition from a weakly to a strongly magnetic state. Magnetic phase diagrams (MPDs) and therefore also the magnetization curves of such ferrimagnets are much more complicated and interesting than in the case of ordinary ferrimagnets with stable sublattices, since in them, together with second-order phase transitions into a noncollinear phase, metamagnetic transitions arise in the unstable subsystem and interference of the two types of transitions is possible. In Ref. 1 all possible MPDs were calculated and the possible types of magnetization curves of these ferrimagnets were presented, but the theoretical investigation neglected the magnetic susceptibilities. Meanwhile, the importance of taking the susceptibility into account follows at least from the well-known fact that even in a simple ferrimagnet, depending on the susceptibility in the collinear phase, different MPDs are formed: A noncollinear phase either arises or does not arise. The existing quite extensive experimental data for intermetallic compounds $YR(CoAl)_2$ of the Laves phases type, whose itinerant *d* subsystem is magnetically unstable and can serve as an example of the class of ferrimagnets under study, likewise shows the necessity of taking into account the susceptibility of the unstable subsystem. The magnetization curves of the compounds $YR(CoAl)_2$ with different rare earths (REs) and different aluminum concentration have been measured in fields up to 100 T. They have a very diverse form.[2–4] Specifically, for Tm compounds two metamagnetic transitions separated by a noncollinear phase were observed on the magnetization curve.[5] To interpret all of these experimental data we have developed a numerical method in which the properties of the unstable sublattice are described by means of an experimental magnetization curve of the base (no RE) compound $Y(CoAl)_2$. This approach made it possible to interpret very successfully the magnetic properties of the compounds under study.[1–5] However, an analytical study is required in order to answer the questions of whether taking the susceptibility into account leads to the appearance of new MPDs, as compared with those presented in Ref. 1, and how the phase-transition fields and critical values of the parameters of a ferrimagnet depend on the susceptibility. The present paper is devoted to such a study.

1. MODEL

Let us consider a two-sublattice ferrimagnet, one magnetic subsystem of which undergoes a metamagnetic transition in a field H_m from a weakly magnetic state (w) with spontaneous magnetization m and magnetic susceptibility χ_w into a strongly magnetic state (s) with magnetization M at the point of the metamagnetic transition and magnetic susceptibility χ_s. This magnetic subsystem is in an effective field as a result of the presence of a negative exchange interaction, characterized by the exchange parameter λ_{12}, $H_{\text{eff}} = H + \lambda_{12} M_2$, where M_2 is the magnetic moment of the second sublattice,

$$M_1 = \begin{cases} m + \chi_w H_{\text{eff}}, & H_{\text{eff}} < H_m, \\ M + \chi_w (H_{\text{eff}} - H_m), & H_{\text{eff}} > H_m. \end{cases} \tag{1}$$

For simplicity the second magnetic subsystem is characterized by a magnetic moment M_2 of constant magnitude, since our numerical calculations showed that for low temperatures this is a good approximation. We shall solve this problem on the basis of the molecular-field theory.

The thermodynamic potential of the ferrimagnet under study can be written in the form

$$G = F - H(M_1 + M_2) + \lambda M_1 M_2,$$

$$\lambda = |\lambda_{12}|, \quad \lambda_{12} < 0. \tag{2}$$

Here F is the thermodynamic potential of the unstable subsystem in an effective field and is different for weakly and

strongly magnetic states. Using the thermodynamic relation $F=\int_0^{M_1} H_{\rm eff}(M_1)dM_1$ and the magnetization curve of the unstable sublattice (1), we obtain

$$F_w=\chi_w H_{\rm eff}^2/2=(M_1-m)^2/2\chi_w,$$
$$F_s=-\chi_w H_m^2/2+H_m(M-m)+\chi_s(H_{\rm eff}^2-H_m^2)/2$$
$$=-\chi_w H_m^2/2+H_m(M-m)+(M_1-M)^2/2\chi_s. \qquad (3)$$

In the noncollinear phases the quantity M_1 and the characteristic energy of the unstable sublattice, determined by it, equal these values in the corresponding ferrimagnetic phases in the phase-transition fields, since, as is well known,[6] in the molecular-field approximation the magnetic moments of the sublattices in the noncollinear phase do not depend on the magnitude of the field.

Let us now determine the contribution of the susceptibility of the unstable sublattice to the formation of magnetic phase diagrams. Following the nomenclature introduced in Ref. 1, we list all possible states of the ferrimagnet under study: AW — ferrimagnetic weak phase, AS — ferrimagnetic strong phase, FW — ferromagnetic weak phase, FS — ferromagnetic strong phase, NW — noncollinear weak phase, and NS — noncollinear strong phase. We shall determine the existence regions of these phases and the fields giving rise to transitions between them in the molecular-field approximation, analyzing the signs and the magnitudes of the effective fields acting on the sublattice and choosing the phase with the minimum value of the equilibrium thermodynamic potential. In Ref. 1 the MPDs are presented in the coordinates (magnetic field H, concentration t of the atoms of the stable subsystem). By varying the concentration t, i.e., the magnetic moment M_2 of the stable subsystem it is possible to vary the effective field acting on the unstable subsystem and to realize different sections of the MPDs. Depending on the magnitude of the exchange interaction, four MPDs differing substantially with respect to their topology were obtained in these coordinates. In analyzing the MPDs taking the susceptibility into account, the following questions must be answered: Are the main types of MPDs the same as before? How do the exhange parameter criteria for classifying MPDs change? How do the phase-transition fields and the critical values of t (or M_2) depend on the susceptibilities χ_w and χ_s? In our analysis we shall adhere to the terminology of Ref. 1, where the field H_m of the metamagnetic transition, the spontaneous magnetization m in the weak phase, and the magnetization M in the strong phase at the point of the metamagnetic transition are the fixed parameters of the unstable subsystem.

2. MAGNETIC PHASE DIAGRAMS TAKING ACCOUNT OF THE SUSCEPTIBILITY

Depending on the strength of the exchange interaction, MPDs are characterized by a different sequence of initial states (for $H=0$) as M_2 increases. For this reason, as done in Ref. 1, we shall classify the MPDs using the exchange parameter λ as the criterion, and we shall examine the effect of the susceptibility separately for each characteristic interval of λ.

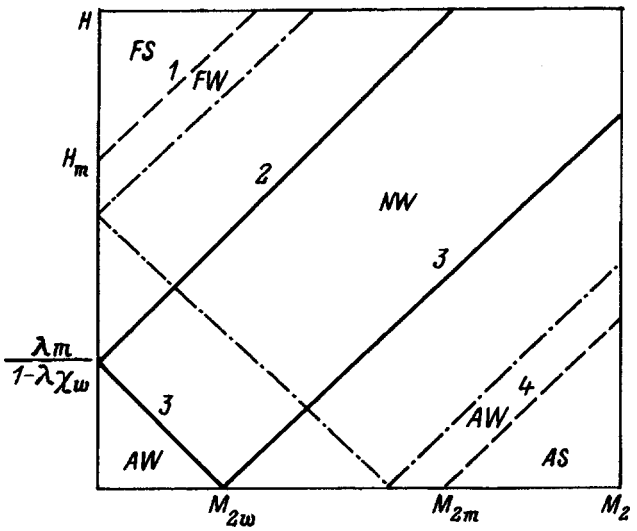

FIG. 1. Magnetic phase diagram of a ferrimagnet with an unstable subsystem in the case of weak exchange $\lambda<H_m/H$. The first- and second-order phase transitions are shown by the dashed and solid lines, respectively. *1* — H_{m1}, *2* — H_{2w}, *3* — H_{1w}, *4* — H_{m2}. The second-order phase transitions for large values of the susceptibilities are shown by the dot-dashed lines.

1) *Weak exchange.* In the case of weak interaction, where

$$\lambda<H_m/M, \qquad (4)$$

the MPD has the form shown in Fig. 1. The fields of the metamagnetic transitions FW $\leftrightarrow$ FS (H_{m1}) and AW $\leftrightarrow$ AS (H_{m2}) do not depend on the susceptibilities and equal, as before,

$$H_{m1}=H_m+\lambda M_2, \quad H_{m2}=\lambda M_2-H_m. \qquad (5)$$

The fields of the second-order phase transitions AW $\leftrightarrow$ NW (H_{1w}) and NW $\leftrightarrow$ FW (H_{2w}) depend on χ_w as follows:

$$H_{1w}=\lambda\left|\frac{m}{1-\lambda\chi_w}-M_2\right|,$$
$$H_{2w}=\lambda\left|\frac{m}{1-\lambda\chi_w}+M_2\right|. \qquad (6)$$

The compensation point M_{2w} with respect to the weakly magnetic state likewise depends on χ_w and equals

$$M_{2w}=\frac{m}{1-\lambda\chi_w}. \qquad (7)$$

One can see from Eqs. (5)–(7) that as χ_w increases, M_{2w} approaches

$$M_{2m}=H_m/\lambda, \qquad (8)$$

H_{2w} approaches H_{m1}, while H_{1w} approaches H_{m2}. For the susceptibility $\chi_w=(1/\lambda)-(m/H_m)$ these points and lines would coincide, but this cannot happen, since χ_w is limited by the condition of the existence of a jump in magnetization on the initial metamagnetic curve of the unstable sublattice

$$\chi_w<\chi_x^{\rm cr}=(M-m)/H_m. \qquad (9)$$

The critical fields with $\chi_w^{\rm cr}$ are shown in Fig. 1 by dot-dashed lines. One can see that the MPDs and the magnetization

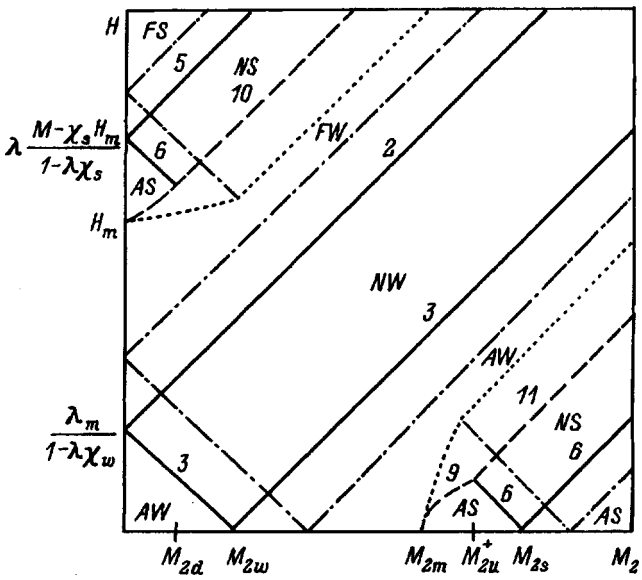

FIG. 2. Same as Fig. 1, for the case of intermediate exchange ($\lambda > H_m/H$, expression (12) is negative). *5* — H_{2s}, *6* — H_{1s}, *9* — H_{m4}, *10* — H_{m6}, *11* — H_{m7}. The first-order phase transitions for large values of the susceptibilities are shown by the dotted lines. The rest of the notation is the same as in Fig. 1.

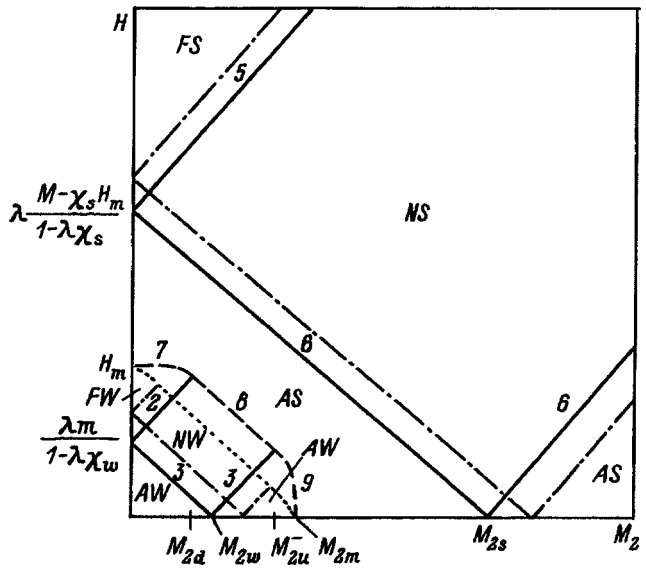

FIG. 3. Same as Fig. 2, for the case of intermediate exchange (the expression (12) is positive, $\lambda < H_m(m+\chi_w H_w)$). *7* — H_{m3}, *8* — H_{m5}.

curves taking account of the susceptibility for weak exchange are qualitatively the same as when exchange is neglected, only the values of the critical fields change. On account of the more stringent restriction (9), the situation $\chi_w > 1/\lambda$ is not realized at all and NW always appear when $m \neq 0$.

2) *Intermediate exchange.* If λ satisfies the condition

$$\frac{H_m}{M} < \lambda < \frac{H_m}{m+\chi_w H_m}, \tag{10}$$

which corresponds to the situation of an intermediate exchange interaction, at $H=0$ there appears a compensation point for the strongly magnetic state

$$M_{2s} = \frac{M-\chi_s H_m}{1-\lambda\chi_s}. \tag{11}$$

The MPD becomes much more complicated, having a different form depending on the sign of the expression

$$\lambda\frac{(M-\chi_s H_m)^2}{1-\lambda\chi_s} - \lambda\frac{m^2}{1-\lambda\chi_w} - 2H_m(M-m) + (\chi_w+\chi_s)H_m^2, \tag{12}$$

and is shown in Fig. 2 for the case when this combination of parameters of the ferrimagnet is negative and in Fig. 3 for the positive case.

Only the fields of the second-order phase transitions AS $\leftrightarrow$ NS (H_{1s}) and NS $\leftrightarrow$ FS (H_{2s}) depend on χ_s:

$$H_{1s} = \lambda\left|M_2 - \frac{M-\chi_s H_m}{1-\lambda\chi_s}\right|,$$

$$H_{2s} = \lambda\left|M_2 + \frac{M-\chi_s H_m}{1-\lambda\chi_s}\right|. \tag{13}$$

All other critical fields and critical points, which are new compared with MPDs for weak exchange, depend on both χ_s and χ_w. In the fields of first-order phase transitions FW $\leftrightarrow$ AS (H_{m3}), AS $\leftrightarrow$ AW (H_{m4}), NW $\leftrightarrow$ AS (H_{m5}), AW $\leftrightarrow$ NS (H_{m6}), and FW $\leftrightarrow$ NS (H_{m7}) the orientation of the magnetic moments of both sublattices relative to the external field changes. This distinguishes them from the metamagnetic transitions in the fields H_{m1} and H_{m2} (5), where only the magnitude of the magnetic moment of the unstable sublattice changes, while the orientation of the magnetic moments does not change,

$$H_{m3} = H_m + \frac{(2H_m-\lambda M-\lambda m)M_2 + \chi_s H_m(H_m-\lambda M_2) + \chi_w(\lambda^2 M_2^2 - H_m^2 - 2\lambda M_2 H_m)/2}{M-m-2M_2+\chi_w\lambda M_2 - \chi_s(H_m-\lambda M_2)},$$

$$H_{m4} = \frac{(H_m-\lambda M_2)(M-m) - \chi_s(H_m+\lambda M_2)^2/2 - \chi_w(H_m^2-\lambda^2 M_2^2)/2}{M+m-2M_2+\chi_w\lambda M_2+\chi_s(H_m+\lambda M_2)},$$

$$H_{m5} = \lambda\left(\frac{M-\chi_s H_m}{1-\lambda\chi_s} - M_2\right) - \left\{\frac{\lambda}{1-\lambda\chi_s}\left[-2H_m(M-m) + \lambda\frac{(M-\chi_s H_m)^2}{1-\lambda\chi_s} - \frac{\lambda m^2}{1-\lambda\chi_w} + (\chi_w+\chi_s)H_m^2\right]\right\}^{1/2}, \tag{14}$$

$$H_{m6}=\lambda\left(M_2+\frac{m}{1-\lambda\chi_w}\right)+\left\{\frac{\lambda}{1-\lambda\chi_w}\left[2H_m(M-m)-\lambda\frac{(M-\chi_sH_m)^2}{1-\lambda\chi_s}+\frac{\lambda m^2}{1-\lambda\chi_w}-(\chi_w+\chi_s)H_m^2\right]\right\}^{1/2},$$

$$H_{m7}=\lambda\left(M_2-\frac{m}{1-\lambda\chi_w}\right)-\left\{\frac{\lambda}{1-\lambda\chi_w}\left[2H_m(M-m)-\lambda\frac{(M-\chi_sH_m)^2}{1-\lambda\chi_s}+\frac{\lambda m^2}{1-\lambda\chi_w}-(\chi_w+\chi_s)H_m^2\right]\right\}^{1/2}.$$

The expressions for H_{m3} and H_{m4} were written out for the condition $\chi_w<1/\lambda$, $(M-m)/H_m$, $\chi_s<1/\lambda$.

The critical values of M_2 in the diagrams presented in Figs. 2 and 3 equal

$$M_{2u}^{\pm}=\frac{1}{2}\left(\frac{M-\chi_sH_m}{1-\lambda\chi_s}+\frac{m}{1-\lambda\chi_w}\right)\pm\frac{1}{2\lambda}\left\{\frac{\lambda}{1-\lambda\chi_w}\left|2H_m(M-m)-\lambda\frac{(M-\chi_sH_m)^2}{1-\lambda\chi_s}+\frac{\lambda m^2}{1-\lambda\chi_w}-(\chi_w+\chi_s)H_m^2\right|\right\}^{1/2},$$

$$M_{2d}=\frac{1}{2}\left(\frac{M-\chi_sH_m}{1-\lambda\chi_s}-\frac{m}{1-\lambda\chi_w}\right)-\frac{1}{2\lambda}\left\{\frac{\lambda}{1-\lambda\chi_w}\left|2H_m(M-m)-\lambda\frac{(M-\chi_sH_m)^2}{1-\lambda\chi_s}+\frac{\lambda m^2}{1-\lambda\chi_w}-(\chi_w+\chi_s)H_m^2\right|\right\}^{1/2}. \quad (15)$$

The motion of the critical fields as χ_w and χ_s increase is shown in Figs. 2 and 3 (dot-dashed lines for second-order phase transitions and dotted lines for first-order phase transitions). Thus, for a fixed value of the exchange parameter $\lambda>H_m/H$, when the MPD has the form shown in Fig. 2, taking account of the susceptibilities χ_m and χ_s with adequate magnitudes leads to collapse of the lines H_{2w}, H_{m6}, and H_{1w},H_{m7} and to the appearance of a line H_{m5}; the phase diagram has the form shown in Fig. 3. This occurs at the moment when the expression (12) changes sign. When it equals zero, the field $H_{m3}=H_m$, while the field H_{m4} is described by the equation $M_2=M_{2m}$. We note that such equations are obtained from an analysis of the complete expressions for H_{m3} and H_{m4}; only the main terms are presented in Eq. (14). We underscore once again that a change in the sign of the expression (12) and the transition from the MPD shown in Fig. 2 to the MPD shown in Fig. 3 are possible both as a result of an increase in χ_w and as a result of an increase in χ_s. Further growth of χ_w and χ_s leads to a decrease in the regions of existence of NW, FW and AW (between M_{2w} and M_{2m}), as shown in Fig. 3, but these regions can vanish only if the exchange interaction increases, but not on account of the susceptibility χ_w, which for intermediate exchange (see Eq. (10)) is limited by the relation $\chi_w<(1/\lambda)-(m/H_m)$.

3) *Strong exchange.* For $\lambda>H_m/(m+\chi_wH_m)$, which corresponds to the situation of strong exchange, the regions NW, FW, and AW (between M_{2w} and M_{2m}) in Fig. 3 vanish, and a line of the phase transition AW $\leftrightarrow$ AS (H_{m2}) appears. The rest of the MPD has the same form as that shown in Fig. 3, with the same evolution of the states as χ_s increases.

In summary, taking account of the susceptibility of the unstable sublattice of a two-sublattice ferrimagnet does not change the form of the magnetic phase diagrams calculated neglecting it, if $\chi_s<1/\lambda$. Moreover, the division into situations of weak, intermediate, and strong exchange interaction is virtually independent of the susceptibility. This is understandable, since the spectrum of the initial states of the ferrimagnet does not depend on the susceptibility for different values of the magnetic moment M_2 of the stable sublattice, which determines the gradation of the exchange-interaction strengths. However, in the case of intermediate exchange the particular MPD (presented in Figs. 2 or 3) that will materialize does depend very strongly on the susceptibilities. In addition, a transition from one MPD to another with a fixed value of the exchange parameter λ is possible as a result of an increase in both χ_w and χ_s. Both susceptibilities strongly limit the existence region of MPDs which is presented in Fig. 2. A large value of χ_s qualitatively changes the MPD, a noncollinear phase does not arise, and magnetization reversal of the ferrimagnet occurs as a result of χ_s. We note that taking account of the smearing of the metamagnetic transition over some interval of fields, which could be due to, for example, the nonuniformity of the sample, leads to a single result — all metamagnetic transitions in which the orientation of the unstable sublattice relative to the external field does not change are broadened over the same interval of fields. As our numerical calculations showed,[1–5] the nonlinearity of the magnetization curve of the unstable subsystem results in corresponding nonlinearities in the magnetization curves of a ferrimagnet in collinear phases.

This work was supported by the Russian Fund for Fundamental Research (Project 96-02-16373) and INTAS–RFFI (Project 96-IN-RU-641).

[1] I. S. Dubenko, N. P. Kolmakova, R. Z. Levitin, A. S. Markosyan, and A. K. Zvezdin, J. Magn. Magn. Mater. **153**, 207 (1996).
[2] T. Goto, I. S. Dubenko, N. P. Kolmakova, K. Koui, R. Z. Levitin, and M. Yu. Nekrasova, Fiz. Tverd. Tela (St. Petersburg) **38**, 1037 (1996) [Phys. Solid State **38**, 575 (1996)].
[3] T. Goto, I. S. Dubenko, N. P. Kolmakova, K. Koui, R. Z. Levitin, and M. Yu. Nekrasova, Fiz. Met. Metalloved. **82**, 4 (1997).
[4] M. I. Bartashevich, T. Goto, I. S. Dubenko, N. P. Kolmakova, S. A. Kolonogii, R. Z. Levitin, and A. S. Markosyan, Physica B (1998), in press.
[5] P. E. Brommer, I. S. Dubenko, J. J. M. Franse, F. Kayzel, N. P. Kolmakova, R. Z. Levitin, A. S. Markosyan, and A. Yu. Sokolov, Phys. Lett. A **189**, 253 (1994).
[6] K. P. Belov, A. K. Zvezdin, A. M. Kadomtsev, and R. Z. Levitin, *Orientational Transitions in Rare-Earth Magnets* [in Russian], Nauka, Moscow (1979), 317 pp.

Translated by M. E. Alferieff

Relation between relaxation losses in domain-wall motion and ferromagnetic resonance in garnet films

V. A. Bokov, V. V. Volkov, and N. L. Petrichenko

A. F. Ioffe Physicotechnical Institute, Russian Academy of Sciences, 194021 St. Petersburg, Russia

M. Maryshko

Institute of Physics, Czech Academy of Sciences, 16200 Prague, Czech Republic
(Submitted January 27, 1998)
Fiz. Tverd. Tela (St. Petersburg) **40**, 1519–1525 (August 1998)

Domain-wall mobility has been studied in garnet films having perpendicular magnetic anisotropy and a narrow FMR line. An analysis of the obtained and published experimental data shows that for the value of the Landau-Lifshits reduced damping parameter derived from FMR measurements, $\Lambda_{FMR} > 2.4\times10^{-9}$ Oe$^2\cdot$s, the domain-wall mobility is inversely proportional to Λ_{FMR}, which is in agreement with classical theory. For $\Lambda_{FMR} < 2.4\times10^{-9}$ Oe$^2\cdot$s, the mobility decreases with decreasing Λ_{FMR}. Possible reasons for this behavior are discussed. An empirical expression relating the losses entailed in domain motion to FMR-related losses for small Λ_{FMR} is proposed. © *1998 American Institute of Physics.* [S1063-7834(98)02508-8]

The damping parameter entering the Landau-Lifshits equation of magnetization motion is contained both in the expression for the FMR linewidth and in the relation for the domain-wall mobility, which offers two ways of its determination. The correspondence between the damping parameters derived from mobility and FMR measurements is a problem discussed repeatedly in the literature. The parameters obtained by the two ways were compared first in a study of single-crystal magnetite and nickel ferrite,[1] and, later, for manganese ferrite.[2] While the values extracted from the mobility data differed somewhat from those found from FMR measurements, they were of the same order of magnitude. The domain-wall mobility μ determined in YIG single crystals exhibiting a very narrow FMR line turned out to be more than two orders of magnitude smaller than that obtained from FMR data.[3] A similar large discrepancy was observed also in YIG crystals doped slightly with Yb^{3+} above 100 K.[4] The damping parameters found from domain-wall resonance and FMR measurements were observed to agree for a number of rare-earth garnets, with YIG again being an exception.[5] An attempt made in Ref. 6 to explain the measurements on YIG failed.[7] It was shown that a moving domain wall in YIG may contain a large number of vertical Bloch lines, which move along the wall when a drive field is applied. While this effect provided a partial explanation for the observed relatively small wall mobility, it was found that a wall not containing vertical Bloch lines at all has a mobility almost seven times smaller than expected based on FMR measurements. The experimental data derived for ferrite-garnet films were likewise contradictory. For instance, Refs. 8 and 9 and some other studies quoted agreement between the damping parameters extracted from FMR and domain-wall mobility measurements. On the other hand, other publications[10–12] maintained that the damping parameters found from mobility measurements exceed noticeably those following from FMR data. A theoretical study[13] suggested that motion of a domain wall entails, besides the conventional relativistic losses characteristic of uniform precession, additional losses caused by the so-called exchange relaxation. It was also suggested[14,15] that there should exist in materials having a narrow FMR line a substantial additional contribution to the losses, which is associated with the perturbation of the modulus of the magnetization vector by a change in the effective field in the moving domain wall, with subsequent relaxation of this perturbation. An idea was put forward[14] that the various contributions to relaxation in garnet films having perpendicular magnetic anisotropy can be separated by analyzing data on the dependence of wall mobility on the strength of the in-plane dc magnetic field H_p applied parallel to the wall. An attempt at such a separation of the contributions to losses in films with a narrow FMR line was made.[16–18] In Ref. 16 it was unsuccessful, and Ref. 18 quoted qualitative disagreement between the experimental results and predictions of theory[14] on the dependence of wall mobility on field H_p. One observed also a quantitative disagreement between the mobilities derived for $H_p = 0$ and those calculated from the relations proposed in Ref. 14. The question of the relation between the relaxation losses due to domain wall motion and those due to FMR remained unclear.

To find this relation, a study has been made of domain-wall mobility in films with different characteristics, in particular, with different but small FMR linewidths. The measurements were performed on (111) oriented YBiFeGa samples, and their characteristics, found by standard techniques, are listed in Table I (samples 3 and 4). When determining the damping parameter, the contribution due to the inhomogeneous broadening of the FMR line was excluded. The wall dynamics were studied by the well-known method

of bubble domain translation. The domains were in state S_0 with two vertical Bloch lines of negative sign, and therefore they moved along the gradient ∇H of a pulsed drive field $H_g = r\nabla H$, where r is the bubble-domain radius. The distance traversed by a domain driven by an H_g field pulse was measured by a high-speed image-recording technique, with a Rhodamine 6G dye laser pumped by an ILGI-503 pulsed nitrogen laser serving as a source of pulsed illumination. The receiver was a TV camera with a high-sensitivity vidicon and the image thus obtained could be stored and displayed on the monitor screen. The measurements were carried out under a dc field H_p applied in the film plane and oriented perpendicular to the direction of bubble-domain displacement. It is known that application of H_p increases the field at which steady-state wall motion breaks down, and therefore starting with a certain H_p one can observe the initial portion of the dependence $V(H_g)$ of the wall velocity on H_g pulse amplitude and, hence, measure the mobility. Besides, the field H_p stabilizes the S_0-domain wall structure, because it maintains vertical Bloch lines at the opposite ends of the diameter perpendicular to the bubble-domain translation and prevents the vertical Bloch lines from displacing along the wall when the domain is in motion.

The $V(H_g)$ dependences were studied within a broad range of in-plane fields for the films under investigation: for sample 3, the field H_p was varied from 0.17 to $0.34H_A$, and for sample 4, from 0.13 to $0.35H_A$, where H_A is the anisotropy field. The initial portions of these plots were used to determine the wall mobilities μ in different fields H_p, with Fig. 1 presenting the data obtained for film 3. Let us compare them with theory. Several expressions relating the wall mobility to field H_p can be found in literature. We shall use here a general expression[14]

$$\mu = \mu_0 \left\{ \left[1 - \left(\frac{H_p}{H_A} \right)^2 \right]^{1/2} - \frac{H_p}{H_A} \arccos \frac{H_p}{H_A} \right\}^{-1}. \quad (1)$$

Here μ_0 is the mobility in a field $H_p = 0$,

$$\mu_0 = \alpha^{-1} \Delta \gamma, \quad (2)$$

where Δ is a wall-thickness parameter, γ is the gyromagnetic ratio, and α is the Gilbert damping parameter found from measurements of either FMR (α_{FMR}) or wall mobility (α_{DW}). In weak fields $H_p \ll H_A$, Eq. (1) reduces to the well-known expression

$$\mu = \mu_0 \left(1 + \frac{\pi H_p}{2H_A} \right). \quad (3)$$

The experimental data plotted in Fig. 1 were approximated, as in Ref. 18, with Eq. (1), with the mobility at the field $H_p = 0$, $\mu_0 = \mu_{01}$, used as a fitting parameter. The results of the fitting are shown in Fig. 1 with a solid line to yield $\mu_{01} = 240\ \mathrm{m \cdot s^{-1} \cdot Oe^{-1}}$. Substituting α_{FMR} into Eq. (2) yields for the mobility $\mu_0 = \mu_{\mathrm{FMR}} = 340\ \mathrm{m \cdot s^{-1} \cdot Oe^{-1}}$ (it is also shown in Fig. 1), which is substantially in excess of the experimental value. Consider whether this discrepancy can be explained in terms of an additional mechanism[14,15] responsible for energy losses suffered in wall motion. The mobility in the presence of a field H_p can be written[14]

$$\mu^{-1} = \alpha_{\mathrm{FMR}} \left[\gamma \Delta I \left(\frac{H_p}{H_A} \right) \right]^{-1} + \alpha_\chi \left[\gamma \Delta F \left(\frac{H_p}{H_A} \right) \right]^{-1}, \quad (4)$$

where $I(H_p/H_A)$ is the expression in braces in Eq. (1), and the damping parameter α_χ takes into account the additional contribution to the losses [the expression for $F(H_p/H_A)$ will be considered later]. For $H_p = 0$ we obtain $I(H_p/H_A) = F(H_p/H_A) = 1$, so that

TABLE I. Sample characteristics.

Sample No.	System	$4\pi M$, G	K, 10^3 erg·cm^{-3}	Δ, 10^{-5} cm	γ, 10^7 Oe^{-1}·s^{-1}	α_{FMR}	α_{DW}	Ref.
1	YBiGa	157	10.6	0.35	1.82	0.0012	0.007	18
2	YBiGa	156	38.5	0.2	1.67	0.002	0.0056	18
3	YBiGa	320	27.3	0.28	1.84	0.0015	0.0021	
4	YBiGa	236	32.4	0.23	1.67	0.0034	0.0032	
5	YGdGa	105	0.66	1.15	1.72	0.0088*	0.0088	9
6	YEuTmGa	184	22.6	0.26	1.1	0.026	0.06	19
7	EuLuGa	440	82	0.17	1.12	0.028	0.041	8
8	YEuGa	160	9.03	0.44	1.21	0.03	0.0345**	20
9	EuLuCaGe	510	58	0.21	1.32	0.034	0.03	8
10	YGdTmGa	149	8.8	0.48	1.27	0.035	0.032**	21,22
11	EuLuAl	440	78	0.15	1.12	0.035	0.032	8
12	YSmLuCaGe	340	17	0.37	1.86	0.07	0.076	8
13	YSmCaGe	139	4.88	0.72	1.81	0.08	0.096**	21,22
14	YEuYbCaGe	265	12.6	0.42	1.5	0.12	0.11***	23
15	YSmLuCaGe	370	26	0.31	1.82	0.12	0.125	8
16	YEuYbCaGe	262	12.4	0.4	1.5	0.12	0.137***	23
17	YSmLuCaGe	400	32	0.31	1.86	0.14	0.137	8

Notes: The value of α_{DW} for sample 6 was derived from Fig. 5 in Ref. 19, that for sample 8—from Fig. 2 in Ref. 20, that for sample 10—from Fig. 3 in Ref. 21, that for sample 13—from Fig. 1 in Ref. 21, and that for samples 14 and 16—from Fig. 2 in Ref. 23.

* FMR measurements were performed for two dc field orientations, parallel and perpendicular to the film plane, with their average taken for α_{FMR}.

** The mobility was determined in low fields H_p; the specified values of α_{DW} were derived from the mobility for H_p calculated using Eq. (1).

*** The measurements were carried out on $S = 1$ magnetic bubbles, but the gyrotropic effect may be disregarded in finding the mobility because of the large values of α_{FMR} and small domain-deflection angles.

$$\alpha = \alpha_{\mathrm{DW}} = \alpha_{\mathrm{FMR}} + \alpha_{\chi}, \tag{5}$$

$$\mu_0 = \Delta\gamma(\alpha_{\mathrm{FMR}} + \alpha_{\chi})^{-1}. \tag{6}$$

Two possible limiting cases were considered.[15] In the first of them, where impurity-induced relaxation processes dominate,

$$\alpha_{\chi} = \alpha'_{\chi} = \frac{32}{15\alpha_{\mathrm{FMR}}}\left(\frac{\chi H_A}{M}\right)^2, \tag{7}$$

where $4\pi M$ is the saturation magnetization, and χ is the longitudinal susceptibility in the region of the paraprocess described by the expression[16]

$$\chi = \frac{kTM^2}{32\pi(KA^3)^{1/2}}. \tag{8}$$

Here k is the Boltzmann constant, and T is the temperature. We shall denote the mobility calculated using Eqs. (6) and (7) by μ_{02}. For small in-plane fields $H_p \ll H_A$ and for domain-wall velocities $V < V_c = 0.5\pi\Delta\gamma H_p$ (V_c is the maximum velocity of steady-state wall motion in fields $H_p \gg 8M$), the function $F(H_p/H_A)$ on the right-hand side of Eq. (4) can be written

$$F\left(\frac{H_p}{H_A}\right) = 1 + \frac{75\pi H_p}{64 H_A}. \tag{9}$$

For higher fields H_p the form of this function has not been established.

In the second limiting case, where intrinsic relaxation processes are dominant,

$$\alpha_{\chi} = \alpha''_{\chi} = 2.5\alpha'_{\chi}. \tag{10}$$

The mobility calculated from Eqs. (6), (7), and (10) will be denoted by μ_{03}. The expression for $F(H_p/H_A)$ in Eq. (4) becomes in this case too cumbersome [see Eq. (7) in Ref. 9] to be presented here.

Assuming impurity-induced relaxation to be dominant, and that the field $H_p = 0$, calculations yield $\mu_{02} = 128\ \mathrm{m\cdot s^{-1}\cdot Oe^{-1}}$ for film 3. If, however, intrinsic relaxation is assumed to be dominant, calculations will give $\mu_{03} = 65\ \mathrm{m\cdot s^{-1}\cdot Oe^{-1}}$. Both these values are smaller than the experimentally measured mobility (see Fig. 1).

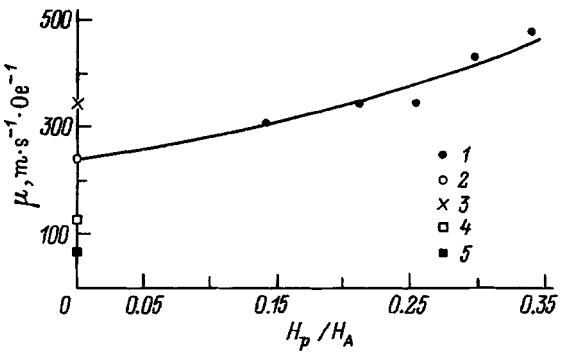

FIG. 1. Domain-wall mobility vs in-plane dc field for film 1 from Table I. (*1*) experimental data, solid line—approximation with Eq. (1) using the mobility at $H_p = 0, \mu_{01}$ (*2*) as a fitting parameter. Mobilities calculated for $H_p = 0$: (*3*) μ_{FMR}, (*4*) μ_{02}, (*5*) μ_{03}.

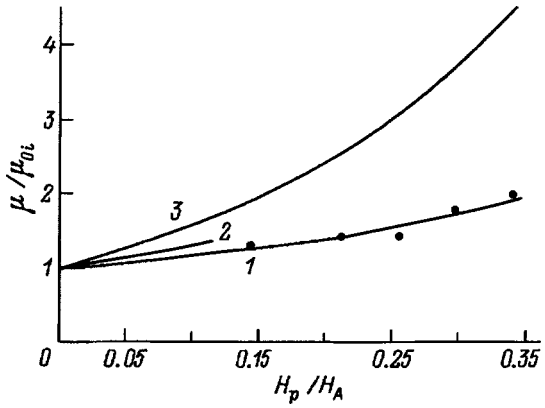

FIG. 2. Reduced domain-wall mobility μ/μ_{0i}, where $i = 1,2,3$, *vs* the ratio of in-plane dc field to the uniaxial-anisotropy field for film 1 from Table I. *1*—plot of Eq. (1), filled circles—ratios of experimental mobilities to μ_{01}; *2*—calculation using Eqs. (4), (6), (7), and (9); *3*—calculation using Eqs. (4), (6), and (10). The function $F(H_p/H_A)$ was calculated using Eq. (7) from Ref. 9.

Figure 2 presents the experimental dependence of wall mobility on the in-plane dc field and compares it with the results of calculations. For conveniency of comparison, the reduced mobility μ/μ_{0i} $(i = 1,2,3)$ is plotted here *vs* the ratio H_p/H_A. Curve *1* is a plot of Eq. (1), and filled circles refer to the ratios of experimental values of the mobility to μ_{01}. For both cases including the additional loss mechanism calculations were made using Eq. (4), and their results are presented by curves *2* and *3*. We readily see that the experimental dependence of wall mobility on the in-plane field is substantially weaker than this follows from theory.[14,15] This supports the conclusion drawn in Ref. 18 that the dependence of mobility on the field H_p is best of all described by Eq. (1).

The experimental relationship $\mu(H_P/H_A)$ for film 4 was determined in the same way as that for film 3. The results of the measurements were likewise approximated by Eq. (1), and mobility μ_{01} used in this case as a fitting parameter was found to be $120\ \mathrm{m\cdot s^{-1}\cdot Oe^{-1}}$, which coincides with the value calculated using Eq. (2) with $\alpha = \alpha_{\mathrm{FMR}}/\mu_{\mathrm{FMR}} = 113\ \mathrm{m\cdot s^{-1}\cdot Oe^{-1}}$. For this reason no analysis similar to that described above was performed for sample 2.

For films 3 and 4, as well as for films 1 and 2 studied earlier,[18] the values of mobility μ_{01} extracted from experimental data were substituted into Eq. (2) to yield the damping parameters α_{DW}, which are presented in Table I.

Let us discuss now the results of this work and of Ref. 18 in combination with the other available data. There are a number of studies of domain-wall dynamics made on garnet films of different compositions with perpendicular magnetic anisotropy, where one can find information both on experimental values of μ and on the damping parameters derived from FMR measurements made on the same films. We used for the analysis the results obtained in measurements[8,9,19–23] carried out either by high-speed photography or using domain-wall resonance in low fields, and containing information on the magnetic characteristics of the samples. The parameters of the films studied in Refs. 8, 9, 19–23 are given in Table I (samples 5–17).

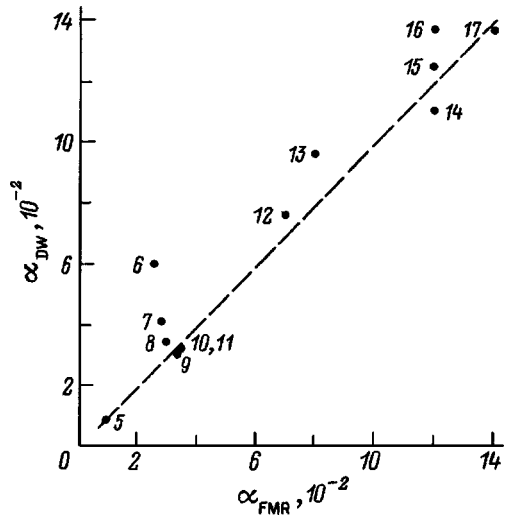

FIG. 3. Relation between the Gilbert damping parameter α_{DW} and α_{FMR} for films 5–17 from Table I. Figures at the points are film numbers (see Table I).

Figure 3 compares the Gilbert damping parameters found from FMR and mobility measurements for films 5–17 from Table I. In Fig. 4, α_{FMR} and α_{DW} are compared for samples having a narrow resonance line, both studied in this work and quoted in Ref. 18, for a YIG sample from Ref. 7, and for film 5; also given are the α parameters calculated for these samples using Eqs. (5) and (7). We readily see that for $\alpha_{FMR} > 3\times10^{-3}$ the figures derived from FMR linewidth and domain-wall mobility coincide. The point obtained for sample 6 obviously does not fit into the pattern, which is apparently associated with some features of the methodology used. The same applies possibly also to the above-mentioned data quoted in Refs. 10–12, because their values of α_{FMR} are too large and belong rather to the region in Fig. 3, where both methods yield the same damping parameters.

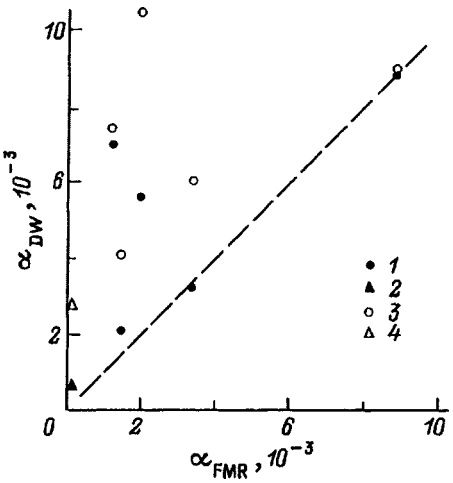

FIG. 4. Plot of the Gilbert damping parameter α_{DW} *vs* α_{FMR} for samples with a relatively narrow FMR line. *1*—films 1–5 from Table I, *2*—YIG sample from Ref. 7 (the values $\alpha_{FMR}=9.4\times10^{-5}$ and $\alpha_{DW}=6.2\times10^{-4}$ were derived from data of this work on wall mobility and parameters of the material), *3,4*—calculation of α_{DW} using Eqs. (5) and (7).

As seen from Fig. 4, samples with a narrow FMR line exhibit noticeable differences between the α_{FMR} and α_{DW} parameters, but their values do not appear to be in any relation to one another. Interestingly, a relation between the losses connected with the wall motion and with FMR can be revealed if one describes the losses in terms of the so-called reduced Landau-Lifshits damping parameter Λ. As is well known, for $\alpha \ll 1$

$$\Lambda = \alpha M \gamma^{-1}, \tag{11}$$

$$\mu_0 = \Lambda^{-1} M \Delta. \tag{12}$$

Parameter Λ can also be expressed through the Landau-Lifshits damping parameter λ as $\Lambda = \lambda/\gamma^2$. An essential difference between these damping parameters can be seen from their relation to the magnetic characteristics of the samples. It was established[24] that the ratio α/γ does not depend on γ, i.e., $\alpha \propto \gamma$. A comparison of FMR linewidth ΔH_{FMR} with $4\pi M$ measured[25] on different samples showed that a decrease of $4\pi M$ by an order of magnitude entails an increase of ΔH_{FMR}, likewise by an order of magnitude, which implies that $\alpha^{-1}\gamma \propto M$. A nearly sevenfold variation of $4\pi M$ achieved by properly varying the film composition did not produce a noticeable effect on γ, and the damping parameter derived from domain-wall resonance measurements, $\lambda = \alpha\gamma M$, remained constant.[26] A study[27] of the relation between ΔH_{FMR} and magnetization, which was varied by changing the film composition, led to the conclusion that the quantity Λ does not depend on $4\pi M$, γ, or frequency.

We also studied the effect of magnetization on FMR linewidth on YEuFeGa and YSmFeGa films (these studies are partially quoted in Ref. 28). The magnetization was varied by high-temperature anneal of the films in oxygen, with their subsequent quenching. By properly varying the anneal temperature T_{ann}, one could change the magnitude of $4\pi M$ and, thus, observe the variation of ΔH_{FMR} in the same sample. The FMR linewidth decreased with increasing magnetization, and this effect was found to be reversible. For a YEuFeGa film, a change of $4\pi M$ from 125 to 195 G resulted in a change of α from 0.044 to 0.03, and that of γ, from 1.19×10^7 to 1.34×10^7 $Oe^{-1}\cdot s^{-1}$. The parameter Λ did not change and was $\sim 0.36\times10^{-7}$ $Oe^2\cdot s$. The results obtained for the YSmFeGa films are as follows: in sample A, a change in T_{ann} from 925 to 1190 °C increased $4\pi M$ from 175 to 250 G, with α_{FMR} decreasing from 0.23 to 0.145, and $\Lambda \sim 1.71\times10^{-7}$ $Oe^2\cdot s$. In another sample, a change of T_{ann} from 890 to 1150 °C increased $4\pi M$ from 157 to 212 G. Here α_{FMR} decreased from 0.245 to 0.16, with $\Lambda \sim 1.74\times10^{-7}$ $Oe^2\cdot s$.

One can thus conclude that the Gilbert damping parameter $\alpha \propto \gamma M^{-1}$, and the reduced damping parameter Λ depends neither on M nor on γ, at any rate within a very broad range of film characteristics. Therefore this parameter can be used to advantage in comparing losses in films with different magnetizations and γ. Obviously enough, for comparatively large losses, when $\alpha_{FMR} = \alpha_{DW}$, transition to Λ_{FMR} and Λ_{DW} will result only in a diagonal displacement of the corresponding points in Figs. 3 and 4 with respect to one another. (This

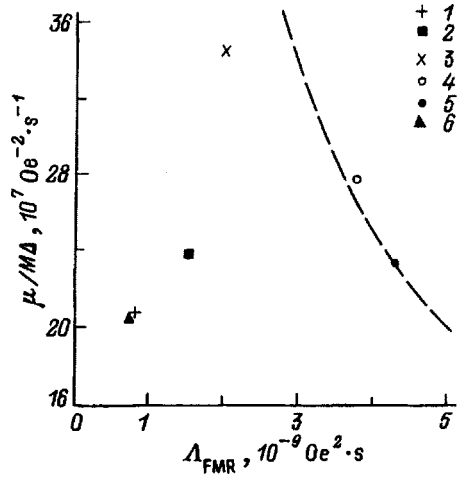

FIG. 5. Reduced domain-wall mobility for $H_p=0$ *vs* reduced Landau-Lifshits damping parameter Λ_{FMR}. *1–5*—samples 1–5 from Table I, *6*—YIG film from Ref. 7, dashed line—calculation using Eq. (12) for $\Lambda=\Lambda_{\mathrm{FMR}}$.

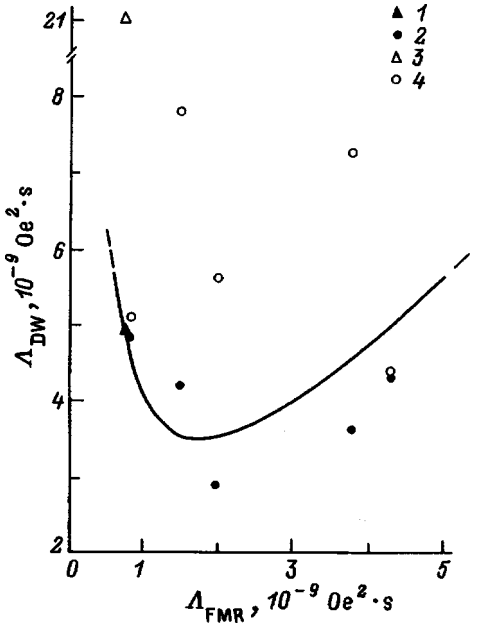

FIG. 6. Plot of reduced Landau-Lifshits damping parameter Λ_{DW} *vs* Λ_{FMR}. *1*—YIG sample from Ref. 7; *1–5*—films 1–5 from Table I (film number increases from left to right with increasing Λ_{FMR}); solid line—fitting with Eq. (14); *3,4*—calculation of Λ_{DW} using Eq. (11) and taking into account Eqs. (5) and (7) (*3*—the YIG film from Ref. 7, and *4*—films 1–5 from Ref. 4).

is the case for $\Lambda_{\mathrm{FMR}}>2.4\times10^{-9}$ Oe$^2\cdot$s). As we shall show later on, the situation for $\alpha_{\mathrm{DW}}>\alpha_{\mathrm{FMR}}$ is different.

The experimental values of μ_{01} obtained for films 1–5 (Table I) and the YIG sample[7] were used to calculate the reduced wall mobilities $\mu_{01}/M\Delta$. Figure 5 plots this mobility as a function of Λ_{FMR}. We also calculated the theoretical dependence of reduced mobility on Λ_{FMR} using Eq. (12) for $\Lambda=\Lambda_{\mathrm{FMR}}$, i.e., for the case where the losses in wall motion are taken into account completely by the damping parameter derived from FMR measurements. A portion of this relation, which is naturally a section of a hyperbola, is shown in Fig. 5 with a dashed line. The mobility data for films having small values of parameter Λ_{FMR} suggest that as the damping parameter decreases the wall mobility first grows as $\Lambda_{\mathrm{FMR}}^{-1}$, as long as this parameter is greater than $\sim2.4\times10^{-9}$ Oe$^2\cdot$s. As Λ_{FMR} is reduced still more, the experimental values of the wall mobility decrease.

Consider possible reasons for this decrease in mobility. A general theory of motion of one-dimensional wall developed in Ref. 29 shows that the mean wall velocity $\langle V\rangle \geqslant(\alpha+\alpha^{-1})^{-1}\Delta\gamma H$, and that as long as the damping losses are small, $\alpha\to0$,

$$\langle V\rangle\simeq\alpha\Delta\gamma H. \tag{13}$$

In the absence of losses, the mean velocity of translational wall motion is zero.[29] At first glance it might seem that our data are in agreement with these conclusions; it should be pointed out, however, that Eq. (13) was derived for the case of nonsteady-state wall motion, and the experimental data on wall mobility exceed by several orders of magnitude the values obtained from Eq. (13). A similar expression ($\langle V\rangle \propto\alpha BH$, where coefficient B includes a number of film characteristics) was obtained also in a theory developed for a two-dimensional wall.[30] It also related to the region of nonsteady-state motion, where periodic nucleation, displacement, and annihilation of Bloch lines take place in the wall. In this case, theoretical estimates of mobility are likewise smaller by nearly three orders of magnitude than the experimental data.

One can also attempt to explain the decrease in mobility for small Λ_{FMR} by assuming the losses suffered by a moving wall to differ from those induced by FMR. The experimental data on mobility μ_{01} can be used to calculate by means of Eq. (12) the Λ_{DW} parameters for the YIG sample and films 1–5. Figure 6 relates these parameters to the corresponding values of Λ_{FMR}. Assuming that for very small Λ_{FMR} the wall mobility may be considered proportional to this parameter (see Fig. 5), and taking into account that when FMR-induced losses increase, $\Lambda_{\mathrm{DW}}=\Lambda_{\mathrm{FMR}}$, the relation connecting these parameters can be expressed by a simple formula

$$\Lambda_{\mathrm{DW}}=\Lambda_{\mathrm{FMR}}+\frac{C}{\Lambda_{\mathrm{FMR}}} \tag{14}$$

(the curve in Fig. 6), where C is a fitting parameter equal to 3×10^{-18} Oe$^4\cdot$s^2. Relation (14) resembles Eq. (5) written taking into account Eq. (7). Therefore Fig. 6 shows also the damping parameters calculated by means of Eqs. (5), (7), and (11), i.e., for the case where theory[15] predicts impurity-induced relaxation to be dominant. (In the second case considered in the theory, the values of Λ_{DW} are about twice larger, and therefore they are not shown in Fig. 6.) Some of the calculated parameters are seen to be close to those derived from mobility measurements. One apparently should not expect a close agreement between these values, if for no other reason than the approximations made when deriving Eq. (8). Thus the decrease of mobility for small Λ_{FMR} could be attributed, in principle, to the operation in this region of an additional effective damping-loss mechanism, of the type

proposed in Ref. 15. As shown in this work and in Ref. 18, however, the experimental dependence of the wall mobility on the in-plane dc field is weaker than this follows from the theory of Refs. 14 and 15.

Thus when the reduced Landau-Lifshits damping parameter Λ_{FMR} derived from FMR measurements is smaller than some small critical threshold the domain-wall mobility grows with increasing Λ_{FMR}. The same conclusion follows also from the general theory of wall motion, but for a nonsteady-state mode, and the theoretical mobility obtained here is found to be several orders of magnitude smaller than the experimental value. Another possible explanation for this effect involves the onset of a damping-loss mechanism which acts in parallel to that operative under uniform precession. The theory proposing a mechanism of this kind predicts, however, a dependence of wall mobility on in-plane dc field differing from the relation following from experiment. When the Δ_{FMR} parameter is in excess of the threshold, mobility and FMR measurements yield the same damping parameters. Hence the damping losses observed in this region originate from the same mechanism as those caused by FMR. In these conditions, the wall mobility is described by the classical relation, by which mobility decreases with increasing damping parameter inversely proportional to the latter.

Support of the Russian Fund for Fundamental Research (Grant 96-02-16890a) is gratefully acknowledged.

[1] J. K. Galt, Bell Syst. Tech. J. **33**, 1023 (1954).
[2] J. F. Dillon and H. E. Earl, J. Appl. Phys. **30**, 202 (1959).
[3] F. B. Hagedorn and E. M. Gyorgy, J. Appl. Phys. **32**, 282S (1961).
[4] H. Harper and R. W. Teale, J. Phys. C **2**, 1926 (1969).
[5] G. P. Vella-Coleiro, D. H. Smith, and L. G. Van Uitert, Appl. Phys. Lett. **21**, 36 (1972).
[6] R. W. Teale, J. Phys. C **13**, 2061 (1980).
[7] V. S. Gornakov, L. M. Dedukh, V. I. Nikitenko, and V. T. Synogach, Zh. Éksp. Teor. Fiz. **90**, 2090 (1986) [Sov. Phys. JETP **63**, 1225 (1986)].
[8] D. Challeton, H. Jouve, and J. Magnin, J. Appl. Phys. **50**, 7853 (1979).
[9] B. E. Argule, J. C. Slonczewski, W. Jantz, J. H. Spreen, and M. H. Kryder, IEEE Trans. Magn. **18**, 1325 (1982).
[10] F. G. Bar'yakhtar, V. L. Dorman, and V. L. Sobolev, Fiz. Tverd. Tela (Leningrad) **27**, 2105 (1985) [Sov. Phys. Solid State **27**, 1261 (1985)].
[11] P. D. Kim, D. Sci. Thesis, Krasnoyarsk (1988).
[12] T. V. Drokina and Yu. V. Starostin, Fiz. Tverd. Tela (Leningrad) **23**, 1195 (1981) [Sov. Phys. Solid State **23**, 699 (1981)].
[13] V. G. Bar'yakhtar, Zh. Éksp. Teor. Fiz. **87**, 1501 (1984) [Sov. Phys. JETP **60**, 863 (1984)].
[14] B. A. Ivanov and K. A. Safaryan, Fiz. Tverd. Tela (Leningrad) **32**, 3507 (1990) [Sov. Phys. Solid State **32**, 2034 (1990)].
[15] B. A. Ivanov and K. A. Safaryan, Fiz. Nizk. Temp. **18**, 722 (1992) [Sov. J. Low Temp. Phys. **18**, 511 (1992)].
[16] B. A. Ivanov, A. Stankiewicz, A. Maziewski, N. L. Petrichenko, and K. A. Safaryan, in *Proceedings of the Sixth International Conference on Ferrites* (Tokyo, 1992), p. 775.
[17] V. A. Bokov, V. V. Volkov, N. L. Petrichenko, and M. Marysko, Pis'ma Zh. Tekh. Fiz. **19**, No. 22, 89 (1993) [Tech. Phys. Lett. **19**, 734 (1993)].
[18] V. A. Bokov, V. V. Volkov, N. L. Petrichenko, and M. Marysko, Fiz. Tverd. Tela (St. Petersburg) **39**, 1253 (1997) [Phys. Solid State **39**, 1112 (1997)].
[19] K. Yu and F. B. Humphrey, J. Appl. Phys. **48**, 4656 (1977).
[20] A. P. Malozemoff, J. Appl. Phys. **48**, 795 (1977).
[21] J. C. DeLuca and A. P. Malozemoff, AIP Conf. Proc. **34**, 151 (1976).
[22] A. P. Malozemoff, J. C. Slonczewski, and J. C. DeLuca, AIP Conf. Proc. **29**, 58 (1976).
[23] J. Mada, J. Appl. Phys. **18**, 95 (1979).
[24] G. P. Vella-Coleiro, S. L. Blank, and R. C. LeCraw, Appl. Phys. Lett. **26**, 722 (1975).
[25] E. I. Nikolaev, A. I. Linnik, and V. N. Sayapin, Zh. Tekh. Fiz. **64**, No. 6, 113 (1994) [Tech. Phys. **39**, 580 (1994)].
[26] G. P. Vella-Coleiro, D. H. Smith, and L. G. Van Uitert, J. Appl. Phys. **43**, 2428 (1972).
[27] T. Ikeda, N. Ohta, F. Ishida, and Y. Sugita, J. Appl. Phys. **51**, 5502 (1980).
[28] V. V. Volkov, V. A. Bokov, and V. I. Karpovich, Fiz. Tverd. Tela (Leningrad) **24**, 2318 (1982) [Sov. Phys. Solid State **24**, 1315 (1982)].
[29] J. C. Slonczewski, Int. J. Magn. **2**, 85 (1972).
[30] A. P. Malozemoff, J. Appl. Phys. **44**, 5080 (1973).

Translated by G. Skrebtsov

Critical dynamics of disordered magnets in the three-loop approximation

V. V. Prudnikov, S. V. Belim, E. V. Osintsev, and A. A. Fedorenko

Omsk State University, 644077 Omsk, Russia
(Submitted October 20, 1997; resubmitted February 16, 1998)
Fiz. Tverd. Tela (St. Petersburg) **40**, 1526–1531 (August 1998)

A field-theoretic description of the critical dynamics of magnetic systems with frozen nonmagnetic impurities is given. The values of the dynamical critical exponent in the three-loop approximation are obtained directly for three-dimensional systems using the Padé–Borel summation technique. A comparison is made with the values of the dynamical exponent for homogeneous systems calculated in the four-loop approximation as well as with the values obtained by Monte Carlo methods. © *1998 American Institute of Physics.* [S1063-7834(98)02608-2]

It is well known that phase transitions in homogeneous magnets change only for Ising magnets when randomly distributed frozen impurities are introduced into the system.[1] The ε-expansion method makes it possible to calculate the critical exponents for dilute magnets.[2] However, the asymptotic convergence of the ε-expansion series in this case is even weaker than for homogeneous magnets.[3] The renormalization-group approach to the description of disordered magnets used in Refs. 4 and 5 directly for three-dimensional systems, made it possible to obtain the values of the static critical exponents in the four-loop approximation. However, calculations to such accuracy are lacking for the description of the critical dynamics of disordered systems. This is due to the rapid growth of the volume of the calculations even in the lowest orders of perturbation theory.

In the present paper a field-theoretic description is constructed for the critical dynamics of disordered magnets directly for $d=3$ in the three-loop approximation. The model considered is a classic spin system with nonmagnetic impurity atoms frozen at the lattice sites. The model is described by the Hamiltonian

$$H=\frac{1}{2}\sum_{ij} J_{ij}p_i p_j \mathbf{S}_i\cdot\mathbf{S}_j,$$

where $\mathbf{S}_i$ is a n-component spin variable, J_{ij} are the exchange translationally-invariant short-range ferromagnetic interaction constants, p_i is a random variable described by the distribution function

$$P(p_i)=p\,\delta(p_i-1)+(1-p)\,\delta(p_i)$$

with $p=1-c$, where c is the concentration of nonmagnetic impurity atoms. Spin-phonon interaction effects lead in the general case to nonconservation of the total spin of the system. Taking them into account, a thermodynamically equivalent Ginzburg–Landau–Wilson model determined by the following effective Hamiltonian can be introduced to describe the critical behavior of spin impurity systems

$$H[\varphi,V]=\int d^dx\left\{\frac{1}{2}[|\nabla\varphi|^2+r_0\varphi^2+V(x)\varphi^2]+\frac{g_0}{4!}\varphi^4\right\}, \tag{1}$$

where $\varphi(x,t)$ is a n-component order parameter, $V(x)$ is the potential of the random impurity field, $r_0\sim T-T_{0c}(p)$, T_{0c} is the critical temperature, determined in the mean-field theory, of a disordered magnet, g_0 is a positive constant, and d is the dimension of the system. We prescribe the impurity potential by a Gaussian distribution

$$P_V=A_V\exp\left[-(8\delta_0)^{-1}\int d^dx V^2(x)\right],$$

where A_V is a normalization constant and δ_0 is a positive constant, proportional to the impurity concentration and the squared impurity potential.

The dynamic behavior of the magnet near the critical temperature, taking account of the spin-lattice relaxation, can be described by a Langevin-type kinetic equation for the order parameter

$$\frac{\partial\varphi}{\partial t}=-\lambda_0\frac{\delta H}{\delta\varphi}+\eta+\lambda_0 h, \tag{2}$$

where λ_0 is the kinetic constant, $\eta(x,t)$ is a Gaussian random force characterizing the effect of a heat reservoir and prescribed by the distribution function

$$P_\eta=A_\eta\exp\left[-(4\lambda_0)^{-1}\int d^dx\,dt\,\eta^2(x,t)\right]$$

with normalization constant A_η, and $h(t)$ is an external field thermodynamically conjugate to the order parameter. The time correlation function $G(x,t)$ of the order parameter is determined by solving Eq. (2) with $H[\varphi,V]$, given by Eq. (1), for $\varphi[\eta,h,V]$ and then averaging over the Gaussian random field η by means of P_η and over the random impurity potential $V(x)$ by means of P_V and singling out the part of the solution that is linear in $h(0)$, i.e.,

$$G(x,t)=\frac{\delta}{\delta h(0)}[\langle\varphi(x,t)\rangle]_{\mathrm{imp}}\Big|_{h=0},$$

where

$$[\langle\varphi(x,t)\rangle]_{\text{imp}}=B^{-1}\int D\{\eta\}D\{V\}\varphi(x,t)P_{\eta}P_{V},$$

$$B=\int D\{\eta\}D\{V\}P_{\eta}P_{V}.$$

The application of the standard renormalization-group technique to this dynamical problem encounters substantial difficulties. However, for homogeneous systems in the absence of the disorder introduced by the presence of impurities it has been shown[6] that the critical dynamical model based on Langevin-type equations is completely equivalent to the standard Lagrangian system[7] with the Lagrangian

$$L=\int d^dxdt\left\{\lambda_0^{-1}\varphi^2+i\varphi^*\left(\lambda_0^{-1}\frac{\partial\varphi}{\partial t}+\frac{\delta H}{\delta\varphi}\right)\right\}.$$

Here the correlation function $G(x,t)$ of the order parameter for a homogeneous system is determined as

$$G(x,t)=\langle\varphi(0,0)\varphi(x,t)\rangle$$
$$=\Omega^{-1}\int D\{\varphi\}D\{\varphi^*\}\varphi(0,0)\varphi(x,t)$$
$$\times\exp(-L[\varphi,\varphi^*]),$$

where

$$\Omega=\int D\{\varphi\}D\{\varphi^*\}\exp(-L[\varphi,\varphi^*]).$$

A generalization of this field-theoretic approach and details of its application to the critical dynamics of disordered magnets with frozen point impurities and extended defects are expounded in Ref. 8. In Ref. 8 a procedure for obtaining a replica Lagrangian averaged over the impurities, the generating-functional formalism for coupled Green's functions, and the diagrammatic rules which eliminate the contribution of closed loops from the Green's functions in all orders are presented.

Instead of the correlation function it is more convenient to study its vertex part, which can be represented in the Feynman diagram formalism in the three-loop approximation in the form

$$\Gamma^{(2)}(k,\omega;r_0,g_0,\delta_0,\lambda_0)$$
$$=r_0+k^2-\frac{i\omega}{\lambda_0}-4\delta_0D_1-\frac{n+2}{18}g_0^2D_2$$
$$+\frac{4(n+2)}{3}g_0\delta_0D_3-16\delta_0^2(D_4+D_5)$$
$$+\frac{(n+2)(n+8)}{108}g_0^3\left(\sum_{i=6}^{8}D_i\right)-\frac{2(n+2)^2}{9}g_0^2\delta_0\left(\sum_{i=9}^{18}D_i\right)$$
$$+\frac{16(n+2)}{3}g_0\delta_0^2\left(\sum_{i=19}^{31}D_i\right)-64\delta_0^3\left(\sum_{i=32}^{39}D_i\right). \qquad (3)$$

The diagrams corresponding to D_i are presented in Fig. 1. The Feynman diagrams contain a d-dimensional integration over the momenta and are characterized near the critical point in the limit with the cutoff parameter $\Lambda\to\infty$ by an ultraviolet divergence at large momenta k with pole-type singularities. These poles are eliminated by using a dimensional regularization scheme, involving the introduction of renormalized quantities.[9] We shall determine the renormalized order parameter as $\varphi=Z^{-1/2}\varphi_0$. Then the renormalized vertex functions will have the generalized form

$$\Gamma_R^{(m)}(k,\omega;r,g,\delta,\lambda,\mu)=Z^{m/2}\Gamma^{(m)}(k,\omega;r_0,g_0,\delta_0,\lambda_0) \qquad (4)$$

with the renormalized coupling constants g and δ, temperature r, and kinetic coefficient λ

$$g_0=\mu^{4-d}Z_gg,\quad \delta_0=\mu^{4-d}Z_\delta\delta,$$
$$r_0=\mu^2Z_rr,\quad \lambda_0^{-1}=\mu^2Z_\lambda\lambda^{-1}. \qquad (5)$$

The scaling parameter μ is introduced to make the quantities dimensionless. In Eq. (4) $\Gamma^{(2)}$ corresponds to the reciprocal of the correlation function $G(k,\omega)$ of the order parameter, while $\Gamma^{(4)}$ corresponds to the four-tail vertex functions $\Gamma_g^{(4)}$ and $\Gamma_\delta^{(4)}$ for the coupling constants g and δ, respectively. The Z factors are determined from the requirement that the renormalized vertex functions be regular, which is expressed in the normalization conditions

$$Z\frac{\partial\Gamma^{(2)}(k)}{\partial k^2}\bigg|_{k^2=0}=1,\quad Z^2\Gamma_g^{(4)}|_{k_i=0}=\mu^{4-d}g,$$
$$Z^2\Gamma_\delta^{(4)}|_{k_i=0}=\mu^{4-d}g,\quad Z\frac{\partial\Gamma^{(2)}(k,\omega)}{\partial(-i\omega)}\bigg|_{k^2,\omega=0}=\lambda^{-1}. \qquad (6)$$

We carried out this regularization procedure for the vertex functions in the three-loop approximation. For this purpose, we present the values of the vertex functions, appearing in the normalization conditions, in the form

$$\Gamma_g^{(4)}|_{k_i=0}=g_0\sum_{i,j=0}^{3}A_{ij}g_0^i\delta_0^j,$$

$$\Gamma_\delta^{(4)}|_{k_i=0}=\delta_0\sum_{i,j=0}^{3}B_{ij}g_0^i\delta_0^j,$$

$$\frac{\partial\Gamma^{(2)}}{\partial k^2}\bigg|_{k^2=0}=\sum_{i,j=0}^{3}C_{ij}g_0^i\delta_0^j,$$

$$\frac{\partial\Gamma^{(2)}}{\partial(-i\omega/\lambda)}\bigg|_{k=0,\omega=0}=\sum_{i,j=0}^{3}D_{ij}g_0^i\delta_o^j, \qquad (7)$$

where the coefficients are sums of the corresponding diagrams or their derivatives at zero external momenta and frequencies. Thus, the numerical values of the derivatives of the diagrams (see Fig. 1) $D_i'=\partial D_i/\partial(-i\omega/\lambda)|_{k=0,\omega=0}$, generating the coefficients D_{ij} and obtained by using the subtraction scheme of Ref. 10, are presented in Table I, where $J=\int d^dq/(q^2+1)^2=(S_d/2)\Gamma(d/2)\Gamma(2-d/2)$ is a one-loop integral with $S_d=2\pi^{d/2}/(2\pi)^d\Gamma(d/2)$, and $\Gamma(x)$ is the gamma function. We write the expansion for the quantities g_0, δ_0, Z, and Z_λ in terms of the renormalized coupling constants g and δ in the form

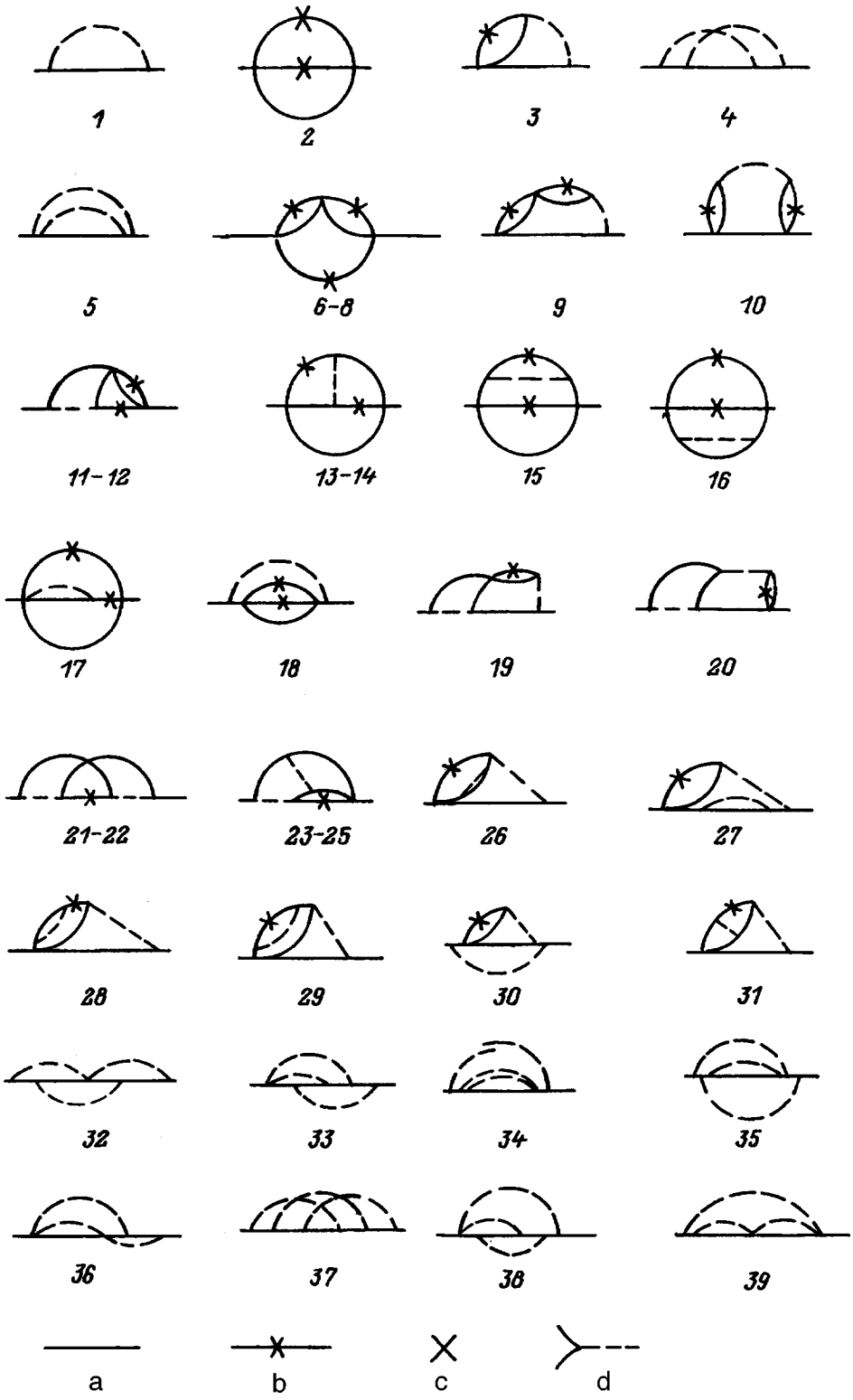

FIG. 1. Diagrammatic representation of contributions to the vertex function $\Gamma^2(k,\omega)=G^{-1}(k,\omega)$ in the three-loop approximation. The line a corresponds to $G_0(k,\omega)=(r_0+k^2-i\omega/\lambda_0)^{-1}$, the line b corresponds to $G_0(k,\omega)=2\lambda^{-1}((r_0+k^2)^2+(\omega/\lambda_0))^{-1}$, the vertex c corresponds to g_0, and the vertex d to $\delta_0\delta(\omega)$.

$$g_0=g\sum_{i,j=0}^{3}a_{ij}g^i\delta^j,\quad \delta_0=\delta\sum_{i,j=0}^{3}b_{ij}g^i\delta^j,$$

$$Z=\sum_{i,j=0}^{3}c_{ij}g^i\delta^j,\quad Z_\lambda=\sum_{i,j=0}^{3}d_{ij}g^i\delta^j, \tag{8}$$

where the unknowns a_{ij}, b_{ij}, c_{ij}, and d_{ij} are expressed in terms of A_{ij}, B_{ij}, C_{ij}, and D_{ij} by means of the normalization conditions. The next step in the field-theoretic approach is to determine the scaling functions $\beta_g(g,\delta)$, $\beta_\delta(g,\delta)$, $\gamma_r(g,\delta)$, $\gamma_\varphi(g,\delta)$, and $\gamma_\lambda(g,\delta)$, which give the renormalization-group differential equation for the vertex functions:

$$\left[\mu\frac{\partial}{\partial\mu}+\beta_g\frac{\partial}{\partial g}+\beta_\delta\frac{\partial}{\partial\delta}-\gamma_r r\frac{\partial}{\partial r}+\gamma_\lambda\lambda\frac{\partial}{\partial\lambda}-\frac{m}{2}\gamma_\varphi\right]$$
$$\times\Gamma^{(m)}(k,\omega;r,g,\delta,\lambda,\mu)=0.$$

TABLE I. Values of the derivatives of the diagrams displayed in Fig. 1, $D_i' = \partial D_i / \partial(-i\omega/\lambda)|_{k=0,\omega=0}$.

D_1'/J	−1.000000	D_{14}'/J^3	−0.032279	D_{27}'/J^3	−0.666667
D_2'/J^2	−0.130768	D_{15}'/J^3	0.061515	D_{28}'/J^3	0.584625
D_3'/J^2	−0.666667	D_{16}'/J^3	0.004666	D_{29}'/J^3	−0.092766
D_4'/J^2	−2.000000	D_{17}'/J^3	−0.333557	D_{30}'/J^3	−0.074202
D_5'/J^2	−1.000000	D_{18}'/J^3	0.042034	D_{31}'/J^3	−0.194407
D_6'/J^3	−0.104778	D_{19}'/J^3	−2.053736	D_{32}'/J^3	−2.053736
D_7'/J^3	−0.032835	D_{20}'/J^3	−2.053736	D_{33}'/J^3	−2.053736
D_8'/J^3	−0.032835	D_{21}'/J^3	−1.142275	D_{34}'/J^3	−1.000000
D_9'/J^3	−0.519431	D_{22}'/J^3	−0.396553	D_{35}'/J^3	0.666667
D_{10}'/J^3	−0.519431	D_{23}'/J^3	−1.142275	D_{36}'/J^3	0.666667
D_{11}'/J^3	−0.276601	D_{24}'/J^3	−0.396553	D_{37}'/J^3	−2.053736
D_{12}'/J^3	−0.468697	D_{25}'/J^3	−0.396553	D_{38}'/J^3	−0.074202
D_{13}'/J^3	−0.032279	D_{26}'/J^3	0.226932	D_{39}'/J^3	0.000000

In the following discussion of the dynamical behavior we shall require only the functions β_g and β_δ and the dynamical scaling function γ_γ, determined by the relations

$$4-d+\beta_g\frac{\partial \ln gZ_g}{\partial g}+\beta_\delta\frac{\partial \ln gZ_g}{\partial \delta}=0,$$

$$4-d+\beta_g\frac{\partial \ln \delta Z_\delta}{\partial g}+\beta_\delta\frac{\partial \ln \delta Z_\delta}{\partial \delta}=0,$$

$$\gamma_\lambda=\beta_g\frac{\partial \ln Z_\lambda}{\partial g}+\beta_\delta\frac{\partial \ln Z_\lambda}{\partial \delta}. \tag{9}$$

The explicit form of the functions β_g and β_δ in the four-loop approximation was obtained in Ref. 5, where the coupling constants ν and u were introduced, which are related to g and δ as $\nu=(n+8)J_g/6$ and $u=-16J\delta$. Prescribing the functions β and γ_λ in the form

$$\beta_\nu=\nu\sum_{i,j=0}^{3}\beta_{ij}^{(v)}\nu^i u^j, \quad \beta_u=u\sum_{i,j=0}^{3}\beta_{ij}^{(u)}\nu^i u^j,$$

$$\gamma_\lambda=\sum_{i,j=0}^{3}\gamma_{ij}^{i}u^j, \tag{10}$$

we present in Table II the values of the coefficients in Eq. (10) for the three-dimensional Ising model ($n=1$). The nature of the critical point for each value of n and d is completely determined by the stable fixed point for the coupling constants (ν^*,u^*), which is determined from the requirement that the β function vanish, i.e.,

TABLE II. Values of the coefficients in the expressions for the scaling functions.

(i,j)	$\beta_{i,j}^{(u)}$	$\beta_{i,j}^{(v)}$	$\gamma_{i,j}$
(0,0)	−1	1	0
(1,0)	1	3/2	−0.25
(0,1)	2/3	1	0
(2,0)	−95/216	−185/216	0.053240
(1,1)	−50/81	−104/81	0.030862
(0,2)	−92/729	−308/729	0.008400
(3,0)	0.389922	0.916667	−0.049995
(2,1)	0.857363	2.132996	−0.152964
(1,2)	0.467388	1.478058	−0.041167
(0,3)	0.090448	0.351069	−0.012642

$$\beta_\nu(\nu^*,u^*)=0, \quad \beta_u(\nu^*,u^*)=0.$$

The quantities ν^* and u^* are of order $4-d$, so that the series expansions of the scaling functions with $d=3$ in powers of ν and u are asymptotically convergent. The Padé–Borel method has found wide application for summing them.[11] Numerical analysis of the equations for determining the fixed points and the conditions under which they are stable shows that in contrast to the ε-expansion with $d=3$ the accidental degeneracy of the fixed points with $n=1$ does not arise. Only two of the four fixed points are of interest: the fixed point for homogeneous systems ($\nu^*\neq 0$, $u^*\neq 0$) and the impurity fixed point ($\nu^*\neq 0$, $u^*\neq 0$), which determines the new critical properties of disordered magnets. The impurity fixed point is stable only for $n=1$, while for $n\geqslant 2$ the presence of disorder associated with the presence of the frozen impurities is not important for the critical behavior of magnets. The impurity fixed point point for the three-dimensional Ising model in the three-loop approximation is given by the values $\nu^*=2.256938$, $u^*=-0.728168$.

Substituting the values of the coupling constants at a fixed point into the scaling function $\gamma_\lambda(\nu,u)$ allows us to determine the dynamical critical exponent z, characterizing the critical slowing down of relaxation processes,

$$z=2+\gamma_\lambda(\nu^*,u^*). \tag{11}$$

But the series expansion of $\gamma_\lambda(\nu^*,u^*)$ in powers of ν^* and u^* with $d=3$ is, in the best case, asymptotically convergent, and to obtain reasonable values it cannot be directly summed. We summed it by the generalized Padé–Borel method, which consists of applying to the series the Borel transformation

$$\gamma_\lambda(\nu,u)=\sum_{i,j}\gamma_{ij}\nu^i u^j=\int_0^\infty e^{-t}\Gamma_\lambda(\nu t,ut)dt,$$

$$\Gamma_\lambda(x,y)=\sum_{i,j}\frac{\gamma_{ij}}{(i+j)!}x^i y^j, \tag{12}$$

and then using the Padé–Chisholm approximants

$$[M,N/K,L]=\sum_{i=0}^{M}\sum_{j=0}^{N}a_{ij}\nu^i u^j\left(\sum_{p=0}^{K}\sum_{q=0}^{L}b_{pq}\nu^p u^q\right)^{-1}.$$

The expansion obtained for $\gamma_\lambda(\nu,u)$ in powers of ν and u in the three-loop approximation makes it possible to use approximants of the form [1,1/1,1] and [2,2/1,1]. The application of the approximants [1,1/1,1] corresponds to an earlier description[12] of the critical dynamics of disordered magnets in the two-loop approximation and gives the value of the dynamical exponent $z^{(2)}_{\rm imp}=2.169849$. The approximants [2,2/1,1] make it possible to obtain the exponent z in the form

$$z=2+\frac{\alpha_1 u}{\beta}+\frac{\beta-1}{\beta^2}(\alpha_2 u^2+\alpha_3 u\nu+\alpha_4\nu^2)+\frac{2\beta^2-\beta+1}{\beta^3}$$
$$\times(\alpha_5 u^2\nu+\alpha_6 u\nu^2)-\frac{1}{\beta}\left[\alpha_1 u+\frac{1}{\beta}(\alpha_2 u^2+\alpha_3 u\nu+\alpha_4\nu^2)\right.$$
$$\left.+\frac{1}{\beta^2}(\alpha_5 u^2\nu+\alpha_6 u\nu^2)\right]_2 F_0(1,1,\beta), \qquad (13)$$

where ${}_2F_0(1,1,\beta)$ is the confluent hypergeometric function, while the functions α_i and β can be calculated from the following relations:

$$\alpha_1=\gamma_{1,0},\quad \alpha_2=\frac{\gamma_{2,0}}{2}-\frac{\gamma_{1,0}\gamma_{3,0}}{3\gamma_{2,0}},$$

$$\alpha_3=\frac{\gamma_{1,1}}{2}-\frac{\gamma_{1,0}\gamma_{0.3}}{3\gamma_{0,2}},\quad \alpha_4=\frac{\gamma_{0,2}}{2},$$

$$\alpha_5=\frac{\gamma_{2,1}}{6}-\frac{\gamma_{1,1}\gamma_{3,0}}{6\gamma_{2,0}}-\frac{\gamma_{2,0}\gamma_{0,3}}{6\gamma_{0,2}},$$

$$\alpha_6=\frac{\gamma_{1,2}}{6}-\frac{\gamma_{1,1}\gamma_{0,3}}{6\gamma_{0,2}}-\frac{\gamma_{0,2}\gamma_{3,0}}{6\gamma_{2,0}},$$

$$\beta=\beta_1 u+\beta_2\nu,$$

$$\beta_1=-\frac{\gamma_{3,0}}{3\gamma_{2,0}},\quad \beta_2=-\frac{\gamma_{0,3}}{3\gamma_{0,2}}.$$

The use of the coupling constants at the impurity fixed point $\nu^*=2.256938$ and $u^*=-0.728168$ gives the following value for the dynamical exponent:

$$z^{(3)}_{\rm imp}=2.165319. \qquad (14)$$

The small change in the value of the exponent $z_{\rm imp}$ calculated in the three- and two-loop approximations shows that higher-order corrections will give only very small changes. The calculations performed in Ref. 12 on the basis of the ε-expansion in the two-loop approximation gave at the same time the value $z^{(2)}_{\rm imp}=2.336$, which substantiates the need to use the renormalization-group procedure directly with $d=3$ to describe the critical behavior of dilute magnets.

In Ref. 13 we performed a calculation of the dynamical critical exponent for the homogeneous three- and two-dimensional ferromagnetic systems in the four-loop approximation on the basis of the Ginzburg–Landau–Wilson dynamical relaxation model. Specifically, for the three-dimensional Ising model the value $z^{(4)}_{\rm pure}=2.017$ was obtained for the dynamical exponent using the Padé–Borel summation technique. The large numerical differences between the values of the dynamical exponent for homogeneous and dilute Ising models make it possible to determine the effect of impurities on the dynamical critical behavior both in real physical experiments and in computer experiments using Monte Carlo methods.

Let us compare with the results of computer modeling of the dynamic critical behavior of the disordered Ising model the value obtained for the dynamical exponent $z^{(3)}_{\rm imp}$.[14–16] In Refs. 14 and 15 computer modeling of the critical relaxation of magnetization in a system with dimensions 48^3 and spin concentration $0.4\leqslant p\leqslant 1$ was performed. The Monte Carlo method combined with the dynamical renormalization-group method[17] was used to determine the dynamical critical exponent z. For homogeneous and weakly disordered systems with $p=0.95$ and 0.8, the following values were obtained for the exponents: $z(1.0)=1.97\pm0.08$, $z(0.95)=2.19\pm0.07$, and $z(0.8)=2.20\pm0.08$, which are in good agreement with our computational results. In Ref. 16 the values of the exponent z were obtained on the basis of an analysis of the asymptotic properties of the dynamical autocorrelation function for a system in a state of equilibrium and demonstrating strong fluctuations of the magnetization. Thus, the following values were obtained: $z(1.0)=2.095\pm0.008$ for a uniform system, $z(0.95)=2.16\pm0.01$, $z(0.9)=2.232\pm0.004$, and $z(0.8)=2.38\pm0.01$ for weakly disordered systems, and $z(0.6)=2.93\pm0.03$ with $p=0.6$. Adhering to the concept that the fixed point of the critical behavior of weakly disordered systems, which does not depend on the impurity concentration, is also a fixed point for any impurity concentration, in Ref. 16 the asymptotic value of the dynamical exponent was estimated to be $z=2.4\pm0.1$. The value of the exponent z obtained in Ref. 16 for a homogeneous system strongly conflicts with the results of the field-theoretic approach, while for $p=0.95$ the agreement between the values is good. Our point of view concerning the universality of the critical behavior of disordered systems was stated in Refs. 14 and 15, where we suggested that the universal critical behavior of weakly disordered systems be determined from the analogous behavior for strongly disordered systems and we advanced the hypothesis of step universality of critical exponents for three-dimensional disordered systems.

The prediction of the theory as to the effect of impurities on the dynamical critical behavior of magnets (higher value of $z_{\rm imp}(d=3)$ compared with $z_{\rm pure}(d=3)$) can be detected in a number of experimental methods: inelastic neutron scattering—the linewidth $\omega_\varphi\propto|T-T_c|^{z\nu}$ at $q=0$ and $\omega_\varphi\propto q^z$ at $T=T_c$; ESR and NMR magnetic resonance—the width of the resonance line $\Delta\omega\propto|T-T_c|^{(d-2+\eta-z)\nu}$, where η is the Fisher exponent; measuring the dynamical susceptibility for a high-frequency external magnetic field $\chi(\omega)\propto\omega^{-\gamma/z\nu}$ at $T=T_c$, where γ is the susceptibility exponent; ultrasonic experiments, where the sound absorption coefficient $\alpha(\omega)\propto|T-T_c|^{-(\alpha+z\nu)}w^2 g(\omega/|T-T_c|^{z\nu})$, the sound dispersion $C^2(\omega)-C^2(0)\propto|T-T_c|^{-\alpha}f(\omega/|T-T_c|^{z\nu})$. Unfortunately, we know of no works where an experimental investigation of the dynamical critical behavior of weakly dilute Ising-like magnets was performed.

This work was supported by the Russian Fund for Fundamental Research under Grant No. 97-02-16124.

[1] A. B. Harris, J. Phys. C **7**, 1671 (1974).
[2] D. E. Khmel'nitskiĭ, Zh. Éksp. Teor. Fiz. **68**, 1960 (1975) [Sov. Phys. JETP **41**, 981 (1975)].
[3] C. Jayaprakach and H. J. Katz, Phys. Rev. B **16**, 3987 (1977).
[4] I. O. Mayer, A. I. Sokolov, and B. N. Shalaev, Ferroelectrics **95**, 93 (1989).
[5] I. O. Mayer, J. Phys. A **22**, 2815 (1989).
[6] C. De Dominicis, Nuovo Cimento Lett. **12**, 567 (1975).
[7] E. Brezin *et al.*, Phys. Rev. D **8**, 434 (1973); *ibid.*, , 2418 (1973).
[8] V. V. Prudnikov and I. D. Lawrie, J. Phys. C **17**, 1655 (1984).
[9] N. N. Bogolyubov and D. V. Shirkov, *Introduction to the Theory of Quantum Fields* [Wiley, N.Y., 3rd edition, 1980; Nauka, Moscow, 1976, 416 pp.].
[10] S. L. Ginzburg, Zh. Éksp. Teor. Fiz. **68**, 273 (1975) [Sov. Phys. Solid State **41**, 133 (1975)].
[11] G. A. Baker, B. G. Nickel, and D. I. Meiron, Phys. Rev. B **17**, 1365 (1978).
[12] V. V. Prudnikov and A. N. Vakilov, Zh. Éksp. Teor. Fiz. **101**, 1853 (1992) [Sov. Phys. JETP **74**, 990 (1992)].
[13] A. V. Ivanov, V. V. Prudnikov, and A. A. Fedorenko, Vestn. Omsk. universiteta, No. 3, 27 (1997).
[14] V. V. Prudnikov and A. N. Vakilov, JETP Lett. **55**, 741 (1992).
[15] V. V. Prudnikov and A. H. Vakilov, Zh. Éksp. Teor. Fiz. **103**, 962 (1993) [J. Exp. Theor. Phys. **76**, 469 (1993)].
[16] H.-O. Heuer, J. Phys. A **26**, L-341 (1993).
[17] N. Jan, L. L. Moseley, and D. Stauffer, J. Stat. Phys. **33**, 1 (1983).

Translated by M. E. Alferieff

Surface spin dynamics of magnets near spin-orientational phase transitions

S. V. Tarasenko

Donetsk Physicotechnical Institute of the Ukrainian Academy of Sciences, 340114 Donetsk, Ukraine
(Submitted February 23, 1998)
Fiz. Tverd. Tela (St. Petersburg) **40**, 1532–1536 (August 1998)

The sufficient conditions for the formation of a dipole-exchange generalized surface spin wave which softens near a volume spin-orientational phase transition are found for a definite form of the high-frequency magnetic susceptibility tensor. © *1998 American Institute of Physics.* [S1063-7834(98)02708-7]

The development of high-quality sources of coherent optical-range electromagnetic radiation has made optical spectroscopy one of the most promising methods for studying the critical dynamics of condensed media near the stability boundaries of the thermodynamic state under examination,[1] including near spin-orientational phase transitions (SOPTs). However, in the case of optically opaque materials, the study of light scattering by crystral surface excitations whose dynamical characteristics vary substantially near the phase transition under study takes on special significance. This concerns first of all surface acoustic waves (SAWs), among which first and foremost are Rayleigh-type SAWs, Love waves, and Gulyaev–Blyushteĭn waves. In Ref. 2 it is shown that analysis of the conditions for Rayleigh-wave propagation likewise can also be an effective tool for studying the critical spin dynamics at SOPTs in the case of magnetic phase transitions. Specifically, the conditions under which a sharp decrease of velocity (right down to zero on the line of second-order SOPTs itself) and an increase of the damping of a Rayleigh-type surface acoustic wave (SAW) occur at a mechanically free boundary of a magnet near a proper ferroelastic SOPT were found in Ref. 2. This requires that the propagation direction of a SAW in the plane of the crystal boundary coincide with the directions in **k** space which, for the SOPT under study in an unbounded magnet, correspond to anomalously diverging critical fluctuations. It is easy to show that the other types of SAWs listed above will also possess similar anomalies in the dynamical characteristics near second-order SOPTs. However, the practical use of the anomalies, indicated in Ref. 2, of the dynamical characteristics of SAWs near SOPTs shows a number of substantial limitations in an entire series of cases. In the first place, most SOPTs by far are dipole-active,[3] and therefore the above-listed effects in the SAW spectrum can be effectively suppressed by a magnetic-dipole (or magnetoelectric) interaction. In the second place, the geometry of a specific sample can be such that the propagating SAW will not soften near the SOPT of interest. In the third place, as shown in Ref. 4, some SOPTs are not proper ferroelastic transitions and therefore the anomalies found in Ref. 2 in the dynamics of surface phonons will not occur in them for any relative orientations of the equilibrium order parameter vector, the vector normal to the surface of the sample, and the propagation vector of any of the above-indicated types of SAWs. Finally, the elastic boundary conditions can differ so much from the conditions on a mechanically free boundary of a crystal (for example, rigid clamping of the surface) that propagation of all of the above-listed types of SAWs will, in principle, become impossible.[5] On this basis it is of special interest to investigate surface spin waves (SSWs) that soften near second-order SOPTs. In the case of magnetic-dipole-active spin oscillations such excitations can be *H*-type surface magnetic polaritons, whose short-wavelength limit are surface magnetostatic spin waves (MSWs).[6] The number of works devoted to the investigation of these excitations in different multisublattice magnetic structures (and, first and foremost, antiferromagnetic) is now increasing unabatedly.[7–10] The interest in these magnetic objects is due not only to the technological progress made in preparing high-quality antiferromagnetic crystals but also the fact that magnetic superlattices of the type ferromagnet — nonmagnetic metal, which are now being intensively investigated, in the case of antiferromagnetic coupling between the layers can also be described in the effective-medium approximation by the indicated model of an antiferromagnet.[11,12] The theory of surface MSWs in a model of a semibounded antiferromagnet was first developed in Refs. 13–15. Specifically, it follows from this model that if an antiferromagnetic crystal with spatially uniform magnetic ordering is located in an external magnetic field **H**, then surface MSWs are not realized either in the polar magnetooptic configuration ($\mathbf{H} \parallel \mathbf{n} \perp \mathbf{k}_\perp$) or in the longitudinal magnetooptic configuration ($\mathbf{n} \perp \mathbf{H} \parallel \mathbf{k}_\perp$). Here **n** is the normal to the interface of the magnetic and nonmagnetic media, while $\mathbf{k}_\perp$ is the wave vector of the surface MSW. In the special case that the external magnetic field $\mathbf{H}=0$, a necessary condition for the existence of a surface MSW is that the relations $\mathbf{n}\hat{\mu}\mathbf{n}<0$ and $\mathbf{k}_\perp \hat{\mu} \mathbf{k}_\perp <0$, where $\hat{\mu}$ is the magnetic susceptibility tensor of the antiferromagnet under study, must be satisfied simultaneously. Finally, in the case of a transverse magnetooptic configuration ($\mathbf{n} \perp \mathbf{H} \perp \mathbf{k}_\perp$) the frequency of the surface MSW formed in a two-sublattice antiferromagnet (AFM) lies between the uniform AFMR frequencies.[13–15] Thus, when the nonuniform exchange interaction is taken into account, surface excitations of this type (just as their analog Damon–Eshbach waves in a ferromagnet) become pseudosurface or leaky surface spin waves. At the same time, it was indicated

first in Ref. 16 that as a result of hybridization of the magnetic-dipole and exchange mechanisms of the spin-spin interaction, the formation of a dipole-exchange SSW is possible near the surface of a magnet. As an example, a semibounded easy-axis ferromagnet with easy axis $OZ \| \mathbf{n}$ was studied in Ref. 16. A similar magnon-localization mechanism was investigated in Ref. 17 for an easy-axis AFM under the assumption that the equilibrium orientation of the antiferromagnetism vector is perpendicular to the interface of the magnetic and nonmagnetic media. Thus far, however, the question important for the optical spectroscopy of SOPTs in opaque magnets of a criterion which the dipole-exchange spectrum of the soft magnon mode of an unbounded magnet must satisfy so that the formation of a generalized dipole-exchange SSW which softens near the SOPT under study would be possible at the interface of magnetic and nonmagnetic media has remained unresolved. The objective of the present paper is to determine this criterion.

The paper consists of several sections. The general formulation of the dipole-exchange boundary-value problem for a two-sublattice model of an orthorhombic AFM occupying a half-space on whose surface the spins are completely free is given in Sec. 1. The analysis is performed for a quite general form of the magnetic susceptibility tensor of an orthorhombic AFM, characteristic, specifically, for all uniaxial magnetic structures, both even and odd relative to the principal axis. On this basis the conditions determining the character of the localization of dipole-exchange spin oscillations near an interface of magnetic and nonmagnetic media are obtained in Sec. 2. The dispersion relation for a generalized dipole-exchange SSW which travels along the surface of the interface and softens near a second-order SOPT is also found and investigated in this section. A criterion for the formation of a generalized dipole-exchange SSW whose frequency softens near the second-order SOPT under study is proposed in Sec. 3, using the results obtained in the preceding sections. The relations obtained are specified for the case of a Morin-type phase transition in an easy-axis antiferromagnet (EA-AFM) in a magnetic field **H** perpendicular to the easy axis.

1. BASIC RELATIONS

As an example of a magnetic medium we shall consider a model of an exchange-collinear two-sublattice AFM. As is well known, the dipole-exchange dynamics of such a dynamical system is described by a closed system of equations, consisting of the Landau–Lifshitz equations for the ferro- and antiferromagnetism vectors (**m** and **l**) and the equations of magnetostatics. Assuming that the uniformly magnetized AFM medium occupies the half-space $\nu<0$ with normal **n** to the interface of the magnetic and nonmagnetic media (ν is the running coordinate along the direction **n**), this system of dynamical equations must be supplemented by appropriate boundary conditions. In the present case we shall assume that the spins at the AFM surface $\nu=0$ are free, $\tilde{\mathbf{m}}$ and $\tilde{\mathbf{l}}$ describe small deviations of the ferromagnetism and antiferromagnetism vectors from the equilibrium orientations

$$\frac{\partial \tilde{m}}{\partial \nu}=\frac{\partial \tilde{l}}{\partial \nu}=0, \tag{1}$$

and, in addition, a standard system of electrodynamic boundary conditions for the normal component of the magnetic induction vector $\mathbf{B}_m(\mathbf{B})$ and the tangential component of the magnetic field $\mathbf{H}_m(\mathbf{H})$ of the magnetic (nonmagnetic) medium must be imposed:

$$\mathbf{B}\cdot\mathbf{n}=\mathbf{B}_m\cdot\mathbf{n}, \quad \mathbf{H}\times\mathbf{n}=\mathbf{H}_m\times\mathbf{n}, \quad \nu=0. \tag{2}$$

Since the objective of the present paper is to analyze the conditions under which surface dipole-exchange magnons are formed, it will be assumed below that, together with the relations (1) and (2), the following conditions are also satisfied ($\varphi_m(\varphi)$ is the magnetostatic potential in the magnetic (nonmagnetic) medium)

$$|\tilde{\mathbf{m}}|,\varphi_m,|\tilde{\mathbf{l}}|\to 0, \quad \nu\to-\infty,$$
$$\varphi\to 0, \quad \nu\to\infty. \tag{3}$$

As an example, in the present paper we shall analyze the dipole-exchange spin dynamics of two-sublattice AFMs such that the branches of the spectrum in the model of an unbounded magnet can be divided, according to the type of their excitation by a microwave field **h**, into quasiferromagnetic ($\mathbf{h}\perp\mathbf{H}$, ω_F) and quasiantiferromagnetic ($\mathbf{h}\|\mathbf{H}$, ω_{AF}).[18] If terms no higher than second order in the components of the magnetization vectors of the sublattices $\mathbf{M}_{1,2}$ ($|\mathbf{M}_1|=|\mathbf{M}_2|=M_0$) are retained in the magnetic energy, then in the case when the external magnetic field $\mathbf{H}\| \mathbf{M}\| OX$ ($\mathbf{m}=(\mathbf{M}_1+\mathbf{M}_2)/2M_0$) while the antiferromagnetism vector $\mathbf{l}\| OY$ ($\mathbf{l}=(\mathbf{M}_1-\mathbf{M}_2)/2M_0$), the structure of the high-frequency magnetic susceptibility tensor $\hat{\chi}(\omega,\mathbf{k})$ taking account of the nonuniform exchange interaction can be represented in the form (c — phase velocity of the spin waves, χ_0 — static magnetic susceptibility)

$$\chi_{xx}=\chi_0\frac{\omega_{AF}^2+c^2\mathbf{k}^2}{\omega_{AF}^2+c^2\mathbf{k}^2-\omega^2},$$

$$\chi_{yz}=-\chi_{zy}=\chi_0\frac{i\omega_*\omega}{\omega_F^2+c^2\mathbf{k}^2-\omega^2},$$

$$\chi_{yy}=\chi_0\frac{\omega_*^2}{\omega_F^2+c^2\mathbf{k}^2-\omega^2},$$

$$\chi_{zz}=\chi_0\frac{\omega_F^2+c^2\mathbf{k}^2}{\omega_F^2+c^2\mathbf{k}^2-\omega^2},$$

$$\chi_{xy}=\chi_{xz}=\chi_{yx}=\chi_{zx}=0. \tag{4}$$

As shown in Refs. 18 and 19, a weak orthorhombic ferromagnet, whose different special cases are all uniaxial structures, both even and odd relative to the principal axis, is such a magnet. Specifically, a similar structure of $\hat{\chi}(\omega,k)$ occurs in the spin-flop phase of an EA-AFM in a magnetic field **H** directed along the easy axis, in an EP-AFM in the case that **H** is collinear or perpendicular to the hard axis, in the case of a Morin-type phase transition, and so on. For the unbounded

model of an AFM the expression corresponding to (4) for the spectrum of normal dipole-exchange spin waves can be represented in the form

$$\mathbf{k}^4+A\mathbf{k}^2+B=0, \tag{5}$$

$$A=(\omega_F^2+\omega_{AF}^2-2\omega^2+\tilde{A}_F+\tilde{B}_{AF})c^{-2},$$

$$B=((\omega_F^2-\omega^2)(\omega_{AF}^2-\omega^2)+\tilde{A}_F(\omega_{AF}^2-\omega^2)+\tilde{B}_{AF}(\omega_F^2-\omega^2))c^{-4},$$

$$C=1+4\pi\chi_0\left(\frac{k_x^2}{k^2}+\frac{k_z^2}{k^2}\right),\quad \tilde{B}_{AF}=\left(4\pi\omega^2\frac{k_x^2}{k^2}\right)C^{-1},$$

$$\tilde{A}_F=4\pi\omega_*^2\left(\frac{k_y^2}{k^2}+\frac{k_y^2}{k^2}\right)C^{-1}.$$

In summary, for the model (4) considered here for an AFM, neglecting the boundary conditions, the isofrequency surface of normal dipole-exchange spin oscillations (5) as a function of the frequency ω consists of one ($\omega_{AF}>\omega>\omega_F$ or $\omega_F>\omega>\omega_{AF}$) or two ($\omega>\omega_F$, ω_{AF}) concavities.

2. DIPOLE-EXCHANGE MECHANISM OF LOCALIZING OF A SOFT MAGNON MODE AT THE INTERFACE OF MAGNETIC AND NONMAGNETIC MEDIA

Since here we are studying the spin dynamics of magnets near SOPTs of a soft magnon mode type, to simplify the analytical calculations we shall confine ourselves below to the analysis of Eq. (5) under the assumption that there is a strong inequality between the frequencies ω_F and ω_{AF} of the quasiferromagnetic and quasiantiferromagnetic, respectively, AFMR modes of an unbounded AFM. On this basis we neglect the indirect coupling via the magnetic-dipole field between the high- and low-frequency modes of the spin-wave spectrum of the AFM under study. Such an approximation will make it possible to study generalized SSWs, which are a result of the dipole-exchange mechanism of coupling near the crystal surface only of the type of normal spin oscillations of an unbounded magnet that corresponds to a soft magnon mode (quasiferromagnetic or quasiantiferromagnetic).

As result, the characteristic equation following from Eq. (5) for solving the boundary-value problem (1) and (2) will be quadratic in $q^2=-(\mathbf{k}\cdot\mathbf{n})^2$. In this case, the structure of, for example, the amplitude of the magnetostatic potential φ_m in the magnet in a direction along the normal to the interface can be represented in the form ($A_{1,2}$ — independent constants)

$$\varphi_m=A_1\exp(i\omega t-q_1\nu)+A_2\exp(i\omega t-q_2\nu). \tag{6}$$

It follows from Eq. (5) that for $\mathbf{k}\in XZ$, in both the cases $\omega_F\ll\omega_{AF}$ and $\omega_F\gg\omega_{AF}$, the form of the equation determining the form of the section of the isofrequency surface for a normal dipole-exchange spin wave that softens near a SOPT irrespective of its type of excitation by the microwave field (ferromagnetic or antiferromagnetic) can be represented in the form (at the point of the second-order SOPT $\omega_0=0$)

$$k^2=\omega^2(1+4\pi\chi_0\sin^2\vartheta)-\omega_0^2,\quad k^2=k_x^2+k_z^2. \tag{7}$$

In the case of a soft quasiantiferromagnetic mode $\omega_0=\omega_{AF}$ and $\sin^2\vartheta\equiv k_z^2/\mathbf{k}^2$, while for a soft quasiferromagnetic mode $\omega_0=\omega_F$ and $\sin^2\vartheta\equiv k_x^2/\mathbf{k}^2$.

It also follows from Eq. (5) that in the case $|\mathbf{H}|=0$ the section of the isofrequency curve for a soft quasiferromagnetic mode also occurs for $\mathbf{k}\in YZ$: $k^2=\omega^2(1+4\pi\chi_0(k_z^2/\mathbf{k}^2))^{-1}$. The necessary conditions under which, for a given excitation frequency ω and wave number $k_\perp$ of the spin oscillations, localization of a soft dipole-exchange spin wave with the dispersion law (7) is possible near the interface of magnetic and nonmagnetic media, can be determined with the aid of Eqs. (6) and (7). Analysis shows that for $\mathbf{n}\parallel OY$ $\omega_0\equiv\omega_{AF}$ ($\omega_{AF}\ll\omega_F$), while for $\mathbf{n}\parallel OZ$ $\omega_0\equiv\omega_F$ ($\omega_{AF}\gg\omega_F$): condensation of a volume dipole-exchange soft magnon mode into a bipartite SSW with $q_{1,2}^2>0$ occurs only for ω and $k_\perp$ satisfying the condition

$$\omega^2<\frac{\omega_0^2+c^2k_\perp^2}{1+4\pi\chi_0}. \tag{8}$$

Dipole-exchange SSWs of a similar type are also possible in the case that with $\mathbf{n}\parallel OZ$ $\omega_0\equiv\omega_{AF}$ ($\omega_{AF}\ll\omega_F$) and with $\mathbf{n}\parallel OY$ $\omega_0\equiv\omega_F$ ($\omega_{AF}\gg\omega_F$) ω and $k_\perp$ lie in the interval

$$\omega_0^2+c^2k_\perp^2<\omega^2<\omega_+^2(k_\perp), k_\perp>k_*,$$

$$\omega^2<\omega_-^2(k_\perp),\quad \omega_\pm^2\equiv N_1\pm(N_1^2-N_2)^{1/2},$$

$$N_1\equiv\frac{2c^2k_\perp^2 4\pi\chi_0+\omega_0^2(1+4\pi\chi_0)}{(1+4\pi\chi)^2},$$

$$N_2\equiv\frac{\omega_0^4}{(1+4\pi\chi_0)^2}. \tag{9}$$

However, in contrast to Eq. (8), in the same geometry formation of a bipartite generalized dipole-exchange SSW (Re $q_{1,2}^2\neq0$, Im $q_{1,2}^2\neq0$)

$$\omega_-^2<\omega^2<\omega_+^2 \tag{10}$$

at the interface of the magnetic and nonmagnetic media is also possible. The condition for the system (1)–(3) to have a nontrivial solution for the amplitudes of the partial waves $A_{1,2}$ (6) is sufficient for the existence of a dipole-exchange SSW, propagating along the free surface of a semiinfinite AFM, with a prescribed direction of the wave vector $\mathbf{k}$ of the magnetic oscillations in the plane of the boundary. In the case (7) a calculation of n shows that for $\mathbf{k}\in XZ$ with $\mathbf{n}\parallel OX$ ($\omega_F\ll\omega_{AF}$) or $\mathbf{n}\parallel OZ$ ($\omega_F\gg\omega_{AF}$) the corresponding dispersion equation for the spectrum of a dipole-exchange SSW that softens near a volume SOPT can be represented in the form

$$(q_1+q_2+k_\perp)q_1q_2+k_\perp(q_1^2+q_2^2)=k_\perp^3,$$

$$q_{1,2}^2=\frac{P_1}{2}\pm\left(\left(\frac{P1}{2}\right)^2-P_2\right)^{1/2},$$

$$P_1=\frac{2c^2k_\perp^2+\omega_0^2-\omega^2(1+4\pi\chi_0)}{c^2},$$

$$P_2 = k_\perp^2 \frac{c^2 k_\perp^2 + \omega_0^2 - \omega^2}{c^2}. \quad (11)$$

As follows from Eq. (8), this type of SSW is not realized either in a strictly magnetostatic approximation ($c \to 0$) or in a strictly exchange approximation (formally in Eqs. (7) and (8) the term with 4π must be neglected).

The character of the localization, at the interface of magnetic and nonmagnetic media, of the solution found can be analyzed with the aid of Eqs. (6) and (8)–(10). It is not difficult to show that for $k_\perp < k_*$ the propagating dipole-exchange SSW (11) is a generalized type of SSW, i.e., for it Re $q_{1,2}^2 \neq 0$, Im $q_{1,2}^2 \neq 0$. For $k_\perp = k_*$ this type of localized spin-wave excitation of a semibounded AFM smoothly passes into a bipartite dipole-exchange SSW with $q_{1,2}^2 > 0$. Here k_* is determined from Eq. (10) with the condition

$$\omega_+(k_*) = \omega. \quad (12)$$

Using Eq. (11), it is possible to obtain in the short-wavelength limit ($k_\perp \geqslant k_{**}$, $k_{**}^2 \equiv \omega_0^2 4\pi\chi_0/(1-4\pi\chi_0)$) in an explicit form the dispersion law for dipole-exchange SSW (11) with $q_{1,2}^2 > 0$, if it is assumed that the relation $4\pi\chi_0 \ll 1$ is satisfied. In this case

$$\omega^2 \approx \omega_0^2 + c^2 k_\perp^2 - \frac{(4\pi\chi_0)^2(\omega_0^2 + c^2 k_\perp^2)}{4k_\perp^4}. \quad (13)$$

3. CRITERION FOR THE FORMATION OF DIPOLE-EXCHANGE GENERALIZED SSWS

It is of unquestionable interest to indicate a criterion on whose basis the conditions under which the formation of a generalized dipole-exchange SSW, that softens near the volume SOPT under study, is possible, along a chosen direction of propagation $\mathbf{k}_\perp$ at the interface of magnetic and nonmagnetic media, can be determined by analyzing the character of the isofrequency surface of a soft magnon mode of an unbounded magnet. For this, let us consider the section of an isofrequency surface of a soft magnon mode of an unbounded magnet by a plane determined by the normal **n** to the interface of the magnetic and nonmagnetic media and the direction of propagation $\mathbf{k}_\perp$ of the SSW under study. Analysis of Eq. (7) shows that for $k_\perp < k_*$ under the condition

$$\omega^2 < \frac{\omega_0^2}{1-4\pi\chi_0} \quad (14)$$

a region with maximum negative curvature forms on the section of the isofrequency surface of the soft magnon mode (7) along the direction of the generalized SSW found above.

As a result, comparing the conditions found above for the existence of a dipole-exchange generalized SSW (11) and the relation (14) it can be concluded that, a sufficient condition for the formation on the surface of an unbounded magnet, with the system of boundary conditoins (1)–(13) of a generalized dipole-exchange SSW that softens near the boundary of the SOPT under study, is the presence on a corresponding section of the isofrequency surface of the self-magnon mode of an unbounded magnet of a section with maximum negative curvature along the propagation direction of the SSW.

As an example, let us consider the expression for the spectrum of a soft magnon mode ω_0 in the case of a phase transition of an EA-AFM in a magnetic field perpendicular to the easy axis (Morin-type phase transition).[3] The density of the thermodynamic potential in this case can be represented in the form

$$W = \frac{\delta}{2}\mathbf{m}^2 + \frac{\alpha}{2}(\nabla \mathbf{l})^2 - \frac{b}{2}l_z^2 + \frac{b_2}{4}l_z^4 - d(m_x l_y - m_y l_x) - \mathbf{M}\cdot\mathbf{H}, \quad (15)$$

where δ and α are, respectively, the uniform and nonuniform exchange interaction constants, b and b_2 are the uniaxial magnetic anisotropy constants, and d is the Dzyaloshinskiĭ interaction constant. The presence of an external magnetic field $\mathbf{H} \parallel OX$ leads to the possibility of a SOPT from an antiferromagnetic state ($\mathbf{l} \parallel OZ$) into a weakly ferromagnetic state ($\mathbf{l} \parallel OY$, $\mathbf{m} \parallel OX$). The Morin-type SOPT can be a first-order phase transition for $H < H_*$, $T < T_*$, which for

$$H_* \equiv \frac{8|K_2|}{M_*}, \quad K_1(T_*) - 8|K_2| = 0,$$
$$K_1 \equiv \frac{d^2 - b\delta}{2\delta}, \quad M_* \equiv \frac{2d}{\delta}, \quad K_2 \equiv -\frac{-b_2}{2} \quad (16)$$

becomes a second-order phase transition.[3] Analysis of Eq. (15) shows that in both phases the structure of the high-frequency magnetic susceptibility tensor $\hat{\chi}(\omega, \mathbf{k})$ is identical to Eqs. (4). In the present case the soft magnon mode is a quasiantiferromagnetic mode of the spin-wave spectrum of the antiferromagnet (15) under study. The dispersion law of the mode is determined by the following expression [g — gyromagnetic ratio, $c^2 = g^2 M_0^2 \delta\alpha$ — phase velocity of spin waves in Eqs. (4) in the model (15)]:

$$\omega_0^2 = g^2 \sin\vartheta(2K_1\cos\vartheta + 4K_2\sin^2\vartheta\cos\vartheta + M_* H). \quad (17)$$

Since in the canted phase $l_{y,z} \neq 0$ the equation for the angle ϑ in Eq. (17) is determined by the relation

$$\cos^3\vartheta - 3p\cos\vartheta + 2q = 0,$$
$$3p \equiv \frac{1-K_1}{2|K_2|}, \quad 2q \equiv \frac{M_* H}{4|K_2|}, \quad (18)$$

it is easy to see that the frequency of the soft magnon mode (17) decreases to zero (in the model under consideration) not only on the second-order phase transition line

$$2K_1 + M_* H = 0, \quad (19)$$

but also as the critical point (16) is approached along the first-order SOPT line. As follows from the calculations presented above, these same features will also be observed for the type of generalized dipole-exchange SSW (11) found above with $\mathbf{n} \parallel OZ$ ($\mathbf{k} \in XZ$). It is easy to show that surface magnetostatic spin waves, similar to those studied in Refs. 13–15 and softening near the type of SOPT under study, do not materialize in the geometry under study.

We note that the above-studied dipole-exchange type of generalized SSWs does not materialize in the case that the surface of a magnet with completely free spins is metallized or in the absence of metallization the spins on the surface of the magnet are pinned.

Thus, a sufficient criterion, under which a generalized dipole-exchange surface spin wave, which softens near a second-order SOPT and whose polarization is identical to that of a volume soft magnon mode, forms on a nonmetallized surface of a magnet with free spins, has been formulated on the basis of an analysis of the form of the isofrequency surface of a soft magnon mode of the spectrum of normal spin oscillations of an unbounded orthorhombic AFM whose high-frequency magnetic susceptibility tensor satisfies Eqs. (4).

[1] H. Z. Cummins and A. P. Levanyuk [Eds.], *Light Scattering Near Phase Transition Points* [Elsevier, North-Holland, 1984; Nauka, Moscow, 1990, 414 pp.].
[2] S. V. Gerus and V. V. Tarasenko, Fiz. Tverd. Tela (St. Petersburg) **17**, 2247 (1975) [Phys. Solid State **17**, 1487 (1975)].
[3] K. P. Belov, A. K. Zvezdin, A. M. Kadomtseva, and R. A. Levitin, *Orientational Phase Transitions in Magnets* [in Russian], Moscow, Nauka (1979), 317 pp.
[4] V. G. Bar'yakhtar, I. M. Vitebskiĭ, Yu. G. Pashkevich, V. L. Sobolev, and V. V. Tarasenko, Zh. Éksp. Teor. Fiz. **87**, 1028 (1984) [Sov. Phys. JETP **60**, 587 (1984)].
[5] V. I. Al'shits, V. N. Lyubimov, and A. L. Shuvalov, Zh. Éksp. Teor. Fiz. **106**, 828 (1994) [J. Exp. Theor. Phys. **79**, 455 (1994)].
[6] A. G. Gurevich and G. N. Melkov, *Magnetic Oscillations and Waves* [in Russian], Nauka, Moscow (1994), 461 pp.
[7] F. S. Nortemann, R. L. Stamp, and R. E. Camley *et al.*, Phys. Rev. B **47**, 3225 (1993).
[8] Xuang-Zhang Wang and D. R. Tilley, Phys. Rev. B **52**, 13353 (1995).
[9] T. L. Fanseca, A. S. Carrica, and N. S. Almeida, Phys. Rev. **46**, 11 626 (1992).
[10] M. I. Kaganov, N. B. Pustyl'nik, and T. I. Shalaeva, Usp. Fiz. Nauk **191**(2), 167 (1997).
[11] N. S. Almeida and D. L. Mills, Phys. Rev. B **38**, 6698 (1988).
[12] N. Raj and D. R. Tilley, Phys. Rev. B **36**, 7003 (1987).
[13] V. V. Tarasenko and V. D. Kharitonov, Zh. Éksp. Teor. Fiz. **60**, 2321 (1971) [Sov. Phys. JETP **33**, 1246 (1971)].
[14] R. E. Camley, Phys. Rev. Lett. **45**, 283 (1980).
[15] B. Luthi, D. L. Mills, and R. E. Camley, Phys. Rev. B **28**, 1475 (1983).
[16] R. E. De Wames and T. J. Wolfram, J. Appl. Phys. **41**, 987 (1970).
[17] B. A. Ivanov, V. F. Lapchenko, and A. L. Sukstanskiĭ, Fiz. Tverd. Tela (Leningrad) **27**, 173 (1985) [Sov. Phys. Solid State **27**, 101 (1985)].
[18] E. A. Turov, *Physical Properties of Magnetically Ordered Crystals* [Academic Press, N. Y., 1965; Nauka, Moscow, 1967, 230 pp.].
[19] V. G. Bar'yakhtar, V. A. L'vov, and D. A. Yablonskiĭ, Fiz. Tverd. Tela (Leningrad) **25**, 797 (1983) [Sov. Phys. Solid State **25**, 455 (1983)].

Translated by M. E. Alferieff

Anomalous light diffusion in ferroelectrics having a diffuse phase transition

A. L. Korzhenevskiĭ and L. S. Kamzina

A. F. Ioffe Physicotechnical Institute, Russian Academy of Sciences, 194021 St. Petersburg, Russia
(Submitted January 20, 1998)
Fiz. Tverd. Tela (St. Petersburg) **40**, 1537–1541 (August 1998)

It has been shown by using the statistical approach that the angular dependence of intensity $I(\theta)$ in multiple small-angle light scattering can be described by Lévy's universal distribution functions. The fundamental property of the stability of these distributions permits one to extract information on the characteristics of fractal media as complete as it is possible in the simple single-scattering case. In particular, an analysis of the polarization characteristics of $I(\theta)$ in disordered PST reveals that the surface fractals observed in these crystals are of the heterophase rather than domain origin. © *1998 American Institute of Physics.* [S1063-7834(98)02808-1]

The idea of a possible existence of percolation-type processes in ferroelectrics undergoing diffuse phase transitions obtained supportive evidence from small-angle scattering (SAS) experiments performed on a number of crystals.[1–4] The existence of percolation processes accompanied by a growth in size of (optical) inhomogeneities is argued for qualitatively by the very observation of sharp peaks in SAS intensity within narrow temperature intervals. To obtain quantitative information on the character of evolution of the internal, spatially inhomogeneous structure in crystals having diffuse phase transitions, one has to develop, however, an appropriate optical model of the inhomogeneous medium and to compare experimental data on the SAS intensity with results obtained within some approximate analytical scheme of scattering calculations. It is well known that the simplest of them (and the most convenient for extracting information about a scattering medium) is the single-scattering (Born or Rayleigh) approximation, where the scattered intensity is proportional to the Fourier transform of the pair-correlation function of dielectric permittivity. This approximation requires, however, measurements on fairly thin samples, with a thickness L less than the light mean-free path l_1, which regrettably entails low intensity of the detected scattered radiation. It was shown[5] that in actual lead scandotantalate (PST) and lead magnoniobate (PMN) samples the angular dependence of the anomalous contribution to SAS intensity behaves as $I(\theta)\sim\theta^{-\alpha}$, with $\alpha=3.2$ and 3.35, respectively, and, thus, falls off rapidly with increasing scattering angle θ. Therefore reliable isolation of this contribution from background scattering can be done only for angles $\theta<10°$ (PST) and $\theta<1.5°$ (PMN). On the other hand, the need of excluding the central (unscattered) beam restricts the minimum angle as well, $\theta^0_{\min}\sim 20'-30'$. It would therefore be difficult to use for studying the angular dependence samples substantially thinner than the ones employed in Ref. 1 ($\sim$1 mm).

In principle, the small spatial scale of measured characteristics is typical of most experiments undertaken in studies of fractal media within any one scattering technique (be it light, neutrons, or x-rays). It is essential to know, however, whether we deal with single scattering, where a power-law asymptotic behavior for $I(\theta)$ would provide evidence for the existence of a fractal structure in a medium (with a Hausdorf dimension $d_f=\alpha$ for $\alpha<3$ or $d_s=6-\alpha$ for $\alpha>3$), or with a multiple process, in which case analysis of SAS experimental data on a log-log scale is, generally speaking, insufficient, because in a fractal medium $I(\theta)$ is no longer described by a simple power law. Multiple scattering introduces complications into the analysis not only of the shape of $I(\theta)$, which yields information on characteristic spatial scales of the scattering medium, but of the polarization characteristics of scattered light as well, because one will now have to allow for possible manifestations of the mutual mode transformation in a vector light field[6] (in the case of tensor fluctuations of the dielectric permittivity in the medium). Therefore interpretation of experimental SAS data obtained on relatively thick samples (where one succeeds in isolating the anomalous contribution within a broader range of scattering angles) would require a separate discussion.

This work proposes a statistical approach for the analysis of multiple light scattering in a fractal medium, which permits one to understand better what characteristics of the medium can be derived from the angular dependence of the SAS intensity. The conclusions drawn from this general approach are applicable to treatment of SAS data obtained on PST and PMN crystals. Besides, an analysis of the polarization characteristics measured in PST crystals permitted us to decide on the heterophase (rather than purely domain-type) origin of small-angle scattering and, in this way, to provide a partial answer to the question[5] concerning the physical nature of the surface fractals responsible for the scattering of light.

Because interaction of radiation with most condensed inhomogeneous media is a weak effect, so that the mean-free path of light l_1 (as well as of neutrons, e.g., for thermal neutrons $l_1\sim 1$ mm) is usually large compared to the sample thickness, it turns out that the scattering intensity can be analyzed in the single-scattering approximation, whose cross section $\sigma(\theta)$ is calculated in the Born or eikonal approximations (for the phase shift $\Delta\varepsilon kR_0\ll 1$ or $\gg 1$, respectively). This does not naturally entail any considerations of statistical

character, and the specific features of treatment of scattering data obtained in a fractal medium become manifest only in the need of taking properly into account the finite scale interval within which it exists ($r_{\min} < r \ll R_{\max}$).[7]

Nevertheless, multiple scattering is possible in ferroelectrics having a diffuse phase transition. This is evidenced both by indirect theoretical estimates of l_1 and by the fact that small-angle scattering in thick and thin samples differs considerably in polarization characteristics[8].

Operation in the multiple-scattering mode makes possible (and convenient) application of the statistical approach to SAS data. It may be appropriate to illustrate it first in terms of a simplified scalar-wave model. Note that we are dealing here with small-angle scattering, and it remains small angle as long as the sample thickness $L \ll l_{tr}$, where l_{tr} is the transport length. The latter can be estimated readily from the condition of small scattering into the backward hemisphere[9]

$$l_{\rm tr}^{-1} = \sigma_{\rm tr} = \int_0^{2\pi} d\varphi \int_{\pi/2}^{\pi} \sin\,\theta \sigma(\theta) d\theta. \tag{1}$$

Definition (1) is essentially equivalent to the definition $l_{\rm tr}^{-1} = \langle \sigma(\theta)(1-\cos\theta)\rangle$ used in transport theory.

For isotropic fractal media with $\sigma(\theta) \propto \theta^{-\alpha}$ (for $\theta_{\min} \ll \theta \ll \theta_{\max}$, $\theta_{\min} = 1/kR_{\max}$, $\theta_{\max} = 1/kR_{\min}$, $k = 2\pi/\lambda \gg 1/R_{\min}$), Eq. (1) reduces to a simple expression relating $l_{\rm tr}$ to l_1:

$$l_{\rm tr} = l_1(\theta_{\min})^{2-\alpha} \gg l_1. \tag{2}$$

For sample thicknesses $l_1 \ll L \ll l_{\rm tr}$, scattering remains small angle, and, because the scattered waves are incoherent, it can be identified with a Markovian random process, in which the coordinate z along the axis of the incident beam plays the part of time. The probability density for light to be scattered through a given angle θ in any scattering event coincides with the optical indicatrix of scattering $\varphi(\theta) = \sigma(\theta)/\sigma_{\rm tot}$, where $\sigma_{\rm tot} = \int \sigma(\theta) d\Omega$ is the total single-scattering cross section $\sigma_{\rm tot} \propto \theta_{\min}^{2-\alpha}$. The individual scattering events are statistically independent because, in media that are macroscopically (i.e., on average) isotropic, the scattering cross section $\sigma(\theta)$ depends only on the scattering angle $\theta = \theta_{\rm inc} - \theta_{\rm scat}$. The total (observed) scattering angle Θ_N is a vector sum of all N single-scattering angles θ_i

$$\boldsymbol{\Theta}_N = \sum_{i=1}^{N} \boldsymbol{\theta}_i, \tag{3}$$

where the number of small-angle scattering events $N = L/l_1 \gg 1$, and the SAS intensity $I(\theta)$ coincides with the distribution function of the sum (3) of independent random variables with the same distribution $\varphi(\theta) \sim \theta^{-\alpha}$. Thus the problem of determining the angular relation $I(\theta)$ under small-angle scattering conditions ($N \gg 1$) turns out to be equivalent to the classical statistical problem of the limiting behavior of expansion (3). It was solved by P. Levy, who showed that the distribution function of expansion (3), $P_\alpha(\Theta)$, is a stable distribution, whose attraction basin is fully determined by the exponent α of the function $\varphi(\theta)$. Prior to writing out the expression for $P_\alpha(\Theta)$, it would, however, be expedient to understand the behavior of expansion (3) on a qualitative level. To do this, estimate the number of scattering events N among which one would find with a probability $w \sim 1$ an angle greater than a given one ($\theta = \theta_*$):

$$w = N \int_{\theta_*}^{\infty} \varphi(\theta)\theta d\theta = L \int_{\theta_*}^{\infty} \sigma(\theta)\theta d\theta \approx L/l_1 \theta_*^{2-\alpha} \approx 1. \tag{4}$$

The latter approximate equality in (4) may be considered also as an estimate of the maximum possible scattering angle realized in N events, so that one may use in estimating the typical value of sum (3), $\theta^{\rm typ}$, the function $\varphi(\theta)$ truncated at $\theta > \theta_* \sim L^{1/(\alpha-2)}$:

$$\Theta_N^{\rm typ} \simeq \left[N \int_{\theta_{\min}}^{\theta_*} \theta^2 \varphi(\theta)\theta d\theta \right]^{1/2} \simeq [L L^{\frac{4-\alpha}{\alpha-2}}]^{1/2} = L^{\frac{1}{\alpha-2}} \simeq \theta_*(L). \tag{5}$$

We readily see that, first, for $2 < \alpha < 4$ the behavior of expansion (3) is in accord with the law of anomalous diffusion ($\theta_N^{\rm typ} \propto N^{1/(\alpha-2)} > N^{1/2}$) and, second, for large N sum (3) behaves as one (the largest) term [compare with (4)]. The latter property is in a striking contrast to the behavior of additive random quantities obeying Gaussian statistics, where the behavior of a sum is determined by a large number of contributions, and the probability for a term to be of the order of the total sum tends asymptotically to zero. In the case of multiple small-angle scattering $I(\theta)$ will be described by a normal distribution only for scattering indicatrices $\varphi(\theta)$ which decrease rapidly with increasing θ (for $\alpha > 4$), while in the $2 < \alpha < 4$ case we come for $I(\theta)$, in accordance with Eq. (5), to two-dimensional symmetric distribution functions of Lévy[10] $I(\theta) = P_\alpha(\theta)$:

$$P_\alpha(\theta) = \frac{1}{(2\pi)^2} \int \exp(i\mathbf{k}\boldsymbol{\theta} - b|k|^{\alpha-2}) d^2k, \tag{6}$$

where b is a normalization constant.

As follows from Eq. (6), the wings of $P_\alpha(\theta)$ follow for $\theta \gg \theta^{\rm typ}$ the power-law asymptotic behavior $\varphi(\theta) \propto \theta^{-\alpha}$, a point that demonstrates the Levy distribution-function stability, whose origin was illustrated by estimates (4) and (5). The fundamental property of stability of the Levy distributions makes it in principle possible to determine the index α (and, hence, the Hausdorf fractal dimension of a medium) from data on the angular dependence $I(\theta)$ for $\theta \gg \theta^{\rm typ}$. Taking into account the anomalous character of light diffusion, Eqs. (1), (2), and (5) permit us to derive the following relation for $\theta^{\rm typ}$:

$$\theta^{\rm typ} \simeq \theta_{\min}(L/l_1)^{\frac{1}{\alpha-2}} = (L/l_{\rm tr})^{\frac{1}{\alpha-2}}, \tag{7}$$

whence one immediately sees that the typical scattering angle remains small up to sample thicknesses of the order of $l_{\rm tr}$, which makes the above statistical description self-consistent.

When processing experimental data one naturally cannot know in advance whether the scattering from inhomogeneities is of a diffraction nature or refraction is dominant. It is therefore essential to establish the exact conditions of applicability of Eq. (6) to analysis of the angular dependence

$I(\theta)$. A number of works dealing with multiple small-angle scattering proposed $R_{\max} \ll l_1$ as the necessary condition. This condition may serve as a revealing starting point in a standard derivation of the transport equation whose transformation to the Focker–Planck differential equation suggests an analogy between scattering and normal diffusion. Nevertheless, the statistical approach is based directly on the wave rather than transport equation. In the approximation of a Markovian process (i.e., the approximation where inhomogeneities of a medium in the direction of wave propagation are assumed to be δ correlated), this equation permits one to derive coupled equations for scattered wave-field correlators without presenting this field in the form of a Born perturbative expansion and, accordingly, without invoking any diagram summation procedure. In particular, the solution to the equation for the second-order pair-coherence function $\Gamma(\boldsymbol{\rho},z)$ in the case of a plane incident wave can be written[9]

$$\Gamma(\boldsymbol{\rho},z)=I_0 \exp[-\pi k^2 z H(\boldsymbol{\rho})],$$

$$H(\boldsymbol{\rho})=\frac{1}{2}\int [1-\cos(\mathbf{q}_\perp \boldsymbol{\rho})] G_\varepsilon(\mathbf{q}_\perp,0) d^2 q_\perp , \qquad (8)$$

where $G_\varepsilon(\mathbf{q})$ is the Fourier transform of the pair correlation function of the dielectric permittivity of a medium. The condition of applicability of the above description of multiple light scattering can be formulated[9] in the form of an inequality for solution (8):

$$\lambda \frac{\partial \ln \Gamma}{\partial \rho} \ll 1 , \qquad (9)$$

which, in contrast to the condition of applicability of the Markovian approximation to calculation of the mean wave field, does not contain any restrictions on the mean-free path l_1, because the small-angle region does not contribute to $H(\boldsymbol{\rho})$. For power-law correlators $G_\varepsilon(q) \sim q^{-\alpha}$, the case of interest to us here, condition (9) can be presented as

$$k\rho_{\mathrm{coh}}(L) \simeq (l_{\mathrm{tr}}/L)^{\frac{1}{\alpha-2}} \gg 1 ,$$

$$k^2 z H[\rho_{\mathrm{coh}}(z)] \simeq 1 , \qquad (10)$$

where the second equality may serve as a definition of the wave-field coherence length ρ_{coh}. The first equality in Eq. (10) shows that the Markovian approximation is valid for analysis of small-angle light scattering in isotropic fractal media for sample thicknesses $L \ll l_{\mathrm{tr}}$, i.e., actually within the total small-angle region. Note that in the case of power-law dielectric-permittivity correlators Eq. (8) can be obtained already within the eikonal approximation.[11] The latter cannot, however, in contrast to the Markovian approximation, be considered a priori valid for description of small-angle light scattering for all $L < l_{\mathrm{tr}}$, because it disregards completely the diffraction effects. On the other hand, Eq. (8) is obtained also from the equation of transport of small-angle scattered radiation, which can be derived, however, only under the condition of weak scattering, $R_{\max} \ll l_1$.[9,12] As shown above, this additional condition is unnecessary.

If the coherence function (8) is known, one can readily find the angular dependence of the SAS intensity $I(\theta)$:

$$I(\theta \neq 0) \simeq \frac{k^2 S_\perp}{4\pi^2 R^2}\int d^2\rho \exp(-i\mathbf{k}\boldsymbol{\rho})\Gamma(\rho,L), \qquad (11)$$

where $S_\perp$ is the sample area, and R is the distance to the sample. For isotropic fractal media this angular dependence coincides with the Lévy distribution function (6).

Let us turn now to data on small-angle light scattering in ferroelectrics with a diffuse PT. As follows from the above general statistical treatment of the SAS process, for scattering angles $\theta > \theta^{\mathrm{typ}} \simeq \theta_{\min}(L/l_1)^{1/(\alpha-2)}$ the angular dependence $I(\theta)$ retains its power-law behavior in multiple scattering as well. It appears thus correct, as well as convenient, to measure the angular dependence of intensity on relatively thick samples, provided the observed scattering retains its small-angle pattern (i.e., $L \ll l_{\mathrm{tr}}$). Accordingly, our earlier conclusions[4,5] on the fractal character of the spatial structure in PST crystals may be considered reliably substantiated.

At the same time SAS polarization measurements can also yield valuable information on the symmetry properties of fluctuations in the dielectric permittivity of fractal structures in ferroelectrics with a diffuse PT. Similar to the analysis of spatial characteristics of a medium, the optimum method of treatment of polarization data becomes obvious, even in the presence of multiple light scattering, if one takes into account the following consequence of the statistical approach developed above, namely, that for $\theta > \theta^{\mathrm{typ}}$ small-angle scattering occurs only in rare single-scattering events. Hence the polarization dependence in this region of θ angles can be analyzed in the Born scattering approximation:

$$I(\mathbf{q}) = I_0 k^4 \left\{ G_s(|q|)\,\delta_{ij}\delta_{km} + G_t(|q|) \times \left[\delta_{ik}\delta_{jm} + \delta_{im}\delta_{kj} - \frac{2}{3}\delta_{ij}\delta_{km} \right] \right\} t_i^i t_k^i t_j^s t_m^s , \qquad (12)$$

where t^i and t^s are the polarization vectors of the incident and scattered light, respectively. Equation (12) takes into account that analysis of small-angle scattering (i.e., for $q \to 0$) in a macroisotropic optical medium involves only two independent functions, $G_s(|q|)$ and $G_t(|q|)$, which describe scattering from scalar and tensor fluctuations of dielectric permittivity, respectively:

$$G_s(|q|) = \frac{1}{4}\langle \mathrm{Tr}\Delta\varepsilon(q)\mathrm{Tr}\Delta\varepsilon(-q)\rangle,$$

$$G_t(|q|) = \langle \mathrm{dev}\Delta\varepsilon(q)\mathrm{dev}\Delta\varepsilon(-q)\rangle,$$

$$\mathrm{dev}\Delta\varepsilon = \Delta\varepsilon_{ik} - \frac{1}{3}\delta_{ik}\mathrm{Tr}\Delta\varepsilon,$$

$$\Delta\varepsilon_{ik}^{(\gamma)}(\mathbf{r}) = a_{iklm} P_l^{(\gamma)}(\mathbf{r}) P_m^{(\gamma)}(\mathbf{r}). \qquad (13)$$

The superscript γ in the last equality in (13) identifies a point in the sample with a (γ)-domain polar state. Because the ferroelectric PT in PST crystals occurs from the paraelectric cubic to rhombohedral phase, the polarization vectors of different domains have the following structure: $P^{(\gamma)} = (\pm 1, \pm 1, \pm 1) P_0$, $\gamma = 1, \ldots, 8$.

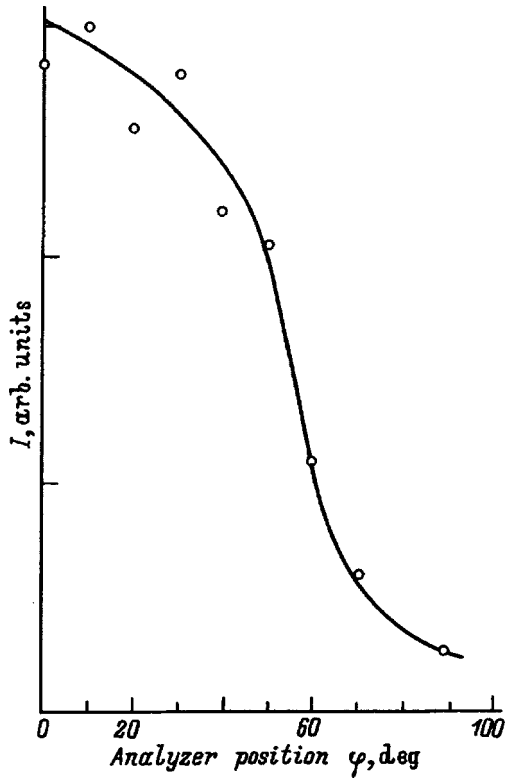

FIG. 1. Polarization dependence of small-angle light-scattering intensity $I(\theta)$ in a PST crystal obtained at the temperature of the anomalous peak. Scattering angle $\theta = 30'$.

We measured the polarization characteristics of SAS intensity on thin PST samples (degree of ordering $s = 0.95$, $T_c = 38$ °C, sample thickness $L = 200$ μm), where the SAS intensity $I(\theta)$ retains its power-law behavior down to the smallest allowable angles $\theta^0_{\min} = 20'$ (Ref. 5).

Figure 1 presents an experimental $I(\theta)$ relation (φ is the angle between t^i and t^s). We readily see that anomalous small-angle scattering cannot be assigned to a single-phase polar state with microdomain structure. Indeed, in the latter case only fluctuations $\Delta\varepsilon_{ik}$ with $i \neq k$ would be nonzero (and, hence, $G_s = 0$), and one would have $I(\varphi) \sim (1 + 1/3\cos^2\varphi)$, which is obviously at odds with the observed dependence on φ. The contribution of scalar fluctuations to scattering appears only in the case of a heterogeneous medium, where polar clusters of the low-temperature phase coexist with regions of the cubic phase.

Thus the polarization dependence of $I(\varphi)$ obtained argues convincingly for the existence in PST crystals of such a heterophase structure. The contribution of domain walls to SAS at the scattering angle $\theta = 30'$ used in our measurements is insignificant, which is apparently associated with the fairly small size of the domains at temperatures close to the position of the SAS peak ($T_c = 38$ °C).

We note in conclusion that the possibility of an adequate description of the polarization dependence of $I(\varphi)$ within the Born approximation, as well as the fact that angular measurements of the SAS intensity $I(\varphi)$ yield for the characteristic angle Θ a value less than $\Theta_{\min} \sim 20'$, suggest that the mean free path of light in PST crystals with $s = 0.95$ and $T_c = 38$ °C is of the order of (or greater than) 200 μm.

Support of the Russian Fund for Fundamental Research (Grants 96-02-16958 and 96-02-16893) is gratefully acknowledged.

[1] L. S. Kamzina and A. L. Korzhenevskiĭ, JETP Lett. **50**, 163 (1989).
[2] L. S. Kamzina and A. L. Korzhenevskiĭ, Fiz. Tverd. Tela (Leningrad) **34**, 1795 (1992) [Sov. Phys. Solid State **34**, 957 (1992)].
[3] L. S. Kamzina, A. L. Korzhenevskiĭ, and N. N. Kraĭnik, JETP Lett. **56**, 519 (1992).
[4] L. S. Kamzina, N. N. Kraĭnik, and O. Yu. Korshunov, Fiz. Tverd. Tela (St. Petersburg) **37**, 2765 (1995) [Phys. Solid State **37**, 1523 (1995)].
[5] A. L. Korzhenevskiĭ, L. S. Kamzina, and O. Yu. Korshunov, JETP Lett. **61**, 219 (1995).
[6] A. Yu. Val'kov and T. I. Tipyasova, Opt. Spektrosk. **79**, 125 (1995) [*sic*].
[7] A. Pearson and R. W. Anderson, Phys. Rev. B **48**, 5865 (1993).
[8] L. S. Kamzina, A. L. Korzhenevskiĭ, N. N. Kraĭnik, and L. M. Sapozhnikova, Izv. Akad. Nauk SSSR, Ser. Fiz. **54**, 614 (1990).
[9] S. M. Rytov, Yu. A. Kravtsov, and V. I. Tatarskiĭ, *Introduction to Statistical Radio Physics*, Vol. 2 [in Russian], Nauka, Moscow, 1978.
[10] J.-P. Bouchaud and F. Georges, Phys. Rep. **195**, 127 (1990).
[11] A. Yu. Val'kov, V. P. Romanov, and T. I. Tipyasova, Zh. Éksp. Teor. Fiz. **99**, 1283 (1991) [Sov. Phys. JETP **72**, 714 (1991)].
[12] S. V. Maleev and B. P. Toperverg, Zh. Éksp. Teor. Fiz. **78**, 315 (1980) [Sov. Phys. JETP **51**, 158 (1980)].

Translated by G. Skrebtsov

Dielectric relaxation in deuterated triglycine sulfate crystals

S. N. Drozhdin and M. A. Kuyantsev

Voronezh State University, 394693 Voronezh, Russia
(Submitted February 10, 1998)
Fiz. Tverd. Tela (St. Petersburg) **40**, 1542–1545 (August 1998)

A study has been made of the slow relaxation of the dielectric permittivity of deuterated triglycine sulfate (DTGS) initiated by application of a dc electric field. The field and temperature dependences of the relaxation time associated with domain-wall motion were obtained. The effect of the internal electric field on relaxation processes is seen in different behavior of the field and temperature dependences under different orientations of the external field. The existence in DTGS crystals of two temperature regions of domain-structure rearrangement lying 7–8 and 15–18 °C below the Curie point has been established. [S1063-7834(98)02908-6]

The behavior of the domain structure of ferroelectrics in applied electric fields is most frequently studied by various indirect methods, because they provide information on the dynamics of the associated processes not only in near-surface layers but in the bulk of the sample as well. Among such methods are, in particular, the relaxation techniques, which permit one to extract the dynamic properties of the domain structure of a crystal from the evolution of various macroscopic parameters (dielectric permittivity, pyroelectric coefficient, loss tangent etc.). The relaxation properties of the domain structure have thus far been studied in most detail in TGS crystals, both nominally pure[1–3] and containing defects of various origin[4,5]. Despite the considerable interest in deuterated TGS (DTGS), both of a purely scientific and applied nature, information on the dynamic properties of its domain structure is very scarce, and the relaxation characteristics have not been investigated at all.

This work reports a study of the relaxation behavior of DGTS domain structure made by measuring the evolution in time of the low-frequency dielectric permittivity ε. The relaxation process was initiated by application of a dc electric field $E_=$.

1. EXPERIMENTAL TECHNIQUES

The DGTS samples were 0.08-cm thick polar-cut plates 1 cm^2 in area, with silver electrodes deposited in vacuum. The dielectric hysteresis loops measured on all samples at 60 Hz yielded the temperature dependence of the coercive, E_c, and internal, E_i, fields, which at $T=25$ °C were found to be, respectively, 270–300 and 40–50 V/cm.

The phase-transition temperature T_c was determined from the maximum of the dielectric permittivity measured by the bridge technique at 1.592 kHz in an ac electric field of amplitude $E_0 \cong 3.7$ V/cm. The values of T_c were found to lie within the interval 57–59 °C for all the samples selected, which yields ~80% for the degree of deuteration of the samples under study.

The relaxation time dependences of the capacitance (dielectric permittivity) were measured under polarization switching of the sample with a dc electric field (Fig. 1). When the external electric-field polarity is reversed, one observes a nonmonotonic behavior of the capacitance in time, which first grows and reaches a maximum value C_0 corresponding to the depolarized state of the sample, to decrease subsequently to a steady-state level C_∞. The falling-off portion of the $C(t)$ dependence displays the transition of the sample to the single-domain state with oppositely directed polarization. At each temperature, from room level to the Curie point T_c, the dc electric field applied to the sample

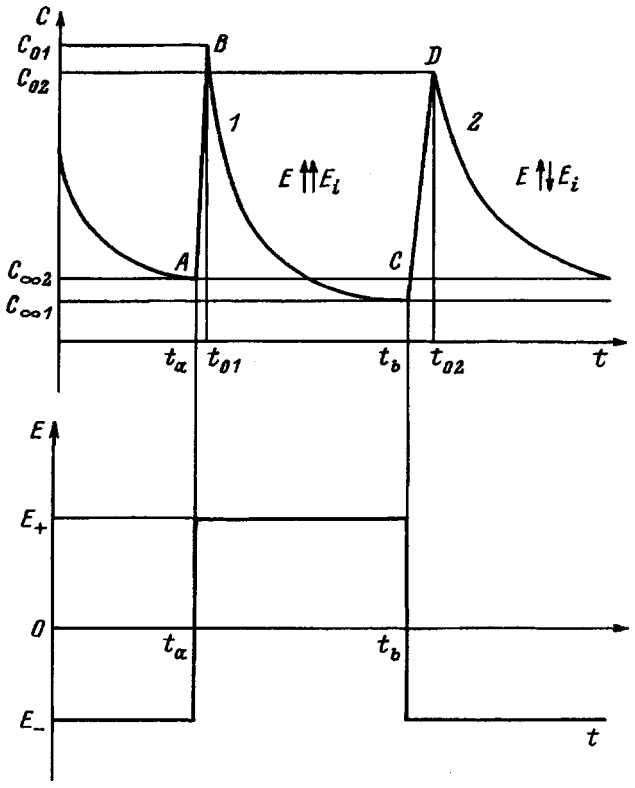

FIG. 1. Schematic presentation of the $C(t)$ relation under consecutive polarization reversal with a dc electric field $E_=$. *1* — $E_=\uparrow\uparrow E_i$, *2* — $E_=\uparrow\downarrow E_i$.

was given in fractions of E_c. This technique ensures a constant initial state of the crystal, which is the state of maximum depolarization.

The falling-off parts of the experimental $C(t)$ curves were fitted with exponential functions of the type[1]

$$C(t)=C_\infty+(C_0-C_\infty)\exp(-t/\tau), \quad (1)$$

where C_0 is the initial capacitance, C_∞ is the steady-state capacitance, τ is the relaxation time, and $C(t)$ is the capacitance at time t.

The validity of this selection of the fitting functions was seen from the quasi-linear behavior of the $f(t)$ relation

$$f(t)=\ln\{[C_0-C_\infty]/[C(t)-C_\infty]\}=t/\tau. \quad (2)$$

The slope of the quasi-linear portions of the $f(t)$ relations yielded the relaxation time for different polarizing fields in the 0.5–2.0 E_c range and different temperatures from 20 °C to the Curie point.

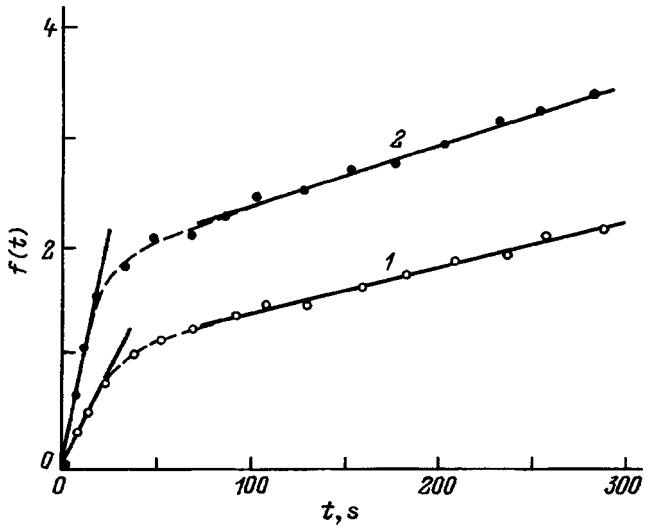

FIG. 3. $f(t)=\ln\{[C_0-C_\infty]/[C(t)-C_\infty]\}$ for two directions of the $E_=$ field: *1* — $E_=\uparrow\uparrow E_i$, *2* — $E_=\uparrow\downarrow E_i$. $T=46$ °C, $E_==1.5\,E_c$.

2. RESULTS OF MEASUREMENTS

Figure 2 presents typical dependences of the capacitance of a DTGS sample on time measured under polarization reversal for two different directions of the applied field $E_=$. We readily see that for one direction of field $E_=$ the initial capacitance C_{01} is larger than that for the other, C_{02}, and conversely, the steady-state value $C_{\infty 1}$ is smaller than $C_{\infty 2}$. This situation is illustrated schematically in Fig. 1.

This difference can be due to the internal field, which for different directions of the external field may either favor relaxation or inhibit it. Thus curve *1* in Fig. 2 corresponds to the external field aligned with the internal field, and for curve *2* the external and internal fields are antiparallel.

The relaxation processes initiated by reversal of the sign of field $E_=$ occur in parallel with the crystal being switched over from one polarization state to the other, with the opposite direction of polarization. Therefore the experimentally observed $C(t)$ relations reflect actually the dynamics of the crystal's domain structure under polarization reversal, and, hence, they should display the various stages of this process[6] with their characteristic times (initial nucleation with τ_1, end-face growth of nuclei with τ_2, lateral motion of domain walls with τ_3, and domain coalescence with τ_4), although these stages do not have distinct boundaries in time.

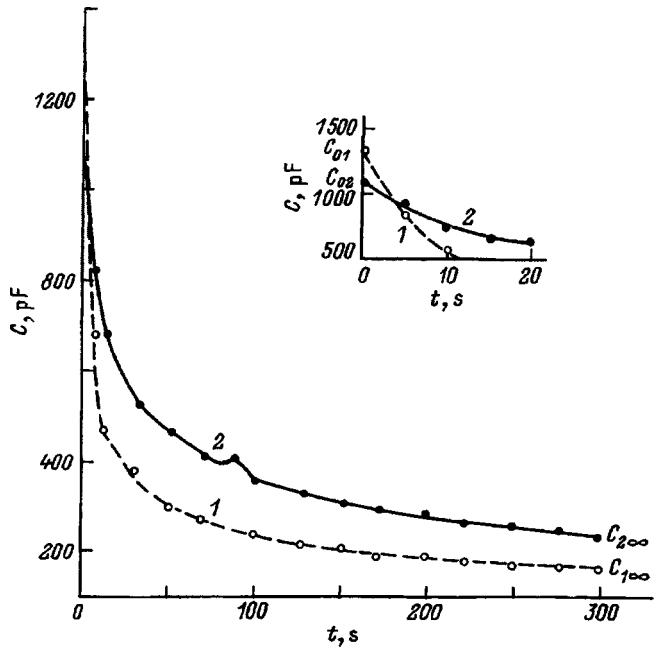

FIG. 2. $C(t)$ relation for a DTGS crystal sample. *1* — $E_=\uparrow\uparrow E_i$, *2* — $E_=\uparrow\downarrow E_i$. $T=35$ °C, $E_==1.5\,E_c$.

Obviously enough, the rapid increase of C (on the time scale of about 5 s) observed following the field reversal (Fig. 1) is due primarily to the first two switching stages, after which the crystal transfers to a depolarized polydomain state with the largest number of domain walls possible in these conditions. This portion of the experimental curves was not studied in this work because of its short duration and the correspondingly large measurement errors.

Fitting Eq. (2) to the falling-off branches of the experimental relaxation curves $C(t)$ reveals clearly two quasi-linear portions (Fig. 3), which correspond apparently to the third and fourth stages of the switching process characterized by the relaxation times τ_3 and $\tau_4>\tau_3$. These portions are of major interest, because, while they both are connected with the lateral motion of domain walls, in the second of them interaction between neighboring walls becomes essential.[6] The fact that the intermediate part in the $C(t)$ relation, as seen from Fig. 3, cannot be described by a single relaxation time probably indicates a change from one polarization reversal stage to another, accompanied by a gradual onset and enhancement of interaction between domain walls.

Figure 4 plots the relaxation time $\tau_3(E_=)$ for two different directions of the polarizing field. One clearly sees that the characteristic relaxation times in the case where the applied field is parallel to the internal field (curve *1*) are shorter than those observed under switching in the opposite direction (curve *2*). In weak fields ($E_=<E_c$), the behavior of the $\tau_3(E_=)$ relations is qualitatively different. Curve *1* exhibits in this field interval a portion with saturation, and the relax-

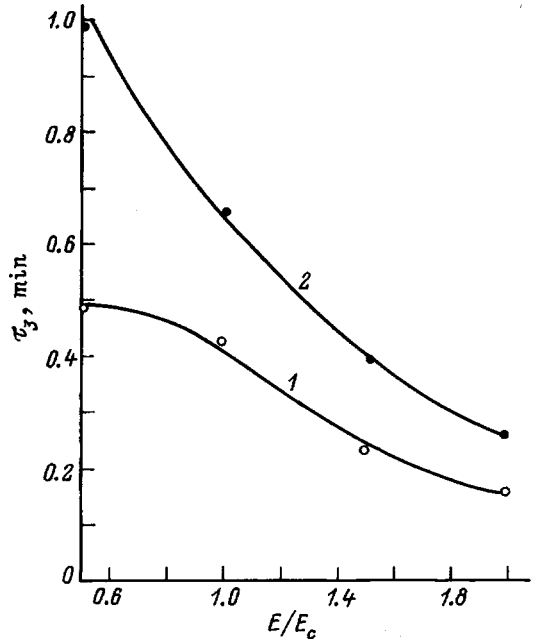

FIG. 4. Field dependences of relaxation time τ_3 for two directions of the $E_=$ field: *1* — $E_=\uparrow\uparrow E_i$, *2* — $E_=\uparrow\downarrow E_i$. $T=33.4$ °C.

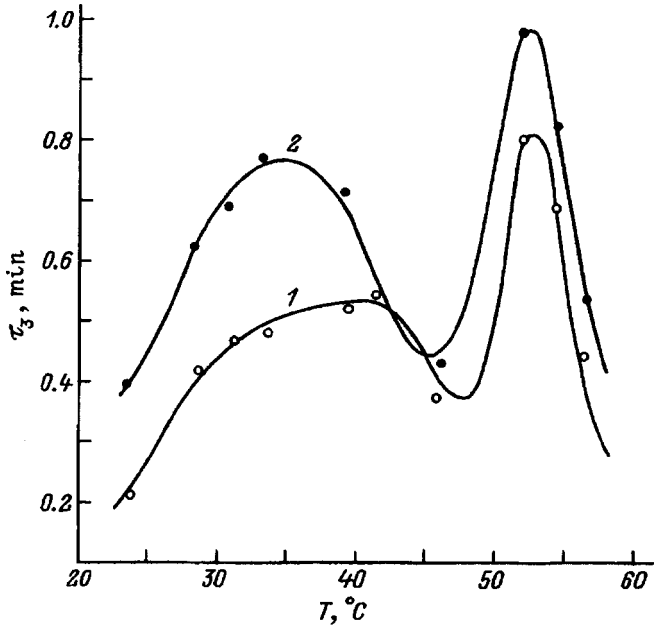

FIG. 6. Temperature dependence of relaxation time τ_3 for two directions of the $E_==E_c$ field: *1* — $E_=\uparrow\uparrow E_i$, *2* — $E_=\uparrow\downarrow E_i$.

ation time observed in these conditions remains finite even for $E_=\cong 0$, which permits one to consider this value of τ_3 as the relaxation time characteristic of spontaneous switching of the sample induced by the internal field. Curve *2* exhibits typically a rapid increase of τ_3 in weak fields, which evidences strongly inhibited polarization with the applied field antiparallel to the internal one.

The field dependences of the relaxation time τ_4 are plotted in Fig. 5. In contrast to the $\tau_3(E_=)$ relations, the $\tau_4(E_=)$ curves obtained for oppositely oriented external fields are seen to behave qualitatively in a similar way throughout the switching field range studied. The $\tau_4(E_=)$ relations are characterized by an increase of relaxation time in both weak and strong fields. Whereas in the weak-field region the increase of τ_4 can be readily explained and is in agreement with the behavior of the field dependences of the TGS relaxation time, the increase of τ_4 at high fields suggests that the interaction between domain walls setting in in this stage of the relaxation process inhibits total transfer of the crystal to the single-domain state, as a result of which the characteristic duration of the process increases.

The temperature dependences of the relaxation times τ_3 and τ_4 obtained in the experiment are shown, respectively, in Figs. 6 and 7. We see that these relations are essentially nonmonotonic and cannot be fitted by the Arrhenius law. These $\tau(T)$ relations exhibit two regions of anomalous growth of the relaxation time, which lie below the Curie point by 7–8 and 15–18 °C, respectively. Such dependences

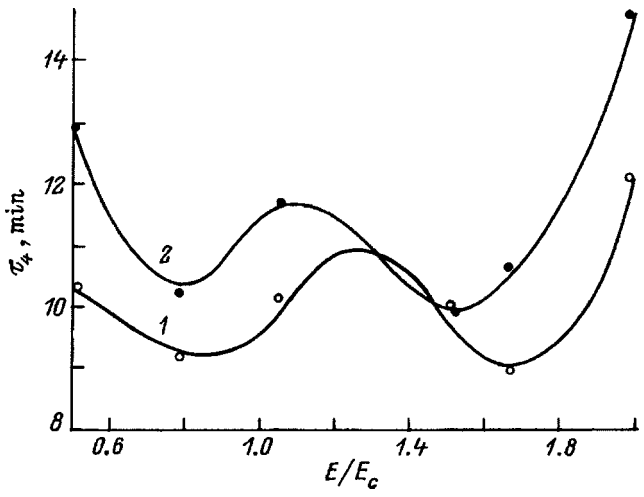

FIG. 5. Field dependences of relaxation time τ_4 for two directions of the $E_=$ field: *1* — $E_=\uparrow\uparrow E_i$, *2* — $E_=\uparrow\downarrow E_i$. $T=52$ °C.

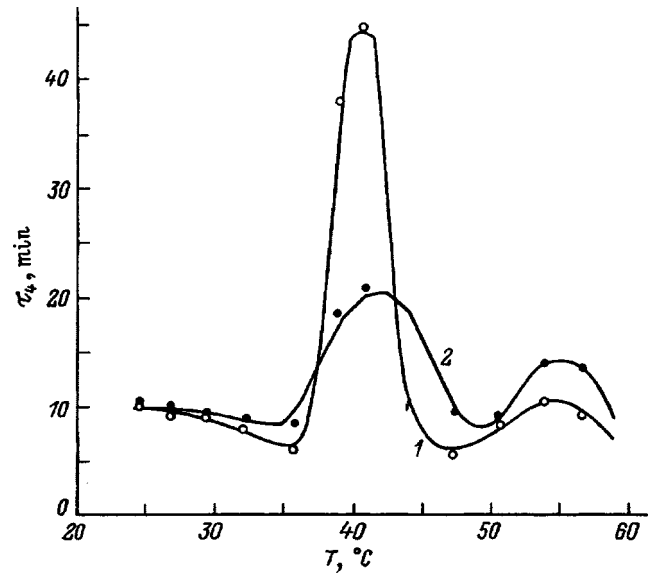

FIG. 7. Temperature dependence of relaxation time τ_4 for two directions of the $E_==2E_c$ field: *1* — $E_=\uparrow\uparrow E_i$, *2* — $E_=\uparrow\downarrow E_i$.

observed on TGS crystals are attributed to the existence of temperature regions within which the domain structure of the crystal undergoes rearrangement. Our results suggest that such regions of spontaneous domain-structure rearrangement exist in DTGS too, although here they are displaced toward higher temperatures by 8–10 °C because of the protons being replaced by the heavier and less mobile deuterons.

The presence of the internal field manifests itself also in the temperature behavior of τ, where it is seen in different absolute values of τ measured at the same temperature for different directions of the applied switching field (Figs. 6 and 7).

3. INTERNAL FIELD IN DTGS CRYSTALS

DTGS crystals studied in this work represent a system with mixed deuteron-proton bonds, because only 80–90% of protons are replaced by deuterons. Thus the crystal has both fast hydrogen bonds, which are capable of responding rapidly to an external field, with protons in the double potential well, and more sluggish deuteron bonds. One may consider the glycine complexes with unsubstituted protons as defects, which create in the crystal an internal bias field producing a certain influence on its properties.

Our measurements showed that this field is not large (40–50 V/cm) and is practically temperature independent throughout the temperature interval studied. Annealing of samples at 110 °C for one hour does not result in disappearance of E_i and even in a noticeable change of its magnitude.

It may be conjectured that bonds with protons, which are the lighter mediators, experience the strongest influence of the external electric field. As a result, the glycine complexes with unsubstituted protons play in the DTGS crystals studied the part of low-energy nucleation centers, where new domains appear under polarization reversal.

To sum up, the problem of the nature and properties of the internal field in crystals with mixed proton-deuteron bonds is of significant interest and deserves both experimental and theoretical investigation.

[1] S. N. Drozhdin, L. N. Kamysheva, and O. M. Golitsyna, Vestnik VGTU, Ser. Fiz. Mater. **1**, No. 1, 96 (1996).
[2] S. A. Gridnev, V. M. Popov, and L. A. Shuvalov, Izv. Akad. Nauk SSSR, Ser. Fiz. Ser. Fiz. **48**, 1226 (1984).
[3] V. V. Gladkiĭ, V. A. Kirikov, and E. S. Ivanova, Fiz. Tverd. Tela (St. Petersburg) **39**, 353 (1997) [Phys. Solid State **39**, 308 (1997)].
[4] L. N. Kamysheva, S. N. Drozhdin, and O. M. Serdyuk, Phys. Status Solidi A **97**, K29 (1986).
[5] L. N. Kamysheva, S. N. Drozhdin, and O. M. Serdyuk, Zh. Tekh. Fiz. **58**, 1607 (1988) [Sov. Phys. Tech. Phys. **33**, 971 (1988)].
[6] L. I. Dontsova, N. A. Tikhomirova, and L. A. Shuvalov, Kristallografiya **39**, 158 (1994) [Sov. Phys. Crystallogr. **39** 140 (1994)].

Translated by G. Skrebtsov

Size effect in isometric $PbTiO_3$ crystals

V. G. Gavrilyachenko

Rostov State University, 344090 Rostov-on-the-Don, Russia

V. D. Komarov and E. G. Fesenko

Scientific-Research Institute of Physics Rostov State University, 344090 Rostov-on-the-Don, Russia

A. V. Leĭderman

Physics Department, University of Puerto Rico at Mayagüez, Mayagüez, Puerto Rico 00680, US

(Submitted February 19, 1998)
Fiz. Tverd. Tela (St. Petersburg) **40**, 1546–1547 (August 1998)

The phase transitions $Pm3m \rightleftarrows P4mm$ and domain-structure formation in 5–500 μm isometric $PbTiO_3$ crystals were investigated. The phase transition is characterized by a high rate and by the formation of a single flat interphase boundary {023}. A size effect was observed: In crystals smaller than a critical size (about 20 μm), formation of 90° domains stops and, in agreement with a phenomenological theory, the temperature hysteresis of the phase transition doubles. © *1998 American Institute of Physics.* [S1063-7834(98)03008-1]

The characteristic features of first-order phase transitions and of the domain structure formed as a result of such transitions largely determine the characteristic physical properties of ferroelectric crystals. For this reason their investigation has become of paramount importance in the physics of phase transitions and in ferroelectric materials science. As shown in Refs. 1–3, in investigations of extended plate-shaped $PbTiO_3$ crystals these features are determined by the values of a number of factors at the phase-transition temperature: 1) internal factors (the jump ΔP_S in the spontaneous polarization and the accompanying jumps in the electric field (depolarization field), the spontaneous deformation, the latent heat of the transition, and the density of free charge carriers) and 2) external factors (rate of change and gradient of the temperature near a phase transition).

Our objective in the present work was to investigate the effect of still another internal factor (crystal size) and external factor (zero-gradient heating and cooling of a crystal near a phase transition) on the phase transitions and domain structure of isometric $PbTiO_3$ crystals.

1. PRODUCTION AND INVESTIGATION OF THE CRYSTALS

The objects of our investigations were isometric $PbTiO_3$ crystals with edge length ranging from 5 to 50 μm. The crystals were obtained by the crucibleless method. A homogeneous mixture of $PbTiO_3$ and PbO was pressed into a 25 mm in diameter and 5 mm high disk and held for 24 h at 850 °C. After cooling, the agglomerate was ground and PbO was dissolved in a 5% water solution of acetic acid at 80 °C. The crystals obtained in this manner are shown in Fig. 1. They are transparent and have a pale-yellow color, their cell parameters are $a=3.896\times10^{-10}$ m, $c=4.136\times10^{-10}$ m, and $c/a=1.062$, and the temperature of the phase transition $P4mm \rightarrow Pm3m$ is $T_c=492-494$ °C, in agreement with existing data. A polarizing microscope, a thermal chamber with an optical channel, and a video camera were used to investigate the phase transitions and the process leading to the formation of domain structure. The temperature interval of the thermal chamber was 18–600 °C; the heating and cooling rates 0.01–0.5 °C·s^{-1} were regulated automatically. For the investigations, 10–15 well-faceted crystals were placed into the thermal chamber, heated above the temperature T_c, and then cooled. The phase transition was registered with the video camera.

Direct observations of the phase transitions and the formation of domain structure under isothermal conditions and frame-by-frame examination of the video film showed that the phase transitions in the crystals occur with the formation of one flat interphase boundary {023}. We investigated such a transition in plate-shaped crystals in Refs. 1–3, where it was established that the domain structure is formed on the interphase boundary as a superposition of layered regular 90° domains with alternating layers of thickness d_1 and d_2, where $d_1+d_2=4-7$ μm. The hysteresis of the phase transition in such crystals did not exceed 7 °C. In the present work, we established that these features of the phase transi-

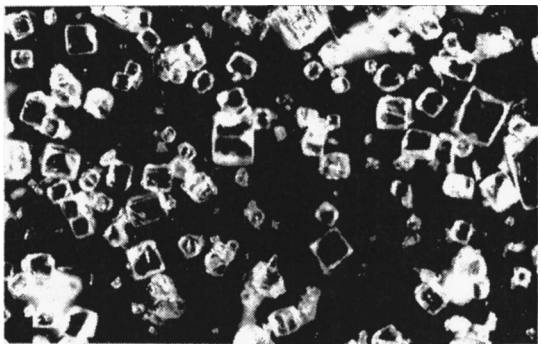

FIG. 1. Isometric $PbTiO_3$ crystals ($\times$400).

tion are characteristic for crystals larger than a critical size, equal to 15–20 μm. As crystal size decreases and approaches the critical size (about 20 μm) the 90° domains formed during the phase transition vanish on completion of the transition. This attests to a loss of stability by the crystals as a result of the fact that the crystal edge becomes of the same order of magnitude as d_1+d_2. In crystals smaller than the critical size 90° domains do not arise at all. Crystal size has no effect on the formation of 180° domain structure. It is significant that in crystals smaller than the critical size (less than 15 μm) the hysteresis of the phase transition reaches 14–17 °C.

2. DISCUSSION

Our results are in agreement with the thermodynamic theory of ferroelectric phase transitions that takes account of the influence of the relaxation of internal mechanical stresses on a phase transition.[4,5] Internal mechanical stresses, which unavoidably accompany the formation of nuclei of a new phase, are taken into account by introducing an effective electrostriction parameter δ. The relaxation of the internal mechanical stresses will be most complete in the case when the phase transition proceeds by means of the appearance and development of a single nucleus of a new phase, while the interphase boundary is (on the average over 90° domains) a plane of zero deformation (so-called optimal twinning).

In $PbTiO_3$ the {023} plane is the zero-deformation plane accompanying a phase transition. Under conditions of optimal twinning in $PbTiO_3$ 90° domains form every time, while the parameter δ is minimum. In the absence of 90° domains the internal mechanical stresses build up on the interphase boundary with indices {023}; this increases the parameter δ by 3 to 4 orders of magnitude as compared with the minimum value.[3–5] The magnitude of the hysteresis of the phase transition is determined by the expression[4]

$$\Delta T = -3\delta(\beta_1+\delta)/4\alpha_0\gamma_1, \quad (1)$$

where α_0, β_1, and γ_1 are coefficients in the expansion of the thermodynamic potential in a series in powers of the polarization. For $PbTiO_3$, in the absence of 90° twinning, $\delta = 32.2\times10^6$ J·m^5·C^{-4} (taken from Table 1.3 of Ref. 3). Near the phase-transition temperature $\alpha_0 = 3.33\times10^5$ J·m·C^2·K^{-1}, $\beta_1 = -5\times10^8$ J·m^5·C^{-4}, $\gamma_1 = 1.2\times10^{10}$ J·m^9·C^{-6} (data from Table 1.1 of Ref. 3). A calculation performed using Eq. (1) and these data gives $\Delta T \approx 19$ °C, which is close to the experimental values (14–17 °C).

As ΔT increases, the phase-transition rate increases, as a result of which minimization of the depolarization field is accomplished by 180°-domain formation with no screening of P_s, since, despite the high density of free charge carriers at the phase-transition temperature, there is not enough time for complete screening of P_S to occur in the $PbTiO_3$ crystal. The vanishing of 90° domains after the completion of the phase transition in crystals larger than a critical size can be explained by the small area of the 90°-domain walls, inadequate for stabilizing the walls at dislocations.[6]

[1] E. G. Fesenko, V. G. Gavrilyachenko, A. F. Semenchev, and S. M. Yufatova, Fiz. Tverd. Tela (Leningrad) **27**, 1194 (1985) [Sov. Phys. Solid State **27**, 719 (1985)].
[2] E. G. Fesenko, U. G. Gavrilyachenko, and A. F. Semenchev, Ferroelectrics **100**, 195 (1989).
[3] E. G. Fesenko, V. G. Gavrilyachenko, and A. F. Semenchev, *Domain Structure of Multiaxial Ferroelectrics* [in Russian], Rostov University, Rostov-on-the-Don, 1990.
[4] A. V. Turik, A. I. Chernobabov, and V. Yu. Topolov, Fiz. Tverd. Tela (Leningrad) **25**, 2839 (1983) [Sov. Phys. Solid State **25**, 1640 (1983)].
[5] A. V. Turik, A. I. Chernobabov, and V. Yu. Topolov, Fiz. Tverd. Tela (Leningrad) **26**, 3618 (1984) [Sov. Phys. Solid State **26**, 2176 (1984)].
[6] V. S. Boĭko, R. I. Garber, and A. M. Kosevich, *Reversible Plasticity of Crystals* [in Russian], Naukova Dumka, Kiev (1990), 280 pp.

Translated by M. E. Alferieff

LATTICE DYNAMICS. PHASE TRANSITIONS

Energetics of the thermoelastic effect in solids

V. L. Gilyarov and A. I. Slutsker

A. F. Ioffe Physicotechnical Institute, Russian Academy of Sciences, 194021 St. Petersburg, Russia

V. P. Volodin and A. I. Laĭus

Institute of Macromolecular Compounds, Russian Academy of Sciences, 199004 St. Petersburg, Russia

(Submitted February 12, 1998)
Fiz. Tverd. Tela (St. Petersburg) **40**, 1548–1551 (August 1998)

The dependence of the temperature on the external adiabatic deformation is determined for a one-dimensional model of a solid — chains of atoms with an anharmonic interaction. The resulting dependences of the average kinetic and potential components of the internal energy on this deformation are compared with a model of adiabatic loading of a single oscillator.
 [S1063-7834(98)03108-6]

The thermoelastic effect consists in a change in the temperature of a solid under elastic adiabatic loading. When a solid with a positive thermal expansion coefficient is stretched, the temperature decreases, and when such a solid is compressed the temperature increases. A good approximation in describing the thermoelastic effect is Kelvin's relation[1,2]

$$\frac{\Delta T}{T} = -\frac{\alpha}{C}\sigma, \tag{1}$$

where T and ΔT are, respectively, the temperature of the body and the change in temperature under a load, σ is the stress, α is the linear thermal expansion coefficient, and C is the specific heat (per unit volume). The presence of the thermal expansion coefficient in Eq. (1) indicates that this effect is due to the anharmonicity of the interatomic interaction.

The energetics of the thermoelastic effect exhibit interesting features. For example, when a body is compressed and its temperature increases, the increase ($C\Delta T$) in the thermal energy of the body is an order of magnitude larger (for small loads) than the measured work of deformation.[3] This fact, as well as the decrease in the thermal energy of a body (decrease of the temperature) on stretching, when work is also performed on the body, make it desirable to perform a detailed investigation of the energetics of the thermoelastic effect.

1. ANALYTICAL ANALYSIS

We shall analyze the energetics of the thermoelastic effect for the example of a one-dimensional chain of atoms.

Since the deformations considered are small, it is sufficient to give the interatomic interaction in the form of a potential with cubic anharmonicity

$$\varphi(x) = \frac{f}{2}x^2 - \frac{g}{3}x^3, \tag{2}$$

where the dynamical variable $x = r - r_0$, and r_0 is the coordinate of the well bottom, equal to the equilibrium interatomic distance a at the mechanical limit.

The self-consistent Einstein approximation can be used to calculate the thermodynamic characteristics.[4] Then the free energy per atom of a chain of $N \gg 1$ atoms, taking account only of the nearest neighbors, has the form[5]

$$F = -\frac{kT}{2} + kT \ln \frac{\hbar}{2kT}\sqrt{\frac{\phi}{m}} + \psi(\Delta a), \tag{3}$$

where $\psi(x)$ is the softened pair-interaction potential, ϕ is the force constant determined from the self-consistency condition, $\Delta a = a\varepsilon$ is the average displacement of an atom from the position of equilibrium, and ε is the relative deformation of the bonds.

On scales much larger than kT/ϕ, which is the mean-square vibrational amplitude of the atoms, long-wavelength expansions are valid for the potential ψ and the force constant ϕ:[5]

$$\psi(x) \approx \frac{kT}{2} + \varphi(x) + O(\varphi^{\mathrm{IV}}/\varphi''),$$

$$\phi(x) \approx 2\varphi''(x) + O(\varphi^{\mathrm{IV}}/\varphi''). \tag{4}$$

Then, for the main thermodynamic functions of the internal energy, stress tensor, and entropy

$$w = F + TS, \quad \sigma = \frac{\partial F}{\partial \varepsilon}, \quad S = -\left(\frac{\partial F}{\partial T}\right)_{\varepsilon}$$

we obtain

$$w = kT + \varphi(\Delta a), \quad P = -\frac{1}{a^2}\left[\varphi' + \frac{1}{2}kT\frac{\varphi'''}{\varphi''}\right],$$

$$S = k\left(1 - \ln \frac{\hbar}{2kT}\sqrt{\frac{\phi}{m}}\right). \tag{5}$$

The stress tensor in the one-dimensional case reduces to the pressure P. A characteristic feature of the internal energy w is that it is additive with respect to two physical components: the thermal energy and the interaction potential energy. Such an expression is exact for a cubic pair-interaction potential. A characteristic feature of the pressure in the system is its additivity with respect to the same two components: a potential component, reflecting elasticity, and a thermal component, associated with the entropy force of the thermal pressure.

Let us now examine the adiabatic deformation of a one-dimensional chain of atoms at constant entropy. The basis of the energetics, considered here, of adiabatic deformation is the law of conservation of energy, which in the present case has the form of the first law of thermodynamics

$$dQ \equiv TdS = dw + Pa^3 d\varepsilon = 0. \tag{6}$$

For finite changes of the quantities the expression (6) must be integrated between the initial and final states. The initial state is the state of thermodynamic equilibrium with temperature T_1 and the corresponding thermal deformation $\varepsilon_1 \simeq gkT_1/af^2$.[6] The final state produced by the external deformation is characterized by the temperature T_2 and deformation ε_2, which in the general case can be represented as

$$\varepsilon_2 = \varepsilon_1 + \varepsilon_f. \tag{7}$$

The expression (7) determines the mechanical deformation ε_f in an adiabatic process.

Integrating Eq. (6), we obtain

$$k\Delta T + \Delta\varphi = -a^3 \int_{\varepsilon_1}^{\varepsilon_2} P(\varepsilon, T)\, d\varepsilon = a \int_{\varepsilon_1}^{\varepsilon_2} \left(\varphi'(\varepsilon) + \frac{kT\varphi'''}{\varphi''} \right) d\varepsilon = \Delta\varphi + kT \ln \sqrt{\frac{\phi_2}{\phi_1}}. \tag{8}$$

The left-hand side of Eq. (8) is the internal-energy change, consisting of thermal and potential parts, in the adiabatic process. The right-hand side is the work of deformation, likewise consisting of two parts: mechanical, compensating exactly the change in the potential part of the internal energy, and entropic, which is the work performed by the thermal pressure. The force constants appearing in Eq. (8) can be found from Eq. (4).

A specific feature of a heated anharmonic body is the thermal expansion of the bonds, in which is manifested the balance of forces in the position of thermodynamic equilibrium, where the thermal pressure force is balanced by the elasticity of the bonds. External deformation results in additional stretching of the bonds, and the entropic force of the thermal pressure performs additional work on this displacement up to establishment of a new position of equilibrium.

For small changes of the state we find from Eq. (8) to first order in the anharmonic force constant

$$\frac{\Delta T}{T_1} = -\frac{ga\varepsilon_f}{f}. \tag{9}$$

This expressions corresponds to the thermoelastic effect—the change in temperature under adiabatic deformation. The expression (9) can be easily reduced to the Kelvin relation (1).[7] In the form (9), however, this expression combined with Eq. (5) for w makes it possible to analyze the behavior of the internal energy in an adiabatic deformation process.

Let us rewrite the expression (5) for the internal energy in the form

$$w = \frac{1}{2}kT + \frac{1}{2}kT + \varphi(\Delta a). \tag{10}$$

Here the first term is the average kinetic energy E_k per degree of freedom, while the last two terms are the average potential energy E_p (by definition, the internal energy is the ensemble-averaged total energy of the system minus its macroscopic motion and the result of the action of the external forces). Using Eq. (9), we find for these components for the final state to first order in g

$$E_k(\varepsilon_f) = E_1\left(1 - \frac{ga\varepsilon_f}{f}\right),$$
$$E_p(\varepsilon_f) = E_1\left(1 + \frac{ga\varepsilon_f}{f}\right) + \varphi(a\varepsilon_f), \tag{11}$$

where $E_1 = (1/2)kT_1$.

In the initial state we have from Eq. (10)

$$E_k = E_1, \quad E_p = E_1 + \varphi(a\varepsilon_1) = E_1 + 2\frac{g^2}{f^3}E_1^2. \tag{12}$$

The expression for E_p differs from Eq. (11) by the term quadratic in g. When it is taken into account, the average potential and kinetic components in Eq. (12) differ from one another. This corresponds to violation of the virial theorem in anharmonic systems. It can be shown, by means of uncomplicated but tedious calculations, that the rest of the corrections in Eq. (11) which are of second order in g are quadratic in the force and are of no consequence in the case of small loads, with which we shall be concerned below. Therefore the expression (11) under small loads can be assumed to equal

$$E_k(\varepsilon_f) = E_1\left(1 - \frac{ga\varepsilon_f}{f}\right),$$
$$E_p(\varepsilon_f) = E_1\left(1 + 2\frac{g^2}{f^3}E_1 + \frac{ga\varepsilon_f}{f}\right) + \varphi(a\varepsilon_f). \tag{13}$$

These energy functions can be traced in the mechanics of adiabatic loading of an anharmonic oscillator, proposed in Ref. 8.

2. COMPARISON WITH ADIABATIC LOADING OF A SINGLE OSCILLATOR

The foregoing construction of the thermodynamics of a chain of atoms employed the self-consistent Einstein model. In this model, which is based on the variational theorem of statistical physics, the free energy of a system is calculated starting from an ensemble of oscillators. For this reason, it is of interest to compare the results obtained here with the re-

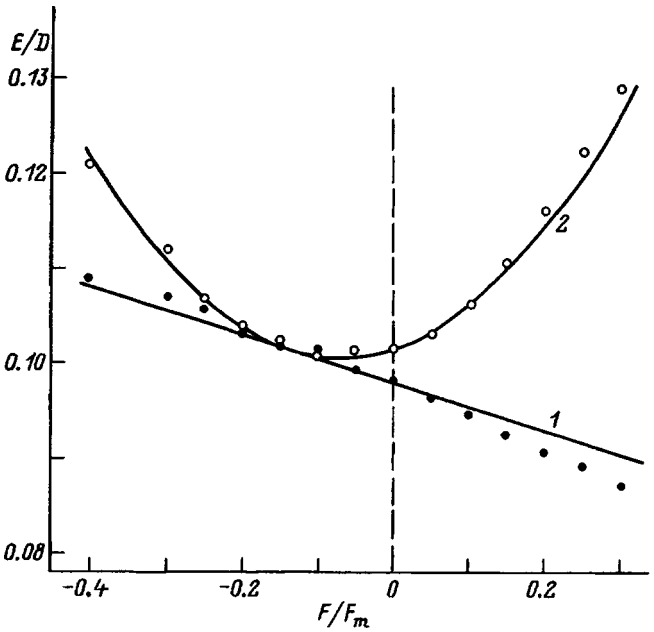

FIG. 1. Comparison of the analytical force dependences of the energy (solid lines) and the numerical results (dots). *1*—Average kinetic energy, *2*—average potential energy.

sults obtained by numerical averaging in the model of adiabatic loading of a single oscillator.[8] This is especially important since we are dealing with time averages in a mechanical model, whereas in the thermodynamic model we are dealing with ensemble averages (ergodic hypothesis). Since the internal energy and its components (13) permit a mechanical analogy, it is natural to use these quantities for comparisons.

In the mechanical model[8] an anharmonic oscillator with energy $E_0=0.2D$, where the dissociation energy of the oscillator (2) $D=f^3/6g^2$, was loaded slowly with an increasing external force. After the system arrived in the final state, time averages of the kinetic and potential components of its energy were obtained for different values of this force. These quantities can be compared with the values calculated from Eqs. (13).

For this, it is necessary to convert the deformation entering in Eq. (13) to the external load $F=-Pa^2$ in the final loaded state. It can be shown that to first order in the anharmonicity this relation is expressed by a nonlinear elasticity law $F=fa\varepsilon_f-g(a\varepsilon_f)^2$. For the loads considered below the contribution of the nonlinear term in this dependence to the energy does not exceed several percent, so that we shall neglect it. The thermodynamic and mechanical energy parameters are compared in Fig. 1. The energies are measured in units of the dissociation energy D and the force is measured in units of the ultimate strength $F_m=f^2/4g$. The agreement between these data is seen to be completely satisfactory. The discrepancies (especially in the stretching region) are apparently mainly due to the force corrections to Eq. (13) which are quadratic in the anharmonic constant g.

The difference of the average potential and kinetic components from one another expresses the deviation of the anharmonic system from the virial theorem. In the absence of an external load the internal energy, according to Eq. (12), equals

$$E_0=E_1\left(2+\frac{E_1}{3D}\right),$$

whence

$$E_k\equiv E_1\cong\frac{1}{2}E_0\left(1-\frac{E_0}{12D}\right),$$

$$E_p\cong\frac{1}{2}E_0\left(1+\frac{E_0}{12D}\right). \tag{14}$$

TABLE I.

Quantity	Eq. (14)	Mechanical system
E_k/D	0.09833	0.09821
E_p/D	0.10167	0.10172

The energies from Eqs. (14) are presented in Table I together with the values obtained numerically for a mechanical system.

Therefore good agreement with the mechanical calculation is observed here as well.

The result of this work is a detailing of the energetics of an adiabatically loaded anharmonic solid. Equations were obtained for the deformation dependences of the average kinetic and potential components of the internal energy. These dependences agree well with the numerical mechanical model and graphically illustrate the breakdown of the virial theorem, as is characteristic for an anharmonic system with a nonuniform potential energy function. The changes in the kinetic and potential components explain the interesting energetics of the thermoelastic effect.

This work was performed under the financial support of the Russian Fund for Fundamental Research (Project code 96-03-32467a).

[1] W. Thompson (Lord Kelvin), Mathematical and Physical Papers. London (1890), 592 pp.
[2] A. Nadin, *Plasticity and Fracture of Solids*, Vol. 2. [in Russian], Moscow, 864 pp.
[3] Yu. K. Godovskiĭ, *Thermophysics of Polymers* [in Russian], Moscow (1982), 280 pp.
[4] T. Matsubara and K. Kamiya, Prog. Theor. Phys. **58**, 767 (1977).
[5] V. L. Gilyarov, in *Nonlinear Effects in Fracture Kinetics* [in Russian], Leningrad, 1988, p. 3.
[6] Ya. I. Frenkel', *Kinetic Theory of Liquids* [Clarendon Press, Oxford, 1946); Nauka, Leningrad, 1945, 460 pp.].
[7] A. I. Slutsker and V. P. Volodin, Theor. Chim. Acta **247**, 111 (1994).
[8] V. L. Gilyarov, A. I. Slutsker, V. P. Volodin, and L. A. Laĭus, Fiz. Tverd. Tela (St. Petersburg) **39**, 153 (1997) [Phys. Solid State **39**, 132 (1997)].

Translated by M. E. Alferieff

LOW-DIMENSIONAL SYSTEMS AND SURFACE PHYSICS

Structural features of solid gallium in microporous glass

I. G. Sorina, E. V. Charnaya, and L. A. Smirnov

Institute of Physics, St. Petersburg State University, 198904 Petrodvorets, Russia

Yu. A. Kumzerov

A. F. Ioffe Physicotechnical Institute, Russian Academy of Sciences, 194021 St. Petersburg, Russia

C. Tien

Cheng Kun National University, 701 Tainan, Taiwan

(Submitted January 23, 1998)
Fiz. Tverd. Tela (St. Petersburg) **40**, 1552–1553 (August 1998)

An experimental Debye-Scherrer study of structural features of gallium in porous glass with pore diameter $d=4$ nm is reported. Gallium structures different from the known bulk modifications have been discovered. © *1998 American Institute of Physics.*
[S1063-7834(98)03208-0]

Porous glasses loaded by various materials have been recently attracting considerable interest. The properties of geometrically confined substances can differ substantially from those of bulk samples. For instance, water freezes in porous glass in cubic structure different from the conventional hexagonal bulk modification, as indicated by neutron diffraction studies of glass with a pore diameter of 5 nm.[1] Solid deuterium in porous glass likewise does not resemble in structure the bulk form.[2] Therefore investigation of the structure of gallium in porous glass is of particular significance because, even in the bulk state, it exhibits a number of specific structural properties. It is known, for instance, that bulk pure gallium crystallizes in a number of modifications differing notably from one another.[3]

The sample under study was prepared of glass obtained by thermal treatment of a sodium borosilicate system, which was subsequently subjected to acid attack.[4] The glasses were tested by mercury porometry and electron microscopy. The pore diameter $d=4$ nm, the pore volume was 0.15 cm^3/g. Liquid gallium was injected into porous glass at a pressure of 9 kbar. The pore volume filling was about 90%.

The structural features of solid gallium in porous glass were studied by the Debye-Scherrer method[5] within the 4.5–300 K range using Cu Kα radiation. The results of the studies are presented schematically in Figs. 1–4. As evident from the experimental data, solid gallium crystallizes in pores in three different modifications. The structure labeled 1 forms in the sample cooled from room temperature to 250 K (Fig. 1) and is present in all Debye patterns without any exclusion (note that gallium filling the pores at room temperature is in the liquid state). As the temperature is lowered down to 150 K, one observes superposition of another structure labeled 2 (Fig. 2). After the sample was warmed to $T=300$ K and cooled again to 200 K, another modification (structure 3), differing from the first two, is seen against the background of structure 1 (Fig. 3). The Debye pattern of the sample again cooled to 150 K contains all three structures (Fig. 4). At other temperatures one observed various combinations of the first and the other two structures.

We have succeeded in deciphering structure 1 using Hell's curves[5]. It exhibits a tetragonal bcc lattice with $a=b=0.325$ nm and $c=0.495$ nm, and differs from the known modifications of bulk gallium. Note that the bulk gallium modification forming at pressures above 3.0 GPa has tetragonal bcc lattice with $a=b=0.2813$ nm and $c=0.4458$ nm.[3] The large difference between the lattice parameters does not,

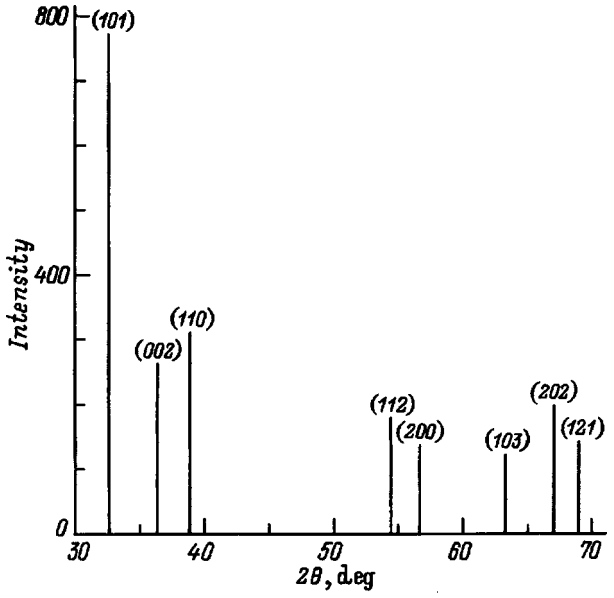

FIG. 1. Debye pattern for gallium in porous glass with $d=4$ nm; structure *1*, $T=250$ K.

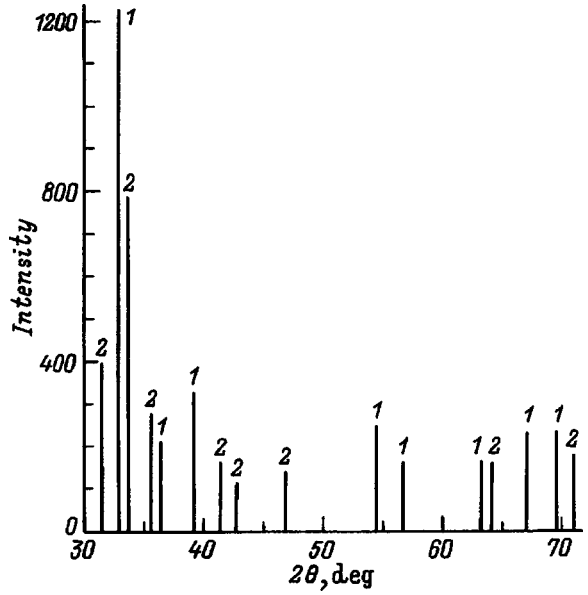

FIG. 2. Debye pattern for gallium in porous glass with $d=4$ nm; structures *1* and *2*, $T=150$ K.

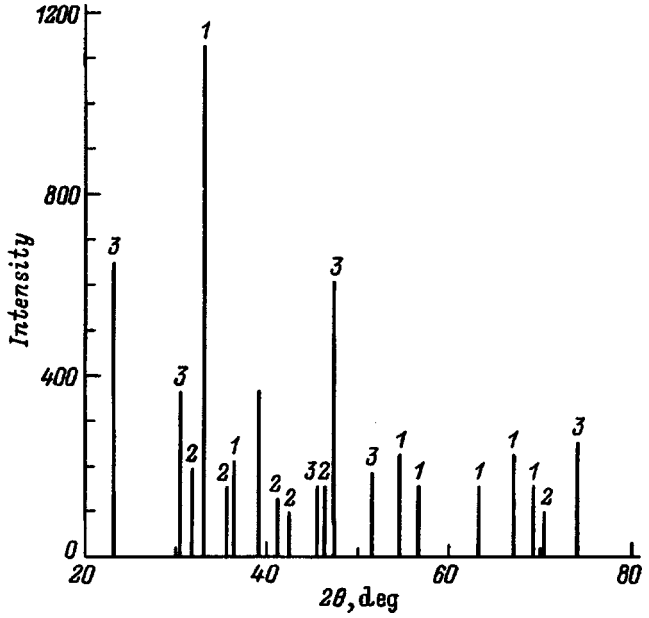

FIG. 4. Debye pattern for gallium in porous glass with $d=4$ nm; structures *1*, *2*, and *3*, $T=150$ K.

however, permit us to consider these structures to be identical.

Structure 2 contains lines belonging to the α modification of bulk gallium. The absence of some α-Ga reflections is possibly due to bulk gallium having graphite-like lattice,[6] and therefore it possibly has atomic planes which are bonded weaker than atoms in the plane itself. Hence these planes can, in principle, shift in porous glass, which may make some reflections forbidden while allowing others.[7] Thus structure 2 is possibly a disordered α modification in which bulk gallium can crystallize under normal conditions.

Structure 3 has a lower symmetry, which makes its assignment considerably more difficult. One can, however, maintain with confidence that the corresponding lines fit to none of the known modifications of bulk gallium.

In this way, our x-ray diffraction studies of solid gallium loaded in porous glass indicate a possibility of formation in porous glass of gallium structures different from the bulk modifications, and of a structure representing a disordered α modification of bulk gallium.

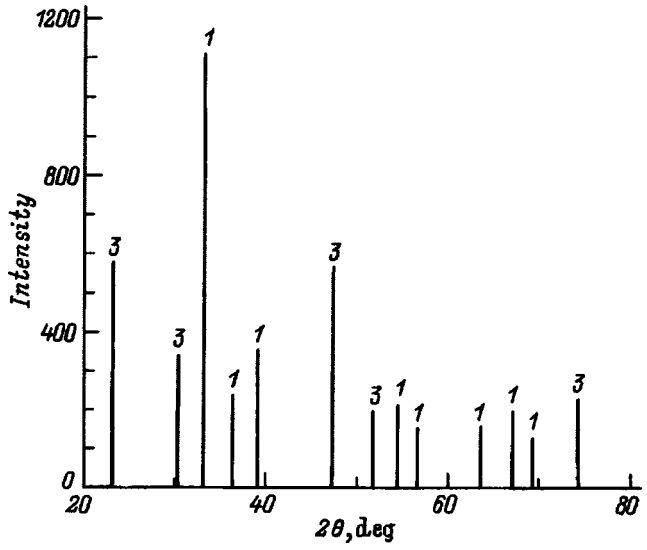

FIG. 3. Debye pattern for gallium in porous glass with $d=4$ nm; structures *1* and *3*, $T=200$ K.

Support of the Russian Fund for Fundamental Research (Grant 96-02-19523) and of the NSC (Taiwan) (Grant 86-2112-M-006-012) is gratefully acknowledged.

[1] M.-C. Bellissent-Funel, J. Lai, and L. Bosio, J. Chem. Phys. **98**, 4246 (1993).
[2] Y. Wang, W. M. Snow, and P. E. Sokol, Low Temp. Phys. **101**, 929 (1995).
[3] *Chemical Encyclopedia*, Vol. 5, edited by I. L. Knunyats [in Russian], Sov. Éntsikl., Moscow (1988), 623 pp.
[4] *Two-Phase Glasses: Structure, Properties, and Applications*, edited by B. G. Varshal [in Russian], Nauka, Leningrad (1991), 275 pp.
[5] *Modern Crystallography*, Vol. 1, edited by B. K. Vainshtein *et al.* [in Russian], Nauka, Moscow (1979), 383 pp.
[6] G. B. Bokiĭ, *Introduction to Crystal Chemistry* [in Russian], Moscow State Univ., Moscow (1954), 490 pp.
[7] B. E. Warren, *X-Ray Diffraction* (Dover, New York, 1990).

Translated by G. Skrebtsov

Quantum corrections to 2*D* hole conductivity in a quantum well on Te$(10\bar{1}0)$

N. S. Averkiev, V. A. Berezovets, G. E. Pikus, N. I. Sablina, and I. I. Farbshtein

A. F. Ioffe Physicotechnical Institute, Russian Academy of Sciences, 194021 St. Petersburg, Russia
(Submitted February 13, 1998)
Fiz. Tverd. Tela (St. Petersburg) **40**, 1554–1558 (August 1998)

The anomalous positive magnetoresistance of a two-dimensional (2*D*) layer on Te$(10\bar{1}0)$ is analyzed, and it is shown that this phenomenon can be described within the weak localization theory taking into account the specific features of the band spectrum symmetry of a 2*D* layer on this tellurium surface and the associated peculiarities in the phase relaxation processes, as well as the existence of several 2*D* subbands. The main parameters of the theory have been determined, and it has been found that this orientation of the 2*D* layer is characterized by an extremely high probability of intersubband transitions in elastic scattering, which makes this case qualitatively different from the 2*D* hole system on the (0001) surface studied previously. The phenomenon is attributed to the difference in the character of electronic states between these crystal interfaces, namely, dangling covalent bonds in the chains making up the tellurium crystal on the (0001) surface, and the disruption of the weaker interchain Van der Waals bonds on the $(10\bar{1}0)$ face representing the cleavage surface. A conclusion is drawn that the wave-state phase-relaxation time in inelastic processes is dominated by electron-electron scattering. © *1998 American Institute of Physics.* [S1063-7834(98)03308-5]

The need to introduce quantum corrections to the conductivity of two-dimensional (2*D*) hole carriers on a tellurium surface was first demonstrated in a study of galvanomagnetic properties of the accumulation layer on Te(0001).[1] This effect was revealed as an anomalous magnetoresistance (AMR), whose sign and behavior varied with temperature and 2*D*-hole concentration. The experimental results were quantitatively interpreted in terms of the weak localization theory for noninteracting particles, which was modified by inclusion of the specific features of the tellurium valence-band energy spectrum (lifted spin degeneracy, many-valley character, trigonal distortion of the spectrum).[1,2] Positive AMR was later found in studies of the accumulation layer on the $(10\bar{1}0)$ surface, which is parallel to the twofold (x) and threefold (z) axes.[3,4] This phenomenon was also described in terms of phenomenological theory of weak localization, but without taking into account the real symmetry of the 2*D*-hole Fermi surface on this plane; in particular, the spectrum was assumed not to be trigonally distorted.

A microscopic theory of the effect of weak localization of 2*D* holes in tellurium, which are localized at the principal crystallographic planes (0001), $(\bar{1}2\bar{1}0)$, and $(10\bar{1}0)$, has recently been developed. This theory takes into account both the real anisotropic band structure of tellurium and the dependence of the 2*D*-hole dispersion on surface orientation, and the dependence of the scattering matrix element on the initial and final quasi-momenta of the holes.[5,6] The specific features of weak localization due to the presence in the quantum well of more than one quantized subbands were also considered.

The present communication reports a study of AMR on the Te$(10\bar{1}0)$ surface and compares its results with the weak localization theory developed for this orientation. This analysis makes use of the 2*D*-hole characteristics found from measurements of the monotonic and oscillatory components of the resistance and Hall effect in a 2*D* layer [the Shubnikov–de Haas (SH) effect] within a broad magnetic-field range.[7]

1. EXPERIMENTAL RESULTS

The samples were cleaved along the C_3 axis from a tellurium single crystal of record-high purity (10^{13} cm^{-3} at 77 K) and represented rectangular plates 0.1–0.4 mm thick, with the broad face being the cleavage plane $(10\bar{1}0)$. The accumulation layer on the broad face was produced by treating it with a polishing etch by the technique[1] employed for the (0001) surface.

Figure 1 displays magnetoresistance measurements, $\Delta\rho/\rho_0$, for a sample with an accumulation layer on the $(10\bar{1}0)$ surface in magnetic fields of up to 100 kOe. The oscillatory behavior of $\Delta\rho(H)/\rho_0$ (the SH effect) indicates the 2*D*-hole gas to be degenerate. An analysis[7] of the behavior of $\Delta\rho(H)/\rho_0$ made within a broad range of magnetic fields permitted one to find such characteristics as the number of 2*D* subbands in the accumulation layer (two), the concentration of the 2*D* holes in each subband p_l and their mobility μ_{zz}^l (see Table I).

The inset to Fig. 1 shows on an enlarged scale the initial portion of this relation. In the weak magnetic-field domain the $\Delta\rho(H)/\rho_0$ relation is seen to follow an anomalous behavior typical of the weak localization effect, namely, a strong, close-to-linear increase starting in a magnetic field of the order of 20 Oe.

Figure 2 shows the $\Delta\sigma(H)$ relation in the AMR region obtained at different temperatures.

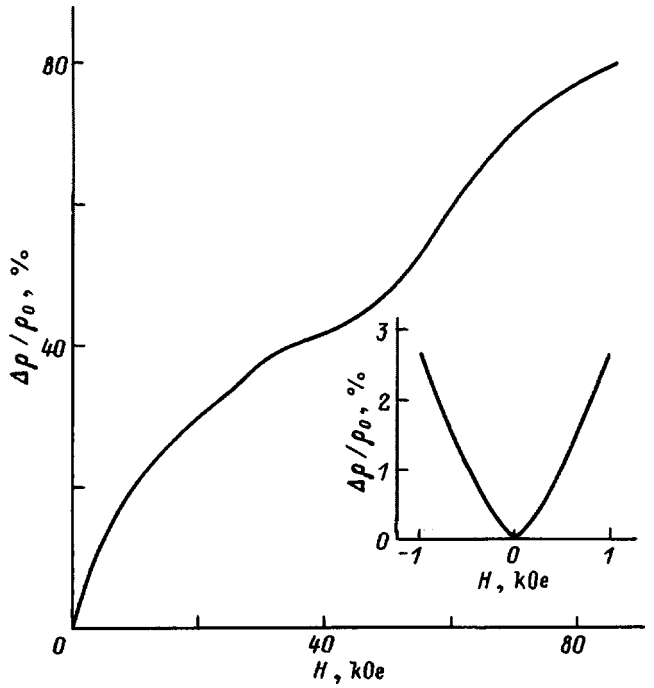

FIG. 1. Magnetic-field dependence of magnetoresistance $\Delta\rho(H)/\rho_0$ of a tellurium sample with accumulation layer on the $(10\bar{1}0)$ surface for $T=1.3$ K. The inset shows the initial portion of the $\Delta\rho(H)/\rho_0$ relation. An anomalously fast increase of the resistance near $H=0$ is evident.

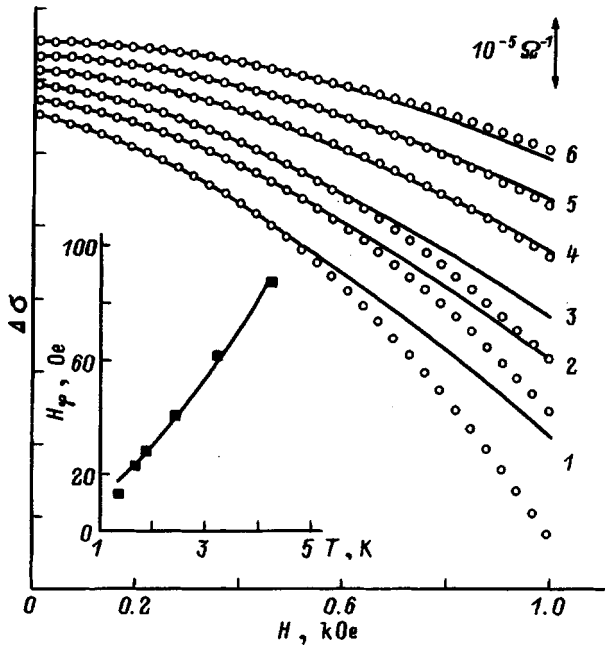

FIG. 2. Magnetic-field dependence of the conductivity $\Delta\sigma(H)$ of a tellurium sample with accumulation layer on the $(10\bar{1}0)$ surface obtained at different temperatures. The conductivity is reduced to unit area. The origins of the curves are displaced. Solid line: experiment, open circles: calculation. T(K): *1*—1.35, *2*—1.67, *3*—1.86, *4*—2.4, *5*—3.2, *6*—4.2. The inset shows the temperature behavior of parameter H_φ. Filled squares—experiment, solid line—theoretical fit.

2. DISCUSSION OF RESULTS

A. The 2D-hole dispersion law for the $(10\bar{1}0)$ surface

In tellurium, the extrema of the valence and conduction bands are located at the M and P corners of the Brillouin zone connected only through the time inversion operation. In three dimensions, the dispersion relation for the upper valence band can be presented in the form (to within terms of order k^3):[8]

$$E=A_v k_z^2+B_v(k_x^2+k_y^2)-(\Delta^2+\beta^2 k_z^2)^{1/2} +\Delta+\frac{1}{2}\gamma_3(k_+^3+k_-^3), \tag{1}$$

where $k_\pm=k_x\pm ik_y$. The constant γ_3 has opposite signs for the M and P extrema. The parameters entering Eq. (1) are such that the valence-band spectrum has a shallow saddle point separated by $E_0=2.3$ meV from the band top. The two-band model taking into account kp interaction of the two upper valence subbands with the conduction band and the lower valence subband permits one to relate the parameters entering Eq. (1) to the band gap E_g and the valence-band spin-orbit splitting Δ_1.[5,6]

When confined along the y axis in a potential well on the Te$(10\bar{1}0)$ surface, 2D holes in a quantized subband with index l obey the following dispersion relation[6]

$$E_l(k_x,k_z)=A_v k_z^2+B_v k_x^2-(\Delta^2+\beta^2 k_z^2)^{1/2} +\Delta+\gamma_3 k_x(k_x^2-3\langle k_y^2\rangle), \tag{2}$$

where $\langle k_y^2\rangle$ is a function depending on potential well shape and the quantized level number l.

According to Eq. (2), the 2D-hole Fermi surface at low energies represents two closely lying ellipses which join at $E_F=E_0$ to acquire a dumbbell shape as E_F continues to increase. As seen from Eq. (2), the trigonal distortion of Fermi trajectories, which was disregarded in Ref. 3, is retained in the 2D layer on Te$(10\bar{1}0)$.

The presence of a saddle point in the spectrum results not only in a strong anisotropy of the 2D-hole effective mass, which varies with Fermi energy, but also in an unusual dependence of the density of 2D-hole states on energy, $\Omega(E)$, shown in Fig. 3 over a broader concentration range than this is done in Refs. 5 and 6. The increase in the density of states observed to occur as one approaches the saddle-point energy increases the contribution to transport effects of quantized subbands with Fermi energies close to the energy E_0, where the number of free carriers is comparatively small.

TABLE I. Characteristics of 2D holes in the accumulation layer on Te$(10\bar{1}0)$.

Quantum-subband number.	ρ_l, 10^{12} cm^{-2}	μ_{zz}^l, 10^3 cm^2/V·s	Ω_l, 10^{13} eV^{-1}	D_{zz}^l, cm^2/s	$(\tau_0^0)^l$, 10^{-13} s
0	4.0	5.5	3.66	600.8	4.44
1	0.54	12.0	8.54	75.85	24.4

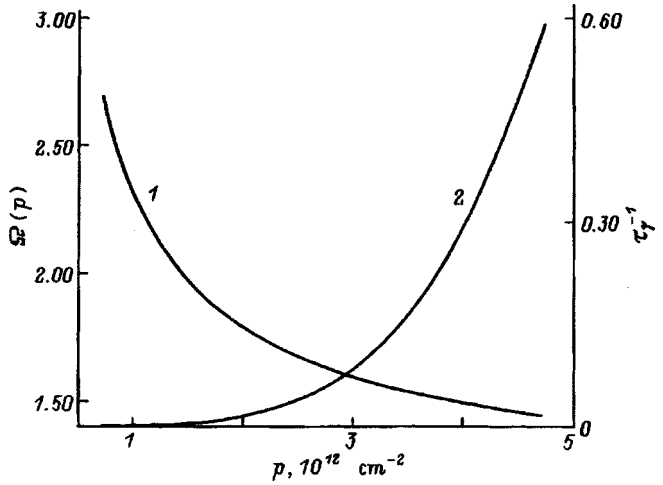

FIG. 3. Calculated dependences of the density of states Ω at Fermi level and of the quantity $1/\tau_\gamma$ on 2*D*-hole concentration on the Te$(10\bar{1}0)$ surface. *1*—a plot of $\Omega \cdot 4\pi B_v$, *2*—a plot of $1/\tau_\gamma\ \gamma_3^2\ 100/\tau_0^0(A_v/\Delta)^3$.

B. Weak-localization effect on Te$(10\bar{1}0)$. The case of strong effective-mass anisotropy and of several quantized subbands

After taking into account the anisotropic properties of the diffusion coefficient, weak-localization theory of noninteracting particles yields the following standard expression for the dependence of the 2*D*-hole conductivity on Te$(10\bar{1}0)$ on magnetic field[5,6]

$$\Delta\sigma_{ii}(H)=\sigma_0\left\{ f_2\left(\frac{H}{H_\varphi+H_v+H_\gamma}\right)+\frac{1}{2}f_2\left(\frac{H}{H_\varphi+2H_v}\right)-\frac{1}{2}f_2\left(\frac{H}{H_\varphi}\right)\right\}, \tag{3}$$

where $\sigma_0=(D_{ii}/\overline{D})e^2/2\pi^2\hbar$, $f_2(x)=\ln x+\Psi(\frac{1}{2}+1/x)$, and Ψ is the digamma function. The characteristic magnetic fields H_φ, H_v, and H_γ entering Eq. (3) are related to the corresponding phase relaxation times τ_φ, τ_v, and τ_γ through

$$H_\alpha=\frac{\hbar c}{4e\overline{D}\tau_\alpha}, \tag{4}$$

where $\alpha=\varphi,v,\gamma$; $\overline{D}=(D_{zz}D_{xx})^{1/2}$ is the direction-averaged mass-diffusion coefficient, τ_φ is the wave-state phase-relaxation time under inelastic scattering, and τ_v and τ_γ are the elastic-scattering phase-relaxation times for inter- and intravalley transitions, respectively. The latter is inversely proportional to the parameter γ_3 describing the ''trigonal distortion'' of 2*D*-hole Fermi trajectories on the Te$(10\bar{1}0)$ surface.

The relation between the diffusion-coefficient tensor components D_{zz} and D_{xx} and the microscopic parameters entering the matrix Hamiltonian in the effective-mass approximation is given in Refs. 5 and 6 for the case of scattering from a short-range potential. The Einstein relation for degenerate electron gas

$$D_{ii}=p\mu_{ii}/e\Omega, \tag{5}$$

was used to find the dependence of the mobility tensor components μ_{xx} and μ_{zz} on the 2*D*-hole concentration.

Equation (3) describes the weak-localization effect for the case of only one 2*D* subband existing in the 2*D* layer. If more than one 2*D* subband is present, one has to take into account the probability of intersubband transitions. If the intersubband transition time within each valley is substantially shorter than the times determining the characteristic magnetic fields H_φ, H_v, and H_γ, the contributions due to all 2*D* subbands are averaged proportionally to the density of states at the Fermi level Ω_l. In doing this, all parameters in Eqs. (3) and (4) should be replaced with their averages[6]

$$D_{ii}=\frac{\sum_l D_{ii}^l\Omega_l}{\sum_l\Omega_l},\quad \overline{D}=\frac{\sum_l \overline{D}^l{}_{ii}\Omega_l}{\sum_l\Omega_l},\quad \frac{1}{\tau_i}=\frac{\sum_l(1/\tau_i^l)\Omega_l}{\sum_l\Omega_l}. \tag{6}$$

Note that Eq. (3) is valid as long as the characteristic magnetic fields H_φ do not exceed $H_{\rm tr}=\hbar c/4e\overline{D}\tau_p$, where τ_p is the momentum relaxation time. While in magnetic fields $H\sim H_{\rm tr}$ the weak-localization phenomenon is retained, it does not have a diffusion character.

C. Analysis of experimental results

By combining the theoretical relations shown in Fig. 3 with the experimental values of the concentration p_l and μ_{zz}^l of 2*D* holes in each of the subbands (Table I) one can find a number of characteristics used in the weak-localization theory. These are the density of states Ω_l, the diffusion coefficient at Fermi level D_{zz}^l, and the parameter $(\tau_0^0)^l$, which determines the time between elastic collisions and is equal in order of magnitude to the momentum relaxation time τ_0 (Table I). Knowing the calculated ratio μ_{zz}^l/μ_{xx}^l (see Refs. 5 and 6), one can now transfer, using relations (6), from the characteristics of individual 2*D* subbands to the averaged parameters entering Eqs. (3) and (4).

A comparison of experimental $\Delta\sigma(H)$ relations with Eq. (3) made possible determination, without the inclusion of diffusion-coefficient anisotropy, of the parameter H_φ responsible for the positive AMR, namely, the third term in Eq. (3): $H_\varphi(1.3\ \text{K})=10$ Oe. As for the other two terms in Eq. (3), they become significant in magnetic fields above 300 Oe. This means that $H_\varphi+2H_v\approx H_\varphi+H_v+H_\gamma>300$ Oe. On the other hand, using curve *1* in Fig. 1 in Ref. 6, the above characteristics of the 2*D* holes, and the known coefficient $\gamma_3=2\times10^{-20}$ meV$\cdot$cm^3 (see, e.g., Ref. 1), one can estimate τ_γ and, accordingly, H_γ: $\tau_\gamma\cong10^{-12}$ s, and $H_\gamma\cong20$ Oe. Whence it follows that

$$H_v>H_\varphi,H_\gamma, \tag{7}$$

with $H_v>300$ Oe. Using Eq. (4), one can also estimate the characteristic phase relaxation times τ_φ and τ_v. One comes to

$$\tau_\varphi\sim\tau_\gamma>\tau_p,\tau_v,$$

which means that for 2*D* holes on this surface $\tau_p\sim\tau_v$. Strictly speaking, in this case the diffusion approximation used by us is invalid for description of weak localization. It

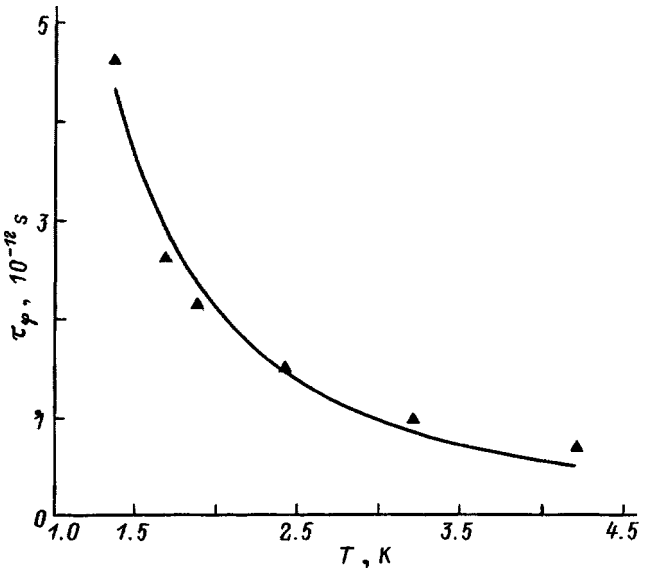

FIG. 4. Temperature dependence of the phase relaxation time τ_φ. Filled triangles—experiment, solid line—theoretical fit.

can be shown, however, that because $\tau_\varphi \gg \tau_p, \tau_v$, the largest contribution to $\Delta\sigma(H)$ is due only to the cooperon, which is antisymmetric under valley interchange. Its contribution to conductivity is described by the third term in Eq. (3), which contains only H_φ (or τ_φ) as a parameter. This means that when comparing Eq. (3) with experiment, one should retain in it only the term $-\frac{1}{2}f_2\, H/H_\varphi$, and consider magnetic fields <300 Oe. As seen from the plots in Fig. 2, such a description does indeed produce a quantitative agreement of calculated relations with experiment in the weak magnetic-field domain (up to ~ 400 Oe). The contribution due to classical magnetoresistance was taken into account, as in Ref. 1, by introducing an additional term bH^2. This approximation showed that parameter H_φ decreases with decreasing temperature. The values of H_φ for various temperatures are presented in the inset to Fig. 2. While the $H_\varphi(T)$ relation can be fit with a straight line, approximation of the form

$$H_\varphi = A_\varphi T + B_\varphi T^2 \tag{8}$$

appears physically more validated. A least-squares fitting yields $A_\varphi = 9.66$ Oe/K, and $B_\varphi = 2.7$ Oe/K^2. Figure 4 displays the phase relaxation times $\tau_\varphi(T)$, which were calculated using experimental data on H_φ, relations (4) and (6), and the values of the diffusion coefficient listed in Table I. The line in Fig. 4 is a plot of the relation derived from Eq. (8)

$$1/\tau_\varphi = 1.58\times 10^{11} T + 0.45\times 10^{11} T^2 (\mathrm{s}^{-1}). \tag{9}$$

The pattern of the $\tau_\varphi(T)$ relation indicates that the phase relaxation of the hole wave state is dominated by electron-electron interaction (see, e.g., Ref. 9). The first term here can be associated with the temperature dependence of the phase relaxation time due to carrier interaction with Nyquist fluctuations: $(1/\tau_\varphi) \cong (1/\tau_\varphi^{(N)}) = T(\pi\sigma_0/\sigma_\square)(k/\hbar)\ln(\sigma_\square/2\pi\sigma_0)$.[9] A calculation made using the 2*D*-hole parameters given in Table I yields $(1/\tau_\varphi^{(N)}) \cong (T/1\mathrm{K})\times 10^{10}\ \mathrm{s}^{-1}$, which agrees quantitatively with the experimental value.

In stronger magnetic fields, the experimental values of $\Delta\sigma(H)$ were found to be higher than the calculated ones because of the contribution to the weak-localization effect due to scattering involving elastic transitions, which, when occurring in a magnetic field, result in a decrease of the magnetoresistance.

To conclude, application of microscopic theory of weak localization[5,6] to the positive AMR effect in a 2*D* layer on Te$(10\bar{1}0)$ has revealed an extremely high probability of intersubband transitions under elastic scattering of 2*D* holes, which makes this case qualitatively different from that of a system of 2*D* holes on the (0001) surface studied earlier. Assuming the scattering to occur primarily from surface roughness, it appears reasonable to relate the above difference to different character of the electronic states on these surfaces, namely, unsaturated covalent bonds on the (0001) surface, which terminate the chains making up the tellurium crystal, and disrupted weaker van der Waals bonds coupling the chains on the $(10\bar{1}0)$ surface, which is the cleavage surface.

The authors are grateful to A. O. Smirnov for assistance in some experiments, and to I. A. Bespalov for the calculations.

Support of the Russian Fund for Fundamental Research (Grants 96-02-16959 and 96-02-17849), ''Physics of Solid-State Nanostructures'' program (Grant 97-1035), ''Support of Young DSc Program'' (Grant 96-15-96955), and of the ''Integration'' Foundation (Grant 326.37) is gratefully acknowledged.

[1] V. A. Berezovets, I. I. Farbshtein, and A. L. Shelankov, JETP Lett. **39**, 74 (1984).
[2] A. I. Shelankov, Solid State Commun. **53**, 465 (1985).
[3] V. A. Berezovets, Yu B. Lyanda-Geller, A. O. Smirnov, and I. I. Farbshtein, JETP Lett. **58**, 770 (1993).
[4] V. A. Berezovets, I. I. Farbshtein, and A. O. Smirnov, Phys. Low-Dimens. Semicond. Struct. **12**, 301 (1995).
[5] N. S. Averkiev and G. E. Pikus, Fiz. Tverd. Tela (St. Petersburg) **38**, 1748 (1996) [Phys. Solid State **38**, 964 (1996)].
[6] N. S. Averkiev and G. E. Pikus, Fiz. Tverd. Tela (St. Petersburg) **39**, 1659 (1997) [Phys. Solid State **39**, 1481 (1997)].
[7] V. A. Berezovets, D. V. Mashovets, A. O. Smirnov, D. V. Smirnov, and I. I. Farbshtein, Fiz. Tverd. Tela (Leningrad) **33**, 3502 (1991) [Sov. Phys. Solid State **33**, 1966 (1991)].
[8] M. S. Bresler, V. G. Veselago, Yu. V. Kosichkin, G. E. Pikus, I. I. Farbshtein, and S. S. Shalyt, Zh. Eksp. Teor. Fiz. **57**, 1479 (1969) [Sov. Phys. JETP **30**, 799 (1969)].
[9] B. L. Altshuler, A. G. Aronov, and D. E. Khmelnitsky, J. Phys. C **15**, 7367 (1982).

Translated by G. Skrebtsov

Polarization spectra of excitonic luminescence of bare ZnCdSe/ZnSe quantum wires

N. V. Lomasov, V. V. Travnikov, S. O. Kognovitskiĭ, S. A. Gurevich, S. I. Nesterov, and V. I. Skopina

A. F. Ioffe Physicotechnical Institute, Russian Academy of Sciences, 194021 St. Petersburg, Russia

M. Rabe and F. Henneberger

Humboldt University, Berlin, Germany
(Submitted February 13, 1998)
Fiz. Tverd. Tela (St. Petersburg) **40**, 1559–1562 (August 1998)

Linearly polarized luminescence spectra of bare (unburied) semiconductor structures with ZnCdSe/ZnSe quantum wires, obtained by reactive ion etching, were investigated. It was found that, regardless of the orientation of the linear polarization of the exciting light, the luminescence radiation of the quantum wires is polarized parallel to the axis of the wires, while the radiation of the buffer layer of the isotropic ZnSe barrier material is oriented perpendicular to the axis of the wires. The polarization features found are due to the modification of the modes of the electromagnetic field near open quantum wires, which occurs as a result of the presence of the vertical interfaces between media with strongly different permittivities. It was also found that, when linearly polarized excitation is used, the alignment of exciton dipole moments strongly influences the polarization properties of the luminescence. © *1998 American Institute of Physics.* [S1063-7834(98)03408-X]

The most direct method to obtain quantum wires (QWs) is etching, through one-dimensional masks, of two-dimensional quantum objects placed in the immdediate vicinity of the surface. If etching is not accompanied by subsequent burial, then a characteristic feature of the resulting bare QWs is the presence of semiconductor/vacuum interfaces at their side walls. As a reslt of the large difference arising in this case between the permittivities of the semiconductor ($\varepsilon \sim 10$) and the surrounding medium ($\varepsilon \sim 1$), there is a substantial difference between the values of the local electric field components inside the QWs that correspond to the external electromagnetic field being polarized in a direction perpendicular or parallel to the axis of the wires. This, in turn, should produce a pronounced polarization anisotropy of the optical properties of bare QWs.[1,2] The anisotropy predicted in Refs. 1 and 2 has been observed in luminescence and Raman-scattering spectra of bare InGaAs quantum wires.[3,4] The present work is devoted to the investigation of the anisotropy of the luminescence spectra of bare ZnCdSe/ZnSe QWs. In contrast to Refs. 3 and 4, where attention was focused mainly on the manifestation of only the anisotropy of optical-transition probabilities in the observed spectra, we also investigated, using resonance excitation, the effect of the kinetics of the spatial-energy relaxation on the polarization properties of the luminescence of bare QWs. Moreover, we also investigated the substantial anisotropy, which we observed, of the radiation of the isotropic buffer-barrier-layer material (ZnSe). It was shown that it is due to the anisotropy of the absorption of light passing through the etched surface region.

1. EXPERIMENT

The samples with quantum wires were prepared by interference lithography, followed by reactive ionic etching[5] of the initial structures, prepared by the MBE method, with single $Zn_{1-x}Cd_xSe$ (5 nm) quantum wells located between the layers of the ZnSe barrier material. Two starting structures were used. In the type-I structure the top ZnSe layer was 60 nm thick, the buffer layer between the GaAs substrate and the quantum well was 400 nm thick, and the Cd concentration $x=0.13$. In the type-II structure the ZnSe layer thicknesses were much smaller (the top layer 25 nm, the buffer layer 20 nm), while the Cd concentration $x=0.16$. Etching was performed to a depth of the order of 60–100 nm. In the type-II samples this led to complete etching of the A_2B_6 materials, as a result of which these samples consisted of ZnSe strips, located directly on the GaAs substrate and insulated from the another, with the QWs located approximately at the center of the strips. The structures obtained as a result of etching remained unburied. The transverse width of the QWs varied in the range 50–100 nm. Since the results obtained on samples with different geometric parameters were essentially identical to one another, in what follows the type-I samples are represented by the results obtained on a sample with a 80-nm-wide quantum well and a 100-nm-deep etched part, while the type-II samples are represented by a sample with a 70-nm-wide QW and 70-nm-high column with a QW.

The photoluminescence (PL) spectra were investigated with excitation by the 441.6 nm line of a He–Cd laser ($T=77$ K). Excitation and detection were performed in linear polarization parallel or perpendicular to the axis of the wires.

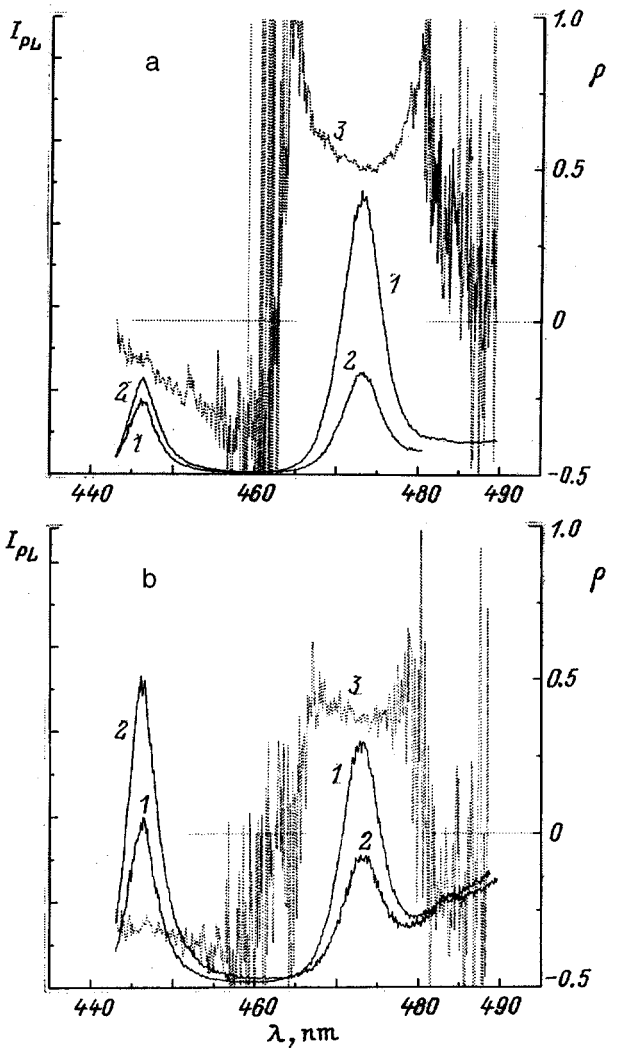

FIG. 1. Luminescence and degree of polarization spectra obtained for a type-I sample with polarization of the exciting light parallel (a) and perpendicular (b) to the axis of the wires. *1, 2* — Luminescence spectra with the radiation polarized parallel and perpendicular to the axis of the wires, respectively; *3* — degree ρ of polarization of the spectra.

Figure 1 shows the PL spectra of the type-I sample with the polarization of the exciting light oriented parallel ($E_{ex} \| Z$) (a) and perpendicular ($E_{ex} \perp Z$) (b) to the axis of the QWs. The spectra *1* correspond to detection of radiation components linearly polarized parallel to the axis of the wires, while the spectra *2* correspond to detection of radiation components perpendicular to the axis of the wires. The spectra *3* are the spectra of the degree of linear polarization, which were determined as

$$\rho = \frac{I_{\|Z} - I_{\perp Z}}{I_{\|Z} + I_{\perp Z}}, \tag{1}$$

where $I_{\|Z}$ ($I_{\perp Z}$) is the intensity of the radiation with polarization parallel (perpendicular) to the axis of the wires. A measurement in accordance with Eq. (1) signifies a measurement of the degree of polarization relative to the axis Z of the wires. Positive values of ρ correspond to the luminescence being polarized mainly along the axis of the wires, while negative values correspond to radiation being polarized perpendicular to the axis of the wires.

The short-wavelength line near 446 nm in Fig. 1 corresponds to radiation of the ZnSe barrier material. The long-wavelength line corresponds to radiation of the ZnCdSe wires. It is evident from Fig. 1 that in type-I samples the radiation of the wires is polarized parallel to the axis of the wires irrespective of the polarization of the exciting light, while the barrier radiation is polarized perpendicular to the axis of the wires (the same polarization ratio is observed with unpolarized excitation). In type-II samples the QW radiation is likewise polarized along the axis of the wires for both polarizations of the exciting light. We were not able to detect barrier luminescence in type-II samples. This is evidently a consequence of efficient trapping of carriers from the barrier into a wire.

In type-I samples the ZnSe buffer-layer thickness is very large, as a result of which the interior regions of this layer should make the main contribution to the barrier luminescence. The buffer layer is an isotropic material (in the plane of the layer), and its radiation (at least the radiation emerging perpendicular to the layer) seemingly should not be polarized. To determine the reasons for the appearance of a negative degree of polarization of the barrier we performed the following experiment. In a type-I sample we investigated the dependence of the intensity of the impurity luminescence of the ZnSe buffer layer ($\lambda_{max} \sim 550$ nm) on the polarization of the exciting light (excitation was likewise performed by the 441.6 nm). It was found that in the case of excitation polarization along the axis of the wires the intensity of this band is approximately 1.4 times less than that of the radiation corresponding to perpendicular excitation polarization (when measuring the intensity ratio we took account of the difference in the reflection coefficients for the two polarizations of the exciting light). Since the ZnSe buffer layer is an isotropic material and the observed dependence on the excitation polarization cannot be due to absorption anisotropy in the buffer layer itself, the results obtained indicate a polarization anisotropy of absorption of the exciting light passing through the ZnCdSe/ZnSe surface lattice. The passage of initially unpolarized isotropic radiation, formed in the interior of the buffer layer, through the same lattice in the opposite direction (out of the crystal) evidently results in the appearance of a negative degree of polarization of the observed barrier luminescence.

In contrast to the sign of the degree of polarization, the magnitude and spectral dependence of the degree of polarization for the two excitation polarizations differ appreciably from one another. This difference increases substantially in type-II samples. This is clearly seen in Fig. 2, where the degree of polarization spectra, obtained with parallel (spectrum *2*) and perpendicular (spectrum *3*) polarizations of the exciting light, are compared with the luminescence spectrum (*1*) for type-II samples. The degree of polarization at the maximum of the luminescence lines for parallel excitation polarization ($\rho_{\|}$) is approximately the same in the two types of samples; at the same time, it is appreciably greater than the degree of polarization corresponding to perpendicular ex-

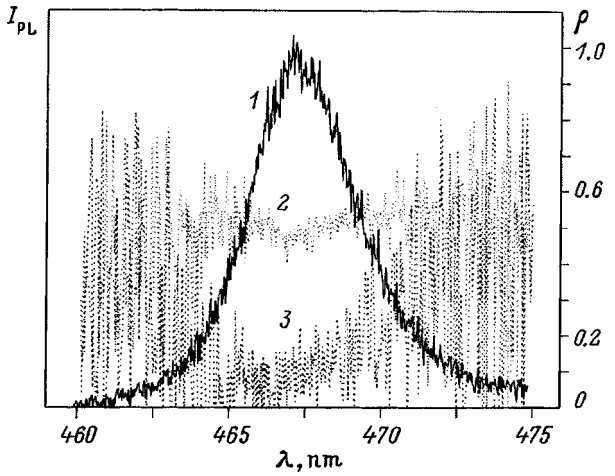

FIG. 2. Luminescence spectrum of a type-II sample (*1*) as well as degree of polarization spectra obtained with the exciting light polarized parallel (*2*) and perpendicular (*3*) to the axis of the wires.

citation ($\rho_\perp$). For type-II samples this excess of the degree of polarization is much larger and $\rho_\perp$ is approximately five times smaller than $\rho_\parallel$. The change in ρ over the contour of the luminescence lines also attracts attention. In type-I samples (Fig. 1), in which the degree of polarization spectra were measured more reliably (the signal/noise ratio was better), a clear increase in ρ is observed as the distance from the center of the line in the direction of lower and higher energies increases. The results presented show that the degree of polarization of the QW radiation depends on both the polarization of the exciting light and the type of sample. Since for our samples the geometric parameters that according to Refs. 1–4 determine the degree of polarization are approximately the same, the results obtained indicate the existence of different factors which affect the polarization of the QW radiation.

2. DISCUSSION

Inside a bare wire, the intensities of the local electric fields, corresponding to $E\|Z$ polarization of the external electromagnetic radiation, are much larger than the intensities of the local fields for $E\perp Z$ polarization.[1,2] It should be noted that this is actually a consequence of Maxwell's boundary conditions. The tangential (parallel to the interface and therefore the axis of the wires) components of the electric vector must be the same on both sides of the interface ($E_{\parallel 1}=E_{\parallel 2}$). The normal (perpendicular) components are related as $\varepsilon_1 E_{\perp 1}=\varepsilon_2 E_{\perp 2}$. As a result, since $\varepsilon_1=1$ in vacuum, the perpendicular component of the electric field at the interface on the QW side is ε_2 (~ 10) times less than the external electric field. The variation of the local fields at the interface, naturally, result in variation of the local electric fields on the average over the entire profile of a QW. Since the matrix elements of the optical transitions are proportional to the scalar product of the intensity of the local electric field and the interband dipole moment, the optical transition probabilities (whose values are obtained after averaging over the electron-hole wave functions) for light polarization along a quantum wire are much higher than the corresponding probabilities for perpendicular polarization.[1,2] This difference should lead to a strong polarization of luminescence along the axis of bare wires.[3] The maximum values (~ 0.5) of the degree of polarization of the QW luminescence line in our case equal the experimental and theoretical values of the degree of polarization of the luminescence which were obtained in Ref. 3. This is entirely natural, since the geometric parameters and permittivity values in our bare wires are approximately the same as the corresponding values for the wires investigated in Refs. 3 and 4.

The observed anisotropy of photoexcitation of the ZnSe buffer layer is essentially a direct proof of the fact that when light passes through a bare surface grating, the absorption coefficient for light polarized along the axis of the wires is much larger than the corresponding coefficient for perpendicular polarization.[1,2] The frequency of the exciting line which we used virtually coincides with the position of the absorption line of the $n=2$ excitonic state of the ZnSe material. This circumstance as well as the fact that the barrier material in the etched part of ZnSe, just as the QW material, lies in the region characterized by the presence of vertical semiconductor/vacuum interfaces attest to the fact that the anisotropic absorption of the exciting light is due to anisotropic excitonic absorption in the etched part of ZnSe, since its thickness is almost an order of magnitude larger than the thickness of the quantum well. As a result of the action of this anisotropic absorption, the barrier radiation, which is in itself unpolarized and formed mainly by the interior volume of the buffer layer, after passing through the surface layer becomes polarized perpendicular to the axis of the wires on account of the fact that the light component polarized along the axis of the wires is absorbed more efficiently.

In the general case the ratio of the intensity of the radiation with parallel and perpendicular polarizations depends not only on the probability W of the corresponding optical transitions but also on the population (N) of the excitonic states with the corresponding dipole moments

$$\frac{I_\parallel}{I_\perp}=\frac{W_\parallel}{W_\perp}\frac{N_\parallel}{N_\perp}. \tag{2}$$

In the case of linearly polarized exciting light and the resonance excitation which we used, a population difference can arise as a result of alignment of the dipole moments of the excitons (see, for example, Refs. 6 and 7).

The maximum degree of alignment of excitons, which arises with the absorption of light as the energy relaxes, decreases as the number of scatterings by phonons increases.[6,7] This is evidently the reason for the pronounced decrease observed with $E\|Z$ in the degree of polarization of excitons as the line center is approached from the high-energy side. The maximum of the QW luminescence line at $T=77$ K approximately corresponds to the bottom of the band of the ground excitonic state of the QWs. Excitons which have reached the band bottom undergo the largest number of scatterings over their lifetime, and the maximum degree of polarization is characteristic for them[7] ($N_\parallel$ maximally approaches $N_\perp$). The observed increase in the degree of polarization on the long-wavelength edge of the luminescence line is apparently due

to trapping of aligned excitons with high energy in a state of localized excitons (in the case of scattering by, for example, LO phonons).

In the case of perpendicular polarization of the exciting light $E_{ex} \perp Z$ absorption directly in the quantum wire material is weak, and in type-I samples most of the exciting light is absorbed in the interior of the ZnSe buffer layer. As a result, the QW radiation is formed largely on account of recombination of excitons which arise as a result of trapping in the QWs of thermalized carriers and excitons from the barrier material. It is natural to infer that in this case the fraction of aligned excitons is very low ($N_\perp \approx N_\parallel$) and the polarization of the radiation is determined mainly by the ratio of the optical transition probabilities. In type-II samples the thickness of the buffer layer is very small, and the relative contribution made to the QW luminescence by excitons formed directly in the wire material and subjected to alignment increases substantially; moreover, excitons arising as a result of trapping from barrier regions directly adjacent to a wire likewise can be partially aligned. For this reason, in the case $E_{ex} \perp Z$ the dipole moments of an appreciable fraction of the excitons are aligned along the excitation polarization, and the population difference ($N_\perp > N_\parallel$) compensates to a large degree the difference of the optical transition probabilities, as a result of which the degree of polarization relative to the axis of the wires is very low.

In the case $E_{ex} \parallel Z$ the absorption coefficient in a wire and in the barrier regions adjacent to it is much larger than in the case of $E_{ex} \perp Z$ polarization. As a result, the fraction of the excitons aligned parallel to the wires is much greater ($N_\parallel > N_\perp$) and, naturally, the degree of polarization is higher than the values which are characteristic for unpolarized exciton, in which case $N_\parallel = N_\perp$.

Our investigations have shown that the luminescence radiation of quantum wires is polarized parallel and the barrier radiation is polarized perpendicular to the axis of the wires. The observed features are due to modification of the modes of the electromagnetic field as a result of the presence of vertical interfaces between media with strongly different permittivities. Polarization of the quantum wires along the axis arises because the probability of radiative transitions for parallel polarization is much higher than the corresponding probabilities for perpendicular polarization. The high absorption probability for parallel polarization in bare wires leads to the fact that the initially unpolarized barrier luminescence radiation formed in the interior of the buffer layer acquires a perpendicular polarization after passing through the surface region with bare wires. It was also found that in the case of the excitation mechanism employed the alignment of exciton dipole moments has a large effect on the polarization properties.

We thank the Russian Fund for Fundamental Research (Grant No. 96-02-00131) and the NATO International Program (NANO. LG 950382) for support.

[1] N. A. Gippius, V. D. Kulakovskiĭ, S. G. Tikhodeev, and A. Forchel, JETP Lett. **59**, 556 (1994).
[2] N. A. Gippius, S. G. Tikhodeev, A. Forchel, and V. D. Kulakovskii, Superlattices Microstruct. **16**, 165 (1994).
[3] P. Ils, Ch. Greus, A. Forchel, V. D. Kulakovskii, N. A. Gippius, and S. G. Tikhodeev, Phys. Rev. B **51**, 4272 (1995).
[4] J. Rubio, Z. H. van Der Meulen, N. Mestres, J. M. Calleja, K. H. Wang, P. Ils, A. Forchel, N. A. Gippius, and S. G. Tikhodeev, Solid-State Electron. **40**, 707 (1996).
[5] S. A. Gurevich, A. V. Kolobov, V. M. Lyubin, S. I. Nesterov, M. M. Kulagina, F. N. Timofeev, and S. I. Troshkov, Pis'ma Zh. Tekh. Fiz. **18**(17), 85 (1992) [Sov. Tech. Phys. Lett. **18**, 581 (1992)].
[6] E. L. Ivchenko, G. E. Pikus, and L. V. Takunov, Fiz. Tverd. Tela (Leningrad) **20**, 1235 (1978) [Sov. Phys. Solid State **20**, 1502 (1978)].
[7] S. A. Permogorov and V. V. Travnikov, Fiz. Tverd. Tela (Leningrad) **22**, 2651 (1980) [Sov. Phys. Solid State **22**, 1547 (1980)].

Translated by M. E. Alferieff

Comparative analysis of Bragg and Laue diffraction from CdF_2–CaF_2 superlattices on Si(111)

R. N. Kyutt, A. Yu. Khil'ko, and N. S. Sokolov

A. F. Ioffe Physicotechnical Institute, Russian Academy of Sciences, 194021 St. Petersburg, Russia
(Submitted November 18, 1997; resubmitted February 15, 1998)
Fiz. Tverd. Tela (St. Petersburg) **40**, 1563–1569 (August 1998)

Short-period superlattices (SL) with periods from 7 to 22 nm were grown by MBE in the CdF_2–CaF_2 system on Si(111). X-ray diffraction measurements of these structures in various reflection and transmission geometries demonstrate the possibility of producing such objects with a high crystal perfection. Specific features of diffraction from an SL with layers possessing substantially different diffracting abilities and strains of opposite signs with respect to the substrate are considered. The main parameters of the grown SLs have been obtained by simulation in semikinematic approximation. The applicability of the model of a perfect SL to objects with structural defects has been demonstrated. © *1998 American Institute of Physics.* [S1063-7834(98)03508-4]

X-ray-diffraction-based determination of the structural parameters of superlattices (SL) makes use in most cases of the symmetric or asymmetric Bragg geometry.[1–4] Other arrangements employ small-angle scattering,[4,5] grazing-incidence diffraction,[6] and tilted-sample symmetric reflection.[7] A possibility of obtaining diffraction patterns from an SL in symmetric Laue geometry has also been demonstrated.[8] This work presents a more comprehensive analysis of diffraction-curve shape and of the effect on it of SL structural parameters in various coplanar diffraction arrangements.

The SLs chosen for the study were CaF_2/CdF_2 fluorides on a Si(111) substrate. The possibility of epitaxial growth of such structures, as well as their high crystal perfection, have recently been demonstrated.[8,9] Both these compounds have the fluoride fcc structure. The substantial difference between the scattering factors of Cd and Ca atoms makes such SLs a convenient subject for diffraction studies. Producing structurally perfect SLs in this system is possible because the lattice constants of both fluorides are close to that of the silicon lattice. Indeed, at room temperature the lattice parameter of CdF_2 is by 0.78% smaller, and that of CaF_2, by 0.6% larger than that of silicon.

1. BRAGG AND LAUE DIFFRACTION FROM AN SL. THEORY

Diffraction from SLs whose total thickness is less than the extinction length can be considered in terms of the semikinematic approximation.[10] This approximation takes into account coherent interaction of waves reflected from the substrate and the SL, so that the total reflectivity can be written

$$R=|A_1+A_{\mathrm{SL}}e^{-2\pi iH_z d}|^2. \tag{1}$$

The scattering amplitude from the substrate (A_0) is calculated using the dynamic theory, and that from the epitaxial layer (A_{SL}), by the kinematic theory. Here d is the interplanar spacing at the interface, and H_z is the projection of the diffraction vector on the surface normal.

By kinematic theory, the amplitude of reflection from an SL

$$A_{\mathrm{SL}}=iF_{\mathrm{SL}}\frac{\sin(m\Phi)}{\sin(\Phi)}e^{i(y-f_1)z_1}, \tag{2}$$

where the scattering ability for an SL consisting of two alternating layers

$$F_{\mathrm{SL}}=\sin[(y-f_1)z_1]\,\frac{K_1}{y-f_1}+\sin[(y-f_2)z_2]\,\frac{K_2}{y-f_2}\exp(i\Phi), \tag{3}$$

$$\Phi=(y-f_1)z_1+(y-f_2)z_2.$$

Here y is a reduced angular variable characterizing the deviation from the substrate reflection center

$$y=\frac{\Delta\theta\,\sin(2\theta)}{|\chi_H|}\sqrt{\frac{\gamma_0}{|\gamma_H|}}, \tag{4}$$

where γ_0 and γ_H are the direction cosines of the angles of incidence and reflection, respectively. The quantities f_1 and f_2 express the reduced angular difference between the reflection centers of layers 1 and 2 and of the substrate. For unrelaxed layers, where the only nonzero strain component is ε_{zz}, which is equal to the relative difference between the interplanar spacings of the layers and of the substrate along the normal,

$$f_i=-\varepsilon_{zz}\frac{(\gamma_H-\gamma_0)\gamma_H}{|\chi_H|}\sqrt{\frac{\gamma_0}{|\gamma_H|}}, \tag{5}$$

z_1 and z_2 are the reduced thicknesses of layers 1 and 2 relative to the substrate extinction length

$$z_i=\frac{\pi t|\chi_H|}{\lambda\sqrt{\gamma_0|\gamma_H|}}, \tag{6}$$

K_1 and K_2 are the ratios of the structural factors of the layers to that of the substrate, m is the number of periods in the SL, and $|\chi_H|$ is the Fourier component of polarizability, which is proportional to the structural factor.

The appearance of satellites is known to be due to periodic variation of the SL parameters in depth. In actual fact, we have here two periodically varying quantities, namely, strain (expressed through f) and scattering ability (structure factor F). They both have the same period and are determined by the composition of the SL layers. There is, however, a substantial difference too. The quantity F is directly connected to the electron density, and for identical layer structure it is determined by the atomic numbers of the atoms contained in the layers. By Vegard's law, the strain profile is basically determined by composition as well, but it depends also on the distribution of tangential strains in the SL, which give rise to additional strains in the layers. The satellite intensity is affected also by possible presence of structural defects, but their distribution is most likely not periodic, and can be taken into account by introducing the static Debye–Waller factor.

The influence of strain on the diffraction pattern is determined by parameter B,

$$B=\Delta f\frac{z_1z_2}{z_1+z_2}=-\Delta\varepsilon_{zz}\frac{\pi}{\lambda}\frac{t_1t_2}{t_1+t_2}\frac{(\gamma_H-\gamma_0)\gamma_H}{|\gamma_H|}, \tag{7}$$

where $\Delta\varepsilon_{zz}$ is the difference between the strains in the two SL layers.[1] For $\Delta\varepsilon_{zz}=0$, satellites will appear if the layers have different scattering abilities.

The diffraction curve yields directly two SL characteristics: the period T from the satellite separation Δ, and the average interplanar spacing $\langle\varepsilon_{zz}\rangle$ from the angular position of the zero satellite with respect to the substrate reflection peak. For an ideal SL made up of layers of stoichiometric composition with known lattice parameters a and elastic properties, this is sufficient to calculate the thicknesses of the two layers

$$T=t_1+t_2=\frac{\lambda|\gamma_H|}{\Delta\ \sin(2\Theta_B)}, \tag{8}$$

$$\langle\varepsilon_{zz}\rangle=\frac{\left(\frac{\Delta a}{a}\right)_1 t_1(1+p_1)+\left(\frac{\Delta a}{a}\right)_2 t_2(1+p_2)}{t_1+t_2}, \tag{9}$$

where p_1 and p_2 are the Poisson coefficients.

In reciprocal space, the diffraction intensity for unrelaxed SLs is distributed along the crystal surface normal with additional centers representing satellites, whose separation is proportional to the SL period. These satellites lie on the same line with the reciprocal lattice point of the substrate for the given reflection. In a general case, an epitaxial layer is characterized by an average distortion tensor $e_{ij}=\omega_{ij}+\varepsilon_{ij}$, which includes strains ε_{ij} and rotations ω_{ij}. For coherent structures grown on high-symmetry surfaces, only the ε_{zz} component is nonzero, and therefore strain affects only reflections with a nonzero component H_z. In the symmetric Bragg geometry, where $H_z=H\mathbf{z}$, the diffraction curves depend both on strain distribution and on the structural factor. The intensity in the scattering plane is distributed along the diffraction vector, and the curve with the satellites can be measured both in the conventional double-crystal arrangement and by $\theta-2\theta$ scanning with an analyzer (Fig. 1a). In Eq. (5) we shall have to set $\gamma_H=-\gamma_0$. Transition to asymmetric Bragg diffraction may change the satellite intensity ratio, because the strain-induced contribution B is proportional to $(\gamma_0+|\gamma_H|)$. It does not, however, depend on the sign of the asymmetry, and the corresponding double-crystal curves measured for the cases of $(\gamma_0<|\gamma_H|)$ and $(\gamma_0>|\gamma_H|)$ differ only in angular scale and are identical in the satellite intensity ratios.

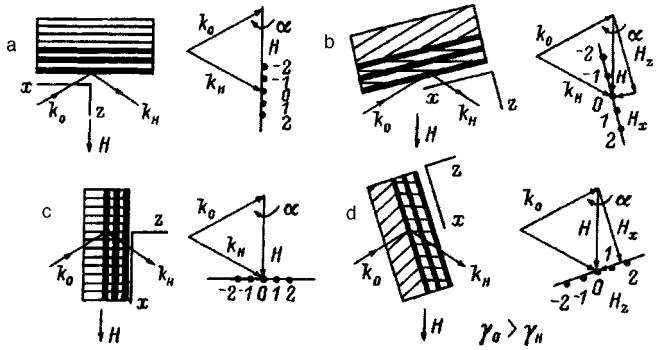

FIG. 1. Schematic of different x-ray measurement geometries: symmetric and asymmetric Bragg (a and b), symmetric and asymmetric Laue (c and d).

In Laue geometry $(\gamma_H>0)$, the strain contribution can reverse its sign depending on that of the asymmetry. Therefore as one goes from one asymmetry case to another, the satellites reverse their sequence (Fig. 1d). In a symmetric Laue arrangement, $f_1=f_2=0$ and $B=0$ for unrelaxed SLs, so that strain cannot affect the diffraction pattern at all, although the latter should nevertheless contain satellites originating from the difference between the structural factors of the two SL layers (Fig. 1c). The intensity of each satellite can in this case be written

$$r_n=m^2\frac{\sin^2(y_nZ_1)}{y_n^2}\frac{(K_1-K_2)^2}{(K_1+K_2)^2}, \tag{10}$$

where y_n is the angular position of the nth satellite. Note that the curve with the satellites is measured in the direction perpendicular to the diffraction vector, i.e., by ω scanning.

2. SAMPLES AND MEASUREMENT TECHNIQUES

The SLs studied in this work were MBE grown in the CdF_2/CaF_2 system.[9] The high molecular binding energy of these fluorides accounts for the molecular character of their sublimation and permits one to simplify considerably the growth technology.

We used for substrates 350-μm thick silicon plates cut in the (111) plane with misorientation not in excess of 10 arcmin. The substrates were chemically treated with subsequent high-temperature cleaning in vacuum. The cleanness of the silicon surface was established from the presence of the 7×7 superstructure in LEED patterns. To improve the crys-

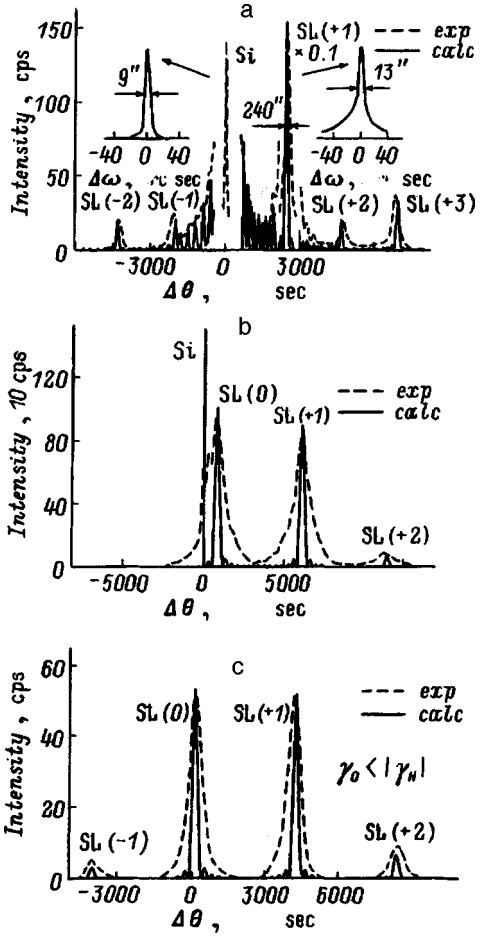

FIG. 2. Experimental and calculated curves for structure 117: (a) 111 and (b) 222 reflections in symmetric Bragg geometry, and (c) 422 reflection in asymmetric Bragg geometry.

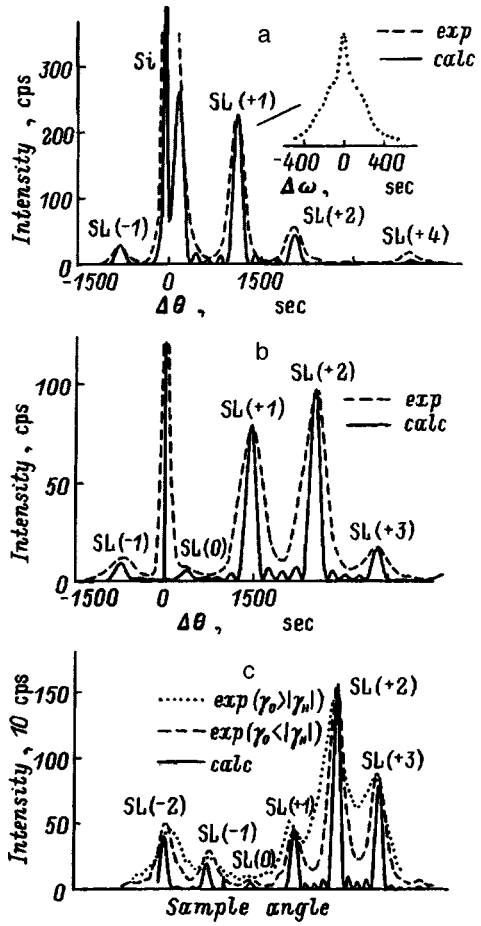

FIG. 3. Experimental and calculated curves for structure 126: (a) 111 and (b) 222 reflections in symmetric Bragg geometry, and (c) 422 reflection in asymmetric Bragg geometry.

talline quality of the structures, a calcium-fluoride buffer layer was deposited on the cleaned silicon surface by the two-temperature technique[11] before the SL growth. The SL growth temperature did not exceed 100 °C. To improve the heterointerface smoothness, the growth was interrupted after deposition of each new CaF_2 layer for two to five min. The fluoride growth rate, calibrated by measuring interference patterns produced by a He–Ne laser, was a few monolayers per min.

The x-ray diffraction measurements were made on a triple-crystal diffractometer with Cu $K\alpha$ radiation, using the 111 and 222 symmetric and the 422 asymmetric Bragg reflections. Laue diffraction was measured for the 220 (symmetric) and 111 and 311 (asymmetric) reflections with Mo $K\alpha$ radiation. Perfect Si(111) single crystals served as a monochromator and an analyzer in the Bragg geometry. For Laue diffraction, a Ge(111) crystal was used as monochromator, with a narrow slit at the detector playing the part of analyzer. All asymmetric reflections were measured in a two-crystal arrangement with the counter window open. The resolution of the three-crystal arrangement was 7 arcsec, and that with the slit analyzer, 56 arcsec.

3. EXPERIMENTAL RESULTS AND SIMULATION OF DIFFRACTION CURVES

Figure 2 presents experimental curves for the 111, 222, and 422 Bragg reflections obtained on sample 117 with a short-period SL. The presence on each of them of several satellites implies good SL periodicity. The periods derived from these three curves coincide to better than 1%. In the 111 reflection curve, the zero satellite of the SL cannot be resolved from the substrate maximum, and therefore in order to improve the accuracy of determination of the average strain $\langle \varepsilon_{zz} \rangle$, it was extracted from second-order reflection curves. Irrespective of the actual reflection type, CdF_2 layers exhibit a larger scattering ability than CaF_2, which accounts for the considerably higher intensity of the satellites on the large-angle side in all diffraction curves. Because the strain parameter B, which increases with increasing reflection order, becomes larger than one for the 222 and 422 reflections even for a short-period SL, the zero satellite is comparable to the $(+1)$ one. The diffraction curves measured for the 422 asymmetric reflection exhibit only SL peaks (Fig. 2c). This can be assigned to the CaF_2/Si(111) interface being of the B type, where the film lattice is turned through 180° with respect to the interface normal.[11]

Figure 3 shows the same set of diffraction curves obtained for sample 126 with a noticeably larger (by 2.5 times) SL period. They also reveal distinct satellites up to $+4$ order. Because the period and, hence, parameter B are larger in this case than those for the preceding sample (for approximately the same layer thicknesses), these curves exhibit

TABLE I. Results of x-ray diffraction measurements.

	111 (Bragg)				220 (Laue)		
Sample No.	$\varepsilon_{zz}\cdot 10^{-3}$	T, nm	W_θ	$W_{\theta-2\theta}$	T, nm	W_θ	$W_{\theta-2\theta}$
117	−3.25	6.84	13″	240″	6.9	390″	50″
126	−3.25	17.5	400−20″	240″	17.6	530″	80″
156	−1.95	21.9	1220″	185″	22.0	190″	760″
211	−1.4	16.9	400−40″	190″			
237	−2.92	15.8	240″	80″			

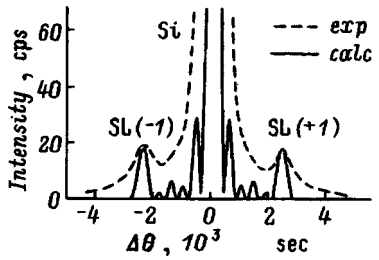

FIG. 4. 220 symmetric Laue reflection for sample 156.

characteristic differences from those displayed in Fig. 2. In particular, the zero satellite in the 222 and 422 reflections is practically suppressed, so that the concept of the SL being one layer with an average lattice constant has no more any meaning. Similar curves were obtained also for other samples. The SL structural parameters derived directly from diffraction curves are listed in Table I.

The calculated curves are presented together with the diffractograms. The parameters inserted in the calculations were as follows: average reduced strain f, scattering ability (structure factor) F, and the thickness of each SL layer. Because the satellites in the experimental curves were found to be broadened substantially, we took the satellite height ratio in the experimental and calculated curves as a criterion for parameter fitting. Because the SL period is determined unambiguously from x-ray measurements, the main variable parameter was the thickness ratio of the calcium and cadmium fluoride layers (t_1 and t_2, respectively) for a fixed period T. The thickness of the buffer layer was assumed to be proportional to that of the CaF_2 layer in the SL derived from the actual growth regime. When the calculated and experimental curves were considered to fit poorly, transition layers with thicknesses t_A and t_B and average values of the strain and scattering factors were introduced as additional parameters. All calculations were performed under the assumption of the layers being in registry with one another. Table II presents the parameters corresponding to the calculated curves which fit most closely to the experimental ones. Most of the calculated parameters are close to those expected from the technological conditions. The deviations observed to exist for some SLs (see Table II) may be explained as due to the fact that the above-mentioned deposition-rate calibration, which usually provided an accuracy within 10%, was not performed for each structure in order to cut expenditures.

The (-1) and $(+1)$ satellites are observed in the experimental ω curves of the 220 symmetric Laue reflection for all the samples studied (such a curve is exemplified in Fig. 4 for sample 156, whose layers had different thicknesses). As predicted by theory, they flank symmetrically the Si maximum. Their separation can be used to derive from the expression $T=\lambda/(\Delta \sin\theta_B)$ the SL period, which is in a good agreement with the values obtained from the Bragg curves (see Table I). The satellites coincide in position on the 2θ scale with the Si peak, which implies the absence of the relaxation component in the strain ($\varepsilon_{zz}=0$ within experimental error).

The curves of the 111 and 113 asymmetric Laue reflections (Fig. 5) having different directions of asymmetry and approximately equal strain parameters B show graphically how the satellites switch places as the geometry changes from $\gamma_0>|\gamma_H|$ in the first case to $\gamma_0<|\gamma_H|$ in the second. This feature of the diffraction curves can be explained by the fact that the main contribution to the difference between the diffraction conditions for the two SL layers is due not to the difference between the interplanar spacings d but rather to different inclination of the reflecting planes in CaF_2 and CdF_2, which are coherently related to the substrate.

TABLE II. Structure parameters derived from numerical simulation.

Sample No.	Number of periods	t_1/t_2, nm (Technol.)	t_1/t_2, nm (Calc.)	t_A, nm	t_B, nm
117	15	3.1/3.1	3.13/3.73	0.97	0.22
126	5	9.4/9.4	8.53/8.97	0.00	0.00
156	5	9.4/9.4	11.91/9.99	0.00	0.00
211	6	10.0/7.5	9.33/7.57	0.00	0.00
237	24	10.0/7.5	7.89/7.92	0.89	0.59

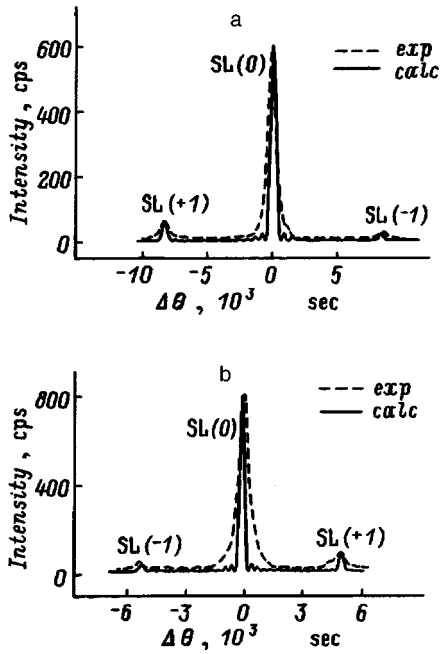

FIG. 5. Asymmetric Laue reflections 111 (a) and 311 (b) for sample 117.

4. DISCUSSION OF RESULTS

As already mentioned, the parameters of an ideal SL with layers of stoichiometric composition can be determined directly from a diffraction curve. The curves calculated using these parameters disagreed noticeably, however, with the experiment. The lattice parameters of CaF_2 and CdF_2 and the Poisson coefficients calculated for the (111) planes from elastic constants [$p(CaF_2)=0.96$ and $p(CdF_2)=1.35$] were matched with x-ray diffraction measurements made on epitaxial layers[12] (which were thicker, however, than the period of our SLs), and we had no grounds for questioning them. Therefore when simulating diffraction curves within a two-layer system the thicknesses could be varied only within the error with which $\langle \varepsilon_{zz} \rangle$ was measured. Even if we take an overestimated value $\delta\langle \varepsilon_{zz} \rangle \approx \pm 10^{-3}$, this corresponds to a change in $\alpha = t_1/t_2$ of ± 0.3. Only by introducing transition layers could one in some cases (see Table II) obtain the required satellite-height ratio with the mean value $\langle \varepsilon \rangle$ left unchanged. These thicknesses, lying within two to three monolayers, have the meaning of effective depth of mutual penetration of the SL layers into one another, which in our case could be due to roughness of the inner interfaces (there is no interdiffusion at the heterointerfaces because of the low growth temperatures). Note that the SLs with transition layers (samples 117 and 237) contain a noticeably larger number of periods compared to the other samples studied.

Obviously enough, the mean strain can be related to elastic strain relaxation as well. Two mechanisms can be conceived here, which involve formation of a dislocation network at the substrate-SL heterointerface or relaxation between the SL layers. In both cases, however, the change in the average SL interplanar spacing is small. In the first case, total relaxation would give rise to a jump in tangential misfit at the heteroboundary of $\varepsilon_{zz} = -9 \times 10^{-4}$ for equal thicknesses of the two layers, and to a change in the normal component $\langle \varepsilon_{zz} \rangle$ ranging from -3.25×10^{-3} (for an unrelaxed SL) to -2.25×10^{-3}. In the second case, total relaxation of all SL layers would make $\langle \varepsilon_{zz} \rangle$ equal to the average misfit of -0.9×10^{-3}.

Measurements made in symmetric Laue geometry yield for the tangential misfit $\langle \varepsilon_{xx} \rangle = 0$, but the measurement error was here $\pm 3 \times 10^{-4}$. Thus we cannot exclude the existence of relaxation of up to 30%. Relaxation by the first mechanism, however, would not result in a noticeable change in the satellite intensity ratio. The latter is dominated by the difference in strains between the two layers, $\Delta\langle \varepsilon_{zz} \rangle$, and this quantity is practically unaffected by relaxation (from -3.01×10^{-2} for an elastically stressed SL to -2.97×10^{-2} for 100% relaxation). Therefore even assuming some relaxation to occur at the heteroboundary, the SL parameters obtained in simulation (Table II) should be considered as reliable enough.

Structural distortions produce some satellite broadening in experimental curves and, therefore, one could hardly expect full agreement with the calculations. The satellite peak-intensity ratio used by us as a fitting criterion can be justified only if all satellites are broadened by structural imperfections in the same way and if no intensity redistribution occurs in these conditions between the satellites. This assumes, in its turn, the absence of noticeable regular variation of the defect structure across the SL, as well as of any irregular fluctuations in the layer periodicity and thickness. The latter are known[1] to result in attenuation of satellites, which is more pronounced in higher orders of diffraction, as well as in the onset of diffuse scattering. Our calculations, however, yielded high-order satellite intensities that were quite frequently below the experimental values (Fig. 3a). Thus this discrepancy cannot be accounted for by fluctuations in periodicity.

One of the criteria by which one could judge the reliability of the SL characteristics thus obtained may be the compatibility of the results derived for different reflections, because they exhibit different sensitivities toward the parameters describing a superlattice. The 222 reflection for the fluoride lattice belongs to the so-called ''difference'' reflections, the value of $F(222)$ for CaF_2 is very small, and therefore scattering in the SL occurs practically only from the CdF_2 layers. As a result, the shape of the diffraction curve does not depend on the scattering factors (the latter affect only the integrated intensity) and is determined solely by strain and the layer thickness. On the other hand, the strain-induced contribution to the asymmetric Laue reflections 111 and 311 is substantially smaller than that in the Bragg geometry, and the satellite height ratio is essentially dependent on the distribution of scattering ability over the period. These reflections can be used to fit the calculated to experimental curves with a minimum set of parameters, which improves the reliability of measurements.

Our fitting did not require considerable variation of the scattering abilities, which attests to a good crystallinity of the SL layers, and the static Debye–Waller factor can be set to one.

Structural perfection of the SLs studied can be estimated from the ω scanning curves in symmetric Bragg geometry. The best was found to be sample 117 with a short-period SL, for which the curves (see inset in Fig. 2a) are only 4 arcsec broader than those for the Si substrate. The satellite width in the ω scan of the symmetric Laue reflection for the same sample is in agreement with the total SL thickness. The other SLs show noticeable satellite broadening in both the transverse and longitudinal directions relative to the **z** normal. Note that the Bragg ω curves exhibit a complex shape with two superimposed maxima, the broader one serving as a pedestal for the more narrow one atop (for sample 156 shown in the inset in Fig. 3a and 211). This shape, characteristic of curves obtained from very thin layers, indicates most frequently the existence of strongly strained, nonoverlapping layers. In this case, the reflection curves are the result of summation of coherent scattering from an unstrained region and of incoherent one, from a strongly distorted region.[13,14] Assuming the maximum allowable extent of relaxation (see above) at the heteroboundary ($\varepsilon_{xx} \leqslant 3 \times 10^{-4}$), it will correspond to a line-dislocation network density of the order of 10^4 cm^{-1}. This yields about 1 μm for the average distance between dislocation lines, which is considerably in excess of the total SL width (0.1–0.4 μm). Theoretical consideration of diffraction from thin layers with dislocation networks hav-

ing the above dimensions yields for the ω curves a shape close to that measured by us.[14] It was shown also[14] that the shape of ω curves is much more sensitive to the onset of relaxation (formation of relaxation-induced defects) than the tangential misfit. It should be pointed out that the extent to which calculations fit an experimental curve does not depend on the shape and width of the ω curves. For instance, a good fit was obtained for sample 156 which exhibited the broadest ω curve possible of a close to Gaussian shape. This supports our conclusion that relaxation at the lower heteroboundary affects only weakly the satellite intensity ratio and the reliability of the SL parameters obtained by us.

In Laue geometry, structural perfection can be better characterized by the angular width of the θ-2θ curve. If an SL contains structural defects, the θ-2θ curve can be broadened due to local fluctuations in ε_{xx} and to the coherent-scattering regions being limited in the x direction. As evident from Table I, for sample 117 the value of $W_{\theta\text{-}2\theta}$ is equal to the angular resolution of the counter slit, while for the other samples it is larger. Note also that when going over from the Bragg to Laue geometry with rotation of the diffraction vector through 90° we change the direction of the local misorientations, because they act on the ω scan curves (perpendicular to the H vector). In the Bragg case, this is the x direction. In the case of a symmetric Laue reflection, the ω curves are measured in the **z** direction, and the reflection width in the x direction is free of their influence. Therefore the considerably smaller width of the θ-2θ curves sensitive to defects which is observed in transmission geometry compared to the ω curves in the Bragg case lends itself to a simple interpretation.

While, generally speaking, the presence of defects in our SLs is connected with stress relaxation, we have here most likely the initial stage of relaxation at the lower heteroboundary. As for the possibility of relaxation between the individual layers in an SL, it can be formally taken into account by variation of the strain parameters f_1 and f_2; this should change their difference (the value of B) and, hence, the satellite height ratio. The absence of such relaxation in our case is evidenced by the compatibility of the parameters obtained for various reflections. The most convincing argument for this is, however, that the curves of the 422 asymmetric Bragg reflection obtained for the $\gamma_0 < |\gamma_H|$ and $\gamma_0 > |\gamma_H|$ cases are identical. An analysis shows that this identity should fail for $\Delta\varepsilon_{xx} \neq 0$. As seen from Figs. 2c and 3c, the satellites of small-period sample No. 117 as in SL with the large-period (sample 126) coincide well in height when matched on the angular scale. The satellites present in the curves measured for $\gamma_0 > |\gamma_H|$ are more poorly resolved, because they extend over a smaller angular interval for the same broadening (caused by structural defects).

By studying an SL in different diffraction geometries one can make determination of its structural parameters more reliably. Two factors are of particular importance in this respect. First, Laue geometry offers a possibility of reducing considerably or even excluding the effect of strain altogether and, thus, of obtaining only the distribution of effective scattering ability. Note that, in contrast to small-angle scattering (which yields the same characteristics), it includes also the static Debye–Waller factor, i.e., information on the structural perfection of layers. Second, the presence of asymmetric reflections with different sensitivity to relaxation permits one to reveal the existence of the latter and its influence on the diffraction pattern.

To conclude, we have considered specific features of diffraction from SLs with layers having misfits of opposite signs with respect to the substrate and essentially different diffracting abilities in the symmetric and asymmetric reflection and transmission geometries. Diffraction curves obtained experimentally in different geometries from a set of samples with CaF_2/CdF_2 superlattices on Si having different periods were presented. Reflection curves were simulated, and their fitting to experimental curves permitted determination of the SL parameters, namely, of the period, strains, scattering abilities, and thicknesses of the layers. The absence of relaxation between individual layers in the samples studied was shown. The SLs were demonstrated to have a regular periodicity. The shape and halfwidth of the diffraction maxima were used to estimate the structural perfection of the SL layers, and an analysis revealed the presence of both fairly perfect (short-period SLs) and more defective samples, which produce satellites broadened in the direction perpendicular to the diffraction vector. The perfect-SL model was shown to be applicable to obtaining structural parameters of superlattices which have structural defects and exhibit broadened satellites in diffraction curves.

Support of the Russian Fund for Fundamental Research and of the Ministry of Science of the Russian Federation is gratefully acknowledged.

[1] V. S. Speriosu and T. Vreeland, Jr., J. Appl. Phys. **56**, 1591 (1984).
[2] J. Kervarez, M. Baudet, J. Gaulet, and P. Auvrey, J. Appl. Crystallogr. **17**, 196 (1984).
[3] A. T. Macrander, G. P. Schwartz, and G. J. Gualtieri, J. Appl. Phys. **64**, 6733 (1988).
[4] T. Baumbach, H.-G. Brühl, U. Pietsch, and H. Terauchi, Phys. Status Solidi A **105**, 197 (1988).
[5] H. Terauchi, S. Sekimoto, K. Kamigaki, H. Sakashita, N. Sano, H. Kato, and M. Nakayama, J. Phys. Soc. Jpn. **54**, 4576 (1985).
[6] U. Pietsch, H. Metzger, S. Rugel, B. Jenichen, and I. K. Robinson, J. Appl. Phys. **74**, 2381 (1993).
[7] K. Nakashima, J. Appl. Phys. **71**, 1189 (1992).
[8] R. N. Kyutt, A. Yu. Khilko, and N. S. Sokolov, Appl. Phys. Lett. **70**, 1563 (1997).
[9] S. V. Novikov, N. N. Faleev, A. Izumi, A. Yu. Khilko, N. S. Sokolov, S. A. Solov'ev, and K. Tsutsui, in *Abstracts of the International Symposium Nanostructures: Physics and Technology* (St. Petersburg, Russia, 1995), p. 387.
[10] R. N. Kyutt, P. V. Petrashen, and L. M. Sorokin, Phys. Status Solidi A **60**, 381 (1980).
[11] N. S. Sokolov, J. C. Alvarez, Yu. V. Shusterman, N. L. Yakovlev, R. M. Overney, Y. Itoh, I. Takahashi, and J. Harada, Appl. Surf. Sci. **104/105**, 402 (1995).
[12] A. Yu. Khilko, R. N. Kyutt, N. S. Sokolov, M. V. Zamoryanskaya, L. J. Schowalter, and Yu. V. Shusterman, in *Abstracts of the 23rd International Symposium Compound Semiconductors* (St. Petersburg, Russia, 1996) (Inst. Phys. Conf. Ser. No. 155, Ch. 12, p. 1021).
[13] P. F. Fewster, Semicond. Sci. Technol. **8**, 1915 (1993).
[14] V. M. Kaganer, R. Köhler, M. Schmidbauer, R. Opitz, and B. Jenichen, Phys. Rev. B **55**, 1793 (1997).

Translated by G. Skrebtsov

Topographic study by scanning-tunneling microscopy of a two-dimensional graphite film on Re$(10\bar{1}0)$

L. N. Bolotov, Z. Vakar, N. R. Gall', I. V. Makarenko, E. V. Rut'kov, A. N. Titkov, A. Ya. Tontegode, and M. M. Usufov

A. F. Ioffe Physicotechnical Institute, Russian Academy of Sciences, 194021 St. Petersburg, Russia
(Submitted January 19, 1998)
Fiz. Tverd. Tela (St. Petersburg) **40**, 1570–1573 (August 1998)

Two-dimensional graphite films on Re$(10\bar{1}0)$ were produced in ultrahigh vacuum by adsorption of benzene vapor on the metal heated to $T=1800$ K. High-resolution Auger spectroscopy used for the film characterization showed the film indeed to have graphitic structure and monolayer thickness. The surface topography was studied in air by scanning-tunneling microscopy. The monolayer thickness was confirmed, and it was shown that a two-dimensional graphite film has a complex topography featuring numerous hillocks with linear dimensions of ~3000 Å and height differences of ~300 Å, while retaining graphitic structure on the atomic scale. The lack of planarity of such a film at room temperature is considered to be due to deformation occurring under cooling from the temperature of formation down to 300 K, which is caused by the difference in thermal expansion coefficients between the graphite sheet and rhenium.
 [S1063-7834(98)03608-9]

Two-dimensional graphite films on metals are remarkable objects because they exhibit chemical bonding characteristic of two-dimensional crystals.[1] In their physicochemical properties, 2D graphite films resemble 2D layers making up layered single-crystal graphite. As a result of valence saturation, 2D graphite films are bonded to the surface only by van der Waals forces, without electron exchange,[2] and they can form without being in registry with the substrate surface, which sets them apart from chemisorbed films (for instance, metallic, semiconductor, diamond, and so on).[1]

2D graphite films can be grown easily on the surface of many metals (Ir, Re, Mo, Ni, Pt, etc.) and, when formed, change radically the surface properties of these materials.[1] Taking into account the influence of such films is essential in many areas of science and technology, such as heterogeneous catalysis, materials science, physics of the surface, and vacuum technology. Regrettably, information on the topography of 2D graphite films on metal surfaces is lacking. This work reports a study of the topography of 2D graphite films on Re$(10\bar{1}0)$ made by scanning-tunneling microscopy (STM).

1. EXPERIMENTAL TECHNIQUES

We used as a substrates texturized rhenium $(10\bar{1}0)$ ribbons measuring $50\times1.5\times0.02$ mm, which were uniform in work function with $e\varphi=5.15$ eV. Purification of ribbons of impurities and aligning the desired crystallographic plane with the surface were achieved by standard techniques.[3] X-ray diffraction showed the orientation of the $(10\bar{1}0)$ plane with respect to the sample surface to be correct to within 99.9%.[4]

2D graphite films were obtained in ultrahigh vacuum by adsorbing benzene vapor on the heated metal.[2] The film growth was monitored by thermionic techniques and Auger-electron spectroscopy.[3]

After the completion of graphite film growth, the rhenium sample was removed from the vacuum chamber and its topography was studied by STM at NTP. The extremely high adsorption passivity of 2D graphite films permits operation with the samples in air without their damage.[1] We used a custom-made STM providing atomic resolution in studies of graphite surfaces. The atomic-scale resolution was demonstrated in surface studies of dichalcogenides of transition metals,[5] and nearly atomic one, in an investigation of single-crystal silicon surfaces.[6]

2. GROWTH AND CHARACTERIZATION OF 2D GRAPHITE FILMS

Interaction of carbon with the Re$(10\bar{1}0)$ surface was examined in detail in Refs. 3 and 4. For this film to form, the bulk of rhenium has first to be saturated with carbon. To do this, rhenium heated to $T_C=1800$ K was exposed to benzene vapor at 1×10^{-5} Torr; benzene molecules striking the heated metal break up, the hydrogen desorbs and is pumped out, and carbon atoms dissolve in the bulk of the sample forming a Re–C solid solution. The surface is coated in these conditions by chemisorbed carbon ″gas″ with concentration $N_C=1.4\times10^{15}$ at/cm^2. The high deposition temperatures favor fast diffusion of carbon into the metal, and the thin ribbons permitted one to saturate the bulk of the sample with carbon in ~30 min. In the final stage of carbon saturation, the carbon surface density increases and at $N_C=2\times10^{15}$ at/cm^2 two-dimensional graphite islands are nucleated. As carbon continues to arrive, the islands grow in area and coalesce to form a continuous 2D graphite film which has a uniform work function.

There is ample experimental evidence in support of the carbon films prepared in this way being indeed two-dimensional and having graphitic structure.[3] We shall present here only three of these arguments.

1) High-resolution carbon Auger spectra exhibit a typical graphitic shape[4], which differs from those obtained from the other chemical forms of surface carbon (surface and bulk carbides, diamond, amorphous carbon);

2) The experimental attenuation of the rhenium Auger peak at $E=176$ eV by a factor 1.6 is in a good agreement with the attenuation (1.8 times) calculated[3,4] for this film;

3) The 2D graphite films are uniform in work function and have $e\varphi=4.45$ eV, which coincides to within 0.05 eV with that of the basal plane of single-crystal graphite.

It was shown[3,4] that, if conditions 2) and 3) are both upheld, the graphite film is uniform and has monolayer thickness. It should be pointed out that the method itself used here to prepare 2D graphite films can produce only one graphite layer, because benzene molecules striking a valence-saturated graphite layer desorb rather than breaking up. Carbon does not build up any more, and the film does not continue to grow beyond the one-layer thickness.

Probing 2D graphite films with CsCl molecules, which dissociate effectively on surface areas coated by nongraphitic carbon or on clean metal, shows that surface defects amount to $\leqslant 10^{-2}$% of the total surface area. This part of the surface area can be identified with the background dissociation of CsCl molecules at defects in the edges of graphite islands which merge when forming a monolayer film (on the islands themselves, there is no CsCl dissociation[2]).

3. BEHAVIOR OF 2D GRAPHITE FILMS UNDER VARIATION OF SAMPLE TEMPERATURE

Two-dimensional graphite films on refractory metals form at medium and high temperatures, 900–1800 K, depending on the nature of the metal. Heating a rhenium sample saturated with carbon at $T_C=1800$ K up to 1900 K results in a complete destruction of the graphite layer, with only chemisorbed ''gas'' remaining on the surface. Transition from 1900 to 1800 K restores the 2D graphite film, and further decrease of temperature to 1700–1100 K gives rise to growth of a graphite film, tens of monolayers thick, from the carbon precipitating from the supersaturated Re–C solid solution.[3,4] For $T<1000$ K, no bulk diffusion occurs. A 2D graphite film formed at a high temperature can be readily preserved by cooling the sample rapidly to room temperature, simply by turning off the ribbon heater current. That the film remained intact under fast cooling is confirmed by the unchanged carbon Auger-signal intensity and by attenuation of the rhenium Auger signal by 1.6 times.

4. SURFACE TOPOGRAPHY OF 2D GRAPHITE FILMS

Figure 1a presents a typical STM image of the surface of a 2D graphite film on rhenium recorded at constant tunneling current. The film is unexpectedly not at all plain, and its surface abounds in hillocks. This pattern is in no way a reflection of nonuniformities on the metal substrate; indeed,

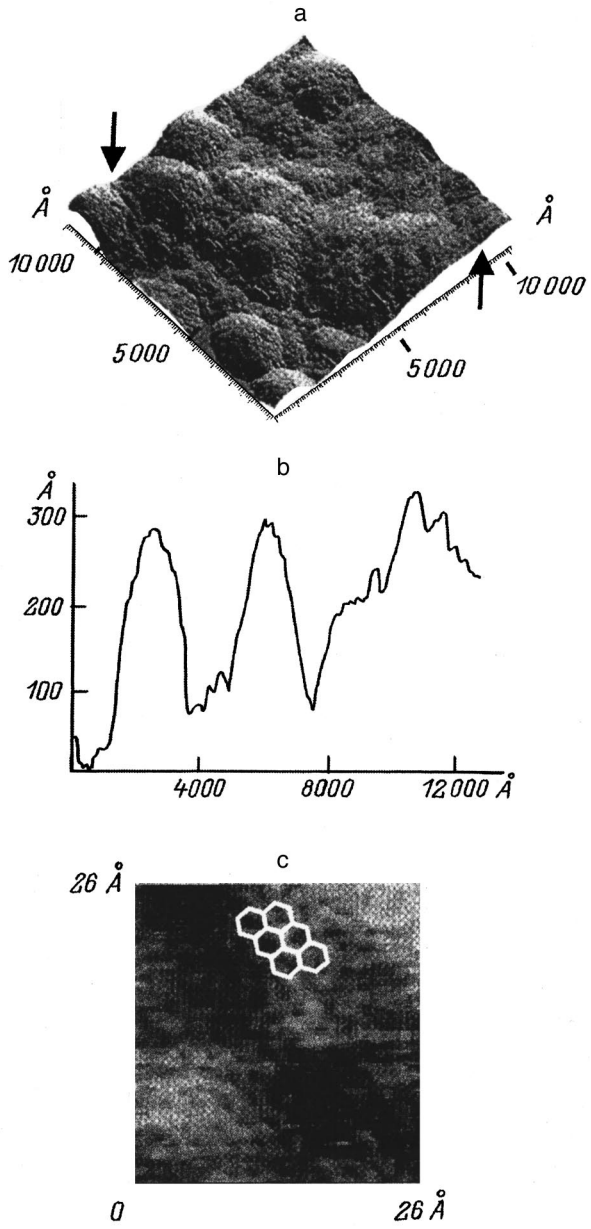

FIG. 1. (a) STM image of topography of a graphite film on a rhenium substrate. Tip potential $U_t=-100$ mV, tunneling current $I_t=40$ pA; (b) Cross-section profile in the plane passing through the two points identified by arrows in Fig. 1a; (c) STM image of a part of the surface measuring 20×26 Å at the top of a hillock. The bright-to-dark transition corresponds to a height difference of ~ 2 Å. The white hexagons in the figure show schematically the crystal structure of a graphite layer.

STM images show the metal surface to be very smooth with a characteristic size of nonuniformities ~ 15 Å.

Figure 1b displays a cross section of the STM image in Fig. 1a cut perpendicular to sample surface. We see that the hillocks are typically $\sim 2500-3500$ Å at the base, and their height is $\sim 250-350$ Å. An increase of STM resolution at the expense of reduced scan area revealed the surface of each hillock to be likewise warped, with an average difference in height of 20–30 Å.

The tops of individual hillocks were studied in the constant tunneling-gap mode, which provides better spatial resolution. The surface of the hillocks was found to have a

clearly pronounced graphitic structure (Fig. 1c). The STM image exhibits distinct hexagons corresponding to the hexagonal carbon-atom arrangement in the graphite-layer lattice, which differentiates this pattern from the reference obtained on single-crystal graphite. In our opinion, this reflects the equivalence of all carbon atoms in a 2D graphite film (in single-crystal graphite, there is no such equivalence because of the effect of the subsurface layer). This observation may be considered as a direct proof that the 2D graphite film is indeed a monolayer.

5. DISCUSSION

Our previous studies[1,2] provide conclusive evidence that a two-dimensional graphite layer is bonded to the surface of a metal, in particular, of rhenium only through weak van der Waals forces, while within the film, the carbon atoms are held together by strong covalent bonding, so that ~ 9 eV have to be expended to remove one carbon atom from the graphite sheet.[2] As for the graphite island edges, they are valence unsaturated and form strong bonding to metal atoms.[2] Thus the 2D graphite film acts like a 2D graphite single crystal adsorbed on the metal surface.

We associate the complex topography of the graphite film shown in Fig. 1a with the effects of cooling a film grown on a metal at a high temperature. Indeed, the thermal expansion coefficients of graphite and of the metal substrate differ significantly, and the temperature difference is large, since a 2D graphite film forms at 1800 K, while STM images were obtained at 300 K.

When cooled, the metal shrinks more than the graphite film does because of the difference in their thermal expansion coefficients. This may result in breaking of the weak van der Waals bonds, whereas chemisorption will continue to bond the island edges to the metal surface. As for the graphite layer itself, which consists of strongly bound carbon atoms, it apparently cannot break up and retains its structure. Nevertheless it bends, and the observed pattern is actually the consequence of such deformation. The bending is seen to be quite large; indeed, the cross section of the film shown in Fig. 1b suggests that it rises above the metal surface by hundreds of Å.

Let us estimate the magnitude of the expected effect. Figure 2 displays schematically the graphite island on a metal surface. The island was grown at $T_C = 1800$ K (Fig. 2a) and cooled down to $T = 300$ K (Fig. 2b). The thermal expansion coefficient of graphite in the plane perpendicular to the c axis, i.e. in the layer plane, varies from $\sim 1.22 \times 10^{-6}$ K^{-1} at $T = 300$ K to -0.02×10^{-6} K^{-1} at $T = 650$ K and -1.5×10^{-6} K^{-1} at $T = 1800$ K,[7] which is about an order of magnitude smaller than that for metals (including rhenium) within the same temperature range. Therefore we shall neglect in our calculation the expansion of the graphite layer.

The $(10\bar{1}0)$ plane emerging onto the surface of the rhenium substrate is parallel to the c axis of the hexagonal rhenium lattice. Reference data reveal a considerable anisotropy in the thermal expansion coefficient, viz. it differs along the [0001] and [1210] directions (i.e., parallel and perpendicular to the c axis) by a factor 2.5.[7] Because both directions lie on the face we are studying, we took for the thermal expansion coefficient its average value, as this is proposed in Ref. 8, and, taking into account the growth of α at high temperatures, we set $\alpha_{\mathrm{Re}} = 7 \times 10^{-6}$ K^{-1}.

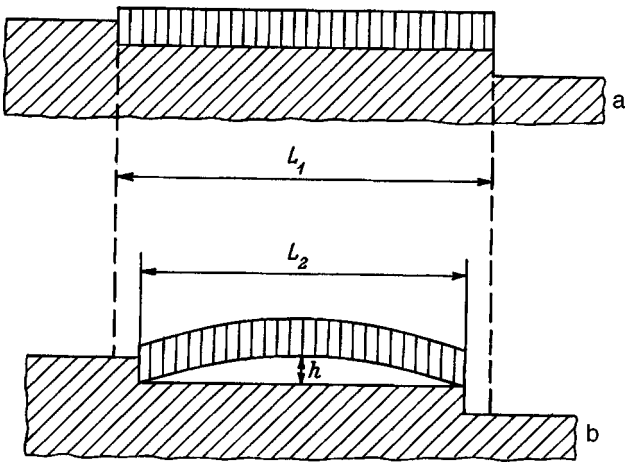

FIG. 2. Schematic representation of a graphite island formed on an atomic step of the rhenium surface when the sample temperature was changed from 1800 K (a) to 300 K (b). Vertical shading — two-dimensional graphite film, slanted shading — Re substrate with the atomic step.

Let L_1 be the length of the part of the substrate underlying the graphite island at the temperature of its formation (Fig. 2a). The island edges are bound strongly to the substrate by chemisorption and, apparently, are pinned to surface defects (atomic steps, the points where dislocations emerge on the surface, subgrain boundaries etc.). When cooled by ΔT, the length of the graphite island remains unchanged to a first approximation, whereas that of the pertinent part of the substrate will decrease to

$$L_2 = L_1(1 + \alpha_{\mathrm{Re}} \Delta T)^{-1}.$$

Assuming $\Delta T = 1500$ K, and $\alpha_{\mathrm{Re}} = 7 \times 10^{-6}$ K^{-1}, we readily calculate the relative elongation of the graphite island compared to the substrate:

$$(L_1 - L_2)/L_1 = \alpha_{\mathrm{Re}} \Delta T \sim 10^{-2} = 1\%.$$

Let us estimate the height to which this will raise the island above the substrate. We calculate this rise by the Pythagorean theorem taking one half of the island length for the hypotenuse, and one half of the substrate length, for the cathetus (leg) of the corresponding right triangle. As seen from Fig. 1b, the measured island diameter is typically $\sim 2500 - 3500$ Å. Taking into account the shortening of the substrate by 1%, this yields for the rise $h = 350 - 500$ Å. The experimentally determined heights (see Fig. 1b) lie within the interval 250–350 Å, which is in a good agreement with the above estimate.

To conclude, our studies show that 2D graphite films formed on rhenium at high temperatures and cooled to room temperature have essentially nonplanar, hillocky surface structure and strictly monolayer thickness. The film is deformed by the stresses associated with considerable differences in the thermal expansion coefficients of the graphite layer and the metal substrate. The strong bonding among carbon atoms within the graphite layer and the very weak

bonding (van der Waals forces) to the metal surface favor deformation of the graphite layer without its destruction. It is reasonable to assume that the layer deformation will be considerably smaller for metals requiring low temperatures for 2D graphite film formation [for instance, for Ni, $T_C = 850$ K (Ref. 9)].

Support of the Russian Program "Physics of Solid State Nanostructures" (Grant 2-025/4) is gratefully acknowledged.

[1] N. R. Gall, E. V. Rut'kov, and A. Ya. Tontegode, Int. J. Mod. Phys. B **11**, 1865 (1997).
[2] A. Ya. Tontegode, Prog. Surf. Sci. **38**, 201 (1991).
[3] N. R. Gall, S. N. Mikhailov, E. V. Rut'kov, and A. Ya. Tontegode, Surf. Sci. **191**, 185 (1987).
[4] N. R. Gall', S. N. Mikhaĭlov, E. V. Rut'kov, and A. Ya. Tontegode, Poverkhnost' **8**, 58 (1986).
[5] L. N. Bolotov, B. E. Derkach, L. F. Ivantsev, I. V. Makarenko, P. B. Plekhanov, and V. I. Safarov, Fiz. Tverd. Tela (Leningrad) **32**, 1523 (1990) [Sov. Phys. Solid State **32**, 889 (1990)].
[6] L. N. Bolotov, I. V. Makarenko, A. N. Titkov, M. I. Veksler, I. V. Grekhov, and A. F. Shulekin, Fiz. Tverd. Tela (St. Petersburg) **38**, 889 (1996) [Phys. Solid State **38**, 491 (1996)].
[7] S. I. Novikova, *Thermal Expansion of Solids* [in Russian], Nauka, Moscow (1974), 378 pp.
[8] *Tables of Physical Quantities: Handbook*, edited by N. S. Grigor'ev and E. Z. Meĭlikhov [in Russian], Énergoizdat, Moscow (1986), 867 pp.
[9] E. V. Rut'kov, A. Ya. Tontegode, and M. M. Usufov, Izv. Ross. Akad. Nauk, Ser. Fiz. **58**, No. 10, 102 (1994).

Translated by G. Skrebtsov

ERRATA

ERRATUM: Luminescence-spectrum and strength properties of rhodamine 6G-doped silica gel films [Phys. of the Solid State 40, 427–431 (March 1998)]

G. E. Malashkevich

Institute of Molecular and Atomic Physics, Academy of Sciences of Belarus, 220072 Minsk, Belarus

E. N. Poddeneznyĭ, I. M. Mil'nichenko, V. B. Prokopenko, and D. V. Dem'yanenko

F. Skorina Geomel State University, 256699 Gomel, Belarus

Fiz. Tverd. Tela (St. Petersburg) **40**, 1574 (August 1998)

[S1063-7834(98)03708-3]

Figures to this article are as follows:

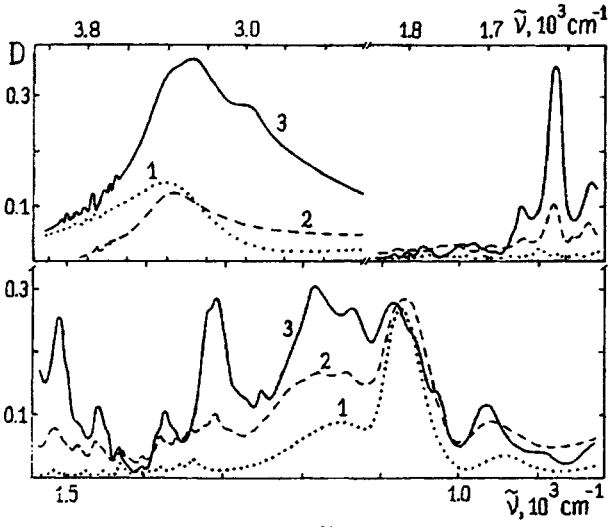

FIG. 1.

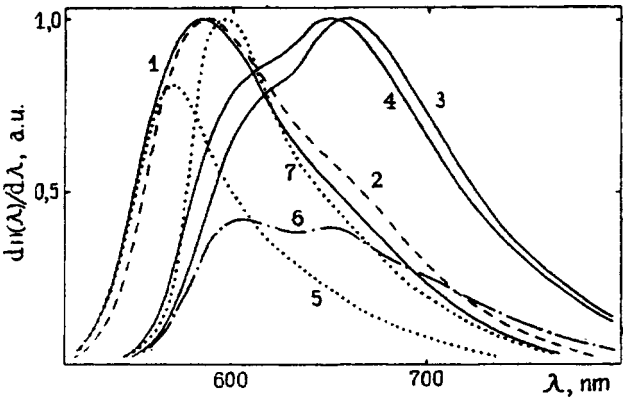

FIG. 3.

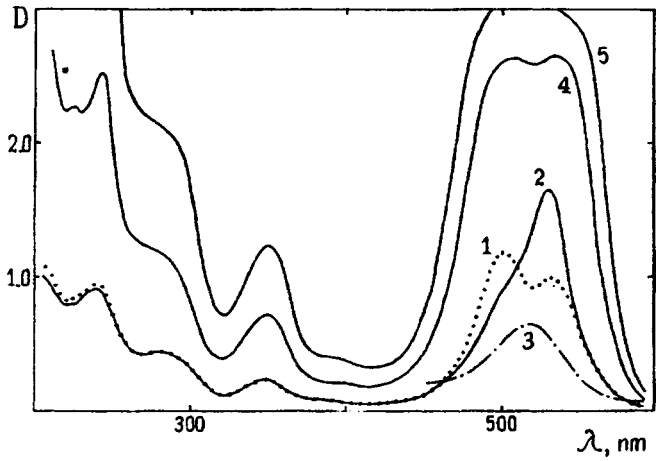

FIG. 2.

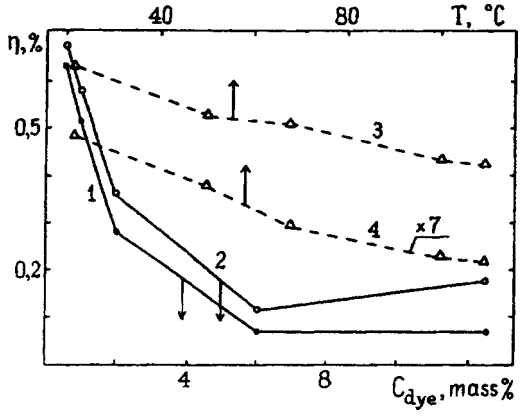

FIG. 4.

Translated by Paul F. Schippnick

